Neuroimaging Pharmacopoeia

Daniel Thomas Ginat
Juan E. Small
Pamela Whitney Schaefer
Editors

Springer

Neuroimaging Pharmacopoeia

Daniel Thomas Ginat • Juan E. Small
Pamela Whitney Schaefer
Editors

Neuroimaging Pharmacopoeia

Springer

Editors
Daniel Thomas Ginat, MD, MS
Department of Radiology
University of Chicago
Pritzker Medical School
Chicago, IL
USA

Pamela Whitney Schaefer, MD
Department of Radiology
Massachusetts General Hospital
Harvard Medical School
Boston, MA
USA

Juan E. Small, MD
Department of Radiology
Lahey Clinic
Burlington, MA
USA

ISBN 978-3-319-12714-9 ISBN 978-3-319-12715-6 (eBook)
DOI 10.1007/978-3-319-12715-6
Springer Cham Heidelberg NewYork Dordrecht London

Library of Congress Control Number: 2015932672

Printed on acid-free paper

Springer is part of Springer Science+Business Media (www.springer.com)

The authors dedicate this book to the wonderful field or neuroradiology and head and neck imaging, the great advances and discoveries in pharmacology, and to a healthy and (illicit) drug-free world.

Foreword

What you have in front of you is a highly original, different, and useful publication and the only one of its kind in all of diagnostic radiology. The classic definition of "pharmacopoeia" is that of a book containing directions for the identification and preparation of drugs or a list of drugs and their uses. So, in a classic sense, this book is not a pharmacopoeia but something that goes beyond one. Each chapter describes one medication or drug and its indications and action mechanisms, and although in many instances this would suffice to be considered a pharmacopoeia, the authors go further and present a unique and complete series of high-quality neuroimaging studies that reflect the side effects and complications of the drugs discussed. It is, in my opinion, the best and most complete collection of this sort of images that I have even come across, and there is no question that it will be very helpful to neuroradiologists, radiologists, emergency physicians, and many others. Although are shorter than others, all 55 chapters are excellent. Just perusing through the images is fun, eye opening, and informative.

Dr. Schaefer, Small, and Ginat join many of the great, Avicenna, Galen, Vesalius and others who in the past have discussed the use of drugs in pharmacopeias. My recommendations: buy the book- you will not be disappointed, look at the images- you will be entertained, read the book- you will be a better radiologist, and keep the book handy- you will help your patients.

Mauricio Castillo, MD, FACR
Professor of Radiology and Chief of Neuroradiology
University of North Carolina at Chapel Hill
Editor in Chief, American Journal of Neuroradiology
President, American Society of Neuroradiology

Preface

Various medicinal and illicit drugs can result in serious complications affecting the brain, head and neck, and spine. Many of these complications are visible on imaging. In addition, less serious complications or innocuous effects can result in diagnostic conundrums for the imaging interpreter unaware of the patient's drug exposures or their imaging manifestations, while others may produce rather characteristic changes on imaging that should be readily recognized as such. Until now, imaging interpreters have been unable to turn to a dedicated source of information relating to this subject. In this work, we have compiled a fairly comprehensive review of the imaging features of the effects of drugs and pharmaceuticals, from A to Z.

Considering the widespread use of medicinal and illicit drug use throughout the world, familiarity with this subject is critical for the imaging interpreter. Thus, the goal of *Neuroimaging Pharmacopoeia* is to serve as a resource for recognizing these effects and formulating an appropriate differential diagnosis. The term *pharmacopoeia* is derived from the two Greek words *pharmakon* for medicine and *poiein* to make. As such, a pharmacopeia is a compilation of medicinal or pharmacological drugs with their formulas, methods of preparation, effects, and directions of use.

This text represents an adaptation of the classical pharmacopeia, in which each chapter essentially comprises an illustrated pharmacological vignette comprising the indications, mechanism of action, discussion, differential diagnosis, and relevant figures for general classes or specific drugs. Although pharmacology is a dynamic field with perpetual development of new agents, this text provides a fundamental approach for understanding and interpreting neuroimaging studies in patients with drug-induced changes. This knowledge can in turn be used to help optimize patient management in certain cases.

Chicago, IL, USA — Daniel Thomas Ginat, MD, MS
Burlington, MA, USA — Juan E. Small, MD
Boston, MA, USA — Pamela Whitney Schaefer, MD

Acknowledgement

Alaa Jaly, Lancashire Teaching Hospitals
Chris Coutinho, MB, FRCR, Lancashire Teaching Hospitals
Jenny Hoang, MBBS, Duke University
Sachin Mathur, MRCP, FRCR, Lancashire Teaching Hospitals
Gregory Christoforidis, MD, University of Chicago
Alisa Gean, MD, University of California, San Francisco
Christine Glastonbury, MBBS, University of California, San Francisco
Vesna Petronic-Rosic, MD, University of Chicago
Caroline Robson, MBChB, Boston Children's Hospital

Contents

Contributors

Mariam Aboian, MD, Department of Radiology, University of California, San Francisco, CA, USA

Eileen C. Ang, MBBS, Department of Diagnostic Imaging, Monash Medical Center, Monash Health, Melbourne, VIC, Australia

Timothy Biega, MD, Department of Radiology, Tripler Army Medical Center, Honolulu, HI, USA

Maria J. Borja, MD, Department of Radiology, Massachusetts General Hospital, Boston, MA, USA

Ronil V. Chandra, MBBS, MMed, FRANZCR, Department of Diagnostic Imaging, Monash Medical Center, Monash Health, Melbourne, VIC, Australia

Ana M. Franceschi, MD, Diagnostic Radiology, New York University Medical Center, New York, NY, USA

Merav Galper, MD, Department of Diagnostic Radiology, Lahey Clinic, Burlington, MA, USA

Daniel Thomas Ginat, MD, MS, Department of Radiology, University of Chicago, Pritzker Medical School, Chicago, IL, USA

Harut Haroyan, MD, Department of Radiology, University of Chicago, Chicago, IL, USA

Jeffrey Hashim, MD, Department of Diagnostic Radiology, Lahey Clinic, Burlington, MA, USA

Rania Hito, MD, Department of Radiology, University of Massachusetts Memorial Medical Center, Worcester, MA, USA

Grayson W. Hooper, DO, Department of Radiology, Tripler Army Medical Center, Honolulu, HI, USA

Jason M. Johnson, MD, Department of Diagnostic Radiology, MD Anderson Cancer Center, Houston, TX, USA

Kimberly Kallianos, MD, Department of Radiology, University of California, San Francisco, CA, USA

Allan Lee, MBBS, FRANZCR, Department of Diagnostic Imaging, Monash Medical Center, Monash Health, Melbourne, VIC, Australia

Yi Li, MD, Department of Radiology, University of California, San Francisco, CA, USA

William A. Mehan, MD, Department of Radiology, Tufts Medical Center, Boston, MA, USA

Gul Moonis, MD, Department of Radiology, Columbia University, New York, NY, USA

Dee Nandurkar, MBBS, FRANZCR, Department of Diagnostic Imaging, Monash Medical Center, Monash Health, Melbourne, VIC, Australia

Daniel Lopes Noujaim, MD, Department of Diagnostic Radiology, Lahey Clinic, Burlington, MA, USA

Janu Pirakalathanan, MBBS, Department of Diagnostic Imaging, Monash Medical Center, Monash Health, Melbourne, VIC, Australia

Marianne S. Reed, MD, Diagnostic Radiology, Yale University, New Haven, CT, USA

Pamela W. Schaefer, MD, Department of Radiology, Massachussetts General Hospital, Harvard Medical School, Boston, MA, USA

Charles J. Schatz, MD, FACR, Department of Radiology, Beverly Tower Wilshire Advanced Imaging, University of Southern California Keck School of Medicine, Los Angeles, CA, USA

Santosh Shah, MD, Department of Radiology, Massachusetts General Hospital, Boston, MA, USA

Juan E. Small, MD, Department of Diagnostic Radiology, Lahey Clinic, Burlington, MA, USA

Lee-Anne Slater, MBBS, MMed, FRANZCR, Department of Diagnostic Imaging, Monash Medical Center, Monash Health, Melbourne, VIC, Australia

Stephen L. Stuckey, MBBS, MMed, MD, FRANZCR, Department of Diagnostic Imaging, Monash Medical Center, Monash Health, Melbourne, VIC, Australia

Nurhan Torun, MD, Department of Ophthalmology, Beth Israel Deaconess Medical Center, Boston, MA, USA

Michael C. Veronesi, MD, PhD, Department of Radiology, University of Chicago, Chicago, IL, USA

Evan Watkins, MD, Department of Diagnostic Radiology, Lahey Clinic, Burlington, MA, USA

Tobacco

1

Michael C. Veronesi and Daniel Thomas Ginat

1.1 Uses

Although tobacco use is legal, it is not recommended or prescribed for any therapeutic or medicinal purposes. It is smoked or chewed for recreational use as a potent temporary stimulant and mood elevator.

1.2 Mechanism

Nicotine, the primary active compound in cigarettes, is considered one of the most addictive of all substances because of its rapid onset and offset effects on the brain's dopamine reward systems. Inhaled nicotine can distribute in the brain within 10 s of inhalation but lasts mere seconds, causing a powerful urge for more. Of note, the long-term devastating sequela from smoking as it relates to neurologic disease are only partially explained by nicotine. Aside from nicotine, tobacco contains over six thousand other chemical compounds. In particular, polycyclic aromatic hydrocarbons and the tobacco-specific nitrosamine 4-(methylnitrosamino)-1-(3-pyridyl)-1-butanone have been implicated as the major carcinogens associated with cigarette smoking. Additional details regarding the mechanisms of action for specific conditions are discussed in subsequent sections.

M.C. Veronesi, MD, PhD
Department of Radiology, University of Chicago, Chicago, IL, USA

D.T. Ginat, MD, MS (✉)
Department of Radiology, University of Chicago, Pritzker Medical School, Chicago, IL, USA
e-mail: ginatd01@gmail.com

1.3 Discussion

Tobacco use is the leading cause of preventable death in the United States. An estimated 400,000 deaths or nearly one of every five deaths in the United States is associated with adverse conditions caused by smoking each year. Nearly every organ system is affected by cigarette smoking. The associated manifestations of cigarette smoking from a neuroimaging standpoint include the direct link between smoking and large vessels and lacunar infarcts, chronic small vessel ischemic disease, cerebral aneurysms, cerebral venous thrombosis, head and neck cancer of the squamous type, lung cancer metastases to the brain, and Warthin tumors.

1.3.1 Stroke

Compared with nonsmokers, cigarette smoking is estimated to increase the risk of stroke by 2–4-fold. Of note, stroke is the third leading cause of death in the United States with significant comorbidity in survivors. Mechanisms by which primary and second-hand tobacco smoke exposure increase the risk of stroke and heart disease

D.T. Ginat et al. (eds.), *Neuroimaging Pharmacopoeia*,
DOI 10.1007/978-3-319-12715-6_1, © Springer International Publishing Switzerland 2015

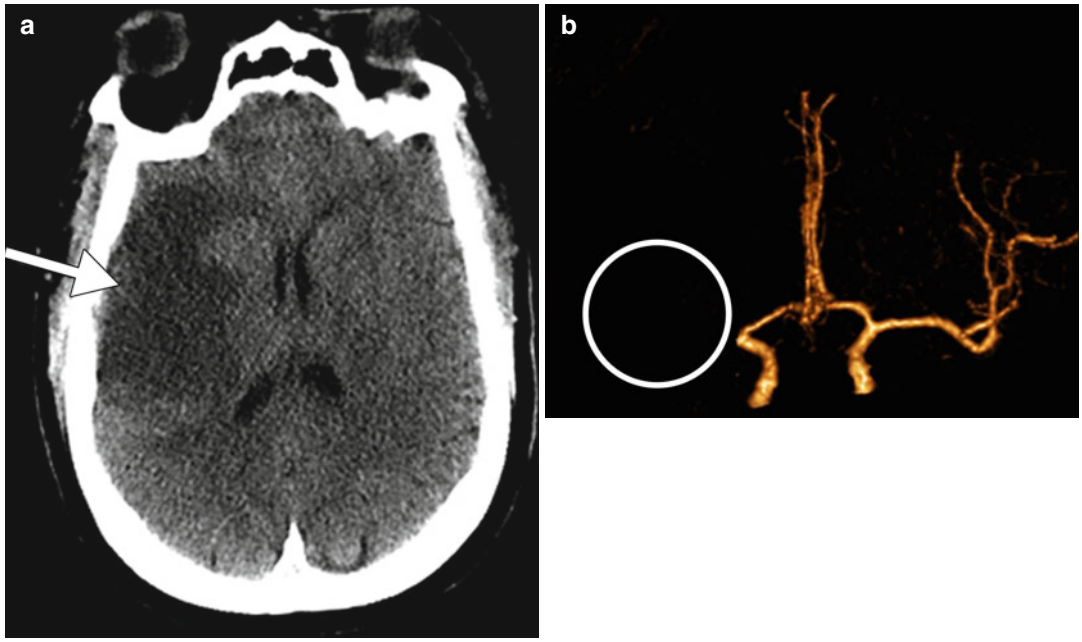

Fig. 1.1 Embolic infarct. This smoker presented with acute left hemiplegia. Non-contrast axial CT image (**a**) shows a hypoattenuation within the right MCA territory (*arrow*). 3D CTA image (**b**) shows occlusion of the right MCA (expected location *encircled*)

include carboxyhemoglobinemia, increased platelet aggregation, increased fibrinogen levels, reduced HDL cholesterol, and direct toxic effects of compounds such as 1,3-butadiene, a vapor phase constituent of environmental tobacco smoke that has been shown to accelerate atherosclerosis. Indeed, atherosclerosis and formation of both occlusive and embolic thrombi are the major causes of cerebrovascular accidents. Smoking is also associated with lacunar infarcts and chronic small vessel ischemic disease. Smoking cessation results in a considerable reduction in stroke risk.

On conventional angiography, CTA or MRA, atherosclerosis manifests as luminal narrowing that may be associated with calcifications. Acute embolic thrombus is suggested by intraluminal high attenuation on non-contrast CT, such as the hyperdense MCA sign, and manifests as an abrupt termination of the artery with absence of flow distally on CTA, MRA, or conventional angiography (Figs. 1.1). Hyperacute infarcts are often unapparent on non-contrast CT, but acute and early subacute infarcts can appear as areas of hypoattenuation with loss of gray white matter differentiation and swelling. MRI with diffusion-weighted imaging is more sensitive for detecting early infarcts, which appear as areas of high T2 signal and restricted diffusion (Fig. 1.2). Besides smoking, other causes and risk factors for stroke include hypertension, hypercholesterolemia, diabetes, use of other drugs, such as cocaine and amphetamines (refer to Chaps. 5 and 6), dissection (Fig. 1.3), and vasculitis, such as lupus or Takayasu arteritis (Fig. 1.4). In addition to large territorial infarcts, smokers are prone to more extensive small vessel ischemic disease, which can manifest as areas of high T2 signal in the cerebral white matter (Fig. 1.5).

1.3.2 Cerebral Aneurysm

Besides smoking, additional risk factors that predispose to aneurysm formation include fenestrated arteries (Fig. 1.6), fibromuscular dysplasia, neurofibromatosis, alpha-1-antytripsyn deficiency, and

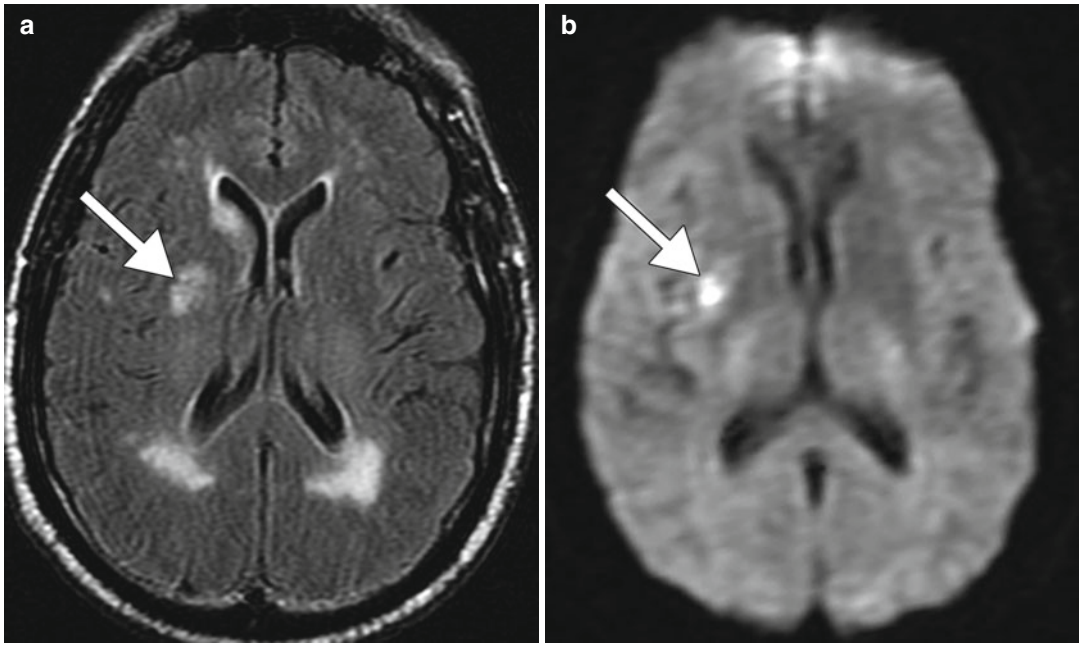

Fig. 1.2 Lacunar infarct and small vessel ischemic disease. The patient is a smoker who presented with acute neurological deficits. Axial FLAIR (**a**) and DWI (**b**) images show a recent right basal ganglia lacunar infarct (*arrows*). There is also diffuse, confluent periventricular white matter T2 hyperintensity as well as mild scattered, punctate subcortical white matter T2 hyperintense foci without corresponding restricted diffusion, which is consistent with chronic small vessel ischemic disease

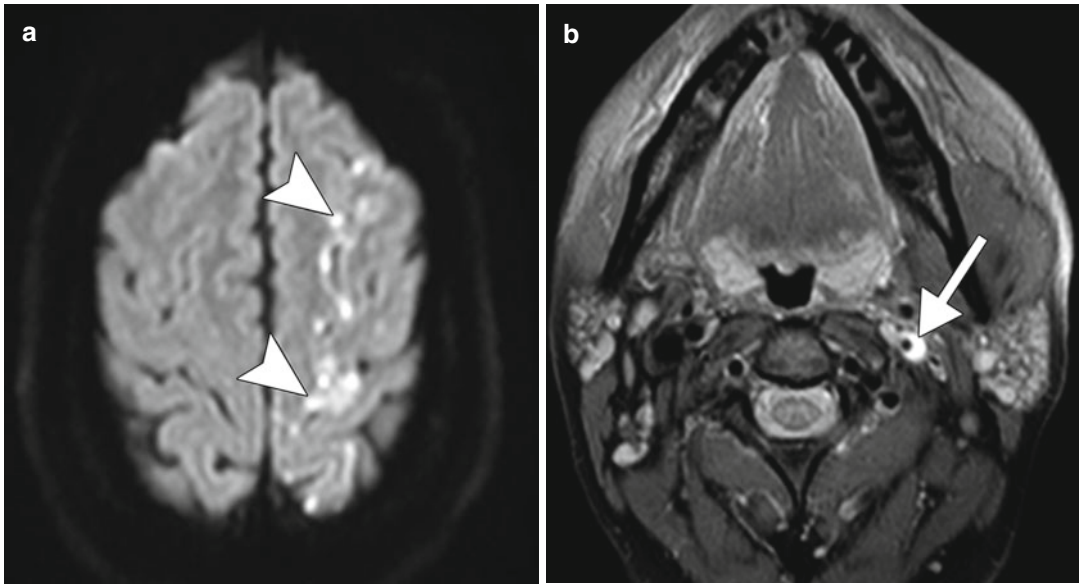

Fig. 1.3 Carotid dissection. Axial DWI (**a**) shows restricted diffusion in the left ACA-MCA watershed territory (*arrowheads*). The axial fat-suppressed T1 MRA (**b**) shows hyperintensity surrounding the narrow left internal carotid artery flow void, compatible with intramural hemorrhage (*arrow*)

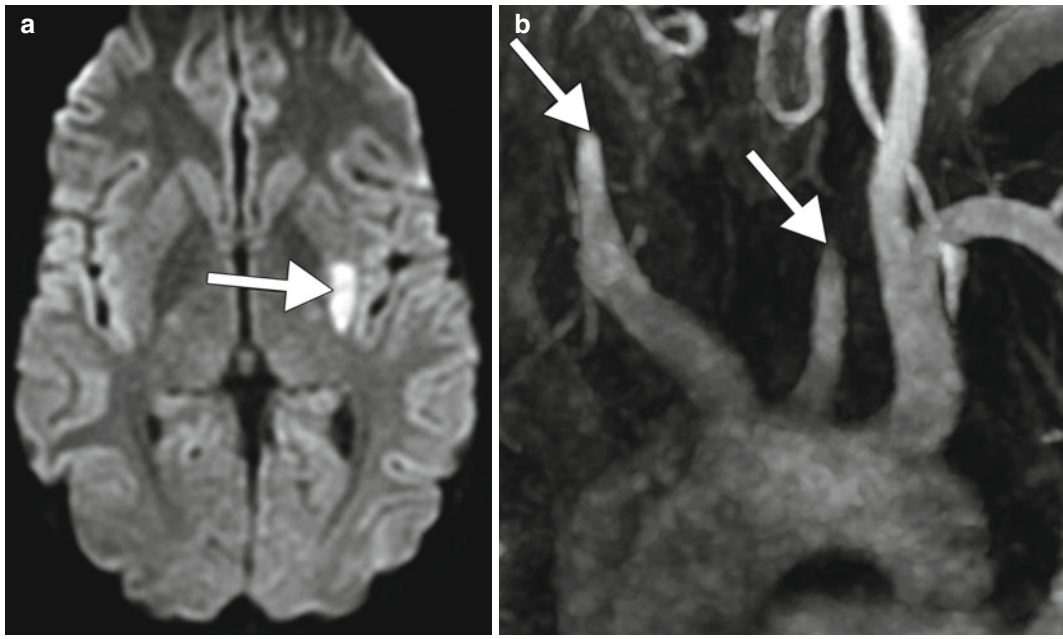

Fig. 1.4 Takayasu arteritis. Axial DWI (**a**) shows a focus of restricted diffusion in the left external capsule (*arrows*). MIP MRA (**b**) shows lack of flow-related enhancement beyond the proximal common carotid arteries bilaterally (*arrows*)

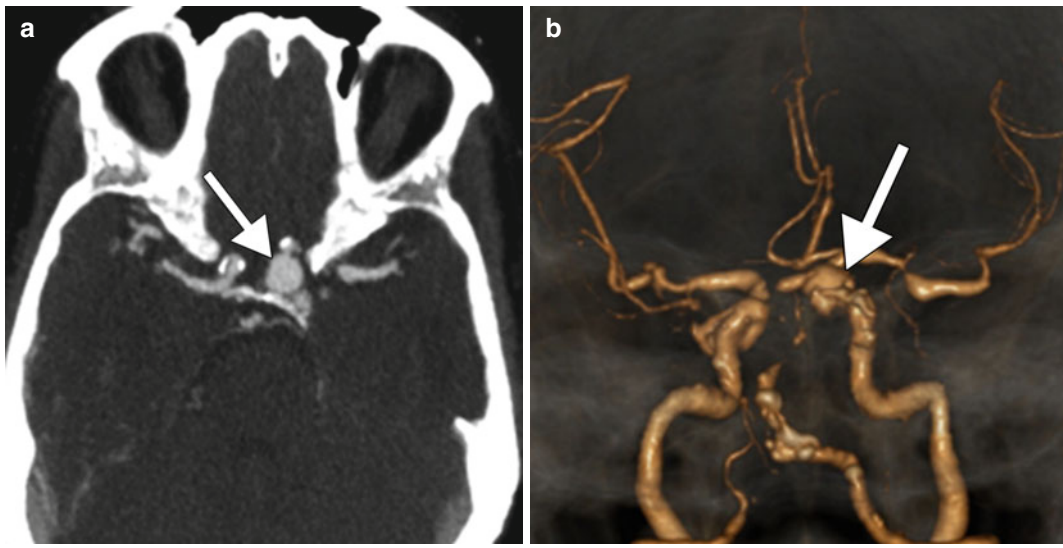

Fig. 1.5 Cerebral aneurysm. A former 20-pack-year smoker underwent evaluation for a suspected stroke. Axial (**a**) and 3D volume rendered (**b**) CTA images show a left paraclinoid internal carotid artery saccular aneurysm (*arrow*). There is also extensive atherosclerotic narrowing of the cerebral vasculature noted in both the anterior and posterior circulation bilaterally

connective tissue disorders, such as Ehlers-Danlos syndrome and Marfan's syndrome and polycystic kidney disease. Otherwise, the differential diagnosis of a cerebral aneurysm on radiologic imaging includes an infundibulum (usually manifests as a triangular dilatation with the vessel arising from the apex that measures less than 2 mm), pseudoaneurysm, and mycotic aneurysm (Fig. 1.7).

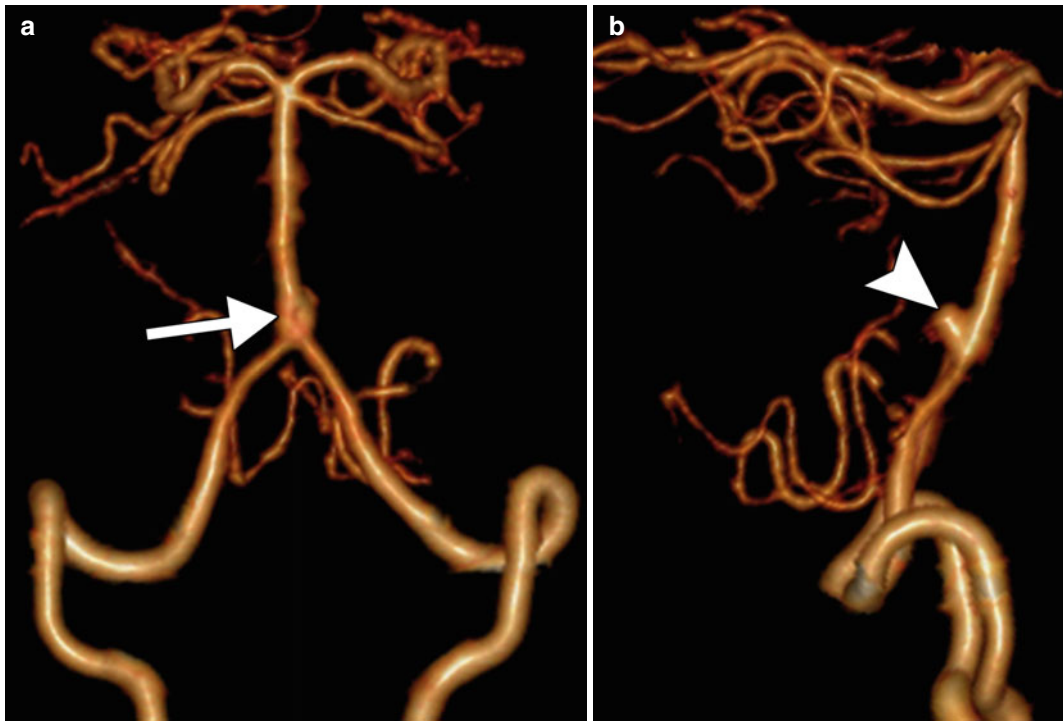

Fig. 1.6 Arterial fenestration. Frontal projection 3D volume rendered CTA image (**a**) shows a fenestration of the proximal basilar artery (*arrow*). Lateral projection 3D volume rendered CTA image (**b**) shows a dorsally oriented aneurysm arising from the caudal aspect of the fenestration (*arrowhead*)

1.3.3 Cerebral Venous Thrombosis

Secondary polycythemia due to chronic smoking is a risk factor developing cerebral venous thrombosis. Refer to the L-asparaginase and oral contraceptives chapters (Chaps. 21 and 47) for examples of venous thrombosis on imaging.

1.3.4 Head and Neck Cancer, Squamous Cell Carcinoma

Tobacco smoking, along with alcohol, is well established as the dominant risk factor for head and neck squamous cell carcinoma (HNSCC). This risk is correlated with the intensity and duration of tobacco use and is synergistic with concomitant alcohol consumption. There are more than sixty recognized compounds in tobacco that have a specific carcinogenic potential. In particular, nitrosamines and polycyclic hydrocarbons can alter the molecular profile of an individual and causes mutations. Nicotine, originally thought only to be responsible for tobacco addiction, is also involved in tumor promotion and progression with antiapoptotic and indirect mitogenic properties. Other factors that can increase the risk of HNSCC include HPV infection and certain occupational exposures. Imaging with contrast-enhanced CT and MRI allows depiction of the anatomy of the larynx and submucosal tumor extension.

Dual-energy CT improves the diagnostic performance and interobserver reproducibility of evaluations of laryngeal cartilage invasion by squamous cell carcinoma. CT, MRI, and PET-CT also provide information regarding cervical nodal disease, systemic metastases, and synchronous malignancies.

On CT or MRI, head and neck squamous cell carcinomas often manifest as ill-defined enhancing masses. Aggressive features of

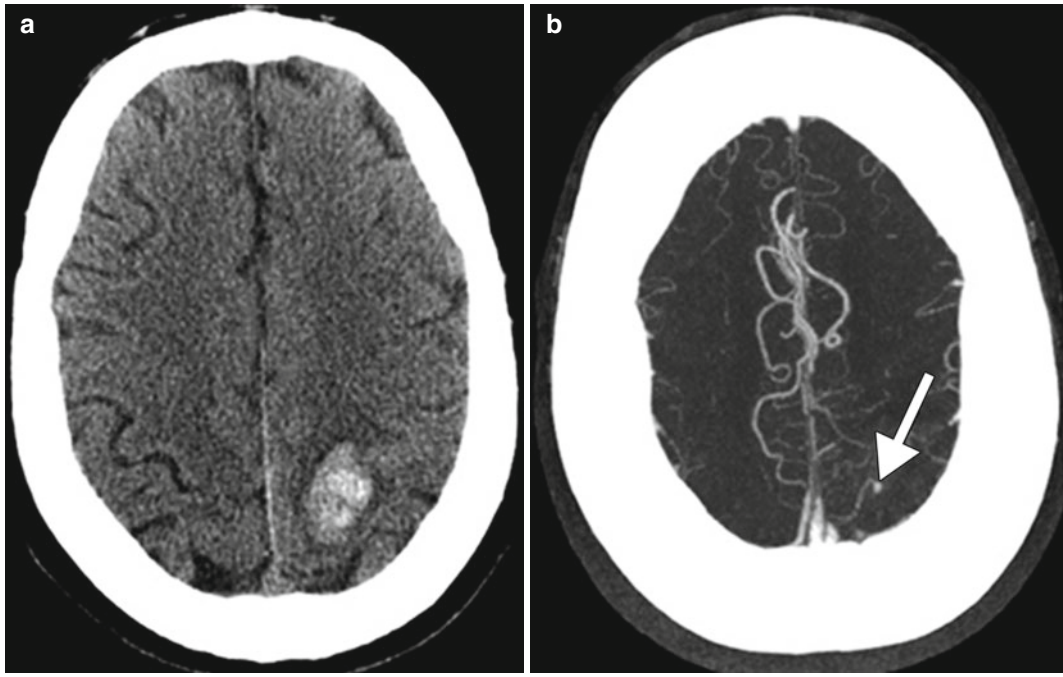

Fig. 1.7 Mycotic aneurysm. Axial CT image (**a**) shows left peri-rolandic hemorrhage. Axial MIP CTA image (**b**) shows a small outpouching arising from a cortical artery (*arrow*)

HNSCC include tissue invasion and necrosis (Fig. 1.8). The most common sites of head and neck squamous cell cancer are the floor of the mouth, tongue, soft palate, anterior tonsillar pillar, and retromolar trigone. In addition to locoregional spread, HNSCC can metastasize to distant organs hematogenously, most commonly to the lungs and bones. Metastasis to the brain is an infrequent, but carries a poor prognostic outcome (Fig. 1.9). Besides smoking, alcohol (refer to Chap. 2), betel nuts (refer to Chap. 8), and HPV are the other major risk factors for head and neck squamous cell carcinoma. Interestingly, HPV-positive squamous cell carcinomas generally have a more favorable prognosis and tend to have tumors that are relatively well-defined and large cystic nodal metastases (Fig. 1.10). Otherwise, the differential for other malignant cancers in the head and neck include thyroid cancer, lymphoma, salivary gland cancer, and sarcoma. Furthermore, head and neck abscesses can sometimes resemble necrotic or ulcerated head and neck squamous cell carcinomas and nodal metastases (Fig. 1.11).

1.3.5 Brain Metastases

In addition to HNSCC, smoking has been shown to be a risk factor for the formation of several other types of cancers, including lung cancer, acute myeloid leukemia, bladder cancer, cervical cancer, renal cancer, esophageal cancer, gastric cancer, pancreatic cancer, and colorectal cancer. The majority of these cancers have at least some potential for metastasizing to the brain, which is the most feared complication of systemic malignancies. If no one smoked, one of every three cancer deaths in the United States would be avoided. Lung cancer has the highest association with smoking, causing an estimated 90 % of all lung cancer deaths in men and 80 % of all lung cancer deaths in women, and is the most common cancer that metastasizes to the brain. Nicotine-derived nitrosamine ketone (NNK) has

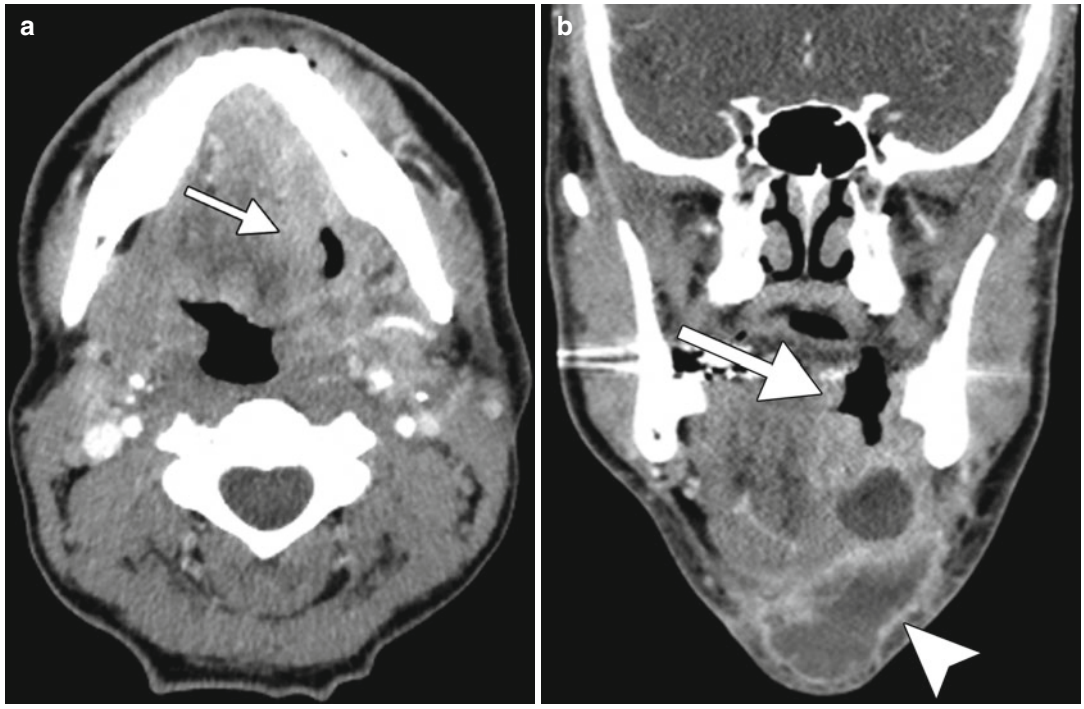

Fig. 1.8 Oral squamous cell carcinoma in a 30-pack-year male smoker. Axial (**a**) and coronal (**b**) post-contrast CT images show an ulcerating mass in the left floor of the mouth and oral tongue (*arrows*) with associated submental necrotic cervical lymphadenopathy (*arrowhead*)

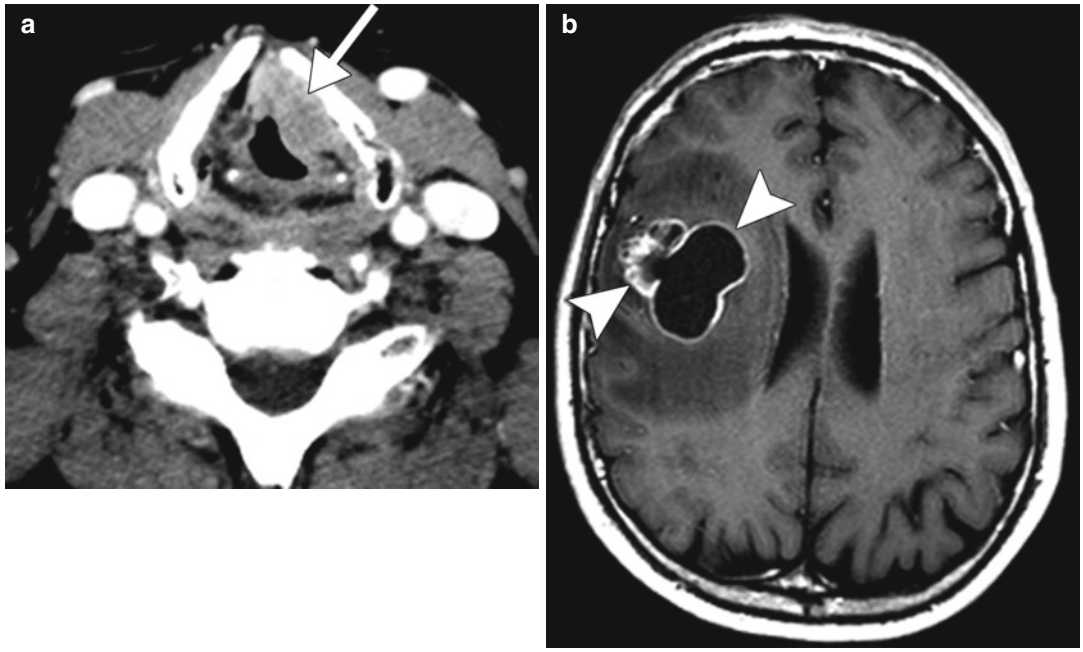

Fig. 1.9 Laryngeal squamous cell carcinoma with brain metastasis. This 25-pack-year smoker had been recently diagnosed with laryngeal squamous cell carcinoma when he developed generalized seizures. Axial CT image (**a**) shows a left vocal cord mass (*arrow*) that also involves the paraglottic fat and anterior commissure. Post-contrast T1-weighted MRI image (**b**) demonstrates a heterogeneous metastatic lesion in the right frontal lobe (*arrowheads*)

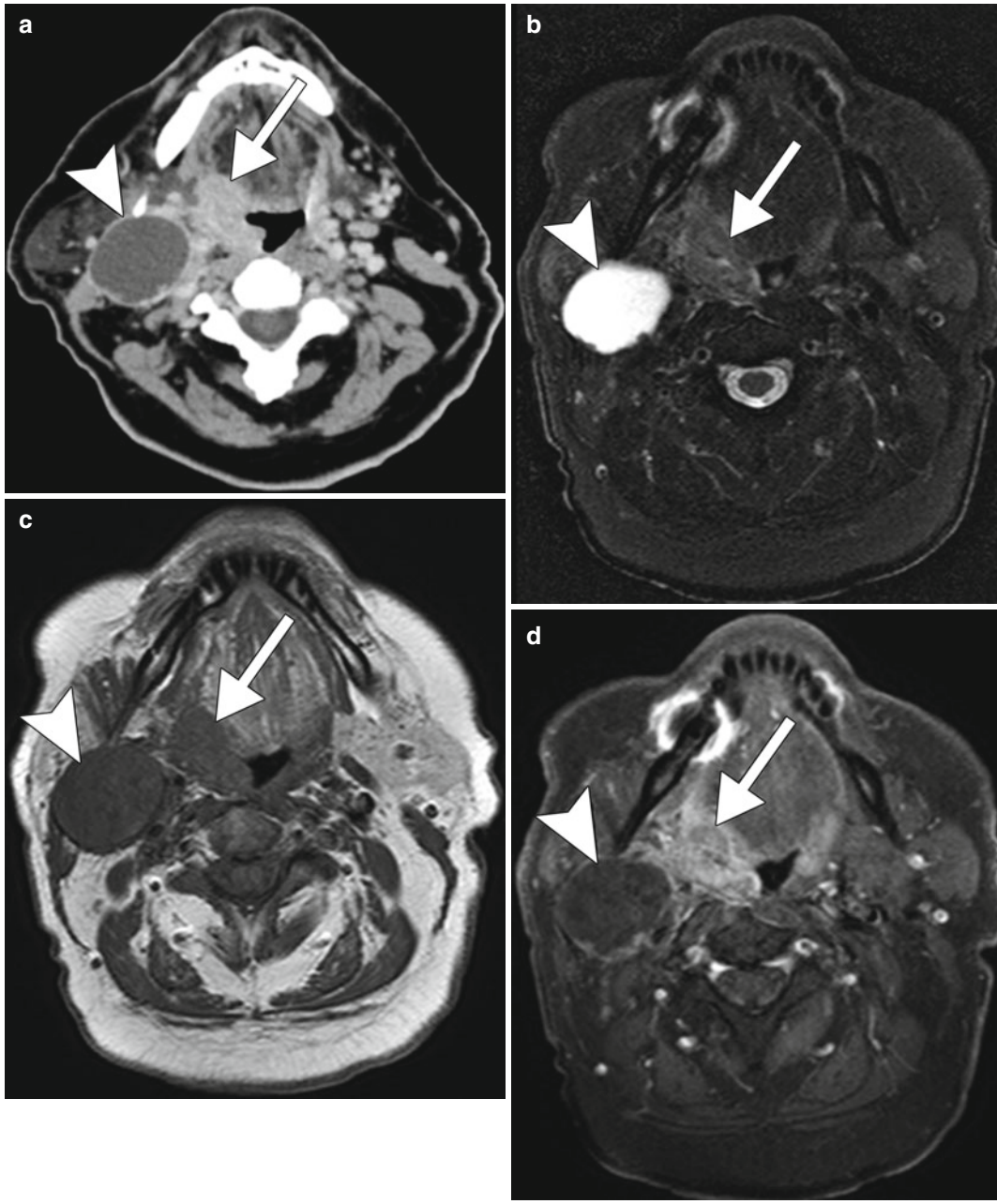

Fig. 1.10 HPV-positive squamous cell carcinoma. Axial CT (**a**) and axial fat-suppressed T2-weighted (**b**), axial T1-weighted (**c**), and axial fat-suppressed post-contrast T1-weighted (**d**) images show a relative well-demarcated right palatine tonsil tumor (*arrows*) and a large metastatic lymph node with cystic necrosis (*arrowheads*)

been identified as a potent procarcinogen specific to the development of lung cancer. The two categories of lung cancer metastases to the brain consist of small cell lung carcinoma (Fig. 1.12) and non-small cell lung carcinoma (NSCLC), such as adenocarcinoma (Fig. 1.13). MRI with contrast is the gold standard for evaluation of brain metastases. Lung cancer metastases to the brain are typically iso- to hypointense on T1 and hyperintense on T2-weighted sequences. The

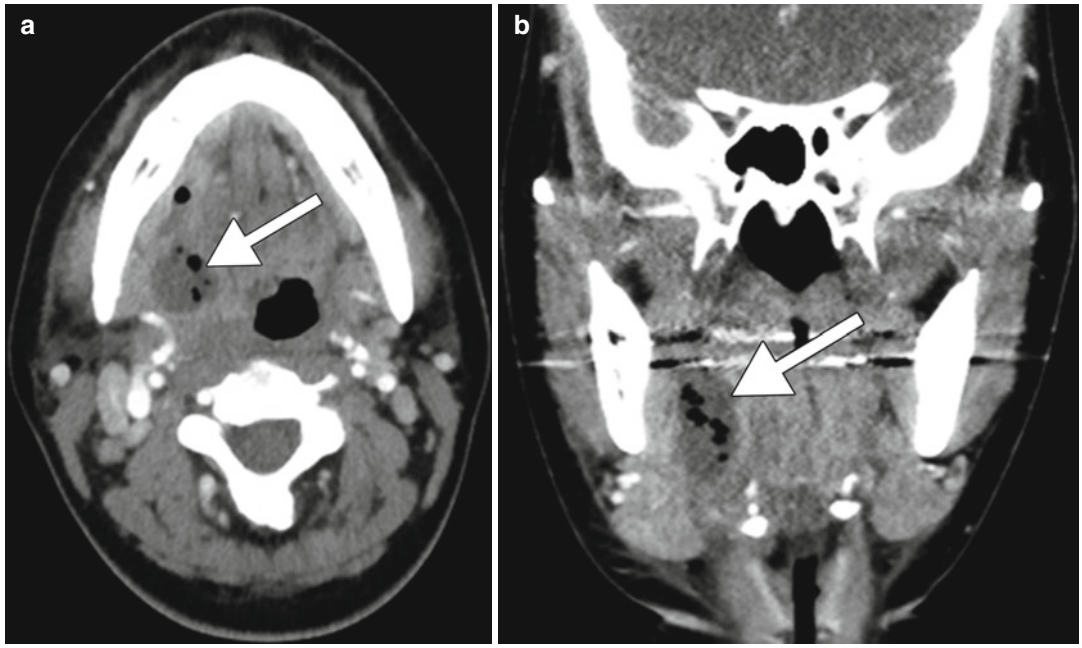

Fig. 1.11 Floor of mouth abscess. Axial (**a**) and coronal (**b**) post-contrast CT images show a fluid collection with internal air in the right floor of the mouth (*arrows*) in a patient with mouth pain and fever

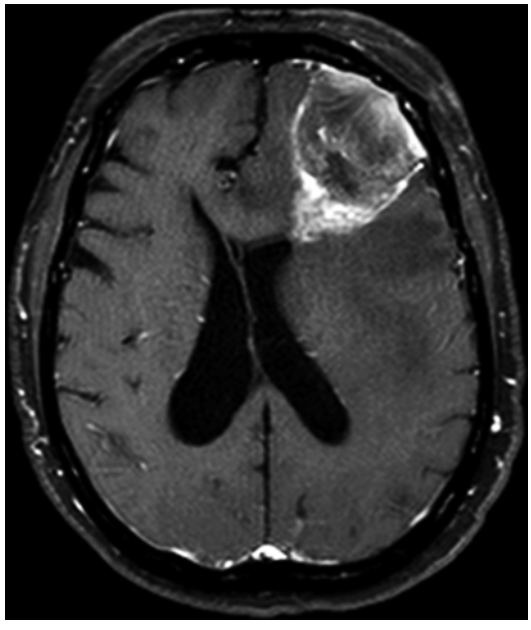

Fig. 1.12 Small cell lung carcinoma metastasis to the brain. The post-contrast T1-weighted MRI in a 40-pack-year smoker who presented with a 2 weeks history of aphasia, forgetfulness, and frequent falls shows a heterogeneously enhancing mass within the left frontal lobe with associated subfalcine herniation

Fig. 1.13 Non-small cell lung cancer brain metastases. The patient has a 40-pack-year smoking history, and known small cell lung cancer metastases to the bone developed altered mental status and intermittent left-sided weakness. The axial post-contrast T1-weighted MRI shows ring-enhancing lesions in the right cerebral hemisphere and a smaller solidly enhancing lesion in the left frontal lobe (*arrow*)

enhancement pattern is usually intense whether uniform, punctate, or ring enhancing. Hemorrhagic lung metastases may display high intrinsic T1 signal. On T2-weighted sequences, metastatic lesions are typically hyperintense with hyperintense peritumoral edema. On MR spectroscopy, there is often an intratumoral choline peak without choline elevation in the peritumoral edema and depletion of NAA. CT may be the initial exam obtained when metastatic disease is not yet known. On precontrast imaging, the mass may be iso- to hypoattenuating, surrounded by variable amounts of vasogenic edema. Similar to MRI, following administration of contrast in CT, enhancement is variable and can be intense, punctate, nodular, or ring enhancing. It is also important to evaluate the skull, soft tissues, and head and neck lymph nodes for additional metastases.

The differential diagnosis for brain metastases includes primary brain tumors (Fig. 1.14), cerebral abscess (refer to Chaps. 7, 16, 19, and 46), focal subacute stroke, and tumefactive demyelinating lesions.

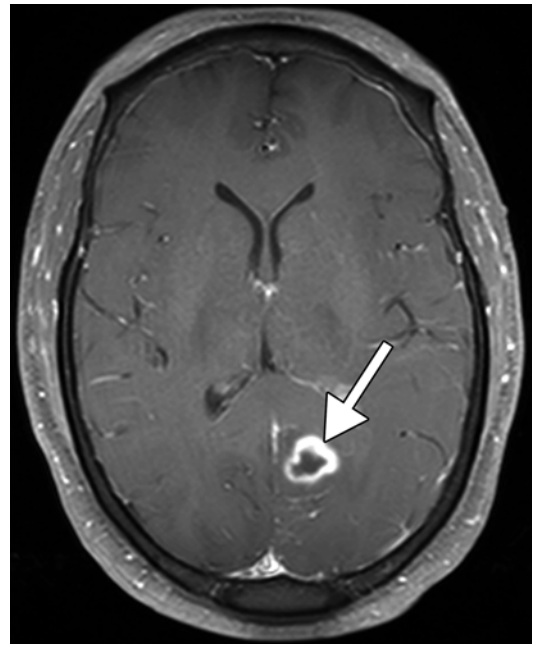

Fig. 1.14 Glioblastoma. Axial post-contrast T1-weighted MR image shows a ring-enhancing mass centered in the left posterior cingulate gyrus (*arrow*)

1.3.6 Warthin Tumor

Papillary lymphomatous cystadenoma of the parotid gland, or Warthin tumor, is significantly associated with a history of cigarette smoking. Indeed, over 90 % of Warthin tumors occur in tobacco smokers. The tumor arises almost exclusively in the parotid gland and has a predilection for male Caucasians. These lesions most commonly present as asymptomatic masses, but may cause facial nerve paralysis or tinnitus. Warthin tumors consists of oncocytic cells containing numerous mitochondria frequently showing structural abnormalities and reduced metabolic function. Smoking can lead to damage to mitochondrial DNA due to the development of numerous reactive oxygen species. In this context, a high rate of deleted mitochondrial DNA has been detected in the oncocytic cells of Warthin tumor. Typical imaging features consist of well-defined solid and/or cystic masses usually within the inferior pole (tail) of the parotid gland, not infrequently multifocal and bilateral (Fig. 1.15).

The differential diagnosis of Warthin tumor includes non-neoplastic conditions, such as benign lymphoepithelial lesions, Sjogren syndrome, and sarcoidosis. For example, benign lymphoepithelial lesions are typically associated with HIV and classically appear as multiple bilateral cystic parotid masses that may contain solid components (Fig. 1.16). Warthin tumors can also resemble pleomorphic adenomas on imaging. However, pleomorphic adenomas are less likely to occur in the parotid tail and display a bosselated appearance and high T2 signal on MRI (Fig. 1.17). While clinical history may be helpful in differentiating some of these possibilities, predictive features of malignancy on imaging include T2 hypointensity of the parotid, ill-defined margins, diffuse growth, infiltration of subcutaneous tissue,

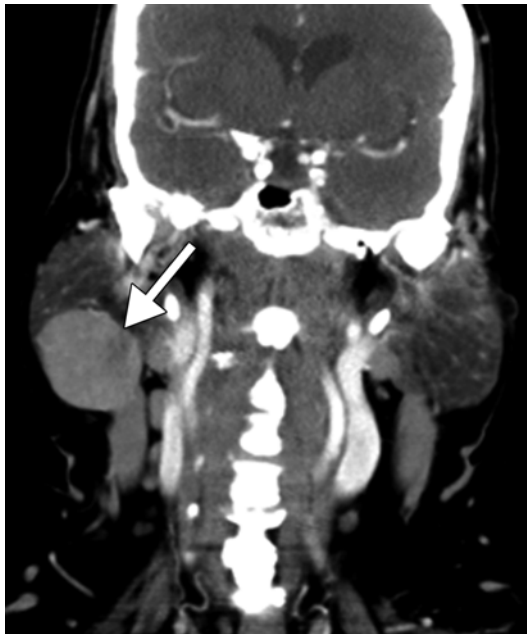

Fig. 1.15 Warthin tumor. This smoker with COPD presented with growing right-sided neck mass. The coronal post-contrast CT image shows a well-defined hyperattenuating mass within the right parotid tail (*arrow*)

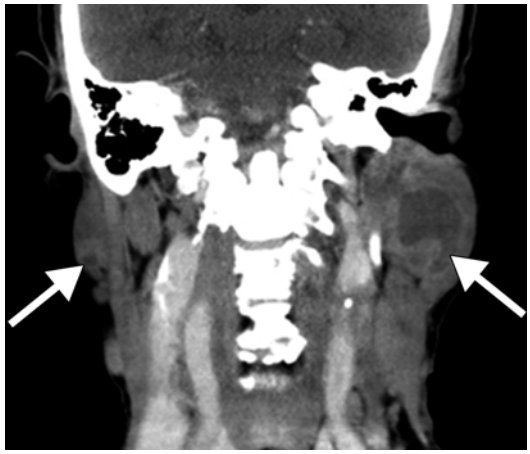

Fig. 1.16 Benign lymphoepithelial lesions in a patient with HIV. The coronal CT image shows cystic lesions in the bilateral parotid glands (*arrows*). The lesion on the left side contains a solid nodule

lymphadenopathy, and perineural spread (Fig. 1.18). However, Warthin tumors often demonstrate T2 hypointense foci and low ADC values and thus cannot be reliably differentiated from many malignant tumors on diffusion-weighted imaging. In addition, Warthin tumors typically display marked hypermetabolism on ^{18}FDG-PET.

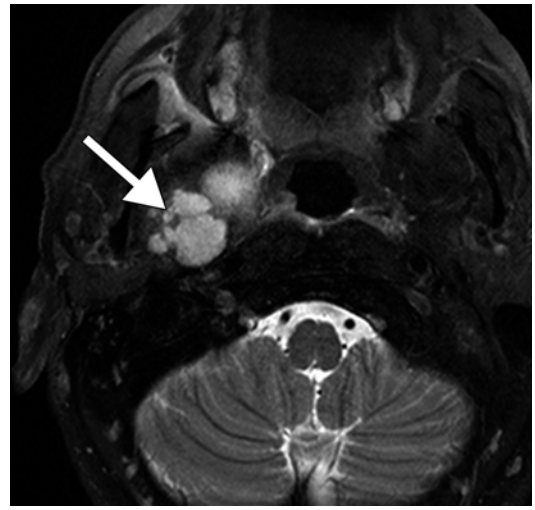

Fig. 1.17 Parotid pleomorphic adenoma. Axial fat-suppressed T2-weighted MRI shows a bosselated T2 hyperintense mass arising from the deep lobe of the right parotid gland (*arrow*)

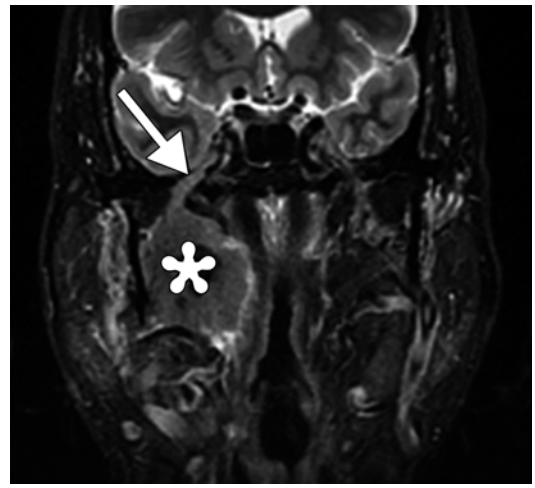

Fig. 1.18 Parotid pleomorphic adenocarcinoma. The coronal STIR MRI shows a heterogeneous mass arising from the deep lobe of the parotid gland (*) with perineural extension along the mandibular nerve across the foramen ovale (*arrow*)

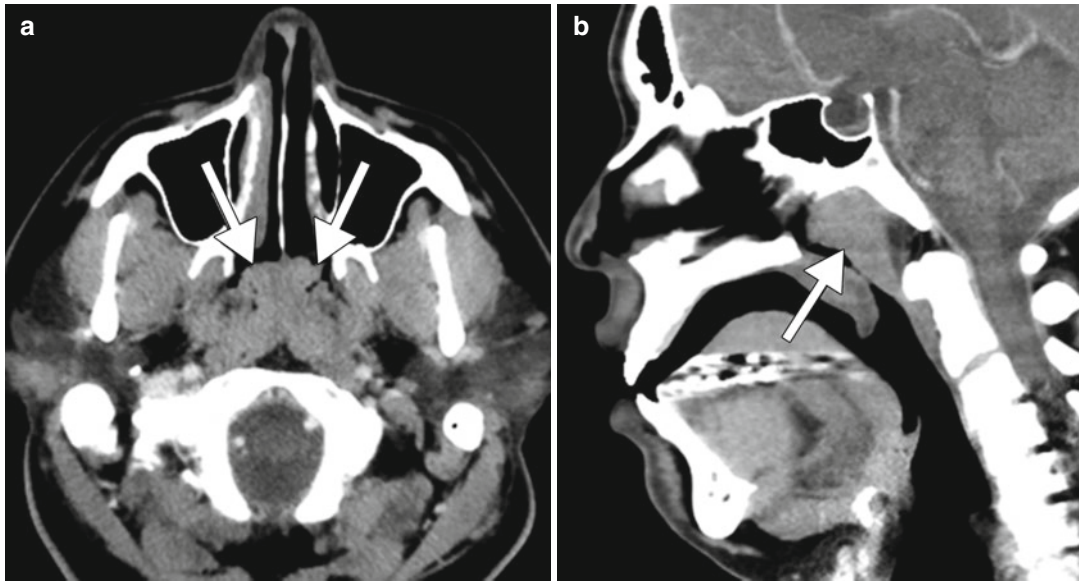

Fig. 1.19 Smoking-induced nasopharyngeal lymphoid hyperplasia. This is a 40-year-old smoker with obstructive symptoms. Axial (**a**) and sagittal (**b**) post-contrast CT images show diffuse marked enlargement of the adenoids (*arrows*)

1.3.7 Smoking-Induced Nasopharyngeal Lymphoid Hyperplasia

Heavy tobacco smoking has been linked to the development of nasopharyngeal lymphoid hyperplasia, which is characterized by the presence of cytotoxic lymphocytes in the nasopharyngeal mucosa. The adenoids may be obstructive in up to 30 % of heavy smokers. On imaging, there is diffuse symmetric enlargement of the adenoidal tissues (Fig. 1.19). Nevertheless, it is important to exclude other conditions, such as nasopharyngeal carcinoma. In contrast to benign lesions, the configuration of nasopharyngeal carcinoma is often asymmetric, in which the mass is centered in the fossa of Rosenmuller, and associated with aggressive features, such as skull base invasion (Fig. 1.20). Other differential considerations for smoking-induced nasopharyngeal lymphoid hyperplasia include reactions to other chemical exposures, Epstein-Barr virus infection, and lymphoproliferative conditions.

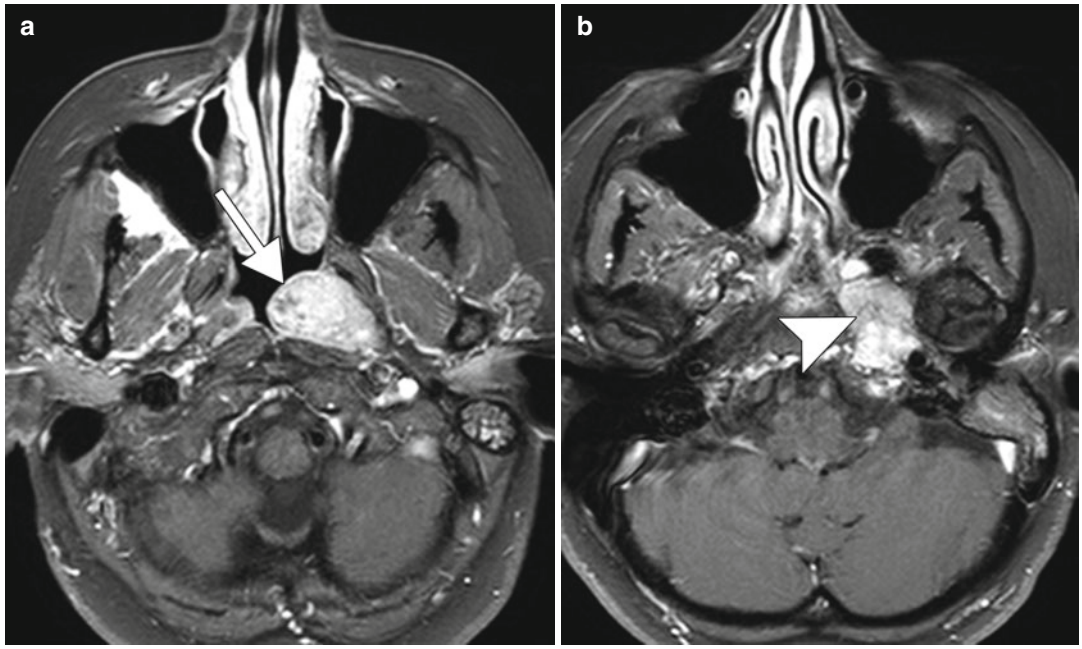

Fig. 1.20 Nasopharyngeal carcinoma. Post-contrast T1-weighted MR images (**a**, **b**) show a bulky mass centered in the left fossa of Rosenmuller (*arrow*). There is associated left skull base invasion (*arrowhead*) and obstructed secretions within the left mastoid air cells

Suggested Reading

Centers for Disease Control and Prevention. Annual smoking-attributable mortality, years of potential life lost, and productivity losses—United States, 2000–2004. MMWR Morb Mortal Wkly Rep. 2008;57(45):1226–8. Accessed 28 June 2014.

Centers for Disease Control and Prevention. QuickStats: number of deaths from 10 leading causes–National Vital Statistics System, United States, 2010. MMWR Morb Mortal Wkly Rep. 2013:62(08);155. Accessed 28 June 2014.

de Ru JA, Plantinga RF, Majoor MH, van Benthem PP, Slootweg PJ, Peeters PH, Hordijk GJ. Warthin's tumour and smoking. B-ENT. 2005;1(2):63–6.

Finkelstein Y, Malik Z, Kopolovic J, Bernheim J, Djaldetti M, Ophir D. Characterization of smoking-induced nasopharyngeal lymphoid hyperplasia. Laryngoscope. 1997;107(12 Pt 1):1635–42.

Galbiatti AL, Padovani-Junior JA, Maníglia JV, et al. Head and neck cancer: causes, prevention and treatment. Braz J Otorhinolaryngol. 2013;79(2):239–47.

Haddad RI, Shin DM. Recent advances in head and neck cancer. N Engl J Med. 2008;359(11):1143–54.

Hashibe M, Brennan P, Benhamou S, et al. Alcohol drinking in never users of tobacco, cigarette smoking in never drinkers, and the risk of head and neck cancer: pooled analysis in the International Head and Neck Cancer Epidemiology Consortium. J Natl Cancer Inst. 2007;99(10):777–89.

Ikeda M, Motoori K, Hanazawa T, Nagai Y, Yamamoto S, Ueda T, Funatsu H, Ito H. Warthin tumor of the parotid gland: diagnostic value of MR imaging with histopathologic correlation. AJNR Am J Neuroradiol. 2004;25(7):1256–62.

Juvela S. Prevalence of risk factors in spontaneous intracerebral hemorrhage and aneurysmal subarachnoid hemorrhage. Arch Neurol. 1996;53:734–40.

Juvela S, Hillbom M, Numminen H, Koskinen P. Cigarette smoking and alcohol consumption as risk factors for aneurysmal subarachnoid hemorrhage. Stroke. 1993;24:639–46.

Juvela S, Porras M, Poussa K. Natural history of unruptured intracranial aneurysms: probability of and risk factors for aneurysm rupture. J Neurosurg. 2000;93:379–87.

Juvela S, Poussa K, Porras M. Factors affecting formation and growth of intracranial aneurysms: a long term follow up study. Stroke. 2001;32:485–91.

Longstreth Jr WT, Nelson LM, Koepsell TD, van Belle G. Cigarette smoking, alcohol use, and subarachnoid hemorrhage. Stroke. 1992;23:1242–9.

Ockene IS, Miller NH. Cigarette smoking, cardiovascular disease, and stroke: a statement for healthcare professionals from the American Heart Association. Circulation. 1997;96(9):3243–7. Accessed 28 June 2014.

Raval M, Paul A. Cerebral venous thrombosis and venous infarction: case report of a rare initial presentation of Smoker's polycythemia. Case Rep Neurol. 2010;2(3): 150–6.

Schuette W. Treatment of brain metastases from lung cancer: chemotherapy. Lung Cancer. 2004;45 Suppl 2:S253–7.

Tonini G, D'Onofrio L, Dell'Aquila E, Pezzuto A. New molecular insights in tobacco-induced lung cancer. Future Oncol. 2013;9(5):649–55.

U.S. Department of Health and Human Services. How tobacco smoke causes disease: what it means to you. Atlanta: U.S. Department of Health and Human Services, Centers for Disease Control and Prevention, National Center for Chronic Disease Prevention and Health Promotion, Office on Smoking and Health; 2010. Accessed 28 June 2014.

U.S. Department of Health and Human Services. Reducing the health consequences of smoking: 25 years of progress. A report of the surgeon general. Rockville: U.S. Department of Health and Human Services, Public Health Service, Centers for Disease Control, National Center for Chronic Disease Prevention and Health Promotion, Office on Smoking and Health; 1989. Accessed 28 June 2014.

U.S. Department of Health and Human Services. The health consequences of smoking: a report of the surgeon general. Atlanta: U.S. Department of Health and Human Services, Centers for Disease Control and Prevention, National Center for Chronic Disease Prevention and Health Promotion, Office on Smoking and Health; 2004. Accessed 28 June 2014.

Weir BK, Kongable GL, Kassell NF, Schultz JR, Truskowski LL, Sigrest A. Cigarette smoking as a cause of aneurysmal subarachnoid hemorrhage and risk for vasospasm: a report. J Neurosurg. 1998;89(3): 405–11.

Alcohol

2

Michael C. Veronesi and Daniel Thomas Ginat

2.1 Uses

Alcoholic beverages are commonly consumed for pleasure and a form of stress reduction since at least the Neolithic period many thousands of years ago. The beverages are produced through the fermentation of various fruit juices and grains. Alcohol can provide an increased sense of self-confidence, disinhibition, mild euphoria, and decreased anxiety but also impaired judgment and attention span, even with low blood levels. There are a few reported health benefits associated with low to moderate alcohol consumption, such as reduction of cardiovascular disease risk factors. Nevertheless, alcohol is one of the most commonly abused substances, and alcohol dependence is a major cause of disease burden. Alcohol in the form of ethanol can be used for sclerotherapy, but this is beyond the scope of the chapter.

2.2 Mechanism

The alcohol found in beverages is ethanol or ethyl alcohol (C_2H_6O). Alcohol metabolism is a complex process with large variations between individuals that are mainly related to genetic factors. Direct absorption of alcohol into the bloodstream occurs in the stomach and small intestine. The liver metabolizes nearly 90 % of alcohol. Alcohol dehydrogenase oxidizes ethanol into acetaldehyde, which is then further oxidized into acetic acid by acetaldehyde dehydrogenase, and finally into carbon dioxide and water through the citric acid cycle. The effects of alcohol upon the central nervous system can be either direct or indirect. The main direct effect of alcohol is volume loss due to neurotoxicity, often mediated by a compromise of neurotransmitters and/or receptors and electrolytes. On the other hand, indirect effects are related to liver cirrhosis, such as hepatic encephalopathy and coagulopathies, and impaired vitamin absorption. In some conditions, it is unclear whether direct or indirect effects or a combination is responsible, such as Wernicke encephalopathy, osmotic myelinolysis, and Marchiafava-Bignami disease.

2.3 Discussion

Marchiafava-Bignami disease. Marchiafava-Bignami disease is a rare condition that mainly affects chronic alcoholics, particularly middle-aged males, and results in progressive demyelination and necrosis of the corpus callosum. Patients present acutely with mental confusion, disorientation, neurocognitive deficits, and seizures, generally ensued by coma and death. On CT, diffuse periventricular hypoattenuation

M.C. Veronesi, MD, PhD
Department of Radiology, University of Chicago, Chicago, IL, USA

D.T. Ginat, MD, MS (✉)
Department of Radiology, University of Chicago, Pritzker Medical School, Chicago, IL, USA
e-mail: ginatd01@gmail.com

D.T. Ginat et al. (eds.), *Neuroimaging Pharmacopoeia*,
DOI 10.1007/978-3-319-12715-6_2,

Fig. 2.1 Marchiafava-Bignami disease depicted on CT. Axial non-contrast CT shows hypoattenuation in the genu of the corpus callosum (*arrow*) and adjacent periventricular white matter (*arrowheads*)

associated with focal areas of hypoattenuation in the splenium and sometimes the genu of the corpus callosum can be observed (Fig. 2.1). On MRI, the affected areas display T2 hyperintensity and variable degrees of restricted diffusion and enhancement depending on the severity and acuity of the disease (Fig. 2.2). In fact, apparent diffusion coefficient restriction of the corpus callosum and cortical lesions were associated with a higher mortality rate and a more severe cognitive impact. MR spectroscopy may reveal decreased NAA-Cr ratio and elevated lactate during the first few months of the disease process. Chronic lesions appear cystic and well marginated. Lesions of the corpus callosum that may have a similar appearance to Marchiafava-Bignami disease include other demyelinating processes, infarction, viral encephalitis, metronidazole (refer to Chap. 25), antiseizure medications (refer to Chap. 27), and shearing injuries (Fig. 2.3).

Traumatic brain injury and hemorrhage related to alcohol. Traumatic brain injury (TBI) is a serious public health problem in the United States. Each year, at least 1.7 million traumatic brain injuries occur and contribute to substantial morbidity and mortality. Preexisting alcohol abuse is common among persons who incur TBI, with as many as 58 % reporting a history of alcohol abuse or dependence and as much as 25 % reporting previous treatment for substance abuse in one study. In a separate study analyzing 2,657 trauma patients experiencing TBI, 58 % had a heavy drinking history, 46 % had a positive blood alcohol level at the time of injury, and 36 % were intoxicated. Alcohol intoxication resulted in a greater likelihood of intubation, intracranial pressure monitoring, respiratory distress, and pneumonia. Timely management of TBI can significantly alter the clinical course if detected with neuroimaging within 48 h of the injury. Clinical manifestations that suggest major injury such as worsening level of consciousness, loss of consciousness for more than 5 min, focal neurological findings, seizure, failure of the mental status to improve over time, signs of a basal or depressed skull fracture, or confusion on examination almost always merit imaging. On the other hand, even patients with absence of clinical findings and high-risk circumstances can have intracerebral hemorrhage on imaging. Neuroimaging also plays an important role in the diagnostic workup of TBI. MRI is superior to CT in detecting axonal injury and cerebral contusions. However, conventional CT generally remains the initial imaging modality of choice during the first 24 h following injury. Alcohol intoxication can lead to severe injuries related to high-speed motor vehicle collisions while driving intoxicated or falls related to drunkenness, resulting in skull fractures, intracranial hemorrhage, cerebral contusions, and shear injury (Figs. 2.3 and 2.4). Alcoholism may also predispose to large and recurrent intracranial hemorrhage with relatively minor trauma due to underlying coagulopathy related to hepatic dysfunction (Fig. 2.5). Alcohol abusers also have a tendency to engage in violent behavior when drunk and may present with maxillofacial fractures, for which CT may be obtained (Fig. 2.6). Incidentally, these individuals often have a high burden of dental disease that may also be encountered on imaging.

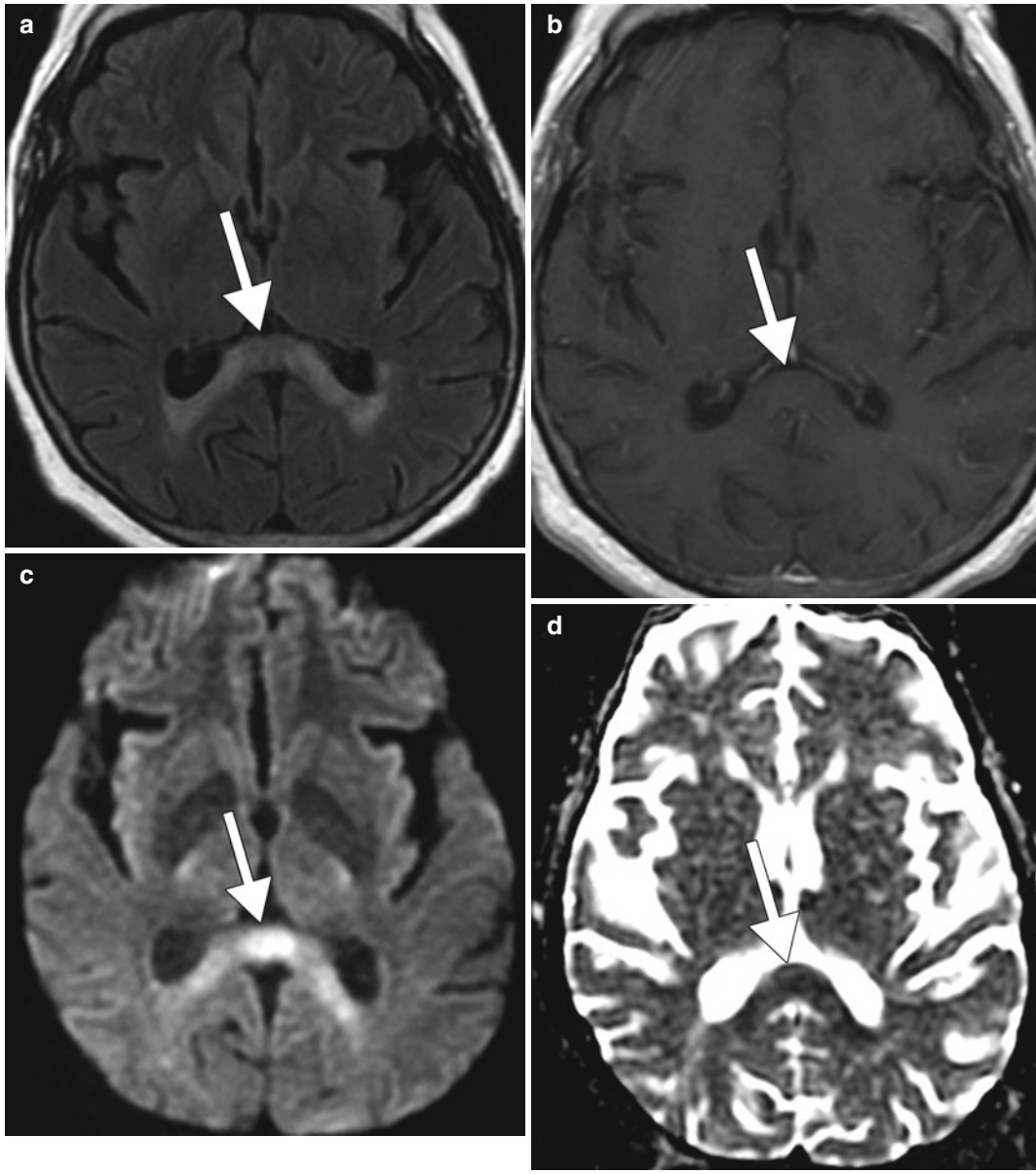

Fig. 2.2 Marchiafava-Bignami disease depicted on MRI. Axial FLAIR MRI (**a**), post-contrast T1-weighted MRI (**b**), DWI (**c**), and ADC map (**d**) show non-enhancing T2 hyperintensity in the splenium of the corpus callosum (*arrows*)

Hepatic encephalopathy (also refer to Chaps. 28, 41, and 49). Hepatic encephalopathy (HE) may occur as an acute, potentially reversible disorder, or it may occur as a chronic, progressive disorder that is associated with chronic liver disease. Depending on the duration and extent of hepatic dysfunction, HE may be classified into fulminant hepatic failure (acute) or portosystemic encephalopathy (chronic). Clinical manifestations of HE can range from mild confusion to coma. Cerebral edema and raised intracranial pressure can result from fulminant hepatic failure and contribute to encephalopathy, but some degree of cerebral edema has been shown in patients with all grades of hepatic encephalopathy. Patients with the portosystemic encephalopathy

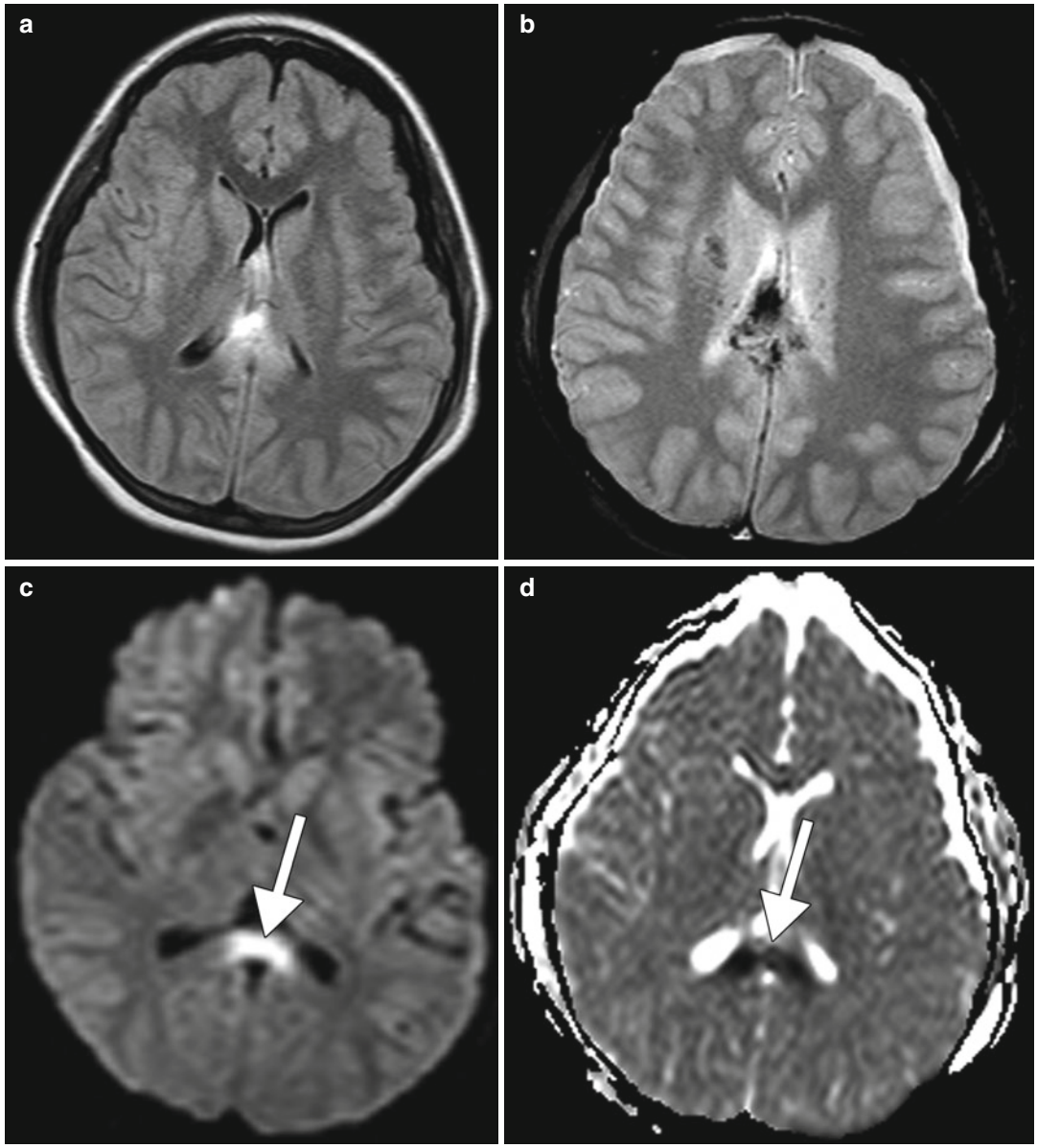

Fig. 2.3 Shear injury. The patient has a recent history of severe trauma to the head. Axial FLAIR MRI (**a**), T2* GRE (**b**), DWI (**c**), and ADC map (**d**) show edema and hemorrhage within the corpus callosum with associated restricted diffusion in the splenium of the corpus callosum (*arrows*)

frequently have pairs and triplets of abnormal astrocytes with a characteristic structure known as Alzheimer type II astrocytosis, in which the astrocytes exhibit physiological and functional abnormalities. When the liver is damaged, either acutely or over time, it can no longer remove neurotoxic substances such as ammonia and manganese from the blood. High levels of ammonia can have deleterious effects on neurotransmitter activity, impairment of cerebral metabolism, and altered neuronal gene expression. Manganese can deposit directly in the basal ganglia and induce extrapyramidal symptomatology. Manganese can also act synergistically with

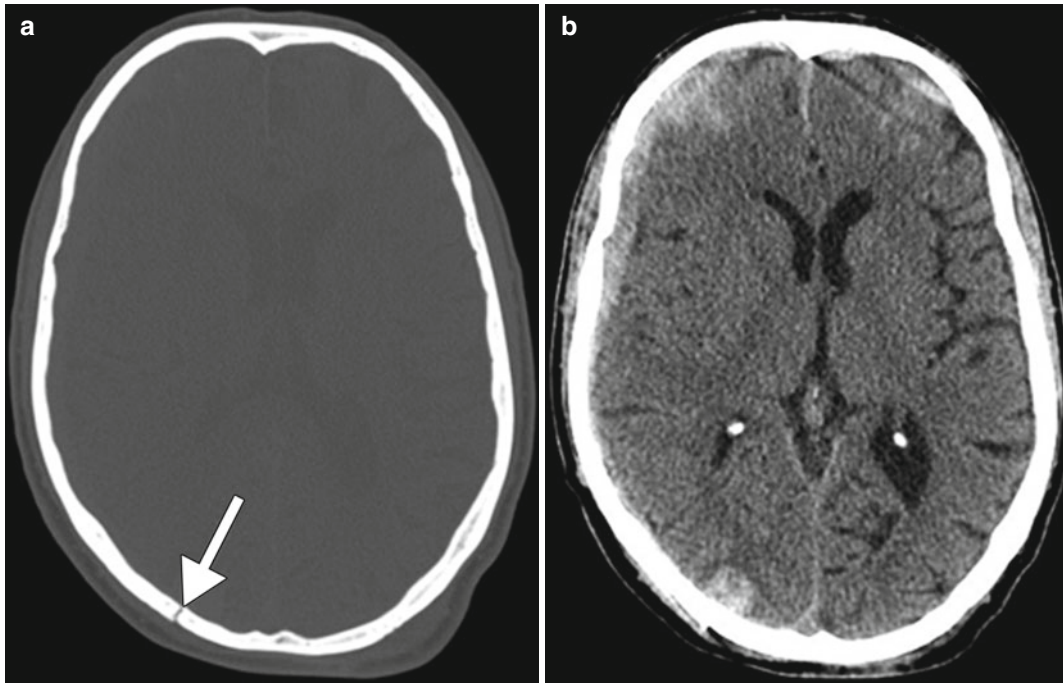

Fig. 2.4 Alcohol-related traumatic brain injury. Axial CT images in the bone (**a**) and brain (**b**) windows show a nondepressed right occipital bone fracture (*arrow*) and scattered acute intraparenchymal hemorrhage, including a right cerebral convexity subdural hematoma, subarachnoid hemorrhage, and hemorrhagic contusions in a patient who fell while drunk

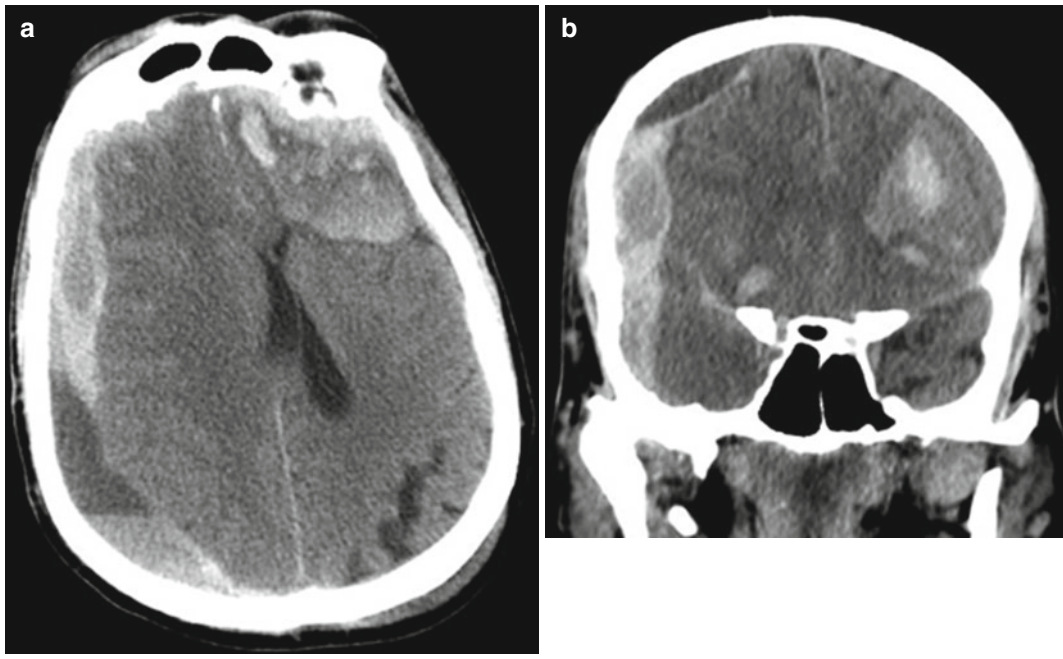

Fig. 2.5 Acute upon chronic intracranial hemorrhage in a patient with alcohol-induced hepatic coagulopathy. Axial (**a**) and coronal (**b**) show a heterogeneous acute upon chronic right cerebral convexity subdural hematoma and a left frontal lobe hemorrhagic contusion and areas of subarachnoid hemorrhage in a patient with alcohol-induced liver failure and trauma

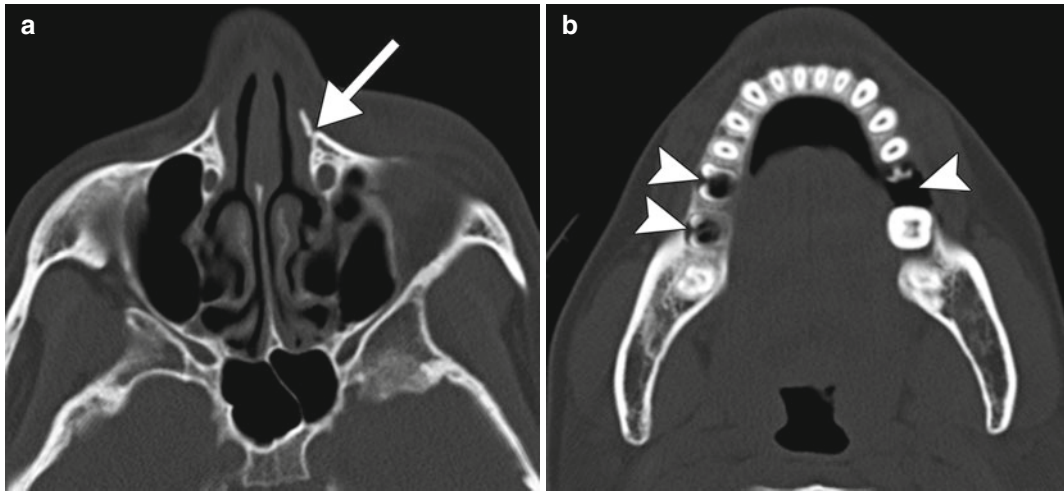

Fig. 2.6 Alcohol-related violence with maxillofacial trauma. Axial maxillofacial CT images (**a**, **b**) show a fracture of the left frontal process of the maxilla (*arrow*) and extensive dental disease (*arrowheads*) in a relatively young patient

ammonia to activate peripheral-type benzodiazepine receptors and the gamma-aminobutyric acid (GABA)-ergic neuroinhibitory system. In acute HE, T2 and DWI abnormalities are present in the cerebral cortex, particularly in the frontal, temporal, and insular lobes, which correspond to edema (Fig. 2.7). MRS often demonstrates an elevated glutamine peak and diminished myoinositol and choline peaks. The differential diagnosis of acute hepatic encephalopathy includes other toxic-metabolic derangements, viral encephalitis, status epilepticus, and Creutzfeldt-Jakob disease. In chronic hepatic encephalopathy, there can be patchy high signal intensity on T1-weighted images in the bilateral globi pallidi, cerebral peduncles, and anterior pituitary (Fig. 2.8), secondary to manganese deposition. The differential diagnosis of hepatic encephalopathy includes total parenteral nutrition also secondary to excess manganese.

Osmotic demyelination (also refer to Chap. 35). Osmotic demyelination consists of vacuolization and intramyelinitic splitting with eventual rupture of the myelin sheaths and most commonly occurs in the setting of rapid correction of hyponatremia in patients with chronic alcohol abuse and malnutrition. The resultant pathologic changes include symmetric myelin disruption in areas with admixed gray and white matter, particularly the basis pontis and basal ganglia but also on occasion the thalamus, and neocortical and cerebellar gray-white junctions with corresponding T2 hyperintensity on MRI (Fig. 2.9). On DWI, corresponding restricted diffusion can be detected within 24 h after onset of symptoms and can serve as an early indication of this disease. The differential diagnosis for osmotic demyelination includes infarcts and microangiopathy, other types of demyelinating processes, neoplasms, and metabolic syndromes, such as Leigh disease and Wilson disease.

Wernicke encephalopathy. Wernicke encephalopathy is an acute neurological syndrome that results from thiamine (vitamin B1) deficiency, which can occur in alcoholics as well as nonalcoholics with nutritional deficiency. Thiamine deficiency impairs enzymes resulting in glutamate accumulation and cell damage with disruption of the cell membrane osmotic gradient, leading to edema. This condition was initially described by Carl Wernicke in 1881 as "superior acute hemorrhagic poliencephalitis." The classic triad of ataxia, oculomotor abnormalities, and confusion is present in only 16–38 % of patients with Wernicke encephalopathy. Consequently, the new diagnostic criteria include 2 out of 4 of the following findings: oculomotor abnormalities, cerebellar dysfunction, and altered mental status or

mild memory impairment. Characteristic imaging findings in alcoholic Wernicke encephalopathy include T2 hyperintensity and variable degrees of enhancement in the medial thalami, mammillary bodies, tectal plate, and periaqueductal gray matter (Fig. 2.10). Diffusion-weighted imaging findings in Wernicke encephalopathy ranges from decreased, normal, or increased ADC values. In contrast to alcoholic Wernicke encephalopathy, involvement of the cerebellum, cerebellar

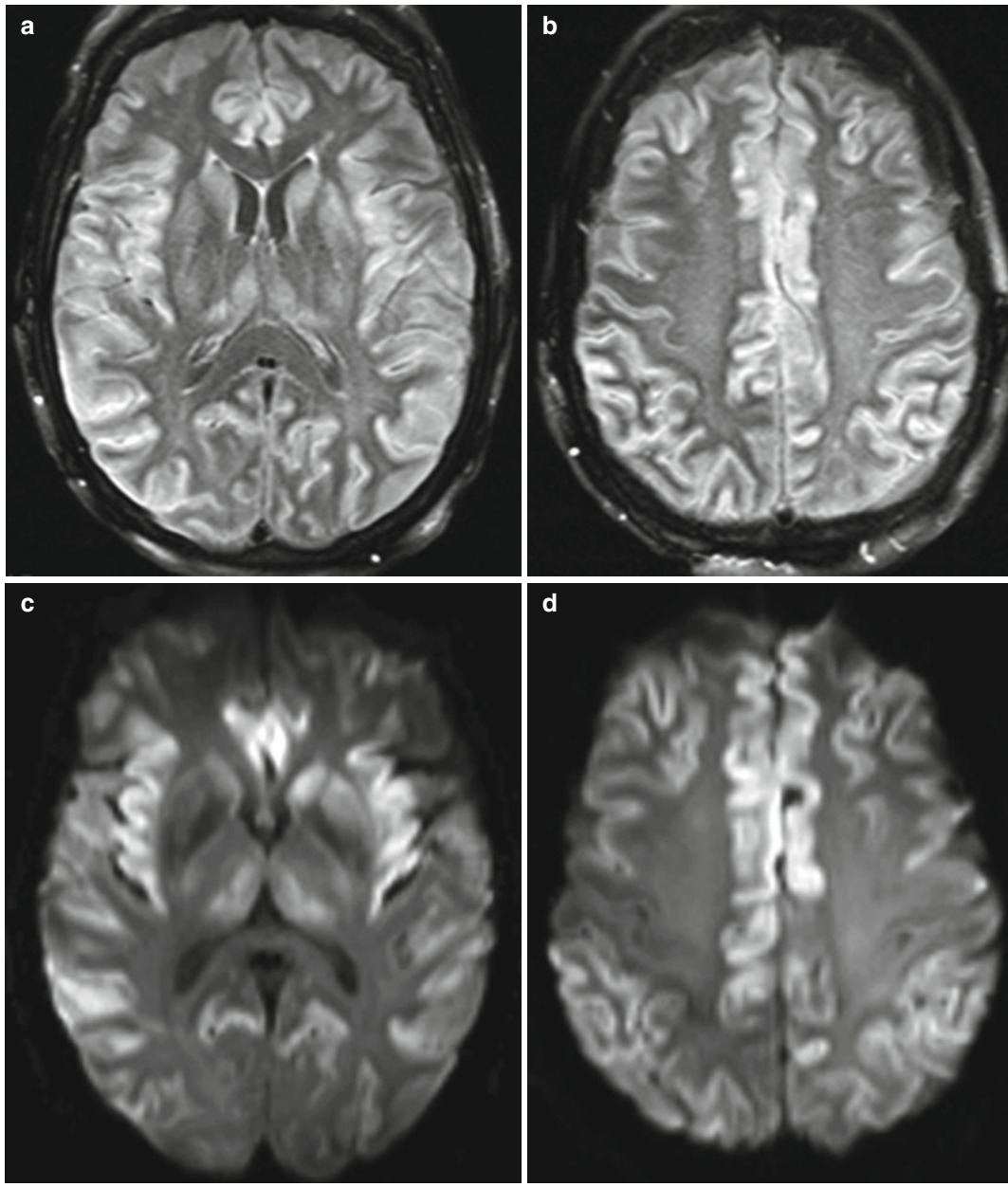

Fig. 2.7 Acute hepatic encephalopathy. Axial FLAIR MR images (**a**, **b**), DWI (**c**, **d**), and ADC maps (**e**, **f**) show diffuse gyriform hyperintensity and restricted diffusion predominantly affecting the bilateral frontal, insular, and temporal lobes

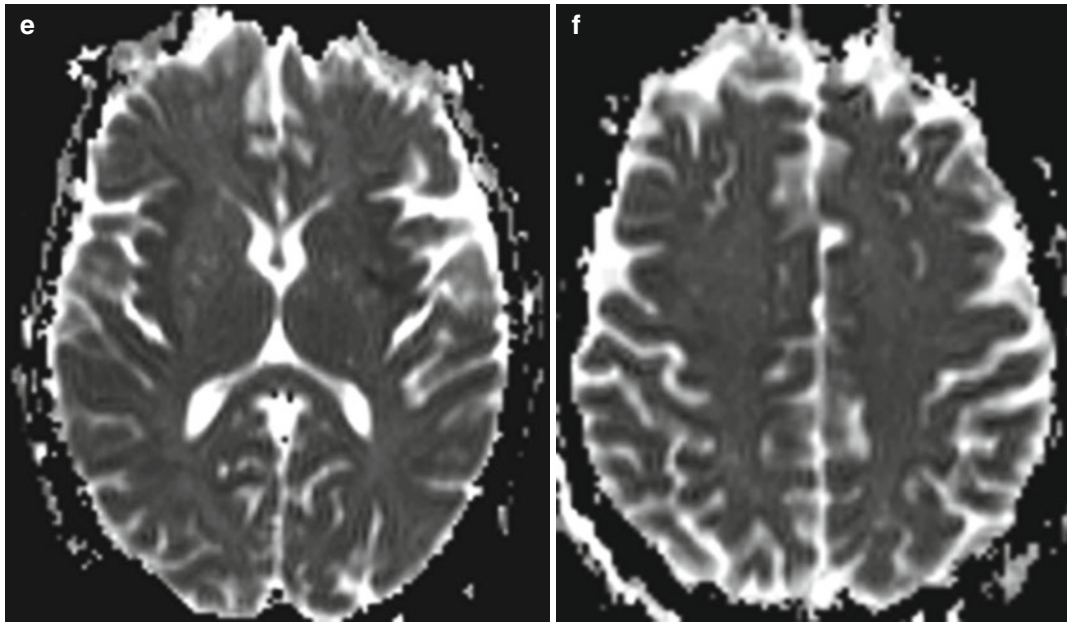

Fig. 2.7 (continued)

vermis, red nuclei, dentate nuclei, splenium of corpus callosum, fornix, cerebral cortex, cranial nerve nuclei, and basal ganglia has been identified only in nonalcoholic and pediatric patients with Wernicke encephalopathy (Fig. 2.11). The differential diagnosis of symmetric lesions of the medial thalami should include artery of Percheron infarct, deep cerebral vein thrombosis, virus encephalitis, acute disseminated encephalomyelitis, CNS lymphoma, and Creutzfeldt-Jakob disease variant (refer to Chap. 49).

Cerebral atrophy. Several studies on alcoholics have demonstrated significant volume loss in cortical and subcortical brain regions. Although there can be diffuse cerebral volume loss with chronic alcoholism, the frontal lobes, hippocampi, and cerebellar vermis are disproportionately affected (Fig. 2.12). Since the frontal lobes help regulate judgment, risk taking, motivation, mood, and wanting, the degeneration that occurs here is contributory to continued drinking despite awareness of these negative consequences. In addition to morphologic volume loss and resultant ex vacuo ventricular dilatation that can be demonstrated on both CT and MRI, ^{1}H MRS generally demonstrates lower concentrations of NAA and choline-containing compounds, most notably in the frontal lobes, medial temporal lobes, and cerebellum. Cross-sectional diffusion tensor imaging studies in alcohol-dependent individuals have indicated decreased fractional anisotropy and increased mean diffusivity in the genu, body and splenium of the corpus callosum, as well as in the centrum semiovale, which suggest compromised axonal/myelin integrity. Several other conditions can cause brain atrophy that resembles the effects of chronic alcoholism, including frontotemporal dementia and the effects of antiepileptic medications, such as dilantin (refer to Chap. 27).

Bilateral symmetric lipomatosis (Madelung disease, multiple symmetric lipomatosis, cephalothoracic lipodystrophy, Launois-Bensaude syndrome). It was originally called "fat neck" (Fetthals) by Madelung in 1888. Launois and Bensaude also characterized this condition in 1898, which accounts for the multiple eponyms. The disorder is characterized by painless symmetrical diffuse hypertrophy of brown adipose tissue. This condition has a propensity to affect alcoholic males, ages 30–60 years. The etiology is believed to be an abnormality in the synthesis of intracellular cyclic

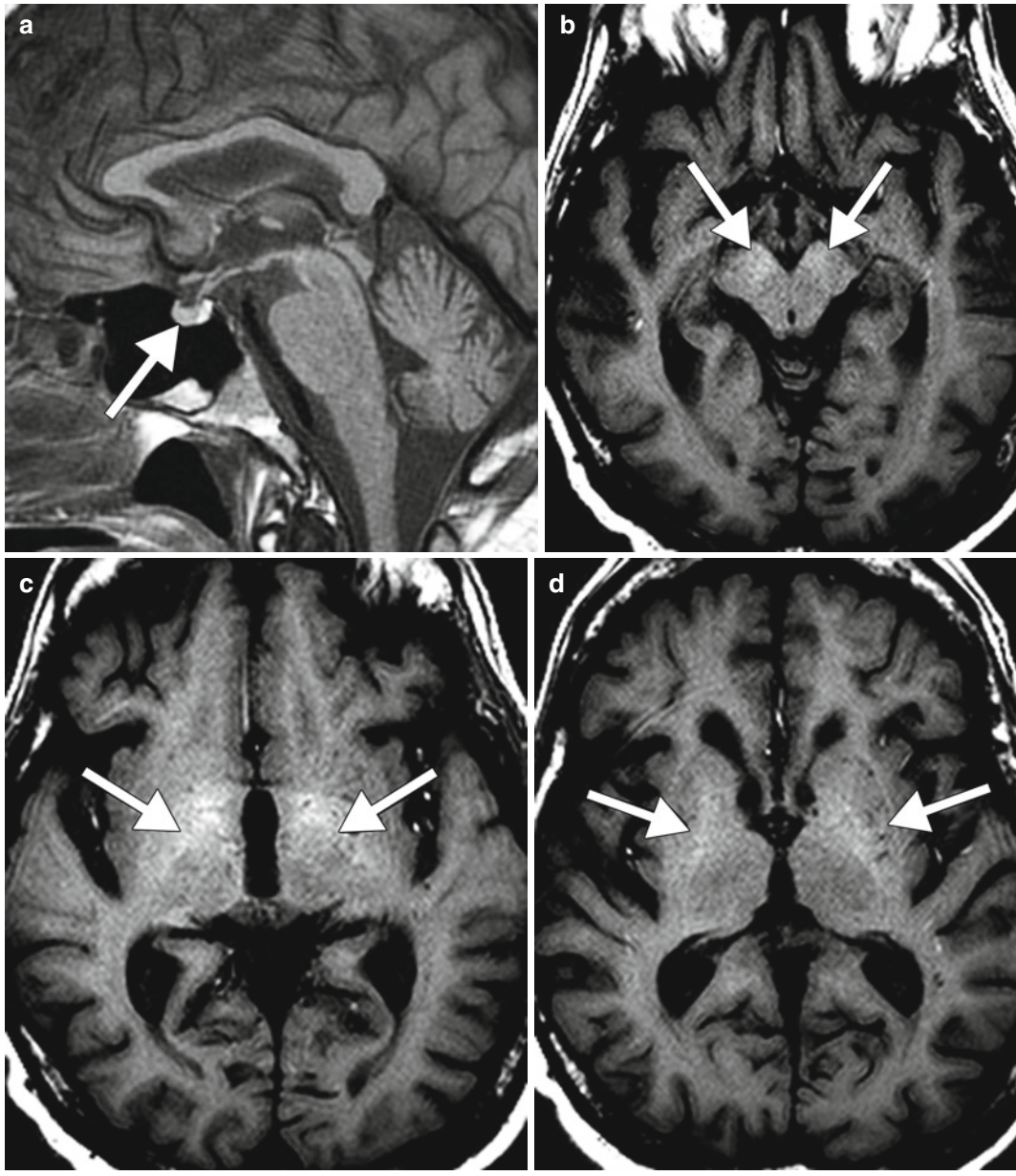

Fig. 2.8 Chronic hepatic encephalopathy. Sagittal T1 MRI (**a**) shows hyperintensity within the anterior pituitary (*arrow*). Axial T1 MR images (**b**–**d**) show hyperintensity within the bilateral basal ganglia and cerebral peduncles (*arrows*)

adenosine monophosphate (cAMP) induced by the stimulation of noradrenaline. The defect in adrenergic-stimulation lipolysis generates the autonomy of fat cells in bilateral symmetric lipomatosis. The main defect is in the catalytic unit of adenyl cyclase, and alcoholism seems to decrease beta-adrenergic receptors and to induce a disturbance in the mitochondrial NA in the adipose tissue, peripheral nerve, muscle, and central nervous system. CT can demonstrate nonencapsulated bilateral fat-attenuation masses in multiple compartments of the neck bilaterally, including the supraclavicular regions,

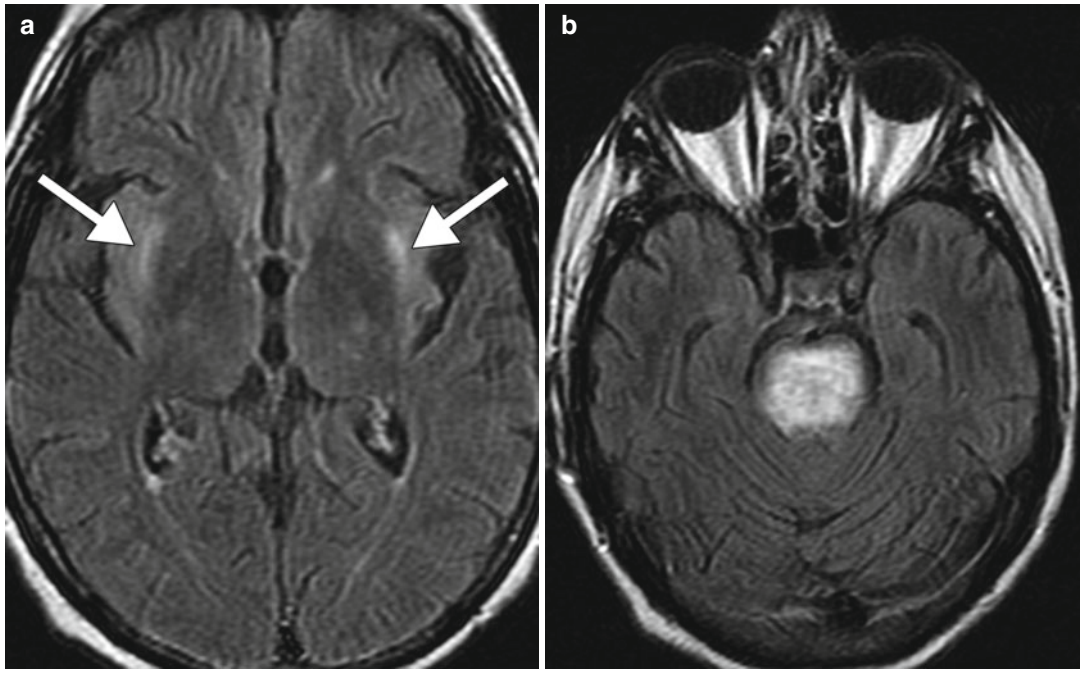

Fig. 2.9 Osmotic demyelination. Axial FLAIR MR images (**a**, **b**) show signal abnormality within the bilateral external capsules (*arrows*) and central pons

subcutaneous tissues, and anterior and posterior triangle of the neck (Fig. 2.13). Alcohol cessation may halt the progression of bilateral symmetric lipomatosis, but the condition does not regress. Rather, the fatty masses are amenable to surgical excision and liposuction. The differential diagnosis for bilateral symmetric lipomatosis includes obesity, the buffalo hump related to steroid use (refer to Chap. 46), and lipoma (Fig. 2.14).

Sialosis. Sialosis (sialadenosis) is a disorder of altered secretory and parenchymal function of the major salivary glands, most commonly the parotid. This condition is caused by autonomic neuropathy. On histology, there is adipose infiltration and edema. The condition presents as an indolent, bilateral, noninflammatory, nonneoplastic, soft, symmetrical, painless, and persistent enlargement of the salivary glands, most often associated with alcoholism, diabetes mellitus, and malnutrition. On imaging, there is bilateral diffuse homogenous enlargement of the affected salivary glands with soft tissue or fat attenuation or signal characteristics (Fig. 2.15). Differential considerations for sialosis include normal variants and Sjogren disease (Fig. 2.16). Imaging may be obtained in patients with sialosis in order to exclude the presence of a tumor.

Alcohol-related cancers. Ethanol in alcoholic beverages is considered a carcinogen. Although its metabolite acetaldehyde has not been shown to be directly carcinogenic in humans, animal studies indicate that it contributes to the increased risk of cancer in chronic alcohol drinkers, since it is known to damage DNA. There is a direct link between prolonged alcohol use and a risk of acquiring certain malignancies, including the oral cavity, pharynx, and larynx, esophageal squamous cell carcinomas, esophageal and gastric adenocarcinomas, hepatocellular carcinoma, and breast adenocarcinomas, among others. Compared to nondrinkers, those who regularly consume 3.5 or more drinks per day have two-to three-fold greater risk of developing head and neck squamous cell carcinoma. The risks are additive if a person smokes tobacco and drinks alcohol chronically (refer to Chap. 1). Squamous cell carcinomas of the head and neck can appear as enhancing or necrotic infiltrative

masses on CT and MRI (Fig. 2.17). ^{18}FDG-PET/CT is useful for detecting pathological lymphadenopathy associated with oral cavity, pharyngeal, and laryngeal squamous cell carcinomas, which typically appear markedly hypermetabolic (Fig. 2.18). Endoscopic ultrasound is useful for

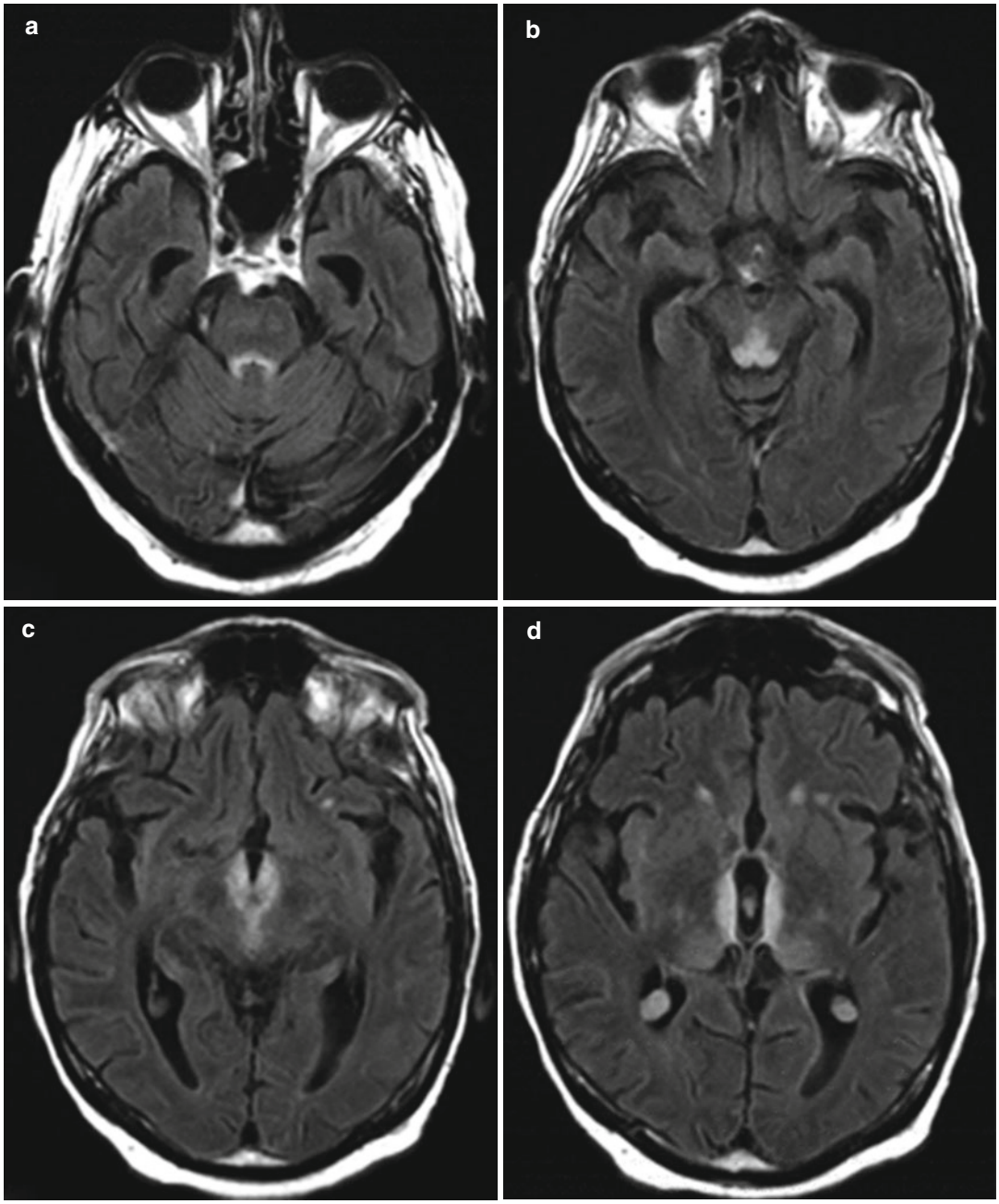

Fig. 2.10 Alcoholic Wernicke encephalopathy. The patient was found confused with whiskey bottles scattered throughout the home. Symmetric, abnormal T2 signal involving the periaqueductal gray, tectal plate, medial thalami, hypothalamus, and mammillary bodies with mild associated enhancement (*arrows*)

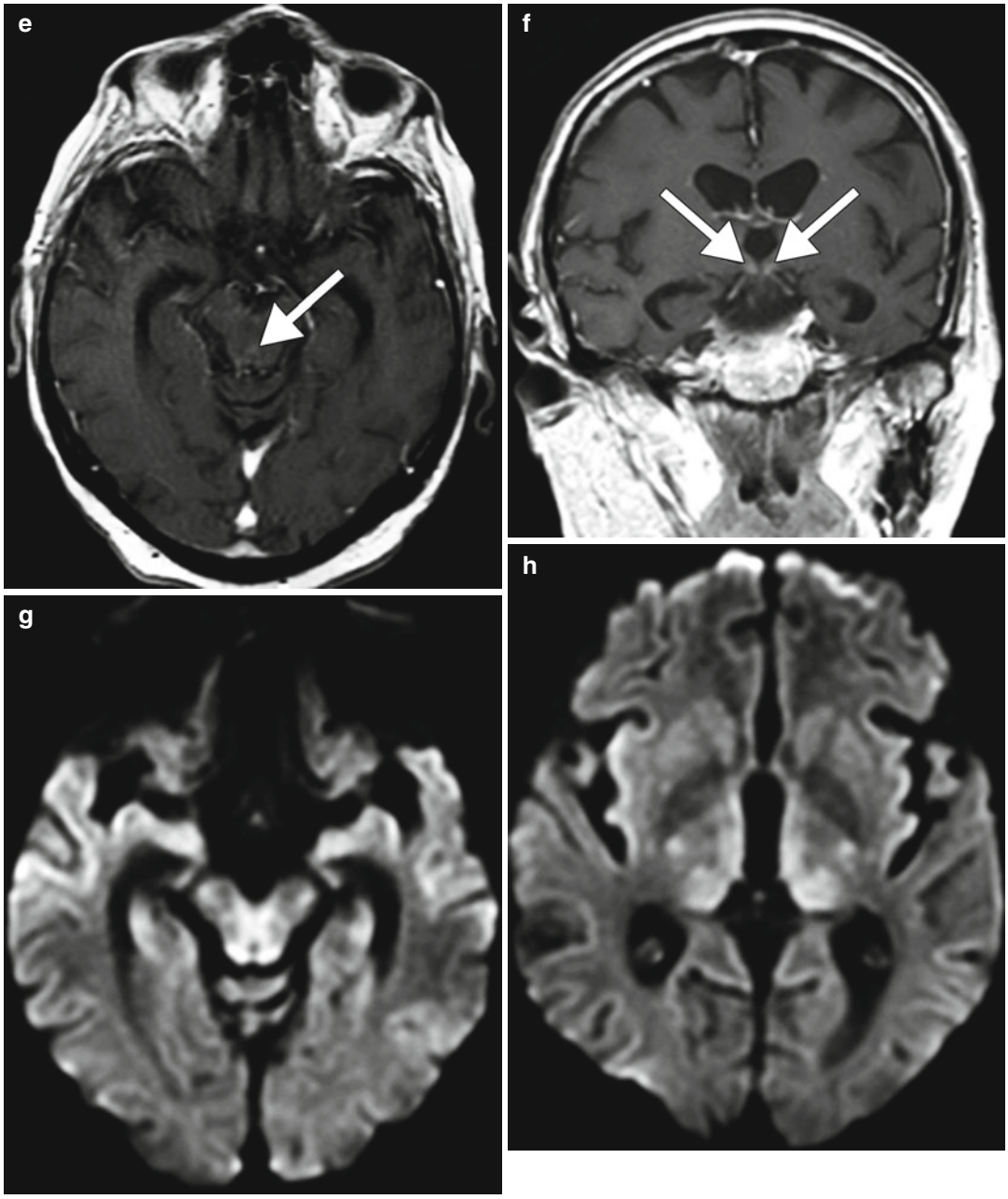

Fig. 2.10 (continued)

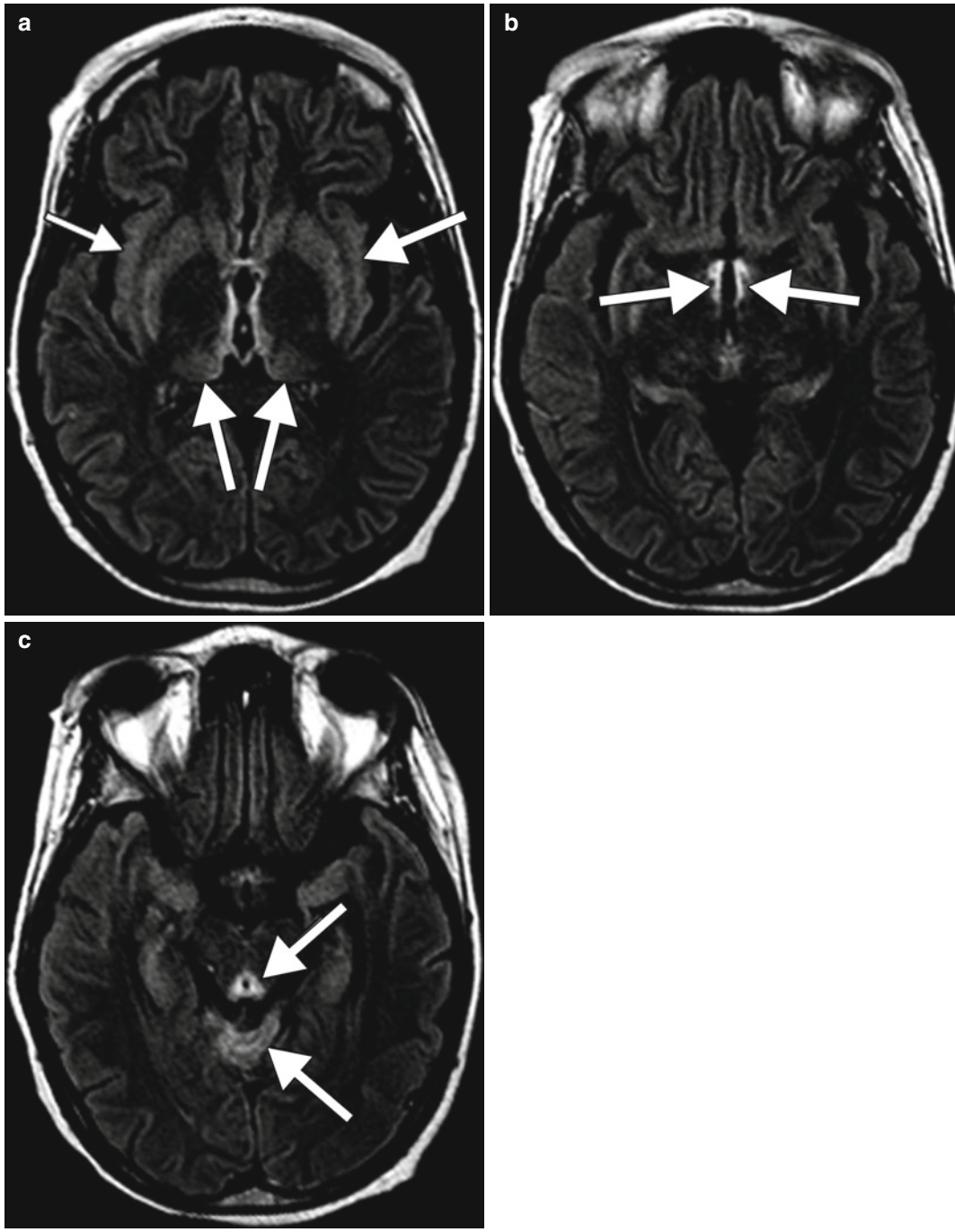

Fig. 2.11 Nonalcoholic Wernicke encephalopathy. Axial FLAIR MR images (**a**–**c**) show hyperintensity in the mammillary bodies, hypothalamus, thalamus, cerebellar vermis, and periaqueductal gray matter in a symmetric distribution (*arrows*)

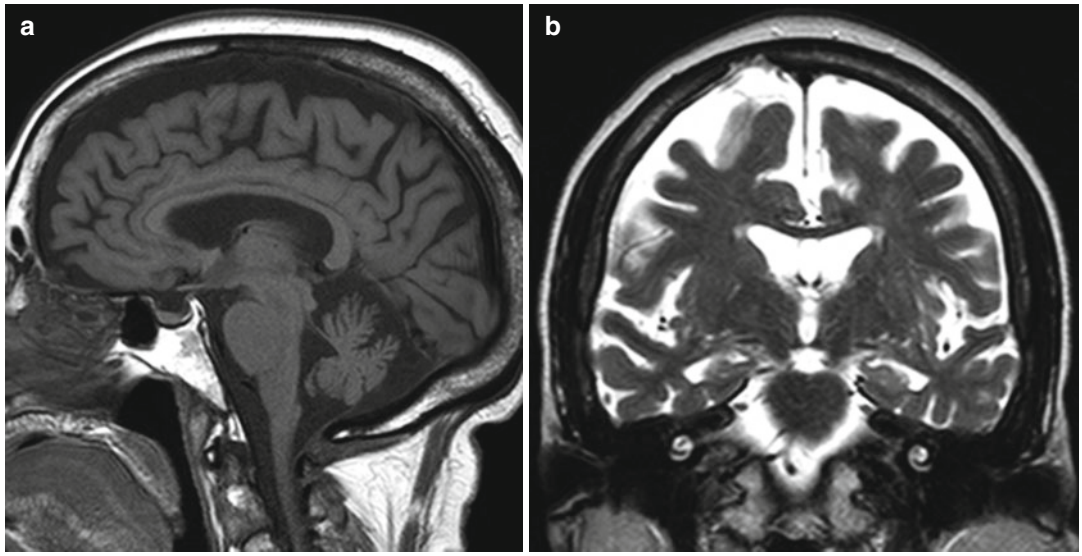

Fig. 2.12 Alcohol brain atrophy. (**a**) Sagittal T1-weighted MRI shows substantial volume loss of the cerebellar vemis. Coronal T2-weighted MRI (**b**) shows volume loss in the frontal lobes and hippocampi

staging esophageal carcinomas in conjunction with CT (Fig. 2.19). MRI is useful for evaluating the presence of intracranial metastases (Figs. 2.20 and 2.21).

Fetal alcohol syndrome (fetal alcohol spectrum disorder). Prenatal callosum alcohol exposure can have a wide spectrum of devastating effects upon the developing fetus. The main diagnostic criteria for fetal alcohol syndrome include maternal exposure to alcohol in utero; characteristic dysmorphic facial features, such as short palpebral fissures and smooth filtrum; growth retardation; and central nervous system malformations. The main structural abnormality that can be encountered on neuroimaging is partial or complete agenesis of the corpus callosum (Fig. 2.22). Neuroimaging may also be obtained to evaluate cleft palate and choanal atresia in patients with fetal alcohol syndrome.

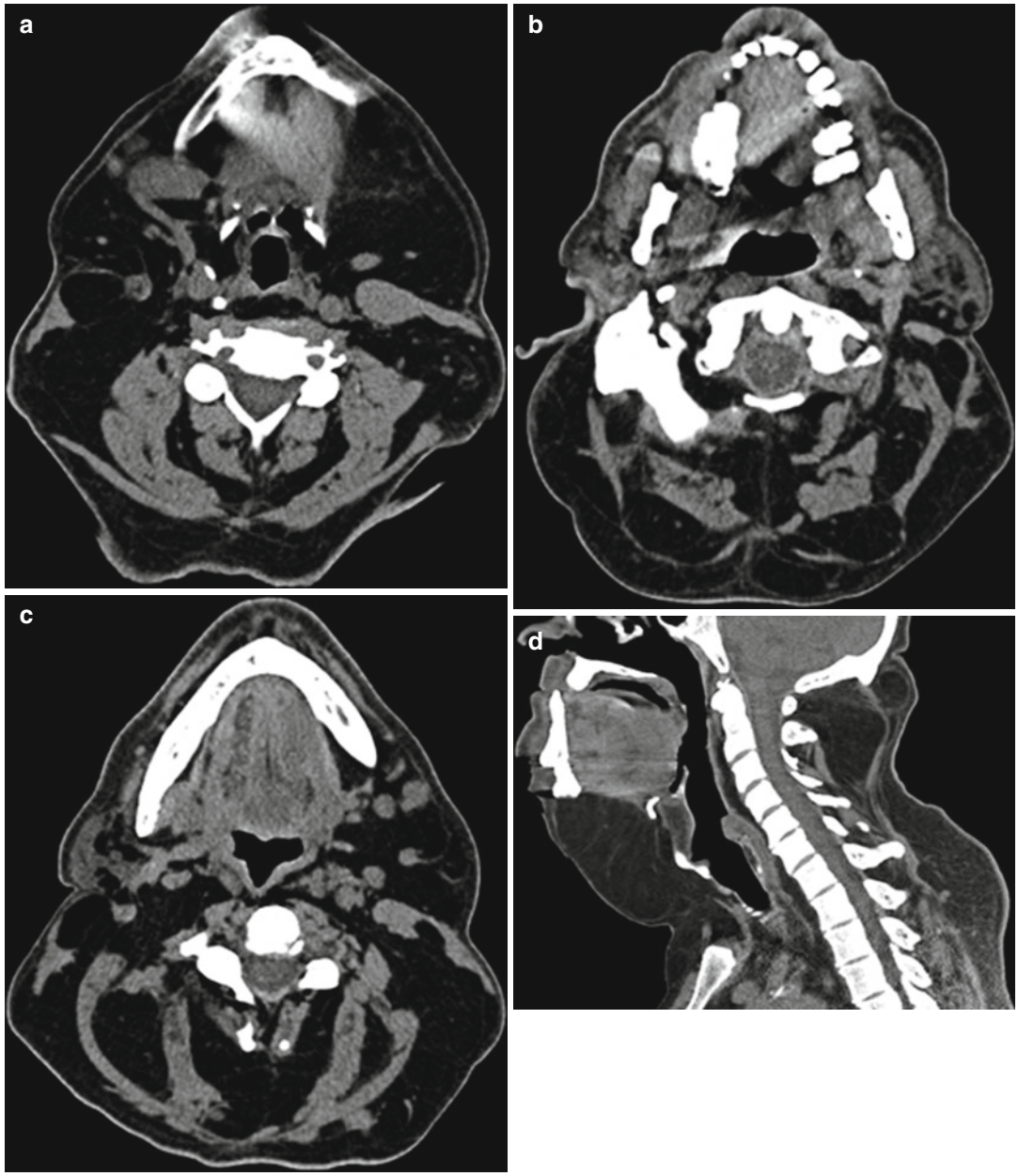

Fig. 2.13 Multiple symmetric lipomatosis. The patient is a middle-aged male with progressive increase in size of the neck and a history of abundant alcohol consumption. Axial (**a**–**c**) and sagittal (**d**) CT images show extensive fat attenuation deposits within the bilateral superficial and deep compartments of the neck in a symmetric distribution that essentially corresponds to the expected location of brown fat

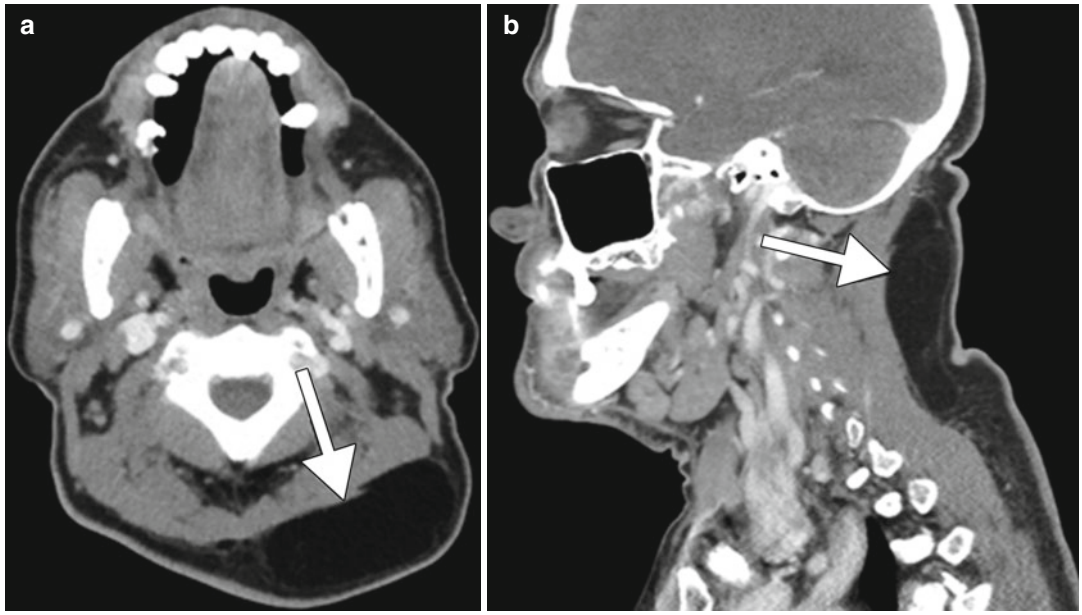

Fig. 2.14 Lipoma. Axial (**a**) and sagittal (**b**) CT images show a homogeneous fat-attenuation mass in the left posterior neck subcutaneous tissues (*arrows*)

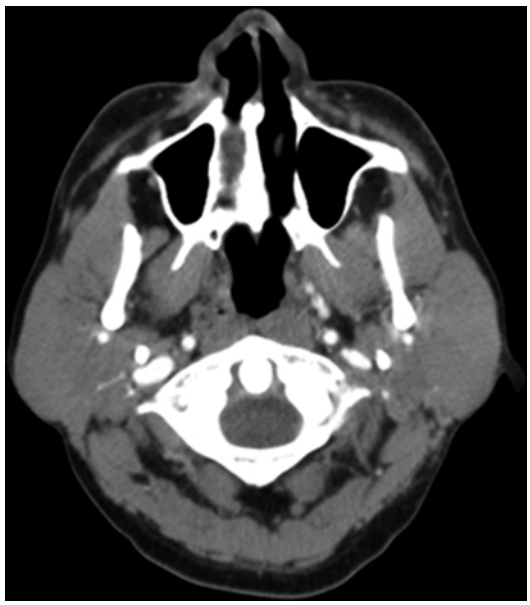

Fig. 2.15 Alcohol-induced sialosis. Axial CT image shows homogeneous diffuse enlargement of the bilateral parotid glands

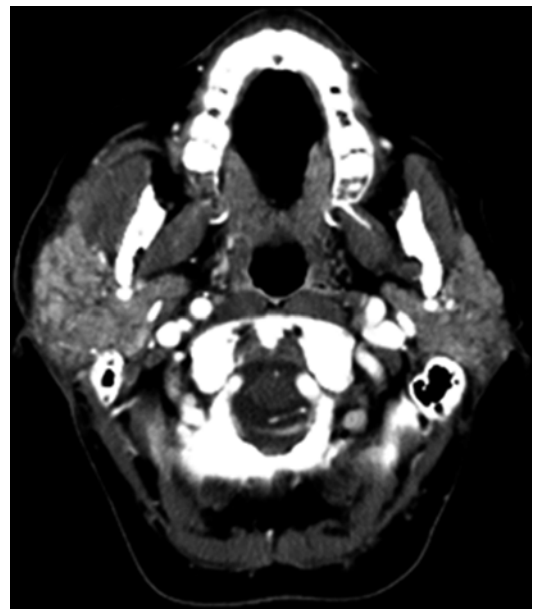

Fig. 2.16 Sjogren disease. Axial CT image shows bilateral enlarged parotid glands with nodular consistency

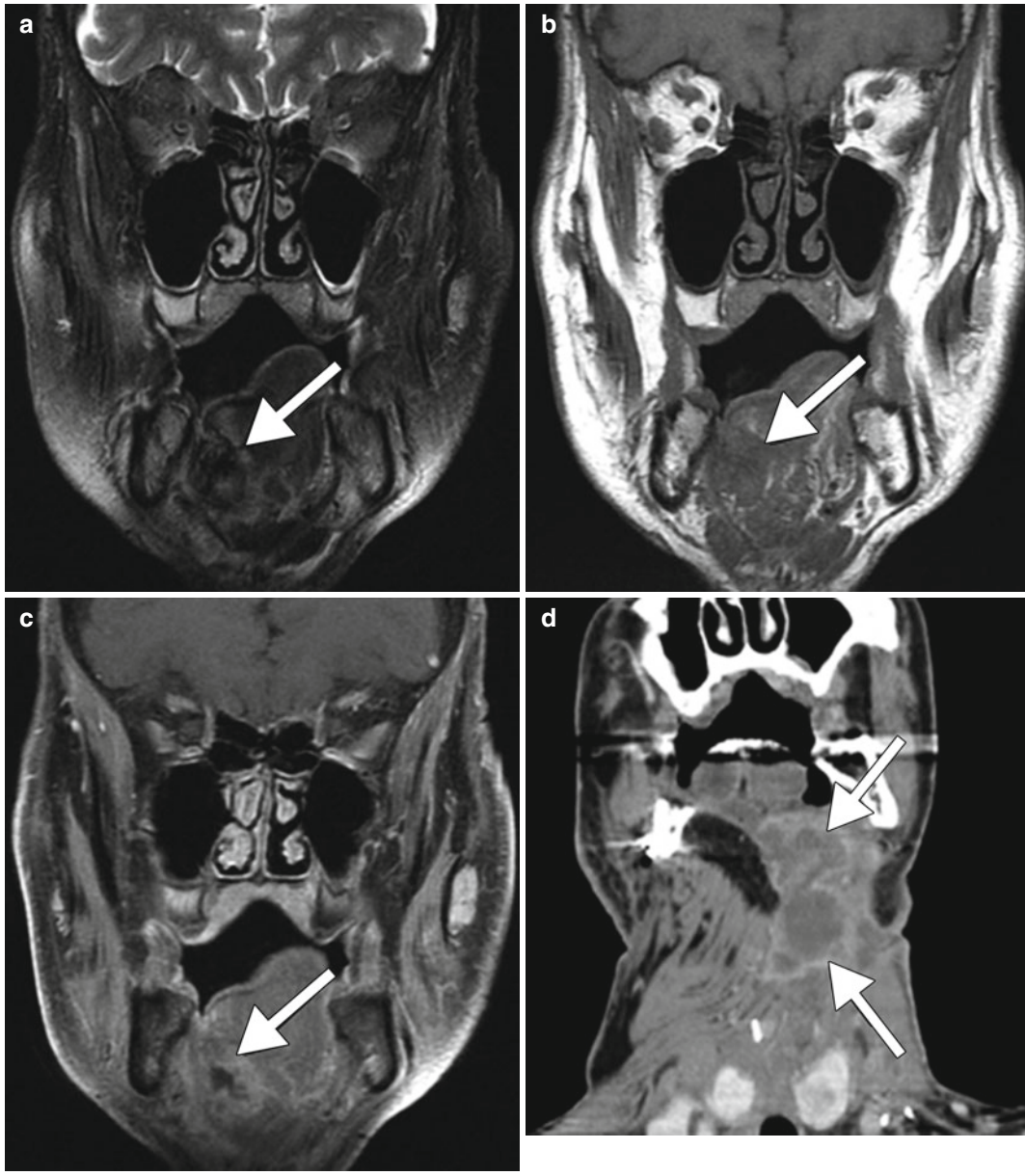

Fig. 2.17 Oral cavity squamous cell carcinoma presumably related to alcohol abuse. Coronal fat-suppressed T2 (**a**), coronal T1 (**b**), and coronal fat-suppressed post-contrast T1 (**c**) show an infiltrative ulcerated heterogeneously enhancing mass that occupies the right floor of the mouth (*arrows*). Postoperative follow-up post-contrast CT (**d**) shows a large necrotic recurrent tumor (*arrows*), adjacent to the graft

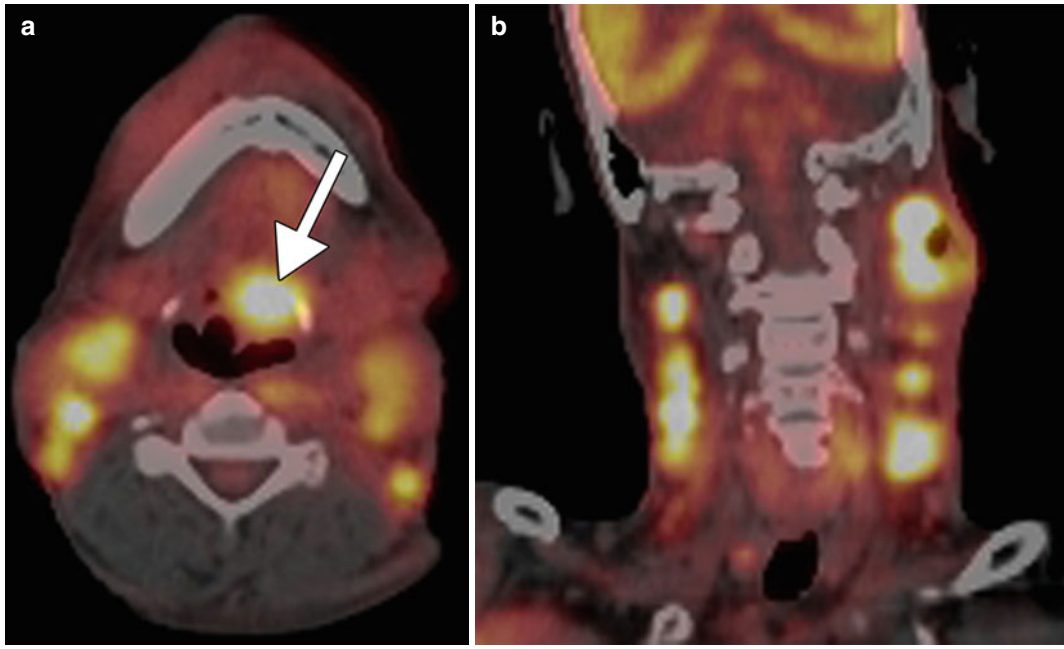

Fig. 2.18 Oropharynx squamous cell carcinoma presumably related to alcohol abuse. Axial (**a**) and coronal (**b**) fusion FDG-PET/CT shows a hypermetabolic left tongue base mass (*arrow*) and extensive bilateral cervical lymphadenopathy

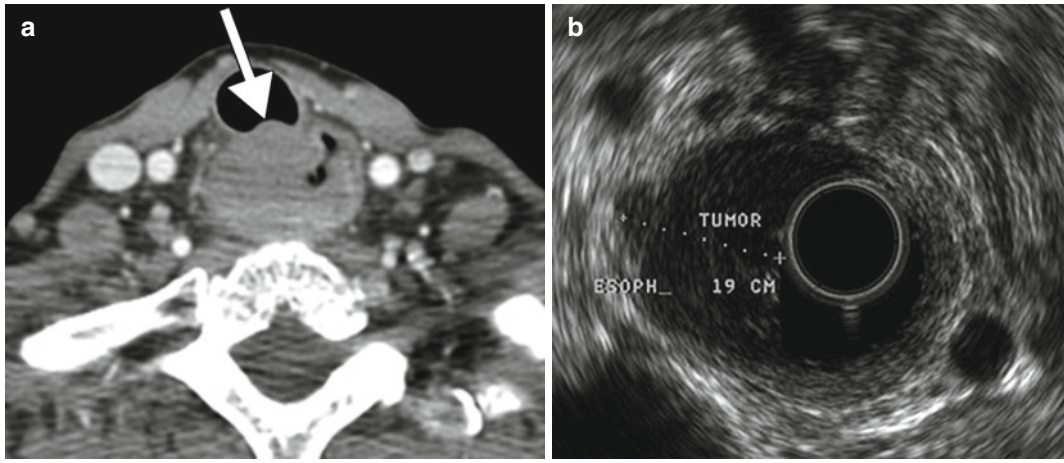

Fig. 2.19 Esophageal squamous cell carcinoma presumably related to alcohol abuse. Axial CT image (**a**) shows bulky right esophageal mass that involves the party wall (*arrow*). Transverse endoscopic ultrasound image (**b**) shows that the infiltrative hypoechoic tumor extends beyond the esophageal wall

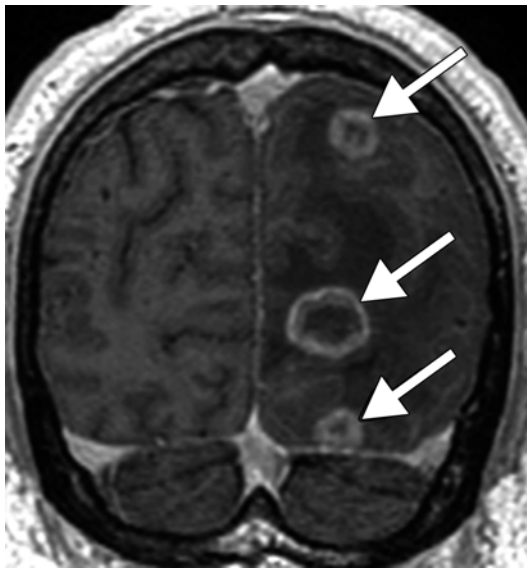

Fig. 2.20 Esophageal squamous cell carcinoma metastases presumably related to alcohol abuse. Coronal post-contrast T1-weighted MRI shows multiple ring-enhancing brain metastases with surrounding vasogenic edema in the left hemisphere (*arrows*)

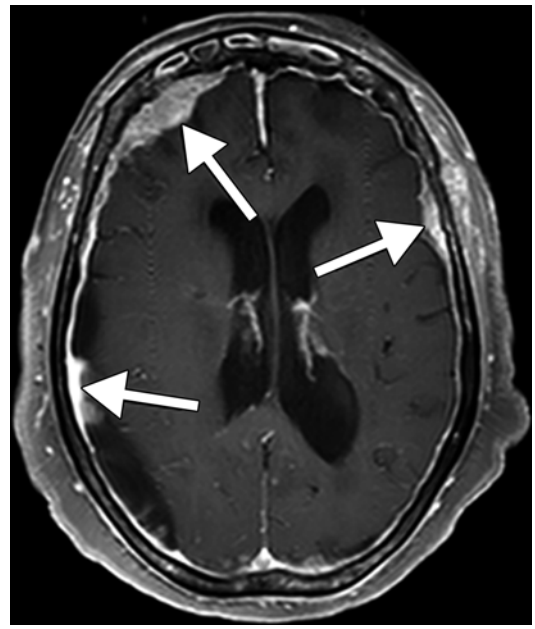

Fig. 2.21 Hepatocellular carcinoma metastases presumably related to alcohol abuse. Axial post-contrast T1-weighted MRI shows multiple dural-based enhancing tumor deposits (*arrows*). There is an associated right cerebral convexity subdural collection (malignant effusion)

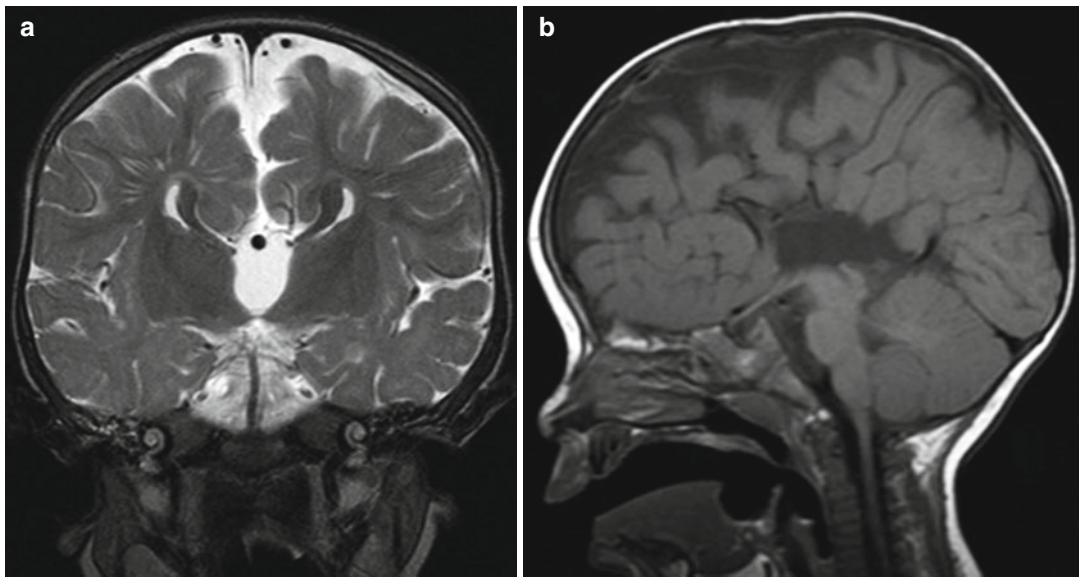

Fig. 2.22 Fetal alcohol syndrome. Coronal T2-weighted MRI (**a**) and sagittal T1-weighted MRI (**b**) show agenesis of the corpus callosum

Suggested Reading

Antunez E, Estruch R, Cardenal C, Nicolas JM, Fernandez-Sola J, Urbano-Marquez A. Usefulness of CT and MR imaging in the diagnosis of acute Wernicke's encephalopathy. AJR Am J Roentgenol. 1998;171(4):1131–7.

Arbelaez A, Pajon A, Castillo M. Acute Marchiafava-Bignami disease: MR findings in two patients. AJNR Am J Neuroradiol. 2003;24(10):1955–7.

Boffetta P, Hashibe M, La Vecchia C, Zatonski W, Rehm J. The burden of cancer attributable to alcohol drinking. Int J Cancer. 2006;119(4):884–7.

Bombardier CH. Alcohol use and traumatic brain injury. West J Med. 1995;162(2):150–1.

Carda C, Gomez de Ferraris C, Arriaga A, Carranza M, Peydró A. Alcoholic parotid sialosis: a structural and ultrastructural study. Med Oral. 2004;9(1):24–32.

Carrilho PE, Santos MB, Piasecki L, Jorge AC. Marchiafava-Bignami disease: a rare entity with a poor outcome. Rev Bras Ter Intensiva. 2013;25(1):68–72.

Crews FT, Nixon K. Mechanisms of neurodegeneration and regeneration in alcoholism. Alcohol Alcohol. 2009;44(2):115–27.

Faul M, Xu L, Wald MM, Coronado VG. Traumatic brain injury in the United States: emergency department visits, hospitalizations, and deaths. Atlanta (GA): Centers for Disease Control and Prevention, National Center for Injury Prevention and Control; 2010.

Freedland ES, McMicken DB, D'Onofria G. Alcohol and trauma. Emerg Med Clin North Am. 1993;11:225–39.

Gadzinski S, Durazzo TC, Mon A, Yeh PH, Meyerhoff DJ. Cerebral white matter recovery in abstinent alcoholics – a multimodality magnetic resonance study. Brain. 2010;133(4):1043–53.

Geibprasert S, Gallucci M, Krings T. Alcohol-induced changes in the brain as assessed by MRI and CT. Eur Radiol. 2010;20(6):1492–501.

González-García R, Rodríguez-Campo FJ, Sastre-Pérez J, Muñoz-Guerra MF. Benign symmetric lipomatosis (Madelung's disease): case reports and current management. Aesthetic Plast Surg. 2004;28(2):108–12; discussion 113.

Gurney JG, Rivara FP, Mueller FP, Mueller BA, Newell DW, Copass MK, Jurkovich GJ. The effects of alcohol intoxication on the initial treatment and hospital course of patients with acute brain injury. J Trauma. 1992;33:709–13.

Ha ND, Weon YC, Jang JC, Kang BS, Choi SH. Spectrum of MR imaging findings in Wernicke encephalopathy: are atypical areas of involvement only present in nonalcoholic patients? AJNR Am J Neuroradiol. 2012;33(7):1398–402.

Hazell AS, Butterworth RF. Hepatic encephalopathy: an update of pathophysiologic mechanisms. Proc Soc Exp Biol Med. 1999;222:99–112.

Hermans R, Verellen S, Vergote G, D'Haenens P, Baert AL. Benign symmetric lipomatosis of the neck or Madelung-Launois-Bensaude syndrome, also known as Madelung's neck: CT findings in two cases. Rofo. 1994;161(3):248–50.

Kastin B, Mandel L. Alcoholic sialosis. N Y State Dent J. 2000;66(6):22–4.

Lee B, Newberg A. Neuroimaging in traumatic brain imaging. NeuroRx. 2005;2:372–83.

Lockwood AH, Weissenborn K, Buttorworth RF. An image of the brain in patients with liver disease. Curr Opin Neurol. 1997;10:525–33.

Ménégon P, Sibon I, Pachai C, Orgogozo JM, Dousset V. Marchiafava-Bignami disease: diffusion-weighted MRI in corpus callosum and cortical lesions. Neurology. 2005;65(3):475–7.

Morgan TR, Mandayam S, Jamal MM. Alcohol and hepatocellular carcinoma. Gastroenterology. 2004;127 (5 Suppl 1):S87–96.

Nelson DE, Jarman DW, Rehm J, et al. Alcohol-attributable cancer deaths and years of potential life lost in the United States. Am J Public Health. 2013;103(4):641–8.

Rovira A, Alonso J, Cordoba J. MR imaging findings in hepatic encephalopathy. AJNR Am J Neuroradiol. 2008;29:1612–21.

Scoccianti C, Straif K, Romieu I. Recent evidence on alcohol and cancer epidemiology. Future Oncol. 2013;9(9): 1315–22.

Sia KJ, Tang IP, Tan TY. Multiple symmetrical lipomatosis: case report and literature review. J Laryngol Otol. 2012;126(7):756–8.

Spadoni AD, McGee CL, Fryer SL, Riley EP. Neuroimaging and fetal alcohol spectrum disorders. Neurosci Biobehav Rev. 2007;31(2):239–45.

Swayze 2nd VW, Johnson VP, Hanson JW, Piven J, Sato Y, Giedd JN, Mosnik D, Andreasen NC. Magnetic resonance imaging of brain anomalies in fetal alcohol syndrome. Pediatrics. 1997;99(2):232–40.

White ML, Zhang Y, Andrew LG, Hadley WL. MR imaging with diffusion-weighted imaging in acute and chronic Wernicke encephalopathy. AJNR Am J Neuroradiol. 2005;26(9):2306–10.

Zuccoli G, Pipitone N. Neuroimaging findings in acute Wernicke's encephalopathy: review of the literature. AJR Am J Roentgenol. 2009;192(2):501–8.

Zuccoli G, Gallucci M, Capellades J, Regnicolo L, Tumiati B, Giadás TC, Bottari W, Mandrioli J, Bertolini M. Wernicke encephalopathy: MR findings at clinical presentation in twenty-six alcoholic and nonalcoholic patients. AJNR Am J Neuroradiol. 2007;28(7):1328–31.

Zuccoli G, Santa Cruz D, Bertolini M, Rovira A, Gallucci M, Carollo C, Pipitone N. MR imaging findings in 56 patients with Wernicke encephalopathy: nonalcoholics may differ from alcoholics. AJNR Am J Neuroradiol. 2009;30(1):171–6.

Zuccoli G, Siddiqui N, Cravo I, Bailey A, Gallucci M, Harper CG. Neuroimaging findings in alcohol-related encephalopathies. AJR Am J Roentgenol. 2010;195(6): 1378–84.

Methanol

3

Allan Lee, Dee Nandurkar, and Ronil V. Chandra

3.1 Uses

Methanol has many uses in industry and automotives, including fuels and antifreeze. Methanol can serve as a denaturant for ethanol, producing "methylated spirit." This was commonly used during the Prohibition to discourage consumption of bootlegged liquor. More recently, abuse of methanol-containing products through inhalation, such as sniffing glue or carburetor cleaner, has been of clinical concern. Methanol intoxication may also occur after suicidal or accidental ingestion of industrial solvents, antifreeze, or fraudulently altered alcoholic beverages.

3.2 Mechanism

Alcohol dehydrogenase metabolizes methanol to formaldehyde, which is then converted to formic acid. Formic acid causes metabolic acidosis and inhibits mitochondrial c oxidase, leading to tissue hypoxia.

A. Lee, MBBS, FRANZCR
D. Nandurkar, MBBS, FRANZCR
R.V. Chandra, MBBS, MMed, FRANZCR (✉)
Department of Diagnostic Imaging,
Monash Medical Center, Monash Health,
Melbourne, VIC, Australia
e-mail: ronilvchandra@gmail.com

3.3 Discussion

There is typically a latent period between 8 and 48 h after initial exposure prior to onset of symptoms. The hallmark initial visual disturbance is due to toxic optic nerve demyelination or necrosis. Associated gastrointestinal symptoms such as nausea, vomiting, and abdominal pain are common. As intoxication ensues, progressive neurological deterioration occurs, ultimately leading to coma.

The characteristic pathological finding is bilateral putaminal hemorrhagic necrosis, which may be evident on both CT and MRI. There may also be extensive focal or confluent subcortical white matter edema or necrosis (Fig. 3.1). Optic nerve, pontine tegmental, and cerebellar edema or necrosis may also occur. The affected areas are typically hyperintense on FLAIR with diffusion restriction, and areas of susceptibility may be evident in the putamina from hemorrhagic necrosis (Fig. 3.2). There may be associated contrast enhancement. If the patient survives, cystic cavities may develop in the putamina.

Emergent management of acute methanol ingestion involves initial resuscitation, enhanced elimination via dialysis, competitive inhibition of alcohol dehydrogenase using enteral or intravenous ethanol or fomepizole, and treatment of the metabolic acidosis. In spite of treatment, mortality rates are extremely high, particularly for patients with seizure or coma on presentation.

D.T. Ginat et al. (eds.), *Neuroimaging Pharmacopoeia*,
DOI 10.1007/978-3-319-12715-6_3,

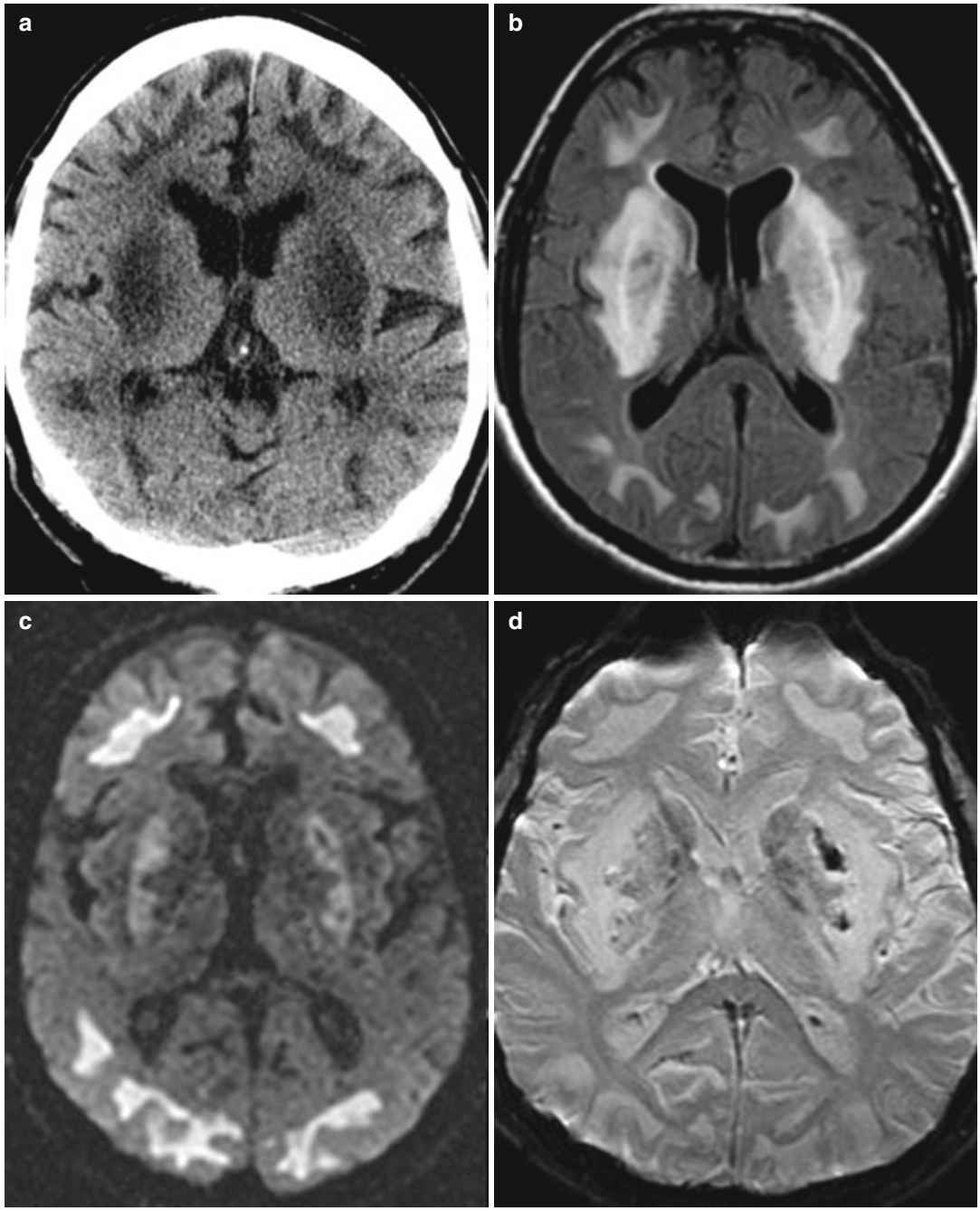

Fig. 3.1 Methanol intoxication. Axial non-contrast CT image (**a**) demonstrates bilateral symmetrical putaminal and subcortical white matter hypoattenuation. Axial FLAIR (**b**), DWI (**c**), and T2*-weighted (**d**) MRI sequences performed 4 days later show symmetrical putaminal and subcortical white matter FLAIR hyperintensity with diffusion restriction. T2* imaging confirms the presence of associated putaminal hemorrhage. The patient did not survive

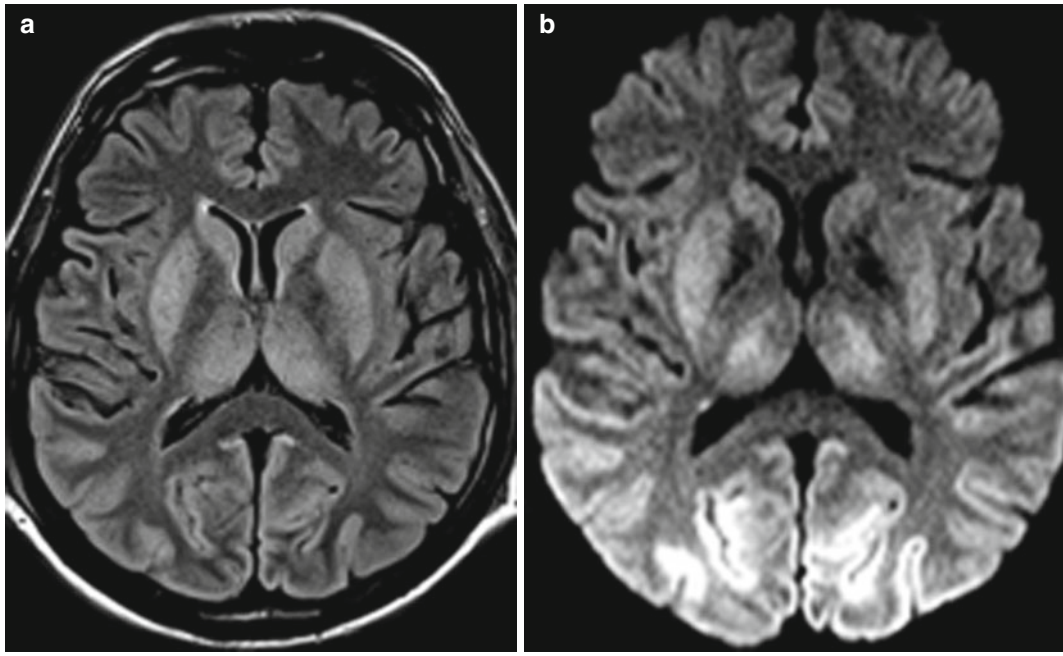

Fig. 3.2 A 60-year-old man with cerebral hypoxic injury from cardiac arrest. Axial FLAIR (**a**) and DWI (**b**) MR images show bilateral symmetrical basal ganglia and thalamic and occipital lobe cortical T2 hyperintensity and diffusion restriction

3.4 Differential Diagnosis

Bilateral putaminal necrosis can be seen in other conditions. However, when a patient presents with initial visual disturbance with imaging revealing bilateral putaminal and subcortical white matter abnormalities, methanol intoxication should be strongly considered.

- *Hypoxic injury:* Brain injury patterns are variable depending on the severity and duration of hypoxia. Symmetrical basal ganglia T2 hyperintensities with diffusion restriction typically occur in severe hypoxic injury. However, this is often accompanied by loss of gray-white differentiation of the cerebral cortex on CT and/or cortical T2 hyperintensities and diffusion restriction on MRI; such cortical changes are not typically associated with methanol intoxication (Fig. 3.2).
- *Viral encephalitis:* Flavivirus infections such as Japanese encephalitis, West Nile fever, and Murray Valley fever typically demonstrate symmetric involvement of the deep gray matter structures. On MRI, this appears as swelling and T2 hyperintensity of these structures (Fig. 3.3). Restricted diffusion and intralesional hemorrhage may also be observed. Other sites that may be involved include the substantia nigra, red nucleus, pons, hippocampi, cerebral cortex, and cerebellum, depending upon the particular virus.
- *Wilson's disease:* An uncommon autosomal recessive inborn defect in copper metabolism resulting in abnormal copper deposition particularly in the brain, liver, and cornea (Kayser-Fleischer ring). Patients usually present in childhood or early adulthood with neurological or hepatic dysfunction and psychiatric disorder. Signal abnormalities on MRI are commonly present in the putamen, caudate nuclei, thalami, and midbrain with less frequent involvement of the white matter and posterior fossa (Fig. 3.4). These may be hyperintense or hypointense on T1- and T2-weighted

Fig. 3.3 Viral encephalitis. Axial FLAIR MRI shows extensive diffuse hyperintensity and swelling of the cerebral cortex, basal ganglia, and posterior thalami (*arrows*)

sequences depending on the underlying pathology of edema, gliosis, necrosis, cavitation, paramagnetic effects of copper, and superimposed hepatic disease.

- *Leigh's disease:* A progressive neurodegenerative disorder that usually presents in infancy or early childhood. The characteristic MRI findings are bilateral symmetrical areas of T2 hyperintensity in the basal ganglia, thalamus, brainstem, cerebellar white matter, and gray matter of the spinal cord (Fig. 3.5).

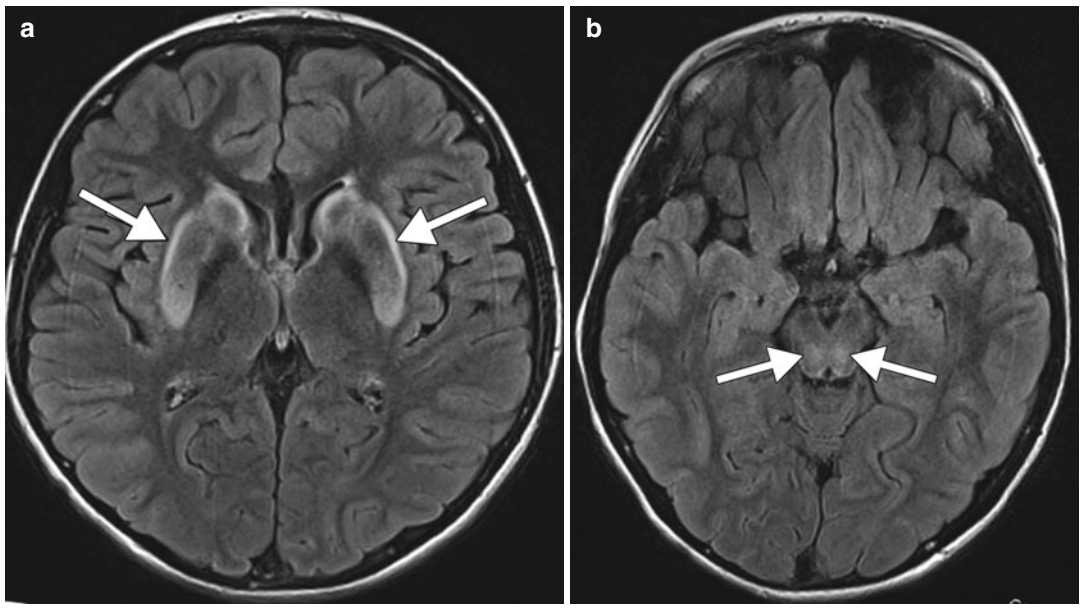

Fig. 3.4 Wilson's disease. Axial FLAIR MR images (**a**, **b**) show abnormal hyperintensity in the bilateral basal ganglia and midbrain (*arrows*)

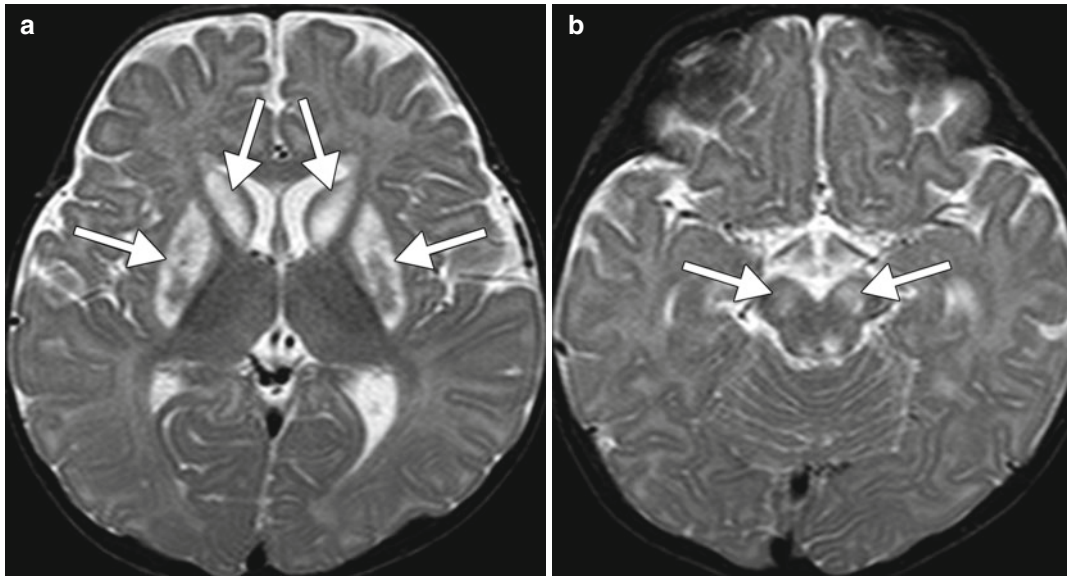

Fig. 3.5 Leigh's disease. Axial T2-weighted MR images (**a**, **b**) show symmetric hyperintensity in the bilateral basal ganglia and midbrain (*arrows*)

Suggested Reading

Blanco M, Casado R, Vazquez F, Pumar JM. CT and MR imaging findings in methanol intoxication. AJNR Am J Neuroradiol. 2006;27:452–4.

Carrasquillo O, Daya MR, Kales SN, Liu JJ. Prognostic factors in patients with methanol poisoning. J Toxicol Clin Toxicol. 1998;36(3):175–81.

Chu BC, Terae S, Takahashi C, Kikuchi Y, Miyasaka K, Abe S, Minowa K, Sawamura T. MRI of the brain in the Kearns-Sayre syndrome: a report of four cases and a review. Neuroradiology. 1999;41(10):759–64.

Gaul HP, Wallace CJ, Auer RN, Fong TC. MR findings in methanol intoxication. AJNR Am J Neuroradiol. 1995;16:1783–6.

Halavaara J, Valanne L, Setala K. Neuroimaging supports the clinical diagnosis of methanol poisoning. Neuroradiology. 2002;44:924–8.

Sefidbakht S, Rasekhi AR, Kamali K, Borhani Haghighi A, Salooti A, Meshksar A, Abbasi HR, Moghadami M, Nabavizadeh SA. Methanol poisoning: acute MR and CT findings in nine patients. Neuroradiology. 2007;49(5):427–35.

Cannabis (Marijuana)

4

Eileen C. Ang, Stephen L. Stuckey,
Daniel Thomas Ginat, and Ronil V. Chandra

4.1 Uses

Cannabis products (marijuana, weed, hashish) are psychoactive drugs that have euphorigenic and anxiolytic properties. Medical use of cannabis is controversial and illegal in most countries. Cannabis is not approved as a medication by the United States Food and Drug Administration. However, some states permit medical treatment with low-dose synthetic cannabinoids for management of pain and nausea in chronically ill patients. Methods for administration include ingestion of extracts or oral capsules, smoking, or inhalation of vaporized fumes.

4.2 Mechanism

Two species of cannabis produce useful amounts of psychoactive cannabinoids. The principal active component in recreational cannabis is Δ^9- tetrahydrocannabinol (THC), extracted from the plant *Cannabis sativa*. THC exerts its central effects by interacting with cannabinoid-1 (CB1) receptors found primarily in the limbic system, frontal cortex, basal ganglia, and cerebellum. In medical cannabis, the principal active ingredient is cannabidiol (CBD), which is found in high concentration in *Cannabis indica*. CBD binds to cannabinoid-2 (CB2) receptors, which are predominantly found in gastrointestinal and immune tissues.

4.3 Discussion

A potential consequence of consumption of cannabis is reversible cerebral vasoconstriction syndrome (RCVS). Indeed, cannabis may represent the most common cause of RCVS in some countries. Cannabis is a vasoactive agent that can alter cerebral vasomotor tone, resulting in multifocal vascular narrowing. Other neurological/psychological effects of cannabis include euphoria, relaxation, and increased appetite, as well as impaired motor skills and speech, reduced short-term memory, lethargy, psychosis, dizziness, and paranoia.

The main clinical presentation of RCVS is sudden-onset severe thunderclap headache associated with photophobia, nausea, and vomiting. The primary radiological CNS manifestation

E.C. Ang, MBBS
S.L. Stuckey, MBBS, MMed, MD, FRANZCR
R.V. Chandra, MBBS, MMed, FRANZCR
Department of Diagnostic Imaging,
Monash Medical Center, Monash Health,
Melbourne, VIC, Australia
e-mail: ronilvchandra@gmail.com

D.T. Ginat, MD, MS (✉)
Department of Radiology, University of Chicago,
Pritzker Medical School, Chicago, IL, USA
e-mail: ginatd01@gmail.com

D.T. Ginat et al. (eds.), *Neuroimaging Pharmacopoeia*,
DOI 10.1007/978-3-319-12715-6_4, © Springer International Publishing Switzerland 2015

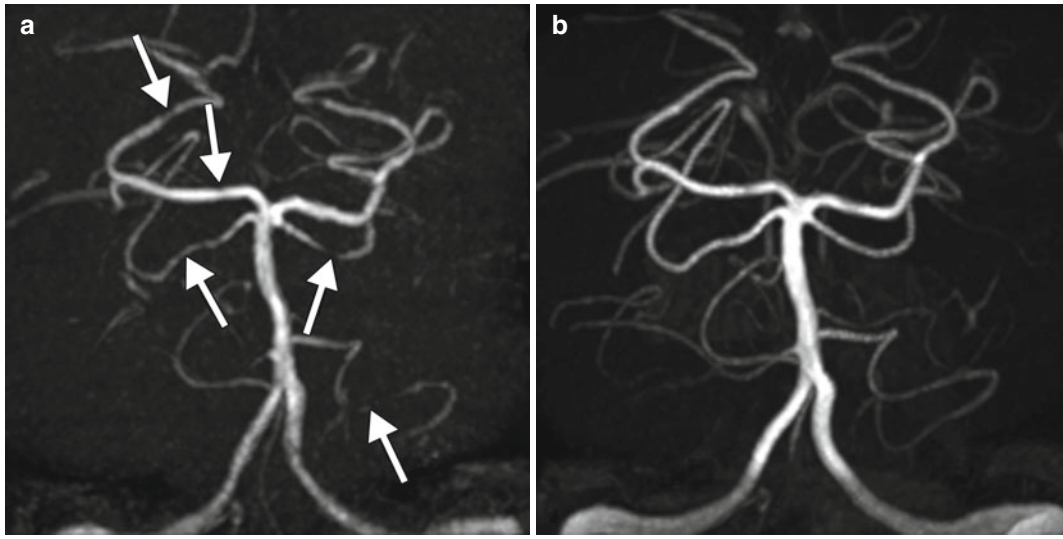

Fig. 4.1 RCVS in the setting of marijuana use. The patient presented with acute thunderclap headache after smoking cannabis. Coronal MIP MRA (**a**) performed 24 h after symptom onset demonstrates multifocal areas of posterior circulation cerebral vasoconstriction (*arrows*). Coronal MIP MRA of the vertebrobasilar system performed 4 months later (**b**) shows resolution of changes

is the presence of alternating multifocal large to medium arterial constriction and dilation, resulting in the characteristic "sausage on a string" appearance on cerebral angiography (Fig. 4.1). A key diagnostic feature is the reversibility upon withdrawal of the stimulus, with spontaneous resolution occurring within 1–3 months. Notably, angiography performed very early in the clinical course may be normal, with vessel narrowing often most marked in the second and third weeks after exposure. Major complications of cannabis-related RCVS include subarachnoid hemorrhage, ischemic stroke, and less commonly, intraparenchymal hemorrhage. The typical patient demographic is a young adult with chronic use of tobacco and cannabis with high levels of consumption just prior to stroke. Although hemorrhagic stroke is not uncommon in RCVS, it has been rarely reported with cannabis use (Fig. 4.2). Individuals who start using marijuana before age 17 have smaller whole-brain and percent cortical gray matter and larger percent white matter volumes than those who begin using marijuana after age 17. In addition, functional imaging studies suggest that resting global and prefrontal blood flow is lower in cannabis users than in controls. Treatment involves cessation of cannabis, supportive care, and management of ischemic and hemorrhagic complications.

Smoking of marijuana using devices such as a narrow outlet bong can result in barotrauma associated with repeated deep inspiration with airflow resistance that is equivalent to performing Müller's maneuver. Successive inhalation through high resistance can result in extreme negative intrathoracic pressure, which causes a transmural pressure gradient inducing barotrauma and release of extra-respiratory air. Air can enter multiple compartments, including the epidural space of the spine, deep neck spaces, subcutaneous tissues, and mediastinum, which can be readily depicted on CT (Fig. 4.3).

4.4 Differential Diagnosis

An important diagnostic consideration for cannabis-induced RCVS is vasospasm secondary to aneurysmal subarachnoid hemorrhage. Other differential considerations include other

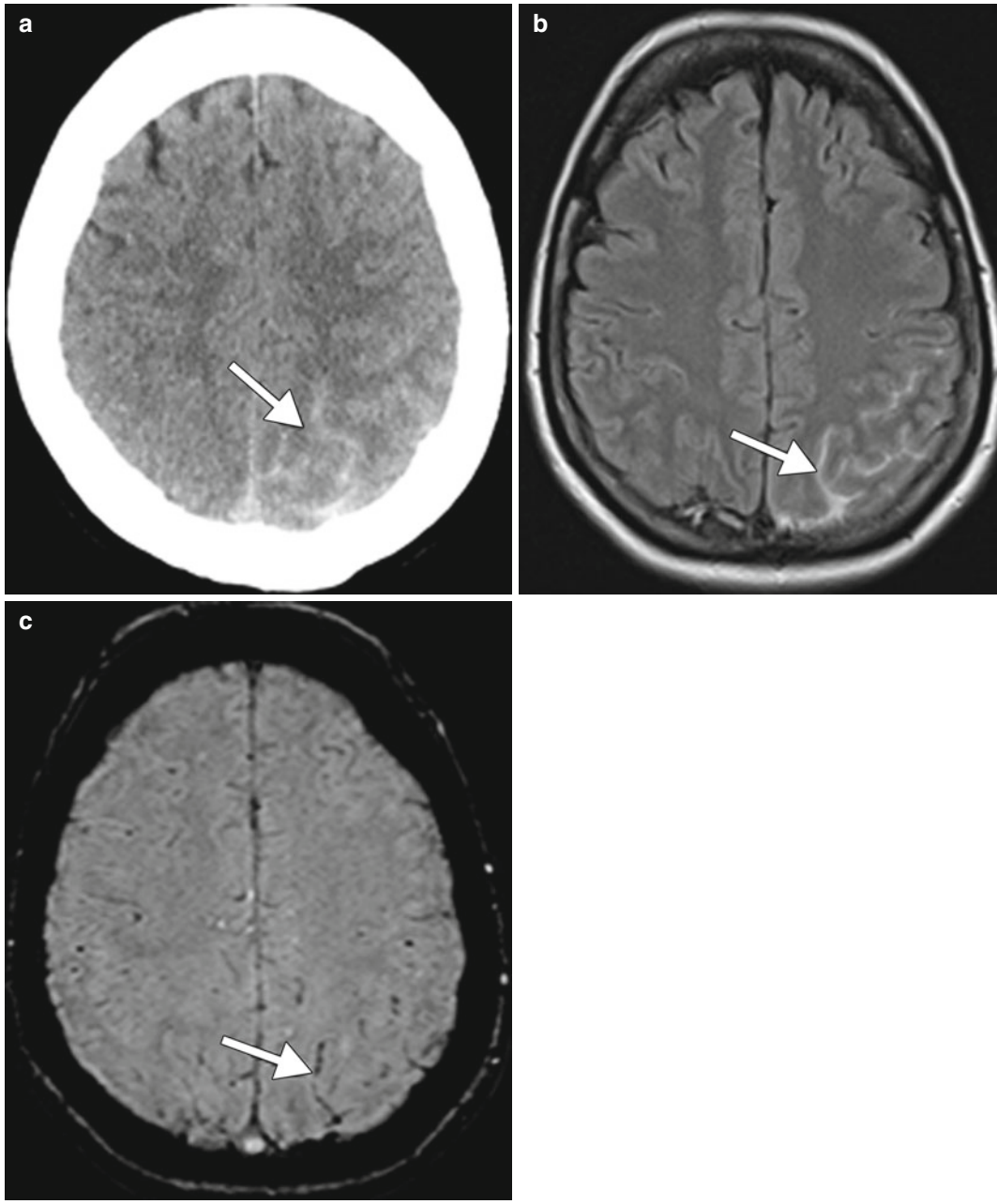

Fig. 4.2 Hemorrhagic stroke due to marijuana. Axial CT on admission (**a**) with corresponding axial FLAIR MRI (**b**) and axial susceptibility-weighted image (SWI) (**c**) reveals left parietal subarachnoid hemorrhage (*arrows*). The acute subarachnoid hemorrhage is more conspicuous on the FLAIR image than the SWI

drug-induced cerebral vasculopathy and other causes of reversible vasoconstriction syndrome such as migrainous angiitis and central nervous system (CNS) vasculitis. Differentiation between the various diagnostic possibilities is aided by the clinical presentation, relevant personal history, and patient demographics.

- *Aneurysmal rupture and secondary vasospasm*: A difficult diagnostic dilemma may arise when an intracranial aneurysm is

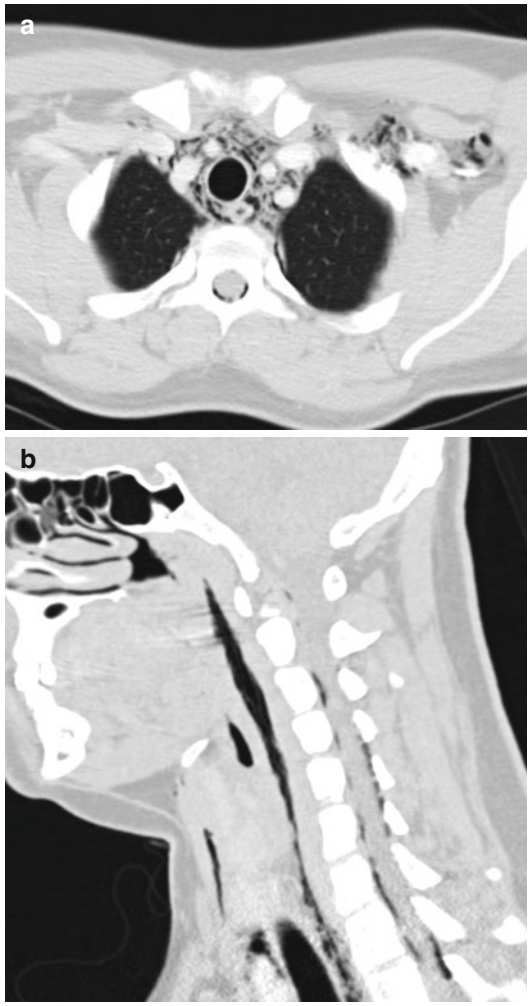

Fig. 4.3 Barotrauma due to marijuana smoking. Axial (**a**) and sagittal (**b**) CT image show extensive air attenuation within the spinal canal, deep spaces of the neck, and upper mediastinum (Courtesy of Alaa Jaly, Chris Coutinho, and Sachin Mathur)

identified on angiography, despite the changes being attributable to RCVS. In this situation, the distribution and extent of subarachnoid blood and the location of cerebral vasospasm is invaluable in ascertaining the diagnosis (Fig. 4.4). In general, cortical subarachnoid hemorrhage is associated with RCVS and basal subarachnoid hemorrhage with aneurysmal rupture. Cortical subarachnoid hemorrhage could be associated with ruptured distal mycotic aneurysm; however, there is usually a history of intravenous drug use or infective endocarditis that predisposes to septic emboli.

- *Other drug-induced RCVS*: A wide range of compounds have been associated with the drug-induced form of RCVS. These include phenylpropanolamine, pseudoephedrine, ergotamine tartrate, methylergonovine, bromocriptine, lisuride, selective serotonin reuptake inhibitors (SSRIs), sumatriptan, isometheptene, cocaine (refer to Chap. 5), amphetamine derivatives (refer to Chap. 6), lysergic acid diethylamide, tacrolimus (FK-506), cyclophosphamide, erythropoietin, intravenous immune globulin (IVIg), interferon alpha, nicotine patches, red blood cell transfusions, licorice (refer to Chap. 9), and oral contraceptives. The radiological features are identical to other causes of RCVS, and the history is invaluable in identifying the offending agent.
- *Migrainous angiitis*: This is radiologically indistinguishable from other causes of RCVS. Often a history of migraines and/or response to treatment may be the only indication that this is the underlying etiology.
- *CNS vasculitis*: This may be primary in etiology, in which the arteritis is confined to the CNS vessels without systemic involvement, or secondary, where there is a history of systemic vasculitis, most often systemic lupus erythematosus (SLE). In the latter situation, CNS involvement is unlikely to be the first manifestation of the disease, as there is almost always a history of systemic vasculitis. While the radiological features of primary CNS vasculitis can overlap with RCVS, the clinical onset of CNS vasculitis is more insidious, the headache is chronic and progressive, and there are usually accompanying cerebrospinal fluid abnormalities. MRI is sensitive for detecting CNS abnormalities in patients with vasculitis. Infarcts are the most

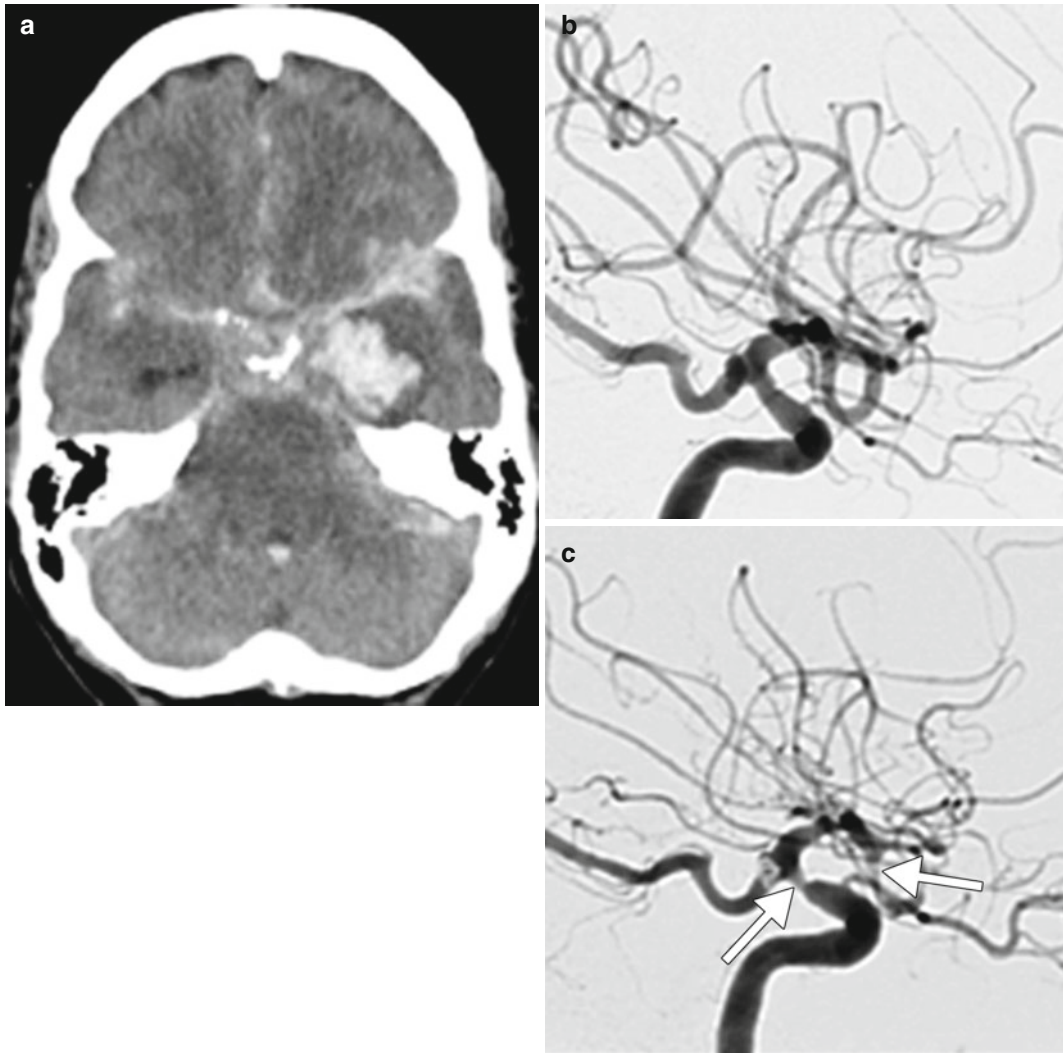

Fig. 4.4 Aneurysmal intracranial hemorrhage. Non-contrast axial CT on admission (**a**) reveals subarachnoid, intraventricular, and left temporal intraparenchymal hemorrhage. Lateral DSA (**b**) performed on the day of admission reveals the normal large cerebral vascular caliber and 4 mm right posterior communicating artery aneurysm. Lateral DSA (**c**) performed for neurological deterioration 10 days later shows marked new focal stenoses of the internal carotid artery and proximal middle cerebral arteries (*arrows*)

common finding, and there is a predilection for the MCA territory (Fig. 4.5).

Subcutaneous and deep neck space emphysema, pneumomediastinum, and pneumorachis can all result from several other factors, such as barotrauma related to paraquat toxicity, penetrating trauma, infections, surgery, and intubation (Fig. 4.6). Pneumorachis, for example, is typically in itself benign and resolves with conservative treatment, but may be a sign of more ominous-associated processes depending upon the clinical scenario.

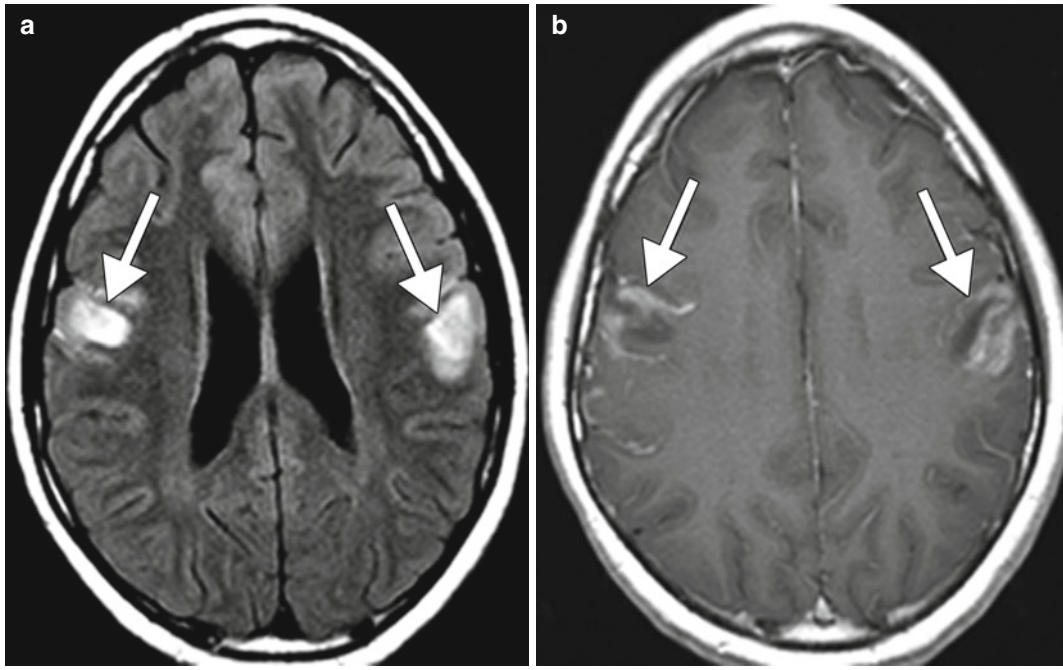

Fig. 4.5 Lupus vasculitis. Axial FLAIR (**a**) and post-contrast T1-weighted (**b**) MR images show subacute infarcts in the bilateral frontal lobes (*arrows*)

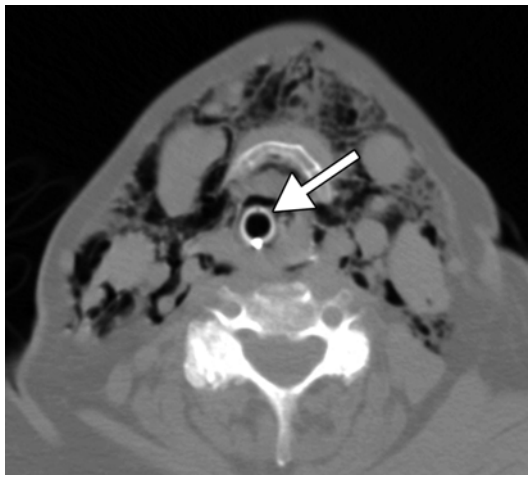

Fig. 4.6 Cervical emphysema after intubation. Axial CT image shows extensive gas within multiple compartments of the neck. An endotracheal tube is present (*arrow*)

Suggested Reading

Ashton C. Pharmacology and effects of cannabis: a brief review. Br J Psychiatry. 2001;178:101–6.

Ducros A, Brousser MG. Reversible cerebral vasoconstriction syndrome. Pract Neurol. 2009;9:256–67.

Ducros A, Boukobza M, Porcher R, Sarov M, Valade D, Brousser MG. The clinical and radiological spectrum of reversible cerebral vasoconstriction syndrome. A prospective of 67 patients. Brain. 2007;130:3091–101.

Hazouard E, Koninck JC, Attucci S, Fauchier-Rolland F, Brunereau L, Diot P. Pneumorachis and pneumomediastinum caused by repeated Müller's maneuvers: complications of marijuana smoking. Ann Emerg Med. 2001;38(6):694–7.

Iversen L. Invited review: cannabis and the brain. Brain. 2003;126:1252–70.

Lupica C, Riegel A, Hoffman A. Mini review: marijuana and cannabinoid regulation of brain reward circuits. Br J Pharmacol. 2004;143:227–34.

Martín-Santos R, Fagundo AB, Crippa JA, Atakan Z, Bhattacharyya S, Allen P, Fusar-Poli P, Borgwardt S,

Seal M, Busatto GF, McGuire P. Neuroimaging in cannabis use: a systematic review of the literature. Psychol Med. 2010;40(3):383–98.

Wilson W, Mathew R, Turkington T, Hawk T, Coleman RE, Provenzale J. Brain morphological changes and early marijuana use: a magnetic resonance and positron emission tomography study. J Addict Dis. 2000; 19(1):1–22.

Wolff V, Armspach JP, Lauer V, Rouyer O, Bataillard M, Marescaux C, Geny B. Cannabis-related stroke: myth or reality? Stroke. 2013;44(2):558–63.

Yucel M, Solowij N, Respondek C, Whittle S, Fornito A, Pantelis C, Lubman D. Regional brain abnormalities associated with long-term heavy cannabis use. Arch Gen Psychiatry. 2008;65(6):694–701.

Crack and Cocaine

5

Rania Hito and Daniel Thomas Ginat

5.1 Uses

In small quantities, cocaine has been used for local anesthesia, predominantly in nasal and lacrimal duct surgery. Until 1903, cocaine was widely available and promoted as a "brain tonic" and "Coca-Cola" in the form of the caffeinated beverage. Otherwise, cocaine in its hydrochloride and alkaloid forms is currently an illicit recreational drug used for stimulant effects and euphoria.

5.2 Mechanism

Cocaine (benzoylmethylecgonine) is derived from the *Erythroxylon* coca plant. The drug can be formulated as the hydrochloride form, which is typically injected intravenously or insufflated (snorted) and absorbed via the mucous membranes, or the alkaloid form (crack), which is volatile when heated and can be smoked. Local anesthetic effects are due to the alteration of sodium and potassium flux in the nerve cell membrane and prevention of the propagation of action potentials, while systemic effects of cocaine are due to activation of the sympathetic nervous system by inhibition of the presynaptic uptake of dopamine and norepinephrine. Sympathetic effects include tachycardia, increased systolic blood pressure, increased cardiac output, and mydriasis. Cocaine-induced vasospasm is believed to be related to the sympathomimetic effect as well as a direct effect on calcium channels. Cocaine also promotes platelet aggregation and decreases antithrombin III and protein C levels. Furthermore, levamisole is a cocaine adulterant that acts as an immunomodulator that can cause neutropenia, skin necrosis, and demyelinating lesions in the brain.

5.3 Discussion

The most common neurological complications of cocaine use are hemorrhagic and ischemic stroke. The hemorrhage is typically in a central location, most commonly in the basal ganglia, followed by the thalamus, brainstem, and cerebellum (Fig. 5.1). There can also be associated intraventricular and subarachnoid hemorrhage. Furthermore, there is an unusual proclivity for bilateral hypothalamic perivascular hemorrhage and edema with subarachnoid hemorrhage (Fig. 5.2), and involvement of this region may be associated with sympathetic overactivity.

Cocaine-induced ischemic strokes can involve both anterior and posterior arterial territories, but most commonly affect the middle cerebral artery territory. Cerebral infarcts from cocaine use are

R. Hito, MD
Department of Radiology, University of Massachusetts Memorial Medical Center, Worcester, MA, USA

D.T. Ginat, MD, MS (✉)
Department of Radiology, University of Chicago, Pritzker Medical School, Chicago, IL, USA
e-mail: ginatd01@gmail.com

D.T. Ginat et al. (eds.), *Neuroimaging Pharmacopoeia*,
DOI 10.1007/978-3-319-12715-6_5,

Fig. 5.1 Cocaine-induced hypertensive hemorrhage. There is a large acute hematoma centered within the left basal ganglia (*arrow*). There is also intraventricular hemorrhage (*arrowheads*)

typically subcortical, although the cortex can be involved (Fig. 5.3). Ischemia can be due to vasculitis and vasospasm or secondary to cocaine's effects on other organ systems, such as myocardial infarctions, respiratory arrest, or embolic events from additives such as talc. In approximately half the cases of cocaine infarcts, angiography does not reveal abnormalities. However, occasionally, intraluminal clot is observed in the intracranial circular due to stasis related to arterial spasm.

Levamisole-tainted cocaine can incite a multifocal demyelinating leukoencephalopathy that can manifest are round or oval lesions in white matter that are hypoattenuating on CT and hyperintense on T2-weighted MRI sequences and there can be diffuse white matter involvement with sparing of the U-fibers (Fig. 5.4). The lesions can also display peripheral ring-enhancement.

Brain parenchymal volume loss has been reported in the setting of chronic cocaine use, predominantly in a frontotemporoparietal distribution, likely related to chronic ischemia. Spinal cord infarction can also result from cocaine use, but is relatively uncommon.

There are a variety of neurovascular changes associated with cocaine use. Cocaine-associated vasculitis syndrome is a hypersensitivity response characterized by nonnecrotizing leukocytoclastic angiitis of the small vessels. Angiography can show multifocal bead of the cerebral arteries (Fig. 5.5), although some cases may not have any appreciable vascular findings. There can be associated hemorrhage and/or ischemia. Cocaine can also result in vasospasm, particularly if there has been subarachnoid hemorrhage, although the drug itself is an independent risk factor for vasospasm. Some patients may develop a moyamoya type of vasculopathy secondary to chronic alkaloidal cocaine use. Finally, cerebral aneurysms, particularly in the anterior circulation, are observed more frequently in cocaine users than in the general population.

Nasal septal perforation is a complication of snorting cocaine, which results from a combination of chemical irritation, ischemic necrosis from intense vasoconstriction, and direct trauma. Nasal septal perforation is preceded by mucosal atrophy and followed by chronic osteolysis that can also affect the hard palate (Fig. 5.6), which can lead to oronasal fistulas. The sinonasal destructive changes that result from cocaine use can also lead to dacryocystitis and orbital cellulitis. Diagnostic imaging is useful for evaluating the orbital complications related to cocaine use, which may manifest as dacryocystitis. Dacryocystitis appears as enlargement of the lacrimal sac with surrounding stranding of the orbital fat (Fig. 5.7). Other complications related to snorting cocaine in the head and neck region include enamel erosion, gingival erosion, and midline granuloma.

Crack cocaine is commonly smoked in a pipe with a metallic filter made from a steel wool scouring pad, such as Brillo. Occasionally, smokers accidentally aspirate and ingest the filter, which can result in a burn injury to the hypopharynx. In such cases, imaging can be obtained in order to assess the degree of burn injury, which can manifest as edema in the hypopharynx, and to localize the foreign body, which is radiopaque (Fig. 5.8).

Maternal cocaine use can result in fetal intraventricular hemorrhage, intraparenchymal hemorrhage,

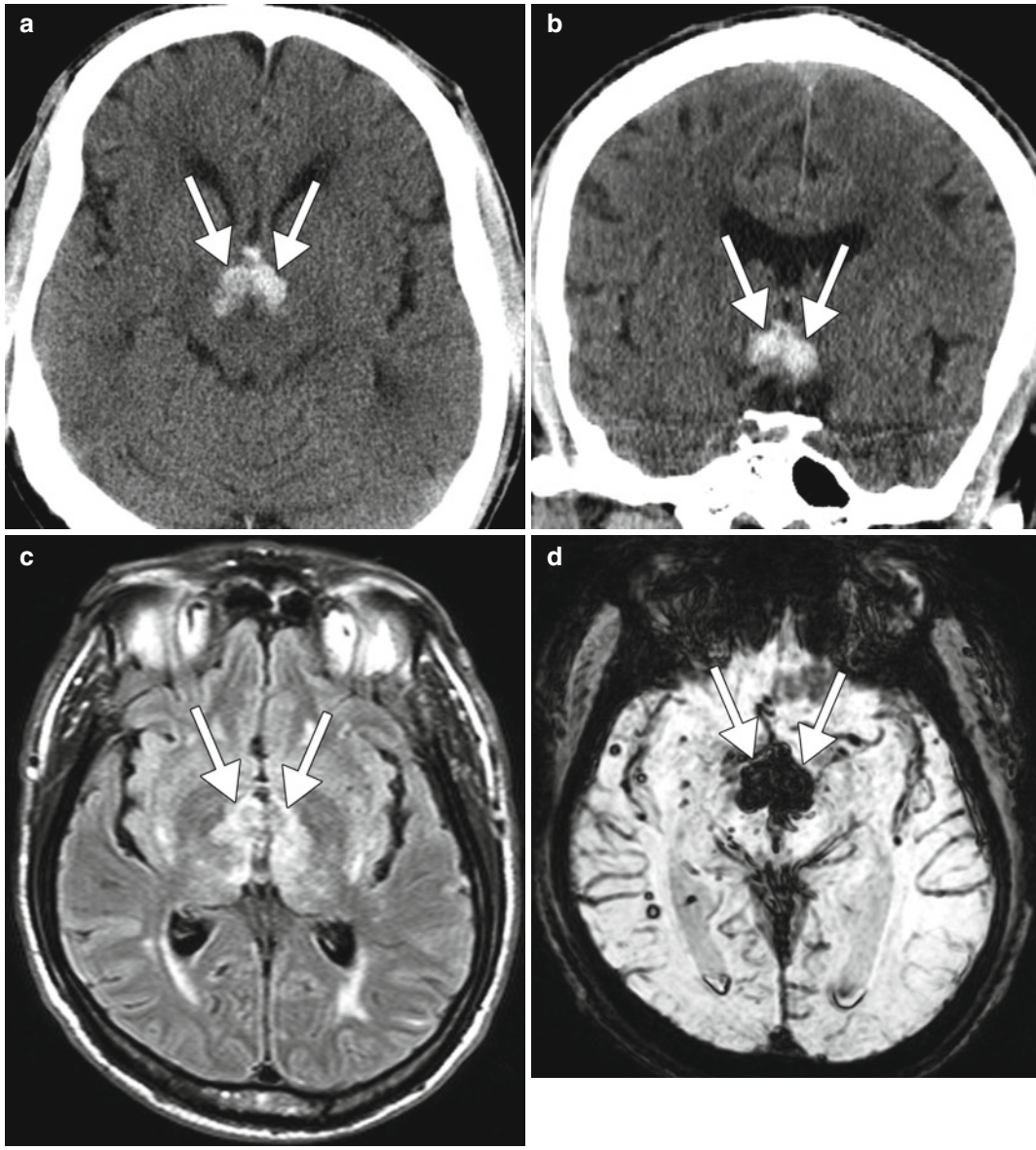

Fig. 5.2 Cocaine-induced hypothalamic hemorrhage. Axial (**a**) and coronal (**b**) CT images show hemorrhage involving the bilateral hypothalamic (*arrows*) with intraventricular hemorrhage. Axial FLAIR (**c**) and SWI (**d**) show the hemorrhage and edema in the bilateral thalami (*arrow*). There are multiple other scattered foci of parenchymal susceptibility effect, which are compatible with microhemorrhages

periventricular leukomalacia, deep brain cysts, and perinatal infarction, likely related to decreased cerebral blood flow from cocaine's effect on the uterine artery. Additionally, studies have shown that fetal skull malformations, encephalocele, and pachygyria can result from prenatal cocaine exposure (Fig. 5.9).

As with any type of intravenous drug use, patients are at risk of acquiring a variety of infections, including HIV and septic brain and spine abscesses from the use of contaminated needles and other unsanitary conditions (also refer to the Chap. 7).

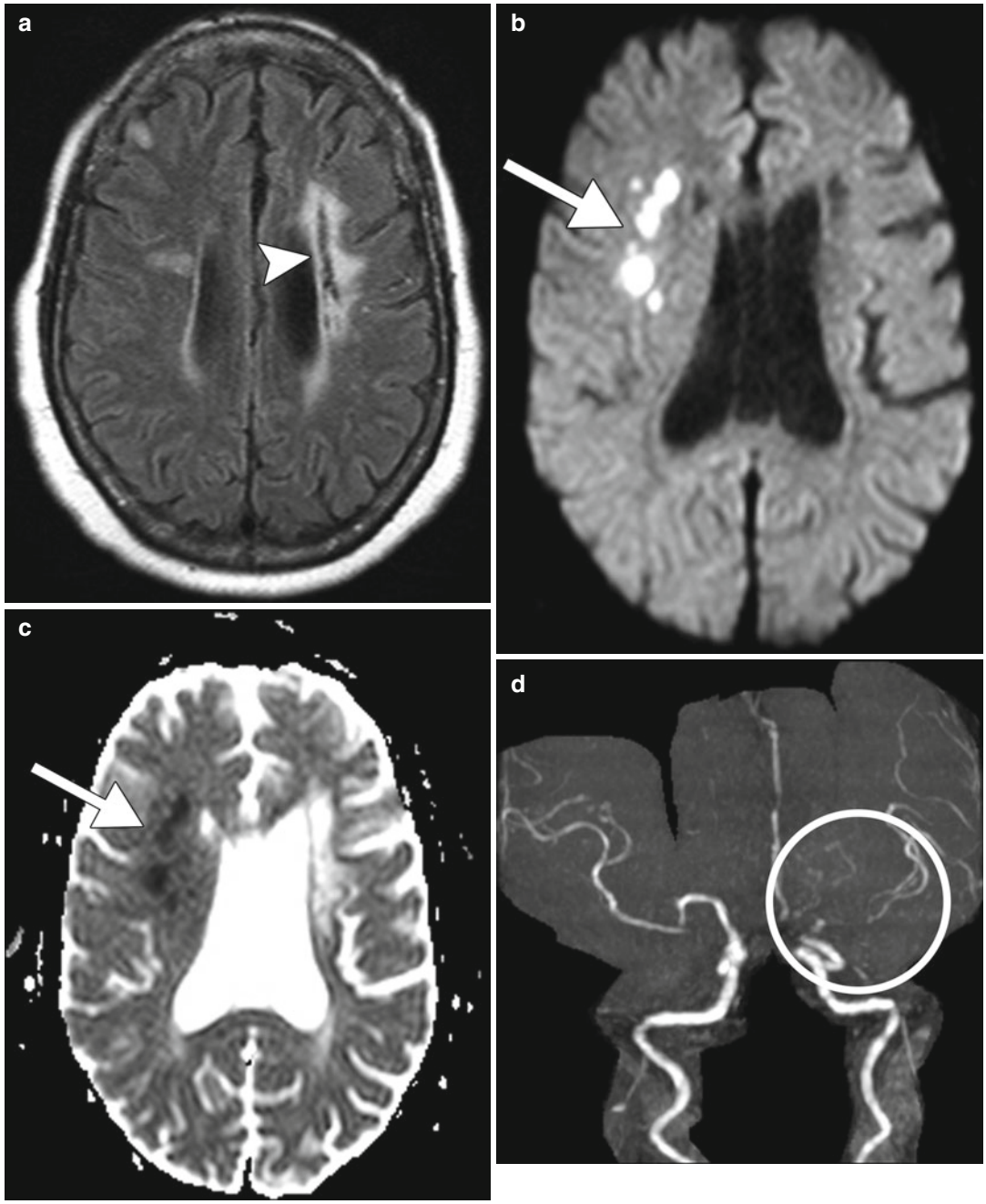

Fig. 5.3 Cocaine-induced ischemia. Axial FLAIR (**a**), DWI (**b**), and ADC map (**c**) show acute infarcts in the right frontal lobe (*arrows*) and chronic encephalomalacia in the left frontal lobe (*arrowhead*). Frontal time-of-flight MRA MIP image (**d**) shows absence of flow-related enhancement in the left supraclinoid internal carotid artery and left middle cerebral artery (*circle*). There is also absent flow-related enhancement within the right anterior cerebral artery

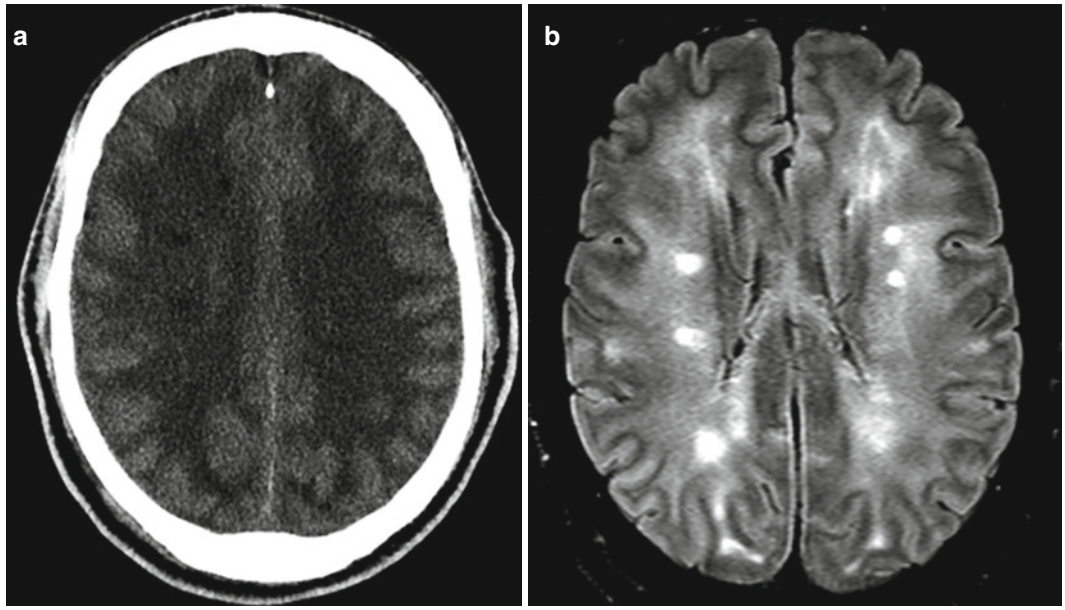

Fig. 5.4 Leukoencephalopathy presumably due to levamisole-tainted cocaine. Axial CT image (**a**) shows diffuse cerebral white matter hypoattenuation and sulcal effacement with scattered areas of more focal hypoattenuation in the centrum semiovale bilaterally. The corresponding axial FLAIR MRI (**b**) shows scattered ovoid areas of high signal superimposed upon a background of fainter and more diffuse white matter hyperintensity

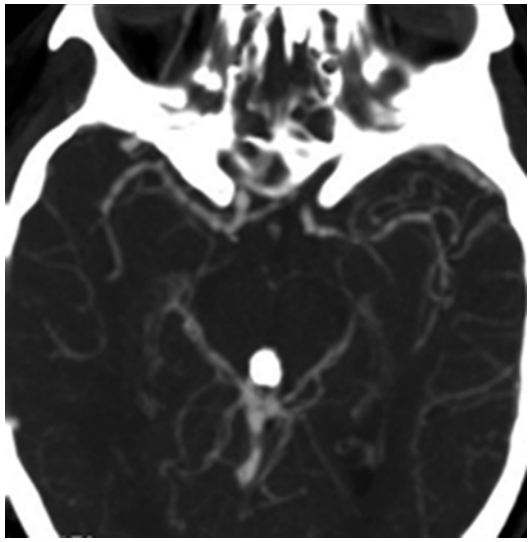

Fig. 5.5 Cocaine-induced vasculitis. Axial image from a CT angiogram demonstrates irregularity of the middle cerebral arteries with a beaded appearance

Fig. 5.6 Nasal septal perforation. Coronal CT image show nasal septal perforation as well as destruction of the right middle turbinate, nasal antral wall, and hard palate

5.4 Differential Diagnosis

Ischemia (also refer to Chaps. 6, 19, 31–34,and 39): The ischemic changes that result from cocaine use can be indistinguishable from other etiologies including thromboembolic stroke and stroke related to dissection and other drug exposures, for example. Likewise, watershed infarctions related to cocaine use can resemble other causes of hypoperfusion, such as a critical ICA stenosis, profound asphyxia, or systemic hypotension.

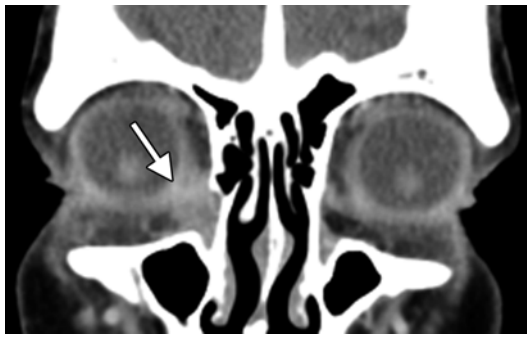

Fig. 5.7 Dacryocystitis in a cocaine user. Coronal contrast-enhanced CT shows enlargement and enhancement of the right lacrimal sac (*arrow*)

Intracranial hemorrhage (also refer to Chaps. 31–34): There is an extensive differential considerations for a spontaneous intracranial hemorrhage, including underlying vascular malformations and aneurysms, underlying neoplasm, venous infarction, vasculitis (besides cocaine-induced vasculitis), coagulopathy, moyamoya disease, and other forms of drug-induced hypertension. Although patient history and urine toxicology screen may reveal cocaine as the likely causative factor, imaging is essential for excluding some of the other potential etiologies.

Vasculitis (also refer to Chaps. 4, 6, and 10): Differential considerations for cocaine-induced vasculitis include vasospasm or atherosclerosis, which can also be related to cocaine use. In addition, primary CNS angiitis, lupus, and other substances, such as amphetamine, heroin, and *Centella asiatica*, can also have similar imaging findings.

Perforated nasal septum: Trauma, surgery, vasoconstrictive or steroid nasal medication, Wegener's granulomatosis, invasive fungal sinusitis, sarcoidosis, and sinonasal neoplasms can cause nasal septal perforation (Figs. 5.10, 5.11,

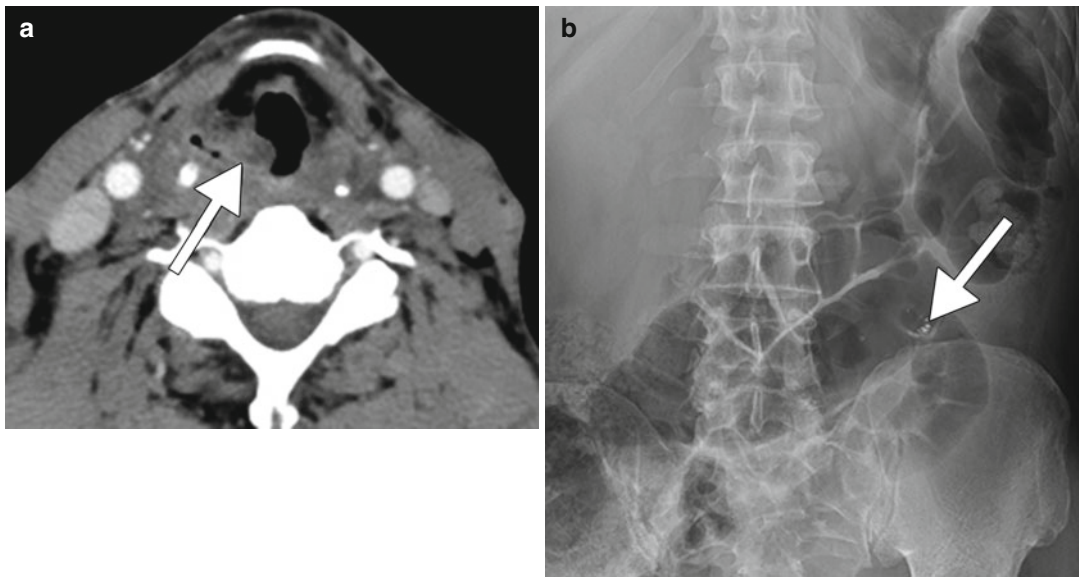

Fig. 5.8 Burn injury from crack paraphernalia ingestion. The patient presents with a sore throat after accidentally ingesting a crack pipe Brillo pad filter. Axial CT image (**a**) shows edema of the right aryepiglottic fold (*arrow*). Frontal radiograph (**b**) shows a metallic structure that is presumed to represent the ingested Brillo pad (*arrow*)

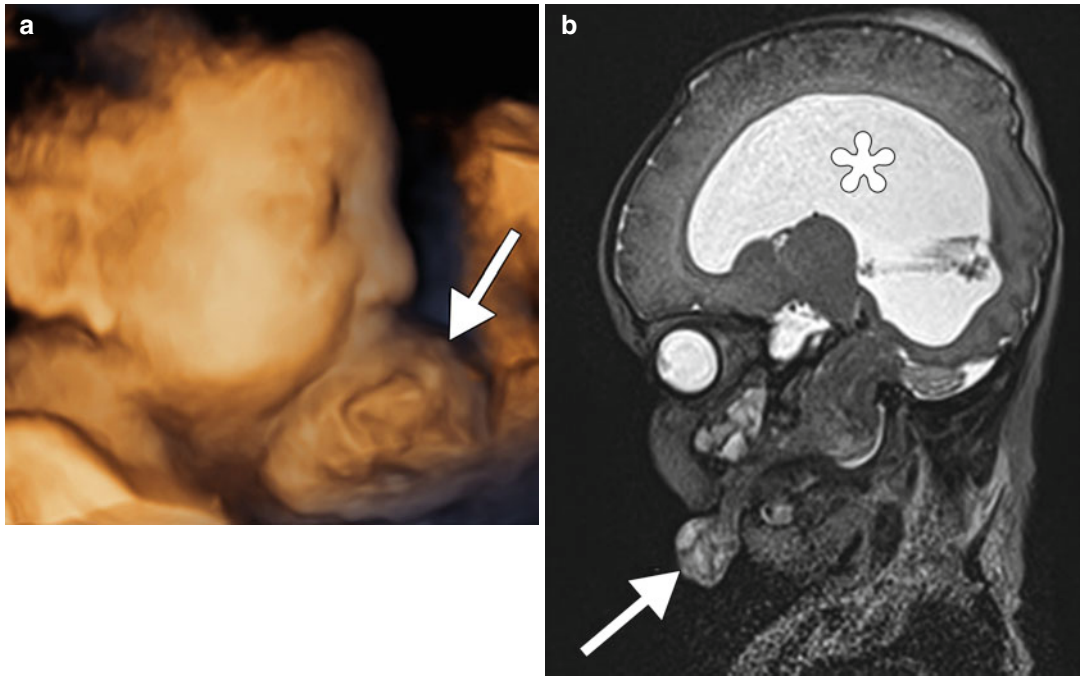

Fig. 5.9 Fetal cocaine exposure. 3D fetal ultrasound image of the face (**a**) shows a perioral mass (*arrow*). Sagittal T2-weighted MRI (**b**) shows that the mass (*arrow*) represents an encephalocele. There is associated ventriculomegaly (*) (Courtesy of Jenny Hoang)

Fig. 5.10 Sinonasal Wegener's granulomatosis. Coronal CT image shows a defect in the nasal septum and mucosal thickening within the paranasal sinuses

Fig. 5.11 Iatrogenic septal perforation. Axial CT image show s cartilaginous nasal septal defect in a patient who underwent endoscopic sinus surgery and septoplasty for sinusitis

Fig. 5.12 Retropharyngeal abscess. Axial CT image shows left hypopharyngeal swelling and a more discrete fluid collection, suggestive of abscess (*arrow*)

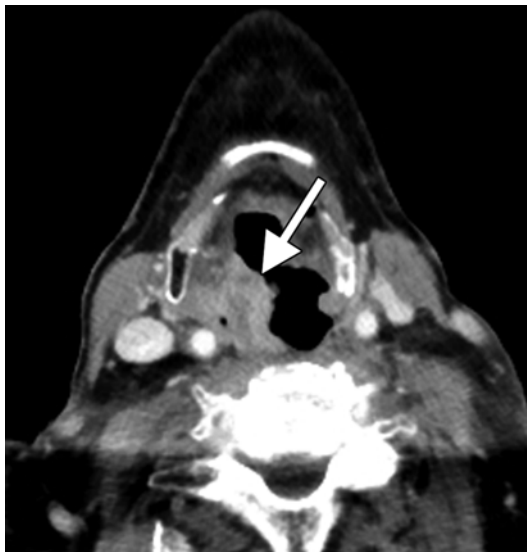

Fig. 5.13 Hypopharyngeal squamous cell carcinoma. Axial CT image shows a heterogeneously enhancing, infiltrative mass in the right hypopharynx (*arrow*)

and 5.12). Involvement of the palatal area can help distinguish patients with cocaine-induced midline destructive lesions from those with sinonasal Wegener's granulomatosis.

Dacryocystitis: Nasolacrimal duct stenosis, dacryocystocele, and dacryocystitis can occur spontaneously, result from various chemotherapeutic agents, radiation therapy, surgery, mass lesions, and fractures. Alternatively, an enlarged lacrimal sac may mimic the presence of a neoplasm or orbital inflammatory syndrome.

Hypopharyngeal burn injury: Burn injury to the hypopharynx from accidental aspiration or ingestion of paraphernalia related to smoking crack cocaine can mimic an infectious process, such as phlegmon or abscess (Fig. 5.12) and malignancy (Fig. 5.13). The clinical history is key for differentiating these conditions.

Suggested Reading

Aggarwal SK, Williams V, Levin SR, Cassin BJ, Garcia JH. Cocaine-associated intracranial hemorrhage: absence of vasculitis in 14 cases. Neurology. 1996; 46(6):1741–3.

Alexandrakis G1, Tse DT, Rosa Jr RH, Johnson TE. Nasolacrimal duct obstruction and orbital cellulitis associated with chronic intranasal cocaine abuse. Arch Ophthalmol. 1999;117(12):1617–22.

Allard FD, Yee EU, Freitag SK. Dacryocystitis secondary to intranasal cocaine abuse: a case report and literature review. Orbit. 2013;32(6):405–8.

Arora NP, Jain R, Bhanot R, Natesan SK. Levamisole-induced leukocytoclastic vasculitis and neutropenia in a patient with cocaine use: an extensive case with necrosis of skin, soft tissue, and cartilage. Addict Sci Clin Pract. 2012;7(1):19.

Bajwa A, Silliman S, Cury JD, et al. Characteristics and outcomes of cocaine-related spontaneous intracerebral hemorrhages. ISRN Neurol. 2013;2013:124390.

Baraban SC, McCarthy EB, Schwartzkroin PA. Evidence for increased seizure susceptibility in rats exposed to cocaine in utero. Brain Res Dev Brain Res. 1997;102: 189–96.

Brown E, Prager J, Lee H, Ramsey RG. CNS complications of cocaine abuse: prevalance, pathophysiology, and neuroradiology. AJR Am J Roentgenol. 1992;159: 137–47.

Buchanan JA, Heard K, Burbach C, et al. Prevalence of levamisole in urine toxicology screens positive for cocaine in an inner-city hospital. JAMA. 2011; 305(16):1657–8.

Dixon SD, Bejar R. Echoencephalographic findings in neonates associated with maternal cocaine and methamphetamine use: incidence and clinical correlates. J Pediatr. 1979;115:770–80.

Drug intelligence brief: Cocaine containing levamisole adversely affecting drug users in the United States Drug Enforcement Administration, Intelligence Production Unit; 2010.

Fessler RD, Esshaki EM, Stankewitz RC, et al. The neurovascular complications of cocaine. Surg Neurol. 1997;47:339–45.

Geibprasert S, Gallucci M, Krings T. Addictive illegal drugs: structural neuroimaging. AJNR Am J Neuroradiol. 2010;31(5):803–8.

González-Duarte A, Williams R. Cocaine-induced recurrent leukoencephalopathy. Neuroradiol J. 2013;26(5):511–3.

Kibayashi K, Mastri AR, Hirsch CS. Cocaine induced intracerebral hemorrhage: analysis of predisposing factors and mechanisms causing hemorrhagic strokes. Hum Pathol. 1995;26(6):659–63.

Levine SR, Brust JCM, Futrell N, et al. Cerebrovascular complications of the use of the "crack" form of alkaloidal cocaine. N Engl J Med. 1990;323(11):699–704.

Moettus A, Tandberg D. Brillo pad crack screen aspiration and ingestion. J Emerg Med. 1998;16(6):861–3.

Schneider JW, Chasnoff IJ. Motor assessment of cocaine-exposed infants. Phys Ther. 1988;68:5–15.

Singer L, Arendt R, Minnes S. Neurodevelopmental effects of cocaine. Clin Perinatol. 1993;20:245–62.

Storen EC, Wijdicks EF, Crum BA, Schultz G. Moyamoya-like vasculopathy from cocaine dependency. AJNR Am J Neuroradiol. 2000;21(6):1008–10.

Toossi S, Hess CP, Hills NK, Josephson SA. Neurovascular complications of cocaine use at a tertiary stroke center. J Stroke Cerebrovasc Dis. 2010;19(4):273–8.

Wu V, Huang J, Lien H, et al. Levamisole-induced multifocal inflammatory leukoencephalopathy: clinical characteristics, outcome, and impact of treatment in 31 patients. Medicine. 2006;85(4):203–13.

Amphetamines

6

Ronil V. Chandra, Daniel Thomas Ginat, and Juan E. Small

6.1 Uses

Amphetamines are a class of central nervous system stimulants. Amphetamine (alphamethylphenethylamine or α-methylphenethylamine) and methylphenidate are used to treat attention-deficit hyperactivity disorder. Amphetamine and dextroamphetamine can also be used to treat narcolepsy. Furthermore, amphetamines have been used as dietary supplements for weight loss and physical performance enhancement. MDMA (3, 4-methylenedioxymethamphetamine or Ecstasy) and methamphetamine are illicit empathogenic recreational drugs of abuse that can produce euphoria, enhanced mental and emotional clarity, sensations of lightness and floating, and other hallucinations.

6.2 Mechanism

Amphetamines act as indirect serotonergic agonists by promoting the release of serotonin through the serotonin transporter by a process of transporter-mediated exchange. Consequently, stimulation of 5-HT2A small vessel receptors leads to prolonged vasospasm. Furthermore, these drugs can interfere with the storage of serotonin within the vesicles and thus increases the amount of serotonin available to be released. Amphetamines also enhance the release of dopamine and noradrenaline. In particular, MDMA can also inhibit monoamine reuptake and delay metabolism by inhibition of monoamine oxidase.

6.3 Discussion

Complications related to amphetamines and methamphetamines are primarily cardiac and neurotoxic, including vasospasm, arteritis, ischemic and hemorrhagic stroke, hemorrhage, gliosis, and neuronal loss. Therefore, ischemia, hemorrhage, leukomalacia, encephalomalacia, and vasospasm are the typical sequela evident on imaging. Acute complications most often result immediately or shortly after administration. As noted previously, Ecstasy or MDMA leads to rapid release of serotonin/5-hydroxytryptamine (5-HT) and potent vasoconstriction. As the occipital cortex and the globus pallidus have high levels of 5-HT and 5-HT2A receptors, these sites

R.V. Chandra, MBBS, MMed, FRANZCR
Department of Diagnostic Imaging,
Monash Medical Center,
Monash Health, Melbourne, VIC, Australia

D.T. Ginat, MD, MS (✉)
Department of Radiology, University of Chicago,
Pritzker Medical School, Chicago, IL, USA
e-mail: ginatd01@gmail.com

J.E. Small, MD
Department of Diagnostic Radiology,
Lahey Clinic, Burlington, MA, USA

D.T. Ginat et al. (eds.), *Neuroimaging Pharmacopoeia*,
DOI 10.1007/978-3-319-12715-6_6,

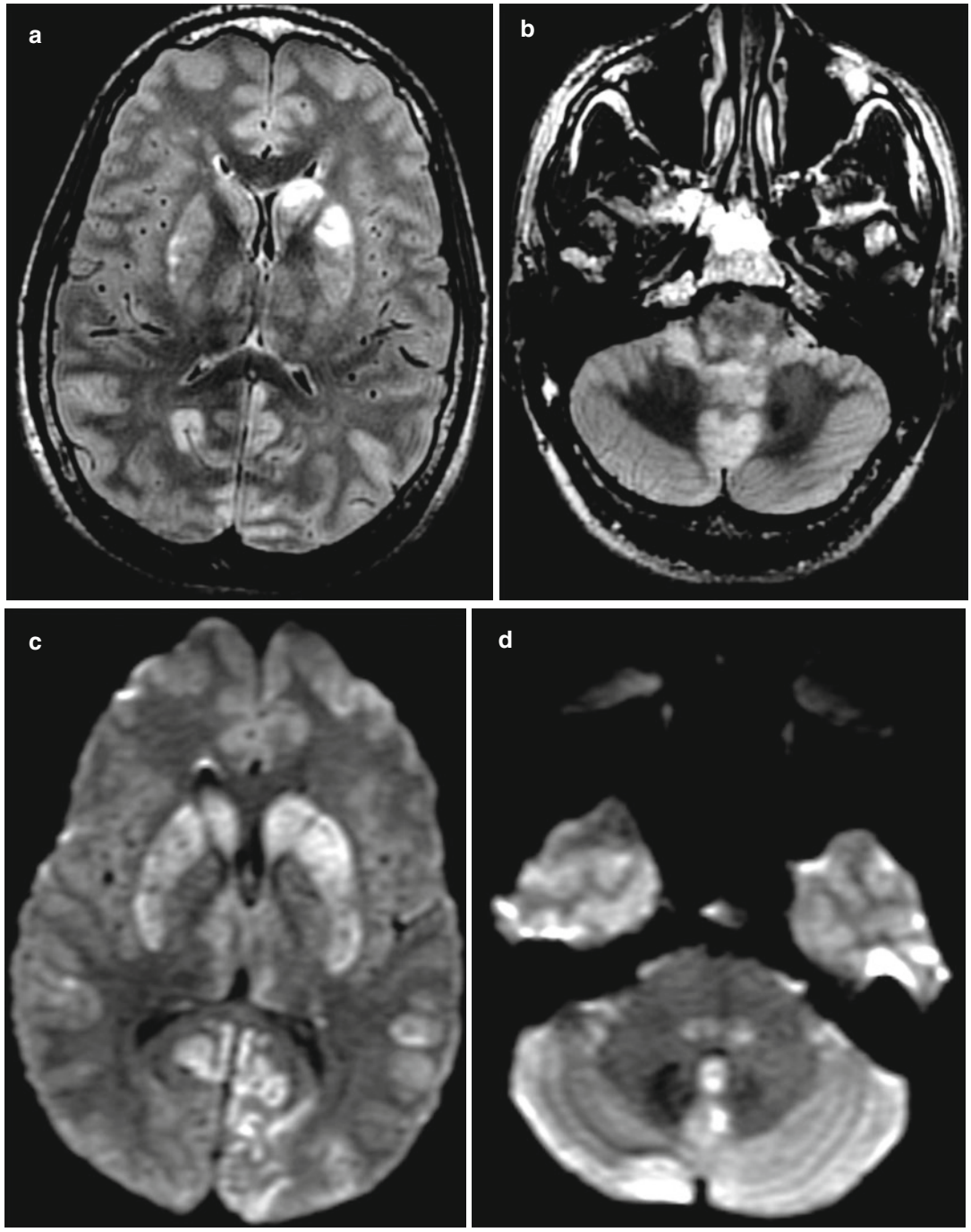

Fig. 6.1 Acute Ecstasy toxicity. Axial FLAIR (**a**, **b**), DWI (**c**, **d**), and ADC map (**e**, **f**) show multiple supratentorial and infratentorial acute infarcts. Courtesy of Alisa Gean

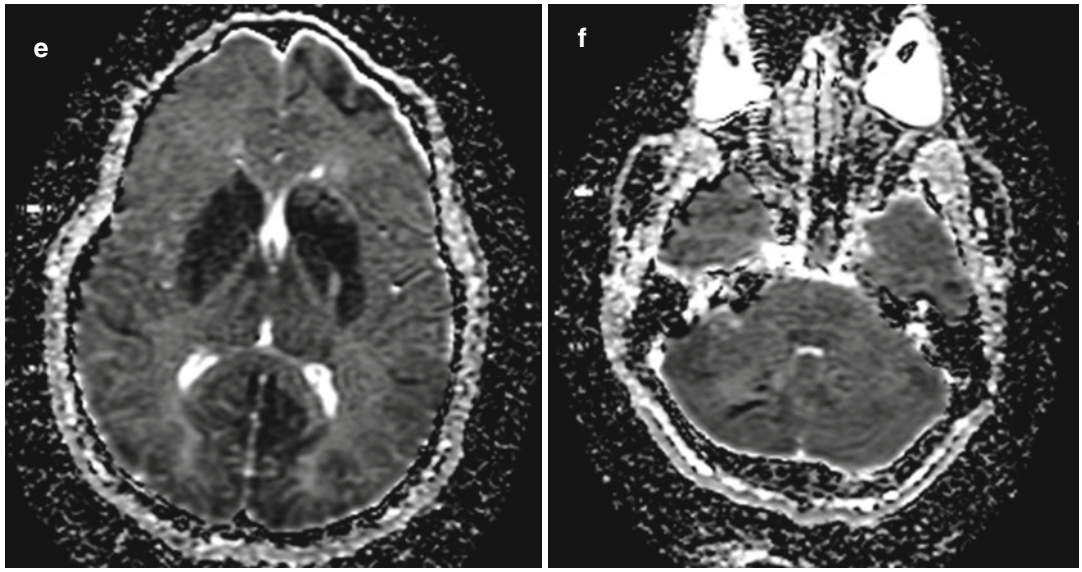

Fig. 6.1 (continued)

Fig. 6.2 Ecstasy-induced hemorrhage. The patient presented with acute severe headache immediately after "two hits" of Ecstasy. Axial CT image demonstrates a large left frontal lobe intraparenchymal hematoma (*arrow*)

are the most vulnerable to ischemia. The abuse of amphetamines has therefore been linked to vasospasm, arteritis, and cerebrovascular accidents (Figs. 6.1, 6.2, and 6.3). Less commonly, amphetamines can result in leukoencephalopathy, which may be associated with abnormalities in the demethylation of debrisoquine hydroxylase. This condition can manifest as extensive cerebral white matter T2 hyperintensity on MRI.

6.4 Differential Diagnosis

- *Reversible cerebral vasoconstriction syndrome (RCVS)*: RCVS encompasses a diverse group of conditions characterized by the acute onset of severe headaches associated with reversible segmental constriction of multiple cerebral arteries. Importantly, the underlying pathophysiology is reversible vasoconstriction rather than vasculitis. Of note, it is not possible to distinguish between RCVS and CNS vasculitis based on imaging. However, several clinical features are helpful in making the diagnosis.

Fig. 6.3 Methamphetamine-induced hemorrhage, infarct, and vasospasm. Sagittal T1 MRI of the spine (**a**) reveals intradural spinal hemorrhage (*arrow*). No intracranial subarachnoid hemorrhage was evident. Axial diffusion-weighted image (**c**) reveals a left occipital lobe infarct (*arrow*). MRA MIP image (**b**) reveals multiple areas of vasoconstriction, most pronounced in the left PCA (*arrow*). The patient was treated with supportive care, and angiography performed 10 weeks later (not shown) confirmed resolution of vasoconstriction

This is essential, as treatment and prognosis of RCVS and CNS vasculitis are quite different. The onset of RCVS is acute with thunderclap headache. However, the severe pain is short lived, lasting from a few minutes to a few hours. Attacks can be single, but patients have a mean of four attacks during a period of approximately 1–4 weeks. A self-limiting, benign outcome is the norm, and resolution is generally within 3 months. CSF analysis is usual normal or near normal. The neuroimaging hallmark of RCVS is vasoconstriction evident as segmental narrowing and dilatation (string of beads) of one or more arteries (Fig. 6.4). The appearance is similar to that of other forms of vasculitis, except the abnormalities resolve within a few months. Bilateral and diffuse anterior and posterior circulation changes are seen in the majority of patients. Although concomitant changes need not be present, subarachnoid hemorrhage, parenchymal edema, parenchymal hemorrhage, and infarction may occur. Of note, RCVS may be accompanied by posterior reversible encephalopathy syndrome (PRES), as these are not mutually exclusive. RCVS patients are treated with nimodipine or verapamil until resolution of angiographic findings.

- *Primary CNS angiitis*: Central nervous system (CNS) vasculitis can be classified as primary when isolated to the CNS and secondary when associated with a systemic condition. Therefore, the diagnosis of primary CNS angiitis requires the absence of a systemic disorder to explain the inflammatory response. Primary CNS angiitis is a rare disorder with a male predominance, characterized by a chronic and insidious onset and frequent headaches (not thunderclap type) with stepwise deterioration typified by transient neurologic deficits, infarcts, and cognitive decline. Neuroimaging generally reveals several infarcts of differing ages, and angiograms may demonstrate irregular, eccentric, and asymmetric arterial narrowing and occlusion of medium- and small-sized vessels (Fig. 6.5). The angiographic abnormalities are frequently irreversible. CSF analysis is abnormal with elevated acute phase reactants such as sedimentation rate and C-reactive protein. Ultimately, this is a diagnosis of exclusion.
- *Secondary CNS vasculitis*: Inflammatory CNS vasculitis can also occur in the context of an underlying systemic condition. An extensive and heterogeneous group of diseases may represent the underlying cause including infections, connective tissue disorders, sarcoidosis, and lymphoproliferative disorders. Infectious etiologies include human immunodeficiency virus (HIV), varicella zoster virus (VZV), hepatitis C virus (HCV) tuberculosis, and syphilis. Systemic vasculitides include polyarteritis nodosa (PAN), Wegener's granulomatosis, and Churg-Strauss syndrome. Connective tissue disorders include systemic lupus erythematosus (SLE), Sjogren's syndrome, rheumatoid arthritis, and mixed connective tissue disorders. The neuroimaging findings in these conditions may be identical to those found with primary CNS angiitis.
- *Acute hypertensive encephalopathy/posterior reversible encephalopathy syndrome (PRES)*: The classic neuroimaging findings are bilaterally predominant parieto-occipital lobe and arterial border zone edema associated with posterior circulation predominant multifocal arterial vasoconstriction (Fig. 6.6; also refer to Chaps. 4, 6, 9, 10, and 16). These findings usually resolve in a few days although cerebral infarction or hemorrhage may be seen. In addition, atypical patterns of PRES on neuroimaging have been extensively reported in the literature. Although generally described in the setting of severe hypertension, up to a quarter of patients are normotensive. PRES is associated with systemic conditions such as eclampsia, transplantation, sepsis, chemotherapy, and autoimmune disease. Although the mechanism of PRES remains controversial, endothelial dysfunction (from a variety of etiologies) preferentially, but not exclusively involving the posterior circulation has been postulated as the inciting cause.

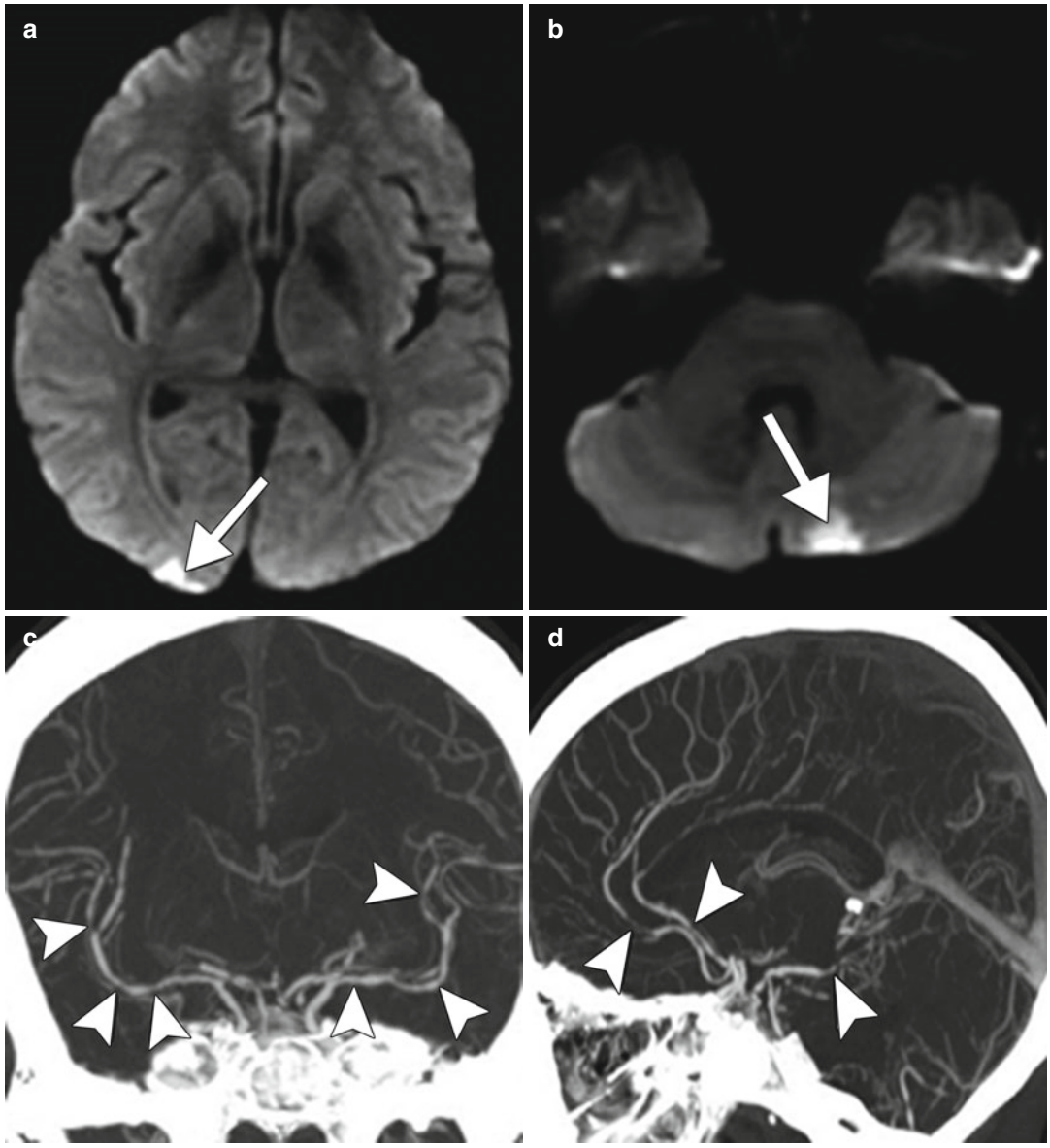

Fig. 6.4 Reversible cerebral vasoconstriction syndrome (RCVS). The patient presented with acute onset of thunderclap headache in the setting of Prozac and Cannabis use. Axial DWI (**a**, **b**) images demonstrate acute areas of infarction (*arrows*). Coronal (**c**) and sagittal (**d**) CTA reconstructions demonstrate multifocal areas of arterial narrowing and irregularity involving the anterior, middle, and posterior cerebral arteries (*arrows*). CSF analysis was normal and symptoms resolved within 3 months

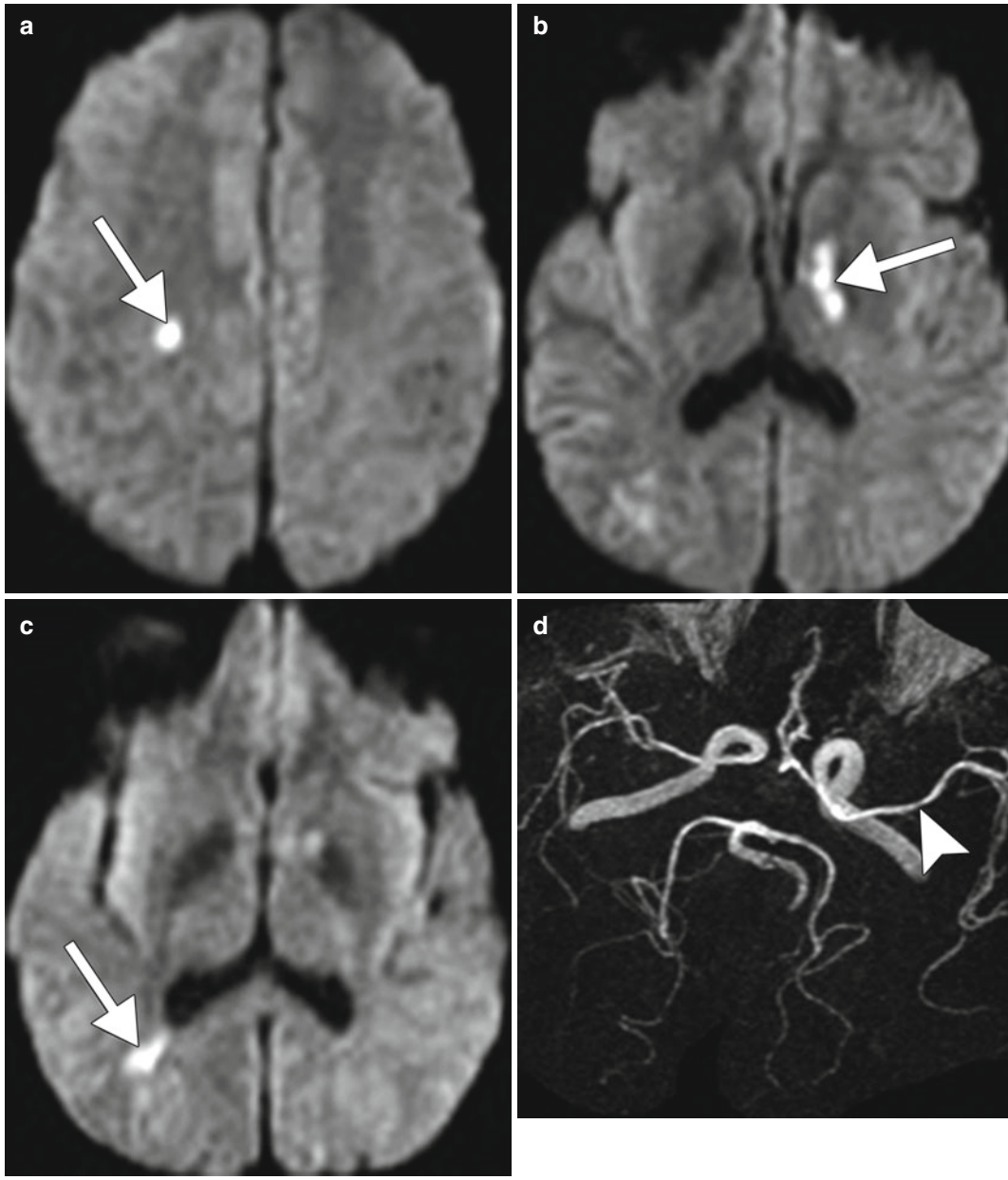

Fig. 6.5 Primary CNS angiitis. DWI (**a**–**c**) shows multifocal acute infarcts (*arrows*). MRA MIP (**d**) image reconstruction demonstrates narrowing of the left M1 segment (*arrows*). AP (**e**) and lateral oblique (**f**) left carotid angiogram images demonstratemultifocal areas of arterial narrowing and irregularity (*arrowheads*). CSF analysis demonstrated acute phase reactants, and over the course of months to years, the patient gradually deteriorated with several more episode of infarction

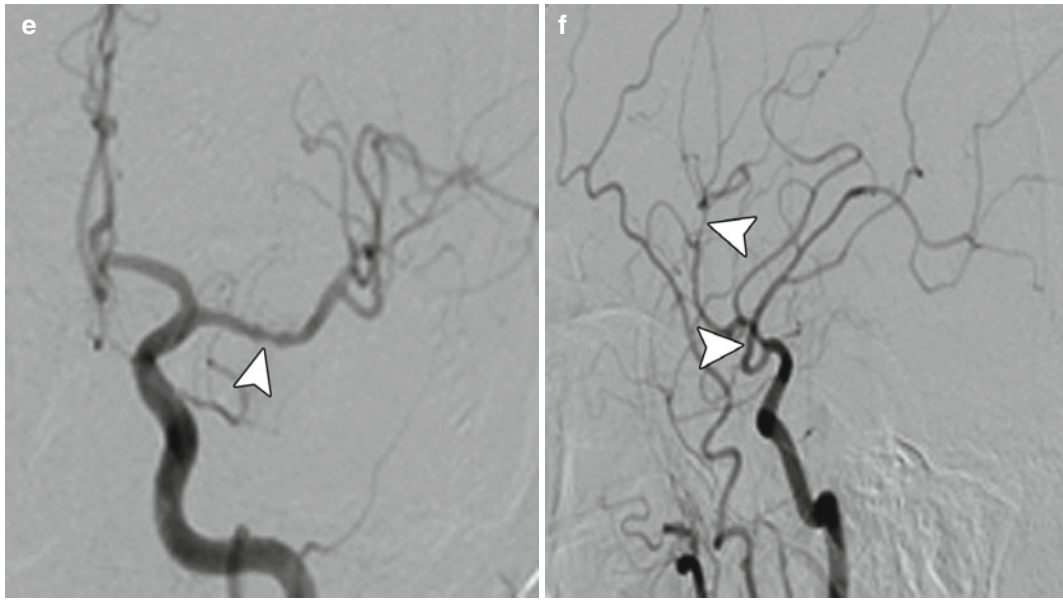

Fig. 6.5 (continued)

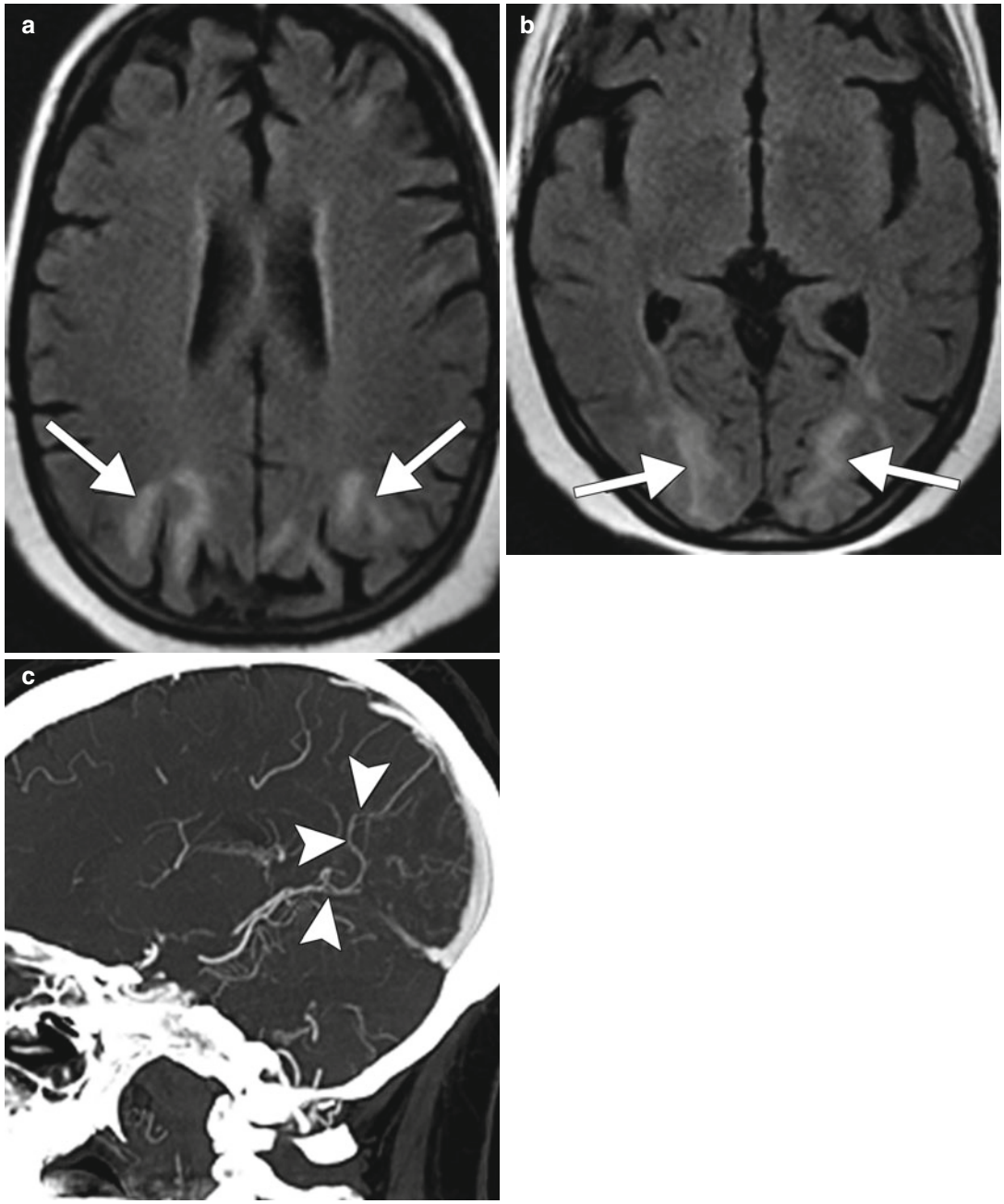

Fig. 6.6 Acute hypertensive encephalopathy (posterior reversible encephalopathy syndrome). Axial FLAIR MR images (**a**, **b**) demonstrate bilateral predominantly parietal and occipital lobe edema. Sagittal CTA MIP image (**c**) of the left posterior cerebral artery reveals multifocal areas of arterial narrowing (*arrows*)

Suggested Reading

Ducros A. Reversible cerebral vasoconstriction syndrome. Lancet Neurol. 2012;11(10):906–17.

Fleckenstein AE, Volz TJ, Riddle EL, Gibb JW, Hanson GR. New insights into the mechanism of action of amphetamines. Annu Rev Pharmacol Toxicol. 2007;47:681–98.

Liu CH, Yang J, Ren JQ, Liu CM, You Z, Liu PK. MRI reveals differential effects of amphetamine exposure on neuroglia in vivo. FASEB J. 2013;27(2):712–24.

Reneman L, Habraken JB, Majoie CB, Booij J, den Heeten GJ. MDMA ("Ecstasy") and its association with cerebrovascular accidents: preliminary findings. AJNR Am J Neuroradiol. 2000;21(6):1001–7.

Stevens CJ, Heran MK. The many faces of posterior reversible encephalopathy syndrome. Br J Radiol. 2012;85(1020):1566–75.

Tucker GT, Lennard MS, Ellis SW, et al. The demethylenation of methylenedioxymethamphetamine ("ecstasy") by debrisoquine hydroxylase (CYP2D6). Biochem Pharmacol. 1994;47:1151–6.

Opioids

7

Daniel Thomas Ginat

7.1 Uses

Opioids can be addictive and prone to dependence and abuse. However, there are many forms of opioids available for clinical use. The main clinical indications for opioids in the United States include the moderate to severe pain related to surgery and induction and maintenance of anesthesia, often in conjunction with other drugs, cough, diarrhea, anxiety due to shortness of breath, and opioid dependence.

7.2 Mechanism

Opioids interact with mu, delta, or kappa opioid receptors, which are coupled to G1 proteins. They close N-type voltage-operated calcium channels and open calcium-dependent inwardly rectifying potassium channels. This results in hyperpolarization and reduction in neuronal excitability. The drugs also decrease intracellular cAMP which modulates the release of nociceptive neurotransmitters. Mu-opioid agonists can also directly increase Ca^{2+} entry and cellular Ca^{2+} concentrations. Changes in cAMP may underlie opioid-induced modulation of the release of neurotransmitters such as substance P. There is a particularly high density of mu-opioid receptors in the periaqueductal gray matter, cerebellum, and limbic systems.

7.3 Discussion

Neurotoxicity related to opioids generally presents in the adult population, but may occur in children due to accidental ingestion. Since patients may not be forthcoming with their drug abuse habits, present comatose, or may truly not know what happened, a toxic-metabolic workup and neuroimaging are important for establishing the diagnosis.

Heroin-induced leukoencephalopathy or "chasing the dragon" syndrome is a toxic spongiform encephalopathy that results from heroin vapor inhalation. "Chasing the dragon" is specific to black-market heroin and involves heating heroin powder on aluminum foil over a flame and inhaling the vapor produced through a straw or pipe. The syndrome may be attributable to an additive or contaminant in street heroin, activated by the heating process. Patients with heroin-induced leukoencephalopathy can present with apathy, cerebellar syndrome, soft (pseudobulbar) speech, and motor restlessness, which can progress to pyramidal tract and pseudobulbar signs, tremor and choreo-athetoid movements, followed by stretching spasms, akinetic mutism, hypotonic paresis, central pyrexia, and death, with a mortality rate of 23 %. Therapy consists of administering antioxidant drug regimens in the form of coenzyme Q, vitamin C, and vitamin E.

D.T. Ginat, MD, MS
Department of Radiology, University of Chicago, Pritzker Medical School, Chicago, IL, USA
e-mail: ginatd01@gmail.com

D.T. Ginat et al. (eds.), *Neuroimaging Pharmacopoeia*,
DOI 10.1007/978-3-319-12715-6_7,

The typical manifestation of heroin-induced leukoencephalopathy on MRI is confluent bilateral and symmetric white matter T2 hyperintensity with relative sparing of the subcortical U-fiber, producing a "dragon's claw" appearance (Fig. 7.1). There is often corresponding restricted diffusion in the acute setting. On MR spectroscopy, decreased NAA and Cho and the presence of Lac are a consistent finding. More uncommonly, heroin inhalation can result in unilateral or bilateral hippocampal

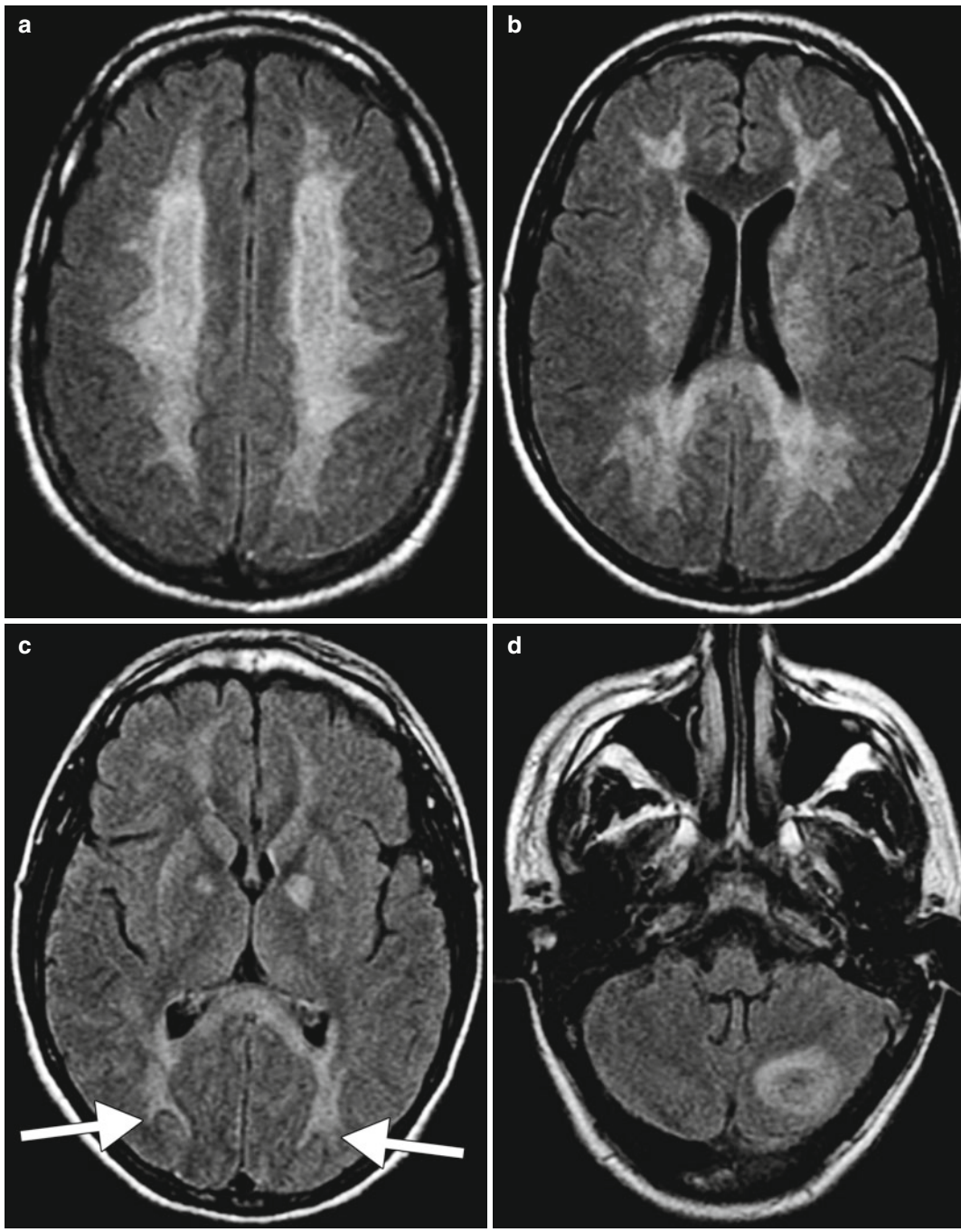

Fig. 7.1 Heroin-induced leukoencephalopathy (chasing the dragon). Axial FLAIR images (**a**–**d**) and ADC maps (**e**–**h**) show diffuse confluent cerebral white matter signal abnormality with restricted diffusion that spares the subcortical white matter, producing a "dragon's claw" appearance (*arrows*)

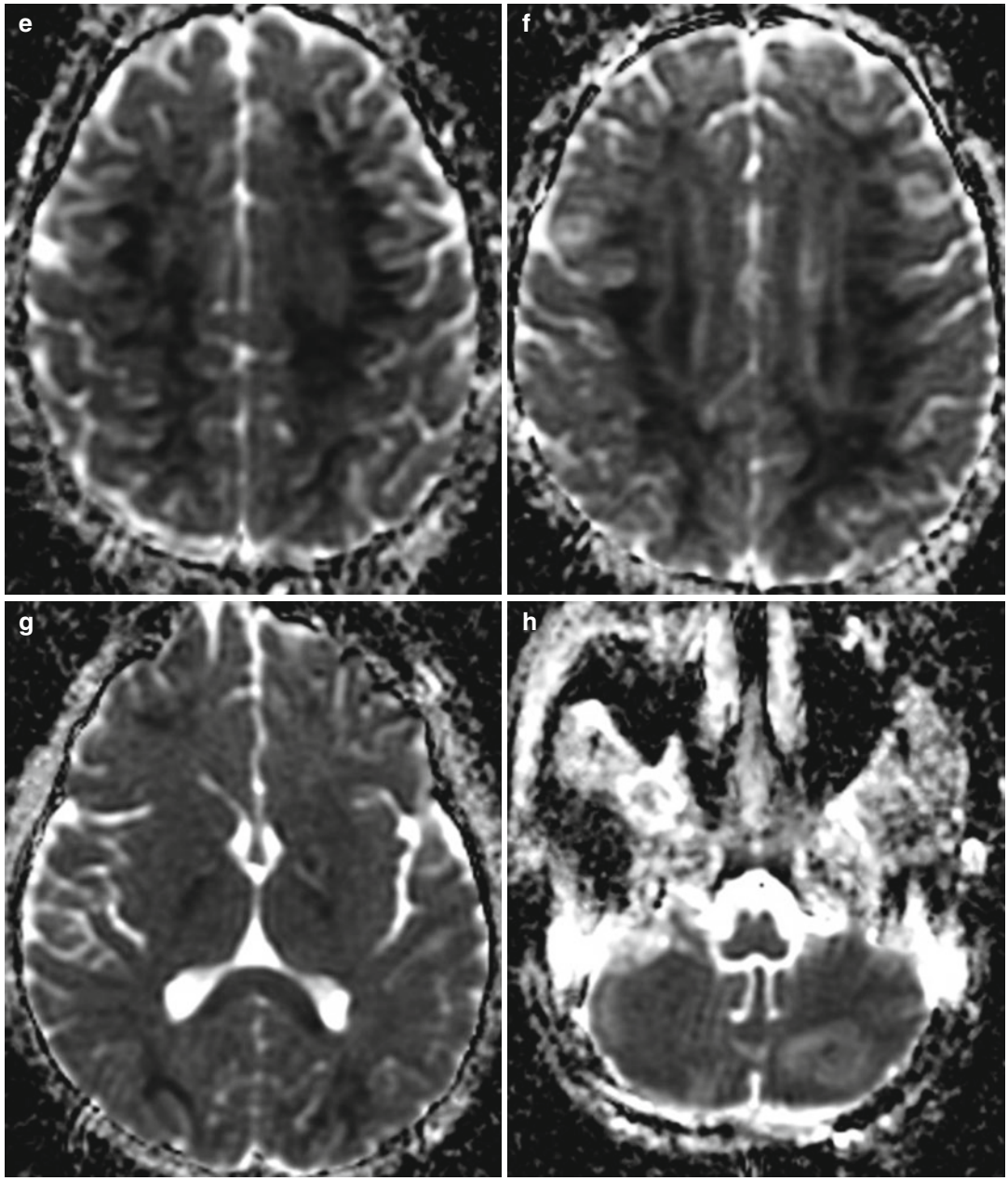

Fig. 7.1 (continued)

infarction, which can occur in isolation of other abnormality. The affected area can initially demonstrate restricted diffusion and subsequently progress toward extensive cortical laminar necrosis with intrinsic T1 hyperintensity on MRI (Fig. 7.2).

Other opioids, such as methadone, can produce toxic leukoencephalopathy with imaging findings that are similar, but not identical to those of heroin inhalation. In addition, other opioids, such as oxycodone, which have a predilection of kappa receptors, can cause acute neurotoxicity with predominant cerebellar and globi pallidi lesions (Fig. 7.3).

Delayed posthypoxic leukoencephalopathy can be caused by opioid overdoses that result in respiratory failure and prolonged cerebral hypo-oxygenation. This condition has a classic

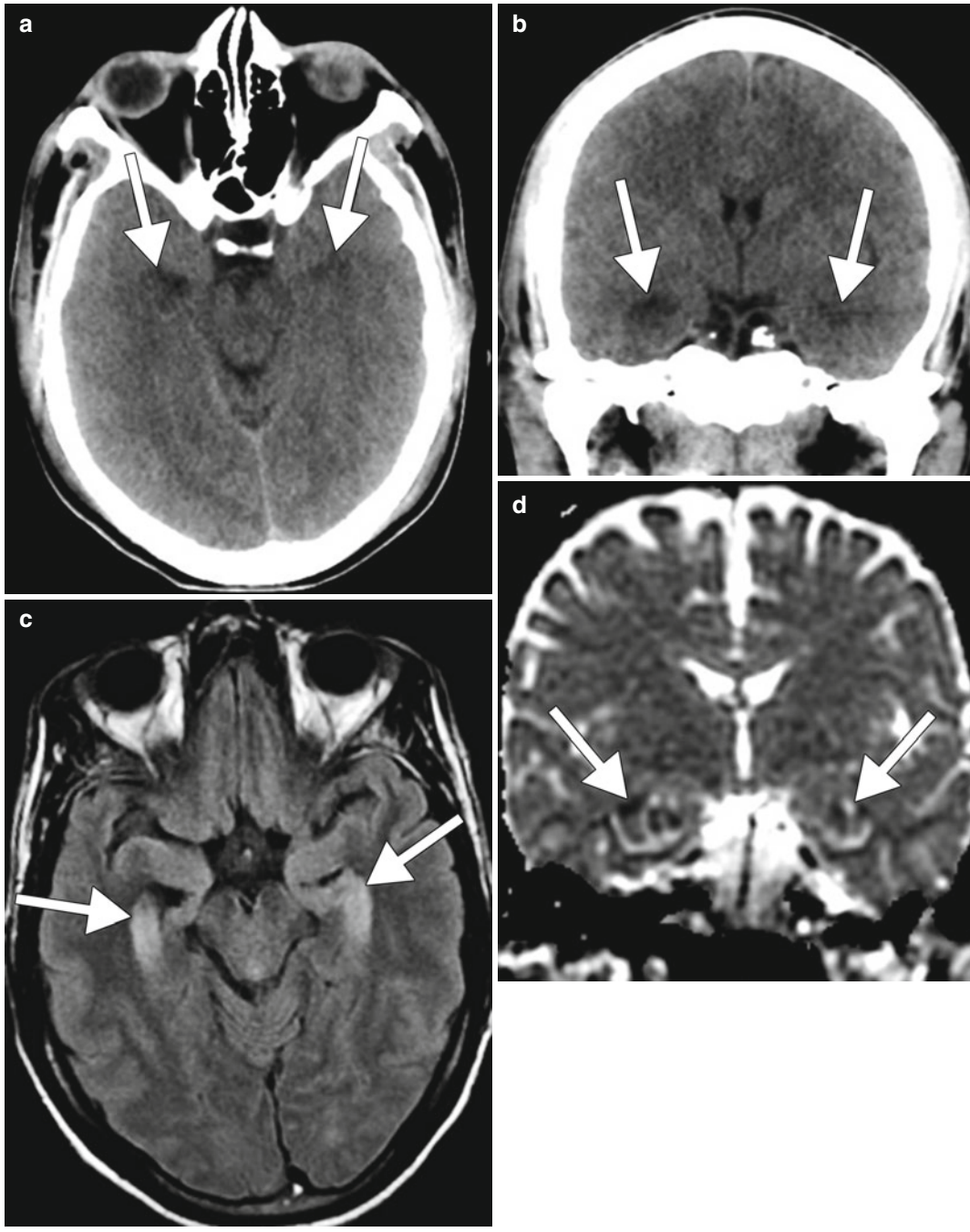

Fig. 7.2 Heroin induced hippocampal infarct. Axial (**a**) and coronal (**b**) CT images show hypoattenuation within the bilateral hippocampi (*arrows*). The corresponding axial FLAIR (**c**) and coronal ADC map (**d**) show signal abnormality with restricted diffusion in the bilateral hippocampi (*arrows*). Axial T1-weighted MRI (**e**) obtained at follow-up shows bilateral hippocampal cortical laminar necrosis (*arrows*)

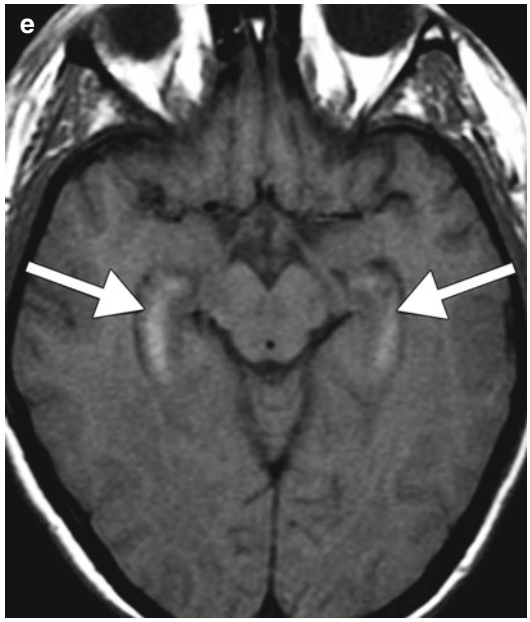

Fig. 7.2 (continued)

biphasic presentation, in which there is full recovery from an obtunded or comatose state followed days or weeks later by an acute onset of neuropsychiatric findings including disorientation, amnesia, hyperreflexia, frontal release signs, parkinsonism, akinetic mutism, or psychosis. MRI demonstrates diffuse demyelination involving white matter of the cerebral hemispheres, usually sparing the posterior fossa with corresponding severe diffuse hypometabolism on ^{18}FDG-PET (Fig. 7.4).

Infections of the central nervous system are potentially devastating consequences of administering heroin and many other illicit drugs via injection. In particular, unsanitary practices such as neglecting to cleanse the skin prior to injection and using contaminated needles can introduce pathogens that cause skin infections and infective endocarditis, which can then lead to the formation of brain abscess. *Staphylococcus aureus* is a common organism found in intravenous drug-use-associated

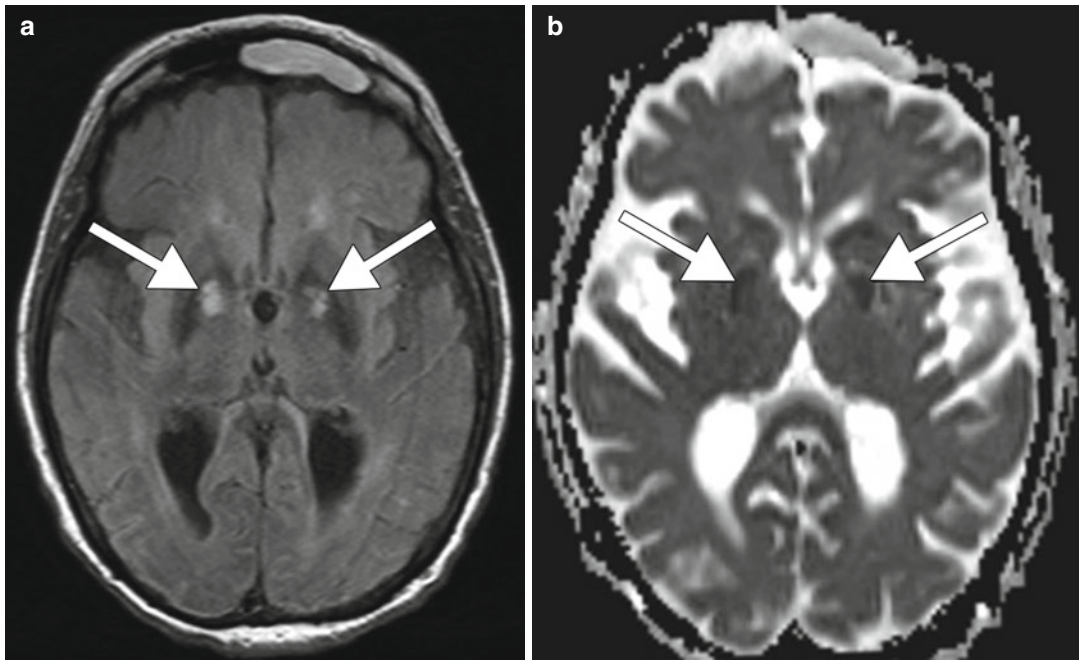

Fig. 7.3 Acute oxycodone intoxication. Axial FLAIR (**a**) and ADC map (**b**) show abnormal signal and restricted diffusion within the bilateral globi pallidi (*arrows*)

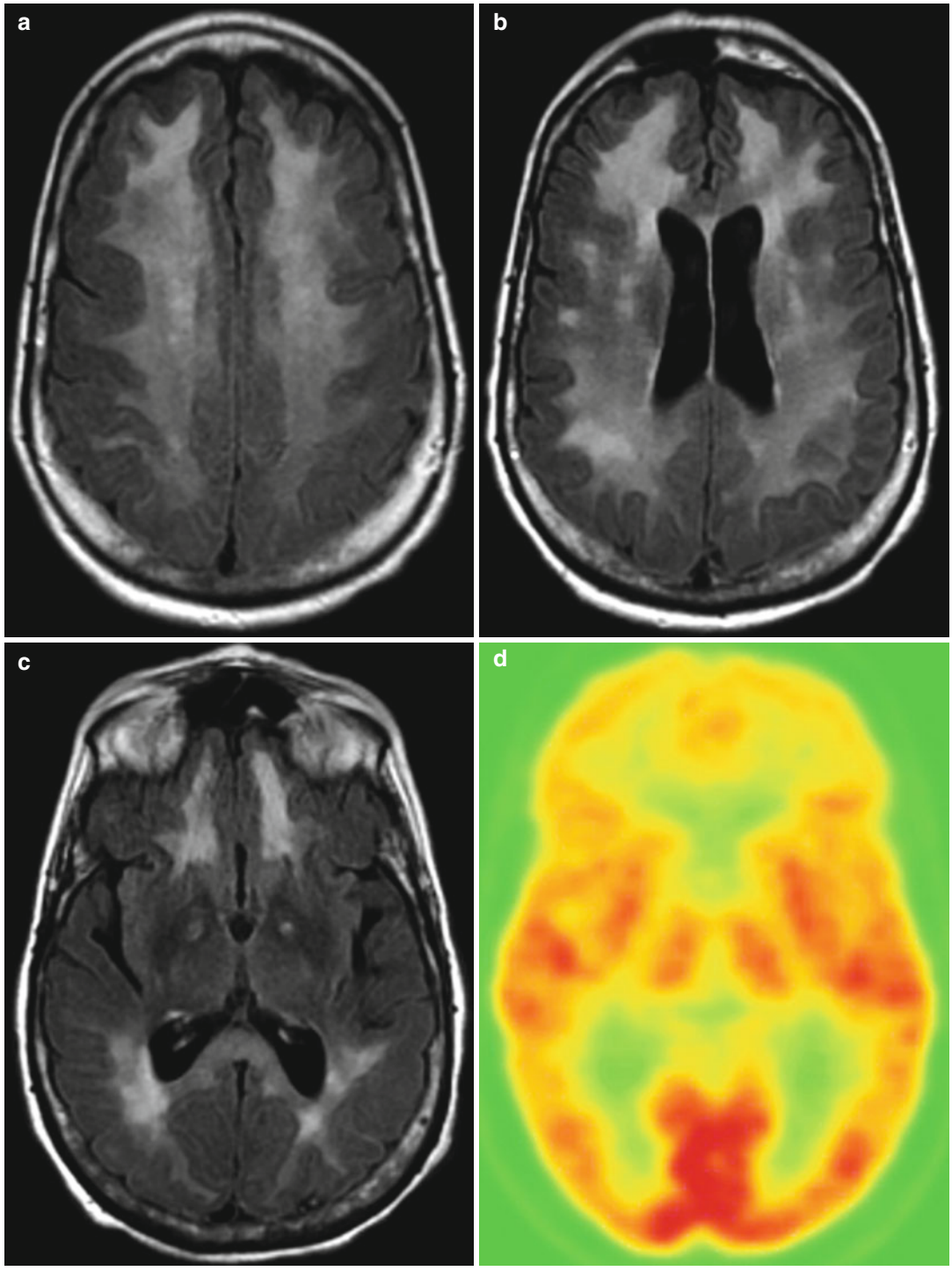

Fig. 7.4 Delayed posthypoxic leukoencephalopathy. Axial FLAIR MR images (**a**–**c**) show extensive bilateral cerebral white matter hyperintensity with corresponding global hypometabolism with relative sparing of the occipital lobes on ^{18}FDG-PET (**d**)

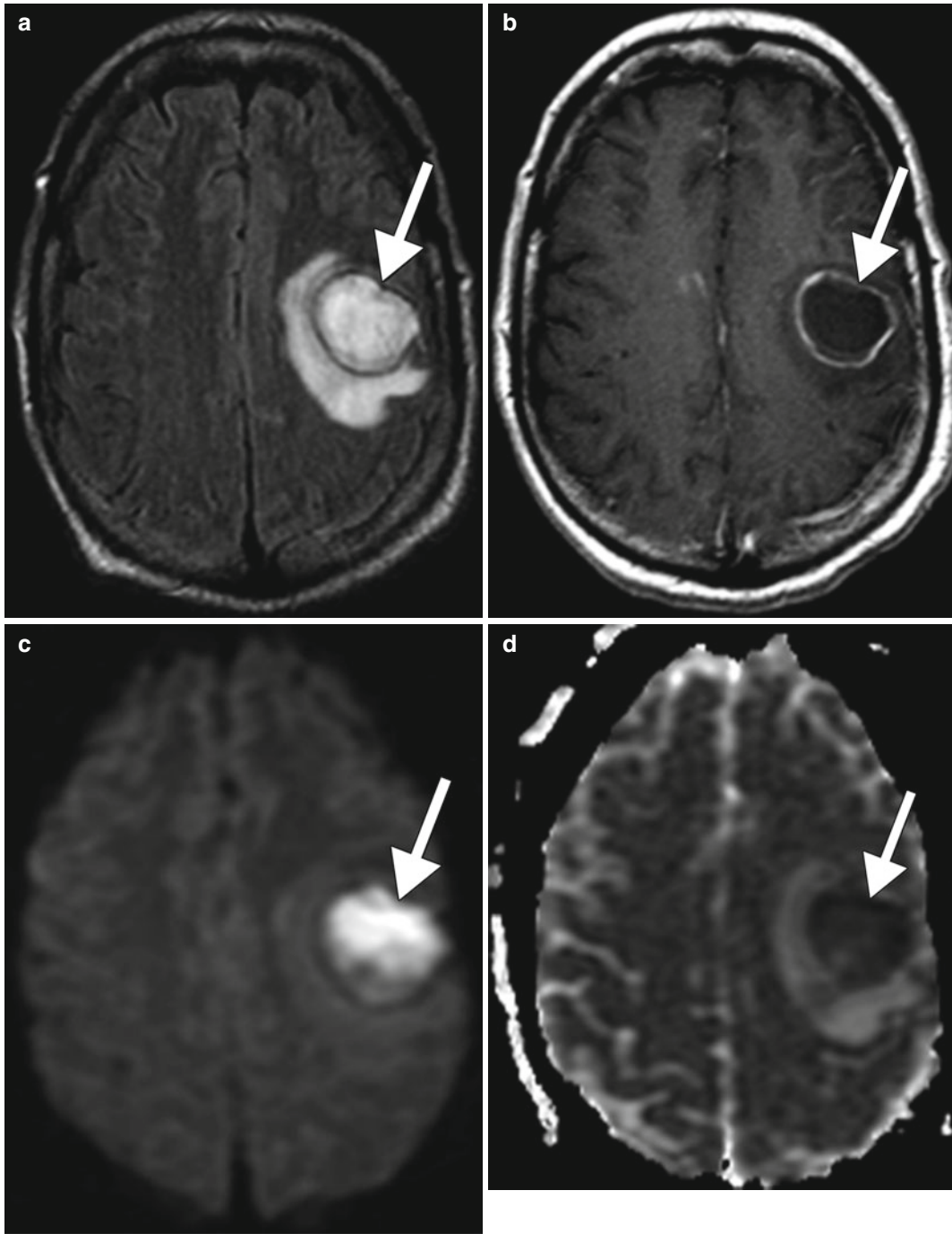

Fig. 7.5 Intravenous drug-use-associated brain abscess. The patient has a history of snorting cocaine and recent intravenous heroin use. Axial FLAIR (**a**), post-contrast T1-weighted (**b**), DWI (**c**), and ADC map (**d**) show a ring-enhancing lesion with restricted diffusion and surrounding edema in the left frontal lobe (*arrows*)

abscess and typically appears as a ring-enhancing lesion with restricted diffusion and surrounding edema (Fig. 7.5). Central nervous system infections can also occur in the absence of infective endocarditis, resulting from bacteremia. This can result in discitis-osteomyelitis and facet joint

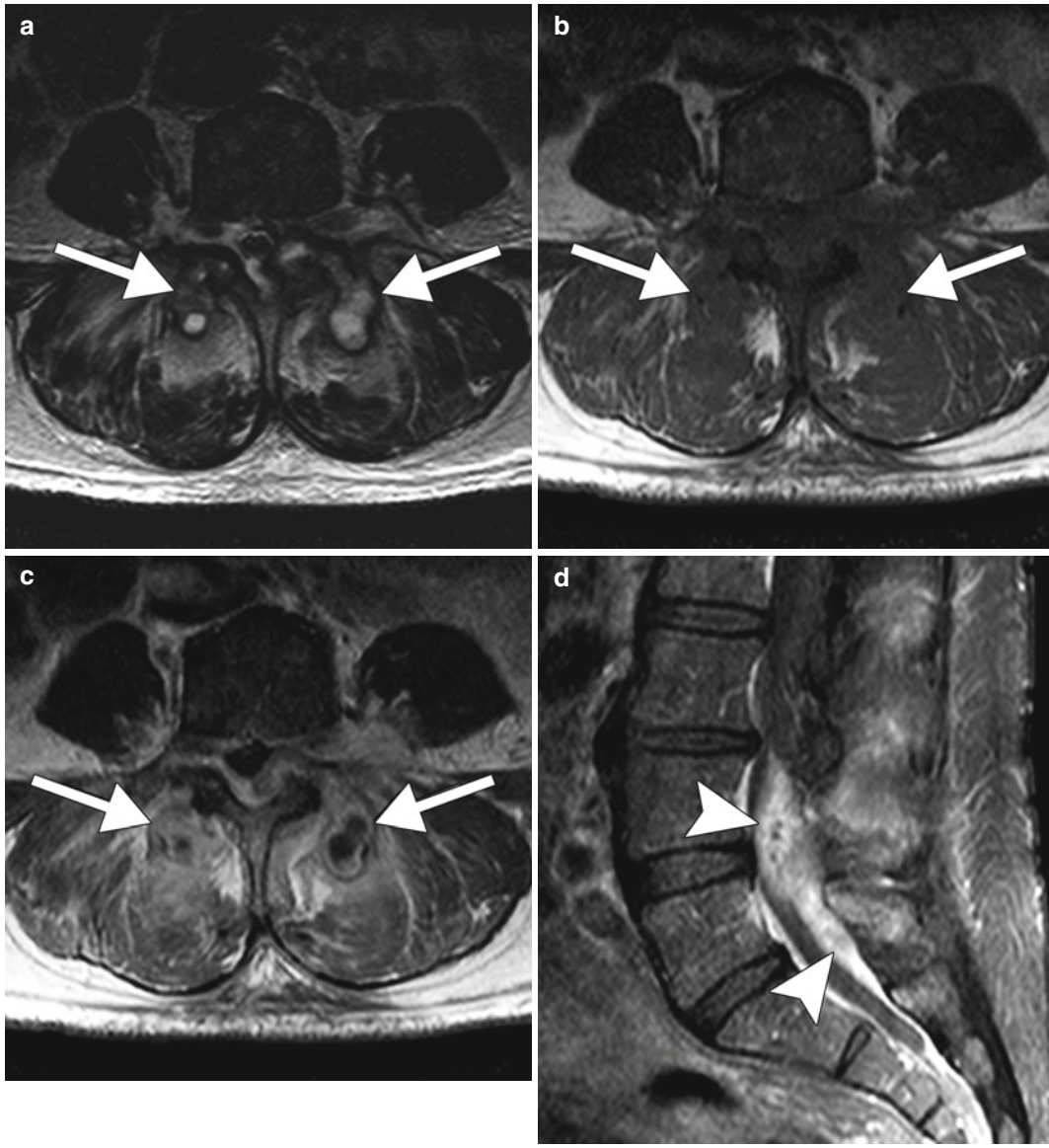

Fig. 7.6 Intravenous drug-use-associated septic arthritis. The patient has a history of recent intravenous heroin use. Axial T2-weighted (**a**), T1-weighted (**b**), and post-contrast T1-weighted (**c**) MR images show septic arthritis of bilateral lumbar facet joints (*arrows*). Sagittal post-contrast T1-weighted MRI (**d**) shows extension of the inflammatory changes into the epidural space (*arrowheads*)

septic arthritis in the spine (Fig. 7.6) and septic thrombophlebitis in the neck (Fig. 7.7). Contrast-enhanced MRI is useful for evaluating these infections and associated spinal canal compromise. Antimicrobial therapy often combined with surgical intervention is necessary to treat these neurologic complications. Individuals that practice injection drug use are also at risk of acquiring HIV, which can also have neurological manifestations, including encephalitis and associated opportunistic infections, such as fungal abscesses, toxoplasmosis, and PML due to immune system compromise (refer to Chap. 26). Furthermore, certain drugs, including marijuana and opioids and cocaine, may have effects on the immune system mediated indirectly by drug interactions in the

central nervous system or directly through activation of cognate receptors on various immune cells, which may predispose to infections.

7.4 Differential Diagnosis

Toxic leukoencephalopathy has been associated with a variety of deleterious substances, including carbon monoxide, solvents, chemotherapeutic agents, cranial radiation, and substances of abuse, such as alcohol and cocaine. However, the combined involvement of the bilateral cerebellar white matter, posterior limb of the internal capsule, with sparing of the anterior limb, and predominantly posterior cerebral white matter with sparing of subcortical U-fibers appears to be highly suggestive of heroin-induced leukoencephalopathy. On the other hand, there is a broader differential diagnosis for heroin-induced hippocampal stroke, including atheroembolic stroke, herpes encephalitis, transient global amnesia (Fig. 7.8), and limbic encephalitis (Fig. 7.9). Acute neurotoxicity affecting the globi pallidi and cerebellum caused by certain opioids such as oxycodone can resemble certain cases of hyperammonemia (refer to Chap. 49), hypoxic ischemic injury, acute Ecstasy toxicity (refer to Chap. 6), mitochondrial disorders, carbon monoxide poisoning (refer to Chap. 40), and methanol toxicity (refer to Chap. 3). Similarly, delayed posthypoxic leukoencephalopathy can result from other of prolonged hypoxia, such as CO poisoning. The imaging findings of delayed posthypoxic leukoencephalopathy are essentially pathognomonic in the appropriate clinical setting.

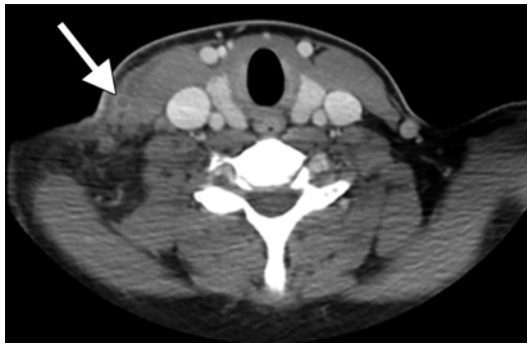

Fig. 7.7 Axial post-contrast CT image shows thrombosis of the right external jugular vein branch (*arrow*) with associated surrounding cellulitis and myositis

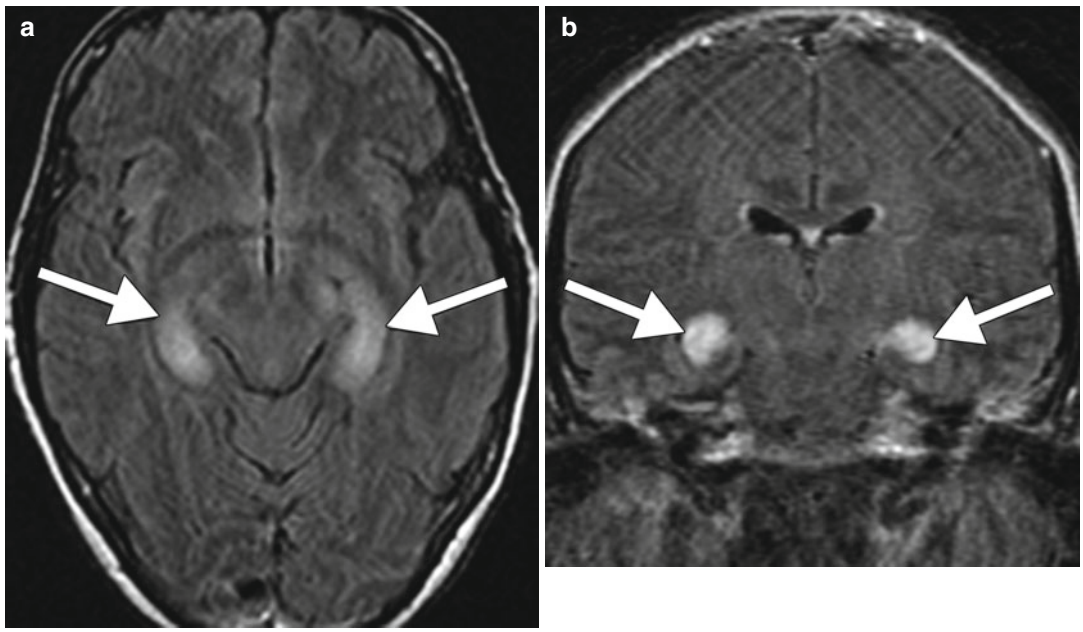

Fig. 7.8 Limbic encephalitis. Axial (**a**) and coronal (**b**) FLAIR MR images show diffuse hyperintensity involving the bilateral hippocampi (*arrows*)

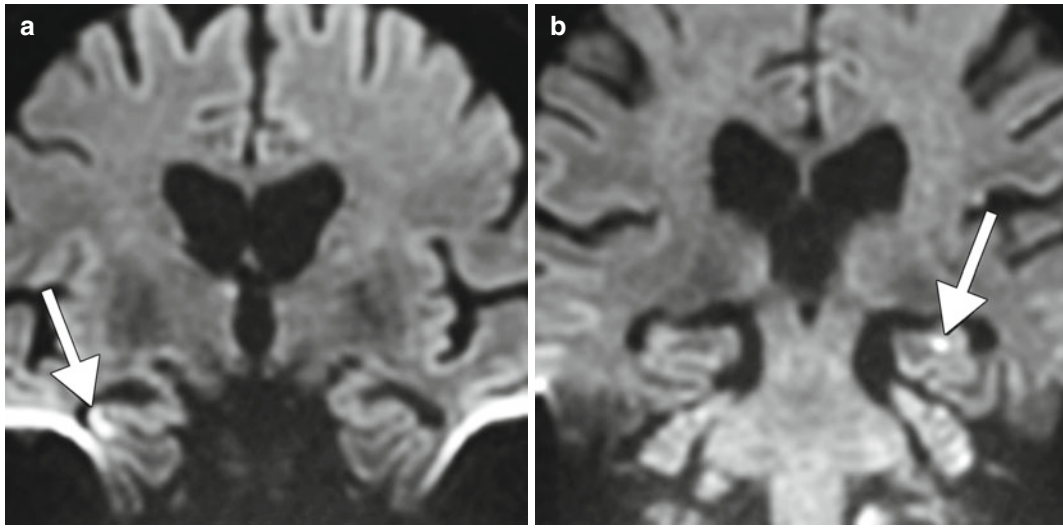

Fig. 7.9 Transient global amnesia. Coronal diffusion-weighted images (**a**, **b**) show punctate foci of restricted diffusion in the bilateral hippocampi (*arrows*)

Suggested Reading

Bartlett E, Mikulis DJ. Chasing "chasing the dragon" with MRI: leukoencephalopathy in drug abuse. Br J Radiol. 2005;78(935):997–1004.

Benoilid A, Collongues N, de Seze J, Blanc F. Heroin inhalation-induced unilateral complete hippocampal stroke. Neurocase. 2013;19(4):313–5.

Cabral GA. Drugs of abuse, immune modulation, and AIDS. J Neuroimmune Pharmacol. 2006;1(3):280–95.

Gordon RJ, Lowy FD. Bacterial infections in drug users. N Engl J Med. 2005;353(18):1945–54.

Gupta PK, Krishnan PR, Sudhakar PJ. Hippocampal involvement due to heroin inhalation–"chasing the dragon". Clin Neurol Neurosurg. 2009;111(3):278–81.

Henriksen G, Willoch F. Imaging of opioid receptors in the central nervous system. Brain. 2008;131(Pt 5):1171–96.

Howland RH. The diverse clinical uses of opioid receptor drugs. J Psychosoc Nurs Ment Health Serv. 2010;48(5):11–4.

Keogh CF, Andrews GT, Spacey SD, Forkheim KE, Graeb DA. Neuroimaging features of heroin inhalation toxicity: "chasing the dragon". AJR Am J Roentgenol. 2003;180(3):847–50.

Molloy S, Soh C, Williams TL. Reversible delayed posthypoxic leukoencephalopathy. AJNR Am J Neuroradiol. 2006;27(8):1763–5.

Salgado RA, Jorens PG, Baar I, Cras P, Hans G, Parizel PM. Methadone-induced toxic leukoencephalopathy: MR imaging and MR proton spectroscopy findings. AJNR Am J Neuroradiol. 2010;31(3):565–6.

Satoh M, Minami M. Molecular pharmacology of the opioid receptors. Pharmacol Ther. 1995;68(3):343–64.

Shprecher D, Mehta L. The syndrome of delayed posthypoxic leukoencephalopathy. NeuroRehabilitation. 2010;26(1):65–72.

Betel Nuts

8

Grayson W. Hooper, Timothy Biega,
and Daniel Thomas Ginat

8.1 Uses

Areca nut (*Areca catechu*) is an ancient cultural and pharmacologic staple that is commonly chewed with the betel leaf (*Piper betle*) and is thus often referred to as the betel nut. If it is chewed with additional ingredients, which can include tobacco, slaked lime, catechu, and a number of flavorants, it is referred to as betel quid or *paan* in South Asia. The use of betel nut dates back as far as 2,000 years and is now estimated to be chewed by up to 10 % of the world's population. The US FDA maintains an import alert for betel nuts, which are considered unacceptable as a non-medicinal ingredient in oral use products. There are innumerable preparations of betel nut with different names and different biochemical effects. Betel nut is primarily masticated for its mild stimulant effect, but it is also used as a palate cleanser, breath freshener, and a simple sweet. In India, for example, popular betel nut preparations known as *Guthka* (with tobacco) and *pan masala* (without tobacco) combine betel nut, slaked lime, and various sweeteners in order to be successfully marketed to the younger demographic as innocuous sweets.

G.W. Hooper, DO • T. Biega, MD
Department of Radiology, Tripler Army Medical Center, Honolulu, HI, USA

D.T. Ginat, MD, MS (✉)
Department of Radiology, University of Chicago, Pritzker Medical School, Chicago, IL, USA
e-mail: ginatd01@gmail.com

8.2 Mechanism

Chewing areca nut liberates four precursor areca-specific alkaloids into the saliva: arecoline, guvacoline, guvacine, and arecaidine, with arecoline accounting for up to 1 % of the dry weight of the nut. These are in addition to tobacco-specific alkaloids if betel quid is chewed. The areca-specific alkaloids undergo nitrosation to form multiple areca-specific nitrosamines, including 3-(methylnitrosamino) propionitrile (MNPN) and 3-(Methylnitrosamino) propionaldehyde (MNPA)—both of which have been shown to be carcinogenic in rat models. Arecoline and arecaidine, without further chemical alteration, have been shown to stimulate fibroblast proliferation, which is implicated in the development of oral submucous fibrosis. In addition, the use of slaked lime (calcium hydroxide) decreases oral pH and facilitates the auto-oxidation of areca polyphenols to produce the reactive oxygen species superoxide and hydrogen peroxide, which directly damage DNA. In Papua New Guinea, users will often add extra lime in the corners of their mouths. Consequently, contrary to the common observation that most oral squamous cell carcinomas arise in the floor of the mouth, those users in Papua New Guinea more often develop the disease in the corners of their mouths. Of note, the use of areca nut is associated with a strong, systemic inflammatory response in humans as measured by CRP. This could be mediated through areca extract-induced

D.T. Ginat et al. (eds.), *Neuroimaging Pharmacopoeia*,
DOI 10.1007/978-3-319-12715-6_8,

inflammatory cytokines, as areca extract has been shown to stimulate tumor necrosis factor alpha (TNF-α) and interleukin-1b (IL-1b).

8.3 Discussion

Betel nut and its myriad preparations are a known cause of oral squamous cell carcinoma, as well as esophageal, gastric, hepatic, and pancreatic carcinomas. In the case of oral squamous cell carcinoma, there is a betel nut dose-dependent relationship and a synergistic relationship with alcohol and tobacco usage. Betel nut usage has also been implicated in the development of multiple debilitating and premalignant conditions, including leukoplakia, malakoplakia, and oral submucosal fibrosis (OSF). Betel nut-associated oral squamous cell carcinomas generally appear as heterogeneous, diffusely enhancing masses on CT (Fig. 8.1). There is often discordance between the ^{18}FDG-PET-CT features of the cervical lymph nodes and their pathologic specimens due to an inflammatory response related to betel nut use (Fig. 8.2). Enlarged and hypermetabolic are often free of tumor on pathologic examination, even in the setting of large primary tumors.

8.4 Differential Diagnosis

Oral region squamous cell carcinomas can be predisposed by other factors besides betel nuts, including tobacco, alcohol, and HPV (refer to Chaps. 1 and 2). The imaging features of squamous cell associated with betel nut use generally appear similar to other squamous cell carcinomas on imaging. However, HPV positive squamous cell carcinomas tend to be well defined with cystic metastatic lymph nodes. In addition, betel nut-induced squamous cell carcinomas are

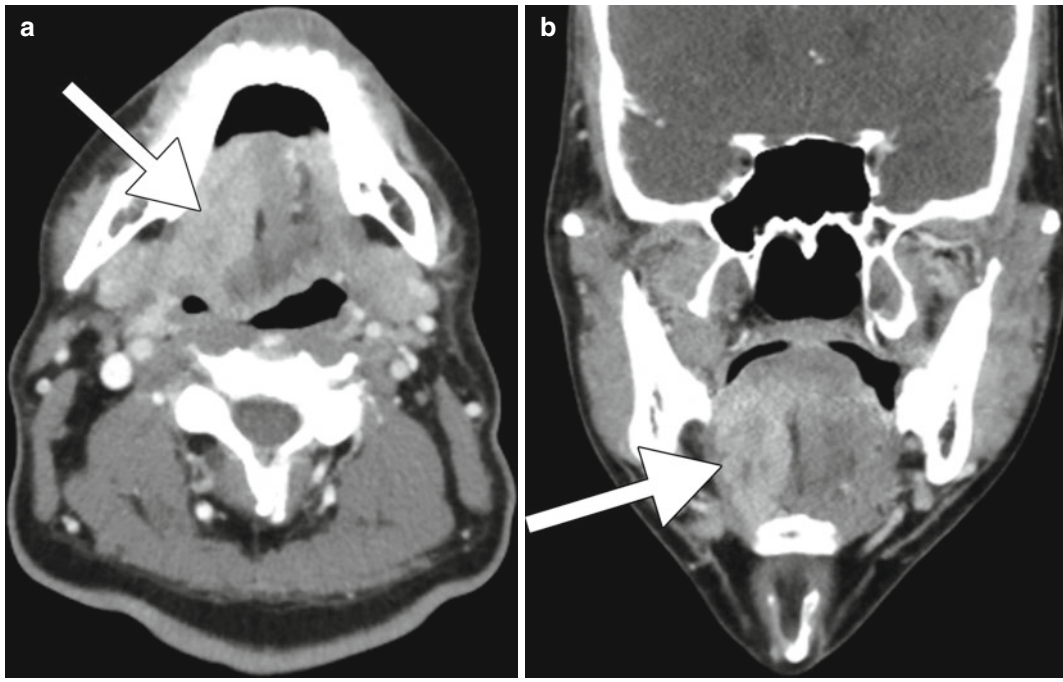

Fig. 8.1 Betel nut-induced oral cavity squamous cell carcinoma. Axial (**a**) and coronal (**b**) contrast-enhanced CT images show an enhancing mass in the right oral tongue (*arrows*)

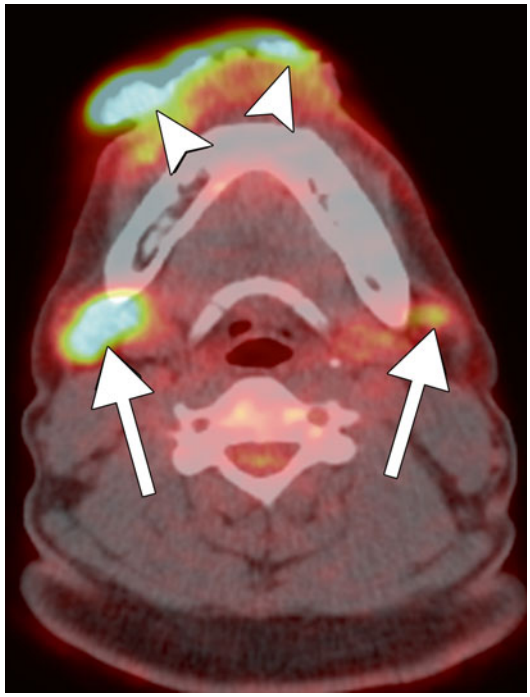

Fig. 8.2 Inflammatory lymph nodes associated with betel nut-induced squamous cell carcinoma. Axial PET-CT fusion image shows an exophytic hypermetabolic lower lip squamous cell carcinoma (*arrowheads*) and bilateral hypermetabolic level 1 lymph nodes (*arrows*) that did not contain malignant cells

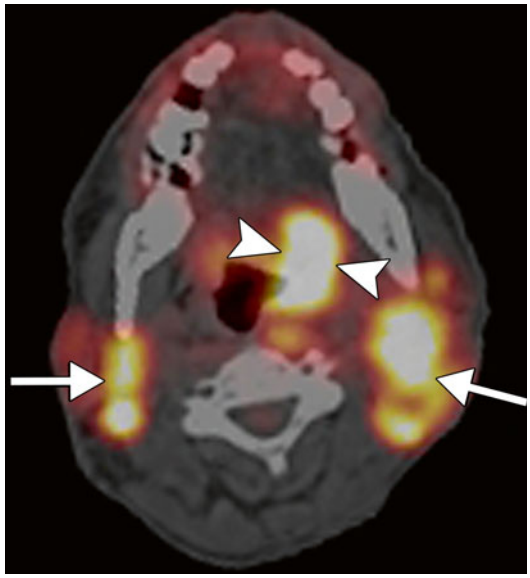

Fig. 8.3 Metastatic lymph nodes. Axial PET-CT fused image shows a hypermetabolic left tongue base squamous cell carcinoma (*arrowheads*) and bilateral hypermetabolic metastatic lymphadenopathy (*arrows*)

particularly frequently associated with enlarged, hypermetabolic inflammatory lymph nodes. The false-positive inflammatory lymph nodes have been shown to have maximum standard uptake values (mSUV) on ^{18}FDG-PET that are indistinguishable from metastatic lymph nodes (Fig. 8.3). Lymph nodes may also exhibit hypermetabolism on PET in the weeks following radiation therapy, but the SUV tends not to be as elevated.

Suggested Reading

Akhtar S, Sheikh AA, Qureshi HU. Chewing areca nut, betel quid, oral snuff, cigarette smoking and the risk of oesophageal squamous-cell carcinoma in South Asians: a multicentre case–control study. Eur J Cancer. 2013;48(5):655–61.

Chang LY, Wan HC, Lai YL, Kuo YF, Liu TY, Chen YT, et al. Areca nut extracts increased expression of inflammatory cytokines, tumor necrosis factor-alpha, interleukin-1beta, interleukin-6 and interleukin-8, in peripheral blood mononuclear cells. J Periodontal Res. 2009;44:175–83.

Gupta PC, Warnakulasuriya S. Global epidemiology of areca nut usage. Addict Biol. 2002;7:77–83.

Jeng JH, Chang MC, Hahn LJ. Role of areca nut in betel quid-associated chemical carcinogenesis: current awareness and future perspectives. Oral Oncol. 2001;37(6):477–92.

Kurkalang S, Banerjee A, Ghoshal N, Dkhar H, Chatterjee A. Induction of chromosome instability and stomach cancer by altering the expression pattern of mitotic checkpoint genes in mice exposed to areca-nut. BMC Cancer. 2013;13:315.

Nair U, Bartsch H, Nair J. Alert for an epidemic of oral cancer due to use of the betel quid substitutes gutkha and pan masala: a review of agents and causative mechanisms. Mutagenesis. 2004;19(4):251–62.

Shafiq K, et al. Areca nut chewing and systemic inflammation: evidence of a common pathway for systemic diseases. J Inflamm. 2012;9:22.

Sharan RN, Mehrotra R, Choudhury Y, Kamlesh A. Association of betel nut with carcinogenesis: revisit with a clinical perspective. PLoS One. 2012;7(8):1–21.

Thomas SJ, MacLennan R. Slaked lime and betel nut cancer in Papua New Guinea. Lancet. 1992;340(8819):577–8.

Wang CC, Lin HL, Wey SP, Jan TR. Areca-nut extract modulates antigen-specific immunity and augments inflammation in ovalbumin-sensitized mice. Immunopharmacol Immunotoxicol. 2011;33:315–22.

Warnakulasuriya S. Areca nut use: an independent risk factor for oral cancer. Br Med J. 2002;324:799–800.

Licorice

9

Juan E. Small and Daniel Thomas Ginat

9.1 Uses

Licorice has been used as a sweetener and a thirst quencher. In certain countries, derivatives of licorice are used for the treatment and control of chronic viral hepatitis due to its presumed hepatoprotective effects. In addition, licorice is used as part of certain alternative medicine therapies for its presumed anticancer, adaptogen, and cough reliever properties. However, the benefits of chronic consumption of licorice generally may not outweigh the potential risks.

9.2 Mechanism

The active ingredient in licorice is glycyrrhizic acid, which inhibits 11ß-hydroxysteroid dehydrogenase (11ß-HSD), leading to sodium reabsorption and potassium secretion. Excessive licorice ingestion therefore results in hypervolemic hypertension, hypokalemia, and metabolic alkalosis. Of note, the pseudohyperaldosteronism induced by excessive licorice ingestion is readily distinguished from primary and secondary hyperaldosteronism by the presence of low plasma renin and aldosterone activity.

9.3 Discussion

The two main categories of documented licorice-induced complications include hypertension and hypokalemic myopathy. With regard to neuroimaging, the glucocorticoid and functional mineral corticoid excess induced by excessive licorice ingestion has been shown to result in hypertension, vasoconstriction, impaired vasorelaxation, and endothelial damage. As such, acute hypertensive encephalopathy or posterior reversible encephalopathy syndrome (PRES) and reversible cerebral vasoconstriction syndrome (RCVS) have been documented in several patients following excessive licorice ingestion. PRES is characterized predominantly by parieto-occipital and other border-zone vasogenic edema with hemorrhagic conversion in up to 20 % of cases. Areas of hemorrhage can also be apparent on imaging. RCVS is characterized by vasoconstriction involving proximal and distal vessels that may lead to border-zone infarctions in 39 % of cases. Small subarachnoid and intraparenchymal hemorrhages can also occur in 22 and 6 % of cases, respectively. There is an overlap between RCVS and PRES, and features of both can be seen in the same patient. Indeed, approximately 10 % of RCVS cases are associated with PRES, regardless of the cause. Conventional

J.E. Small, MD
Department of Diagnostic Radiology, Lahey Clinic, Burlington, MA, USA

D.T. Ginat, MD, MS (✉)
Department of Radiology, University of Chicago, Pritzker Medical School, Chicago, IL, USA
e-mail: ginatd01@gmail.com

D.T. Ginat et al. (eds.), *Neuroimaging Pharmacopoeia*,
DOI 10.1007/978-3-319-12715-6_9,

MRI sequences are suitable for depicting focal areas of vasogenic edema that are primarily distributed in the posterior regions of the cerebral hemispheres related to licorice-induced PRES, and susceptibility-weighted sequences can depict the presence of associated hemorrhage (Fig. 9.1).

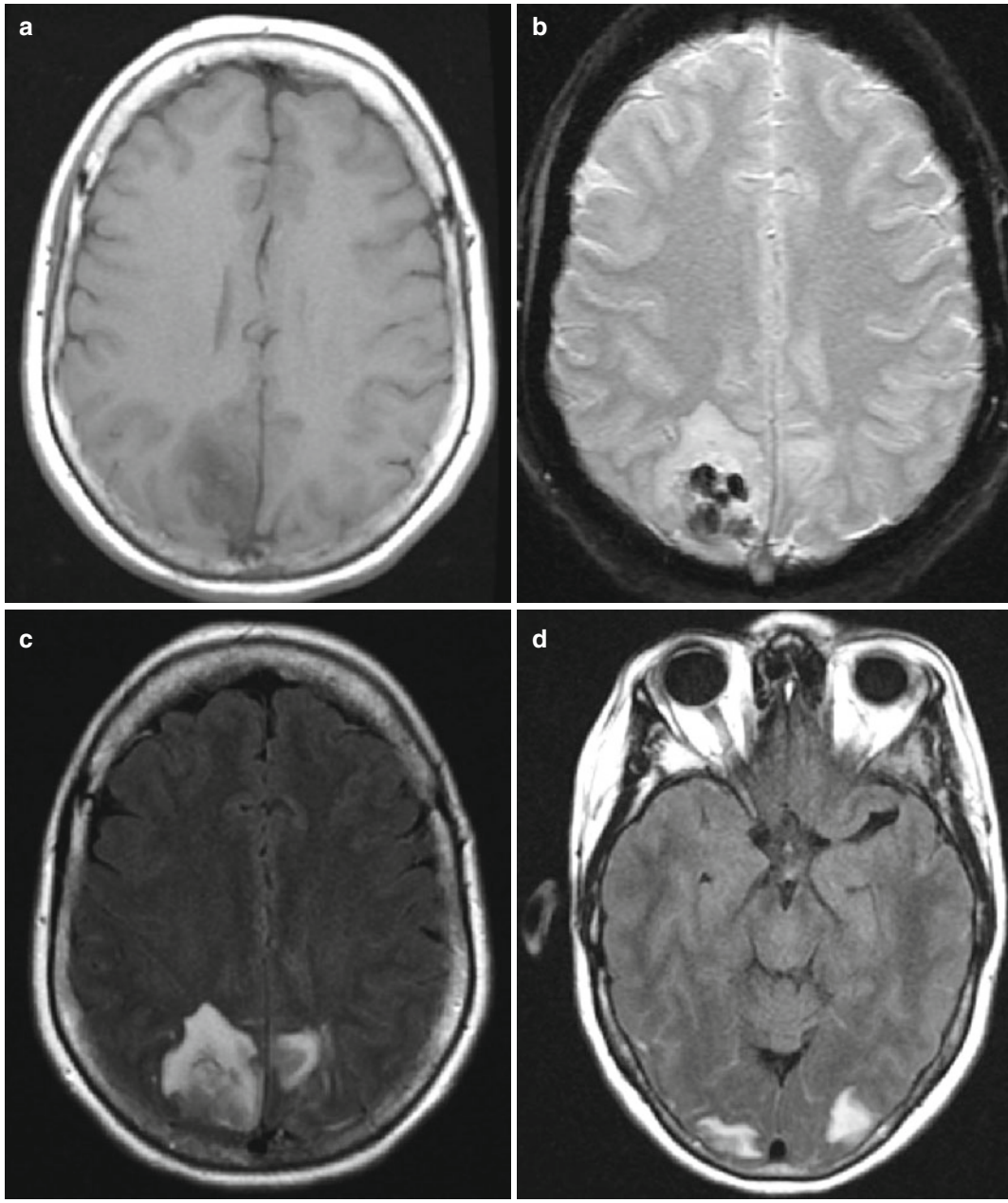

Fig. 9.1 Licorice-induced PRES. Axial T1-weighted (**a**), axial GRE (**b**), and axial FLAIR (**c**, **d**) MR images ofthe brain demonstrate bilateral parieto-occipital edema with superimposed hemorrhage in the right parietal lobe

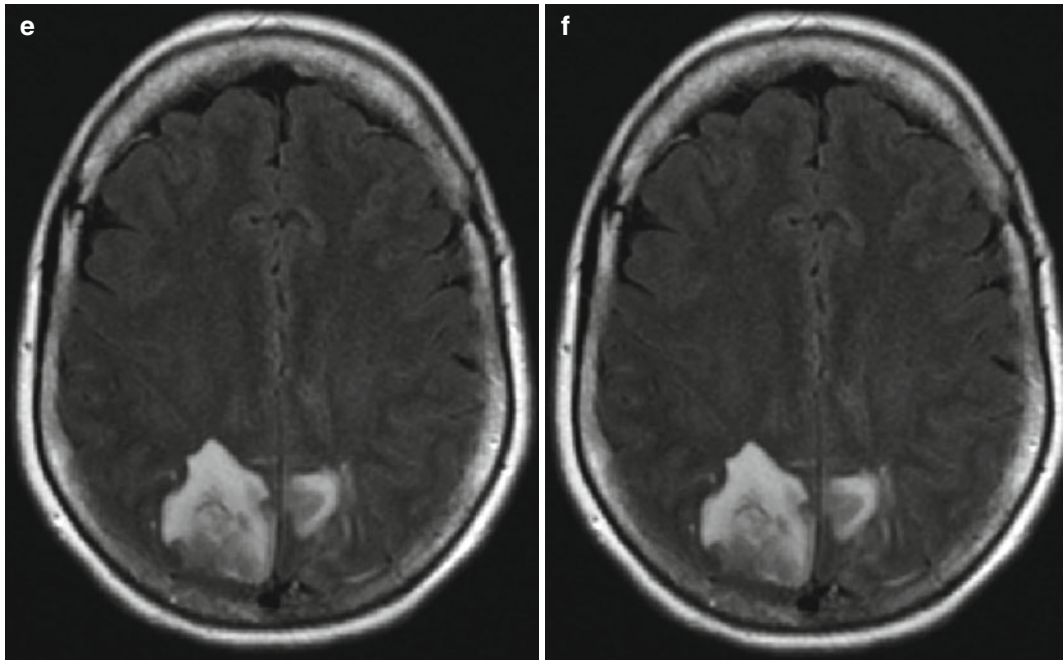

Fig. 9.1 (continued)

Perfusion MRI can be useful for demonstrating hypoperfusion in the deep watershed regions of the ipsilateral cerebral arteries with relative sparing of the superficial cortical regions in cases of RCVS. In addition, angiography can be useful to depict the segmental narrowing and dilatation of multiple cerebral arteries found in licorice-induced RCVS. Predictors of a worse outcome are the presence of cerebral infarction and parenchymal hemorrhage.

9.4 Differential Diagnosis

- PRES due to other causes (refer to Chaps. 6 and 23 for additional details)
- RCVS due to other causes (refer to Chaps. 4, 5, 6, and 10 for additional details)
- Venous sinus thrombosis (refer to Chaps. 21 and 47 for additional details)

Suggested Reading

Chatterjee N, Domoto-Reilly K, Fecci PE, Schwamm LH, Singhal AB. Licorice-associated reversible cerebral vasoconstriction with PRES. Neurology. 2010;75(21):1939–41.

Ducros A, Boukobza M, Porcher R, et al. The clinical and radiological spectrum of reversible cerebral vasoconstriction syndrome. A prospective series of 67 patients. Brain. 2007;130(Pt):3091–101.

Morgan RD, Chou SH, Stelfox HT. Posterior reversible encephalopathy syndrome in a patient following binge liquorice ingestion. J Neurol. 2011;258(9):1720–2.

Omar HR, Komarova I, El-Ghonemi M, Fathy A, Rashad R, Abdelmalak HD, Yerramadha MR, Ali Y, Helal E, Camporesi EM. Licorice abuse: time to send a warning message. Ther Adv Endocrinol Metab. 2012;3(4):125–38.

Singhal AB, Hajj-Ali RA, Topcuoglu MA, Fok J, Bena J, Yang D, Calabrese LH. Reversible cerebral vasoconstriction syndromes: analysis of 139 cases. Arch Neurol. 2011;68(8):1005–12.

van Beers EJ, Stam J, van den Bergh WM. Licorice consumption as a cause of posterior reversible encephalopathy syndrome: a case report. Crit Care. 2011;15(1):R64.

Centella asiatica

10

Janu Pirakalathanan, Stephen L. Stuckey,
and Ronil V. Chandra

10.1 Uses

Centella asiatica is a perennial herbaceous creeper native to India and parts of Asia that is consumed in the plant form. It is integrated into Ayurvedic and Chinese herbal remedies and used for treatment of a variety of ailments, most notably affecting the skin and female genitourinary tract, and to improve memory and concentration. There are also various pharmaceutical formulations aimed at exploiting intrinsic wound-healing, anticonvulsive, antinociceptive, anti-inflammatory, and antioxidative properties.

10.2 Mechanism

The primary active constituent is triterpenoids. In animal models, triterpenoids have been proven to increase collagen and glycosaminoglycan synthesis, promote angiogenesis, and act on the connective tissue of vascular walls.

J. Pirakalathanan, MBBS
S.L. Stuckey, MBBS, MMed, MD, FRANZCR
R.V. Chandra, MBBS, MMed, FRANZCR (✉)
Department of Diagnostic Imaging,
Monash Medical Center, Monash Health,
Melbourne, VIC, Australia
e-mail: ronilvchandra@gmail.com

10.3 Discussion

A rare effect of excessive consumption of *Centella asiatica* is reversible cerebral vasoconstriction syndrome (RVCS). The postulated mechanism is related to the vasoactive effects of triterpenoids, which are known to result in vascular remodeling by interfering with collagen synthesis regulation.

The main clinical presentation of RCVS is sudden onset of severe thunderclap headache associated with photophobia, nausea, and vomiting. The primary radiological CNS manifestation is the presence of alternating multifocal large to medium arterial constriction and dilation, resulting in the characteristic "sausage on a string" appearance on cerebral angiography (Fig. 10.1). A key diagnostic feature is the spontaneous reversibility, upon withdrawal of the stimulus, occurring within 1–3 months. Notably, angiography performed very early in the clinical course can be normal, with vessel narrowing often most marked in the second and third weeks after exposure. Major complications include subarachnoid hemorrhage, ischemic stroke, and, much less commonly, intraparenchymal hemorrhage.

Treatment involves identification and withdrawal of the vasoactive stimulus, supportive care, and management of ischemic and hemorrhagic complications.

D.T. Ginat et al. (eds.), *Neuroimaging Pharmacopoeia*,
DOI 10.1007/978-3-319-12715-6_10,

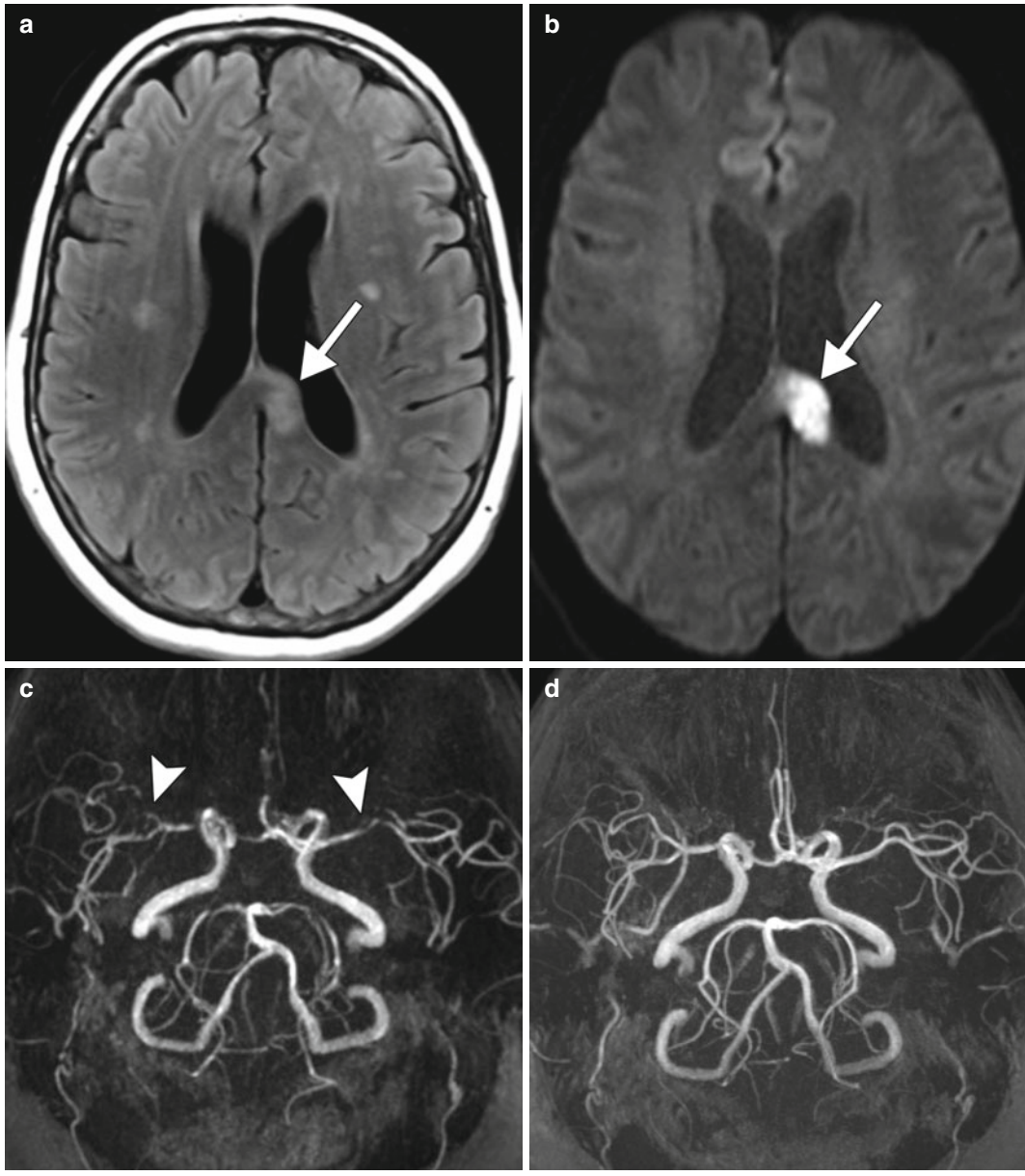

Fig. 10.1 RCVS associated with *Centella asiatica*. Fifty-eight-year-old female presenting 10 days after initial acute thunderclap headache. Symptoms began 48 h after ingestion of a large quantity of *Centella asiatica*. Neurological deterioration 5 days after DSA prompted MRI (**a**, **b**), which shows T2 hyperintensity and restricted diffusion in the splenium of the corpus callosum, consistent with infarction (*arrows*). MIP time-of-flight MRA (**c**) performed in the third week after initial ingestion demonstrates extensive multifocal areas of cerebral vasoconstriction (*arrowheads)*. MIP time-of-flight MRA performed 6 weeks after initial ingestion (**d**) shows resolution of the abnormalities

10.4 Differential Diagnosis

An important diagnostic consideration is vasospasm secondary to aneurysmal subarachnoid hemorrhage. Other differential considerations include central nervous system (CNS) vasculitis, postpartum cerebral angiopathy (PPA), and other causes of reversible vasoconstriction syndrome, such as migrainous angiitis and other drug-induced cerebral vasculopathies. Differentiation

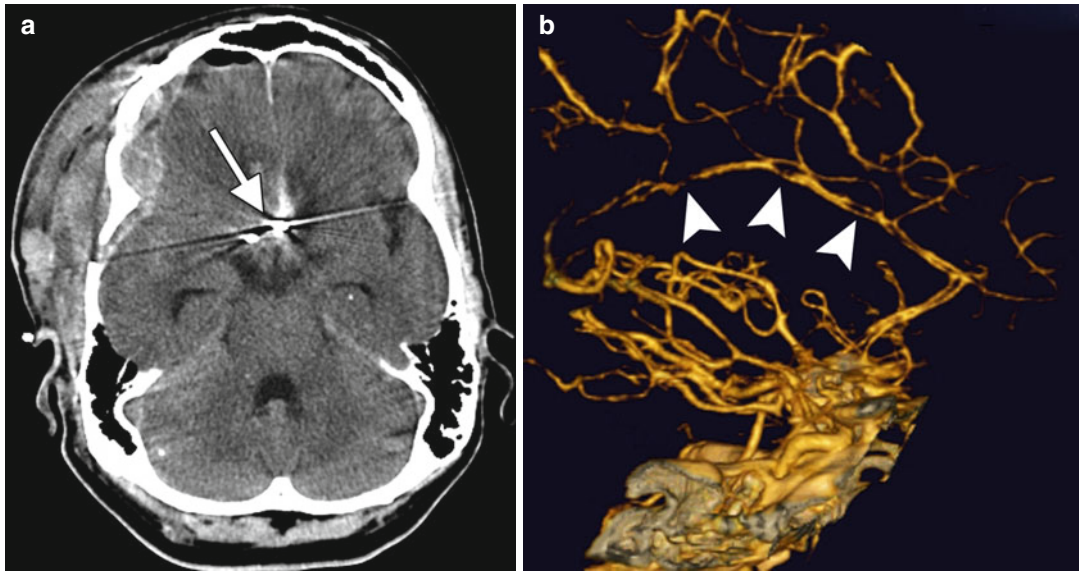

Fig. 10.2 Vasospasm associated with subarachnoid hemorrhage. Axial CT image (**a**) shows anterior communicating artery aneurysm clipping and associated hemorrhage from recent rupture (*arrow*). Lateral 3D CTA (**b**) shows multiple high-grade stenoses of the anterior cerebral arteries (*arrowheads*)

between the various diagnostic possibilities is aided by the clinical presentation, relevant personal history, and patient demographics.

- *Aneurysmal rupture and secondary vasospasm*: A difficult diagnostic dilemma may arise when an intracranial aneurysm is identified on angiography, despite the changes being attributable to RCVS. In this situation, the distribution and extent of subarachnoid hemorrhage and the location of cerebral vasospasm are invaluable in ascertaining the diagnosis. In general, subarachnoid hemorrhage is associated with RCVS and basal subarachnoid hemorrhage with aneurysmal rupture. Subarachnoid hemorrhage could be associated with ruptured distal mycotic aneurysm; however, there is usually a history of intravenous drug use or infective endocarditis that predisposes to septic emboli.
- *CNS vasculitis*: This may be primary in etiology, in which the arteritis is confined to the CNS vessels, or secondary, where there is a history of systemic vasculitis, most often systemic lupus erythematosus (SLE). In the latter situation, CNS involvement is unlikely to be the first manifestation of the disease, as there is almost always a history of systemic vasculitis. While the radiological features of primary CNS vasculitis can overlap with RCVS, the clinical onset of CNS vasculitis is more insidious, the headache is chronic and progressive, and there are usually accompanying cerebrospinal fluid abnormalities. Multiple ischemic lesions can be encountered on MRI (Figs. 10.2 and 10.3).
- *Postpartum cerebral angiopathy*: Perhaps a manifestation of RCVS, the underlying mechanism is thought to relate to hormonal changes that affect vascular smooth muscle or result in endothelial dysfunction that in turn may result in vasogenic edema, vasoconstriction, intracranial hemorrhage, and/or infarction.
- *Migrainous angiitis*: This is radiologically indistinguishable from other causes of RCVS. Often a history of migraines may be the only indication that this is the underlying etiology.
- *Other drug-induced RCVS*: A wide range of compounds have been associated with the drug-induced form of RCVS. These include phenylpropanolamine, pseudoephedrine, ergotamine tartrate, methylergonovine, bromocriptine, lisuride, selective serotonin reuptake inhibitors (SSRIs), sumatriptan, isometheptene, cocaine (refer to Chap. 5), amphetamine derivatives (refer to Chap. 6), marijuana (refer to Chap. 4), lysergic acid diethylamide,

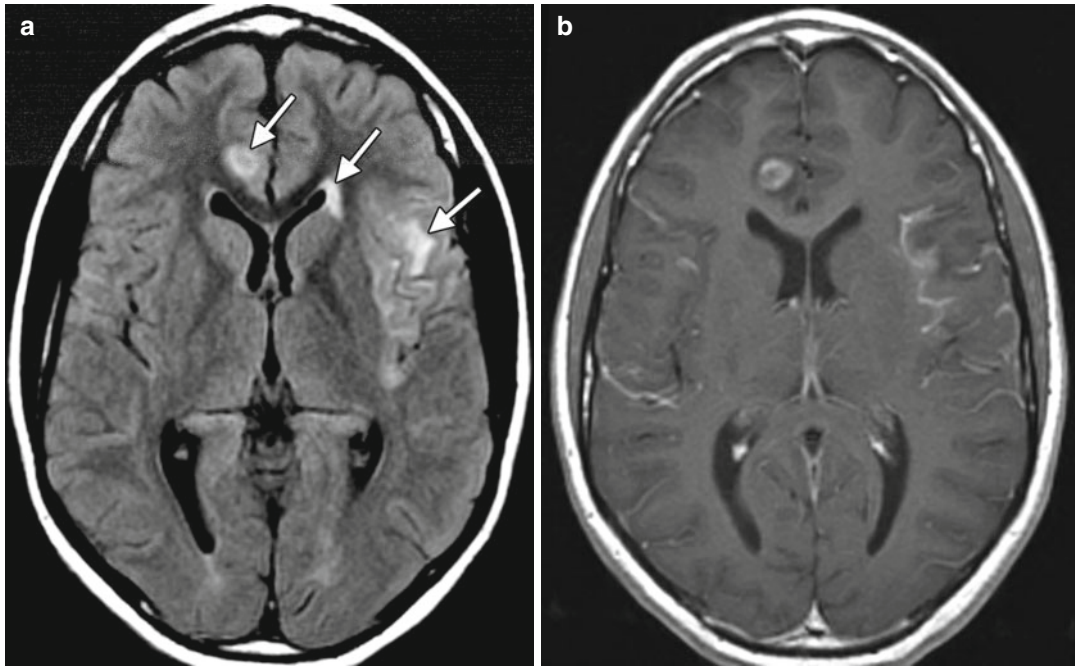

Fig. 10.3 Lupus vasculitis. Axial FLAIR MRI (**a**) shows multifocal areas of cortical and subcortical hyperintense signal abnormality (*arrows*). The corresponding axial post-contrast T1 MRI (**b**) shows abnormal leptomeningeal and parenchymal enhancement associated with the lesions

tacrolimus (FK-506), cyclophosphamide, erythropoietin, intravenous immune globulin (IVIg), interferon alpha, nicotine patches, red blood cell transfusions, licorice (refer to Chap. 9), and oral contraceptives (refer to Chap. 47). The radiological features are identical to other causes of RCVS, and the history is invaluable in identifying the offending agent.

Suggested Reading

Birnbaum J, Hellmann DB. Primary angiitis of the central nervous system. Arch Neurol. 2009;66(6):704–9.

Calabrese LH, Dodick DW, Schwedt TJ, et al. Narrative review: reversible cerebral vasoconstriction syndromes. Ann Intern Med. 2007;146:34–44.

Chong NJ, Aziz Z. A systematic review of the efficacy of *Centella asiatica* for improvement of the signs and symptoms of chronic venous insufficiency. Evid Based Complement Alternat Med. 2013;2013:627182.

Ducros A, Brousser MG. Reversible cerebral vasoconstriction syndrome. Pract Neurol. 2009;9:256–67.

Ducros A, Boukobza M, Porcher R, Sarov M, Valade D, Brousser MG. The clinical and radiological spectrum of reversible cerebral vasoconstriction syndrome. A prospective of 67 patients. Brain. 2007;130:3091–101.

Gohil KJ, Patel JA, Gajjar AK. Pharmacological review on *Centella asiatica*: a potential herbal cure-all. Indian J Pharm Sci. 2010;72(5):546–56.

Koopman K, Uyttenboogaart M, Luijckx GJ, et al. Pitfalls in the diagnosis of reversible cerebral vasoconstriction syndrome and primary angiitis of the central nervous system. Eur J Neurol. 2007;14:1085–7.

Nitrous Oxide (N_2O)

11

Daniel Thomas Ginat

11.1 Uses

Nitrous oxide is used as an inhaled anesthetic and as a propellant in the food industry, such as in whipped cream bulbs. Intentional abuse of or excess occupational exposure to nitrous oxide can result in neurotoxicity.

11.2 Mechanism

Nitrous oxide toxicity results from inactivation of vitamin B12-dependent enzymes. Nitrous oxide irreversibly oxidizes the cobalt ion of vitamin B12 from the +1 to the +3 valence state. Nitrous oxide oxidation of the cobalt ion prevents methylcobalamin from acting as a coenzyme in the production of methionine and subsequently *S*-adenosylmethionine. *S*-adenosylmethionine is necessary for methylation of myelin sheath phospholipids. Conversion of methylmalonyl to succinyl coenzyme A is also inhibited by cobalamin oxidation. Accumulation of methylmalonate and propionate may promote abnormal fatty acid synthesis, which can become incorporated into the myelin sheath.

D.T. Ginat, MD, MS
Department of Radiology, University of Chicago, Pritzker Medical School, Chicago, IL, USA
e-mail: ginatd01@gmail.com

11.3 Discussion

Nitrous oxide toxicity can lead to subacute combined degeneration of the spinal cord, analogous to classic vitamin B12 deficiency. The abnormality leads to progressive demyelination of the spinal cord and demyelination and axonal injury of the peripheral nerves. The posterior columns are predominantly involved with loss of position and vibration senses, ataxia, broad-based gait, and, occasionally, Lhermitte sign. The anterolateral columns can also be affected and swelling of the spinal cord can also be observed. Myelopathy usually develops 2–6 weeks after nitrous oxide exposure, but can occur within hours. Affected patients usually have vitamin B12 deficiency. On MRI, there is typically long-segment high T2 signal along the dorsal columns, without associated enhancement (Fig. 11.1). Treatment consists of ceasing exposure to nitrous oxide and supplementing methionine and vitamin B12. The signal abnormalities encountered on MRI are often reversible following appropriate treatment.

11.4 Differential Diagnosis

The differential diagnosis for T2 hyperintensity selectively involving the dorsal columns mainly includes the following conditions:

- *Vitamin B12 deficiency*: As stated previously, vitamin B12 deficiency has an identical imaging appearance as nitrous oxide toxicity, since it is the endpoint of nitrous oxide toxicity (Fig. 11.2).

D.T. Ginat et al. (eds.), *Neuroimaging Pharmacopoeia*,
DOI 10.1007/978-3-319-12715-6_11,

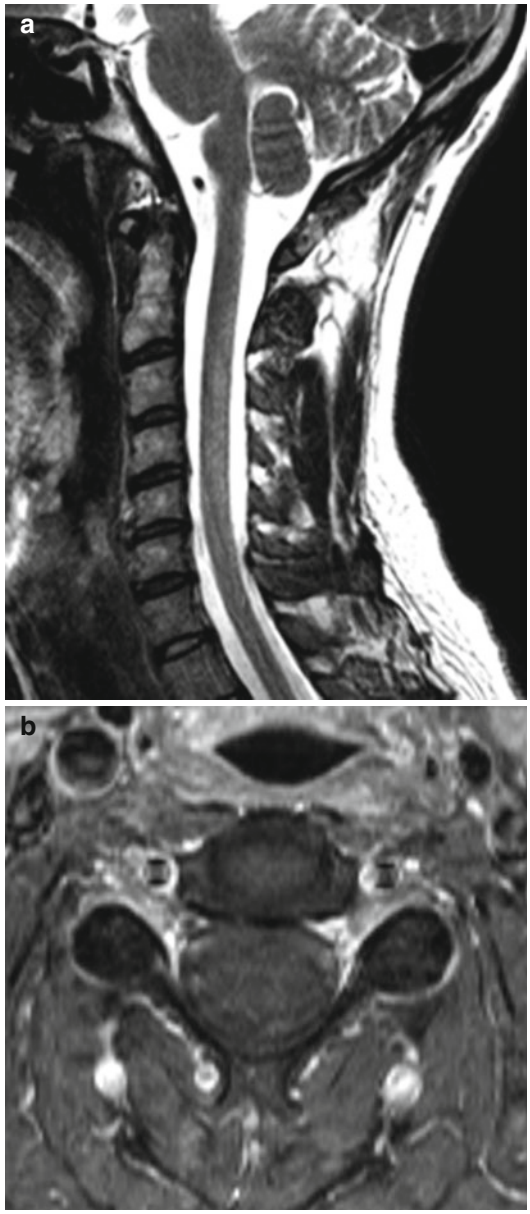

Fig. 11.1 Nitrous oxide myelopathy. The patient presented with progressive sensory changes in the extremities after nitrous oxide use. Sagittal (**a**) T2-weighted MRI shows diffuse high signal within the dorsal columns of the cervical spine. The corresponding axial (**b**) fat-suppressed post-contrast T1-weighted MRI shows no corresponding abnormal enhancement

- *Spinal cord infarction*: Long-segment T2 hyperintensity and swelling in a spinal artery vascular territory, often involving the central gray matter, are characteristic (Fig. 11.3).

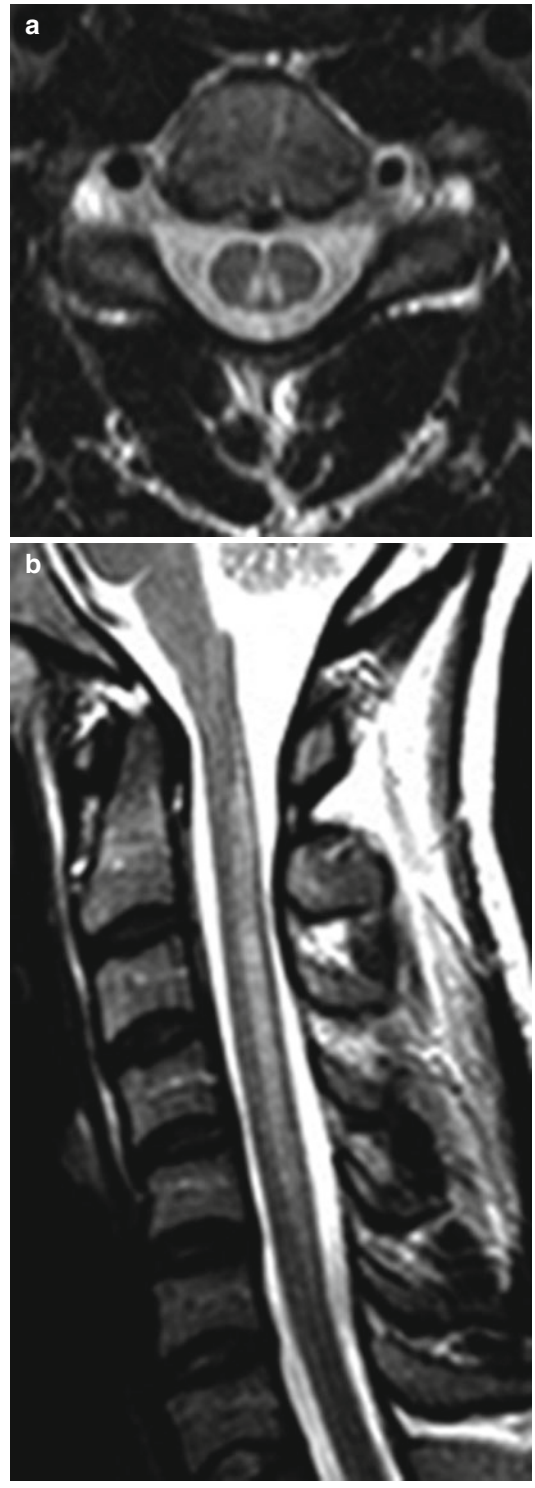

Fig. 11.2 Subacute combined degeneration due to vitamin B12 deficiency. Axial (**a**) and sagittal (**b**) MR images show high signal through much of the bilateral cervical spine dorsal columns

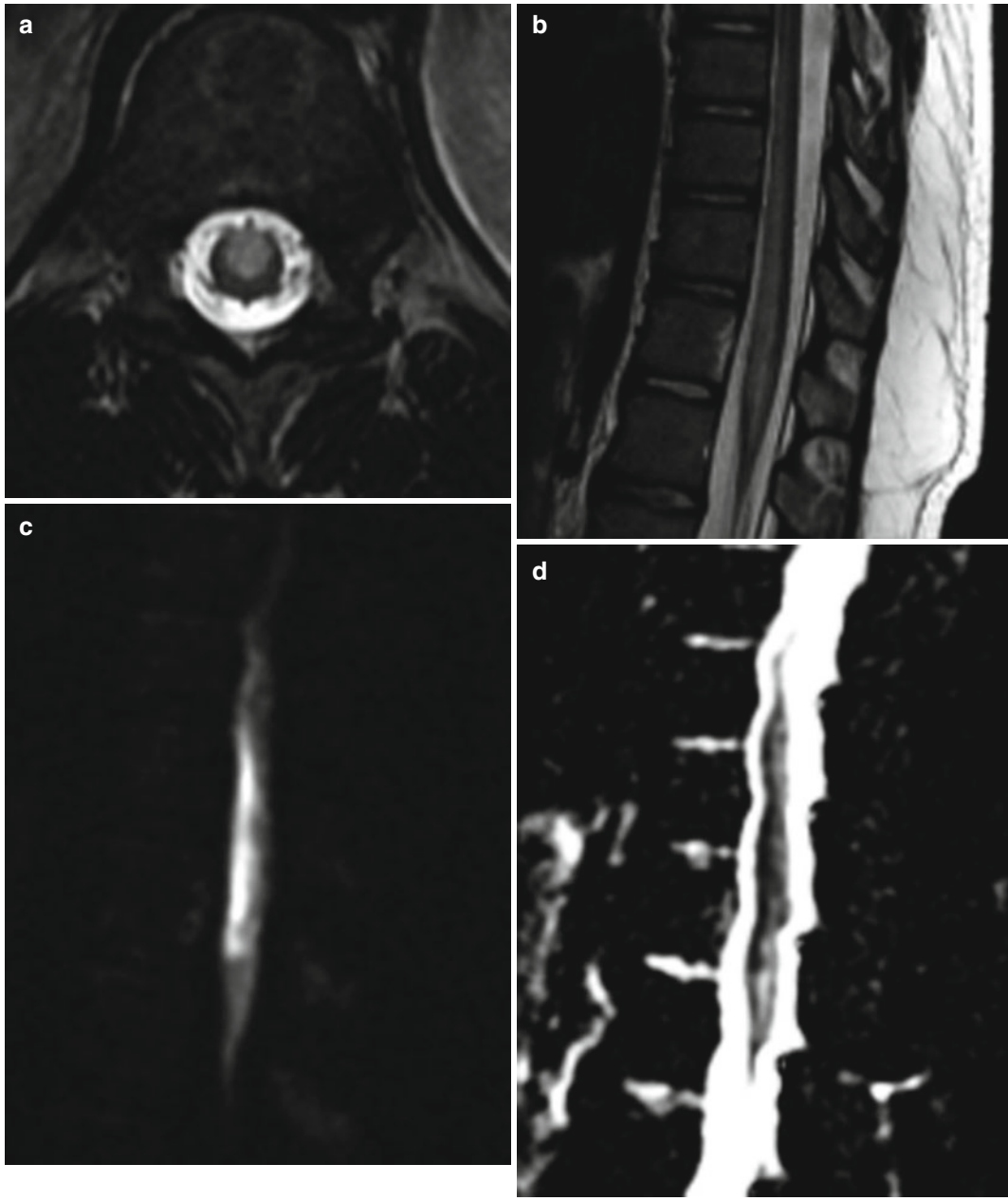

Fig. 11.3 Spinal cord infarction. Axial (**a**) and sagittal (**b**) T2-weighted MR images show high signal in the central spinal cord. There is corresponding restricted diffusion shown on the sagittal DWI (**c**) and ADC map (**d**)

Diffusion-weighted imaging is helpful for confirming acute spinal cord infarction by depicting the presence of restricted diffusion in the affected region.

- *Vacuolar myelopathy due to HIV infection*: This condition can resemble subacute combined degeneration on imaging as well as pathology, and the patient's history of HIV is necessary for the diagnosis.
- *Intrathecal chemotherapy-related myelopathy*: Patients receiving intrathecal chemotherapy can present with ascending numbness and

weakness with corresponding widespread symmetric hyperintensity in the posterior columns of the spinal cord (refer to Chap. 19).

Suggested Reading

Beltramello A, Puppini G, Cerini R, El-Dalati G, Manfredi M, Roncolato G, Idone D, De Togni L, Turazzini M. Subacute combined degeneration of the spinal cord after nitrous oxide anaesthesia: role of magnetic resonance imaging. J Neurol Neurosurg Psychiatry. 1998; 64(4):563–4.

Butzkueven H, King JO. Nitrous oxide myelopathy in an abuser of whipped cream bulbs. J Clin Neurosci. 2000;7(1):73–5.

Ilniczky S, Jelencsik I, Kenéz J, Szirmai I. MR findings in subacute combined degeneration of the spinal cord caused by nitrous oxide anaesthesia–two cases. Eur J Neurol. 2002;9(1):101–4.

Lu CH, Yao M, Liu HM, Chen YF. MR findings of intrathecal chemotherapy-related myelopathy in two cases: mimicker of subacute combined degeneration. J Neuroimaging. 2007;17(2):184–7.

Pema PJ, Horak HA, Wyatt RH. Myelopathy caused by nitrous oxide toxicity. AJNR Am J Neuroradiol. 1998;19(5):894–6.

Ravina B, Loevner LA, Bank W. MR findings in subacute combined degeneration of the spinal cord: a case of reversible cervical myelopathy. AJR Am J Roentgenol. 2000;174(3):863–5.

Sesso RM, Iunes Y, Melo AC. Myeloneuropathy following nitrous oxide anaesthesia in a patient with macrocytic anaemia. Neuroradiology. 1999;41(8):588–90.

Waters MF, Kang GA, Mazziotta JC, DeGiorgio CM. Nitrous oxide inhalation as a cause of cervical myelopathy. Acta Neurol Scand. 2005;112(4):270–2.

Iodinated Contrast Agents

12

Harut Haroyan and Daniel Thomas Ginat

12.1 Uses

In neuroimaging, iodine-based contrast agents are administered intravenously when acquiring CT images mainly for evaluating infectious and inflammatory conditions and tumors. Intravenous administration of iodine-based contrast agents are also an essential part of CT and conventional catheter angiography and CT perfusion studies. Iodine contrast agents can also be administered at different concentrations intrathecally into the subarachnoid space for performing myelography or cisternography and into the ventricular system for performing ventriculography.

12.2 Mechanism

Iodine-based contrast agents consist of various modifications of a 2,4,6-triiodinated benzene ring. Iodine-based contrast has relatively high X-ray attenuation coefficients, particularly near the iodine k-edge of approximately 33 keV, which makes the contrast material appears radio-opaque. Intravenously administered iodinated contrast agents are predominantly excreted through the kidneys (99 % percent where there is normal renal function), with a half-life of approximately 2 h.

12.3 Discussion

Iodine is a chemical element of the halogen group with atomic number 53. Iodine contrasts agents can be oil-based and water soluble. Oil-based contrast agents are not currently used in neuroimaging, and this text focuses on water-soluble iodinated contrast agents, which were actually first developed for urography by Dr. Moses Swick in 1928. Current iodinated contrast agents consist of iodine bound to an organic molecule comprised of one (monomeric) or two (dimeric) benzene rings. Based on whether there is an ionic or covalent bond, iodinated contrast agents can be described as ionic versus nonionic. Ionic contrast agents (i.e., diatrizoate, metrizoate, and ioxaglate) contain carboxyl group, which dissociates in solution, as opposed to nonionic agents (i.e., iopamidol, iohexol, and iopromide), which do not dissociate, but are rendered water soluble due to the presence of hydrophilic hydroxyl groups. In addition, low and high osmolar agents are available, which refers to the amount of iodine yielded per molecule of contrast agent with osmolality that can range from 290 to 1,550 Osm/kg, depending upon the particular agent.

The normal biodistribution of intravenously administered iodine contrast agents on

H. Haroyan, MD
Department of Radiology, University of Chicago, Chicago, IL, USA

D.T. Ginat, MD, MS (✉)
Department of Radiology, University of Chicago, Pritzker Medical School, Chicago, IL, USA
e-mail: ginatd01@gmail.com

D.T. Ginat et al. (eds.), *Neuroimaging Pharmacopoeia*,
DOI 10.1007/978-3-319-12715-6_12,

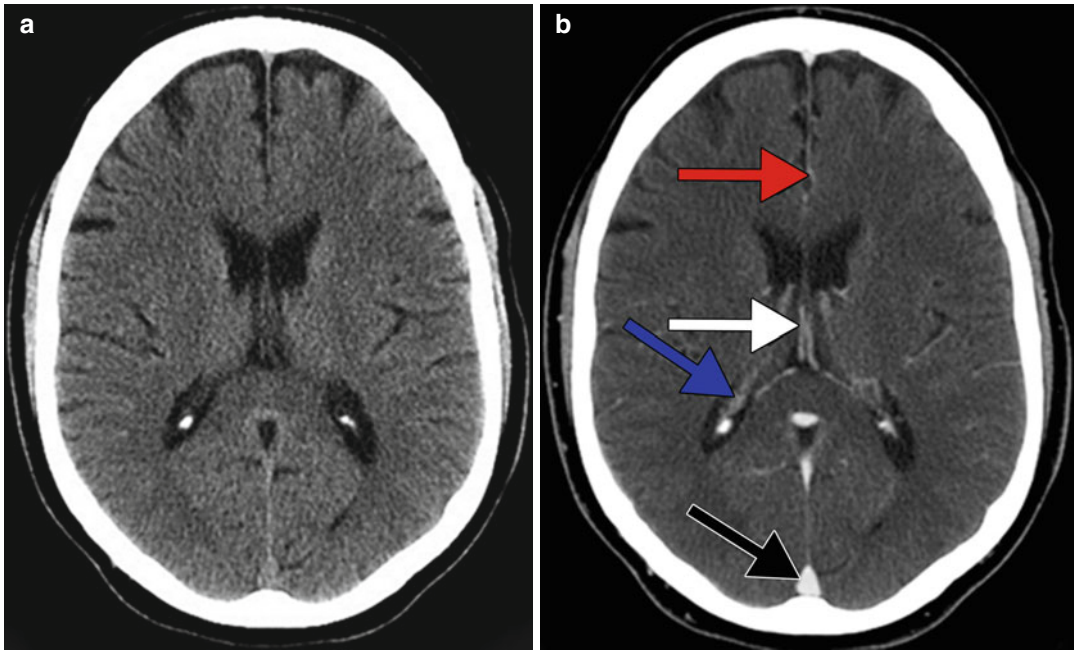

Fig. 12.1 Normal iodinated contrast material distribution. Axial non-contrast CT (**a**) and corresponding post-contrast CT (**b**) show expected enhancement of the dural sinuses (*black arrow*), internal cerebral veins (*white arrow*), choroid plexus (*blue arrow*), and cortical arteries (*red arrow*)

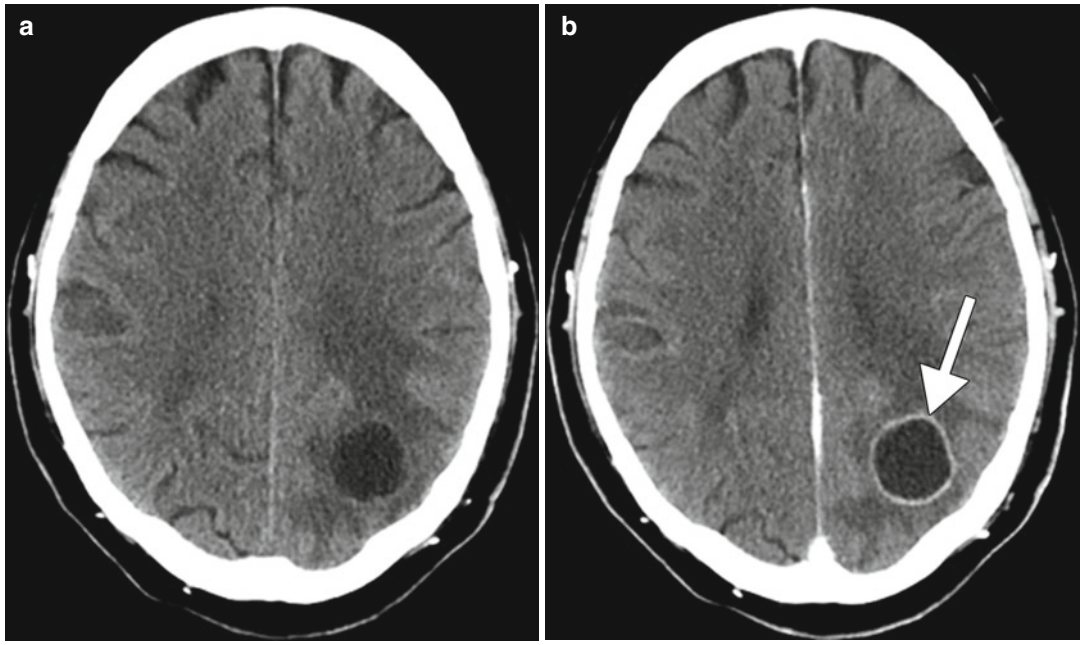

Fig. 12.2 Pre- and post-contrast CT showing a cerebral abscess. Axial pre- (**a**) and post-contrast CT (**b**) images show a thin rim-enhancing fluid collection with surrounding vasogenic edema in the left parietal lobe (*arrow*)

neuroimaging is throughout the cerebrovascular system, choroid plexus, pituitary gland and stalk, muscles, and mucosa (Fig. 12.1). Lesions that disrupt the blood-brain barrier are hypervascular, such as abscess, and certain tumors can also demonstrate enhancement (Figs. 12.2 and

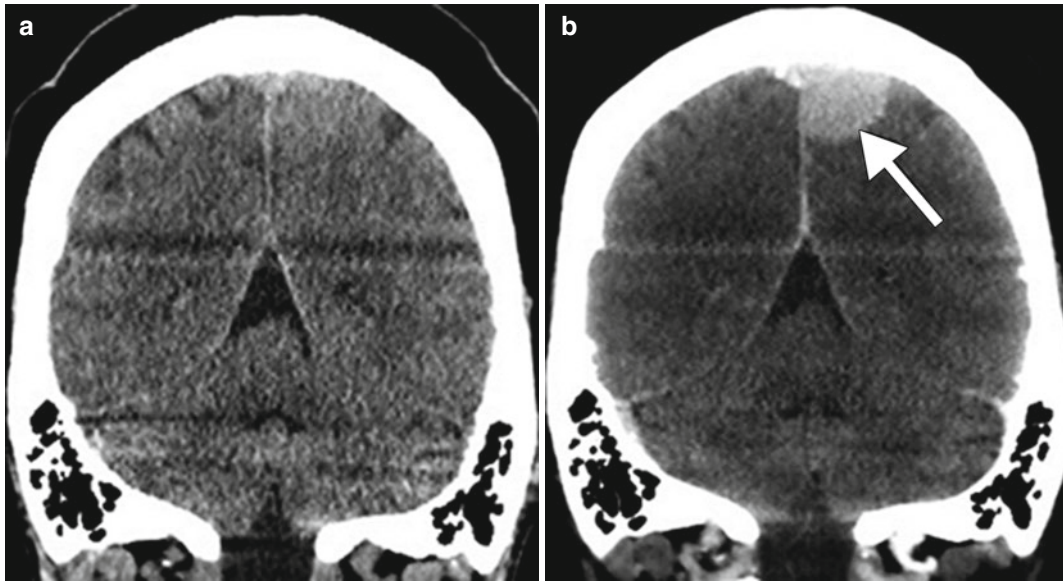

Fig. 12.3 Pre- and post-contrast CT showing a meningioma. Coronal pre- (**a**) and post-contrast (**b**) CT images show a homogeneously enhancing mass in the left parafalcine parietal convexity (*arrow*)

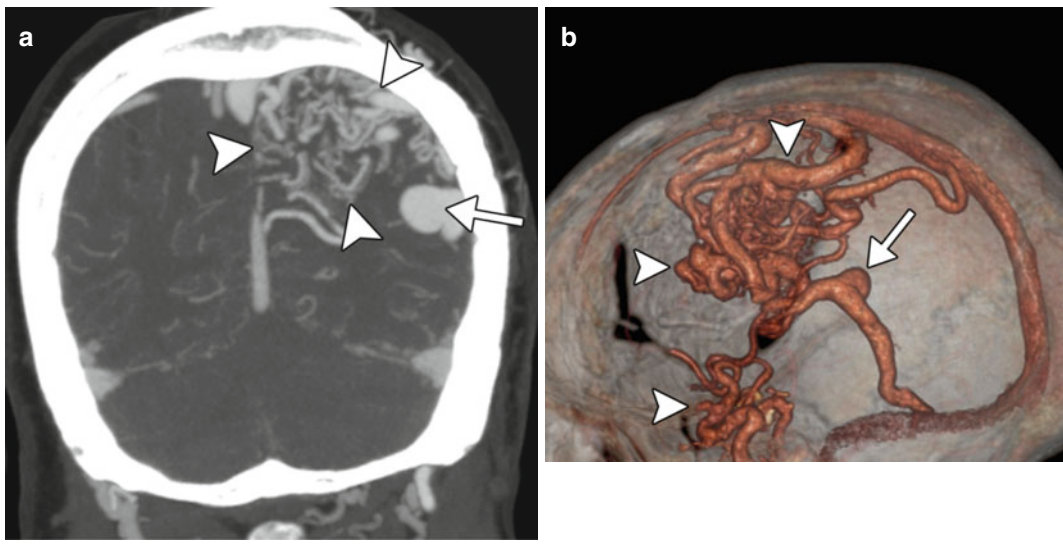

Fig. 12.4 CTA showing an arteriovenous malformation. Coronal CTA MIP (**a**) and 3D CTA volume rendered (**b**) images show a large nidus in the left cerebral hemisphere with associated high-glow aneurysm (*arrow*)

12.3). The degree of enhancement can be quantified by measuring the Hounsfield units on the corresponding pre- and post-contrast images. CTA is performed by acquiring images during the arterial phase (approximately 30 s after intravenous injection of contrast) and is useful for delineating steno-occlusive lesions, aneurysms, and vascular malformations (Fig. 12.4). CT perfusion consists of serial scanning of a limited region at short time intervals during the early phase of contrast administration in order to determine various hemodynamic parameters such as CBV, CBF, and MTT, which can be useful for evaluating ischemic disease and the characteristics of certain tumors (Fig. 12.5). CTV consists of acquiring images during the venous phase (approximately 120 s after intravenous injection of contrast) and is useful for the evaluation of venous

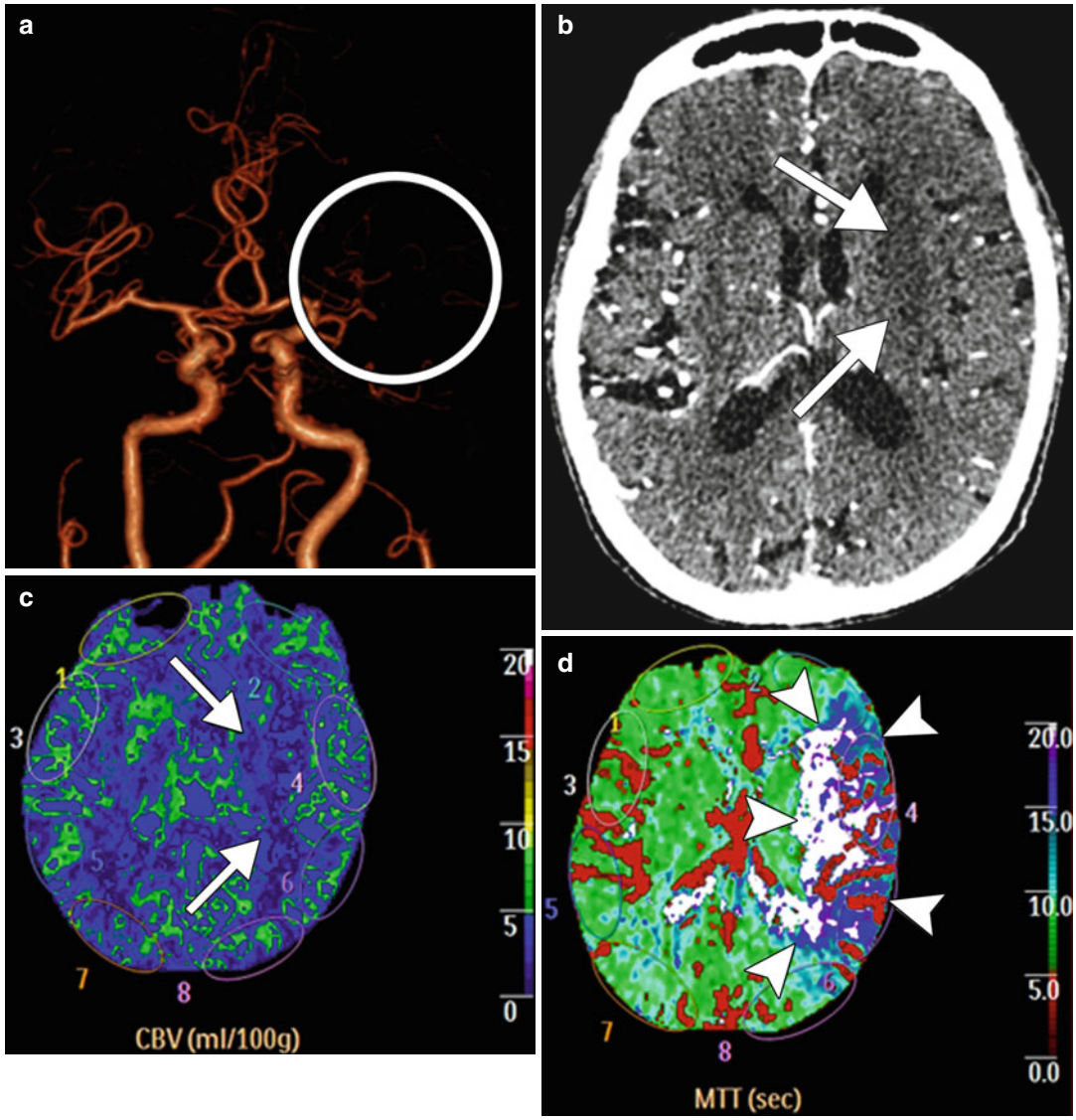

Fig. 12.5 CT perfusion showing acute ischemia. Frontal projection 3D volume rendered CTA image (**a**) shows absent opacification of the left MCA (*circle*). Axial CTA image (**b**) shows hypoattenuation within the left basal ganglia, which corresponds to an acute infarct (*arrows*). The corresponding CBV map (**c**) shows a perfusion defect in the left basal ganglia (*arrows*). However, the MTT map (**d**) shows a much larger area of prolonged transit time, indicating tissue at risk, but potentially salvageable (*arrowheads*)

thrombosis and extrinsic compression or invasion of the venous sinus by tumors (Fig. 12.6). CT myelography consists of injecting contrast into the subarachnoid space, usually via a lumbar puncture, and using the contrast material to outline critical structures, such as the spinal cord or nerve roots that may be compressed (Fig. 12.7). Similarly CT cisternography consists of injecting contrast into the subarachnoid space usually via lumbar puncture and can be used to confirm and localized CSF leaks (Fig. 12.8). CT ventriculography consists of injecting contrast material into the ventricular system, usually via pre-existing ventricular catheter in order to assess for patency

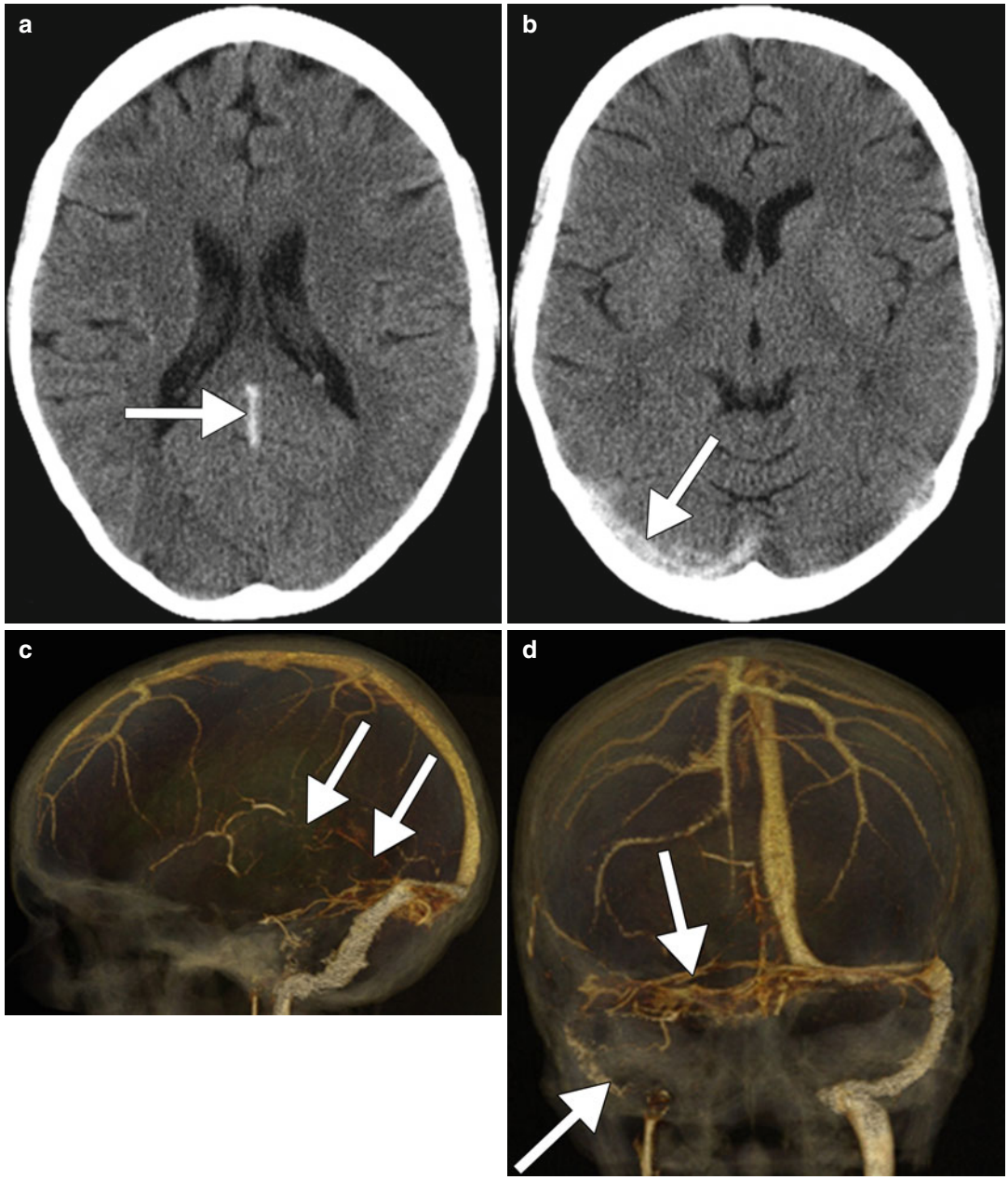

Fig. 12.6 CTV showing venous sinus thrombosis. Axial non-contrast CT images (**a**, **b**) show hyperattenuation within the straight and right transverse venous sinuses (*arrows*). Lateral (**c**) and frontal (**d**) projection 3D CTV volume rendered images show lack of opacification in the corresponding venous sinuses (*arrows*)

of the catheter or localizing the site of obstructive hydrocephalus (Fig. 12.9).

In general, nonionic low osmolar agents are preferred for intravenous use due to better safety profile. Contrast reactions are uncommon and range from 5 to 12 % for high osmolarity contrast media and 1–3 % for low osmolarity contrast media overall. Contrast reactions can be anaphylactoid (urticaria, bronchospasm, laryngeal edema, hypotension and tachycardia, and

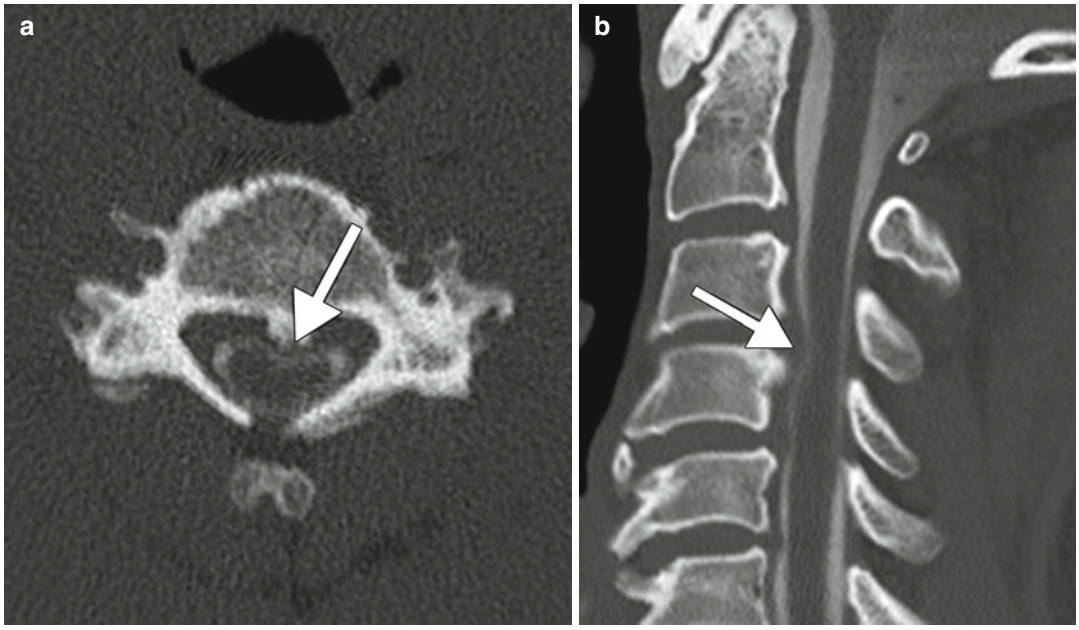

Fig. 12.7 CT myelogram. Axial (**a**) and sagittal (**b**) CT images show contrast material outlining a posterior disc-osteophyte complex (*arrows*) that impinges upon the cervical spinal cord

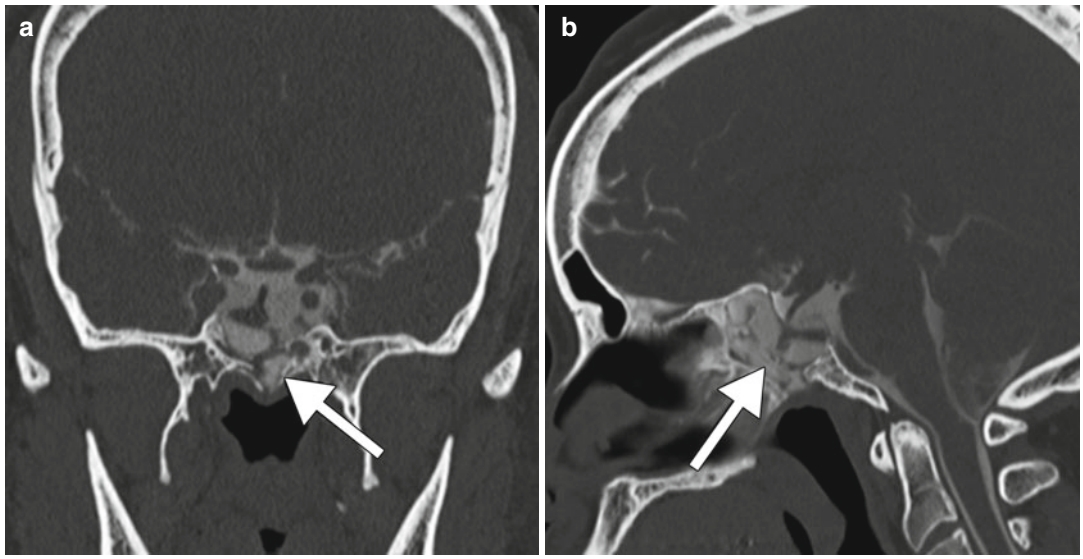

Fig. 12.8 CT cisternogram. The patient has a history of an invasive pituitary adenoma and presents with intermittent clear rhinorrhea. Coronal (**a**) and sagittal (**b**) CT images show the presence of contrast within the sphenoid sinus (*arrows*), extending through a defect in the enlarged sella

hypotension and bradycardia) versus nonanaphylactoid (cardiac arrhythmia, hypertension, seizures, and pulmonary edema). Management of these contrast reactions is beyond the scope of this text. Contrast agent-related nephropathy is defined as an elevation of the serum creatinine level by more than 0.5 mg/dL or more than 50 % of the baseline within 1–3 days following

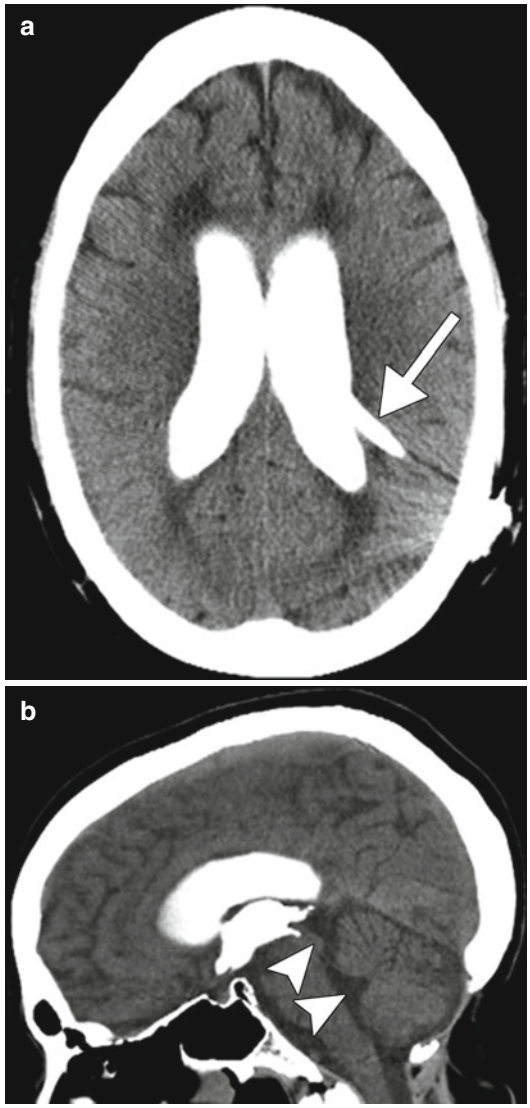

Fig. 12.9 CT ventriculogram. Axial (**a**) and sagittal (**b**) CT images show the lateral and third ventricles filling with contrast administered through a ventricular shunt catheter (*arrow*), but lack of contrast filling the cerebral aqueduct and fourth ventricle (*arrowheads*), indicating the presence of aqueductal stenosis

contrast injection and occurs in 2–7 % of patients. Risk factors include pre-existing renal disease and kidney transplant, diabetes mellitus, collagen vascular diseases, certain antibiotics and chemotherapy agents, among others. Prevention and management of contrast-induced nephropathy is also beyond the scope of this text. Contrast-induced encephalopathy is a rare complication related to large doses of contrast administered during procedures, such as cardiac catheterization and neurovascular procedures. Patients can present with confusion, cortical blindness, focal neurological deficits, and seizures. Most cases of contrast-induced encephalopathy are transient, although permanent deficits result in most severe cases. On CT in the acute setting, focal or diffuse swelling and contrast staining in the brain parenchyma can be observed, which often resolves, although encephalomalacia can ensue in more severe cases (Fig. 12.10).

12.4 Differential Diagnosis

Certain materials besides iodinated contrast appear hyperattenuating on CT, including acute hemorrhage, calcifications, and certain foreign bodies. It is possible to differentiate between intrinsically hyperattenuating materials and contrast enhancement by comparing non-contrast images with corresponding post-contrast images. However, pre-contrast images are not always obtained or may have ambiguous findings, such as the presence of a hyperattenuating area following intra-arterial TPA. In such cases, spectral CT can be helpful for distinguishing between contrast staining and hemorrhage (Fig. 12.11).

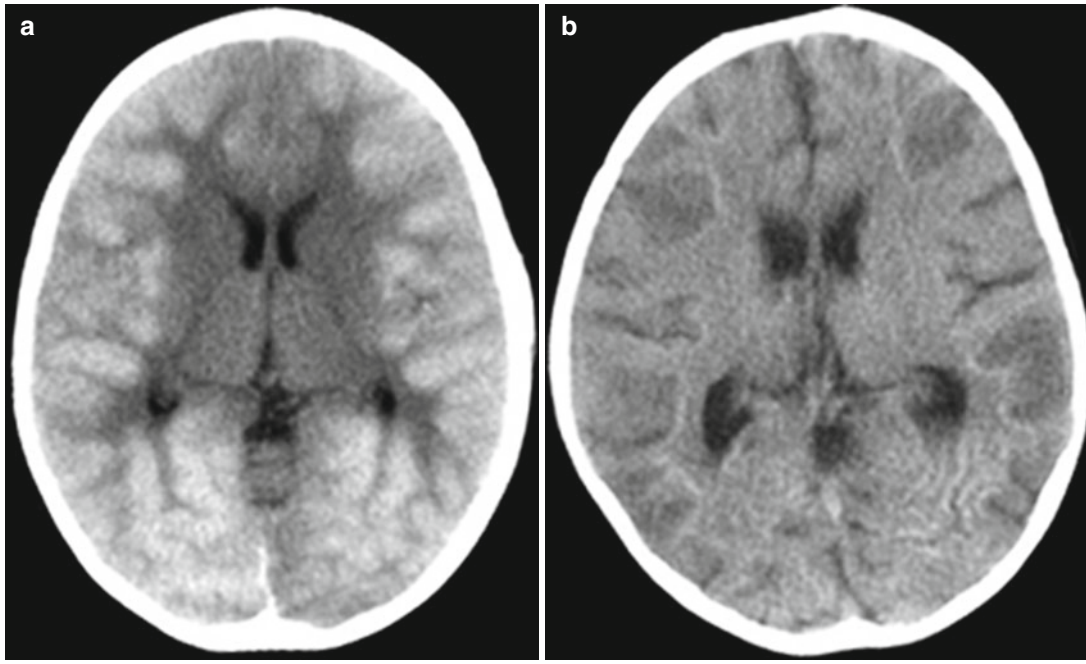

Fig. 12.10 Contrast-induced encephalopathy. The patient presented with altered mental status following cardiac catheterization. Axial CT image (**a**) shows increased attenuation along the cortex with diffuse brain edema. Follow-up non-contrast CT image (**b**) demonstrates diffuse volume loss and cortical laminar necrosis

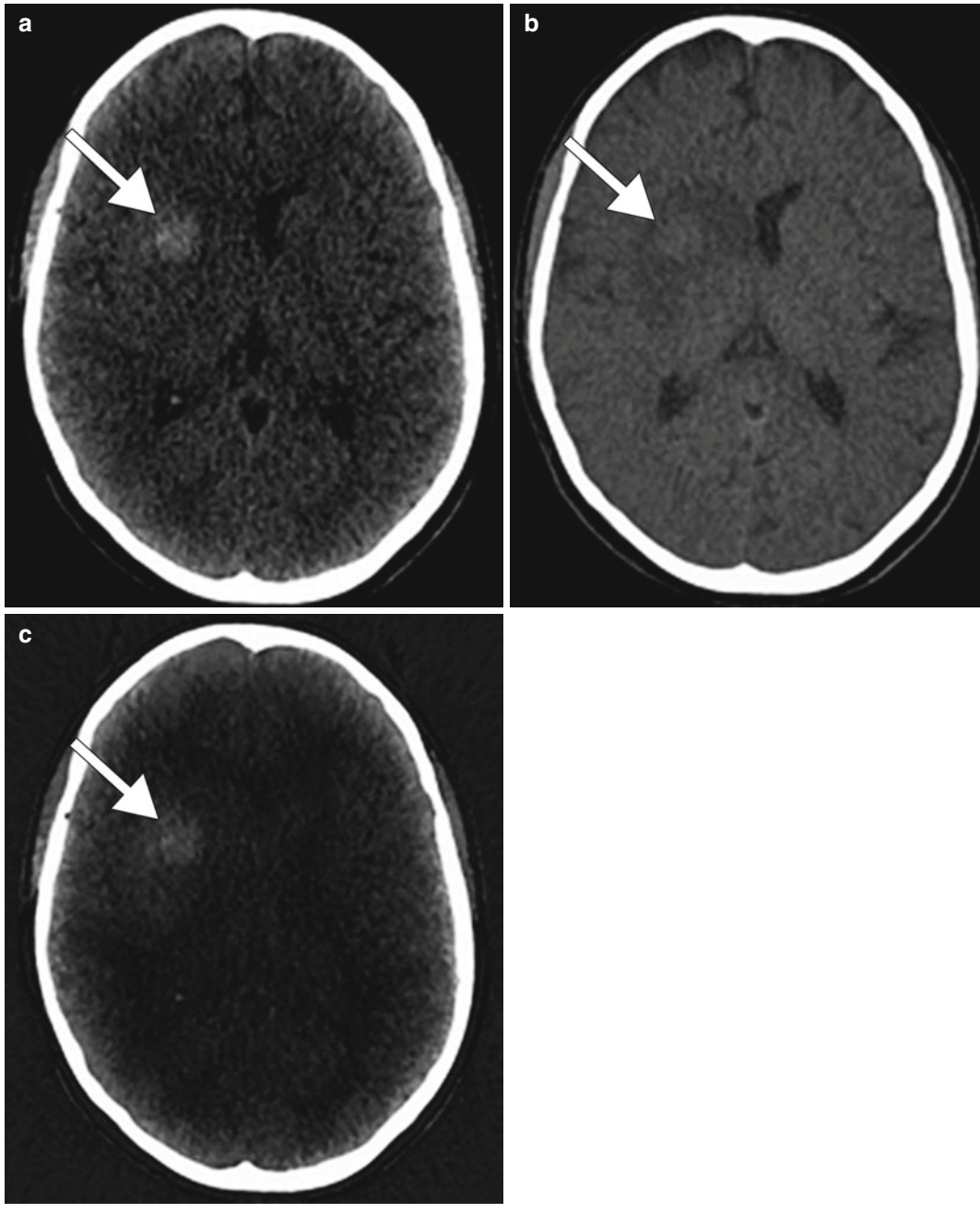

Fig. 12.11 Hemorrhage versus contrast staining resolved using dual energy CT. The patient has a right basal ganglia infarct for which a neurointerventional procedure was performed. Standard axial CT image (**a**) shows a hyperattenuating focus within the right basal ganglia (*arrow*). The water-density (**b**) and iodine-density (**c**) images indicate the presence of both contrast staining and hemorrhage (*arrows*)

Suggested Reading

ACR Committee on Drugs and Contrast Media. ACR manual on contrast media. Version 9. Reston: American College of Radiology; 2013.

Bettmann MA. Frequently asked questions: iodinated contrast agents. Radiographics. 2004;24:S3–10.

Ginat DT, Gupta R. Advances in computed tomography imaging technology. Annu Rev Biomed Eng. 2014;16:431–53.

Gupta R, Phan CM, Leidecker C, Brady TJ, Hirsch JA, Nogueira RG, et al. Evaluation of dual-energy CT for differentiating intracerebral hemorrhage from iodinated contrast material staining. Radiology. 2010;257:205–11.

Preston M. Hickey memorial lecture. Ionic and nonionic iodinated contrast media: evolution and strategies for use. AJR Am J Roentgenol. 1990;155:225–33.

Thomsen HS, Morcos SK. Contrast media and the kidney: European Society of Urogenital Radiology (ESUR) guidelines. Br J Radiol. 2003;76:513–8.

Yu J, Dangas G. Commentary: new insights into the risk factors of contrast-induced encephalopathy. J Endovasc Ther. 2011;18:545–6.

Gadolinium-Based Contrast Agents

13

Harut Haroyan and Daniel Thomas Ginat

13.1 Uses

In neuroimaging, MRI sequences are obtained following intravenous administration of gadolinium-based contrast agents (GBCA) most commonly for the assessment of tumors, inflammatory conditions, and infectious processes. Contrast can also be used for MR angiography and perfusion imaging, although these studies can also be performed without contrast using different techniques.

13.2 Mechanism

Gadolinium-based contrast agents can considerably shorten T1 relaxation time of surrounding protons, resulting in high T1 signal, even if only very small concentrations are present in the blood. Gadolinium-based contrast agents consist of gadolinium incorporated into a chelating agent, which modifies the biodistribution and minimizes toxicity. There are three main categories of FDA-approved GBCA available for clinical use based on the biodistribution: extracellular fluid agents, blood pool agents, and combined extracellular and liver agents. Extracellular agents are most commonly used in practice, distribute mostly in the extracellular space, and do not cross the intact blood–brain barrier. These agents are excreted almost exclusively by kidneys with a half-life of approximately 1.5 h in patients with normal renal function.

13.3 Discussion

Gadolinium (Gd) is a rare earth metal that belongs to the lanthanide family of elements. It has seven unpaired electrons with symmetric S-state that results in a slow electronic relaxation rate. Gadolinium-based contrast agents consist of organic molecules attached to gadolinium. Currently, nine GBCA are approved by FDA for clinical use in the USA. Two groups are recognized based on the type of gadolinium–chelate bond. In one group consisting of Gd-DOTA (Dotarem), Gd-DO3A-butrol (Gadovist), and Gd-HPDO3A (ProHance), gadolinium is in the center of the macrocyclic ring. In the other group consisting of Gd-DTPA (Magnevist), Gd-DTPA-BMA (Omniscan), Gd-DTPA-BMEA (OptiMARK), Gd-BOPTA (MultiHance), Gd-EOB-DTPA (Eovist), and Gadofosveset (Ablavar), gadolinium is attached to a linear chelate. The chelate portion of the molecule affects the biodistribution, excretion, and potential toxicity of the agents. GBCA increase both 1/T1 and 1/T2 to varying degrees depending on the applied magnetic field, which results in significant T1 shortening (bright

H. Haroyan, MD
Department of Radiology, University of Chicago, Chicago, IL, USA

D.T. Ginat, MD, MS (✉)
Department of Radiology, University of Chicago, Pritzker Medical School, Chicago, IL, USA
e-mail: ginatd01@gmail.com

D.T. Ginat et al. (eds.), *Neuroimaging Pharmacopoeia*,
DOI 10.1007/978-3-319-12715-6_13,

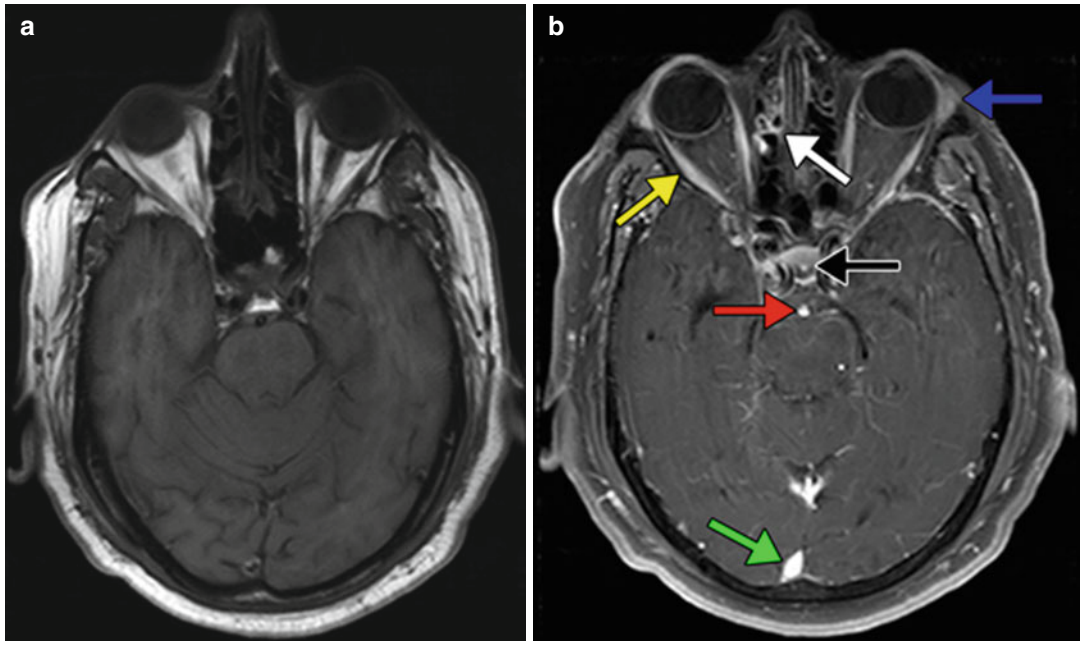

Fig. 13.1 Biodistribution of extracellular gadolinium-based contrast agents. Normal non-contrast T1 image (**a**) and corresponding post-contrast fat-suppressed T1 image (**b**) obtained with intravenous administration of MultiHance show expected enhancement within the venous structures (*green arrow*), basilar artery (*red arrow*), pituitary stalk (*black arrow*), mucosa (*white arrow*), extraocular muscles (*yellow arrow*), and lacrimal gland (*blue arrow*)

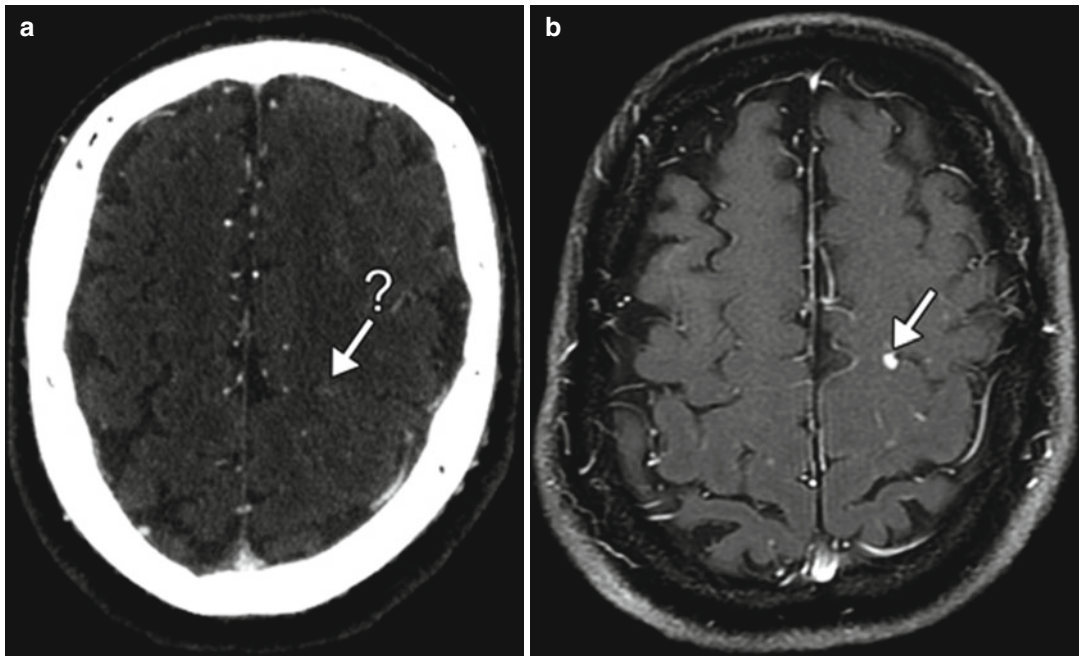

Fig. 13.2 Metastatic disease. Axial post-contrast CT (**a**) shows a very faintly enhancing lesion in the left perirolandic region (*arrow-?*). Post-contrast T1-weighted MRI (**b**) obtained shortly thereafter clearly shows the presence of a metastasis (*arrow*)

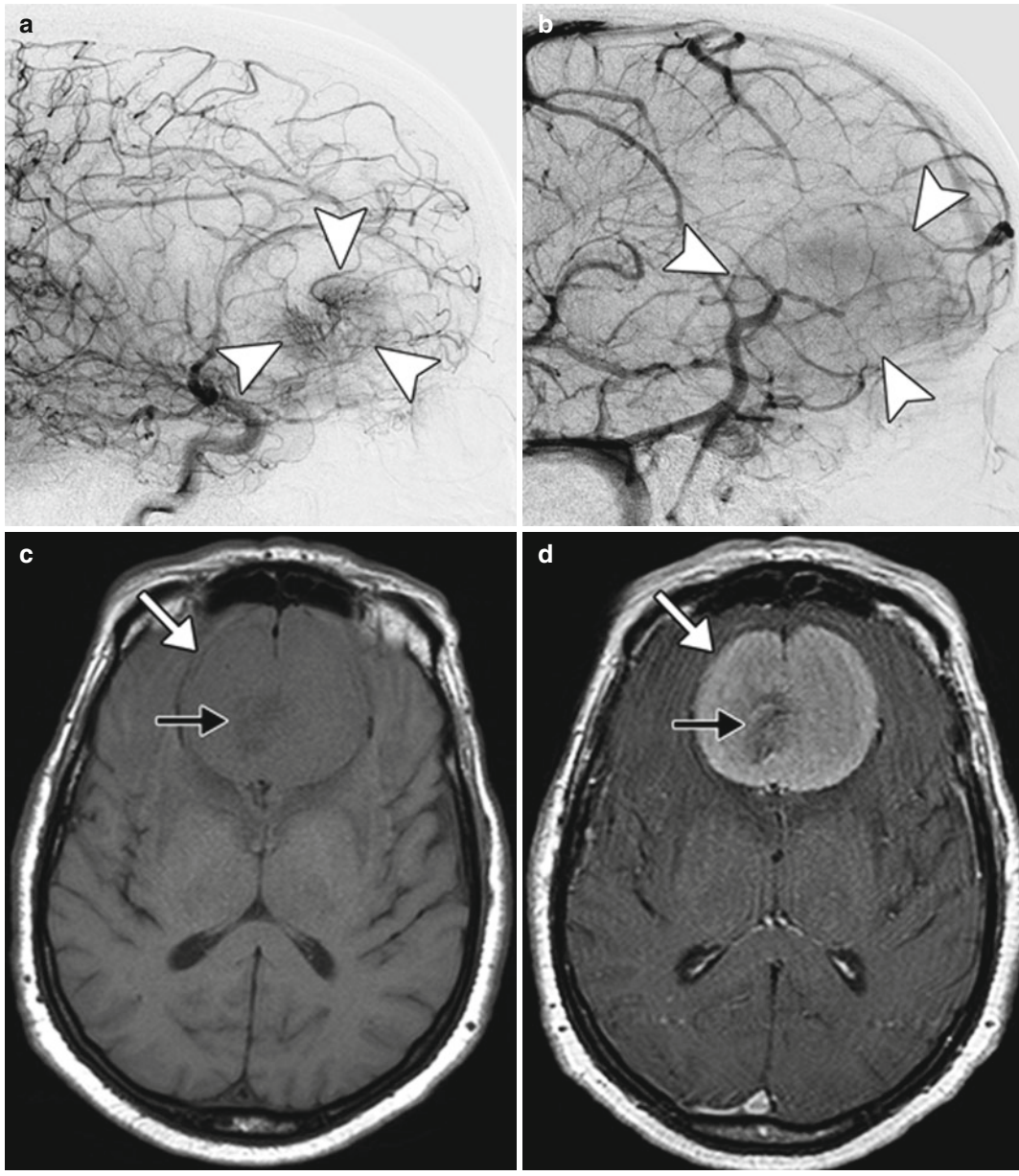

Fig. 13.3 Meningioma. Lateral digital subtraction angiogram images in early (**a**) and late (**b**) phases show a hypervascular mass in the frontal region (*arrowheads*). Axial T1 (**c**) and post-contrast T1 (**d**) images show a large anterior parafalcine mass (*arrows*) with delicate central flow voids (*black arrows*)

signal). Of note, there is no significant effect on T2-weighted images, since the effect is minimal in concentrations used for neuroimaging. Extracellular GBCAs do not cross the intact blood–brain barrier and are normally distributed in vascular structures, choroid plexus, pituitary gland and stalk, pineal gland, area postrema, muscles, and mucosal surfaces (Fig. 13.1). MRI with GCBA is sensitive for the detection of pathological processes associated with blood–brain barrier breakdown, such as abscess, multiple sclerosis, certain primary brain tumors, and metastases. In fact, MRI with contrast is generally more sensitive than CT with contrast for depicting enhancing metastases (Fig. 13.2). MRI with contrast is also useful for depicting hypervascular lesions, such as meningiomas (Fig. 13.3).

In general, GBCA are better tolerated than iodine-based contrast agents used in CT examinations, which can be explained by much smaller doses and biochemical characteristics. The incidence of adverse reactions ranged from 0.07 to 2.4 % when used in doses not exceeding 0.2 mmol/kg. The most common adverse reactions include nausea, headaches, dizziness, paresthesias, and coldness or itching at the injection site. True allergic type reactions are rare, with reported incidence of 0.004–0.7 %, and usually limited to urticaria or hives. Severe allergic reactions are extremely rare.

Fig. 13.4 Nephrogenic systemic fibrosis. Photograph show epidermal atrophy and hairlessness of the affected regions in the legs (Courtesy of Vesna Petronic-Rosic MD, University of Chicago)

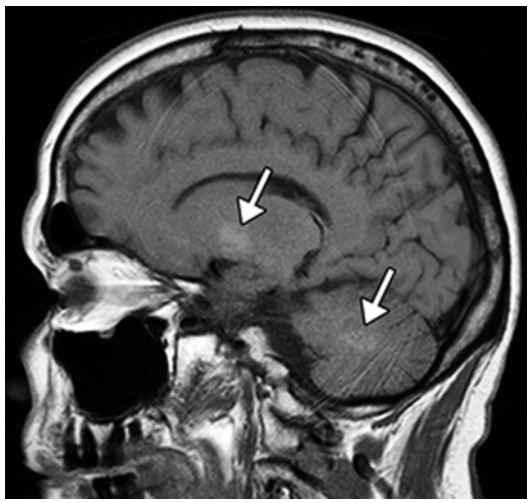

Fig. 13.5 Chronic gadolinium accumulation in the brain. The patient underwent 24 prior contrast-enhanced MRI exams. Sagittal T1 MRI shows patchy hyperintensity in the dentate nucleus and globus pallidus (*arrows)*

Management of anaphylaxis and other contrast reaction is beyond the scope of this text.

A rare delayed complication of GBCA administration is nephrogenic systemic fibrosis (NSF). NSF occurs in patients with end-stage renal disease or severe acute renal failure in association with specific contrast agents (Omniscan, Magnevist, and OptiMARK) and is believed to be dose dependent. Development of NSF is related to *in vivo* release of gadolinium from chelating agents. The dissociation rate of macrocyclic agents is much lower than linear agents, and they are a safer alternative in patients with impaired renal function. NSF predominantly affects the liver, lungs, heart, and skin. In particular, the skin involvement in NSF typically manifests as bilateral symmetric epidermal atrophy and hair loss in the legs (Fig. 13.4). There can also be hyperpigmentation as well as skin hardening or wrinkling. No new cases have been reported in literature in recent years, likely due to increased awareness of the condition, leading to restricted use of GBCA in patients with low GFR.

Even in patients without renal failure, repeated contrast-enhanced MRI scans can lead to accumulation of gadolinium ions in the brain. This can manifest as high signal intensity in the dentate nucleus and globus pallidus on unenhanced T1-weighted images (Fig. 13.5).

13.4 Differential Diagnosis

Differential considerations for hyperintensity on post-contrast T1-weighted MRI include substances that are intrinsically T1 hyperintense, such as subacute blood products (methemoglobin), lipid, proteins, melanin, and certain minerals. Implementation of subtraction maps can be used to discern whether or not there is indeed enhancement in lesions that appear hyperintense on T1 (Fig. 13.6). In addition, the presence of chemical shift artifact or loss of signal with fat-suppression techniques can confirm the presence of lipid in lesions suspected of containing fat. Alternatively, CT can readily depict fat attenuation in lipomatous lesions (Fig. 13.7).

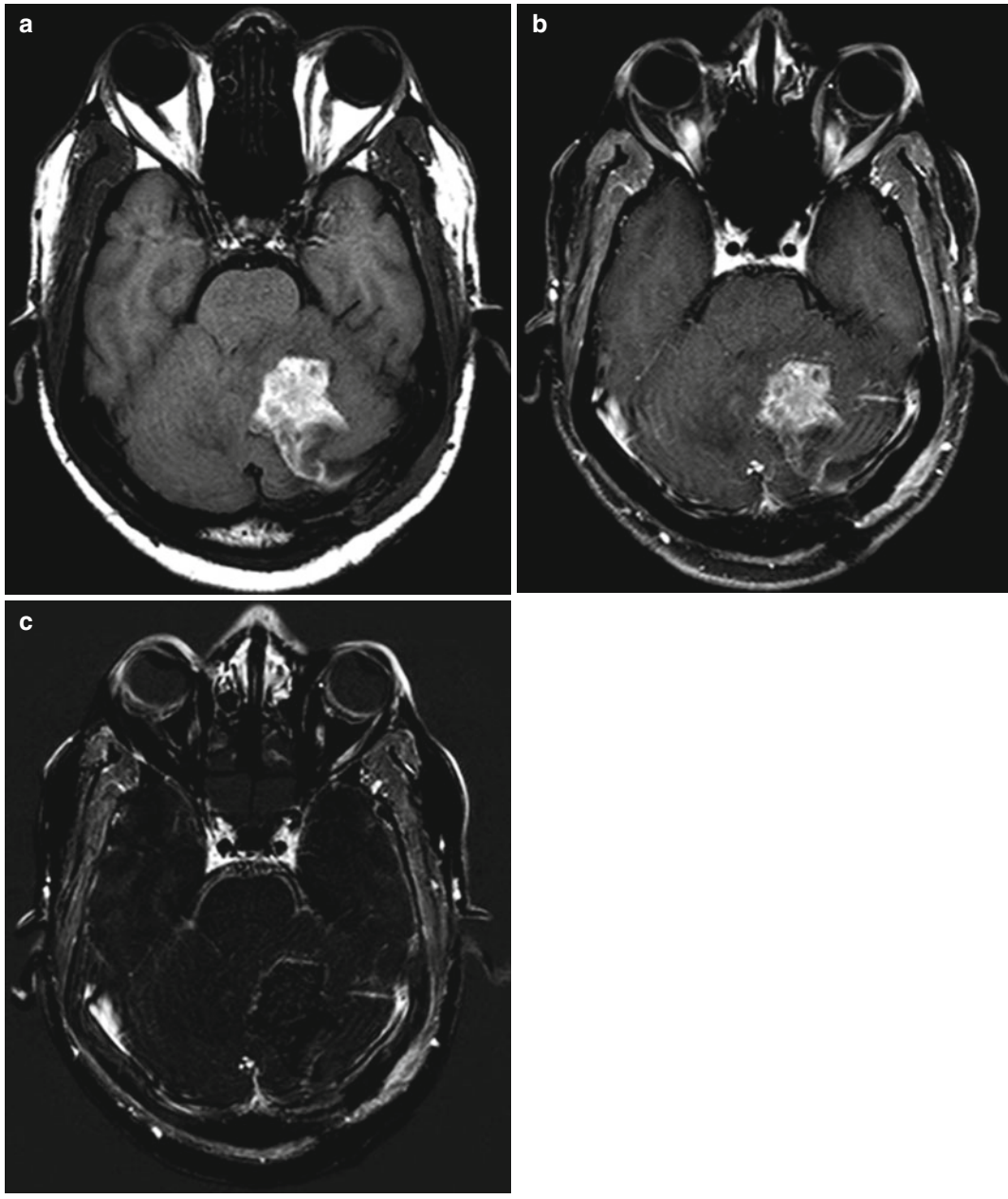

Fig. 13.6 Blood products. The patient underwent recent resection of a left cerebellar tumor. The non-contrast T1 weighted (**a**) and post-contrast T1 weighted (**b**) images show hyperintensity in the resection bed. It is difficult to determinate whether there is indeed a residual enhancing mass amidst subacute blood products with intrinsic T1 hyperintensity. However, the subtraction image (**c**) shows absence of nodular enhancement in the resection bed. A peripheral rim of high signal on subtraction images may result from slight misregistration artifact

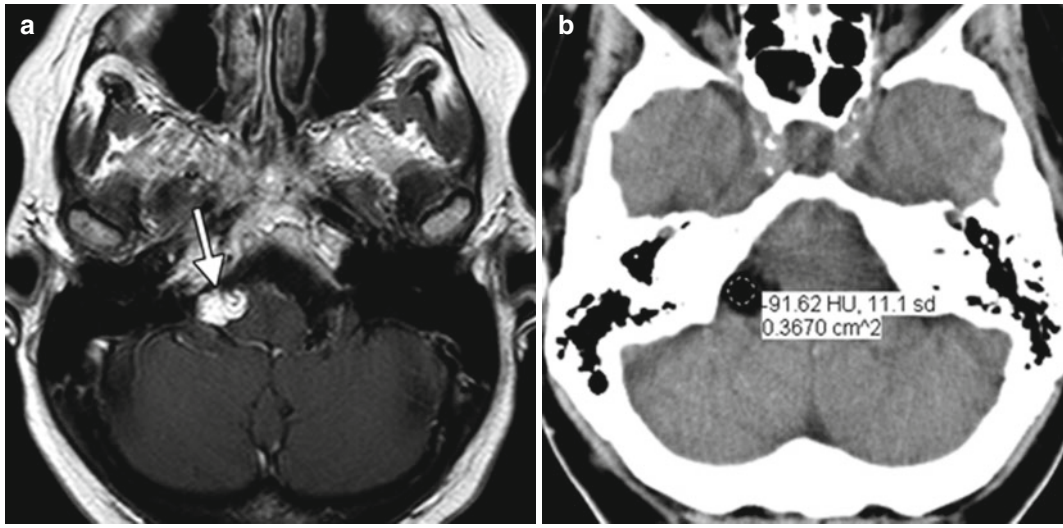

Fig. 13.7 Lipid. Axial post-contrast T1-weighted MRI (**a**) shows a T1 hyperintense lesion in the right cerebellomedullary angle (*arrow*). The corresponding CT image (**b**) shows fat attenuation (−91.62 HU) within the lesion, confirming that it is indeed a lipoma

Suggested Reading

ACR Committee on Drugs and Contrast Media. ACR manual on contrast media. Version 9. Reston: American College of Radiology; 2013.

Aime S, Caravan P. Biodistribution of gadolinium-based contrast agents, including gadolinium deposition. J Magn Reson Imaging. 2009;30:1259–67.

Bennett CL, Qureshi ZP, Oliver Sartor A, Norris LB, Murday A, Xirasagar S, Thomsen HS. Gadolinium-induced nephrogenic systemic fibrosis: the rise and fall of an iatrogenic disease. Clin Kidney J. 2012;5(1):82–8.

Broome DR, Girguis MS, Baron PW, Cottrell AC, Kjellin I, Kirk GA. Gadodiamide-associated nephrogenic systemic fibrosis: why radiologists should be concerned. AJR Am J Roentgenol. 2007;188:586–92.

Cochran ST, Bomyea K, Sayre JW. Trends in adverse events after IV administration of contrast media. AJR Am J Roentgenol. 2001;176:1385–8.

Ginat DT, Meyers SP. Intracranial lesions with high signal intensity on T1-weighted MR images: differential diagnosis. Radiographics. 2012;32(2):499–516.

Jung JW, Kang HR, Kim MH, Lee W, Min KU, Han MH, Cho SH. Immediate hypersensitivity reaction to gadolinium-based MR contrast media. Radiology. 2012;264(2):414–22.

Kanal E, Maravilla K, Rowley HA. Gadolinium Contrast Agents for CNS Imaging: Current Concepts and Clinical Evidence. AJNR Am J Neuroradiol. 2014;35(12):2215–26.

Kanda T, Ishii K, Kawaguchi H, Kitajima K, Takenaka D. High signal intensity in the dentate nucleus and globus pallidus on unenhanced T1-weighted MR images: relationship with increasing cumulative dose of a gadolinium-based contrast material. Radiology. 2014; 270(3):834–41.

Kuo PH, Kanal E, Abu-Alfa AK, Cowper SE. Gadolinium-based MR contrast agents and nephrogenic systemic fibrosis. Radiology. 2007;242:647–9.

Nduom EK, Yang C, Merrill MJ, Zhuang Z, Lonser RR. Characterization of the blood-brain barrier of metastatic and primary malignant neoplasms. J Neurosurg. 2013;119(2):427–33.

Saleh L, Juneman E, Reza Movahed M. The use of gadolinium in patients with contrast allergy or renal failure requiring coronary angiography, coronary intervention, or vascular procedure. Catheter Cardiovasc Interv. 2011;78:747–54.

Seute T, Leffers P, ten Velde GP, Twijnstra A. Detection of brain metastases from small cell lung cancer: consequences of changing imaging techniques (CT versus MRI). Cancer. 2008;112(8):1827–34.

van der Molen AJ, Bellin MF. Extracellular gadolinium-based contrast media: differences in diagnostic efficacy. Eur J Radiol. 2008;66(2):168–74.

Pantopaque (Myodil, Iodophenylundecylic Acid)

14

Daniel Thomas Ginat

14.1 Uses

Pantopaque is an oil-based contrast agent that was mainly used for myelography in the past, but it is now obsolete.

14.2 Mechanism

Pantopaque contains iodine, which renders the contrast agent radio-opaque. The contrast medium is an oil ester, which imparts T1 shortening effects on MRI. Residual Pantopaque droplets are irritating and can cause arachnoiditis and meningitis.

14.3 Discussion

Pantopaque was first used as a contrast agent in 1944 for myelography. The material is radio-opaque on radiography and hyperattenuating on CT. On MRI, Pantopaque is hyperintense on T1-weighted sequences and displays intermediate signal on T2-weighted images. In addition, on T2-weighted images, chemical shift artifact can be observed in the frequency encoding direction (Fig. 14.1). Spinal arachnoiditis frequently occurs in association with Pantopaque years later due to chronic nerve root irritation. The material can also migrate into the intracranial compartment, where it may be encountered incidentally (Fig. 14.2).

14.4 Differential Diagnosis

In the spine, the differential diagnosis for subarachnoid T1 hyperintense lesions on MRI includes fibrolipomas, lipomas, epidural lipomatosis, dermoid, hemorrhage, and melanoma. Without an appropriate clinical history, CT can help differentiate among some of these possibilities; fat is typically very hypoattenuating on CT, while subacute hemorrhage and melanoma have intermediate attenuation. The differential diagnosis for leptomeningeal dissemination of Pantopaque into the intracranial compartment with hyperattenuation on CT mainly includes meningoangiomatosis and subarachnoid hemorrhage. On MRI, ruptured dermoid, leptomeningeal melanoma and/or hemorrhagic metastases, and subacute subarachnoid hemorrhage are potential differential diagnostic considerations.

- *Fibrolipoma*: Filum terminale fibrolipomas typically appear as elongated masses with fat signal characteristics (T1 and T2 hyperintense with loss of signal on fat-suppressed sequences) on MRI (Fig. 14.3).

D.T. Ginat, MD, MS
Department of Radiology, University of Chicago, Pritzker Medical School, Chicago, IL, USA
e-mail: ginatd01@gmail.com

D.T. Ginat et al. (eds.), *Neuroimaging Pharmacopoeia*,
DOI 10.1007/978-3-319-12715-6_14,

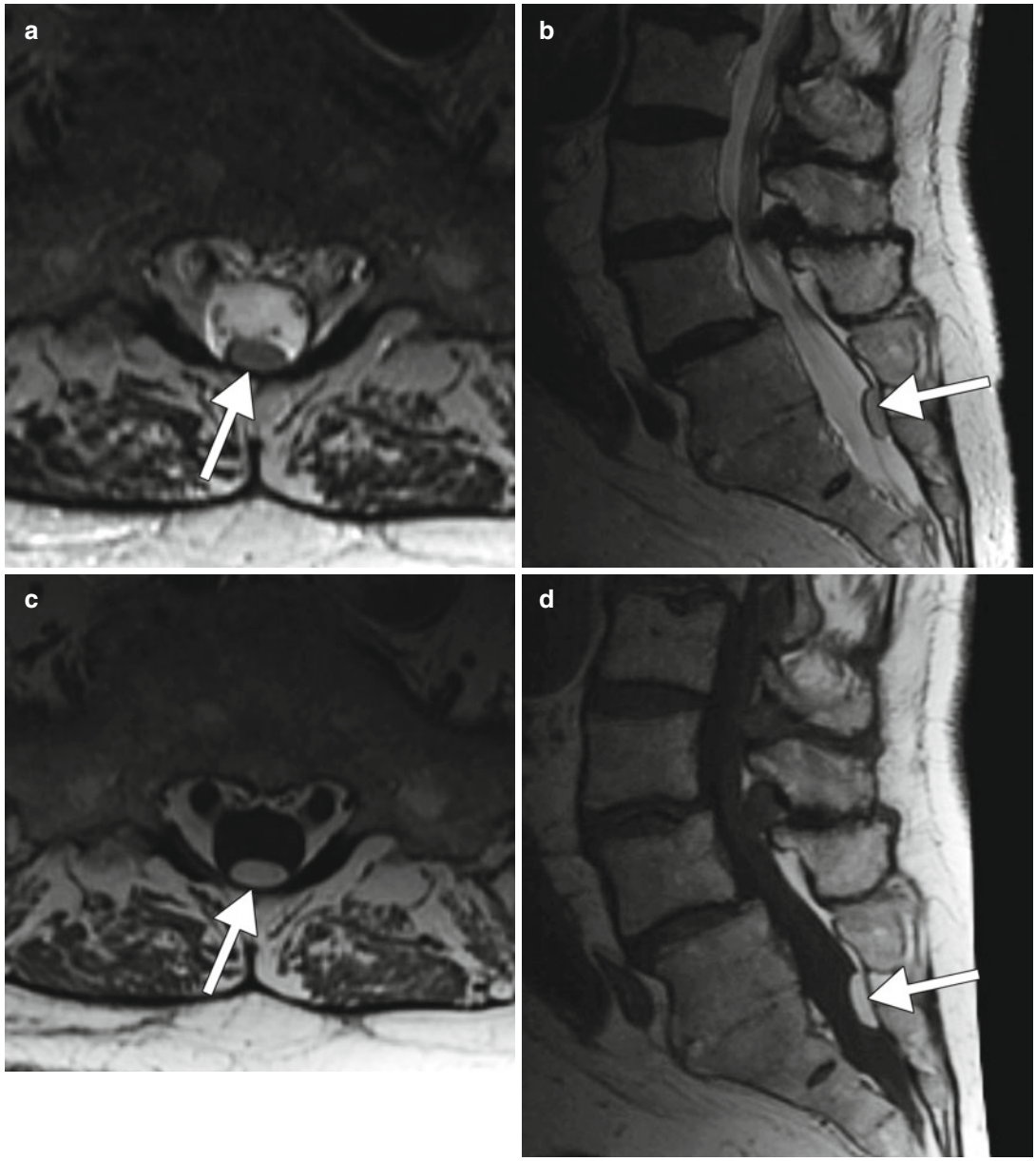

Fig. 14.1 Intraspinal Pantopaque. Axial and sagittal T1-weighted and T2-weighted MR images (**a**–**d**) show high T1 and intermediate T2 signal with associated chemical shift artifact within the spinal canal (*arrows*). Lateral radiograph of the lumbar spine (**e**) shows a high attenuation material in the spinal canal at the level of L5-S1 (*arrows*)

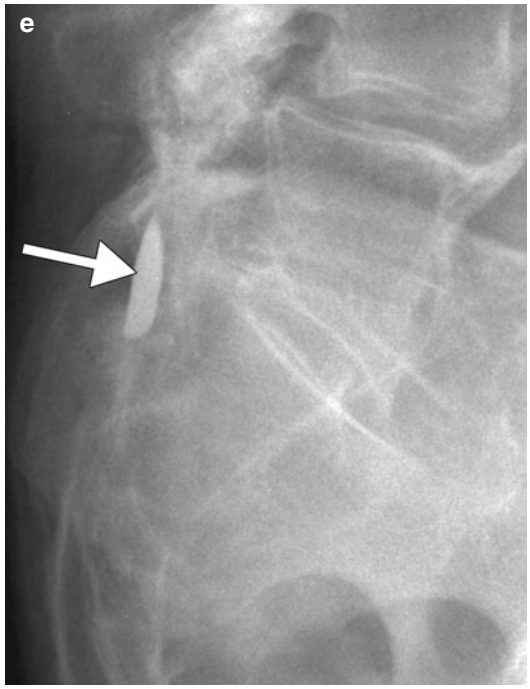

Fig. 14.1 (continued)

- *Ruptured dermoid*: Dermoids typically display properties of fat on CT and MRI. The presence of multiple subarachnoid foci with CT hypoattenuation or T1 hyperintensity suggests rupture (Fig. 14.4).
- *Leptomeningeal metastases*: Metastases may appear intrinsically T1 hyperintense if they are melanotic or if they are characterized by subacute hemorrhage (Fig. 14.5). Unlike Pantopaque, metastases typically enhance.
- *Bullet and bone fragments*: These may enter the intracranial and intraspinal compartments and are hyperattenuating (Fig. 14.6). The presence of entry and/or exit sites, distribution and morphology of the fragments, and clinical history can readily differentiate these from residual Pantopaque.

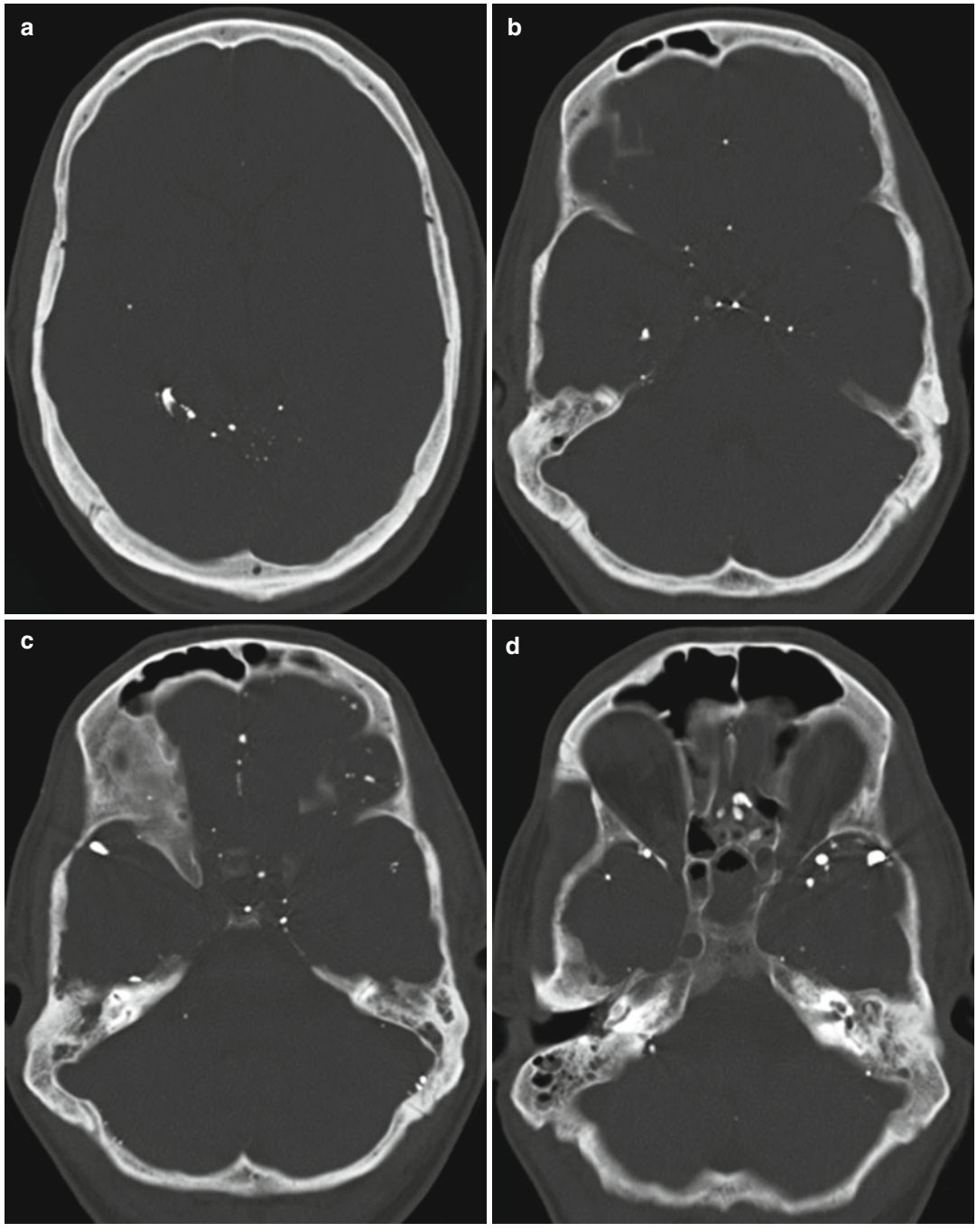

Fig. 14.2 Intracranial Pantopaque. Axial CT images (**a**–**d**) show numerous scattered punctate hyperattenuating foci of residual Pantopaque in the subarachnoid spaces

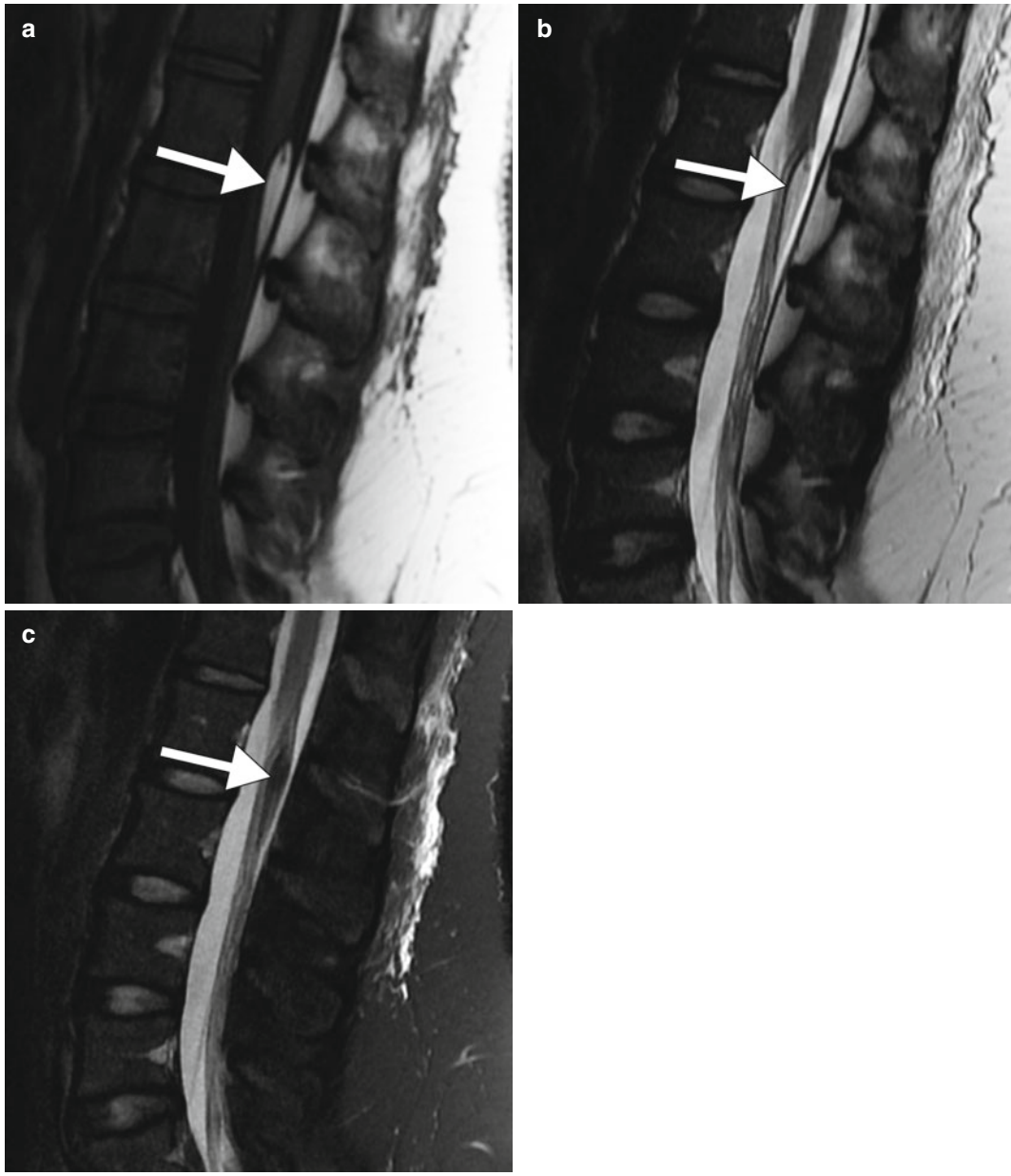

Fig. 14.3 Fibrolipoma of the filum terminale. Sagittal T1-weighted (**a**), T2-weighted (**b**), and fat-suppressed T2-weighted (**c**) MR images show a fusiform mass associated with the filum terminale with signal characteristics of fat (*arrows*)

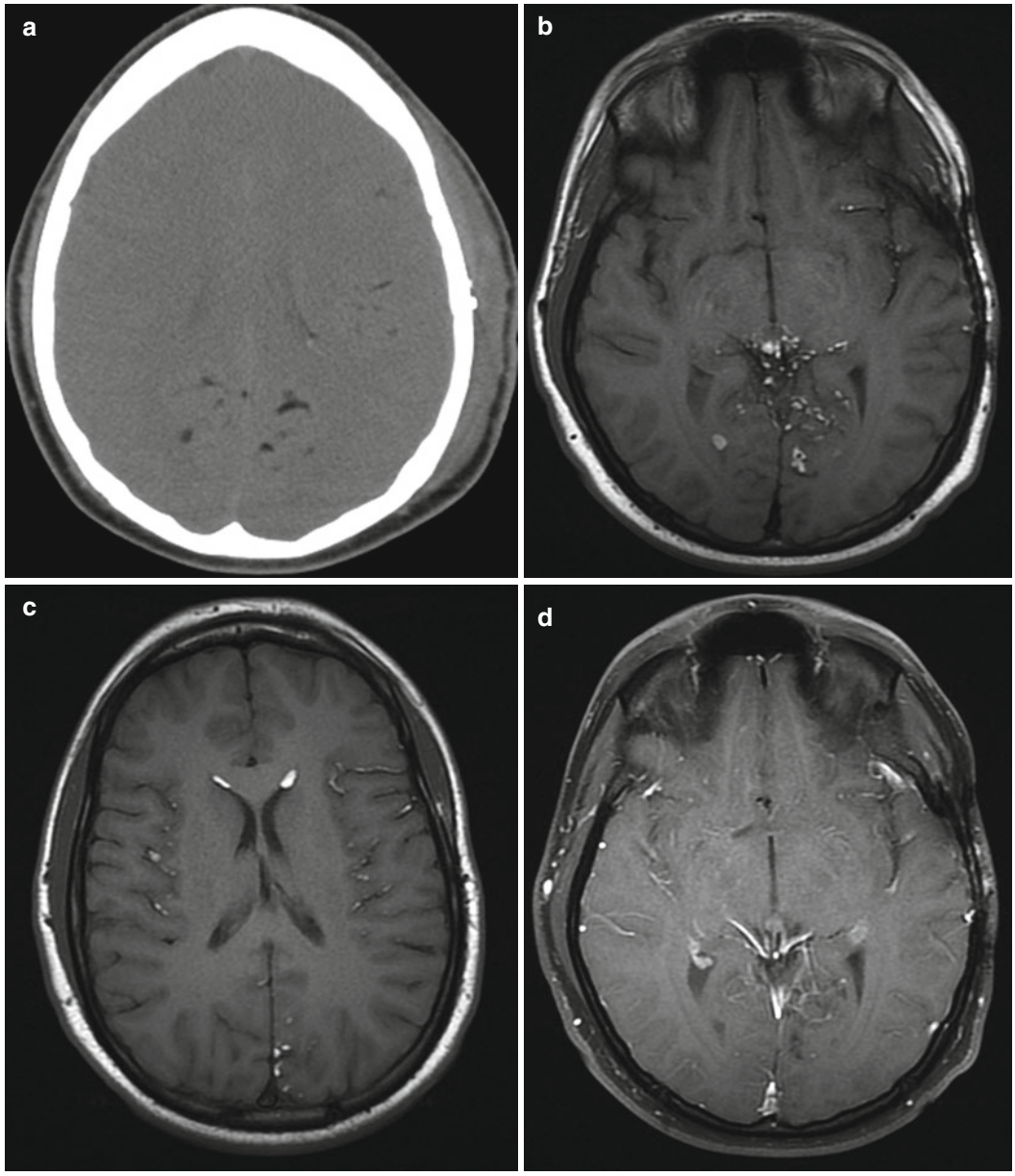

Fig. 14.4 Ruptured dermoid. Axial CT image (**a**) shows a fat-attenuation foci in the bilateral posterior cerebral hemisphere sulci. Axial T1-weighted MR images (**b**, **c**) show scattered foci of T1 hyperintensity within the sulci and ventricular system. Axial fat-suppressed post-contrast T1-weighted MR image (**d**) shows corresponding loss of signal in the lesions

Fig. 14.5 Leptomeningeal melanoma metastases. Sagittal T1 MRI (**a**) of the spine shows intrinsically hyperintense melanoma metastases along the cauda equina nerve roots. The metastases display low signal on T2-weighted MRI (**b**) and enhancement on the post-contrast fat-suppressed T1-weighted MRI (**c**)

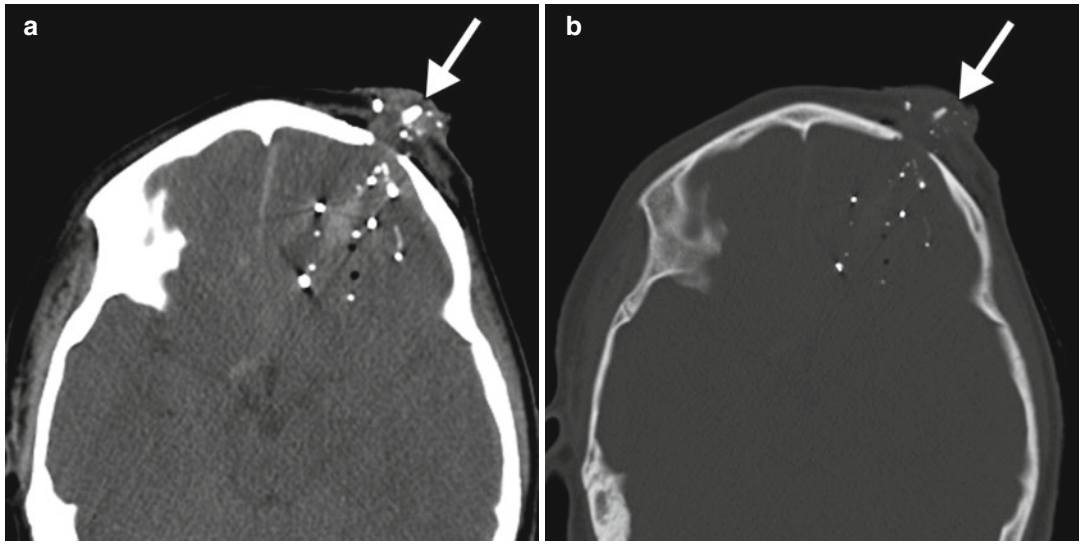

Fig. 14.6 Bullet and bone fragments. Axial CT images (**a**, **b**) show intracranial bullet and bone fragments scattered in the left frontal lobe near the left frontal entry site (*arrow*)

Suggested Reading

Braun IF, Malko JA, Davis PC, Hoffman Jr JC, Jacobs LH. The behavior of Pantopaque on MR: in vivo and in vitro analysis. AJNR Am J Neuroradiol. 1986;7(6):997–1001.

Gnanalingham KK, Joshi SM, Sabin I. Thoracic arachnoiditis, arachnoid cyst and syrinx formation secondary to myelography with Myodil, 30 years previously. Eur Spine J. 2006;15 Suppl 5:661–3.

Mamourian AC, Briggs RW. Appearance of Pantopaque on MR images. Radiology. 1986;158(2):457–60.

Suojanen J, Wang AM, Winston KR. Pantopaque mimicking spinal lipoma: MR pitfall. J Comput Assist Tomogr. 1988;12(2):346–8.

Thorium Dioxide (Thorotrast) 15

Daniel Thomas Ginat

15.1 Uses

Radioactive contrast agent introduced in 1928 and mainly used for cerebral angiography until the 1950s.

15.2 Mechanism

Thorotrast granules can be phagocytosed by macrophages and retained by the reticuloendothelial system Th-203 emits alpha particles and has a biological half-life of several hundred years, so that such patients incur lifetime exposure to internal radiation. In addition, Thorotrast can induce an intense foreign body reaction with a marked cell-deficient fibrosis.

15.3 Discussion

Although obsolete, patients may still present with the sequela of Thorotrast exposure. Extravasated Thorotrast can be retained for many years along the carotid sheath if a transcervical approach was used for the injection. The extravasated Thorotrast can form granulomas (thorotrastomas), which can be complicated by persistent open draining neck wounds. Thorotrast is also carcinogenic and has been implicated in inducing neoplasms, such as hepatic angiosarcoma, cholangiocarcinoma, and hepatocellular carcinoma. Thorotrast is markedly hyperattenuating and readily depicted on CT (Fig. 15.1). Indeed, CT is useful for the delineation of the extent of the deposits and the relationships of the larynx and carotid vessels for treatment planning. Neck dissection and application of doxycycline sclerosis have been used to treat thorotrastomas.

15.4 Differential Diagnosis

The findings in cervical Thorotrast extravasation are rather characteristic and unusual. Conditions that can potentially resemble Thorotrast deposits in the neck on CT are heterotopic ossification, osteosarcoma metastases (Fig. 15.2), treated lymphoma with calcified lymph nodes, and other tumors that have a propensity to calcify, such as papillary thyroid carcinoma (Fig. 15.3), and metal clips (Fig. 15.4).

D.T. Ginat, MD, MS
Department of Radiology, University of Chicago,
Pritzker Medical School, Chicago, IL, USA
e-mail: ginatd01@gmail.com

D.T. Ginat et al. (eds.), *Neuroimaging Pharmacopoeia*,
DOI 10.1007/978-3-319-12715-6_15,

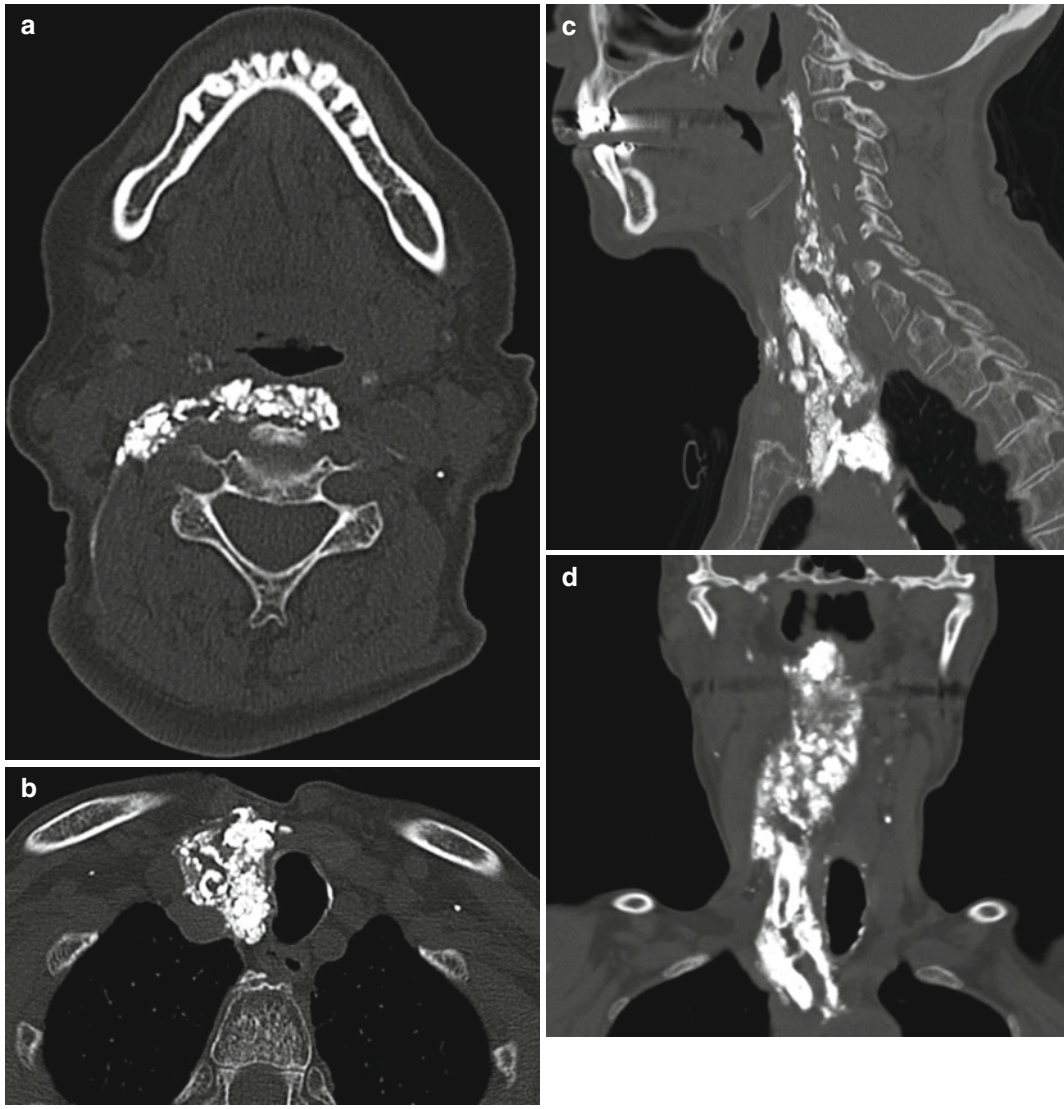

Fig. 15.1 Thorotrastoma. The patient is an 82-year-old female with right vocal cord paralysis and a history of Thorotrast extravasation during an angiogram performed in the 1950s. Axial (**a**, **b**), sagittal (**c**), and coronal (**d**) CT images demonstrate hyperattenuating material surrounding the right carotid sheath, extending superiorly into the retropharyngeal space to the level of C1 and extending inferiorly to the mediastinum

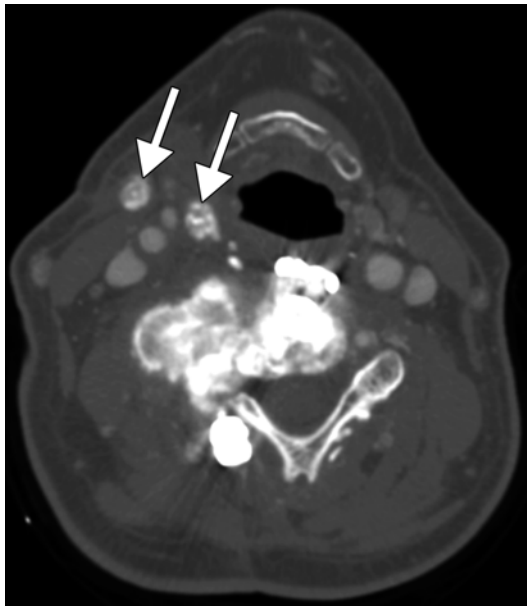

Fig. 15.2 Osteosarcoma metastases. Axial CT image shows an osteoblastic mass arising from a cervical vertebra in a previously operated site. There are also hyperattenuating right cervical lymph node metastases (*arrows*)

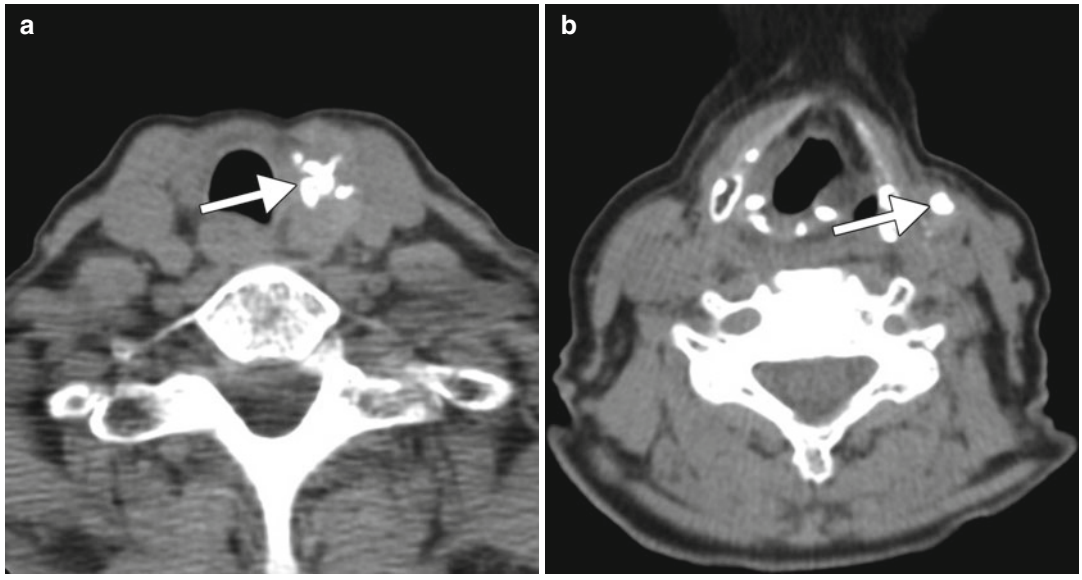

Fig. 15.3 Papillary thyroid carcinoma. Axial CT image (**a**) shows a calcified mass in the left thyroid lobe (*arrow*). Axial CT image at another level (**b**) shows a calcified nodal metastasis (*arrow*)

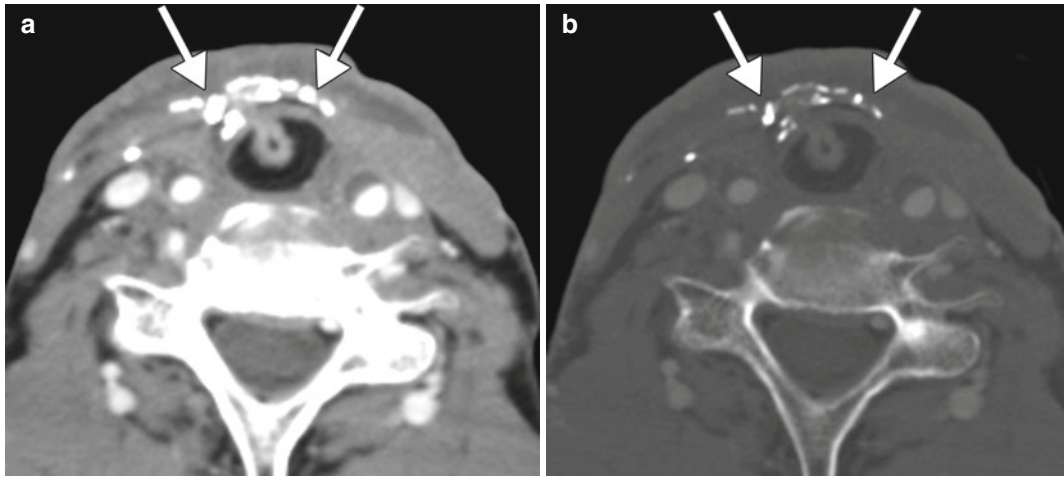

Fig. 15.4 Surgical clips. Axial CT images in soft tissue (**a**) and bone (**b**) windows show numerous metallic clips (*arrows*) in the surgical bed in a patient who underwent laryngopharyngectomy

Suggested Reading

Bohatirchuk FP, Jeletzky TF, Ivan LP. Contact historadiography of nervous tissue impregnated with thorotrast. Am J Roentgenol Radium Ther Nucl Med. 1973;118(4):923–6.

Fishman EK, Gayler BW, Kashima HK, Harris AE, Siegelman SS. Computed tomography in the evaluation of cervical thorotrast granuloma. J Comput Assist Tomogr. 1984;8(2):224–8.

Ishikawa Y, Wada I, Fukumoto M. Alpha-particle carcinogenesis in Thorotrast patients: epidemiology, dosimetry, pathology, and molecular analysis. J Environ Pathol Toxicol Oncol. 2001;20(4):311–5

Stover BJ. Effects of thorotrast in humans. Health Phys. 1983;44 Suppl 1:253–7.

Ung F, Lazor JB, Montgomery WW. Cervical thorotrast granuloma: a review of the literature and a new treatment modality. Ann Otol Rhinol Laryngol. 1998;107(8):708–12.

Wustrow TP, Behbehani AA, Wiebecke B. Thorotrast-induced oro- and hypopharyngeal fibrosis with recurrent bleeding. J Craniomaxillofac Surg. 1988; 16(7):315–9

Zwaga T, Bovée JV, Kroon HM. Osteosarcoma of the femur with skip, lymph node, and lung metastases. Radiographics. 2008;28(1):277–83.

Bevacizumab (Avastin) 16

Daniel Thomas Ginat and William A. Mehan

16.1 Uses

Bevacizumab is used for the treatment of metastatic colorectal cancer, non-squamous cell lung cancer, metastatic renal cell cancer, prostate cancer, and recurrent glioblastoma.

16.2 Mechanism

Bevacizumab is a monoclonal antiangiogenic endothelial growth factor (VEGF) antibody that inhibits the VEGF-A tyrosine kinase receptor. Anti-VEGF agents result in regression of existing microvessels, normalization of surviving mature vasculature, and inhibition of vessel growth and neovascularization. In addition, VEGF inhibition may prevent tumor growth and even result in tumor size reduction.

16.3 Discussion

Certain tumors, such as glioblastoma, have an elevated expression of VEGF. Consequently, glioblastoma patients treated with bevacizumab have achieved response rates of 30–60 % as well as 6 months of progression-free survival rates of 30–50 %. However, there is commonly a transient early apparent response to bevacizumab without a true cytotoxic effect. This is attributable to normalization of a leaky blood–brain barrier in tumor vessels resulting in decreased tumor enhancement and edema. This phenomenon is known as "pseudoresponse" and manifests as decreased enhancement and edema within the tumor and associated clinical improvement that occurs within days to weeks of initiating bevacizumab therapy. On MRI, enlargement of the non-enhancing FLAIR hyperintense signal or new areas of restricted diffusion are signs of tumor progression (Fig. 16.1). Conversely, rebound enhancement and edema can result when bevacizumab is withdrawn.

Stroke-like lesions with diffusion restriction can also result from bevacizumab administration to glioblastoma and metastases (Figs. 16.2 and 16.3). In addition, there is commensurate suppression of abnormal enhancement and normalization of perfusion in the areas of restricted diffusion. These lesions can manifest as early as 4 weeks after initiation of therapy and can persist for at least up to 80 weeks. The histopathology of such lesions consists of atypical necrosis and nuclear hypoxia-inducible factor 1-alpha upregulation, but no tumor recurrence. The cause of these alterations is still uncertain, but may entail atypical necrosis and chronic hypoxia. Other possible neuroimaging findings related to bevacizumab

D.T. Ginat, MD, MS (✉)
Department of Radiology, University of Chicago, Pritzker Medical School, Chicago, IL, USA
e-mail: ginatd01@gmail.com

W.A. Mehan, MD
Department of Radiology, Tufts Medical Center, Boston, MA, USA

D.T. Ginat et al. (eds.), *Neuroimaging Pharmacopoeia*,
DOI 10.1007/978-3-319-12715-6_16,

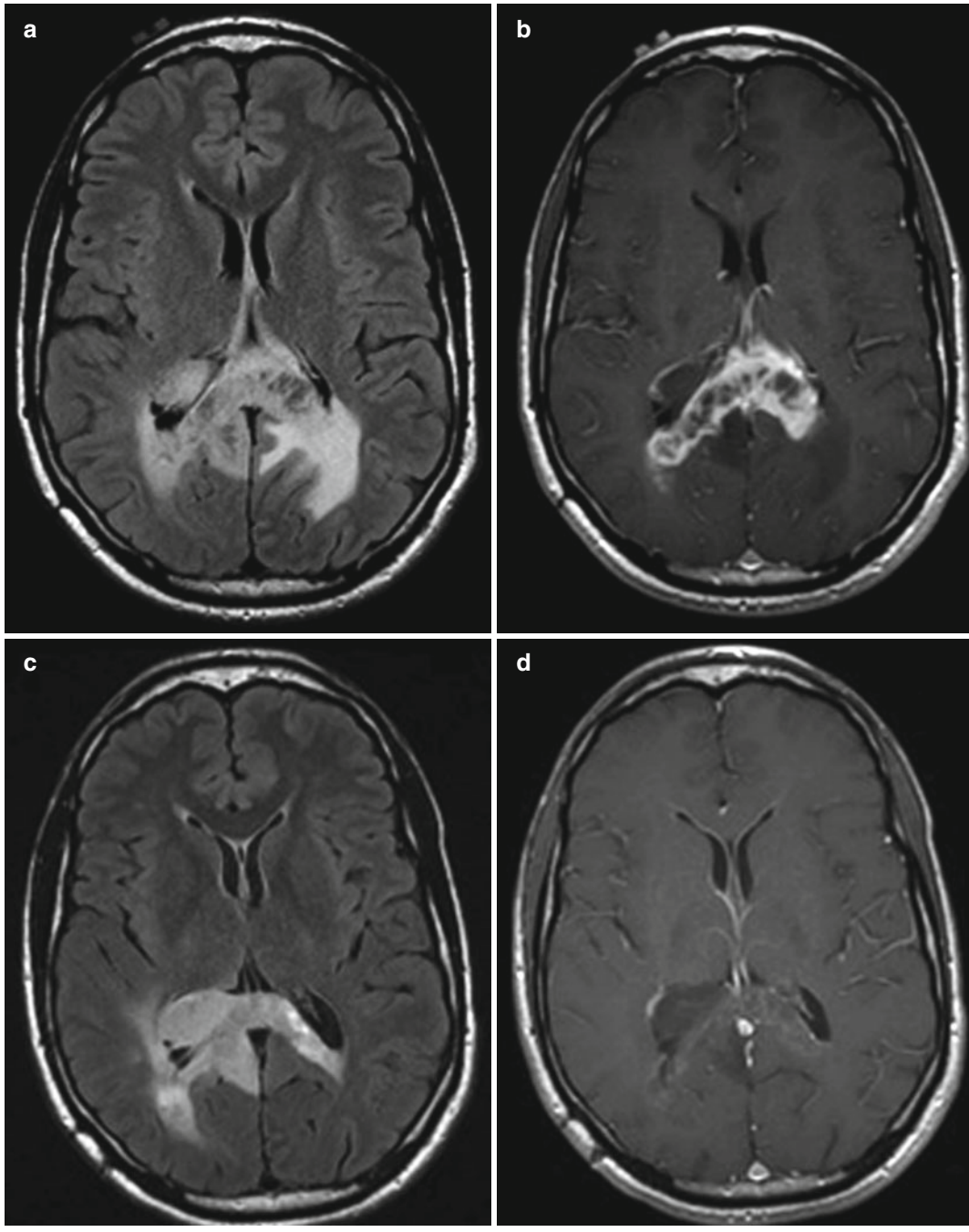

Fig. 16.1 Pseudoresponse. The patient has a history of recurrent glioblastoma in the splenium of the corpus callosum, treated with bevacizumab. Axial FLAIR (**a**) and T1-weighted post-contrast (**b**) MR images show a heterogeneous enhancing mass involving the splenium of the corpus callosum. Axial FLAIR (**c**) and T1-weighted post-contrast (**d**) MR images show marked interval decrease in the degree of enhancement and edema associated with the tumor shortly after bevacizumab administration. Axial FLAIR (**e**) and T1-weighted post-contrast (**f**) MR images show a new area of enhancement and T2 hyperintensity on follow-up imaging obtained 2 months later (*arrows*)

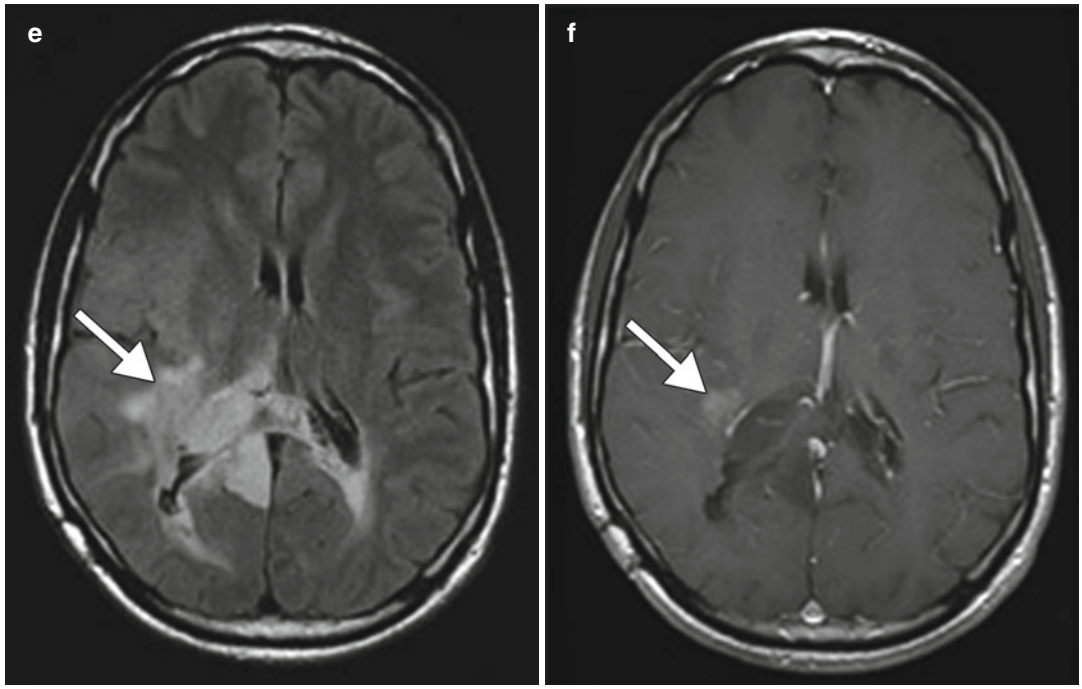

Fig. 16.1 (continued)

administration include nasal septal perforation and posterior reversible encephalopathy syndrome (Fig. 16.4). Although tumor hemorrhage has been reported with bevacizumab use, bevacizumab may not necessarily carry an increased risk for this complication since many tumors have a propensity to hemorrhage spontaneously.

16.4 Differential Diagnosis

The imaging findings related to pseudoresponse related to bevacizumab administration can occur with other anti-VEGF agents, such as cediranib. These findings are analogous to the effects of steroids on brain tumors, in which there can be dramatic reductions of edema and enhancement (refer to Chap. 46). The main differential considerations for bevacizumab-induced stroke-like lesions include true stoke, abscess, and tumor progression or recurrence (Fig. 16.5). These possibilities are less likely, if the clinical condition of the patient improves during therapy, signs of inflammation are absent, and there is no significant enhancement in the lesion with reduced ADC values. Furthermore, stable to slight increase in ADC values suggests nonprogression, while continuous decrease in ADC values suggests tumor progression in cases of glioblastoma treated with bevacizumab. The presence of hypermetabolism on ^{18}FDG-PET and other radiotracers also favors tumor progression or recurrence.

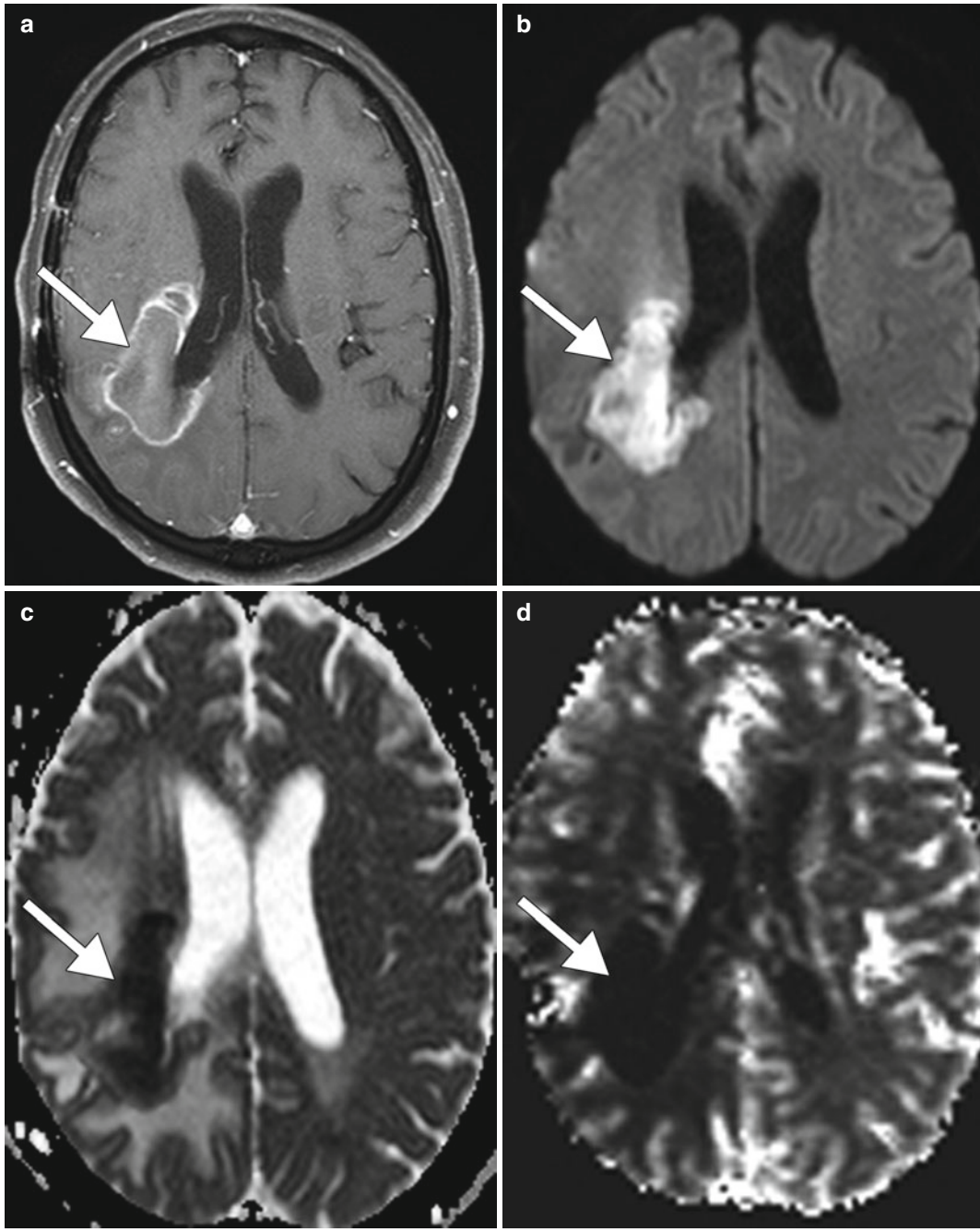

Fig. 16.2 Bevacizumab-induced stroke-like lesions in glioblastoma. The patient has a history of recurrent right frontoparietal glioblastoma treated with bevacizumab monotherapy. Axial post-contrast T1 (**a**), DWI (**b**), ADC map (**c**), and CBV map (**d**) images show hyperintense DWI signal within the previously contrast-enhancing tumor area and corresponding ADC reduction and hypoperfusion (*arrows*)

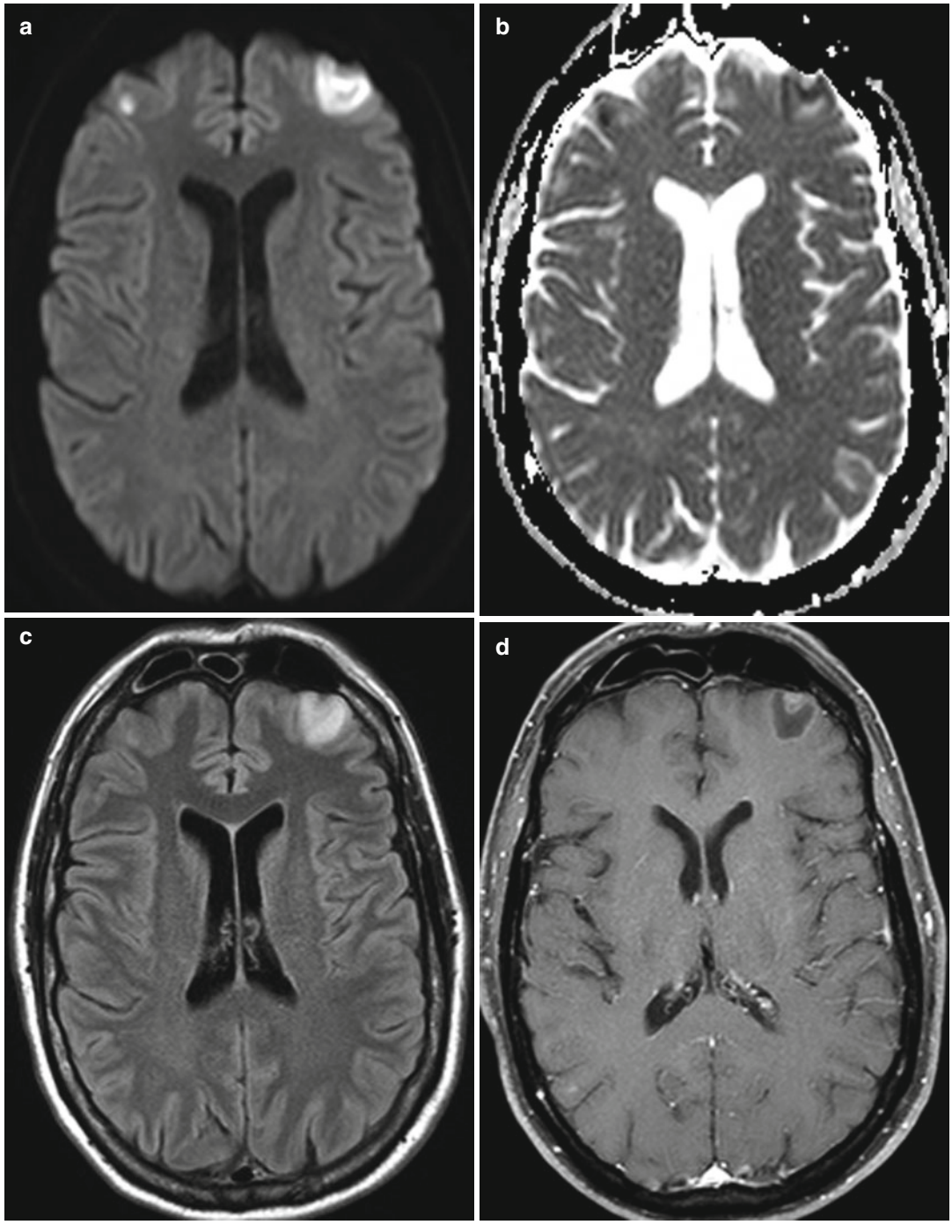

Fig. 16.3 Bevacizumab-induced stroke-like lesions in renal cell carcinoma metastases. Axial DWI (**a**), ADC map (**b**), FLAIR (**c**), and post-contrast T1 (**d**) show restricted diffusion in the bilateral frontal lobe metastases with negligible associated enhancement

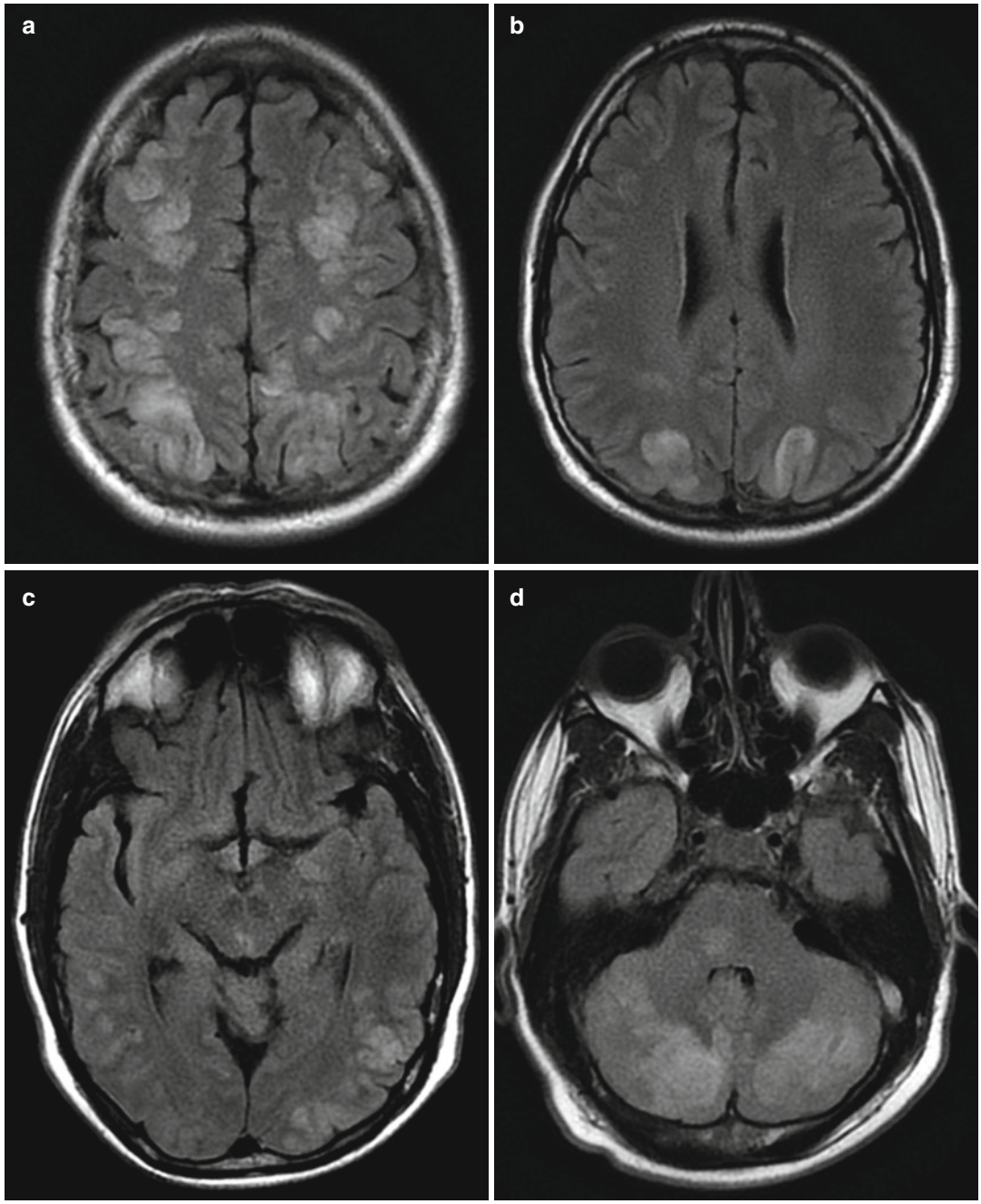

Fig. 16.4 Bevacizumab-induced posterior reversible encephalopathy syndrome. Axial FLAIR images (**a**–**d**) show bilateral symmetric cortical and subcortical edema predominantly in the posterior cerebral hemispheres, but also in atypical locations, including the cerebellum, and pons

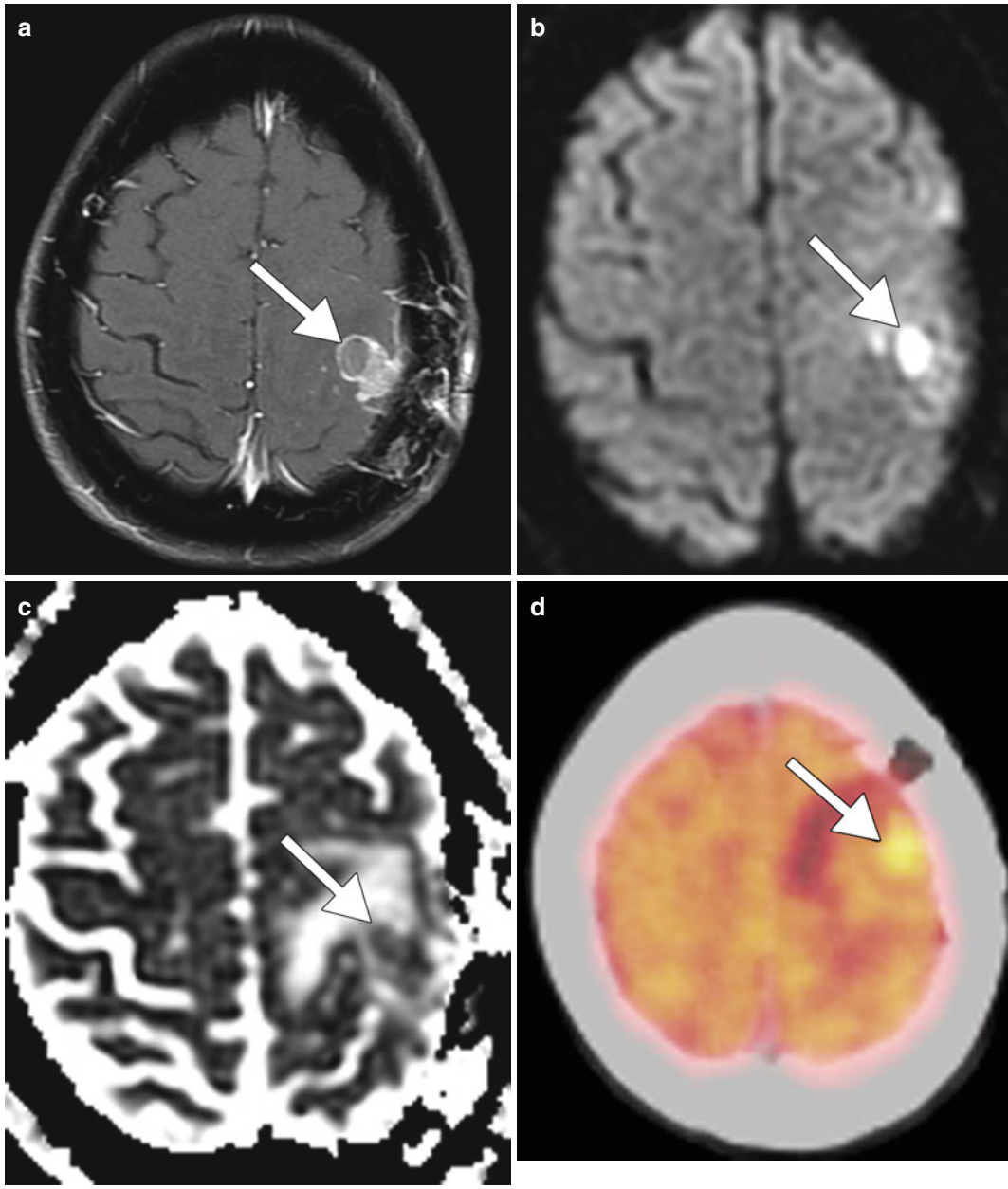

Fig. 16.5 Tumor recurrence. The patient has a history of metastatic lung cancer. Axial post-contrast T1 MRI (**a**), DWI (**b**), and ADC map (**c**) demonstrate tumor recurrence with restricted diffusion (*arrows*) arising in a prior resection cavity. The corresponding ^{18}FDG-PET (**d**) shows hypermetabolism within the lesion (*arrow*)

Suggested Reading

Abbas O, Shamseddin A, Temraz S, Haydar A. Posterior reversible encephalopathy syndrome after bevacizumab therapy in a normotensive patient. BMJ Case Rep. 2013;21:2013.

Allen JA, Adlakha A, Bergethon PR. Reversible posterior leukoencephalopathy syndrome after bevacizumab/FOLFIRI regimen for metastatic colon cancer. Arch Neurol. 2006;63(10):1475–8.

Hygino da Cruz Jr LC, Rodriguez I, Domingues RC, Gasparetto EL, Sorensen AG. Pseudoprogression and pseudoresponse: imaging challenges in the assessment of posttreatment glioma. AJNR Am J Neuroradiol. 2011;32(11):1978–85.

Jain R, Scarpace LM, Ellika S, Torcuator R, Schultz LR, Hearshen D, Mikkelsen T. Imaging response criteria for recurrent gliomas treated with bevacizumab: role of diffusion weighted imaging as an imaging biomarker. J Neurooncol. 2010;96(3):423–31.

Mathews MS, Linskey ME, Hasso AN, Fruehauf JP. The effect of bevacizumab (Avastin) on neuroimaging of brain metastases. Surg Neurol. 2008;70(6):649–52; discussion 653.

Mukherji SK. Bevacizumab (Avastin). AJNR Am J Neuroradiol. 2010;31(2):235–6.

Rieger J, Bähr O, Müller K, Franz K, Steinbach J, Hattingen E. Bevacizumab-induced diffusion-restricted lesions in malignant glioma patients. J Neurooncol. 2010;99(1):49–56.

Temozolamide (Temodar) 17

William A. Mehan and Daniel Thomas Ginat

17.1 Uses

Temozolamide with concurrent radiation is the standard therapy for the treatment of glioblastomas following surgical resection and for relapsing grade III astrocytomas.

17.2 Mechanism

Temozolamide is an alkylating agent prodrug that delivers a methyl group to purine bases of DNA, which ultimately inhibits DNS and cell replication. The primary cytotoxic lesion O6-methylguanine (O6-MeG) can be eliminated by methylguanine methyltransferase (MGMT) in tumors that express this protein or tolerated in mismatch repair (MMR)-deficient tumors. Consequently, MGMT or MMR deficiency confers resistance to TMZ.

17.3 Discussion

Temozolamide with concurrent radiation therapy is associated with pseudoprogression in approximately 10–40 % cases of treated glioblastomas overall and 90 % of cases with MGMT promoter methylation. Pseudoprogression is defined as an increase in size of the enhancing component of high-grade gliomas within 3 months of radiation and temozolamide (Fig. 17.1). Pseudoprogression is believed to be an inflammatory response to the tumor and may portend a better prognosis. Indeed, patients with pseudoprogression had a median survival time of 28 months, compared with 12 months for patients without pseudoprogression.

17.4 Differential Diagnosis

The main differential considerations for pseudoprogression are true tumor progression (Fig. 17.2) and radiation necrosis (Fig. 17.3). The timing of the imaging findings and serial imaging can help differentiate pseudoprogression from true tumor progression. Unlike tumor progression, there is stabilization or eventual decrease in tumor enhancement on follow-up imaging with pseudoprogression. Furthermore, pseudoprogression is observed only in the first few months after treatment, much earlier than radiation necrosis. Various enhancement patterns on MRI have been described with radiation necrosis, including advancing wavefront, cut-pepper appearance, soap bubble appearance, and Swiss cheese appearance. However, the findings are somewhat subjective and there can be substantial overlap between treatment changes and true tumor progression.

W.A. Mehan, MD
Department of Radiology, Tufts Medical Center, Boston, MA, USA

D.T. Ginat, MD, MS (✉)
Department of Radiology, University of Chicago, Pritzker Medical School, Chicago, IL, USA
e-mail: ginatd01@gmail.com

D.T. Ginat et al. (eds.), *Neuroimaging Pharmacopoeia*,
DOI 10.1007/978-3-319-12715-6_17,

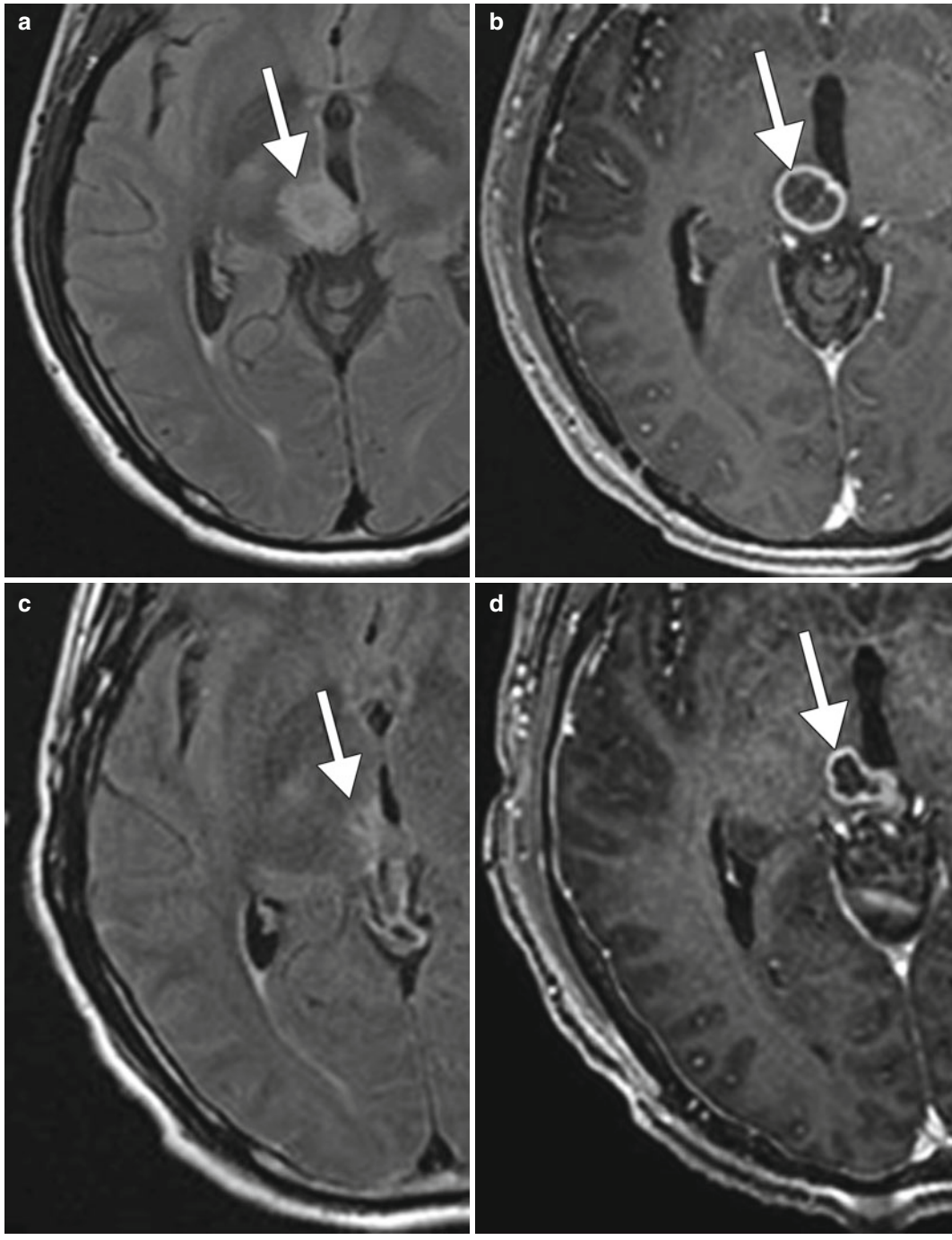

Fig. 17.1 Pseudoprogression. A 32-year-old male with right thalamic glioblastoma treated with surgical debulking followed by temozolamide (TMZ) and radiation (XRT). Serial axial FLAIR (**a**, **c**, **e**, **g**) and T1 post-contrast (**b**, **d**, **f**, **h**) MR images show that the right thalamic glioblastoma (*arrows*) responds to initial treatment then increases in size following TMZ plus XRT with a subsequent decrease in size and enhancement on follow-up

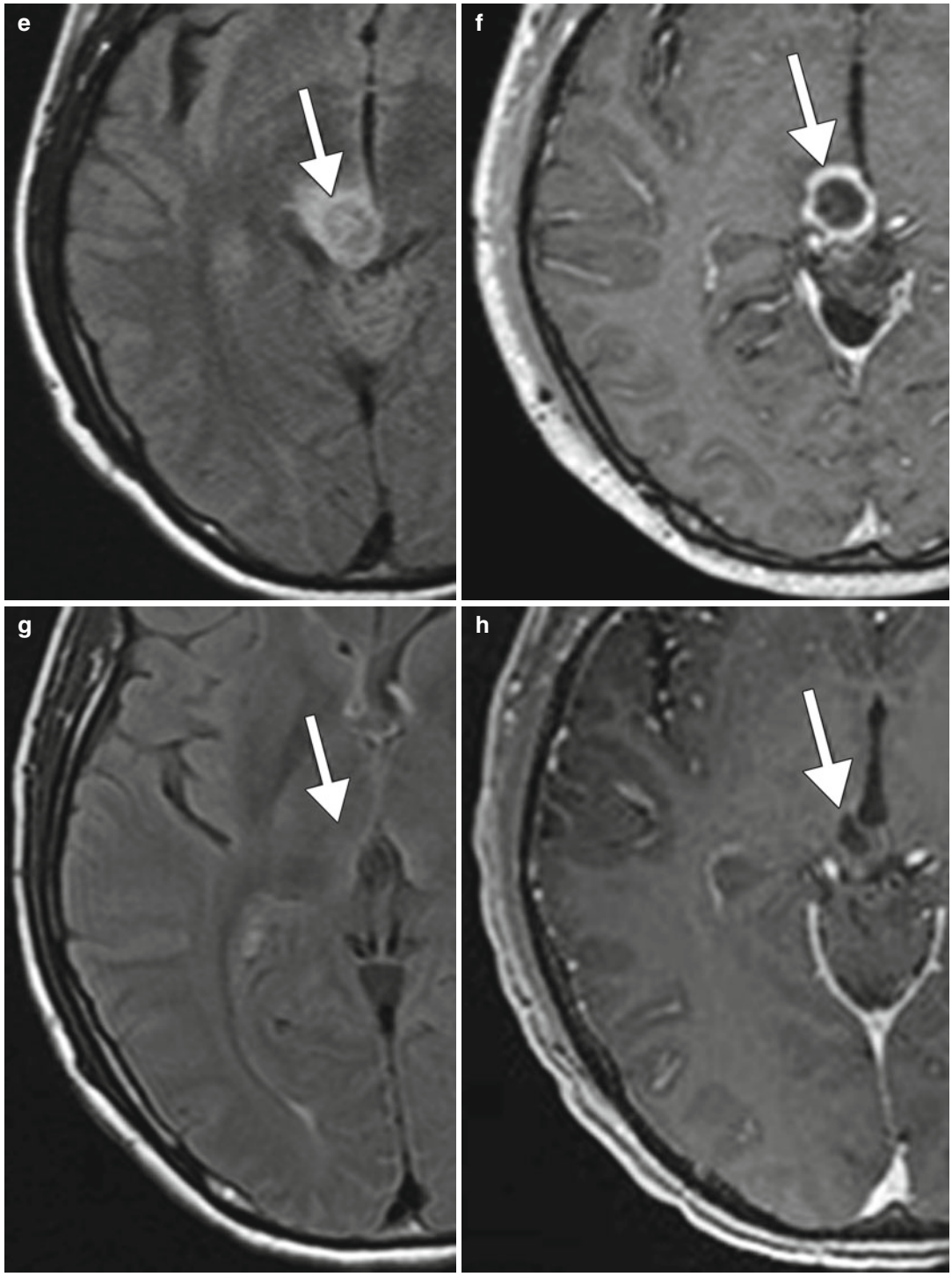

Fig. 17.1 (continued)

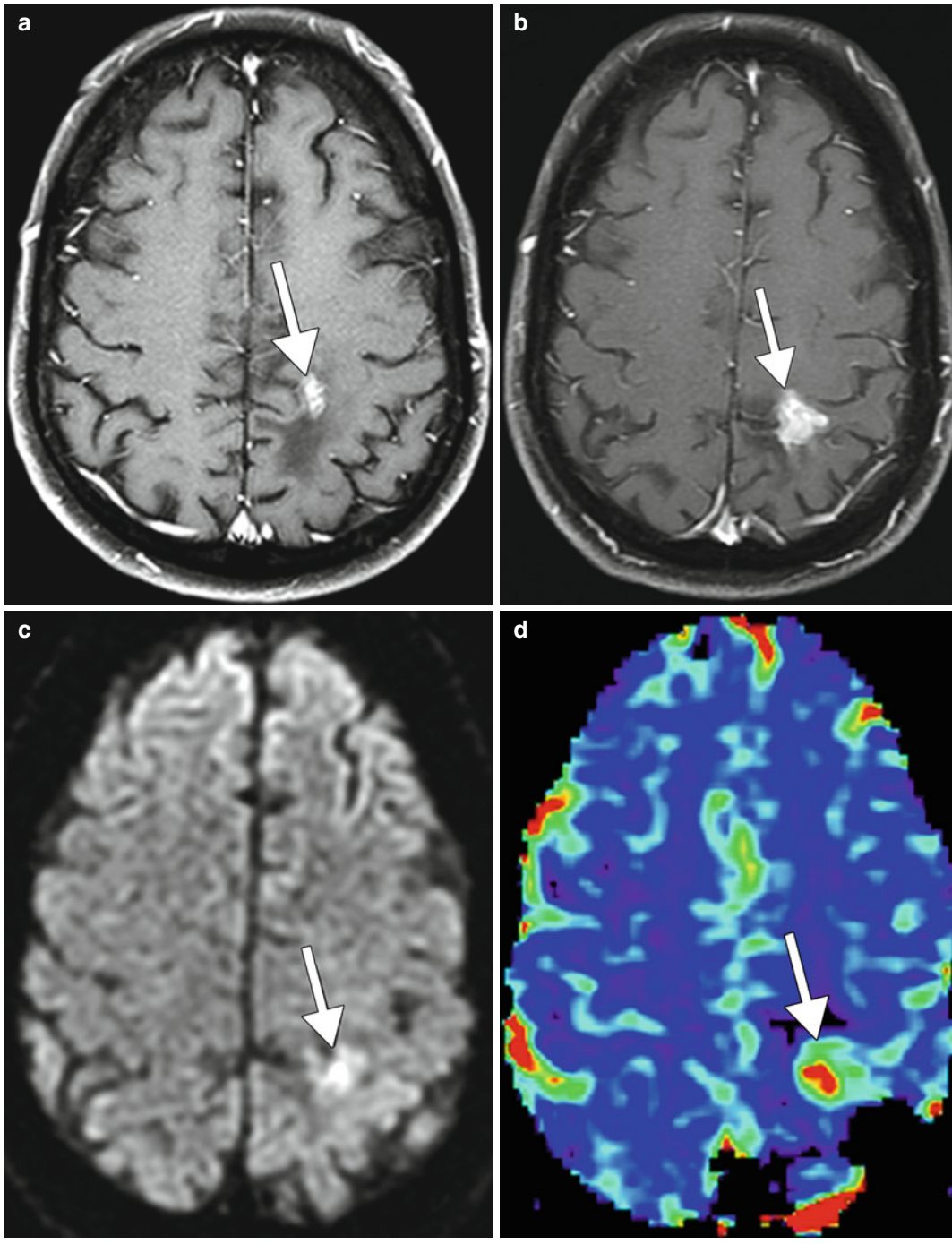

Fig. 17.2 True tumor progression. Axial post-contrast T1-weighted MRI (**a**) shows an enhancing focus in the left paracentral lobular (*arrow*). Follow-up post-contrast T1-weighted MRI (**b**) obtained 6 months later shows interval increase in size of the lesion (*arrow*). There is corresponding high signal on DWI (**c**) and elevated perfusion on the rCBV map (**d**) (*arrows*)

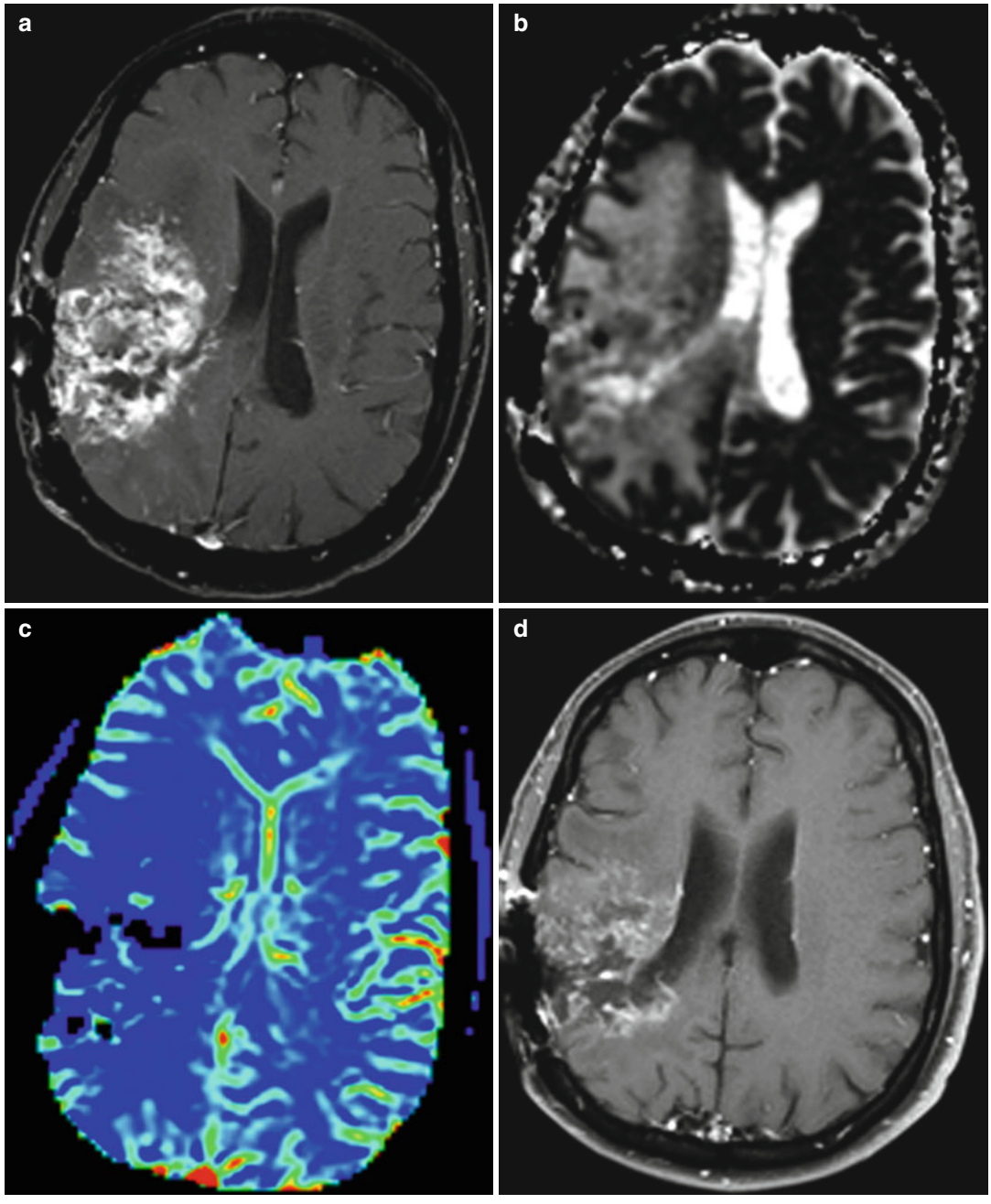

Fig. 17.3 Radiation necrosis. Axial post-contrast T1-weighted MRI (**a**) shows extensive patchy enhancement in the right frontotemporal region. There is no corresponding restricted diffusion on the ADC map (**b**) or hyperperfusion on the rCBV map (**c**). Follow-up post-contrast T1-weighted MRI shows decrease in the degree of enhancement (**d**)

Diffusion-weighted imaging may provide additional insights: true progression tends to display homogeneous or multifocal high signal intensity on DWI, while peripheral high signal or no high signal on DWI is more characteristic of pseudoprogression. With regards to MR perfusion imaging, it has been found that cases with unmethylated MGMT promoter have a significant difference of mean rCBV between pseudoprogression and real progression, while cases with methylated MGMT promoter have no significant difference. On MR spectroscopy, there is a significant increase in the Cho/NAA and Cho/Cre ratios in areas of recurrent tumor compared with areas of treatment-induced necrosis and normal brain tissue. Ultimately, currently available imaging techniques are not 100 % sensitive or specific in diagnosing progression. Furthermore, the frequent coexistence of treatment-induced necrosis and tumor progression can be a confounding factor when interpreting the imaging studies.

Suggested Reading

Chu HH, Choi SH, Ryoo I, Kim SC, Yeom JA, Shin H, Jung SC, Lee AL, Yoon TJ, Kim TM, Lee SH, Park CK, Kim JH, Sohn CH, Park SH, Kim IH. Differentiation of true progression from pseudoprogression in glioblastoma treated with radiation therapy and concomitant temozolomide: comparison study of standard and high-b-value diffusion-weighted imaging. Radiology. 2013;269:831–40.

Hygino da Cruz Jr LC, Rodriguez I, Domingues RC, Gasparetto EL, Sorensen AG. Pseudoprogression and pseudoresponse: imaging challenges in the assessment of posttreatment glioma. AJNR Am J Neuroradiol. 2011;32(11):1978–85.

Jahangiri A, Aghi MK. Pseudoprogression and treatment effect. Neurosurg Clin N Am. 2012;23(2):277–87. doi:10.1016/j.nec.2012.01.002. Epub 2012 Feb 14.

Kong DS, Kim ST, Kim EH, Lim DH, Kim WS, Suh YL, Lee JI, Park K, Kim JH, Nam DH. Diagnostic dilemma of pseudoprogression in the treatment of newly diagnosed glioblastomas: the role of assessing relative cerebral blood flow volume and oxygen-6-methylguanine-DNA methyltransferase promoter methylation status. AJNR Am J Neuroradiol. 2011;32(2):382–7.

Lee WJ, Choi SH, Park CK, Yi KS, Kim TM, Lee SH, Kim JH, Sohn CH, Park SH, Kim IH. Diffusion-weighted MR imaging for the differentiation of true progression from pseudoprogression following concomitant radiotherapy with temozolomide in patients with newly diagnosed high-grade gliomas. Acad Radiol. 2012;19(11):1353–61.

Linhares P, Carvalho B, Figueiredo R, Reis RM, Vaz R. Early pseudoprogression following chemoradiotherapy in glioblastoma patients: the value of RANO evaluation. J Oncol. 2013;2013:690585.

Suh CH, Kim HS, Choi YJ, Kim N, Kim SJ. Prediction of pseudoprogression in patients with glioblastomas using the initial and final area under the curves ratio derived from dynamic contrast-enhanced T1-weighted perfusion MR imaging. AJNR Am J Neuroradiol. 2013;34:2278–86.

Van Mieghem E, Wozniak A, Geussens Y, Menten J, De Vleeschouwer S, Van Calenbergh F, Sciot R, Van Gool S, Bechter OE, Demaerel P, Wilms G, Clement PM. Defining pseudoprogression in glioblastoma multiforme. Eur J Neurol. 2013;20(10):1335–41.

Wesolowski JR, Rajdev P, Mukherji SK. Temozolomide (Temodar). AJNR Am J Neuroradiol. 2010;31(8):1383–4.

Zhang J, Stevens MF, Bradshaw TD. Temozolomide: mechanisms of action, repair and resistance. Curr Mol Pharmacol. 2012;5(1):102–14.

18 1,3-Bis(2-Chloroethyl)-1-Nitrosourea (BCNU; Carmustine) Polymer Wafer (Gliadel)

Daniel Thomas Ginat

18.1 Uses

Carmustine was one of the first systemic chemotherapy agents to gain FDA approval for the treatment of brain tumors. More recently, carmustine-infused polymer wafers (Gliadel) have been used to deliver locally higher doses of chemotherapy directly to the surgical tumor bed, while obviating systemic side effects, such as myelosuppression and pulmonary toxicity.

18.2 Mechanism

Carmustine is a dialkylating agent that forms interstrand cross-links in DNA, thereby preventing DNA replication and DNA transcription. Carmustine is often incorporated into biodegradable discs (Gliadel wafers) for interstitial chemotherapy. The wafers gradually dissolve in the surgical cavity, thereby releasing the chemotherapy agent locally.

18.3 Discussion

Carmustine Gliadel wafers are sometimes implanted within the surgical cavity after malignant brain neoplasm resection. The wafers are used in patients with newly diagnosed high-grade gliomas as an adjunct to surgery and radiation or in patients with recurrent glioblastoma as an adjunct to surgery. Initially, the wafers appear as hypointense thin linear structures on T1- and T2-weighted MRI sequences, but over time, they can become isointense to hyperintense on T1- and T2-weighted sequences and can also display restricted diffusion (Fig. 18.1). The wafers eventually resorb over the course of several months.

The presence of wafers does not alter the pattern of tumor recurrence. Perfusion MRI is particularly useful to monitor treatment effects and differentiate them from recurrent neoplasm. The presence of foci with elevated relative cerebral blood volume (rCBV) suggests tumor recurrence (Fig. 18.2). MR spectroscopy can also be useful for monitoring tumor response to chemotherapy wafers. For example, it has been suggested that increased peritumoral NAA/Cr and decreased peritumoral Cho/NAA compared with normal brain tissue by 3–5 weeks suggest treatment response.

The use of carmustine wafers yields a small, but statistically significant, improvement in survival in patients with newly diagnosed high-grade glial neoplasms. However, the presence of carmustine wafers is associated with a relatively higher incidence of cerebrospinal fluid leaks (5 % vs. 0.8 % in a placebo-treated group) and intracranial hypertension (9.1 % vs. 1.7 % in the placebo group).

D.T. Ginat, MD, MS
Department of Radiology, University of Chicago, Pritzker Medical School, Chicago, IL, USA
e-mail: ginatd01@gmail.com

D.T. Ginat et al. (eds.), *Neuroimaging Pharmacopoeia*,
DOI 10.1007/978-3-319-12715-6_18, © Springer International Publishing Switzerland 2015

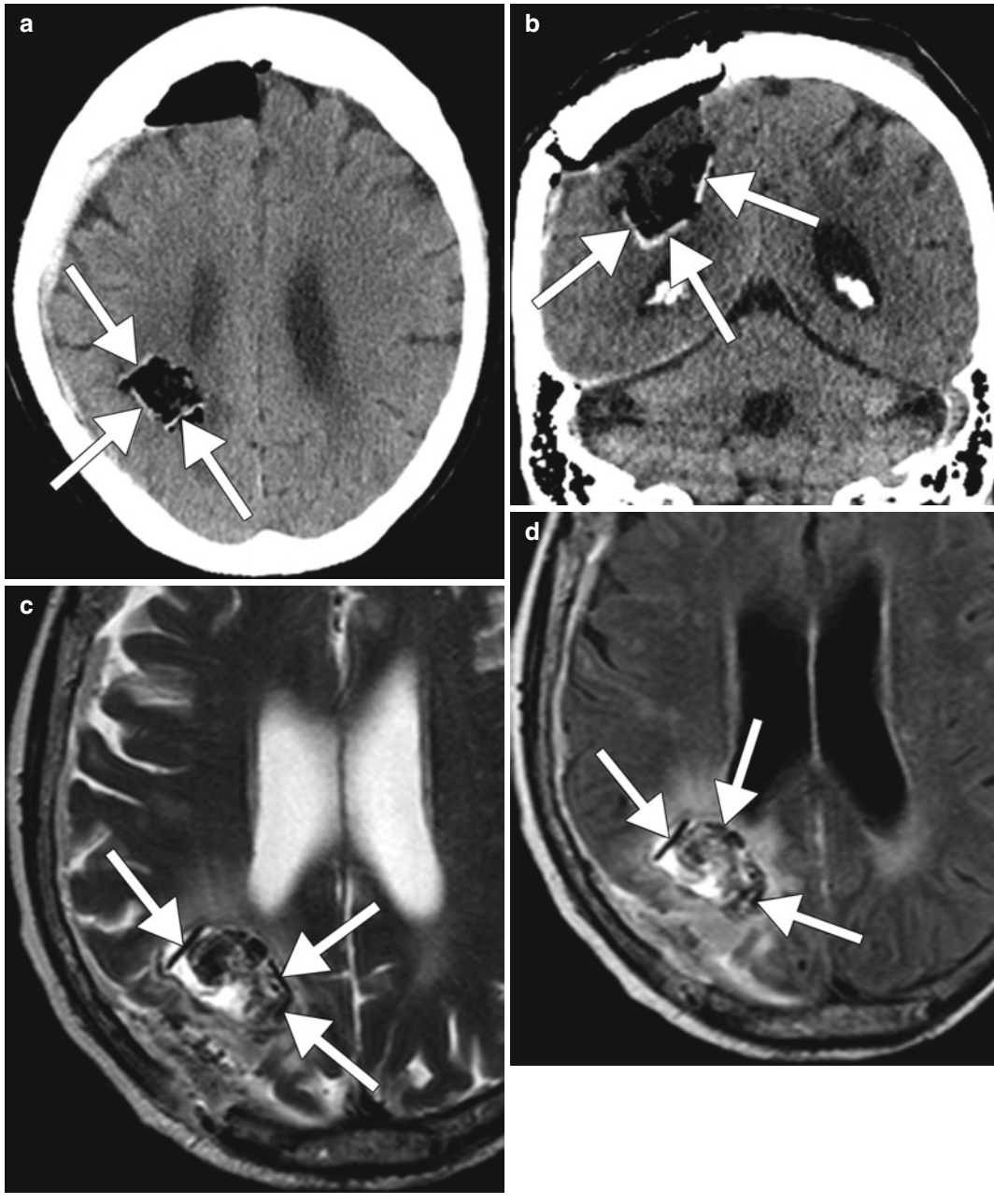

Fig. 18.1 Carmustine Gliadel wafers. Axial (**a**) and coronal (**b**) CT images obtained on the first postoperative day show the linear hyperattenuating wafers (*arrows*) lining the right parietal surgical cavity. Axial T2-weighted (**c**), FLAIR (**d**), T1-weighted (**e**), and post-contrast axial T1-weighted (**f**) MR images obtained at 2 postoperative days show linear low-signal-intensity wafers (*arrows*) along the margins of the resection cavity. Axial T2-weighted (**g**) and T1-weighted (**h**) MR images obtained approximately 2 months later show partial resorption of the wafers

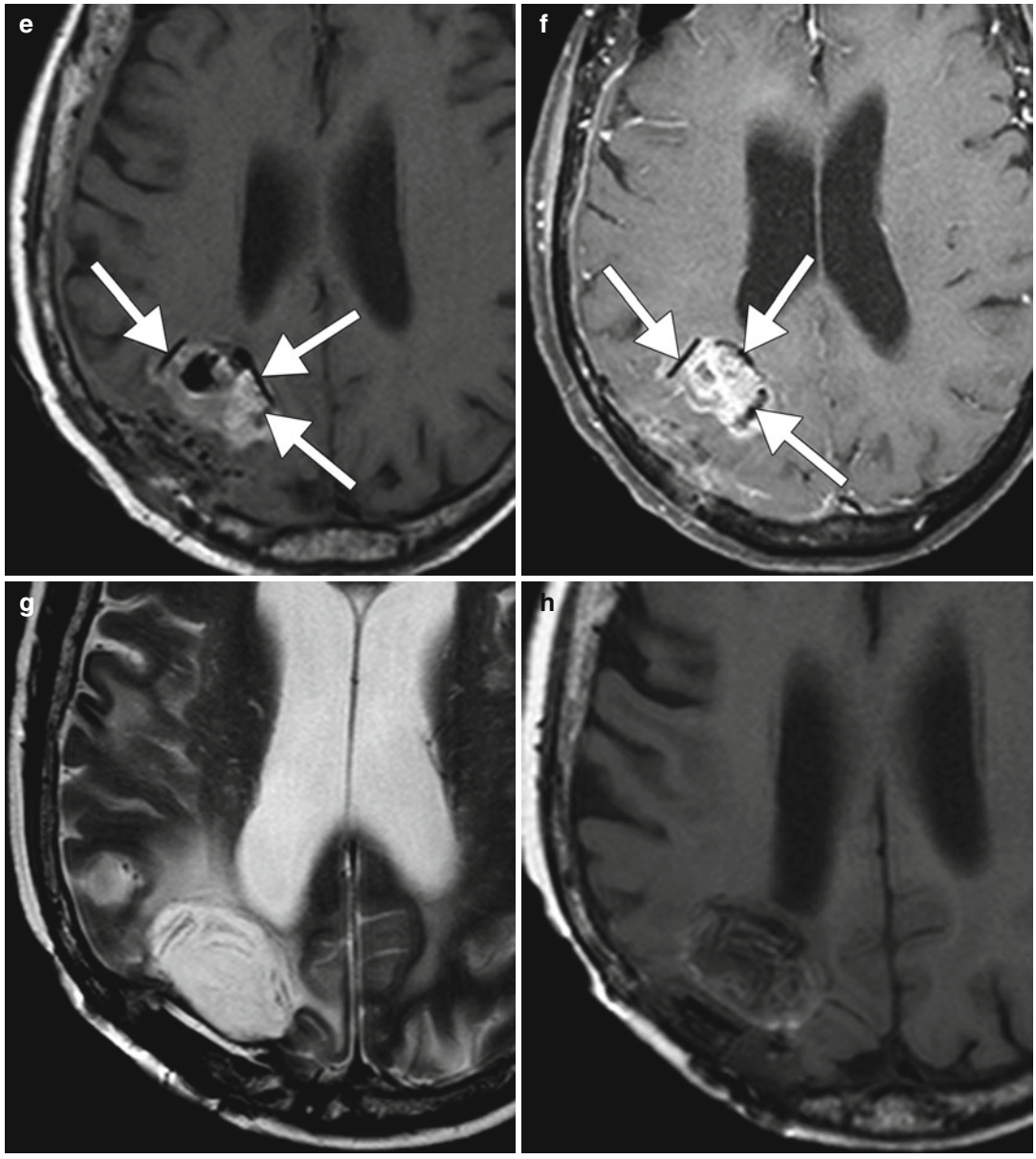

Fig. 18.1 (continued)

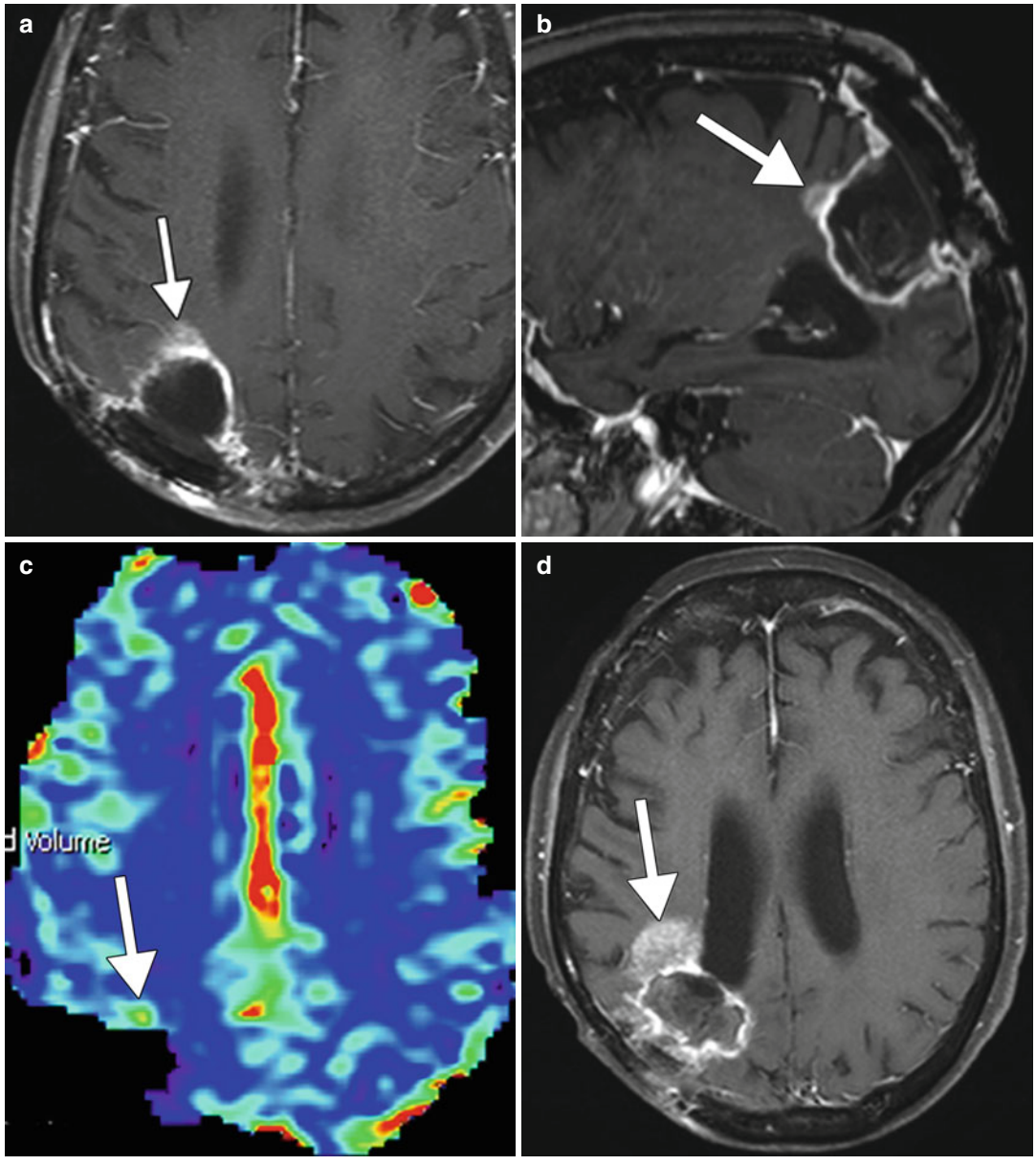

Fig. 18.2 Recurrent tumor. Axial (**a**) and sagittal (**b**) post-contrast T1-weighted MR images show an enhancing focus adjacent to the surgical cavity (*arrow*) with corresponding elevated perfusion on the CBV map (**c**). Follow-up post-contrast T1-weighted MRI (**d**) shows interval of the enhancing mass (*arrow*), compatible with tumor progression in the same patient treated with the carmustine wafers shown in Fig. 18.1

18.4 Differential Diagnosis

The main differential consideration for hyperattenuation in the region of the surgical cavity on CT includes hemorrhage, mineralization, and other implanted materials, such as the Ommaya reservoir and Gliasite (Figs. 18.3, 18.4, 18.5, and 18.6). The thin, linear configuration of the wafers is the key to their proper identification.

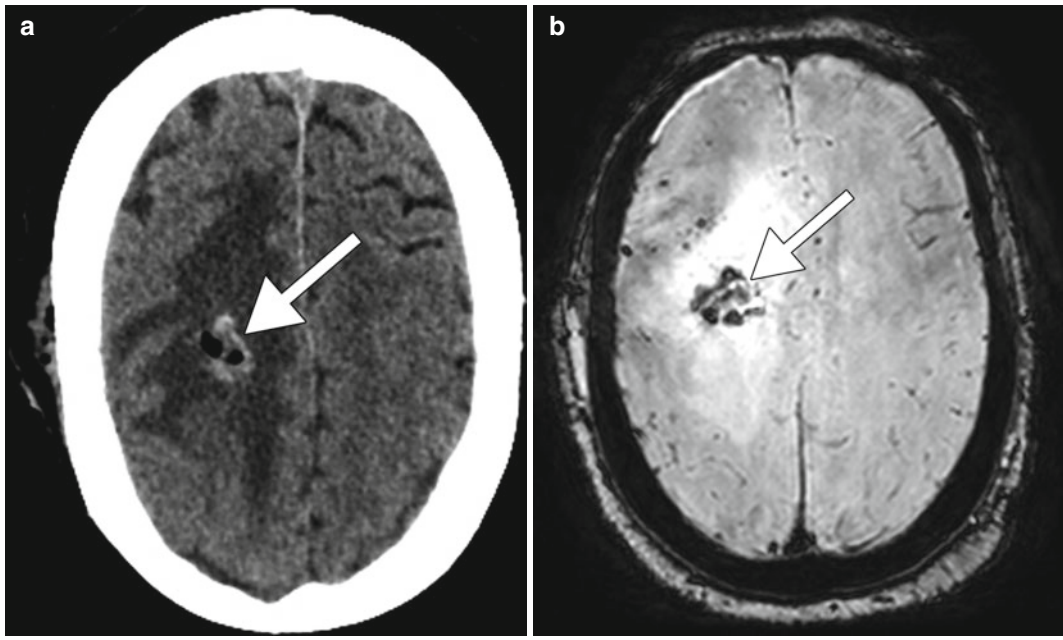

Fig. 18.3 Postoperative hemorrhage. The patient had a right frontal metastasis that was recently resected. Axial CT image (**a**) shows hyperattenuation along the margins of the right frontal lobe resection cavity (*arrow*). The corresponding SWI (**b**) shows susceptibility effect along the margins of the resection cavity (*arrow*)

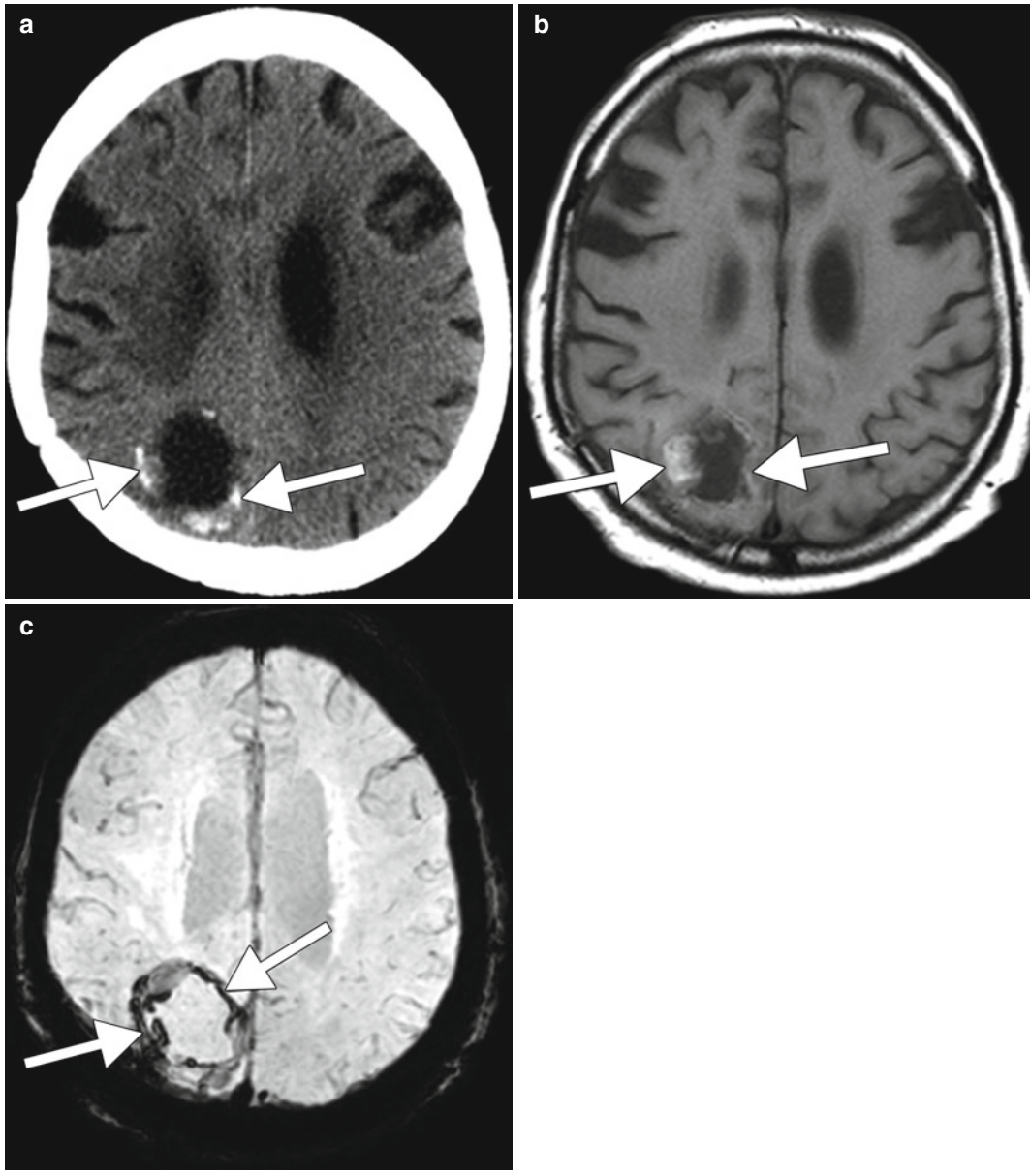

Fig. 18.4 Dystrophic mineralization. Axial CT image (**a**) shows parenchymal calcifications along the periphery of the right parietal resection cavity (*arrow*). There is corresponding T1 hyperintensity and susceptibility effect on the axial T1-weighted (**b**) and susceptibility-weighted (**c**) sequences (*arrows*)

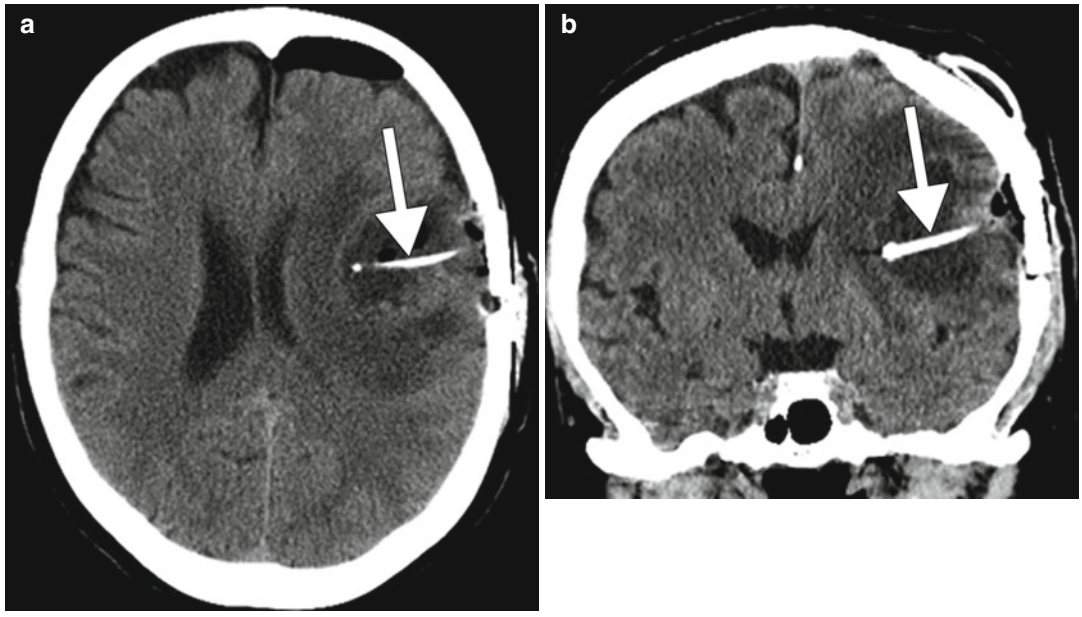

Fig. 18.5 Ommaya reservoir. Axial (**a**) and coronal (**b**) CT images show the hyperattenuating Ommaya catheter (*arrows*) within the left frontal lobe resection cavity

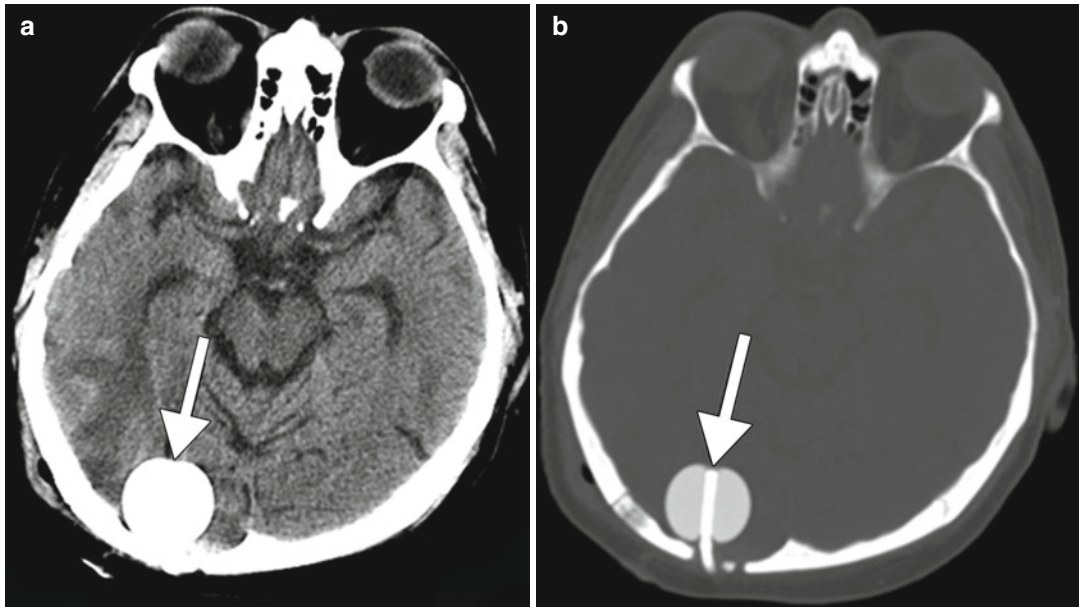

Fig. 18.6 Gliasite device. Axial CT images in soft tissue (**a**) and bone windows (**b**) show the markedly hyperattenuating contents of the inflated Gliasite balloon (*arrows*)

Suggested Reading

Attenello FJ, Mukherjee D, Datoo G, McGirt MJ, Bohan E, Weingart JD, Olivi A, Quinones-Hinojosa A, Brem H. Use of Gliadel (BCNU) wafer in the surgical treatment of malignant glioma: a 10-year institutional experience. Ann Surg Oncol. 2008;15(10):2887–93.

Engelhard HH. The role of interstitial BCNU chemotherapy in the treatment of malignant glioma. Surg Neurol. 2000;53(5):458–64.

Giese A, Kucinski T, Knopp U, Goldbrunner R, Hamel W, Mehdorn HM, Tonn JC, Hilt D, Westphal M. Pattern of recurrence following local chemotherapy with biodegradable carmustine (BCNU) implants in patients with glioblastoma. J Neurooncol. 2004;66(3):351–60.

Nagpal S. The role of BCNU polymer wafers (Gliadel) in the treatment of malignant glioma. Neurosurg Clin N Am. 2012;23(2):289–95, ix.

Ulmer S, Spalek K, Nabavi A, Schultka S, Mehdorn HM, Kesari S, Dörner L. Temporal changes in magnetic resonance imaging characteristics of Gliadel wafers and of the adjacent brain parenchyma. Neuro Oncol. 2012;14(4):482–90.

Westphal M, Hilt DC, Bortey E, Delavault P, Olivares R, Warnke PC, Whittle IR, Jääskeläinen J, Ram Z. A phase 3 trial of local chemotherapy with biodegradable carmustine (BCNU) wafers (Gliadel wafers) in patients with primary malignant glioma. Neuro Oncol. 2003;5(2):79–88.

Methotrexate

19

Daniel Thomas Ginat

19.1 Uses

Methotrexate is a folate antagonist that is used to treat acute leukemia, lymphoma, osteosarcoma, and leptomeningeal metastases. Methotrexate can be administered orally, intravenously, or intrathecally. Methotrexate given intravenously at high dose has been shown to decrease the incidence of hematologic, testicular, and central nervous system relapse.

19.2 Mechanism

Folate antagonism is the main antiproliferative effect of methotrexate, whereby metabolic pathways that require one-carbon moieties supplied by the B9 folate vitamins are disrupted. However, methotrexate also promotes the release of adenosine from fibroblasts, and endothelial cells and elevated adenosine have been demonstrated in CSF after methotrexate therapy. High adenosine levels dilate cerebral blood vessels, modify the release of pre- and postsynaptic neurotransmitters, and may slow the discharge rate of neurons. Consequently, adenosine release may play a role in the pathophysiology of acute methotrexate neurotoxicity. Myelopathy caused by methotrexate is believed to result from local alteration in folate metabolism at the spinal cord level.

19.3 Discussion

Methotrexate can cause acute or chronic encephalopathy, particularly when administered intrathecally. Transient acute encephalopathy has been reported in 3–15 % of cancer patients after high-dose methotrexate. Risk factors for methotrexate-induced neurotoxicity include high-dose treatment, intrathecal treatment, young age, and association with cranial radiation. Patients with acute methotrexate toxicity often present with fluctuating neurologic symptoms, including hemiparesis that may alternate from side to side, dysphasia, altered mental status, headache, choreoathetosis, and seizure. T2 hyperintensities are typically located in the periventricular white matter, particularly in the centrum semiovale bilaterally (Fig. 19.1). Initially, the white matter lesions may not be conspicuous on T2-weighted sequences and can even appear hypointense. On the other hand, presence of restricted diffusion on DWI is a reliable early sign of acute methotrexate encephalopathy and resolves as clinical status improves, despite the persistence of subtle abnormalities on other MRI sequences. Methotrexate encephalopathy can be confidently diagnosed when DWI shows areas of restricted diffusion across multiple vascular

D.T. Ginat, MD, MS
Department of Radiology, University of Chicago, Pritzker Medical School, Chicago, IL, USA
e-mail: ginatd01@gmail.com

D.T. Ginat et al. (eds.), *Neuroimaging Pharmacopoeia*,
DOI 10.1007/978-3-319-12715-6_19,

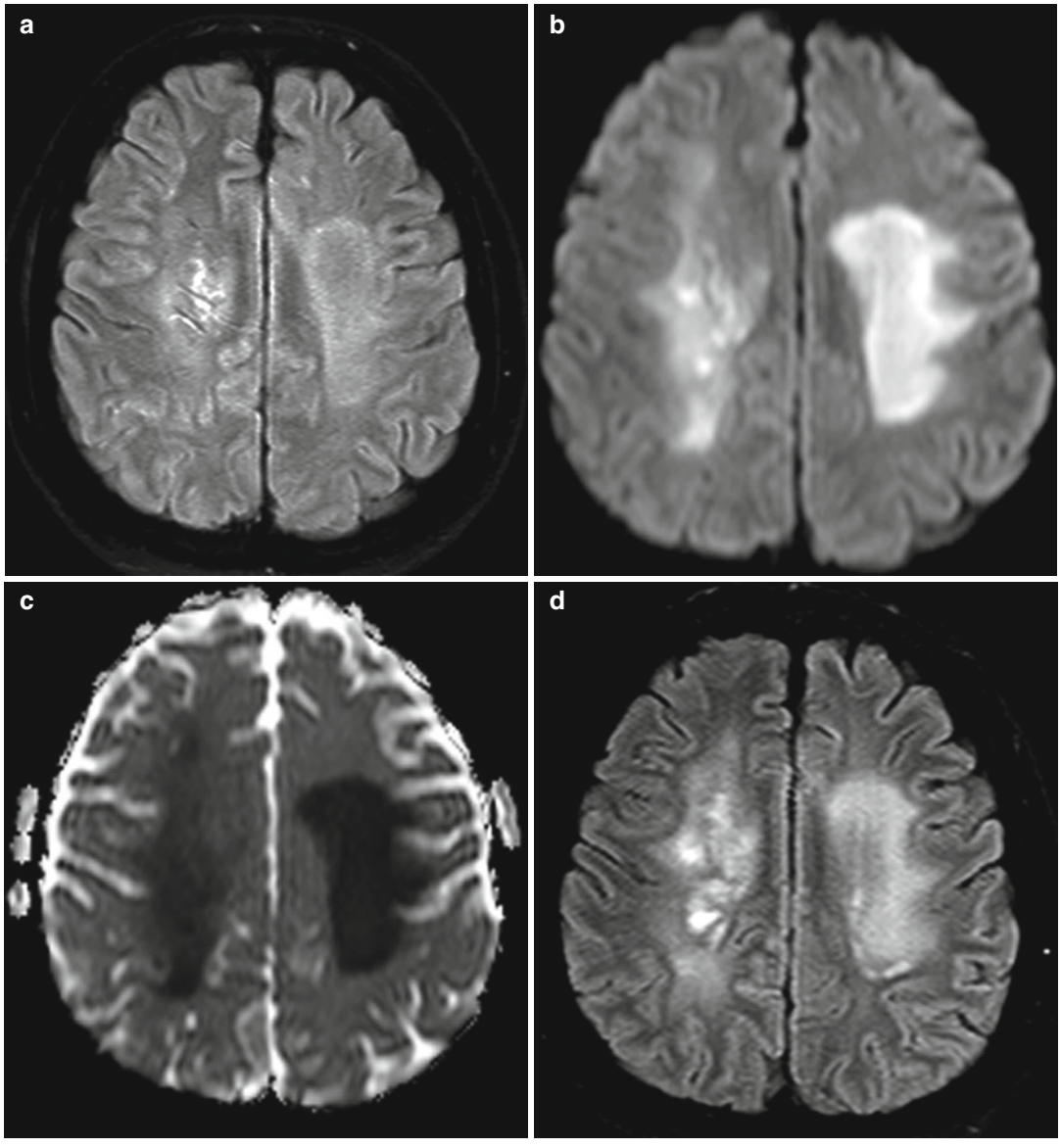

Fig. 19.1 Methotrexate leukoencephalopathy. Axial FLAIR (**a**), axial DWI (**b**), and ADC maps (**c**) show patchy areas of FLAIR hyperintensity in the bilateral white matter of the centrum semiovale with corresponding marked restricted diffusion (*arrows*). Follow up axial FLAIR (**d**), axial DWI (**e**), and ADC maps (**f**) obtained one week later show more pronounced FLAIR signal abnormality, but the restricted diffusion has largely subsided. There was no associated abnormal enhancement (not shown)

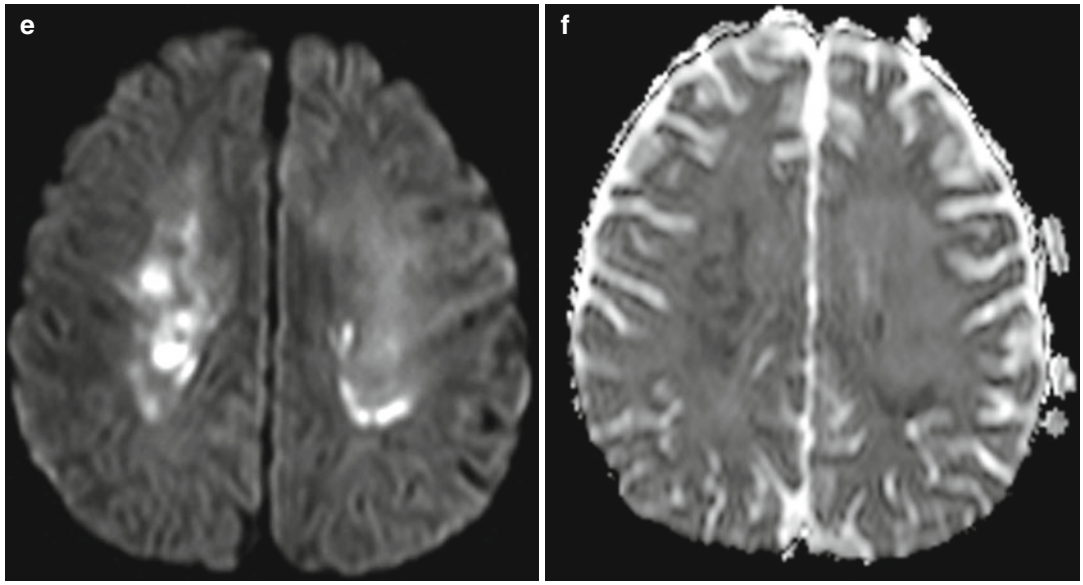

Fig. 19.1 (continued)

beds with involvement of the deep cerebral white matter, in the clinical setting of waxing and waning neurological signs and symptoms. The use of computer-aided detection based on relative differences in quantitative signal intensity measures normalized within each examination can help discern subtle methotrexate-induced leukoencephalopathy.

A more unusual neurotoxic complication of methotrexate is focal brain necrosis after intraparenchymal infusion of methotrexate, which may be caused by catheter disconnection of the Ommaya device. This can result an area of cytotoxic edema adjacent to the catheter track, which in turn is surrounded by more extensive vasogenic edema (Fig. 19.2). Besides halting methotrexate administration, treatment options for methotrexate neurotoxicity include aminophylline, an adenosine antagonist, and dextromethorphan, an antagonist of the NMDA receptor.

Adhesive arachnoiditis that develops after administration of intrathecal methotrexate can cause urinary retention or incontinence in severe cases. The symptoms can begin within hours of administration and sometime resolve. On MRI, adhesive arachnoiditis can appear as clumping of the nerve roots to one another or to the thecal sac (Fig. 19.3). There may or may not be associated enhancement.

Compared to encephalopathy, methotrexate-induced myelopathy is rare. Risk factors for development of methotrexate myelopathy include cumulative intrathecal methotrexate doses, systemic methotrexate, concurrent radiotherapy, and central nervous system involvement of primary disease. On MRI, the myelopathy appears as long-segment T2 hyperintensity within the dorsal columns (Fig. 19.4). The dorsal column signal changes followed by lateral column changes on serial MRI and the gradual caudal-to-rostral extension of lesions are analogous to subacute combined degeneration due to vitamin B_{12}–folate deficiencies. However, a normal spine MRI does not exclude methotrexate myelopathy. Methotrexate myelopathy often has a poor prognosis and can occur in conjunction with arachnoiditis. Treatment with folate metabolites may improve outcome.

Mineralizing microangiopathy consists of dystrophic calcifications in the basal ganglia, subcortical white matter, and dentate nuclei. These are a relatively common finding at cranial CT in children previously treated with radiation therapy and intrathecal methotrexate. On MRI, high signal on

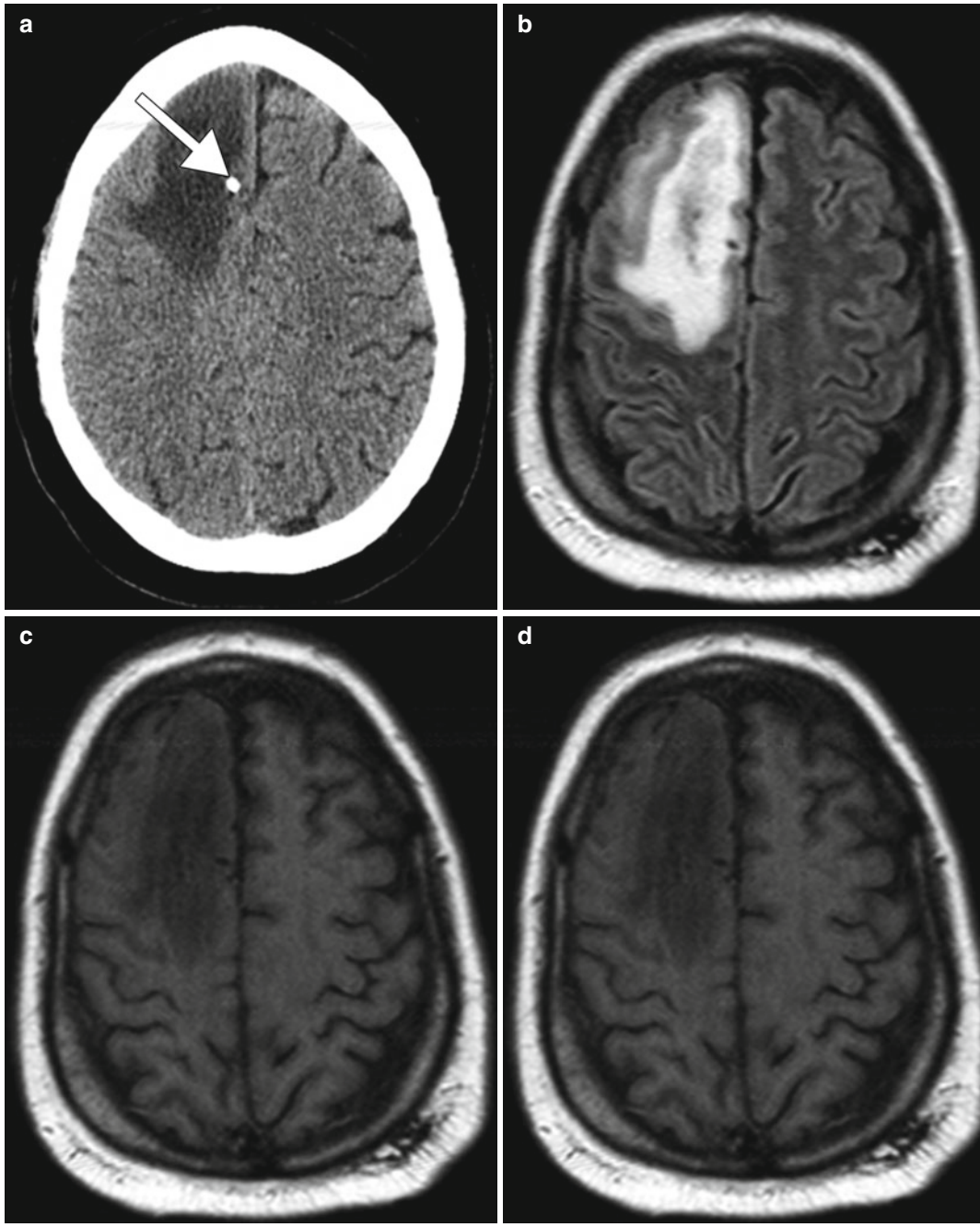

Fig. 19.2 Focal brain necrosis. Axial CT image (**a**) shows extensive confluent hypoattenuation in the right frontal lobe white matter surrounding the Ommaya catheter (*arrow*). Axial FLAIR MRI (**b**), DWI (**c**), and ADC map (**d**) show extensive vasogenic edema surrounding a more focal area of restricted diffusion surrounding the catheter (*arrows*)

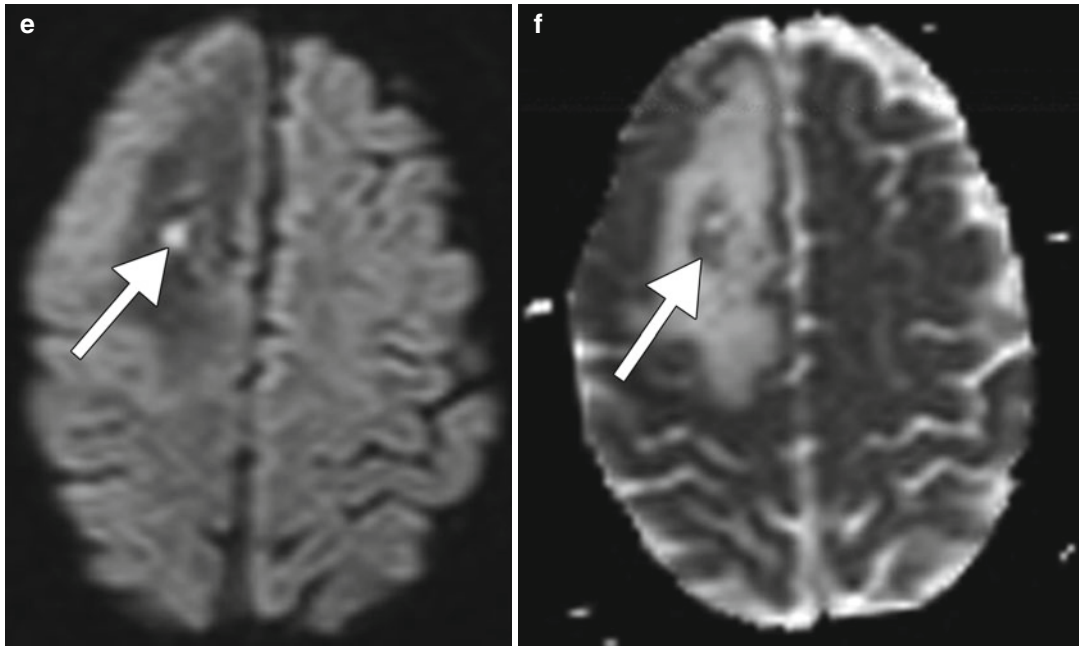

Fig. 19.2 (continued)

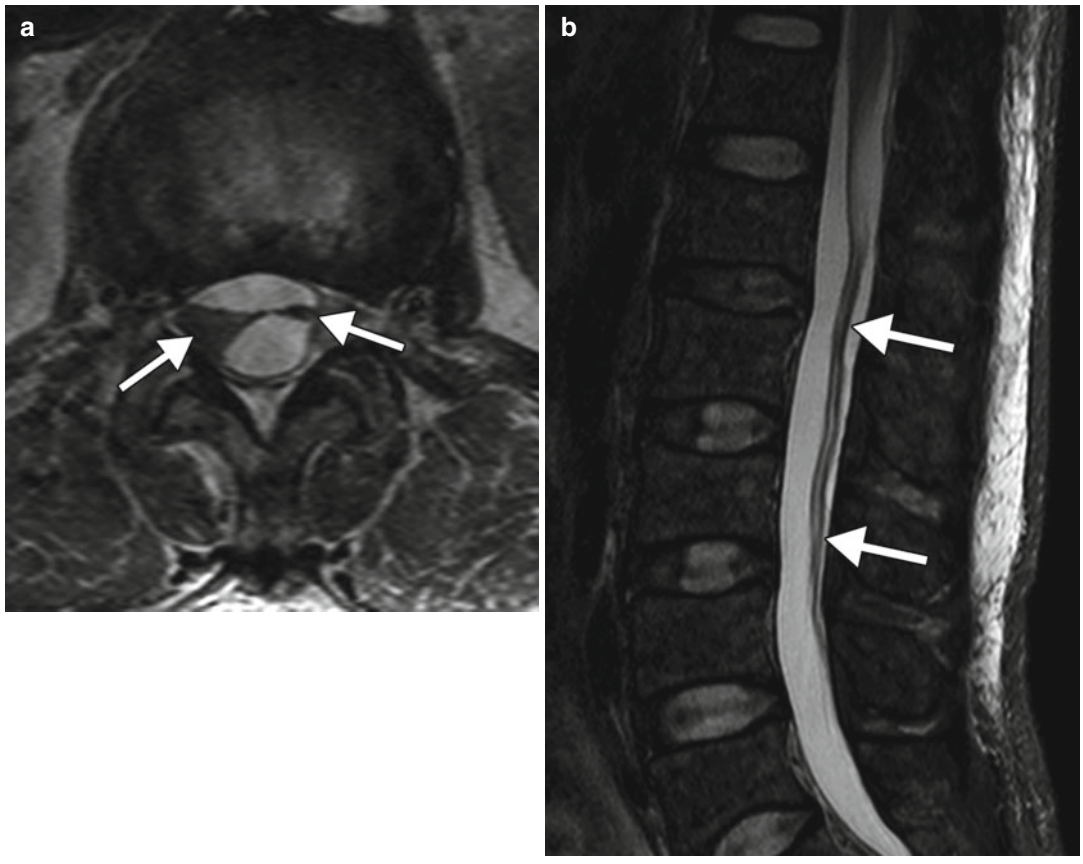

Fig. 19.3 Intrathecal methotrexate-induced adhesive arachnoiditis. Axial (**a**) and sagittal (**b**) T2-weighted MR images show extensive clumping of the cauda equine nerve roots (*arrows*) (Courtesy of Gregory Christoforidis)

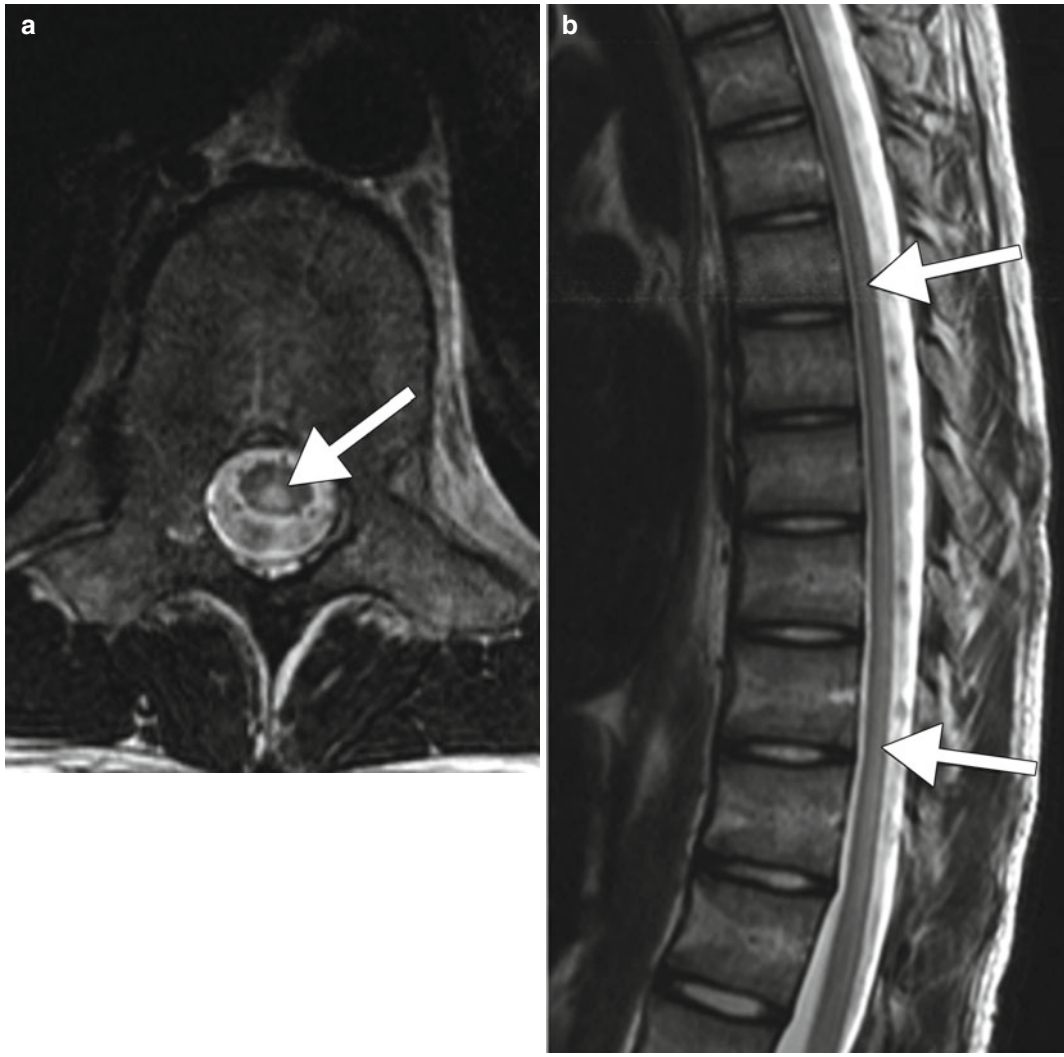

Fig. 19.4 Methotrexate myelopathy. Axial (**a**) and sagittal (**b**) T2-weighted MR images show long-segment hyperintensity affecting the dorsal columns of the thoracic spinal cord (*arrows*)

T1-weighted images is observed in the putamen and decreased signal is on T2-weighted images (Fig. 19.5). These imaging findings appear 2 or more years after treatment. The presence of mineralizing microangiopathy on imaging does not clearly correlate with clinical symptoms.

19.4 Differential Diagnosis

- *Encephalopathy*: Methotrexate-induced encephalopathy resembles delayed leukoencephalopathy with a stroke-like presentation observed with a variety of chemotherapeutic agents. Other differential considerations include hypoxic ischemic encephalopathy (Fig. 19.6), PML, PRES, ADEM, and hereditary demyelinating neuropathies, such as Charcot–Marie–Tooth disease (Fig. 19.7). Restricted diffusion in the splenium of the corpus callosum can result from the use of other medications, such as metronidazole toxicity (refer to Chap. 25).
- *Focal brain necrosis*: The focal nature of the restricted diffusion and surrounding vasogenic edema associated with methotrexate extravasation causing brain necrosis may

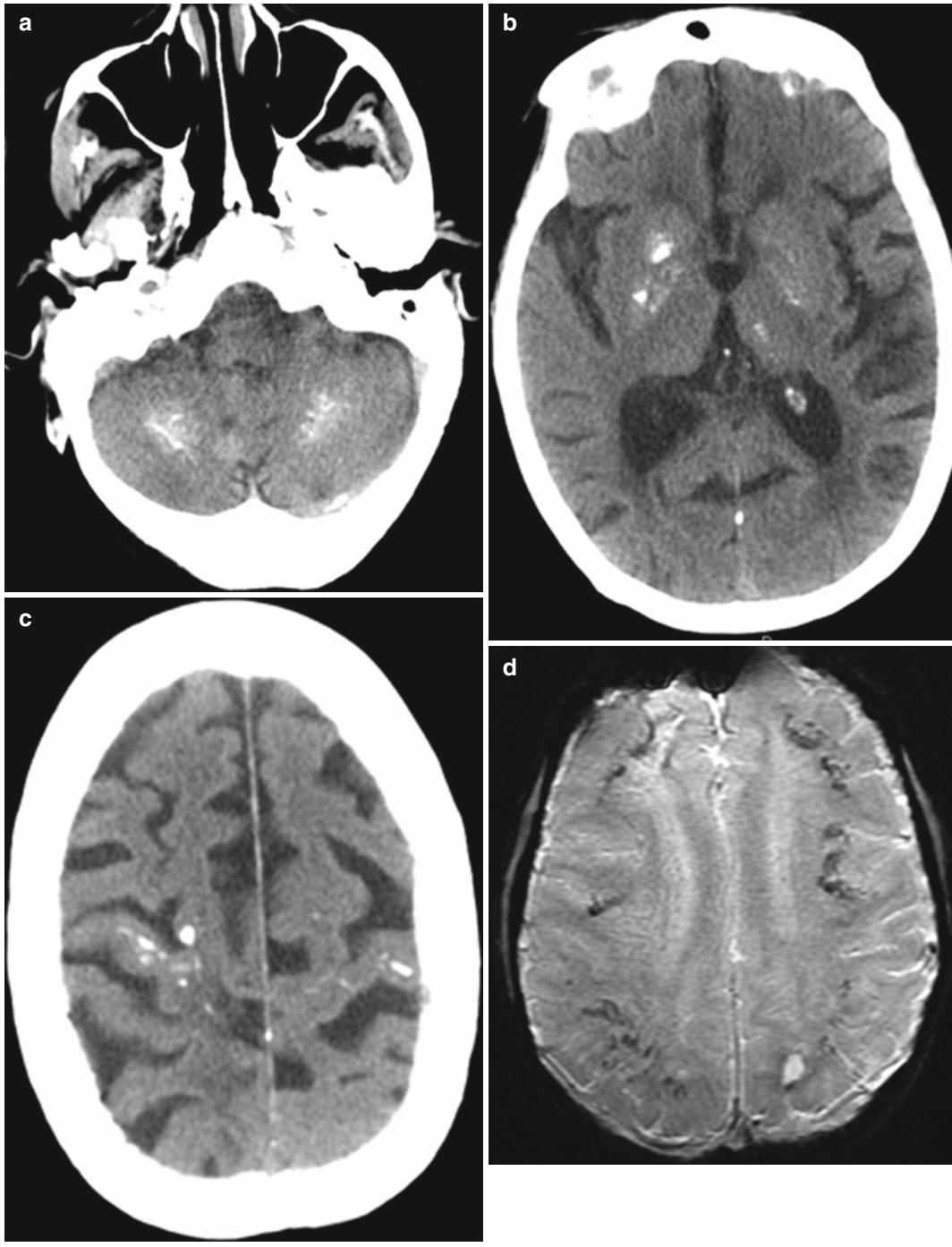

Fig. 19.5 Mineralizing microangiopathy. Axial CT images (**a**–**c**) show calcifications in the bilateral perirolandic subcortical white matter, basal ganglia, and dentate nuclei. The T2* GRE MR images (**d**–**f**) show corresponding low signal in the affected areas. In addition, the axial T1-weighted image (**g**) shows high signal within the basal ganglia

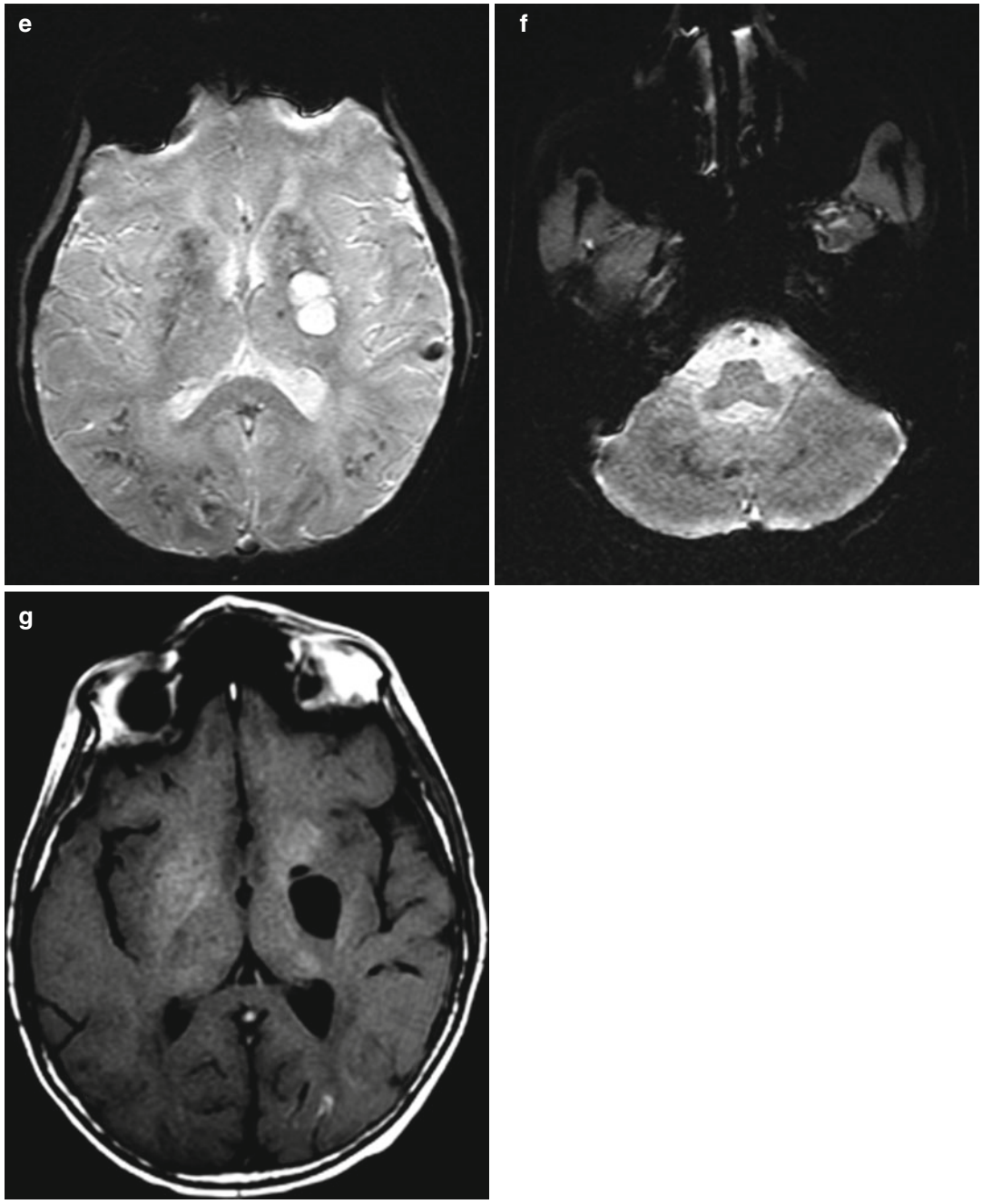

Fig. 19.5 (continued)

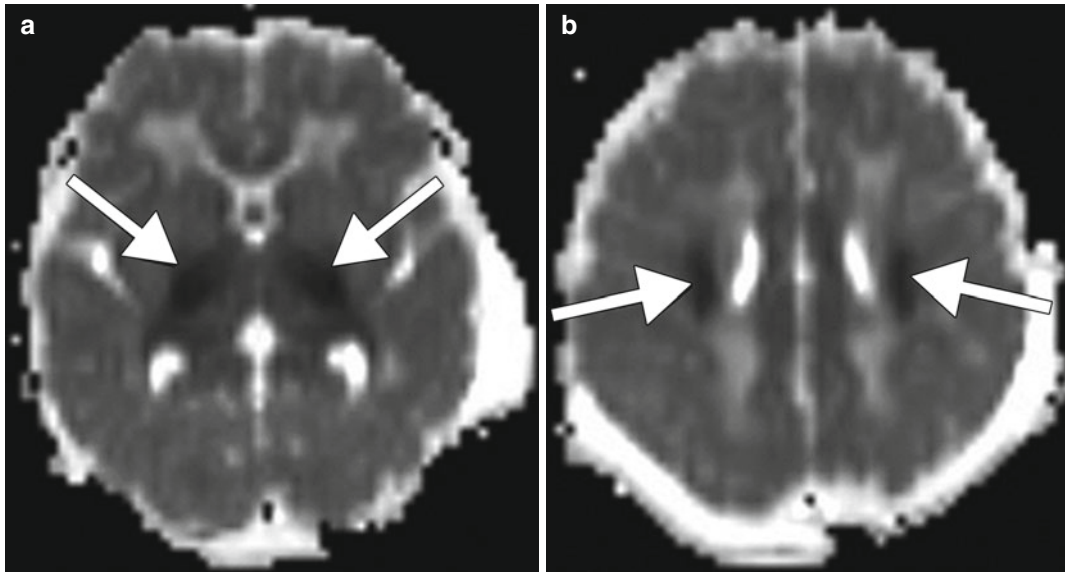

Fig. 19.6 Perinatal hypoxic–ischemic encephalopathy. Axial ADC maps (**a**, **b**) at two different levels show restricted diffusion in the bilateral posterior limbs of the internal capsules and corona radiata (*arrows*)

resemble infectious cerebritis and abscess (Fig. 19.7), for which these immunosuppressed patients are certainly prone.

- *Arachnoiditis*: Besides intrathecal methotrexate, adhesive arachnoiditis can be associated with other chemotherapeutic agents such as cytosine arabinoside and prednisolone and result from repeated lumbar punctures and infection, which can have identical imaging features. Otherwise, clumping of the nerve roots can potentially mimic leptomeningeal dissemination of lymphoma of leukemia, which can manifest as discrete mass lesions or diffuse thickening and enhancement of the nerve roots (Fig. 19.8).
- *Myelopathy*: The main considerations for dorsal column predominant signal abnormality include Wallerian degeneration, subacute combined degeneration (refer to nitrous oxide chapter), HIV vacuolar myelopathy, and demyelination. Spinal cord infarct may also produce long-segment areas of signal abnormality in the spinal cord but typically involve the grey matter, more centrally (Fig. 19.9). Leptomeningeal tumor dissemination in the spine typically demonstrates different features on MRI, including linear or nodular enhancement and occasionally intramedullary edema that is not necessarily limited to the dorsal columns.
- *Mineralizing microanagiopathy*: The calcifications involving the dentate nuclei, basal ganglia, and cerebral white matter can be observed in disorders of calcium metabolism, including hypoparathyroidism or pseudohypoparathyroidism, and Fahr disease (Fig. 19.10). Ischemic and infectious sequelae are other potential differential considerations.

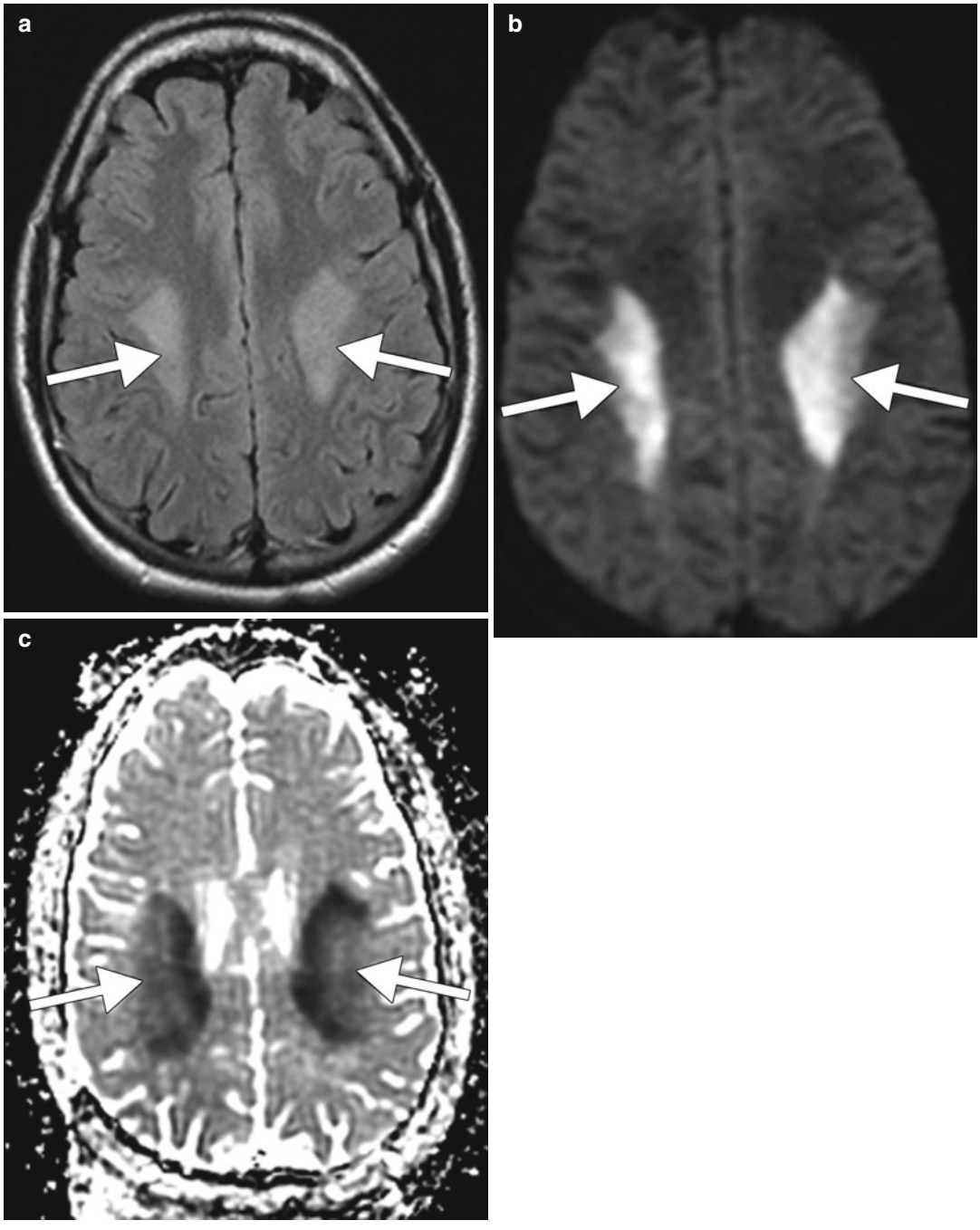

Fig. 19.7 Charcot–Marie–Tooth disease. Axial FLAIR MRI (**a**), DWI (**b**), and ADC map (**c**) show symmetric signal abnormality and restricted diffusion involving the centrum semiovale (*arrows*)

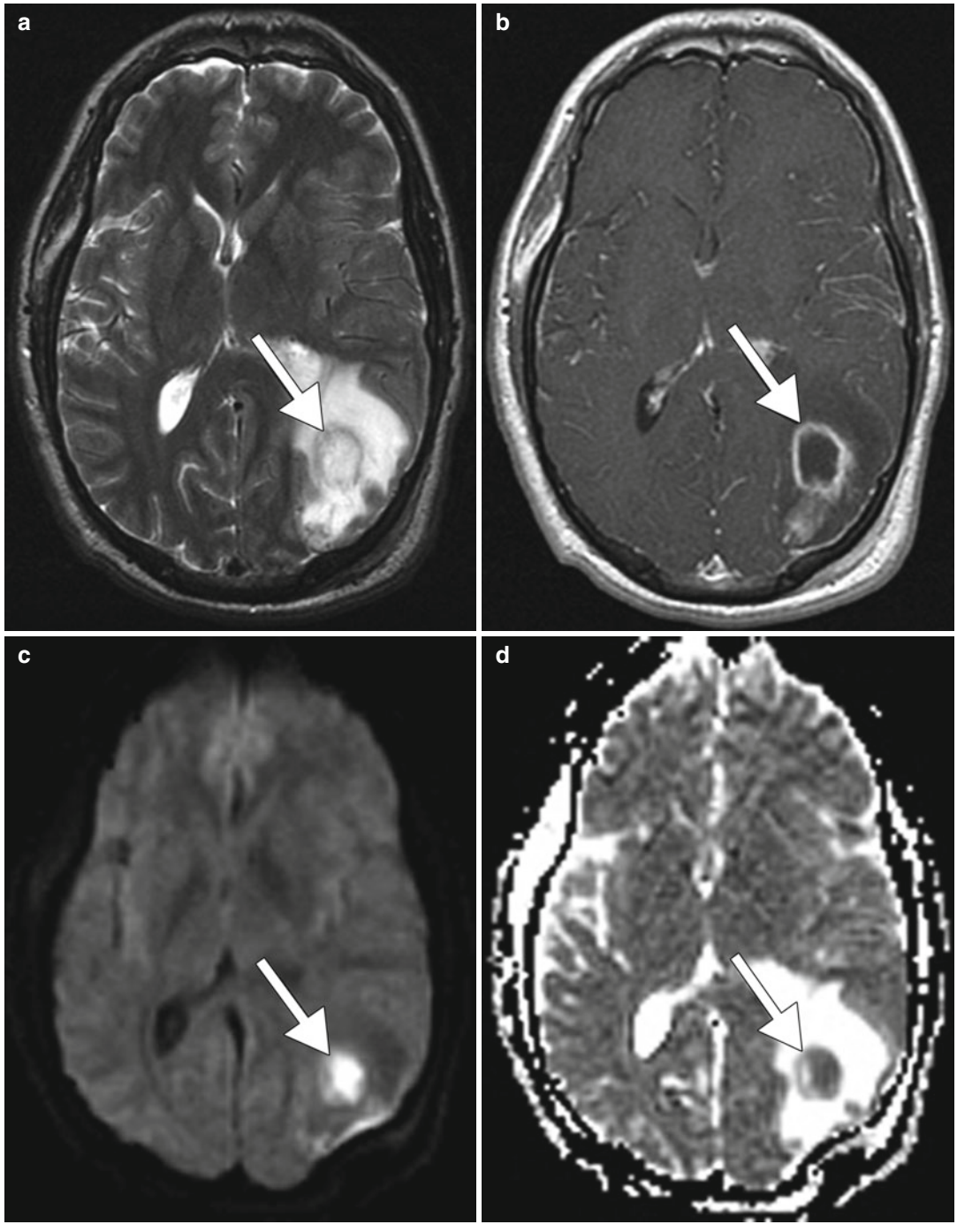

Fig. 19.8 Cerebral abscess. Axial T2-weighted MRI (**a**), post-contrast T1-weighted MRI (**b**), DWI (**c**), and ADC map (**d**) show a rim-enhancing fluid collection with mural T2 hypointensity and restricted diffusion of the contents (*arrows*)

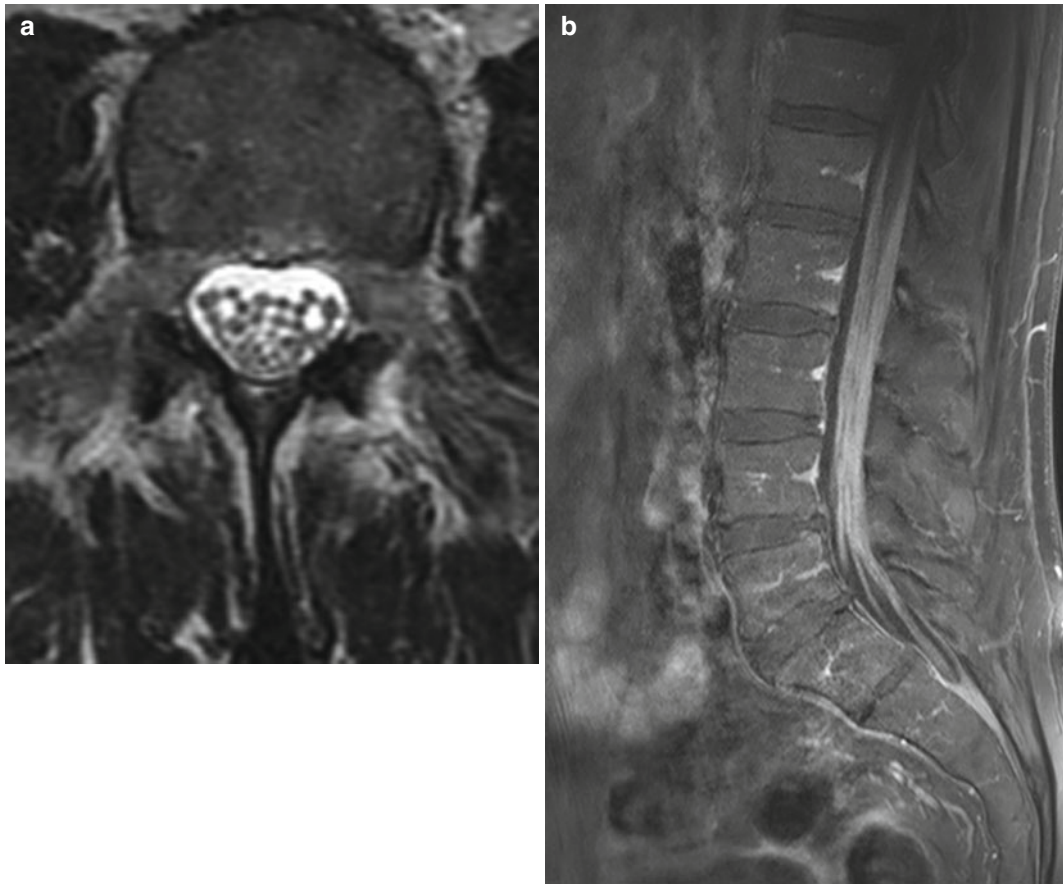

Fig. 19.9 Leptomeningeal lymphoma. Axial T2-weighted MRI (**a**) and sagittal fat-suppressed post-contrast T1-weighted MRI (**b**) show extensive and diffuse thickening and enhancement of the cauda equine nerve roots

Fig. 19.10 Dystrophic intraparenchymal calcifications. Axial CT image shows mineralization of the bilateral basal ganglia and thalami

Suggested Reading

Agarwal A, Vijay K, Thamburaj K, Ouyang T. Transient leukoencephalopathy after intrathecal methotrexate mimicking stroke. Emerg Radiol. 2011;18(4):345–7.

Baehring JM, Fulbright RK. Delayed leukoencephalopathy with stroke-like presentation in chemotherapy recipients. J Neurol Neurosurg Psychiatry. 2008;79:535–9.

Bay A, Oner AF, Etlik O, Yilmaz C, Caksen H. Myelopathy due to intrathecal chemotherapy: report of six cases. J Pediatr Hematol Oncol. 2005;27(5):270–2.

de Waal R, Algra PR, Heimans JJ, Wolbers JG, Scheltens P. Methotrexate induced brain necrosis and severe leukoencephalopathy due to disconnection of an Ommaya device. J Neurooncol. 1993;15(3):269–73.

Glass JO, Reddick WE, Li CS, Laningham FH, Helton KJ, Pui CH. Computer-aided detection of therapy-induced leukoencephalopathy in pediatric acute lymphoblastic leukemia patients treated with intravenous high-dose methotrexate. Magn Reson Imaging. 2006; 24(6):785–91.

Inaba H, Khan RB, Laningham FH, Crews KR, Pui CH, Daw NC. Clinical and radiological characteristics of methotrexate-induced acute encephalopathy in pediatric patients with cancer. Ann Oncol. 2008;19(1): 178–84.

Küker W, Bader P, Herrlinger U, Heckl S, Nägele T. Transient encephalopathy after intrathekal methotrexate chemotherapy: diffusion-weighted MRI. J Neurooncol. 2005;73(1):47–9.

Reddick WE, Glass JO, Helton KJ, Langston JW, Xiong X, Wu S, Pui CH. Prevalence of leukoencephalopathy in children treated for acute lymphoblastic leukemia with high-dose methotrexate. AJNR Am J Neuroradiol. 2005;26(5):1263–9.

Reddick WE, Glass JO, Johnson DP, Laningham FH, Pui CH. Voxel-based analysis of T2 hyperintensities in white matter during treatment of childhood leukemia. AJNR Am J Neuroradiol. 2009;30(10):1947–54.

Sandoval C, Kutscher M, Jayabose S, Tenner M. Neurotoxicity of intrathecal methotrexate: MR imaging findings. AJNR Am J Neuroradiol. 2003;24(9): 1887–90.

Shanley DJ. Mineralizing microangiopathy: CT and MRI. Neuroradiology. 1995;37:331–3.

Visentin M, Zhao R, Goldman ID. The antifolates. Hematol Oncol Clin North Am. 2012;26(3):629–48, ix.

5-Fluorouracil

20

Daniel Thomas Ginat

20.1 Uses

5-fluorouracil (5-FU) and its derivatives, including carmufor (1-hexycarbamly-5-fluorouracil), are most commonly used as adjuvant chemotherapeutic agents for breast and colorectal cancer.

20.2 Mechanism

5-FU is an antimetabolite prodrug. Activation of 5-FU into 5-F-dUMP leads to inhibition of thymidylate synthase and increases dUTP and 5-F-dUTP levels in cells. DNA polymerase-mediated incorporation of dUTP and 5-F-dUTP into DNA produces U/A, 5-FU/A, or 5-FU/G base pairs, which are excised by human uracil excision repair glycosylases, leading to toxic abasic sites in DNA that may precipitate cell death.

20.3 Discussion

Leukoencephalopathy related to 5-FU therapy occurs in less than 5 % of patients treated with this agent. It is believed that dihydropyrimidine dehydrogenase deficiency may predispose to this complication. The toxic leukoencephalopathy associated with 5-FU appears as symmetric high T2 signal in the periventricular and deep white matter of the bilateral cerebral hemispheres, including the corpus callosum, and cerebellar white matter (Fig. 20.1). There can be associated restricted diffusion, and changes on DWI are often the initial neuroimaging manifestation of the toxic leukoencephalopathy. The imaging findings likely correspond to myelin vacuolization and development of intracellular edema. The abnormalities may resolve with cessation of therapy.

20.4 Differential Diagnosis

Toxic leukoencephalopathy can be caused by other chemotherapeutic agents, such as methotrexate (refer to Chap. 19), vincristine, ifosfamide, fludarabine, cytarabine, cisplatin, and the interferons. This condition may also resemble the leukoencephalopathy associated with other pharmaceuticals, such as methotrexate (refer to Chap. 19), metronidazole (refer to Chap. 25) and vigabtrin (refer to Chap. 29), as well as various illicit drugs, such as opioids and amphetamines (refer to Chaps. 6 and 7). Otherwise, 5-FU toxic leukoencephalopathy may resemble other demyelinating conditions, such as acute disseminated encephalomyelitis caused, for example, by vaccines (refer to Chap. 48) and hypoxic-ischemic encephalopathy (refer to Chaps. 3, 9, and 40).

D.T. Ginat, MD, MS
Department of Radiology, University of Chicago, Pritzker Medical School, Chicago, IL, USA
e-mail: ginatd01@gmail.com

D.T. Ginat et al. (eds.), *Neuroimaging Pharmacopoeia*,
DOI 10.1007/978-3-319-12715-6_20,

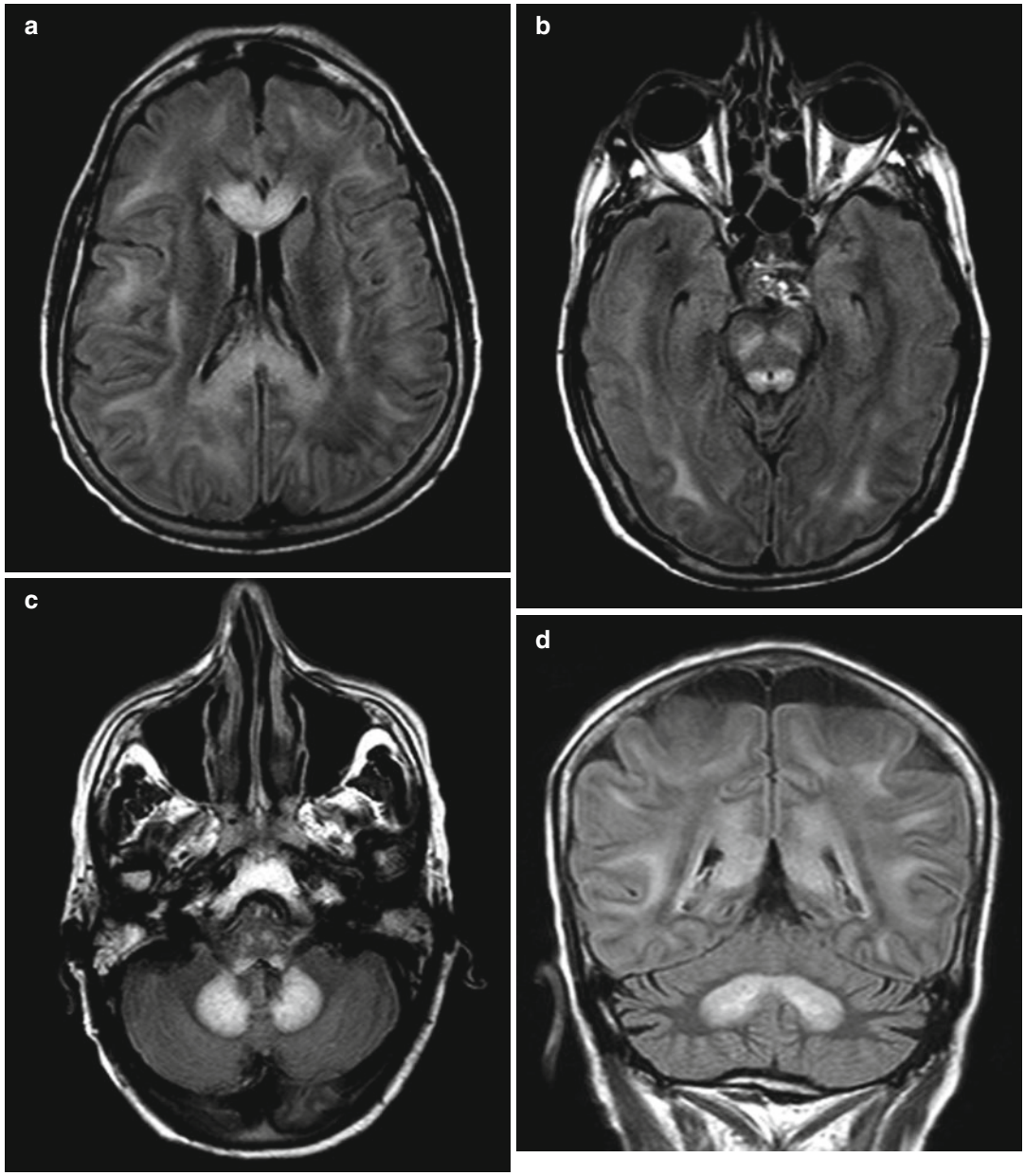

Fig. 20.1 5-FU-induced leukoencephalopathy. The patient presented with acute mental status changes during the course of therapy. Axial (**a**–**c**) and coronal (**d**) FLAIR MR images show extensive bilateral symmetric confluent high T2 signal involving the periventricular and deep cerebral white matter, including the corpus callosum, as well as the cerebellar white matter. DWI (**e**) and ADC map (**f**) obtained a few days earlier show areas of restricted diffusion in the cerebral white matter, which preceded other abnormalities. Treatment was discontinued and the abnormalities resolved on follow-up imaging (not shown)

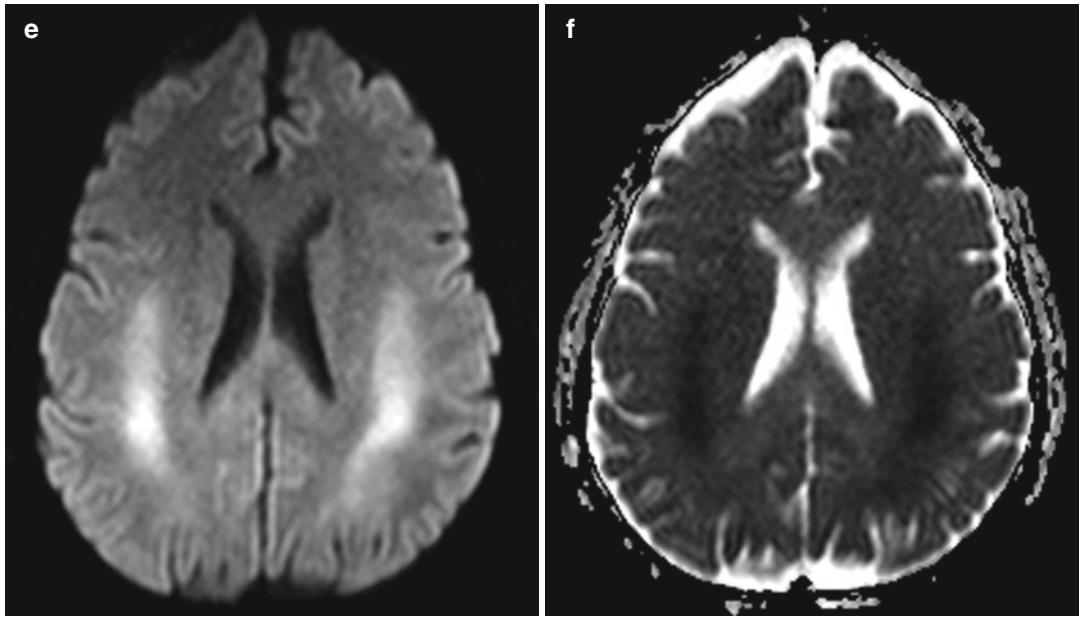

Fig. 20.1 (continued)

Suggested Reading

Fujikawa A, Tsuchiya K, Katase S, Kurosaki Y, Hachiya J. Diffusion-weighted MR imaging of Carmofur-induced leukoencephalopathy. Eur Radiol. 2001;11(12):2602–6.

Mehta S, Singh G, Paul BS. Teaching NeuroImages: 5-FU-induced acute leukoencephalopathy. Neurology. 2013;80(18):e191.

Paul BS, Singh G, Bansal R, Paul G. Diffusion weighted MR imaging of 5-fluorouracil and oxaliplatin-induced leukoencephalopathy. J Postgrad Med. 2013;59(2):135–7.

L-Asparaginase (Elspar/Erwinase) 21

Rania Hito and Ronil V. Chandra

21.1 Uses

L-asparaginase is a form of antineoplastic therapy, mainly for acute lymphoblastic leukemia (ALL) and lymphoblastic lymphoma in adult and pediatric patients.

21.2 Mechanism

The amino acid L-asparagine is an essential nutritional requirement of both normal and cancer cells. Unlike normal cells that can synthesize L-asparagine, certain tumor cells are dependent on external sources. The enzyme L-asparaginase (L-Asp) eliminates the free L-asparagine, starving tumor cells and causing tumor cell death. L-Asp used for antineoplastic therapy is generally derived from *Escherichia coli* or *Erwinia chrysanthemi*.

R. Hito, MD
Department of Radiology,
University of Massachusetts Memorial Medical Center,
Worcester, MA, USA,

R.V. Chandra, MBBS, MMed, FRANZCR (✉)
Department of Diagnostic Imaging,
Monash Medical Center, Monash Health,
Melbourne, VIC, Australia
e-mail: ronilvchandra@gmail.com

21.3 Discussion

The overall incidence of cerebral venous sinus thrombosis in a large meta-analysis of pediatric patients treated for ALL was 1.5 %. Patients with cerebral venous thrombosis (CVT) may present with headache, altered consciousness, focal neurological deficit, and/or seizures during or within 2–3 weeks after treatment with L-Asp. The risk of L-Asp-associated CVT is highest during induction and when used in conjunction with steroids. In a small study, *Escherichia coli*–derived L-Asp had higher rates of thrombosis than *Erwinia chrysanthemi*–derived L-Asp.

There are direct and indirect neuroimaging findings of CVT (Figs. 21.1 and 21.2). Cortical or subcortical edema or hemorrhage are indirect signs that can be identified on non-contrast CT. MRI is more sensitive than CT for these indirect signs. Any area of infarction that does not correspond to an arterial territory should raise suspicion for venous infarction. The location of the lesions can also help guide toward the site of thrombosis—bilateral parietal lesions suggest superior sagittal sinus thrombosis, unilateral temporo-occipital lesions suggest transverse-sigmoid thrombosis, and bilateral thalamic lesions suggest deep venous sinus thrombosis. Thrombus may also be directly identified as hyperattenuation in venous structures on non-contrast CT or as the "empty delta sign" on post-contrast CT where enhancing dura surrounds the thrombus.

D.T. Ginat et al. (eds.), *Neuroimaging Pharmacopoeia*,
DOI 10.1007/978-3-319-12715-6_21,

On MRI, the thrombus may be difficult to directly identify in the acute phase, as deoxyhemoglobin in trapped red blood cells results in T1 isointensity and T2 hypointensity.

The diagnostic test of choice is either CT or MR venography. Any filling defect should raise suspicion of CVT; however, this needs to be distinguished from normal intra-sinus septations, arachnoid granulations, and congenital hypoplastic/aplastic venous structures.

Treatment of L-Asp-associated thrombosis is anticoagulation and cessation of L-Asp.

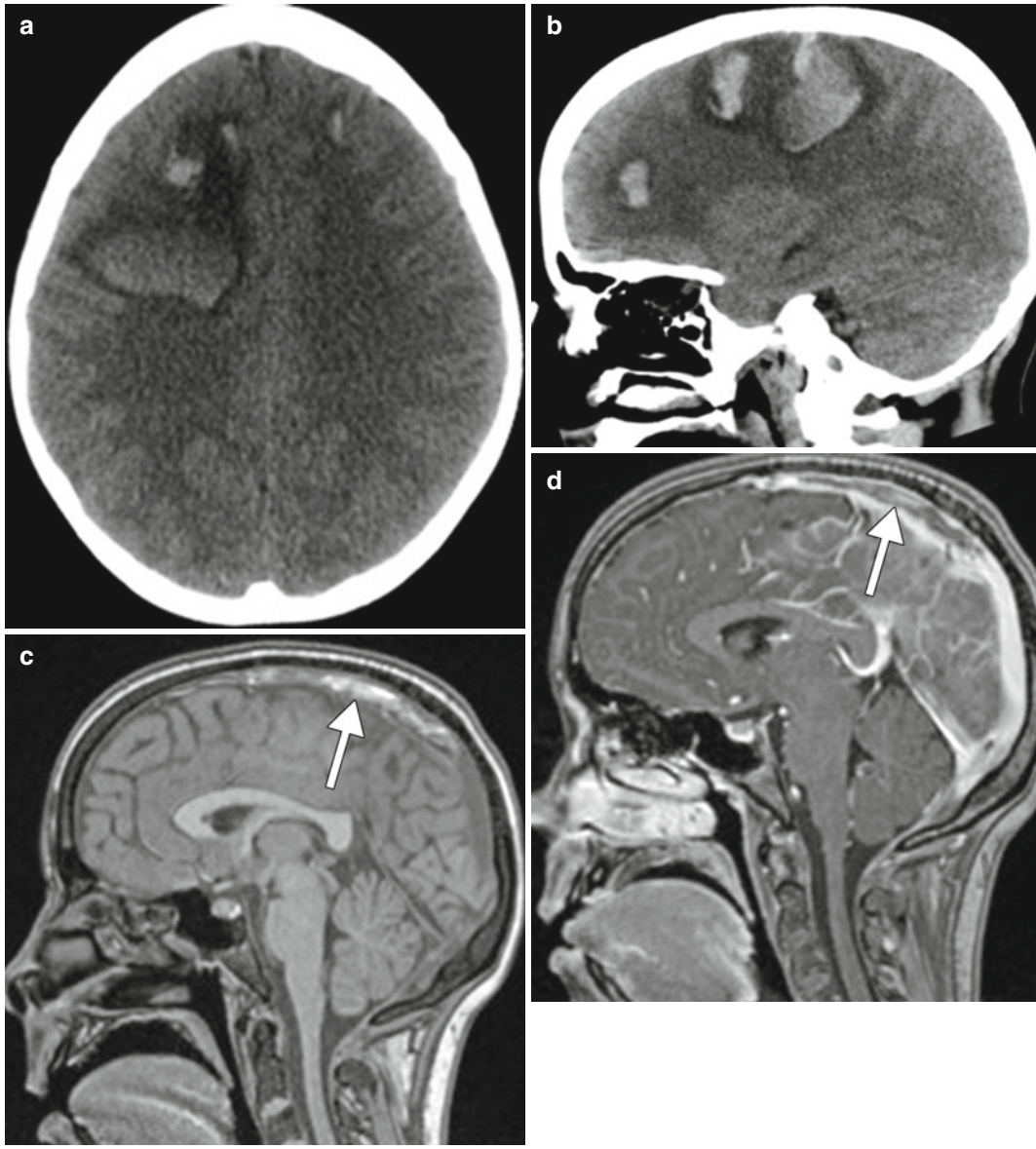

Fig. 21.1 Dural sinus thrombosis and hemorrhage associated with L-Asparaginase. A pediatric patient with newly diagnosed acute lymphoblastic leukemia presented with generalized tonic-clonic seizures and hemiparesis 14 days after treatment with L-Asp. Axial (**a**) and coronal (**b**) non-contrast CT demonstrate bilateral frontal lobe hemorrhages. T1-weighted sagittal non-contrast (**c**) and post-contrast fat-suppressed (**d**) images demonstrating thrombus within the superior sagittal sinus (*arrows*). Axial T2-weighted (**e**) and axial SWI MIP (**f**) images demonstrate the extensive bifrontal hemorrhages with layering blood products in the largest area of hemorrhage

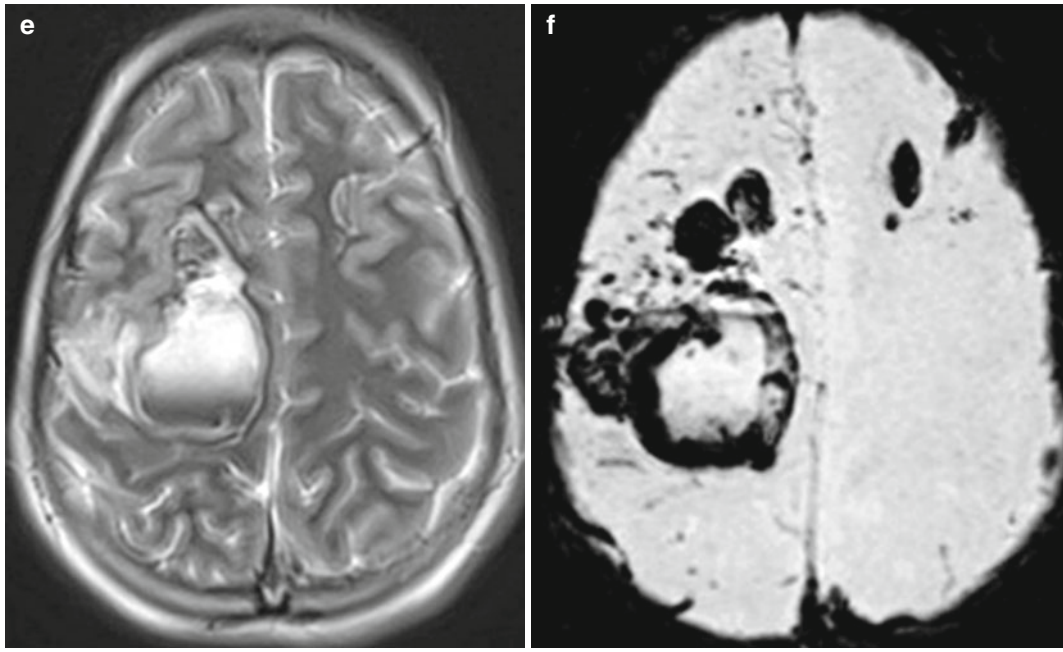

Fig. 21.1 (continued)

Long-term outcomes remain good, and L-Asp may be restarted after imaging shows thrombus stabilization or improvement.

21.4 Differential Diagnosis

A potential drug-induced etiology should be considered for every patient presenting with cerebral venous thrombosis. The most common drug associated with venous thrombosis is the oral contraceptive pill. Other drugs that have been reported to cause venous thrombosis include tamoxifen, androgens, cisplatin, thalidomide, and MDMA. Neuroimaging manifestations are similar to non-drug-induced venous thrombosis. Other conditions that predispose to venous thrombosis in children and young adults should also be considered, such as congenital or acquired prothrombotic conditions, dehydration, infection, anemia, renal disease, trauma, autoimmune disorders, congenital heart disease, central venous line placement, and malignancy.

- *Oral contraceptive pills (OCP) (refer to Chap. 47).* In most developed countries, the most common risk factor for venous thrombosis is OCP use. The use of the estrogen-containing OCP is significantly associated with an increased risk of venous thrombosis, particularly in patients with hereditary prothrombotic states. OCPs containing drospirenone may be associated with higher risks of venous thrombosis than those with levonorgestrel.
- *Tamoxifen:* A selective estrogen receptor modulator commonly used in the treatment of breast cancer. The potential mechanism for a procoagulant effect is unknown but may relate to its weak estrogenic effects.
- *Androgens:* Androgen-induced venous thrombosis has been mainly reported in young body builders. The mechanism is unknown but may relate to increased platelet activation or an increase in coagulation factors.
- *Cisplatin:* Venous thrombosis is a rare complication of patients with germ cell tumors treated with platinum-based chemotherapy. The mechanism is unknown, but may relate to endothelial cell injury.

In addition to various chemotherapy agents, oncology patients may have additional risk factors for the development of venous thrombosis, such as the presence of a central venous catheter. Catheter-related venous thrombosis can appear as a filling defect on contrast-enhance CT, usually

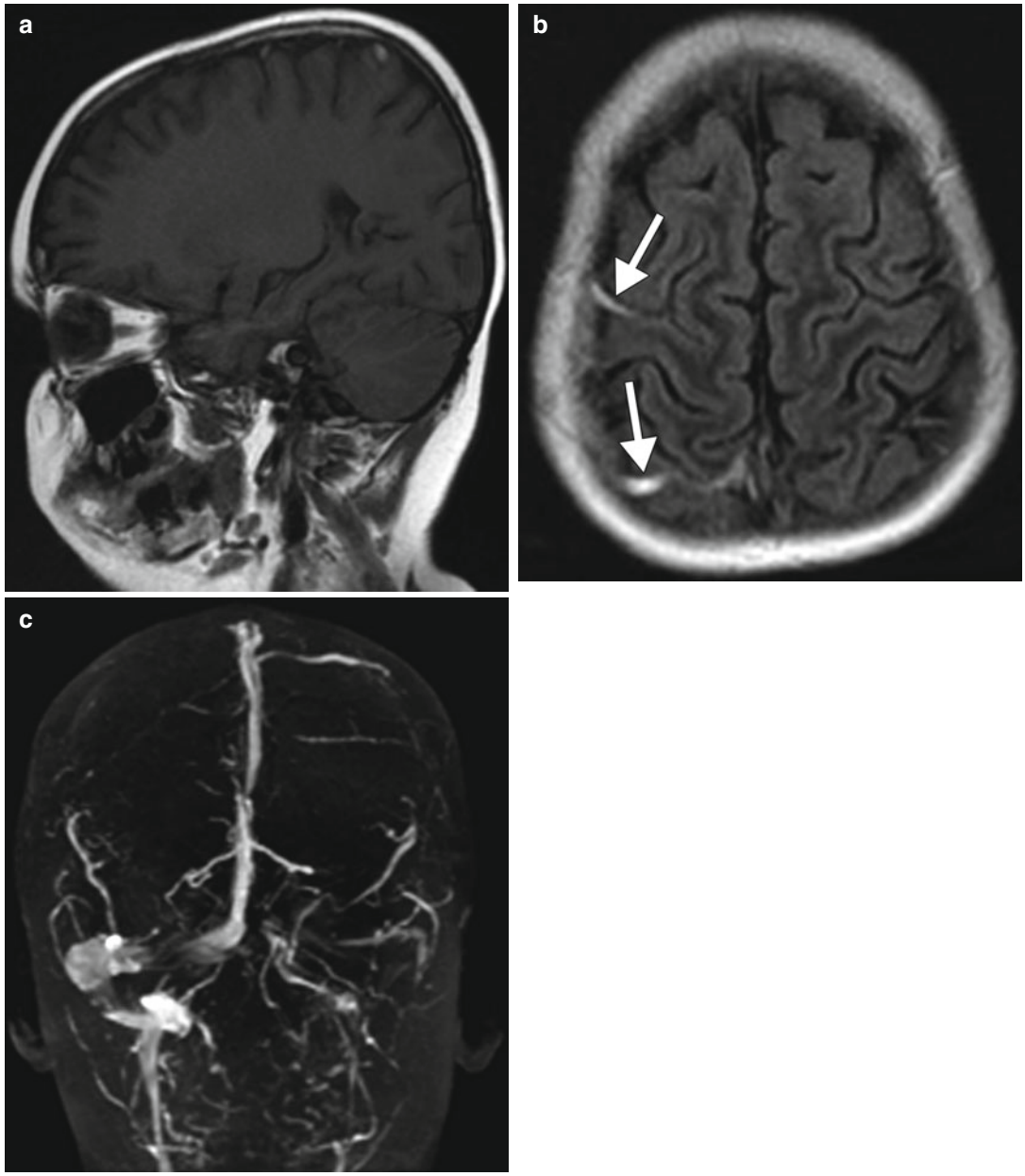

Fig. 21.2 Cortical vein trombosis associated with L-Asparaginase. A 6-year-old female with B-cell ALL presenting with right-sided weakness 1 month after L-Asp induction chemotherapy. Initial sagittal pre-contrast T1-weighted MRI (**a**) shows two foci of hyperintensity in cortical veins over the right cerebral convexity. Axial FLAIR image (**b**) shows hyperintensity in the same two cortical veins (*arrows*). MIP image from an MRV (**c**) shows absence of flow in corresponding right-sided cortical veins

Fig. 21.3 Catheter-related venous thrombosis. The patient has a history of laryngeal cancer treated with chemotherapy. Coronal contrast-enhanced CT shows a hypoattenuating filling defect in the inferior right internal jugular vein (*arrow*), adjacent to the right internal jugular venous catheter (*arrowhead*)

adjacent to the catheter (Fig. 21.3). The vessel can be expanded in the acute setting and narrowed with chronic thrombosis.

Suggested Reading

Athale UH, Chan AK. Thromboembolic complications in pediatric hematologic malignancies. Semin Thromb Hemost. 2007;33:416–26.

Caruso V, Iacoviello L, Di Castelnuovo A, Storti S, Mariani G, de Gaetano G, Donati MB. Thrombotic complications in childhood acute lymphoblastic leukemia: a meta-analysis of 17 prospective studies comprising 1752 pediatric patients. Blood. 2006;108(7):2216–22.

Diamini N, Billinghurst L, Kirkham J. Cerebral venous sinus thrombosis. Neurosurg Clin N Am. 2010;21:511–27.

Grace RF, Dahlberg SE, Neuberg D, Sallan SE, Connors JM, Neufeld EJ, et al. The frequency and management of asparaginase-related thrombosis in paediatric and adult patients with acute lymphoblastic leukaemia treated on Dana-Farber Cancer Institute consortium protocols. Br J Haematol. 2011;152:452–9.

Jaillard AS, Hommel M, Mallaret M. Venous sinus thrombosis associated with androgens in a healthy young man. Stroke. 1994;25(1):212–3.

Kieslich M, Porto L, Lanfermann H, et al. Cerebrovascular complications of l-asparaginase in the therapy of acute lymphoblastic leukemia. J Pediatr Hematol Oncol. 2003;25(6):484–7.

Masjuan J, Pardo J, Callejo JM, Andrés MT, Alvarez-Cermeño JC. Tamoxifen: a new risk factor for cerebral sinus thrombosis. Neurology. 2004;62(2):334–5.

Papet C, Gutzeit A, Pless M. Two cases of cerebral sinus venous thrombosis following chemotherapy for non-seminomatous germ cell tumor. Case Rep Oncol. 2011;4(3):555–9.

Payne JH, Vora JA. Thrombosis and acute lymphoblastic leukaemia. Br J Haematol. 2007;138(4):430–45.

Ross CS, Brown TM, Kotagal S, Rodriguez V. Cerebral venous sinus thrombosis in pediatric cancer patients: long-term neurological outcomes. J Pediatr Hematol Oncol. 2013;35(4):299–302.

Truelove E, Fielding AK, Hunt BJ. The coagulopathy and thrombotic risk associated with L-asparaginase treatment in adults with acute lymphoblastic leukaemia. Leukemia. 2013;27(3):553–9.

Wani NA, Kosar T, Pala NA, Qureshi UA. Sagittal sinus thrombosis due to L-asparaginase. J Pediatr Neurosci. 2010;5:32–5.

Ipilimumab (MDX-010, Yervoy) 22

Daniel Thomas Ginat and Gul Moonis

22.1 Uses

Ipilimumab is a form of Antineoplastic therapy used in the setting of metastatic or unresectable melanoma.

22.2 Mechanism

Ipilimumab is monoclonal antibody against cytotoxic T lymphocyte antigen-4 (CTLA-4). Inhibition of CTLA-4 signaling prolongs T-cell activation and stimulates T-cell proliferation, which augments T-cell-mediated immunity and antitumor immune response.

22.3 Discussion

Ipilimumab can cause various inflammatory reactions as a side effect, including autoimmune hypophysitis. The inflammatory reaction is secondary to specific human monoclonal antibodies that antagonize cytotoxic T-lymphocyte antigen 4 (anti-CTLA-4 mAbs), thereby inducing unrestrained T-cell activation. Ipilimumab-induced hypophysitis occurs in up to 17 % of patients. The hypophysitis can manifest as variable degrees of diffuse enlargement of the pituitary gland and infundibulum (Fig. 22.1). The enhancement is usually homogeneous, but can be heterogeneous. Loss of the hyperintense T1 signal in the posterior pituitary can also be observed. There is often concomitant hypopituitarism. Although the imaging features are rather nonspecific, the findings are reversible with cessation of ipilimumab. However, patients may require long-term hormone replacement therapy.

22.4 Differential Diagnosis

Differential considerations for ipilimumab-induced hypophysitis include metastatic melanoma to the sella, other forms of hypophysitis, pituitary adenoma, craniopharyngioma, germinoma, and lymphoma. Certainly, clinical history and parameters will be helpful in formulating an appropriate differential diagnosis follow-up may be appropriate and decrease in size of the lesion will have indicated that ipilimumab was indeed the etiology.

- *Metastases*: Overall, metastases to the sella are relatively rare, but can mimic ipilimumab-induced hypophysitis (Fig. 22.2). However, intrasellar metastases generally portend widespread systemic disease and are frequently synchronous with leptomeningeal and parenchymal brain metastases. Furthermore, unlike ipilimumab hypophysitis, melanoma metastases are

D.T. Ginat, MD, MS (✉)
Department of Radiology, University of Chicago, Pritzker Medical School, Chicago, IL, USA
e-mail: ginatd01@gmail.com

G. Moonis, MD
Department of Radiology, Columbia University, New York, NY, USA

D.T. Ginat et al. (eds.), *Neuroimaging Pharmacopoeia*,
DOI 10.1007/978-3-319-12715-6_22,

frequently hyperintense on T1-weighted images, are heterogeneous due to intratumoral hemorrhage, and are parasellar (Fig. 22.3).

- *Other causes of hypophysitis*: Lymphocytic and granulomatous hypophysitis can both be considered forms of autoimmune hypophysitis that result from a variety of etiologies besides ipilimumab. For example, IgG4-related disease is a recently recognized systemic inflammatory condition that can manifest as hypophysitis (Fig. 22.4). Typically, autoimmune hypophysitis appears as low signal on T2-weighted images and enhances diffusely with variable degrees of pituitary and or infundibular enlargement. In addition, associated loss of the posterior pituitary bright spot is common and favors

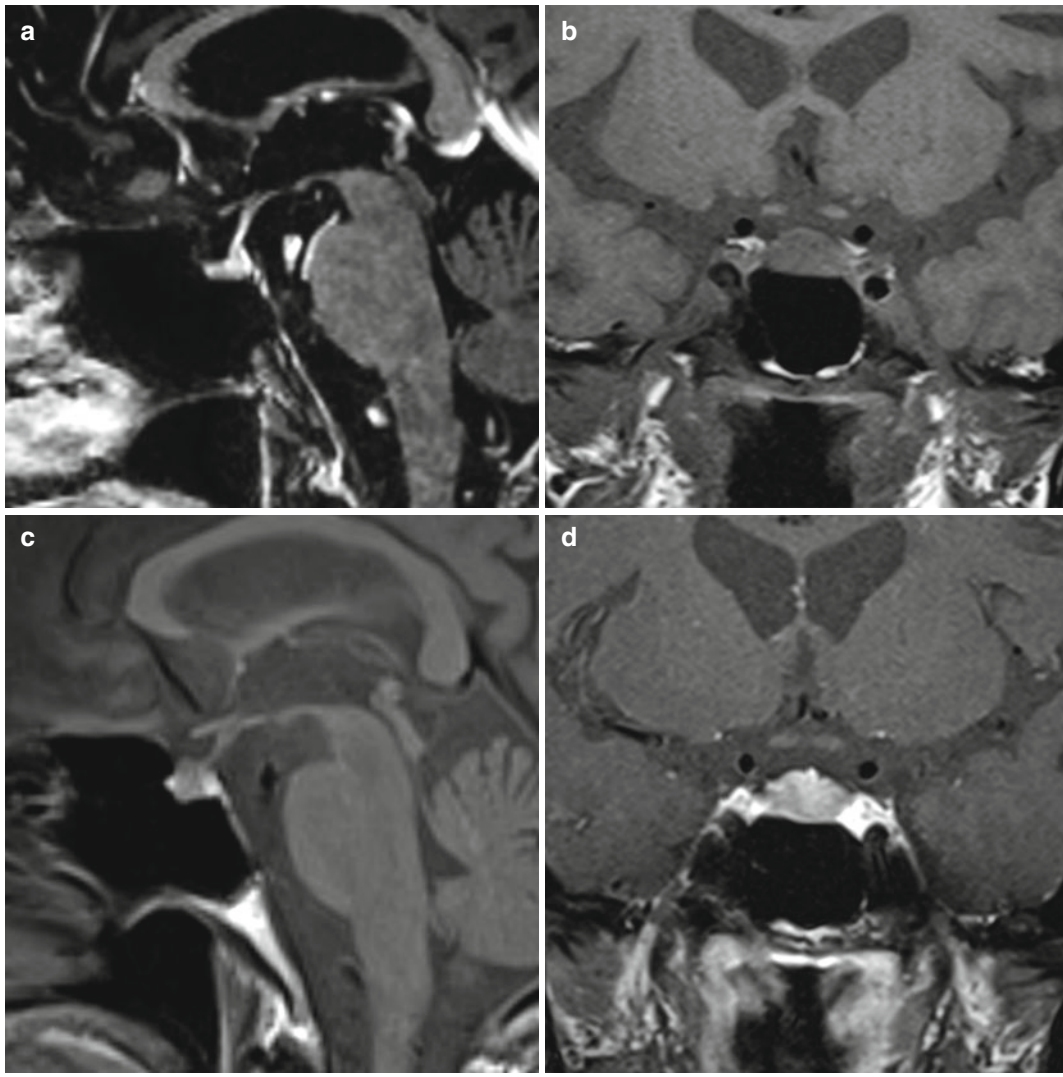

Fig. 22.1 Ipilimumab-induced hypophysitis. The patient has a history of metastatic melanoma treated with ipilimumab. Initial sagittal post-contrast T1 MRI (**a**) shows a normal pituitary gland and stalk. Sagittal and coronal pre- and post-contrast T1-weighted MR images (**b**–**e**) obtained 4 months later after implementation of ipilimumab show interval diffuse enlargement and homogeneous enhancement of the pituitary gland and stalk. Sagittal post-contrast MRI (**f**) obtained 4 months later after discontinuing ipilimumab shows interval decrease in size of the pituitary gland and stalk

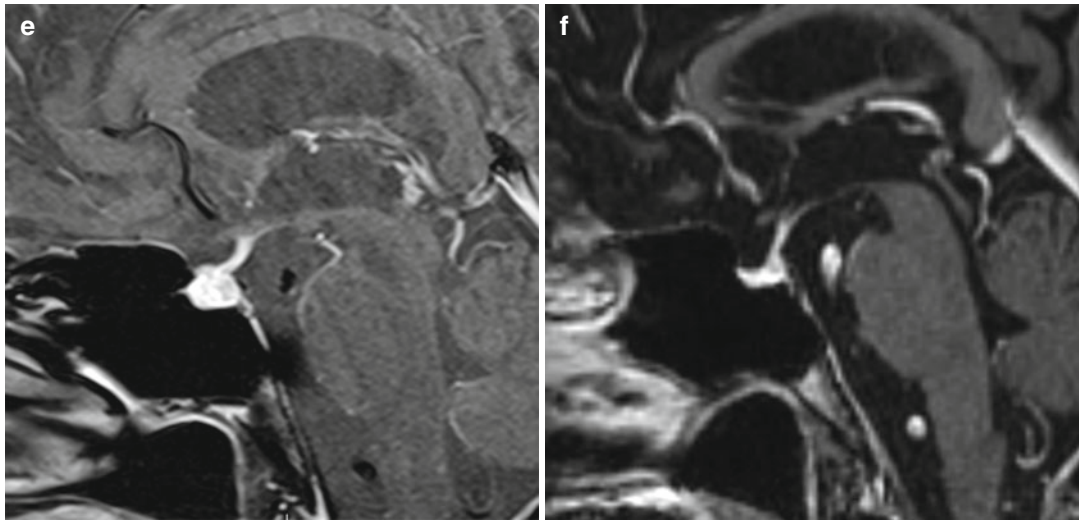

Fig. 22.1 (continued)

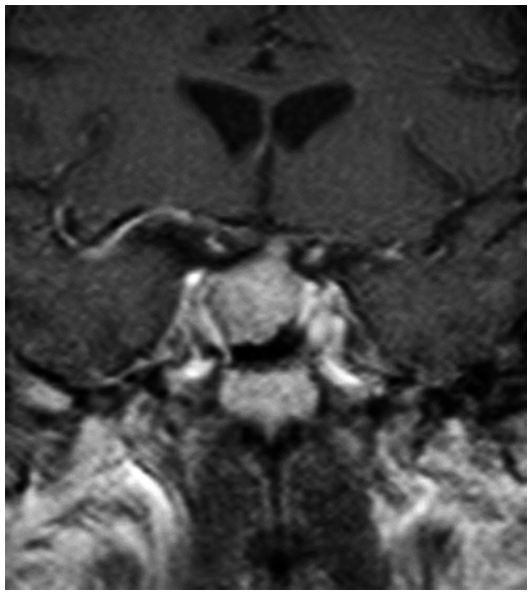

Fig. 22.2 Metastasis (lung cancer). Coronal post-contrast T1-weighted MRI shows a homogeneously enhancing mass within the sella

the diagnosis of autoimmune hypophysitis over pituitary microadenomas. Nevertheless, autoimmune hypophysitis can mimic nonsecreting pituitary adenomas on MRI. Indeed, approximately 40 % of patients with hypophysitis are misdiagnosed as having pituitary macroadenoma and undergo unnecessary surgery.

- *Pituitary adenoma*: Adenomas are the most common sellar mass and patients with melanoma treated with ipilimumab can certainly present with an underlying pituitary adenoma. Adenomas can have variable imaging appearances but generally demonstrate enhancement. In particular, microadenomas display delayed enhancement with respect to the normal pituitary gland and can be identified as a discreet mass. Enhancement tends to be more heterogeneous in macroadenomas compared with ipilimumab-induced hypophysitis. While macroadenomas can extend into the suprasellar cistern, the infundibulum itself usually does not enlarge as it does with hypophysitis. Macroadenomas can also occasionally be invasive, extending into the sphenoid sinus (Fig. 22.5). Interestingly, the presence of mucosal swelling in the sphenoid sinus favors the diagnosis of adenoma over autoimmune hypophysitis.
- *Germinoma*: Neurohypophyseal germinoma is an uncommon WHO grade III neoplasm that tends to occur in children and young adults. Infundibular thickening, absence of the posterior pituitary high signal on T1-weighted MRI, lack of calcification, and hyperattenuation on CT are common imaging features of neurohypophyseal germinoma. In

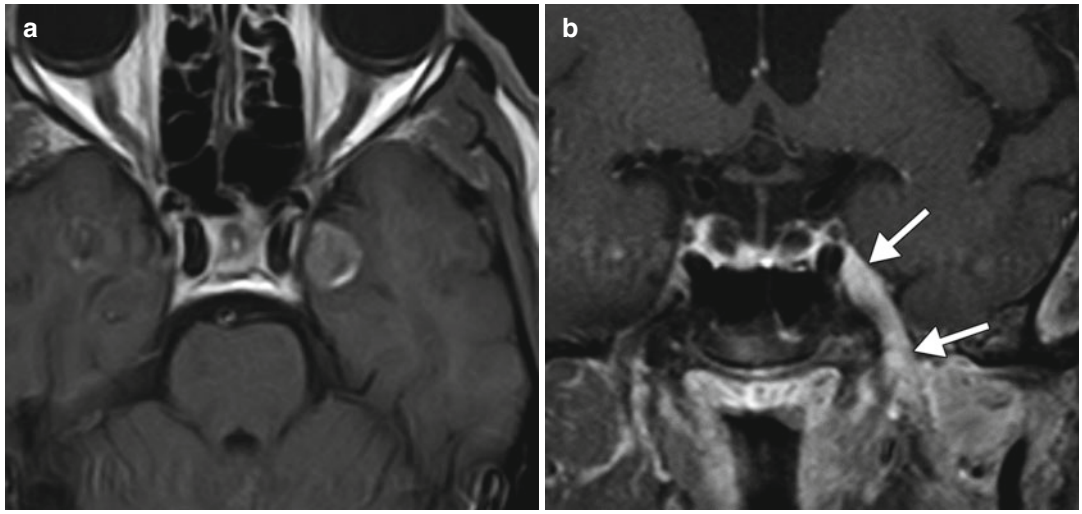

Fig. 22.3 Melanoma metastases in the parasellar region. Axial post-contrast T1-weighed MRI (**a**) shows a heterogeneously enhancing intraparenchymal melanoma metastasis within the left uncus. Coronal post-contrast T1-weighted MRI (**b**) in a different patient shows perineural extension of melanoma (*arrows*) along the left trigeminal nerve in the masticator space across the foramen ovale into Meckel's cave and the cavernous sinus

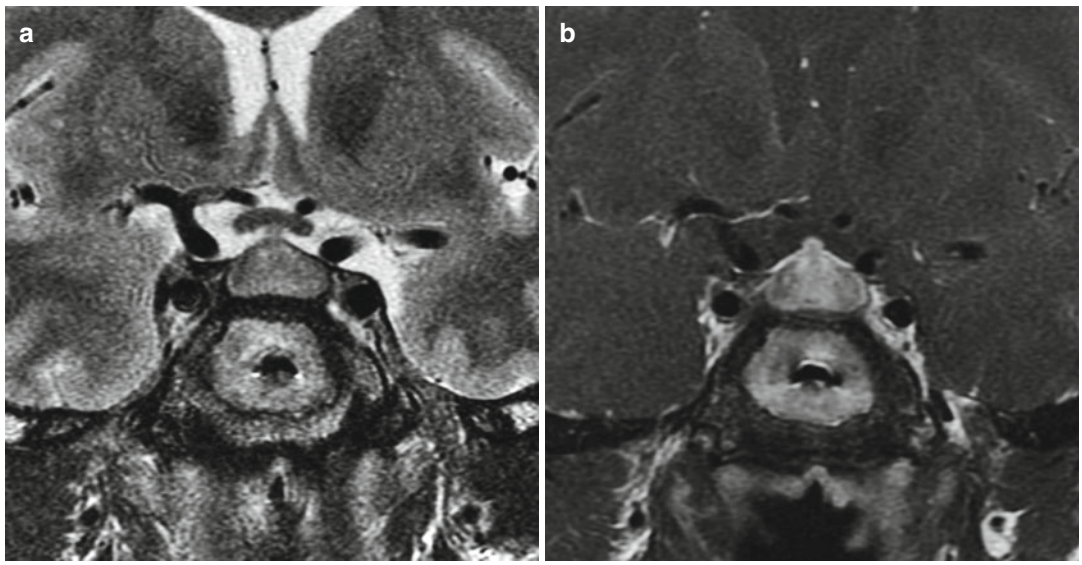

Fig. 22.4 IgG4-related hypophysitis. Coronal T2-weighted (**a**) and coronal T1-weighted (**b**) MR images show diffuse enlargement of the pituitary gland and infundibulum

addition, the presence of concurrent involvement of the pineal gland is suggestive of the diagnosis (Fig. 22.6).

- *Meningioma*: Although these neoplasms occasionally arise in the sellar region and can enhance similarly to the pituitary gland, meningiomas can usually be demarcated from the pituitary gland on MRI (Fig. 22.7). In addition, meningiomas often display a dural tail and may contain calcifications, which are not associated with ipilimumab-induced hypophysitis.

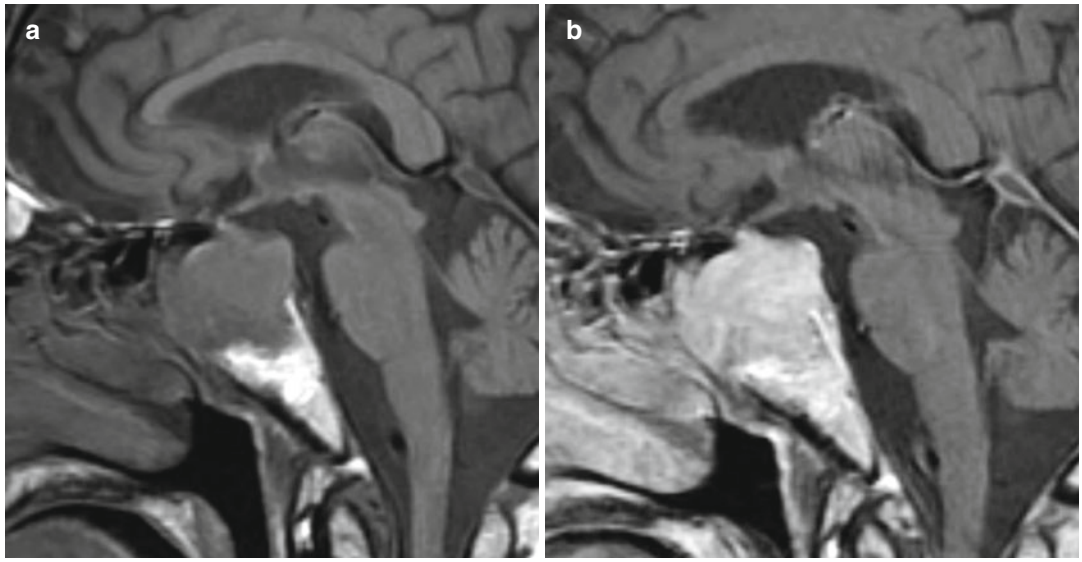

Fig. 22.5 Pituitary adenoma. Sagittal T1-weighted (**a**) and post-contrast sagittal T1-weighted (**b**) MR images show a large, avidly enhancing sellar mass that invades the sphenoid sinuses in a patient with a history of melanoma. Surgical pathology revealed a pituitary adenoma

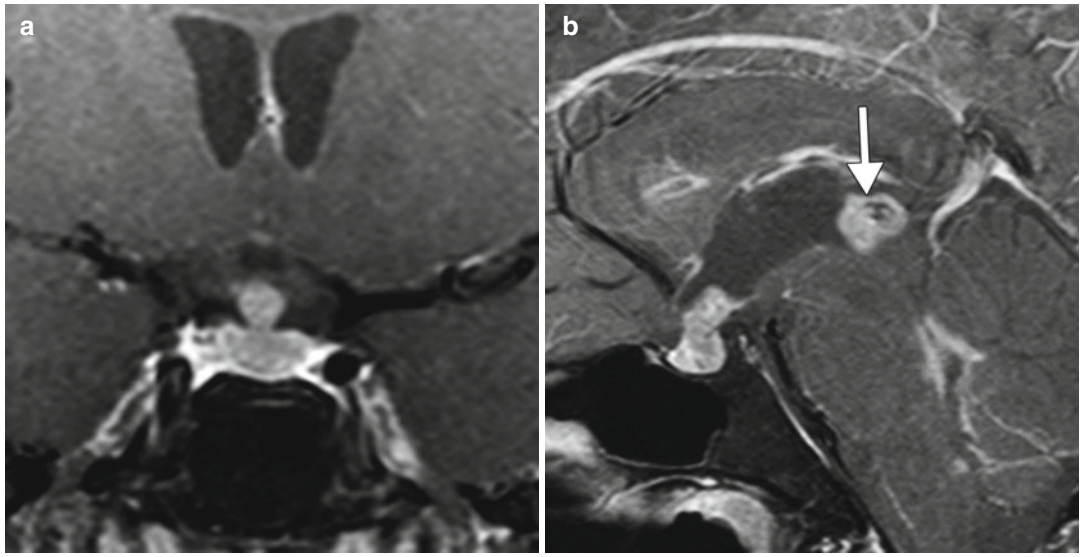

Fig. 22.6 Germinoma. Coronal (**a**) and sagittal (**b**) post-contrast T1-weighted MR images show an avidly enhancing mass centered in the pituitary stalk and central portion of the gland with infiltration. In addition, the sagittal T1 images show a heterogeneously enhancing pineal mass (*arrow*)

- *Lymphoma*: Lymphomatous involvement of the pituitary gland is rare and may coexist with hypophysitis. On MRI, lymphoma typically appears a homogenously enhancing mass (Fig. 22.8). Extension into the cavernous sinuses may be observed.

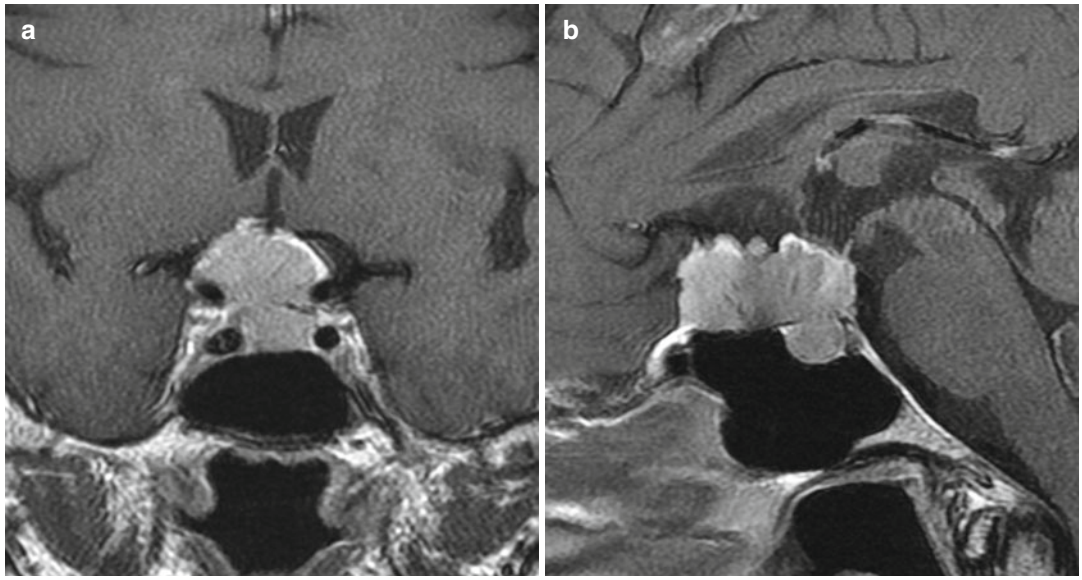

Fig. 22.7 Meningioma. Coronal (**a**) and sagittal (**b**) post-contrast T1-weighted MR images show an avidly enhancing extra-axial dural-based massed centered in the planum sphenoidale and extending into the suprasellar cistern. A dural tail is evident anteriorly. The mass is partially demarcated from the pituitary gland by the hypointense linear diaphragm sella

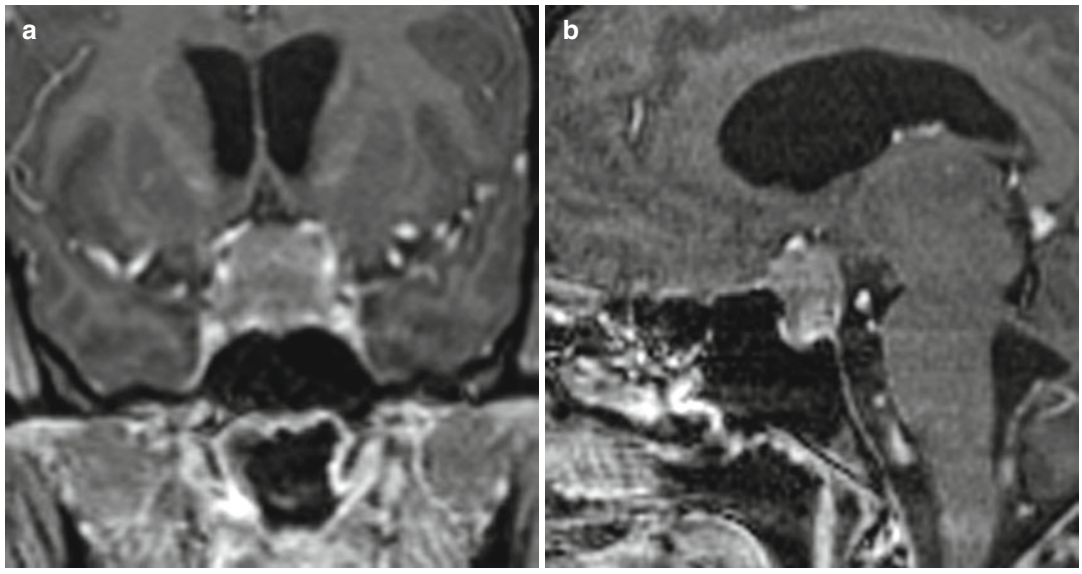

Fig. 22.8 Lymphoma. Coronal (**a**) and sagittal (**b**) post-contrast T1-weighted MR images show a relatively homogeneously enhancing sellar and suprasellar mass

Suggested Reading

Bronstein Y, Ng CS, Hwu P, Hwu WJ. Radiologic manifestations of immune-related adverse events in patients with metastatic melanoma undergoing anti-CTLA-4 antibody therapy. AJR Am J Roentgenol. 2011;197(6): W992–1000.

Carmichael JD. Update on the diagnosis and management of hypophysitis. Curr Opin Endocrinol Diabetes Obes. 2012;19(4):314–21.

Carpenter KJ, Murtagh RD, Lilienfeld H, Weber J, Murtagh FR. Ipilimumab-induced hypophysitis: MR imaging findings. AJNR Am J Neuroradiol. 2009;30(9):1751–3.

Dillard T, Yedinak CG, Alumkal J, Fleseriu M. Anti-CTLA-4 antibody therapy associated autoimmune hypophysitis: serious immune related adverse events across a spectrum of cancer subtypes. Pituitary. 2010;13(1):29–38.

Gutenberg A, Larsen J, Lupi I, Rohde V, Caturegli P. A radiologic score to distinguish autoimmune hypophysitis from nonsecreting pituitary adenoma preoperatively. AJNR Am J Neuroradiol. 2009;30(9):1766–72.

Huang YY, Lin SF, Dunn P, Wai YY, Hsueh C, Tsai JS. Primary pituitary lymphoma presenting as hypophysitis. Endocr J. 2005;52(5):543–9.

Kanagaki M, Miki Y, Takahashi JA, Shibamoto Y, Takahashi T, Ueba T, Hashimoto N, Konishi J. MRI and CT findings of neurohypophyseal germinoma. Eur J Radiol. 2004;49(3):204–11.

McCutcheon IE, Waguespack SG, Fuller GN, Couldwell WT. Metastatic melanoma to the pituitary gland. Can J Neurol Sci. 2007;34(3):322–7.

Rizek P, Seitelbach M, Alturkustani M, Leung A, Fraser JA. Sellar and parasellar intravascular lymphoma mimicking pituitary apoplexy. J Neuroophthalmol. 2012;32(1):33–7.

Tarhini A, Lo E, Minor DR. Releasing the brake on the immune system: ipilimumab in melanoma and other tumors. Cancer Biother Radiopharm. 2010;25(6): 601–13.

Torino F, Barnabei A, De Vecchis L, Salvatori R, Corsello SM. Hypophysitis induced by monoclonal antibodies to cytotoxic T lymphocyte antigen 4: challenges from a new cause of a rare disease. Oncologist. 2012; 17(4):525–35.

Yasuda M, Akiyama N, Miyamoto S, Warabi M, Takahama Y, Kitamura M, Yakushiji F, Kinoshita H. Primary sellar lymphoma: intravascular large B-cell lymphoma diagnosed as a double cancer and improved with chemotherapy, and literature review of primary parasellar lymphoma. Pituitary. 2010;13(1): 39–47.

Calcineurin Inhibitors

23

Santosh Shah and Daniel Thomas Ginat

23.1 Uses

Calcineurin inhibitors (CNI), including cyclosporine, tacrolimus, and sirolimus, are administered for immunosuppressive therapy usually following transplantation in order to reduce rejection rates. These agents are also occasionally used to treat chronic inflammatory/autoimmune diseases.

23.2 Mechanism

Calcineurin inhibitors inhibit the actions of calcineurin, a calcium-dependent protein phosphatase that results in activation of T cells through the upregulation of IL2 and related cytokines, which in turn leads to immunosuppression.

23.3 Discussion

Neurotoxicity from CNI can occur in up to 60 % of patients and clinically present as tremor, decreased responsiveness, seizures, stroke-like episodes, and cortical blindness. In the most severe cases, neuroimaging reveals a pattern consistent with posterior reversible encephalopathy syndrome (PRES). The incidence of PRES in patients on CNI varies from 0.4 to 0.6 % in solid organ transplant patients to as high as 7 to 9 % in allogenic bone marrow transplant patients. Although the exact etiology of PRES is unknown, it is thought to be a disorder of cerebral autoregulation that results in disruption of the blood–brain barrier causing vasogenic edema. PRES has a propensity to involve the territories supplied by the posterior circulation due to its relative paucity of sympathetic innervation, but can also involve anterior vascular distributions. T2-weighted MR imaging typically show bilateral, symmetric areas of hyperintensity in the occipital lobes, posterior parietal, medial frontal lobes, and watershed regions. The basal ganglia, brainstem, and cerebellum are less frequently involved. Large intraparenchymal hemorrhages are rare, although small microhemorrhages are often depicted on susceptibility weighted. The affected sites can display variable degree of enhancement on postcontrast images. Likewise, the findings on diffusion-weighting imaging are variable, and the most severe cases can progress to frank infarction. CT, while less sensitive, may reveal hypoattenuation within the affected areas. Perfusion imaging may show increased cerebral blood flow (CBF). Treatment of CNI toxicity includes decreasing or discontinuing CNI therapy and maintaining strict blood pressure control (Fig. 23.1).

S. Shah, MD
Department of Radiology,
Massachusetts General Hospital, Boston, MA, USA

D.T. Ginat, MD, MS (✉)
Department of Radiology, University of Chicago,
Pritzker Medical School, Chicago, IL, USA
e-mail: ginatd01@gmail.com

D.T. Ginat et al. (eds.), *Neuroimaging Pharmacopoeia*,
DOI 10.1007/978-3-319-12715-6_23,

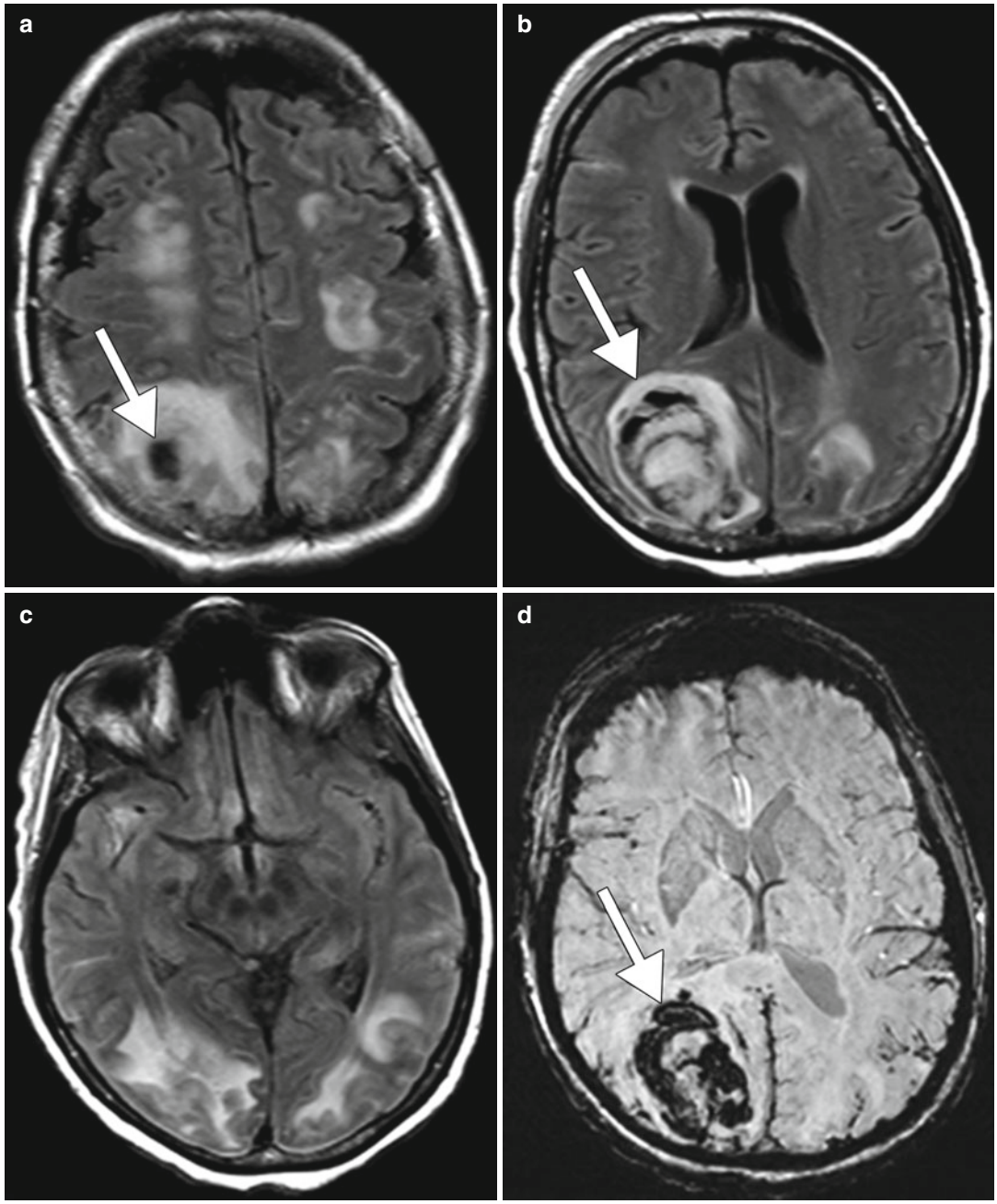

Fig. 23.1 Cyclosporine-induced PRES. Axial FLAIR (**a**–**c**) and SWI (**d**) MR images show cortical and subcortical hyperintensity within the posterior frontal lobes, parietal lobes, and occipital lobes. In addition, there is an associated large right parieto-occipital intraparenchymal hematoma within the right parieto-occipital region (*arrows*)

Posttransplantation lymphoproliferative disorder (PTLD) includes various forms of lymphoid hyperplasia and lymphoid neoplasia that occur in the setting of chronic immunosuppression, including with the use of calcineurin inhibitors, after solid organ transplantation. Most cases of PTLD are of B-cell origin and associated with Epstein-Barr virus infection. The incidence of

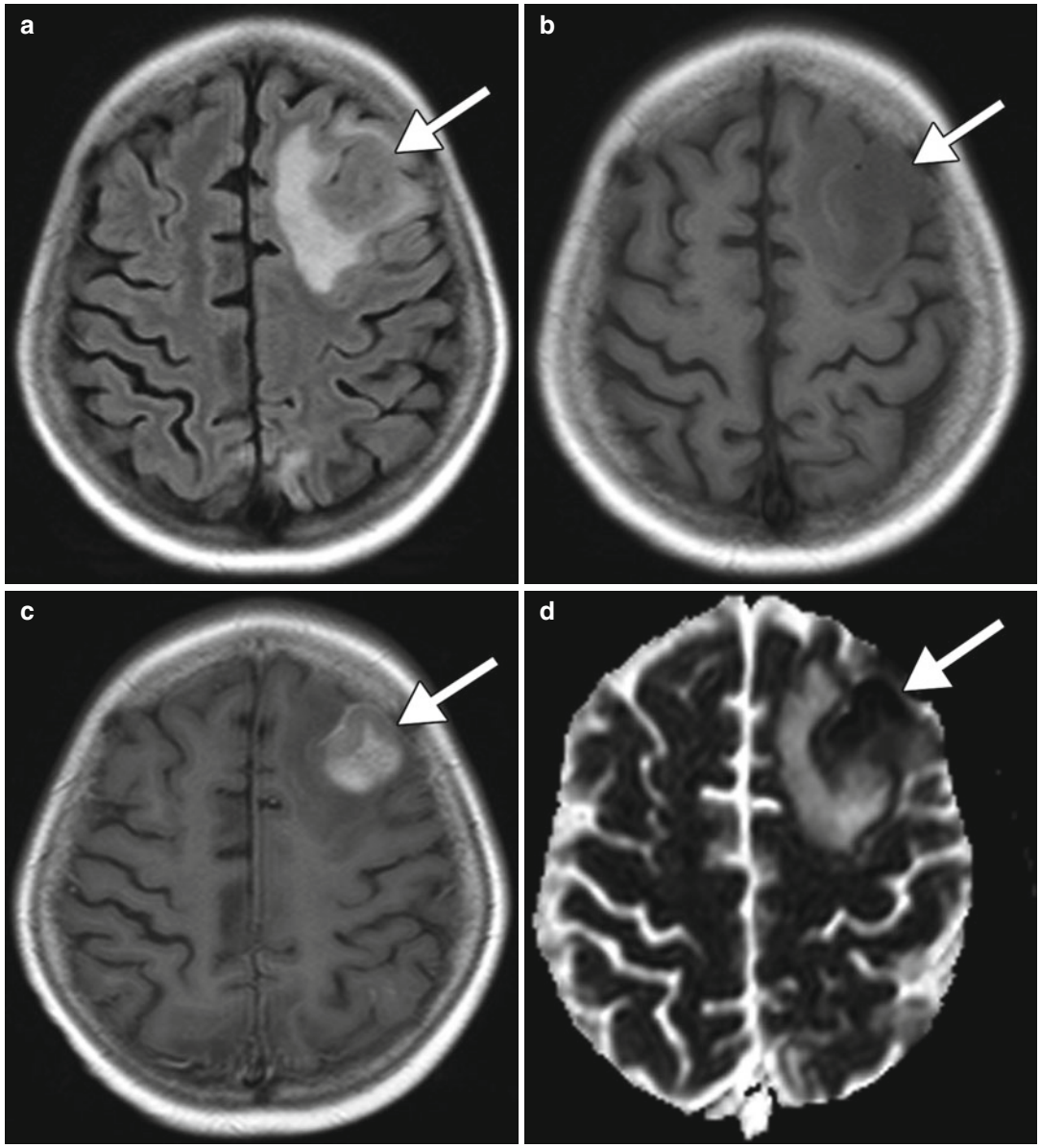

Fig. 23.2 CNS PTLD. Axial FLAIR (**a**), T1-weighted (**b**), and post-contrast T1-weighted (**c**) images show enhancing lesions in the left frontal lobe with surrounding edema (*arrows*). ADC map (**d**) shows restricted diffusion in a portion of the lesion (*arrow*)

PTLD ranges from 1 to 10 % of transplant recipients, depending on the organ transplanted and the type and duration of immunosuppressive therapy. PTLD occurs more frequently in children than in adults, but tends to be more severe in adults. CNS PTLD most commonly appears as focal lobar enhancing masses that display restricted diffusion and surrounding edema (Figs. 23.2 and 23.3). Subdural lesions have also been reported. Involvement of the head and neck most commonly presents as focal masses in the Waldeyer ring and lymphadenopathy (Fig. 23.4). The lymphadenopathy can manifest as large nodal masses or an excessive number of lymph nodes

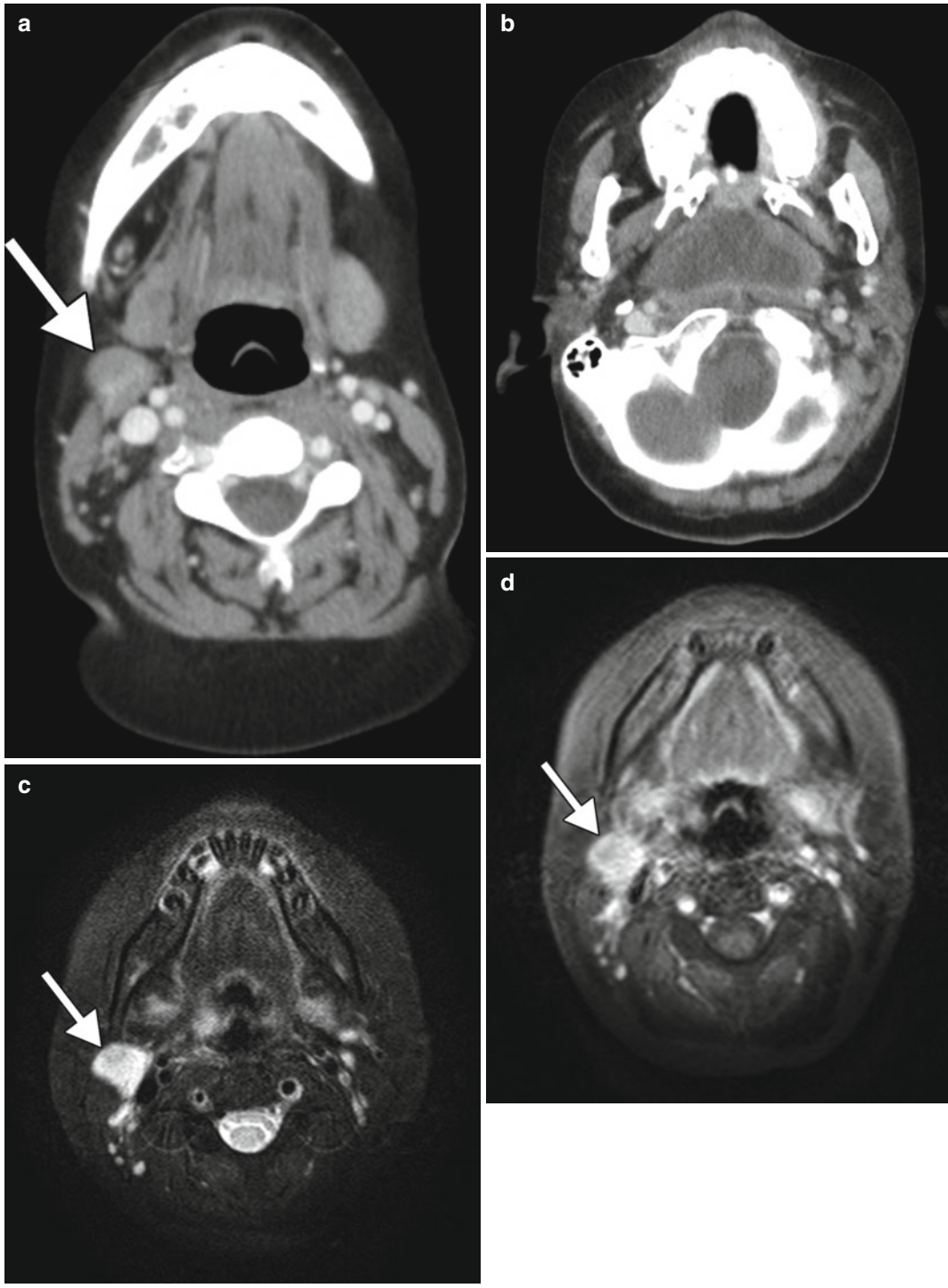

Fig. 23.3 PTLD of the head and neck associated with calcineurin-inhibitor use. The patient received immunosuppressive therapy after bone marrow transplantation and developed neck swelling. Axial CT images (**a**, **b**) show right cervical lymphadenopathy (*arrow*) and a nasopharyngeal mass with central low attenuation. Axial T2-weighted (**c**) and fat-suppressed post-contrast T1-weighted (**d**) MR images show that the abnormal lymph node demonstrates high T2 signal and enhancement (*arrows*). Axial T2-weighted (**e**) and fat-suppressed post-contrast T1-weighted (**f**) MR images show heterogeneous signal and enhancement of the bulky nasopharyngeal mass. DWI (**g**) and ADC map (**h**) show diffusion restriction within portions of the nasopharyngeal lesion

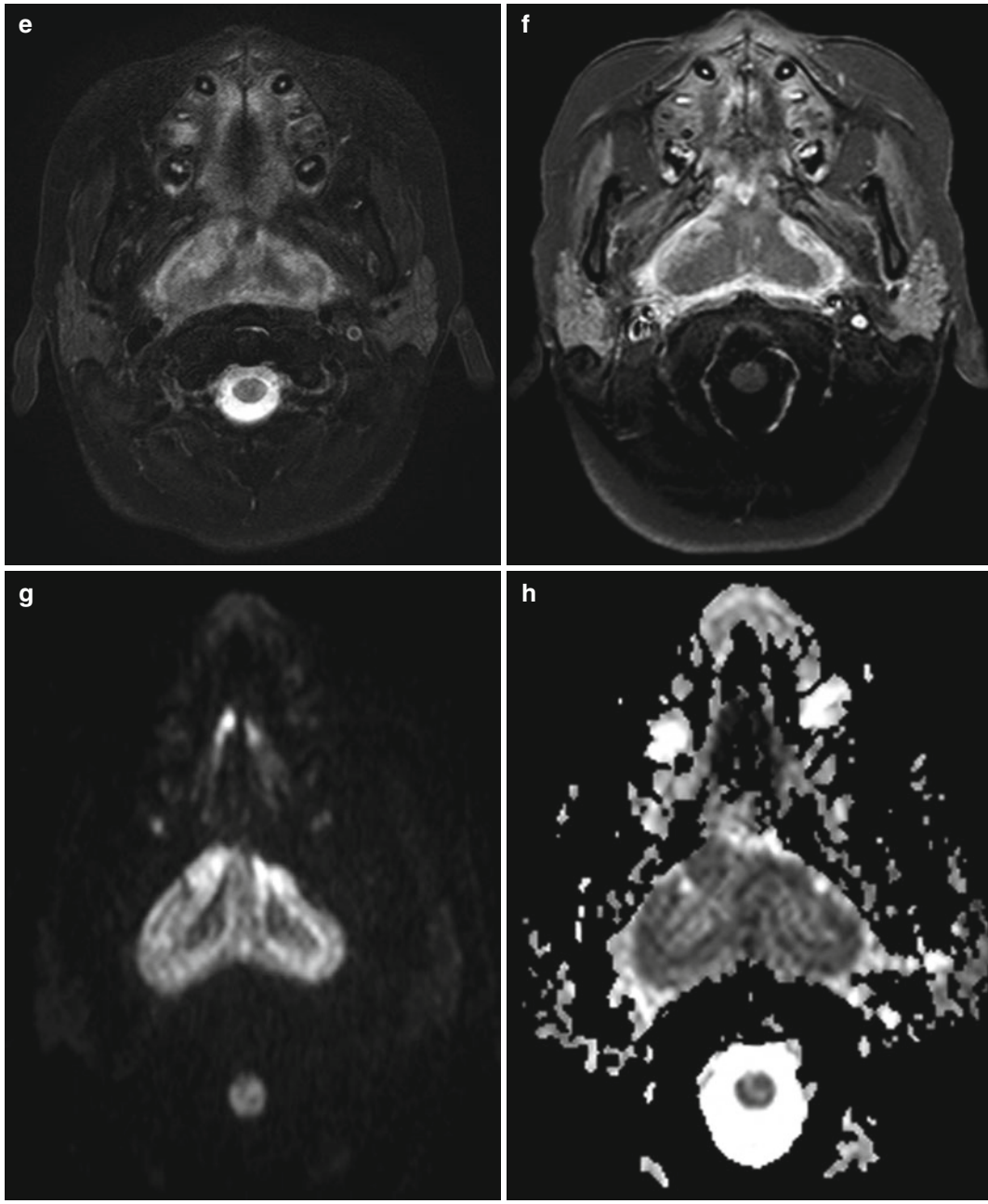

Fig. 23.3 (continued)

that are relatively normal in size. The Waldeyer ring lesions often display central necrosis and submucosal extension into the parapharyngeal space. The main treatment for PTLD is reduction of the immunosuppressive therapy.

23.4 Differential Diagnosis

Differential considerations for CNI-related PRES include other etiologies of PRES: hypertension, other drugs, toxemia of pregnancy, as well as other

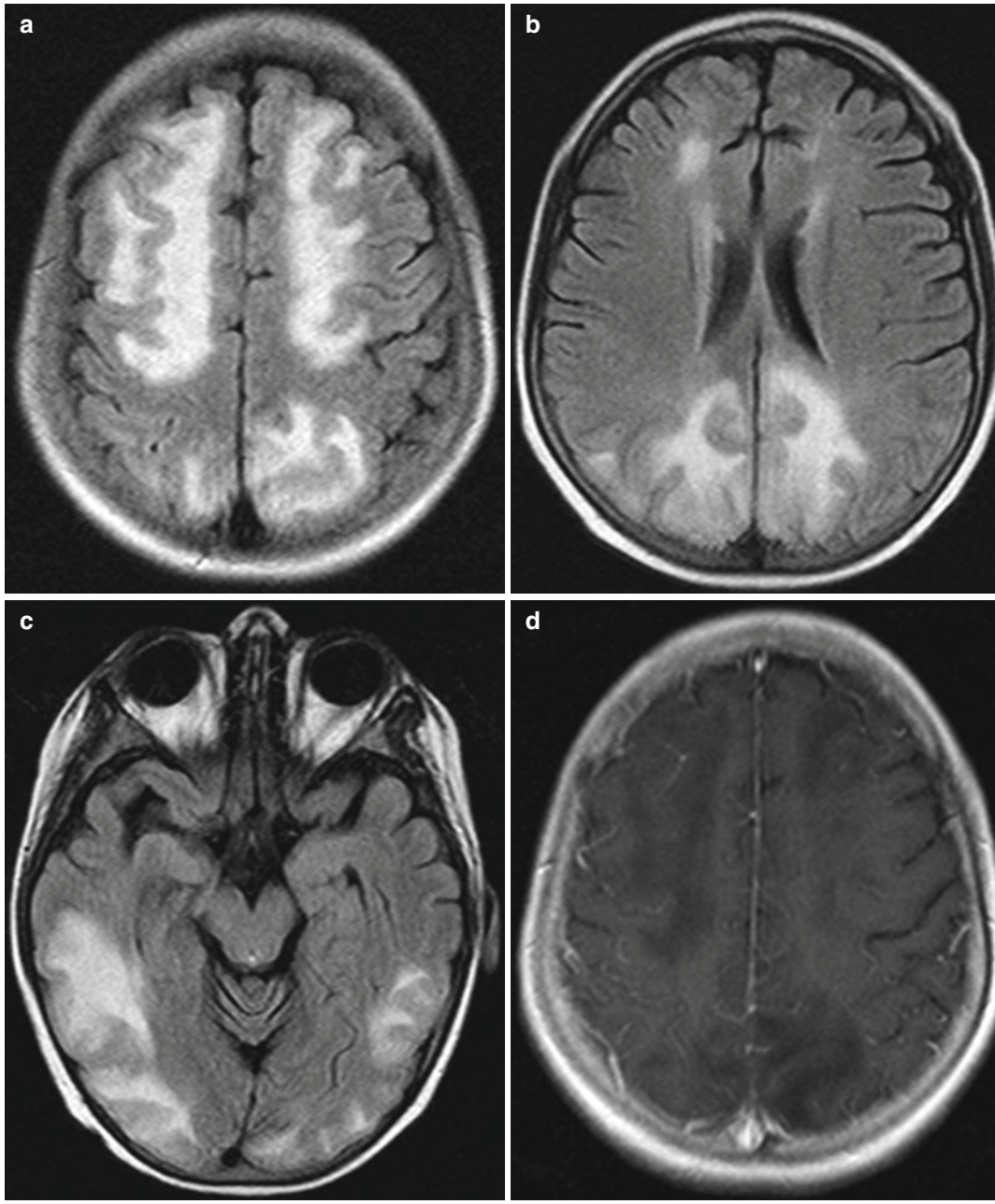

Fig. 23.4 PRES secondary to high-dose combination chemotherapy. Axial FLAIR MR images (**a**–**c**) demonstrate symmetric areas of hyperintensity involving the cortex and subcortical white matter of the paramedian frontal, parietal, and occipital lobes as well as the posterior temporal lobes. There is no evidence of associated abnormal enhancement on the post-contrast T1-weighted MRI (**d**). However, there is elevated diffusivity in the affected areas shown on the ADC map (**e**). The MRI obtained 4 months later (**f**–**h**) shows marked involution of the edema and a few residual punctate foci of hemorrhage in the previously affected sites (*encircled*)

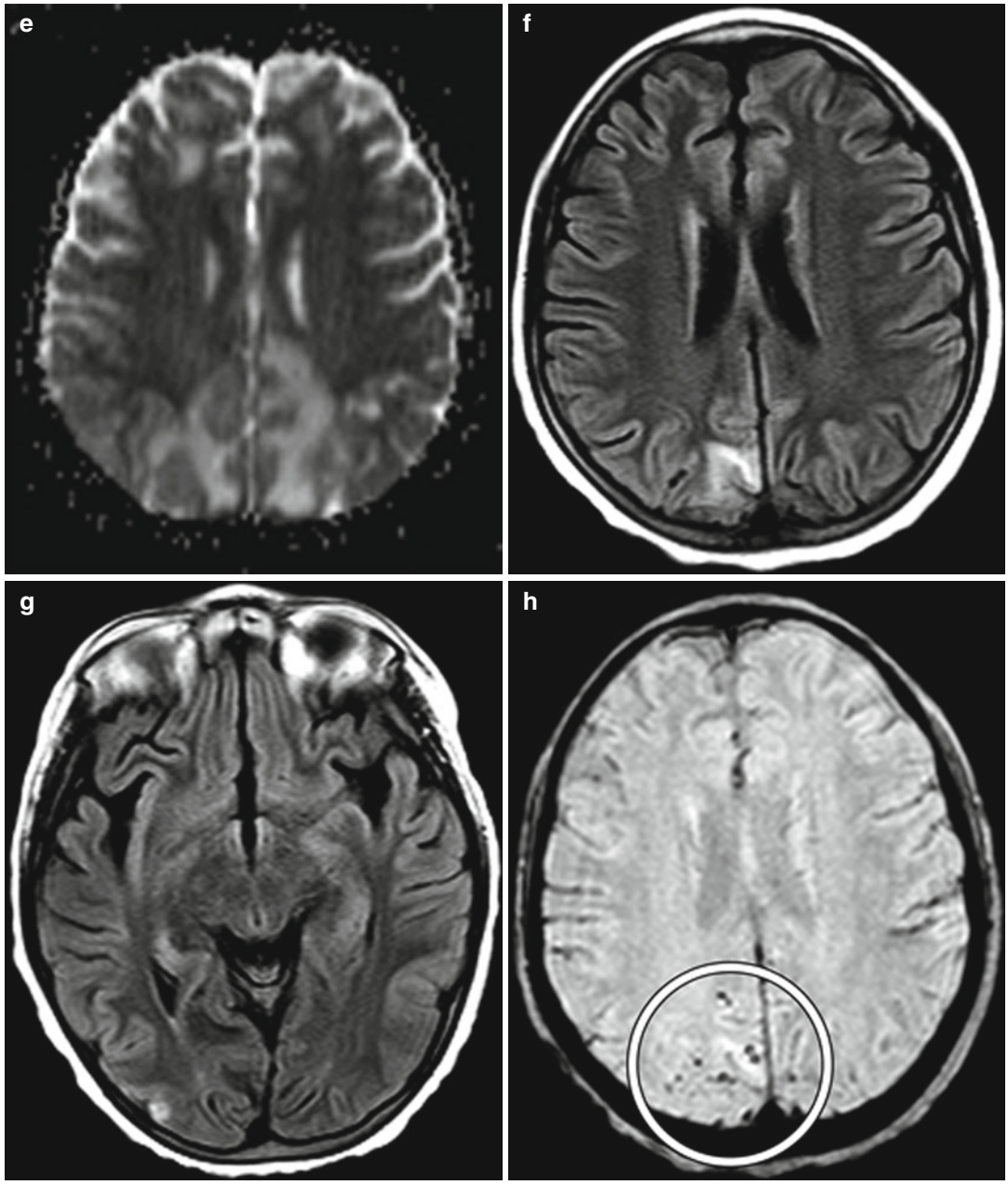

Fig. 23.4 (continued)

non-PRES cortical/subcortical signal abnormalities. PRES has been associated with several other conditions including hypertension, preeclampsia/eclampsia, and other pharmaceuticals and drugs, such as combination high-dose chemotherapy (Fig. 23.4), cisplatin, bevacizumab, triple-H therapy, and cocaine (also refer to Chaps. 6 and 9). Infarction can be distinguished from PRES where there is involvement of a discrete vascular territory and the presence of steno-occlusive lesions with decreased perfusion. Seizures can present as areas of cortical and subcortical T2 hyperintensity

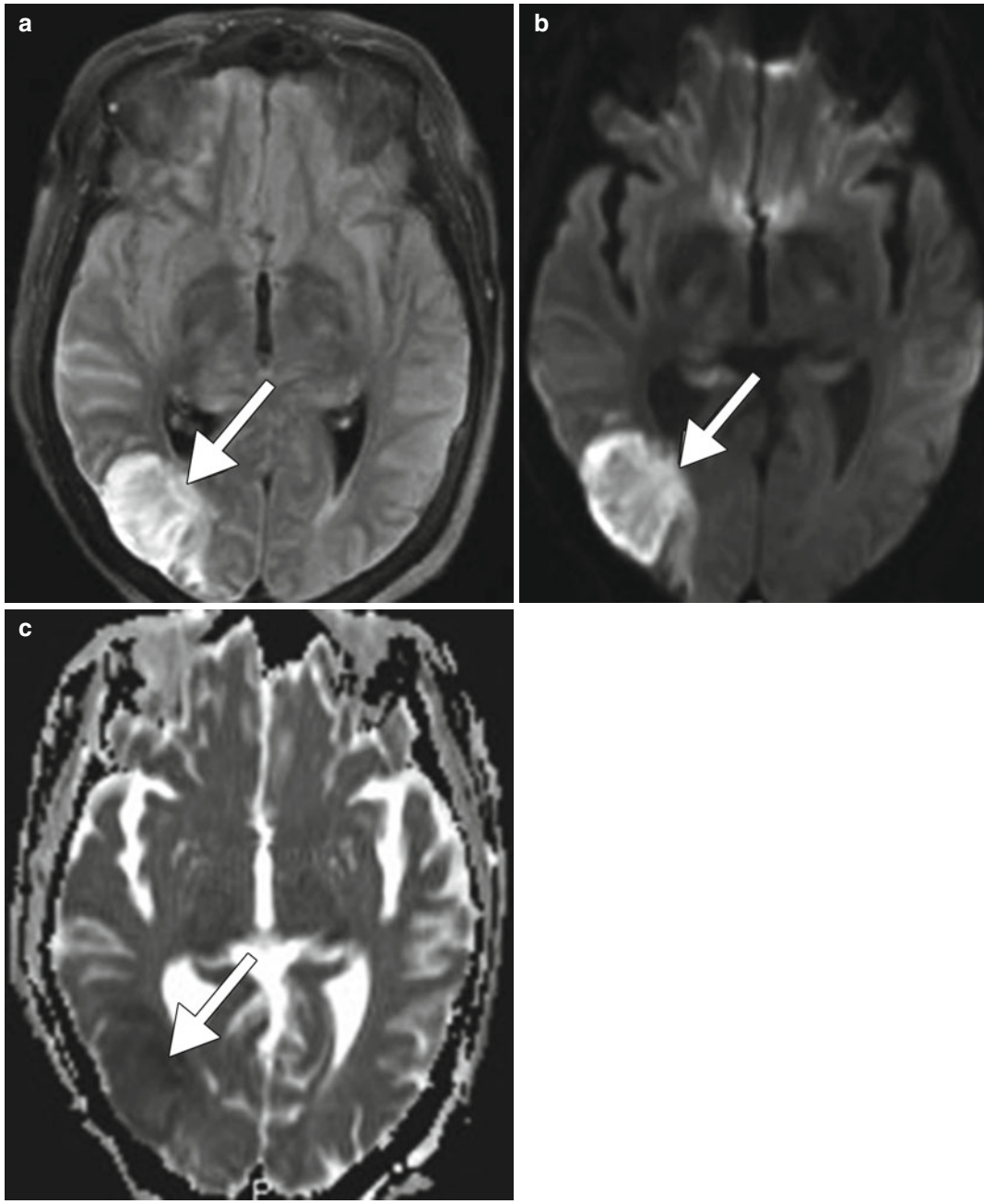

Fig. 23.5 Seizure activity. FLAIR (**a**), DWI (**b**), and ADC map (**c**) cortical and subcortical signal abnormality with corresponding restricted diffusion in the right temporo-occipital region. The abnormality resolved on subsequent imaging

and there can be associated restricted diffusion due to cytotoxic edema (Fig. 23.5).

The differential diagnosis for CNS PTLD includes primary CNS lymphoma, infection, and infarct. Distinguishing the contrast-enhancing lesions of CNS PTLDs or PCNSLs from infection by neuroimaging is not always possible, and a tissue-based diagnosis may be necessary.

Primary CNS lymphoma in immunocompetent patients tends to enhance homogeneously and occur

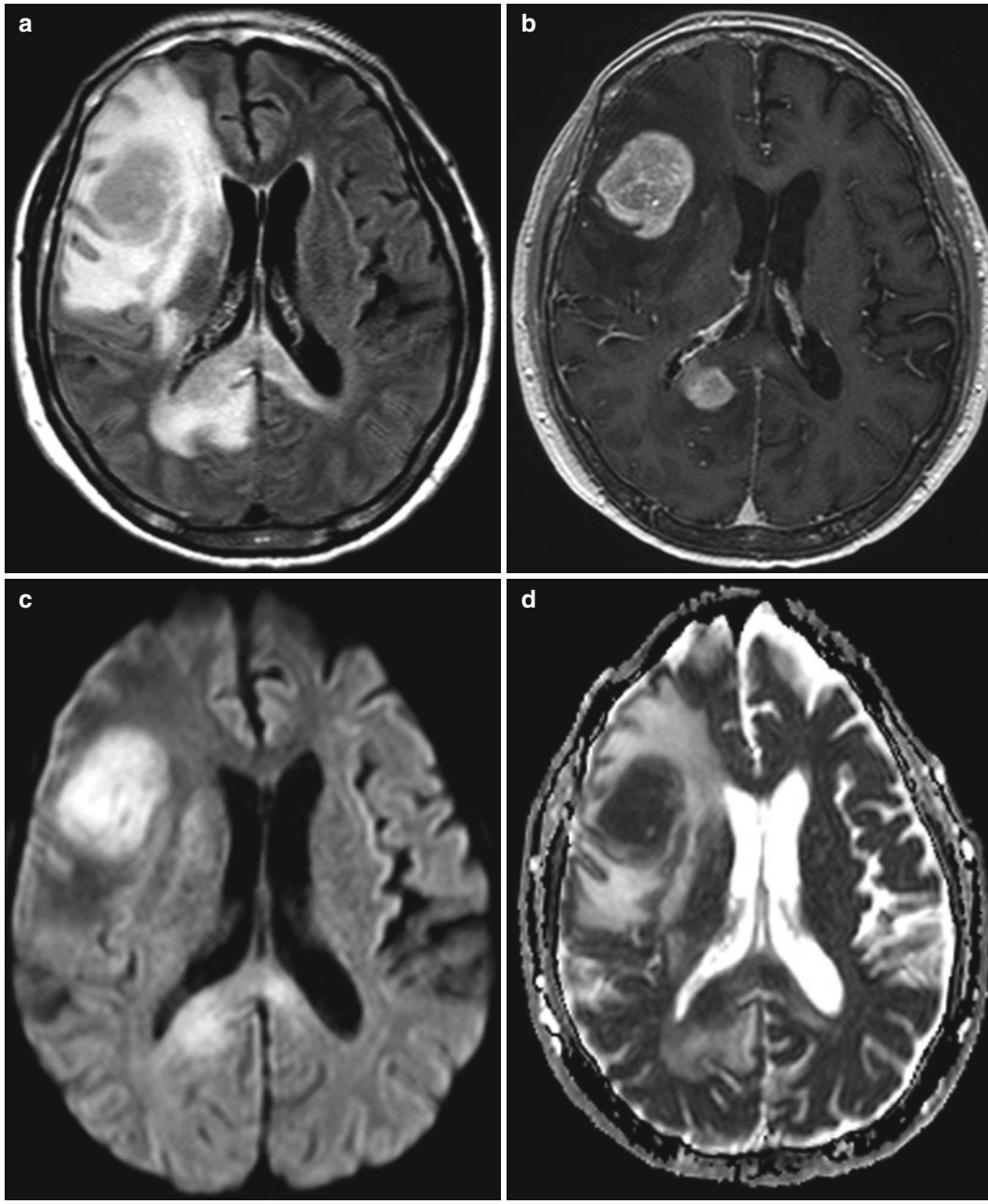

Fig. 23.6 Primary CNS lymphoma. Axial FLAIR MRI (**a**), post-contrast axial T1-weighted MRI (**b**), DWI (**c**), and ADC map (**d**) show multiple homogeneously enhancing periventricular lesions with restricted diffusion

in the periventricular region (Fig. 23.6), while CNS PTLD lesions tend to have a more lobar distribution and may demonstrate more heterogeneous enhancement. Both may demonstrate restricted diffusion. Masses with low attenuation on CT scans or fluid signal intensity on MRI should not be mistaken for abscesses. However, nasopharyngeal abscesses are rare entities and often result from extension of infection that began elsewhere, such as from petrous apicitis or peritonsillar abscess. Alternatively, head and neck PTLD can resemble squamous cell carcinoma, lymphoma, and

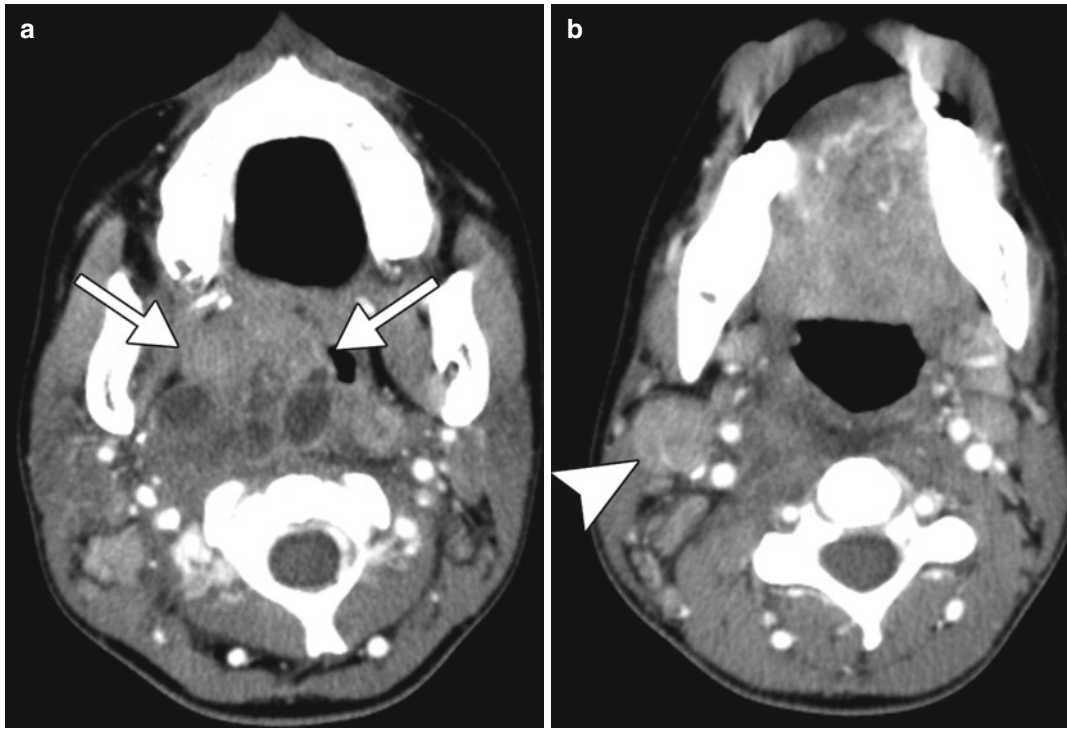

Fig. 23.7 Nasopharyngeal carcinoma. Axial CT images (**a**, **b**) show a bulky necrotic mass centered in the right nasopharynx (*arrows*) and associated right cervical lymphadenopathy (*arrowhead*)

nasopharyngeal carcinoma (Fig. 23.7). Ultimately, the presence of lesions in the Waldeyer ring and/or cervical lymphadenopathy in patients who have undergone organ transplantation and immunosuppressive therapy should increase the index of suspicion for the diagnosis of PTLD.

Suggested Reading

Bartynski WS. Posterior reversible encephalopathy syndrome, part 1: fundamental imaging and clinical features. AJNR Am J Neuroradiol. 2008a;29(6):1036–42.

Bartynski WS. Posterior reversible encephalopathy syndrome, part 2: controversies surrounding pathophysiology of vasogenic edema. AJNR Am J Neuroradiol. 2008b;29(6):1043–9.

Bartynski WS, Tan HP, Boardman JF, Shapiro R, Marsh JW. Posterior reversible encephalopathy syndrome after solid organ transplantation. AJNR Am J Neuroradiol. 2008;29(5):924–30.

Cox KL, Lawrence-Miyasaki LS, Garcia-Kennedy R, Lennette ET, Martinez OM, Krams SM, Berquist WE, So SK, Esquivel CO. An increased incidence of Epstein-Barr virus infection and lymphoproliferative disorder in young children on FK506 after liver transplantation. Transplantation. 1995;59(4):524–9.

Evens AM, Choquet S, Kroll-Desrosiers AR, Jagadeesh D, Smith SM, Morschhauser F, Leblond V, Roy R, Barton B, Gordon LI, Gandhi MK, Dierickx D, Schiff D, Habermann TM, Trappe R. Primary CNS posttransplant lymphoproliferative disease (PTLD): an international report of 84 cases in the modern era. Am J Transplant. 2013 Apr;3.

Gordon AR, Loevner LA, Sonners AI, Bolger WE, Wasik MA. Posttransplantation lymphoproliferative disorder of the paranasal sinuses mimicking invasive fungal sinusitis: case report. AJNR Am J Neuroradiol. 2002;23(5):855–7.

Lattyak BV, Rosenthal P, Mudge C, Roberts JP, Renze JF, Osorio RW, Emond JC, Lalwani AK. Posttransplant lymphoproliferative disorder presenting in the head and neck. Laryngoscope. 1998;108(8 Pt 1):1195–8.

Loevner LA, Karpati RL, Kumar P, Yousem DM, Hsu W, Montone KT. Posttransplantation lymphoproliferative disorder of the head and neck: imaging features in seven adults. Radiology. 2000;216(2):363–9.

McDonald RA, Smith JM, Ho M, Lindblad R, Ikle D, Grimm P, Wyatt R, Arar M, Liereman D, Bridges N, Harmon W, CCTPT Study Group. Incidence of PTLD in pediatric renal transplant recipients receiving

basiliximab, calcineurin inhibitor, sirolimus and steroids. Am J Transplant. 2008;8(5):984–9.

McKinney AM, Sarikaya B, Gustafson C, Truwit CL. Detection of microhemorrhage in posterior reversible encephalopathy syndrome using susceptibility-weighted imaging. AJNR Am J Neuroradiol. 2012; 33(5):896–903.

Santos MM, Tannuri AC, Gibelli NE, Ayoub AA, Maksoud-Filho JG, Andrade WC, Velhote MC, Silva MM, Pinho ML, Miyatani HT, Susuki L, Tannuri U. Posterior reversible encephalopathy syndrome after liver transplantation in children: a rare complication related to calcineurin inhibitor effects. Pediatr Transplant. 2011;15(2):157–60.

Serkova NJ, Christians U, Benet LZ. Biochemical mechanisms of cyclosporine neurotoxicity. Mol Interv. 2004;4(2):97–107.

Shapiro R, Nalesnik M, McCauley J, Fedorek S, Jordan ML, Scantlebury VP, Jain A, Vivas C, Ellis D, Lombardozzi-Lane S, Randhawa P, Johnston J, Hakala TR, Simmons RL, Fung JJ, Starzl TE. Posttransplant lymphoproliferative disorders in adult and pediatric renal transplant patients receiving tacrolimus-based immunosuppression. Transplantation. 1999;68(12): 1851–4.

Vargas H, Nazeer T, Conti D, Parnes SM. Posttransplant lymphoproliferative disorder of the nasopharynx. Am J Rhinol. 2002;16(1):37–42.

Bromocriptine (Parlodel) and Cabergoline (Dostinex)

24

Daniel Thomas Ginat

24.1 Uses

Bromocriptine and cabergoline are used as treatment for patients with idiopathic hyperprolactinemia and prolactinomas.

24.2 Mechanism

Bromocriptine and cabergoline are both ergot derivatives, which are dopamine receptor agonists and inhibitors of prolactin secretion. Cabergoline may also inhibit cell viability also by reducing VEGF secretion via dopamine receptor 2 action in some nonfunctioning adenomas.

24.3 Discussion

Cabergoline and bromocriptine are the most commonly used drugs in the treatment of hyperprolactinemia. They are able to normalize prolactin levels, restore gonadal function, and promote tumor reduction in the majority of patients. Dopamine agonist therapy effectively reduces the size of tumors, which can be apparent within 1 week and typically continues for several years (Fig. 24.1). Chiasmal herniation can occur during the course of therapy, but is not necessarily associated with visual symptoms (Fig. 24.2). However, re-enlargement during therapy can occasionally occur. Over time, dopamine agonist therapy typically results in high T2 signal intensity, indicating increased water content in residual solid tumor tissue. Signal intensity changes on MRI may also correspond to the development of cystic cavities or necrosis and transitions from one pattern to another are also common (Fig. 24.3). Bromocriptine significantly increases the incidence of intratumoral hemorrhage, mainly in tumors with high initial serum prolactin levels. Cabergoline appears to be more efficacious and associated with fewer adverse events than bromocriptine, but intratumoral hemorrhage may nevertheless occur during treatment. This condition can manifest as T1 hyperintensity and fluid-fluid levels within the tumor on MRI (Fig. 24.4). Patients with intratumoral hemorrhage are generally asymptomatic, but some patients may experience headaches, visual field cuts, or cranial nerve deficits.

D.T. Ginat, MD, MS
Department of Radiology, University of Chicago,
Pritzker Medical School, Chicago, IL, USA
e-mail: ginatd01@gmail.com

D.T. Ginat et al. (eds.), *Neuroimaging Pharmacopoeia*,
DOI 10.1007/978-3-319-12715-6_24,

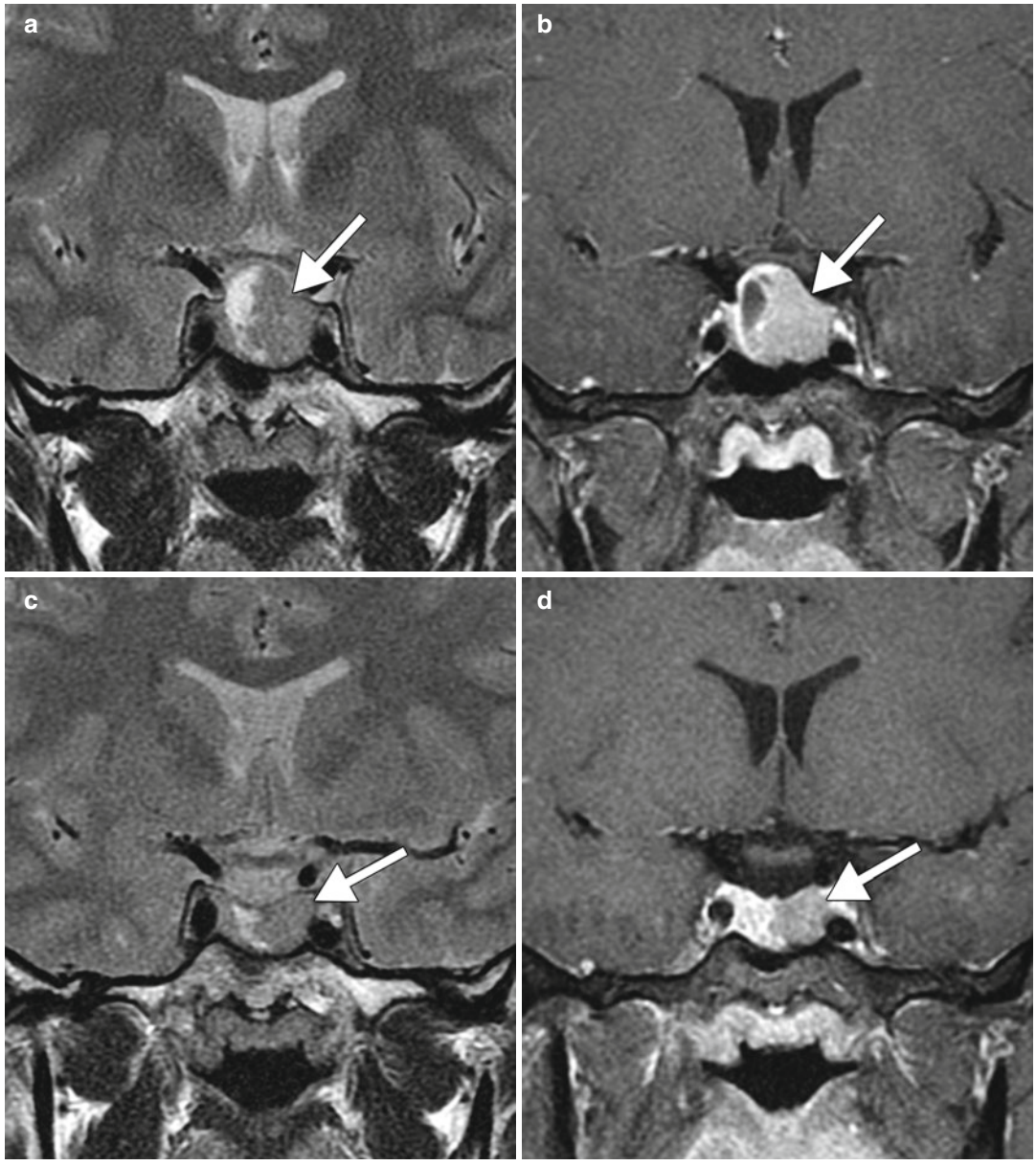

Fig. 24.1 Tumor shrinkage. Coronal T2-weighted (**a**) and coronal post-contrast T1-weighted (**b**) MR images show a pituitary prolactinoma (*arrows*) that compresses the optic apparatus. Coronal T2-weighted (**c**) and coronal post-contrast T1-weighted (**d**) MR images obtained several months after treatment with bromocriptine show interval marked decrease in size of the mass (*arrows*) and no residual compression of the optic apparatus

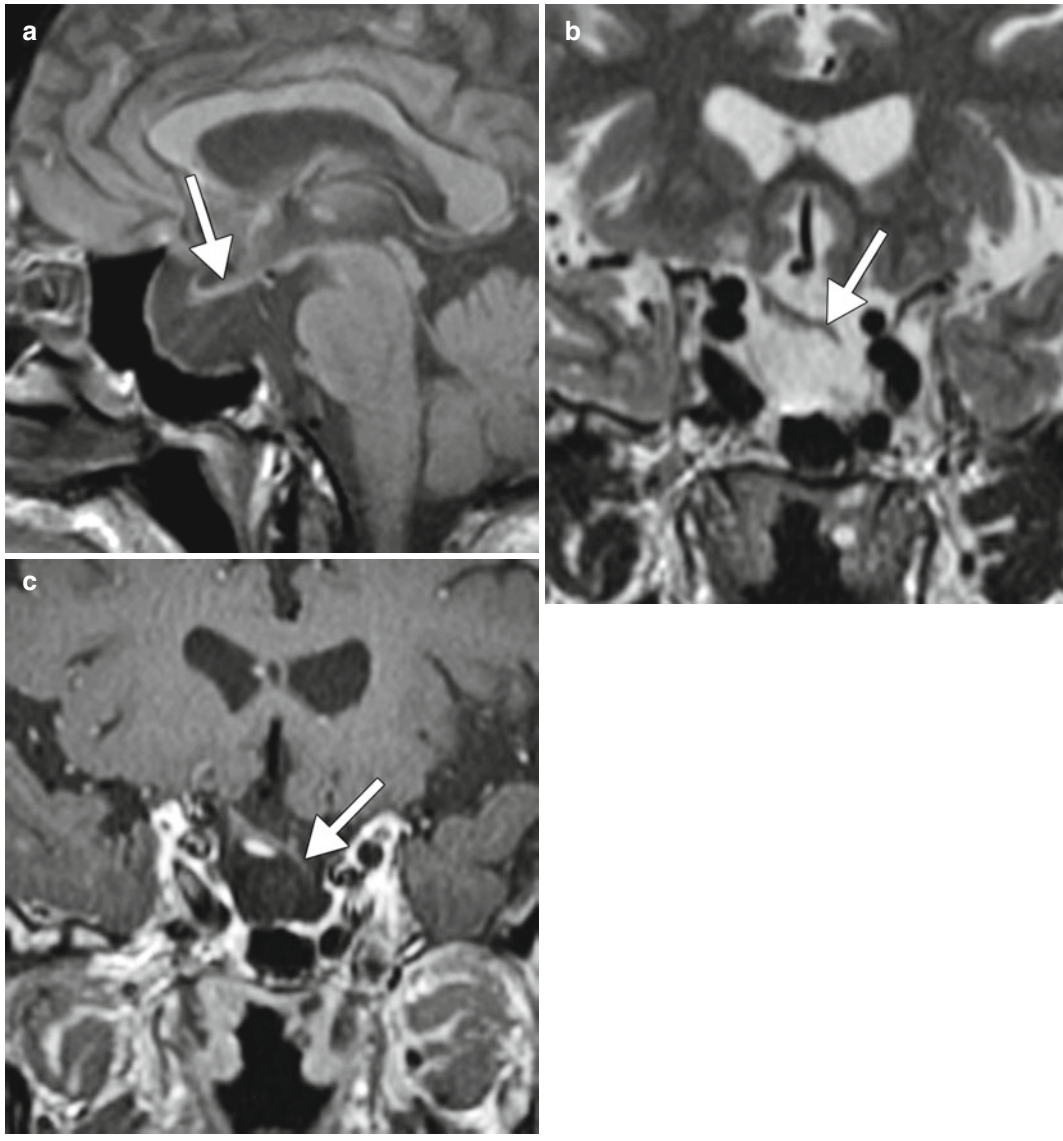

Fig. 24.2 Chiasmal herniation. MR images from a patient with a history of pituitary adenoma, treated with bromocriptine long ago. Of note, the patient never had pituitary surgery. Sagittal T1-weighted (**a**), coronal T2-weighted (**b**), and coronal post-contrast T1-weighted (**c**) MR images show an expanded empty sella with a distorted and inferiorly displaced optic chiasm, particularly on the left side (*arrows*)

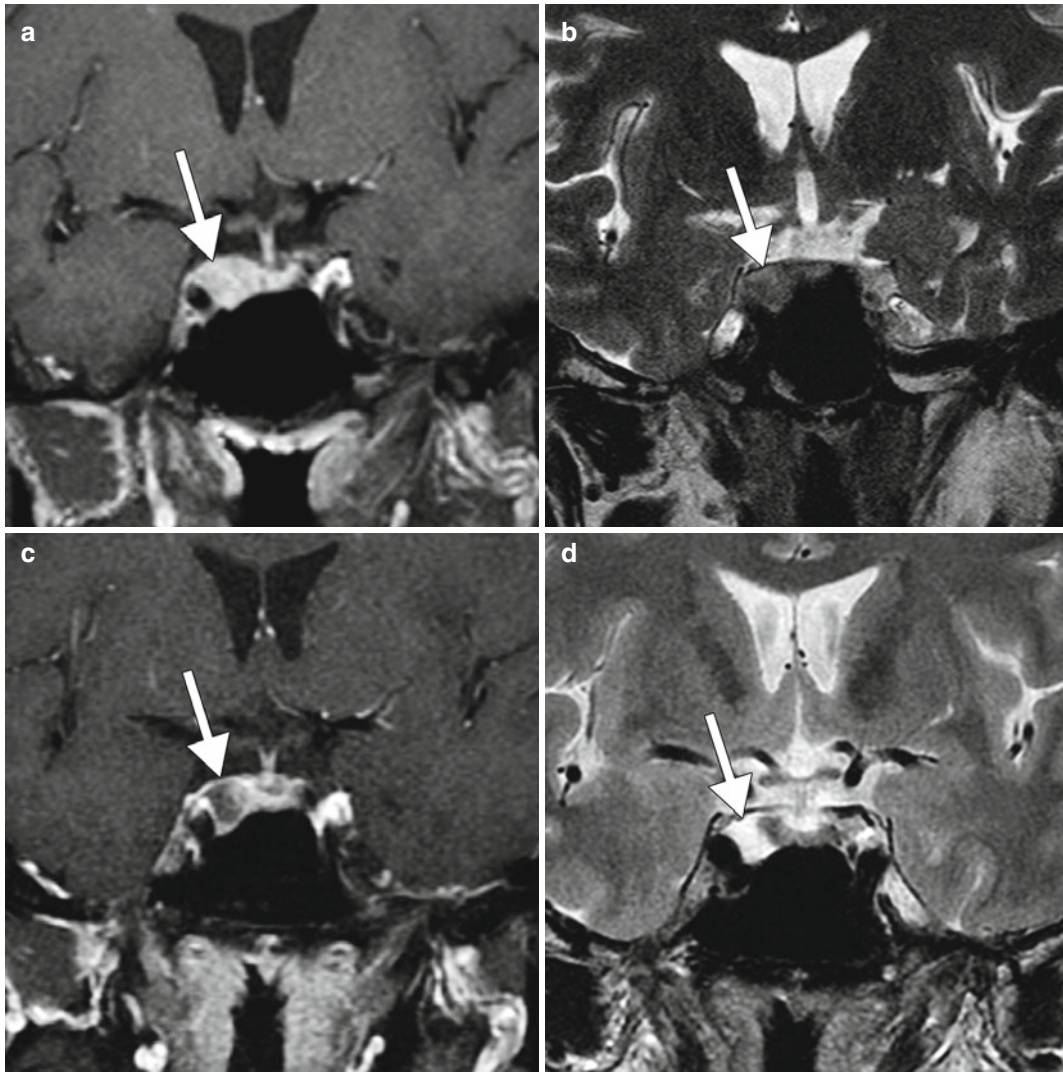

Fig. 24.3 Cystic change. Coronal post-contrast T1-weighted (**a**) and coronal T2-weighted (**b**) MR images before cabergoline treatment show an enhancing T2 hypointense right pituitary microadenoma (*arrows*). Coronal post-contrast T1-weighted (**c**) and coronal T2-weighted (**d**) MR images obtained several months after cabergoline therapy show interval lack of enhancement and T2 hyperintensity with in the lesion (*arrows*)

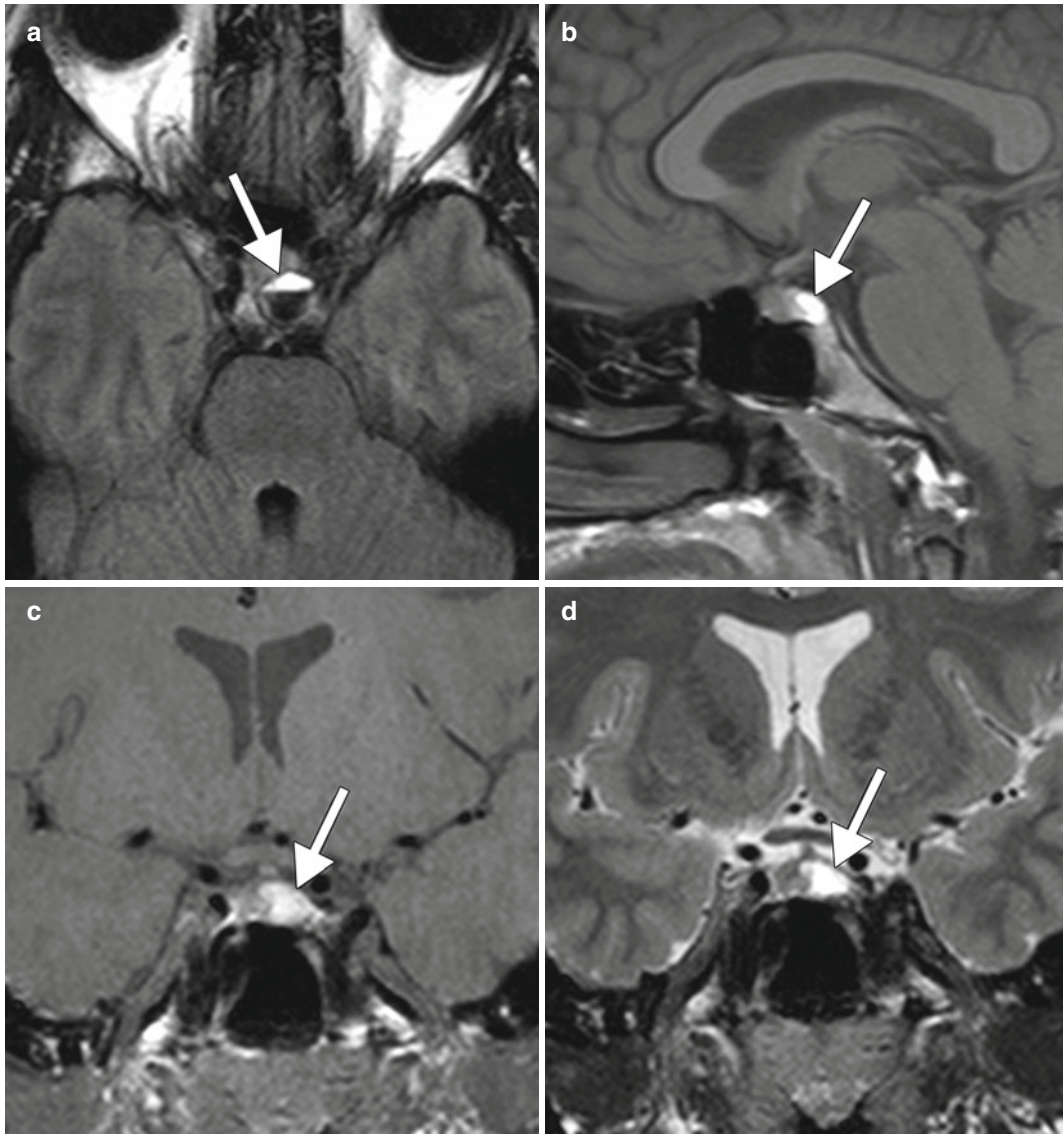

Fig. 24.4 Intratumoral hemorrhage. Axial FLAIR (**a**), sagittal T1-weighted (**b**), coronal T1-weighted (**c**), and coronal T2-weighted (**d**) MR images obtained shortly after starting cabergoline treatment shows hemorrhage within a left pituitary microadenoma with a fluid-fluid level (*arrows*). Follow-up coronal T1-weighted (**e**) and coronal T2-weighted (**f**) MR images obtained several months later show resolution of the hemorrhage with overall slight interval decrease in size of the lesion

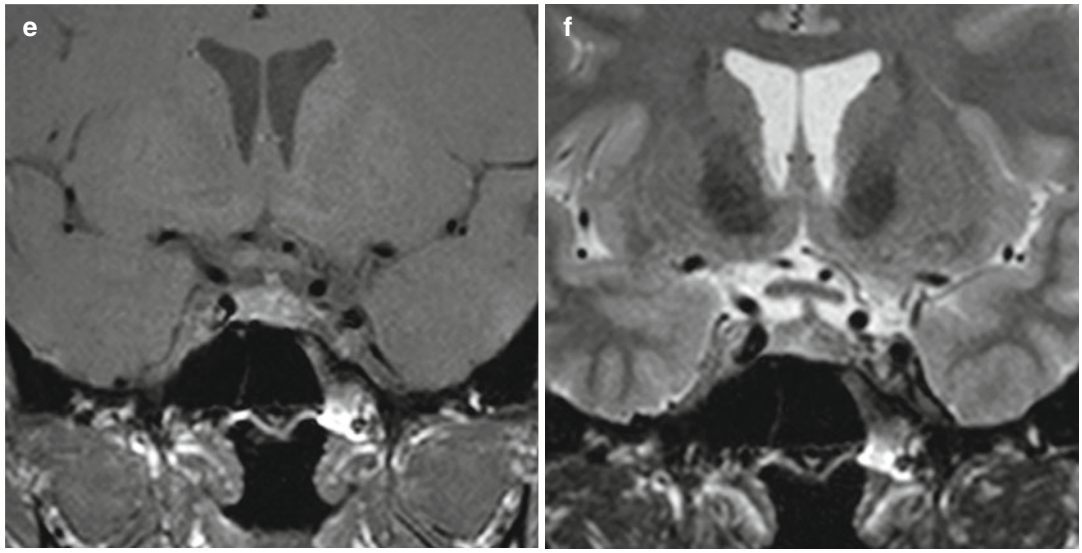

Fig. 24.4 (continued)

24.4 Differential Diagnosis

Pituitary tumors, particularly macroadenomas, may undergo spontaneous hemorrhage without dopamine agonist therapy (Fig. 24.5). Alternatively, apoplexy may occur in pituitary glands that do not contain tumors, particularly in the postpartum period (Sheehan syndrome). Other conditions may resemble hemorrhage, such as cystic tumors, including Rathke cleft cysts, which may also contain layering debris or a T2 hypointense nodule (Fig. 24.6).

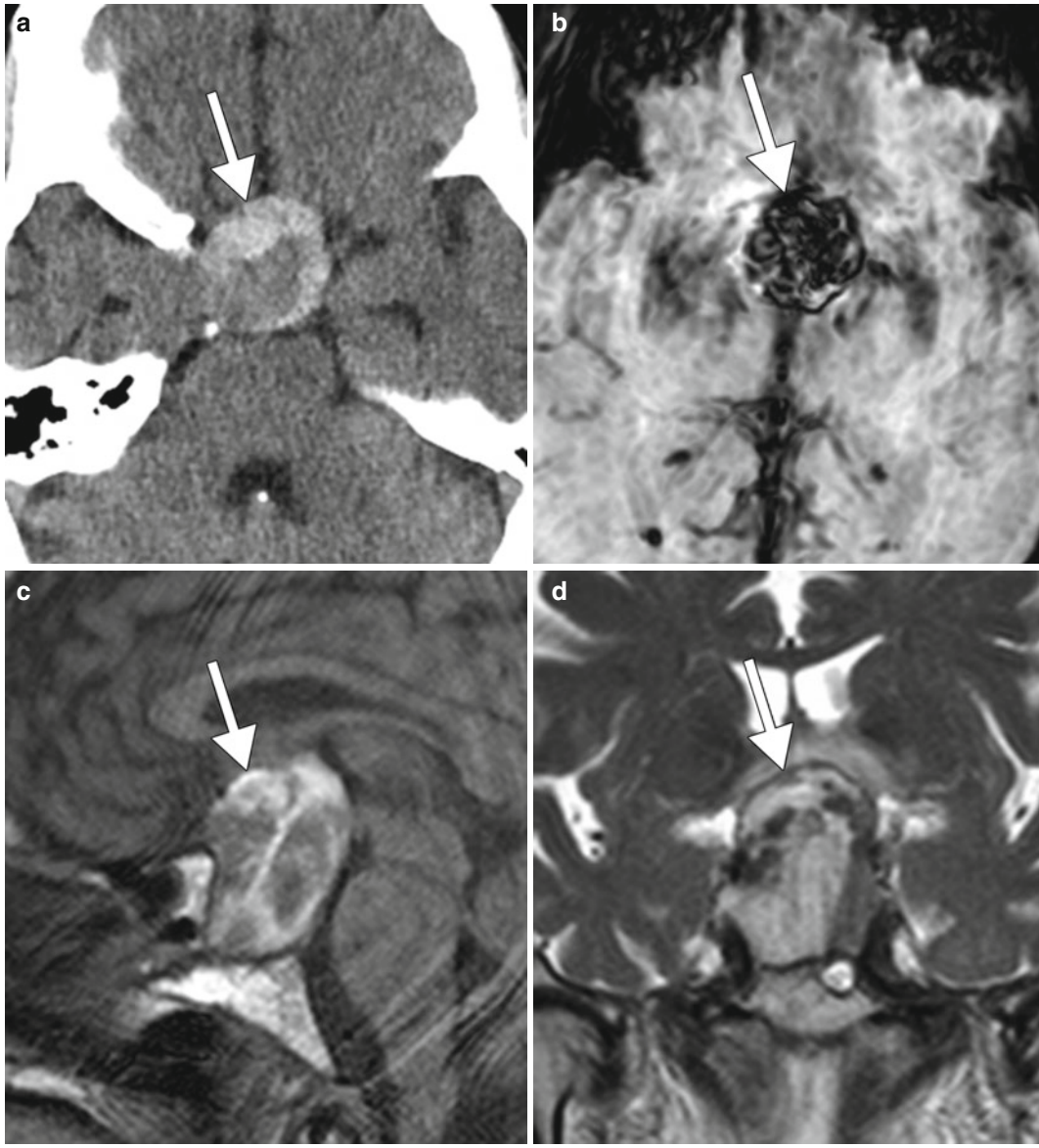

Fig. 24.5 Spontaneous pituitary apoplexy in a pituitary macroadenoma. Axial CT image (**a**) shows a heterogeneously hyperattenuating suprasellar mass (*arrow*). There is corresponding susceptibility effect within the mass on the susceptibility-weighted image (**b**) due to hemorrhage (*arrow*). Sagittal T1-weighted (**c**) and coronal T2-weighted (**d**) MR images show heterogeneous signal within the mass (*arrows*) with areas of intrinsically hyperintense T1 signal consistent with hemorrhage

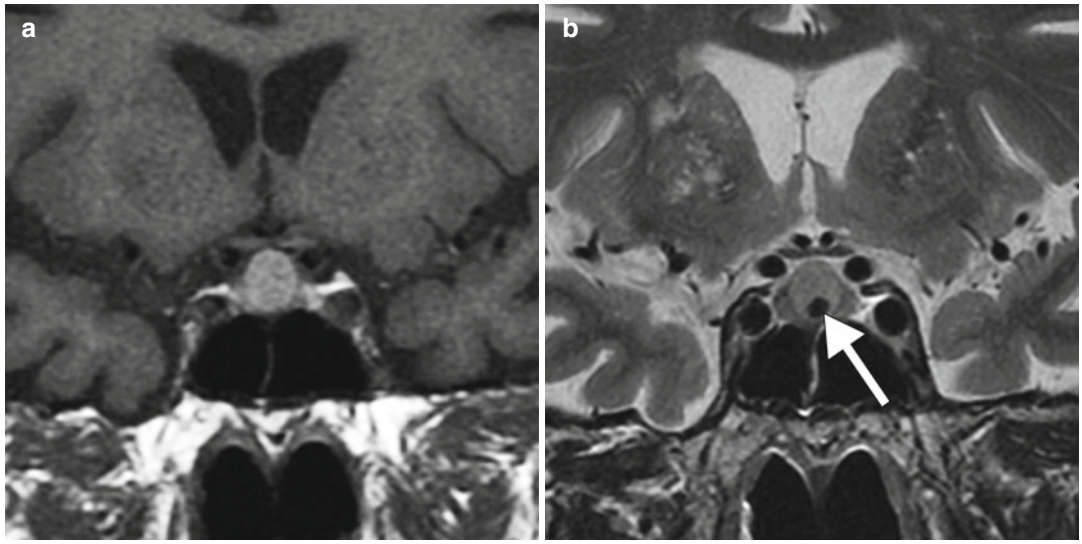

Fig. 24.6 Rathke cleft cyst. Coronal T1-weighted (**a**) and coronal T2-weighted (**b**) MR images show a midline cyst sellar lesion that contains material with intrinsic T1 shortening and a T2 hypointense nodule (*arrow*)

Suggested Reading

Balarini Lima GA, Machado Ede O, Dos Santos Silva CM, Filho PN, Gadelha MR. Pituitary apoplexy during treatment of cystic macroprolactinomas with cabergoline. Pituitary. 2008;11(3):287–92.

dos Santos Nunes V, El Dib R, Boguszewski CL, Nogueira CR. Cabergoline versus bromocriptine in the treatment of hyperprolactinemia: a systematic review of randomized controlled trials and meta-analysis. Pituitary. 2011;14(3):259–65.

Gagliano T, Filieri C, Minoia M, Buratto M, Tagliati F, Ambrosio MR, Lapparelli M, Zoli M, Frank G, Degli Uberti E, Zatelli MC. Cabergoline reduces cell viability in non functioning pituitary adenomas by inhibiting vascular endothelial growth factor secretion. Pituitary. 2013;16(1):91–100.

Lundin P, Bergström K, Nyman R, Lundberg PO, Muhr C. Macroprolactinomas: serial MR imaging in long-term bromocriptine therapy. AJNR Am J Neuroradiol. 1992;13(5):1279–91.

Menucci M, Quiñones-Hinojosa A, Burger P, Salvatori R. Effect of dopaminergic drug treatment on surgical findings in prolactinomas. Pituitary. 2011;14(1):68–74.

Mikhael MA, Ciric IS. MR imaging of pituitary tumors before and after surgical and/or medical treatment. J Comput Assist Tomogr. 1988;12(3):441–5.

Molitch ME. Medical treatment of prolactinomas. Endocrinol Metab Clin North Am. 1999;28(1):143–69, vii.

Rains CP, Bryson HM, Fitton A. Cabergoline. A review of its pharmacological properties and therapeutic potential in the treatment of hyperprolactinaemia and inhibition of lactation. Drugs. 1995;49(2):255–79.

Taxel P, Waitzman DM, Harrington Jr JF, Fagan RH, Rothfield NF, Chen HH, Malchoff CD. Chiasmal herniation as a complication of bromocriptine therapy. J Neuroophthalmol. 1996;16(4):252–7.

Yousem DM, Arrington JA, Zinreich SJ, Kumar AJ, Bryan RN. Pituitary adenomas: possible role of bromocriptine in intratumoral hemorrhage. Radiology. 1989;170(1 Pt 1):239–43.

Metronidazole (Flagyl) 25

Daniel Thomas Ginat

25.1 Uses

Metronidazole is used for the treatment of anaerobic and protozoan infections and prevention of clinical recurrence in Crohn's disease.

25.2 Mechanism

The nitroimidazole antibiotic enters cells as a prodrug by passive diffusion and exerts its cytotoxic effects by production of nitroso free radicals, which leads to DNA breakage and cell death. Metronidazole can easily penetrate the CSF and the central nervous system. The reason for the toxicity is not well elucidated, but is presumably attributable to axonal swelling with increased water content, which may result from local vasospasm and ischemia (Fig. 25.1).

25.3 Discussion

Metronidazole toxicity can produce a characteristic encephalopathy that manifests as ataxia, peripheral neuropathy, and seizures. Affected patients may have normal or toxic serum concentrations. On MRI, high T2 signal in the dentate nuclei is the earliest and most common finding. This initial finding is followed by involvement of the tectum, red nucleus, periaqueductal gray matter, and dorsal pons. The dorsal medulla and the corpus callosum are less commonly involved. Lesions are often bilateral and symmetric, and the splenium is affected in all cases in which the corpus callosum is involved. The lesions are usually characterized by elevated ADC, consistent with vasogenic edema. The lesions do not enhance and do not have significant mass effect. Involvement of supratentorial structures appears to correlate with the severity of toxicity. The abnormal findings on MRI and clinical symptoms typically improve within 8 weeks following discontinuation of metronidazole.

25.4 Differential Diagnosis

The main differential consideration for metronidazole-induced encephalopathy is acute Wernicke's encephalopathy associated with alcohol abuse. Wernicke's encephalopathy is characterized by bilateral symmetric T2 hyperintense lesions in the regions of the mammillary bodies, medial thalami, floor of the third ventricle, periaqueductal gray matter, and tectum of the midbrain.

Other imaging differential diagnoses to consider for metronidazole-induced encephalopathy depend on the particular anatomic sites of involvement:

- *Brainstem*: Osmotic demyelination involves the basis pontis (refer to Chaps. 2 and 36), while metronidazole-induced encephalopathy affects the dorsal pons and nuclear structures.

D.T. Ginat, MD, MS
Department of Radiology, University of Chicago, Pritzker Medical School, Chicago, IL, USA
e-mail: ginatd01@gmail.com

D.T. Ginat et al. (eds.), *Neuroimaging Pharmacopoeia*,
DOI 10.1007/978-3-319-12715-6_25,

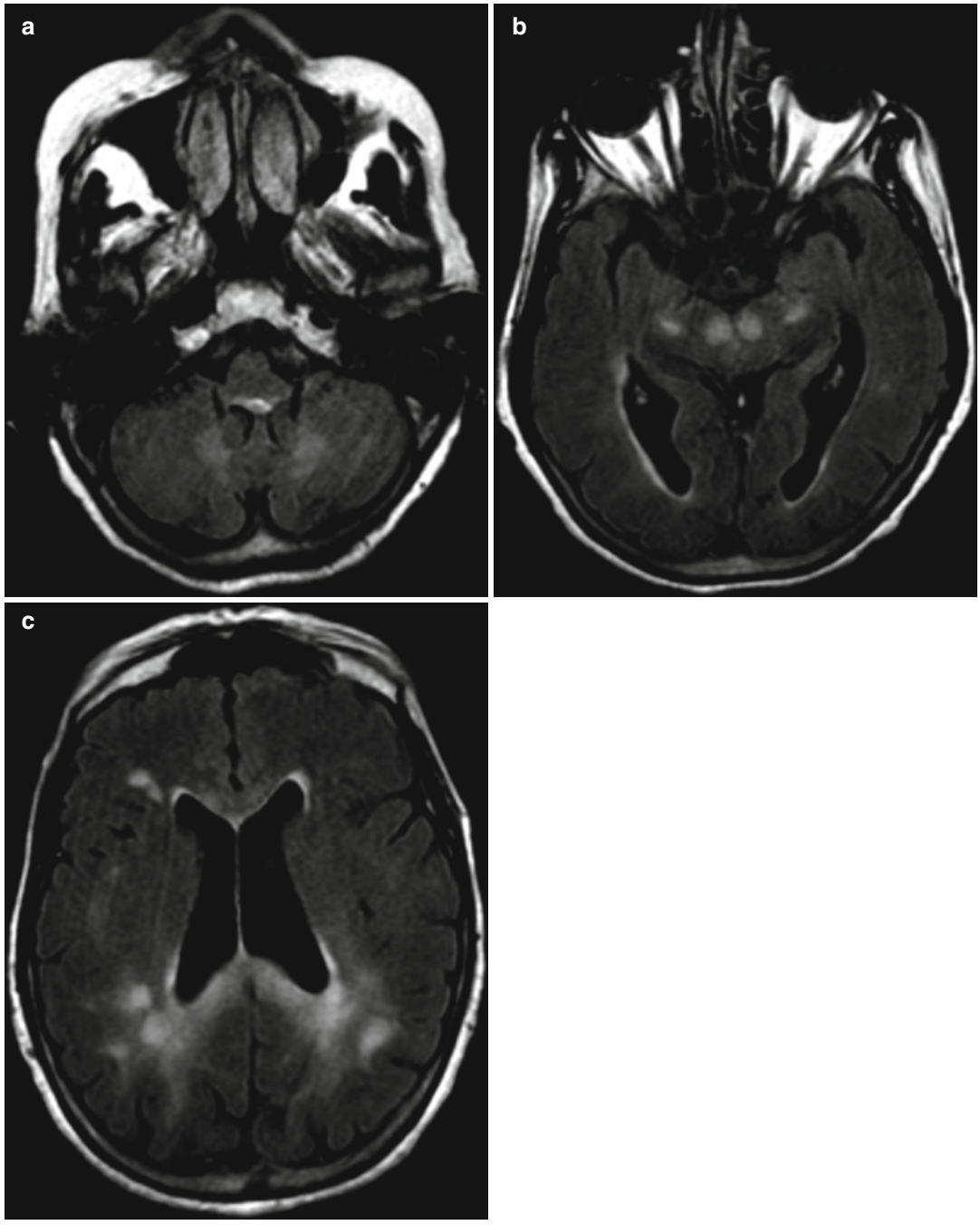

Fig. 25.1 Metronidazole-induced encephalopathy. FLAIR MR images (**a**–**c**) at the time of presentation show bilateral symmetric high signal within the dentate nuclei, red nuclei, cerebral peduncles, corpus callosum, and periventricular and subcortical white matter. An MRI obtained 2 months later (not shown) demonstrated decrease in the signal abnormalities

- *Corpus callosum splenium*: Various demyelinating diseases, such as Marchiafava-Bignami disease (refer to Chap. 2), multiple sclerosis, and Susac's disease (refer to Chap. 27); antiepileptic drugs (refer to Chap. 27); acute infectious encephalitis, such as influenza, *Escherichia*

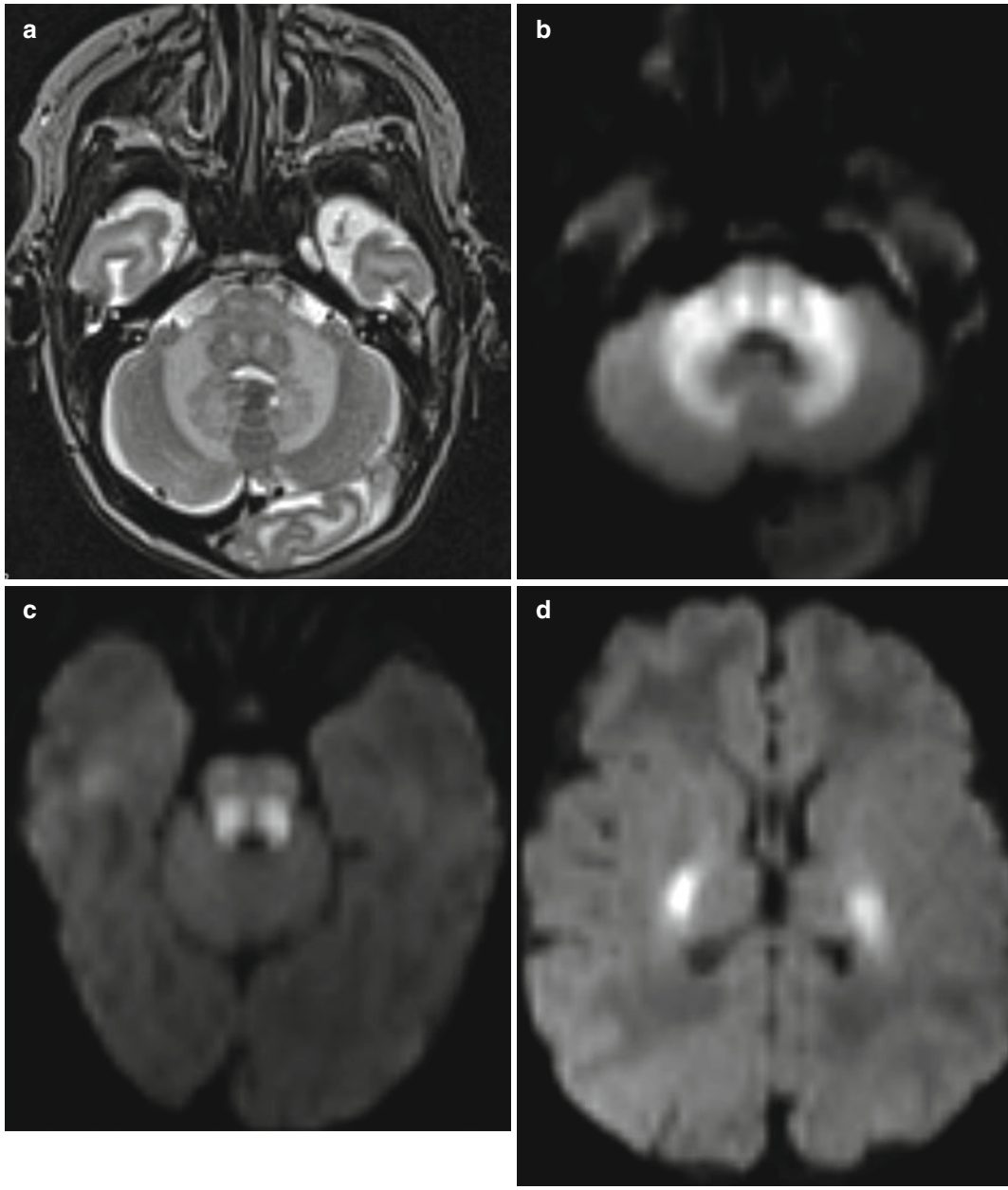

Fig. 25.2 Maple syrup urine disease. Axial T2-weighted MRI (**a**) and diffusion-weighted images (**b**–**d**) show abnormal signal with restricted diffusion involving the bilateral dentate nuclei, brainstem, and corticospinal tracks

coli, mumps, adenovirus, Epstein-Barr virus, and Rotavirus; and acute toxic encephalopathy, such as from methotrexate (refer to Chap. 19) and 5-fluorouracil (refer to Chap. 20), can produce similar findings (Fig. 25.2).

- *Dentate nuclei*: Methyl bromide intoxication, enteroviral encephalomyelitis, and maple syrup urine disease can all produce bilateral dentate nuclei T2 hyperintense lesions (Fig. 25.3).

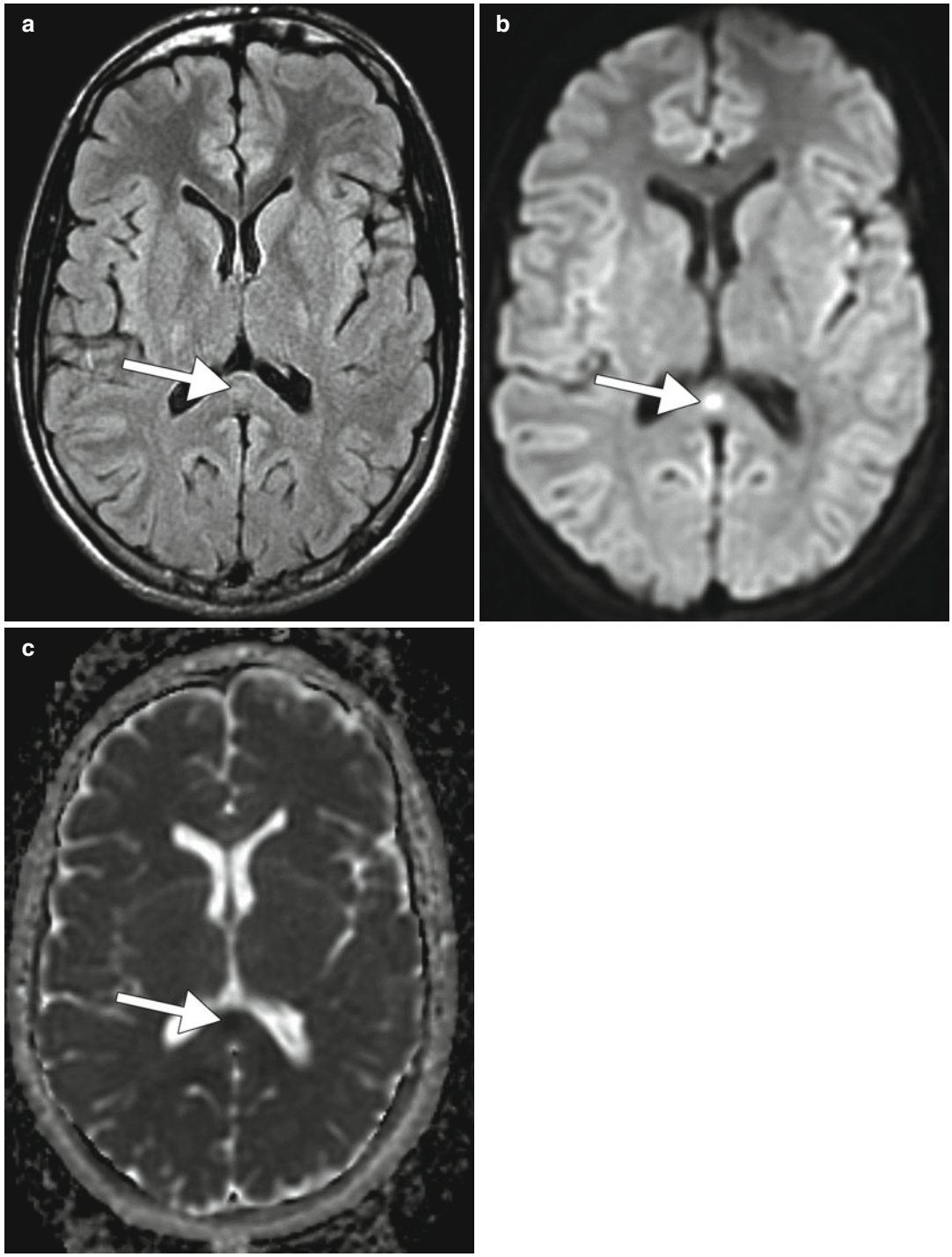

Fig. 25.3 Splenial lesion attributed to influenza infection. The patient tested positive for influenza A. Axial FLAIR (**a**), DWI (**b**), and ADC (**c**) show a focus of high FLAIR signal and restricted diffusion in the midline of the splenium of the corpus callosum (*arrows*)

Suggested Reading

Brismar J, Aqeel A, Brismar G, et al. Maple syrup urine disease: findings on CT and MR scans of the brain in 10 infants. AJNR Am J Neuroradiol. 1990;11:1219–28.

Freeman CD, Klutman NE, Lamp KC. Metronidazole: a therapeutic review and update. Drugs. 1997;54:679–708.

Graves TD, Condon M, Loucaidou M, Perry RJ. Reversible metronidazole-induced cerebellar toxicity in a multiple transplant recipient. J Neurol Sci. 2009;285(1–2):238–40.

Heaney CJ, Campeau NG, Lindell EP. MR imaging and diffusion-weighted imaging changes in metronidazole (Flagyl)-induced cerebellar toxicity. AJNR Am J Neuroradiol. 2003;24(8):1615–7.

Kim E, Na DG, Kim EY, Kim JH, Son KR, Chang KH. MR imaging of metronidazole-induced encephalopathy: lesion distribution and diffusion-weighted imaging findings. AJNR Am J Neuroradiol. 2007;28:1652–8.

Kuriyama A, et al. Metronidazole-induced central nervous system toxicity: a systematic review. Clin Neuropharmacol. 2011;34(6):241–7.

Woodruff BK, Wijdicks EF, Marshall WF. Reversible metronidazole-induced lesions of the cerebellar dentate nuclei. N Engl J Med. 2002;346(1):68–9.

Highly Active Antiretroviral Therapy (HAART)

26

Daniel Thomas Ginat and Pamela Whitney Schaefer

26.1 Uses

Highly active antiretroviral therapy (HAART) is a treatment strategy for HIV (human immunodeficiency virus)-infected patients that consists of administering three or more different drugs, including nucleoside reverse transcriptase inhibitors, protease inhibitors, and non-nucleoside reverse transcriptase inhibitors.

26.2 Mechanism

IRIS results from restored immunity to infectious or noninfectious antigens. Potential mechanisms for the syndrome include a partial recovery of the immune system or exuberant host immunological responses to antigenic stimuli, perhaps related to elevated levels of interleukin-6 (IL-6) and CD8+ T-cell lymphocytic infiltration.

D.T. Ginat, MD, MS
Department of Radiology, University of Chicago, Pritzker Medical School, Chicago, IL, USA
e-mail: ginatd01@gmail.com

P.W. Schaefer, MD
Department of Radiology, Massachusetts General Hospital, Harvard Medical School, Boston, MA, USA

26.3 Discussion

IRIS is an inflammatory response to a subclinical or previously treated infection that occurs after initiation of HAART. CNS IRIS affects approximately 25 % of patients with human immunodeficiency virus (HIV) infection and typically occurs within two months after administration of HAART but may occur up to 2 years later. IRIS can also occur in other immunocompromised patients, such as after stem cell transplantation. The most commonly implicated organisms in the CNS include the JC virus and Cryptococcus. CNS IRIS can also occur with varicella zoster virus (VZV), cytomegalovirus (CMV), *Candida* organisms, *Mycobacterium tuberculosis*, and *Toxoplasma gondii*, or no identifiable organism at all. Diagnostic criteria for IRIS include (1) a prior response to antimicrobial therapy, (2) the return of original symptoms or new inflammatory syndromes after initiation of HAART, and (3) negative CSF cultures. Indeed, IRIS presents with paradoxical clinical deterioration resulting from restoration of the capacity to mount an inflammatory immune response after treatment with antiretroviral drugs.

On imaging, IRIS tends to display parenchymal and/or leptomeningeal contrast enhancement, transient increase in parenchymal abnormalities with high signal on FLAIR and T2-weighted images, and mass effect (Fig. 26.1). Areas of restricted diffusion can also be observed. Ultimately, the neuroimaging features of IRIS vary depending upon the specific underlying pathogen (Table 26.1).

D.T. Ginat et al. (eds.), *Neuroimaging Pharmacopoeia*,
DOI 10.1007/978-3-319-12715-6_26,

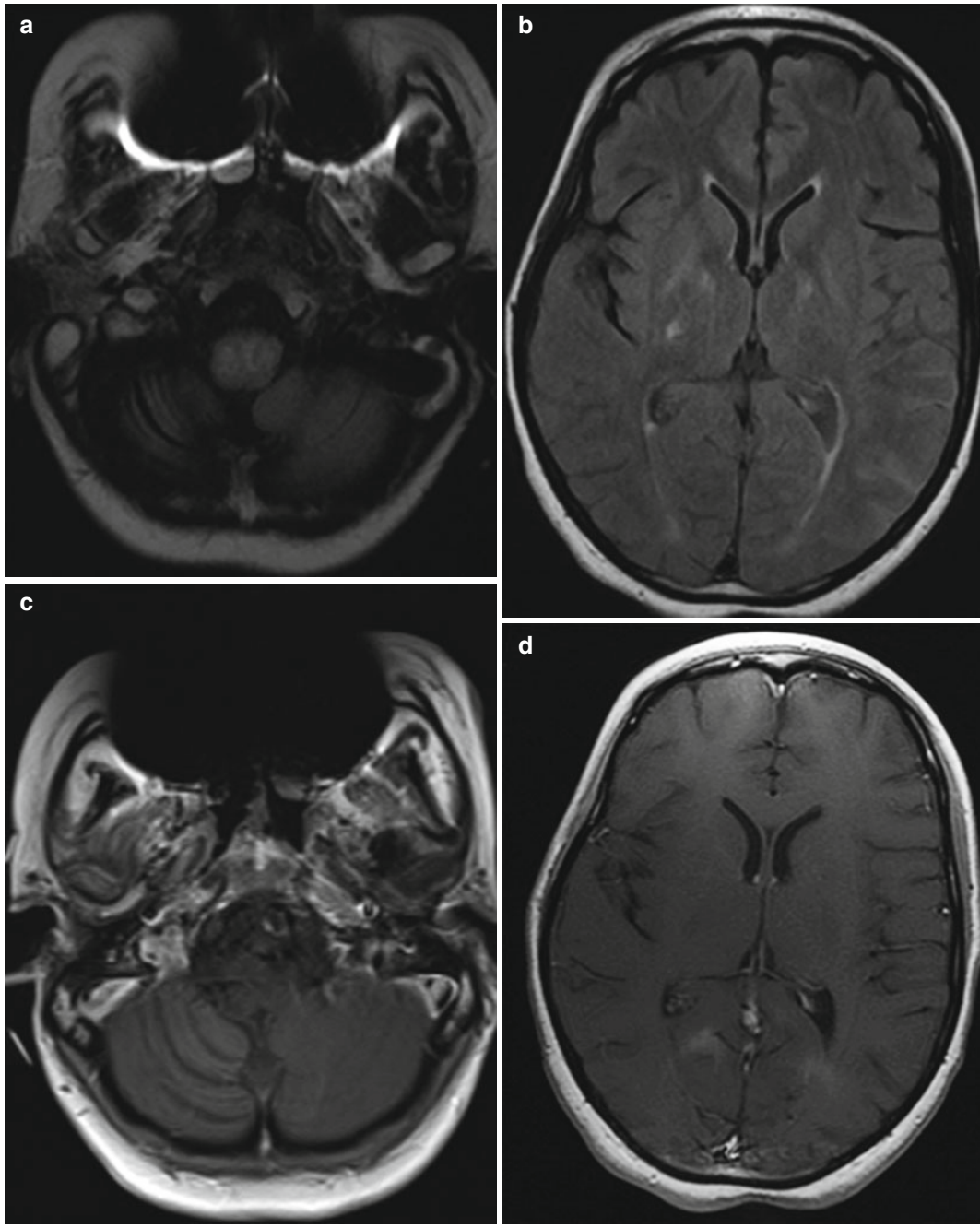

Fig. 26.1 CNS PML-IRIS. The patient was HIV positive and presented with subacute onset of right-sided weakness, slurred speech, and left beating nystagmus. The CD4 count at admission was 5 and the viral load was 82,000. The patient was then started on HAART with three drugs (efavirenz , tenofovir, and emtricitabine). Axial FLAIR (**a**, **b**) and post-contrast T1-weighted (**c**, **d**) MR images at initial presentation show patchy areas of signal abnormality without associated enhancement in the brainstem, cerebellum, and right basal ganglia. Subsequently, the patient presented with worsening neurologic symptoms, although the viral load decreased to 96 and the CD4 count increased to 11. Axial FLAIR (**e**–**h**) and post-contrast T1 (**i**–**l**) MR images obtained 1 month after initial presentation show marked interval progression of the signal abnormality in the brainstem, cerebellum, and supratentorial white matter with patchy enhancement (*arrows*). Corresponding DWI (**m**) and ADC map (**n**) show elevated diffusion in the affected white matter

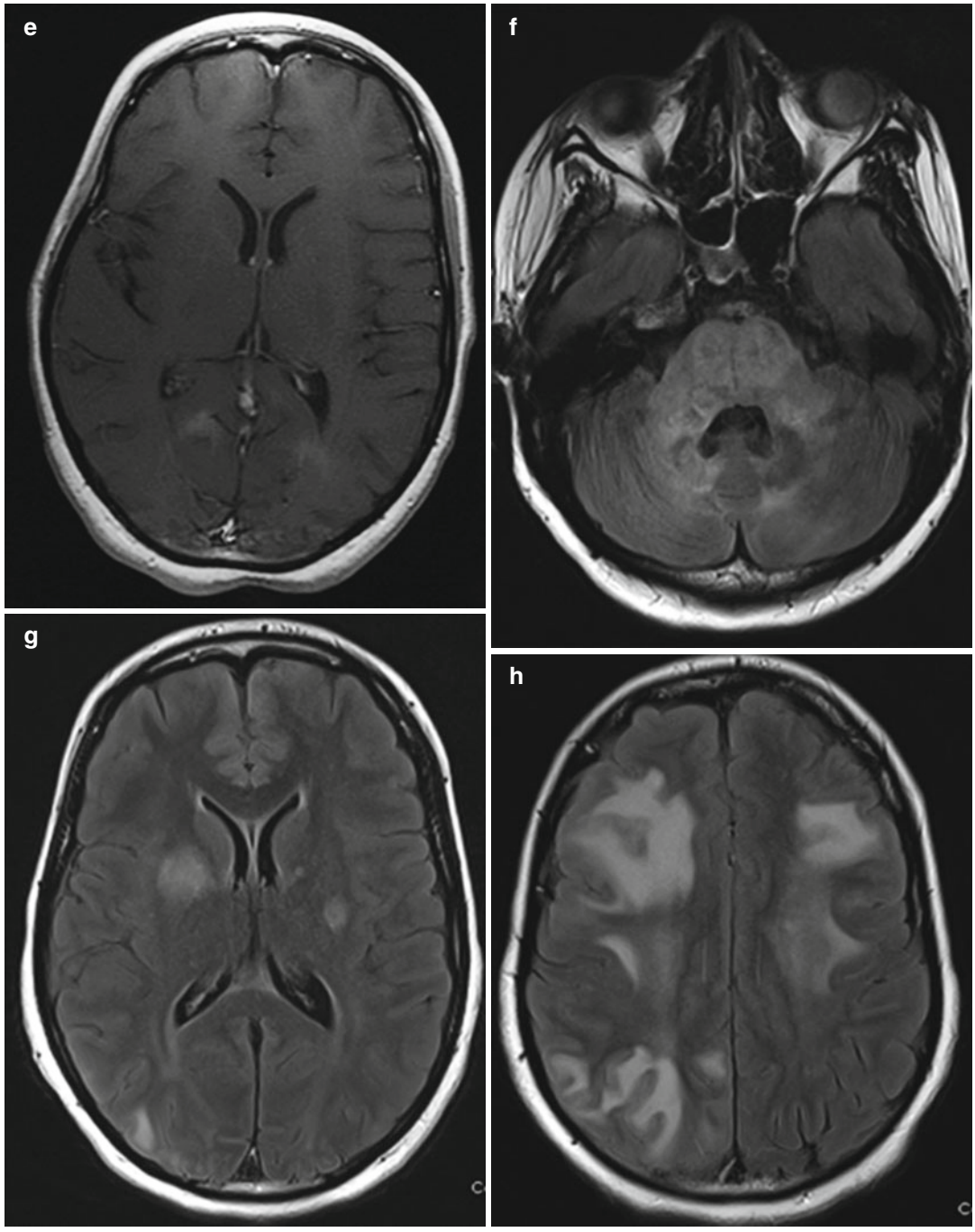

Fig. 26.1 (continued)

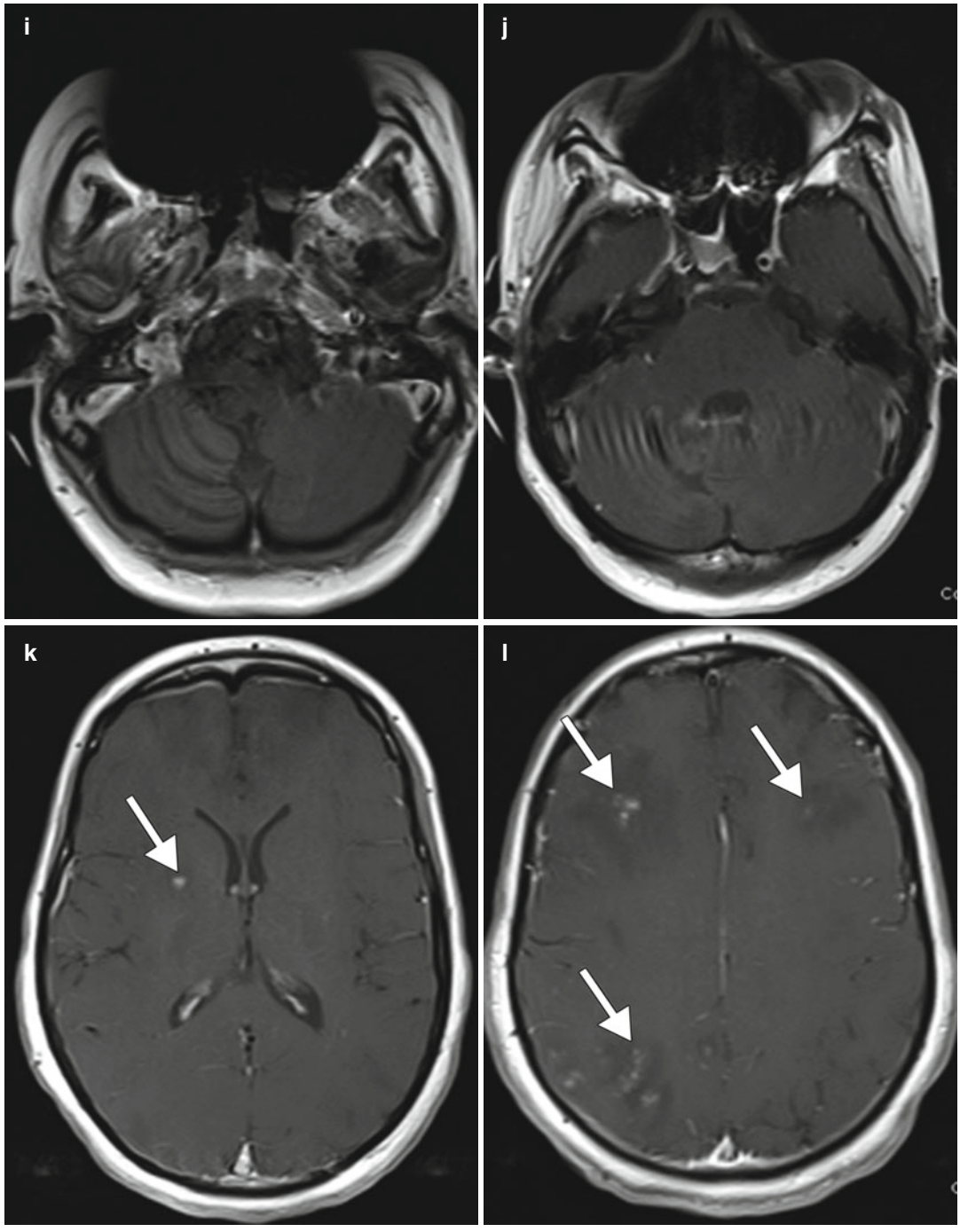

Fig. 26.1 (continued)

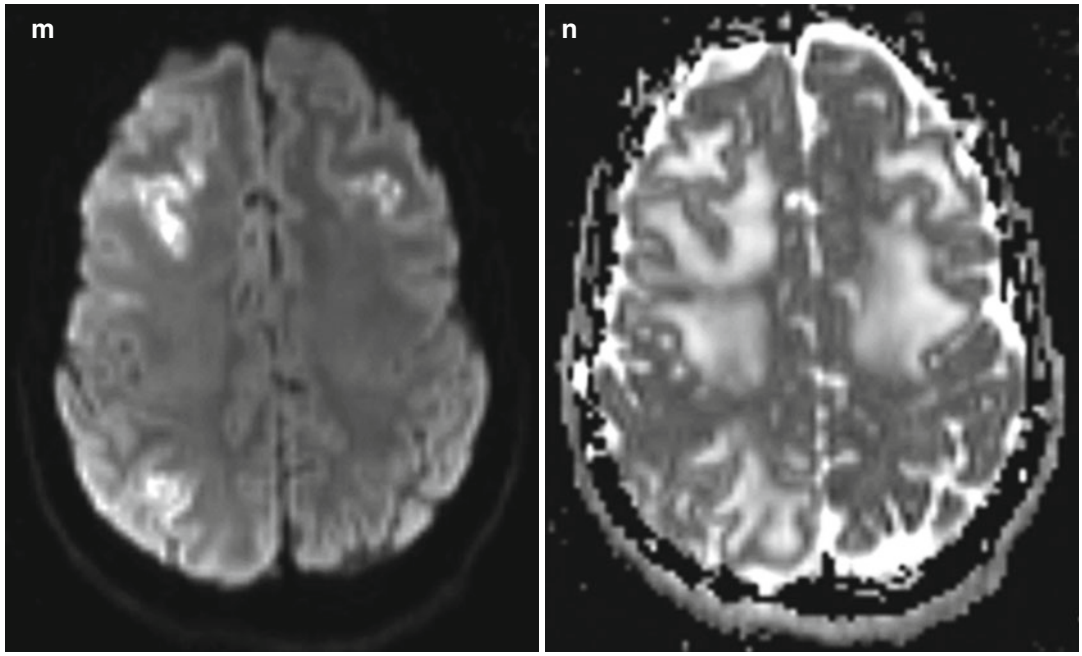

Fig. 26.1 (continued)

Table 26.1 Imaging findings for the different types of IRIS

Pathogen	Neuroimaging findings
JC virus PML	Interstitial edema, mass effect, and on contrast T1WI parenchymal and perivascular enhancement
Mycobacterium tuberculosis	Tuberculoma, basal leptomeningeal enhancement, and hydrocephalus
Atypical mycobacterium	Lymphadenitis; rarely enhancing lesions in the brain
Cytomegalovirus	Cerebral vasculitis and infarcts; ventriculitis; retinitis
Varicella	Cerebral vasculitis and infarcts, which may be associated with parenchymal and leptomeningeal enhancement
Cryptococcus	Lymphadenitis; gelatinous pseudocysts with restricted diffusion and parenchymal enhancement; cryptococcoma meningitis with meningeal or choroid plexus enhancement
Toxoplasma	Focal-enhancing parenchymal mass lesions, often with edema

The keys to the diagnosis of IRIS are the symptomatic and radiologic progression of disease after the initiation of HAART, despite an increasing CD4 T-cell count and the suppression of HIV viremia and the absence of a new opportunistic infection. Treatment for CNS IRIS related to HAART mainly consists of steroids. Patients may succumb to the disease, with mortality rates as high as 30 %.

26.4 Differential Diagnosis

The main alternative diagnostic considerations to IRIS include treatment failure and opportunistic infections without the superimposed effects of HAART. The imaging manifestations of opportunistic infections depend upon the specific pathogen, such as the JC virus, toxoplasmosis, *Mycobacterium tuberculosis*, or Cryptococcus.

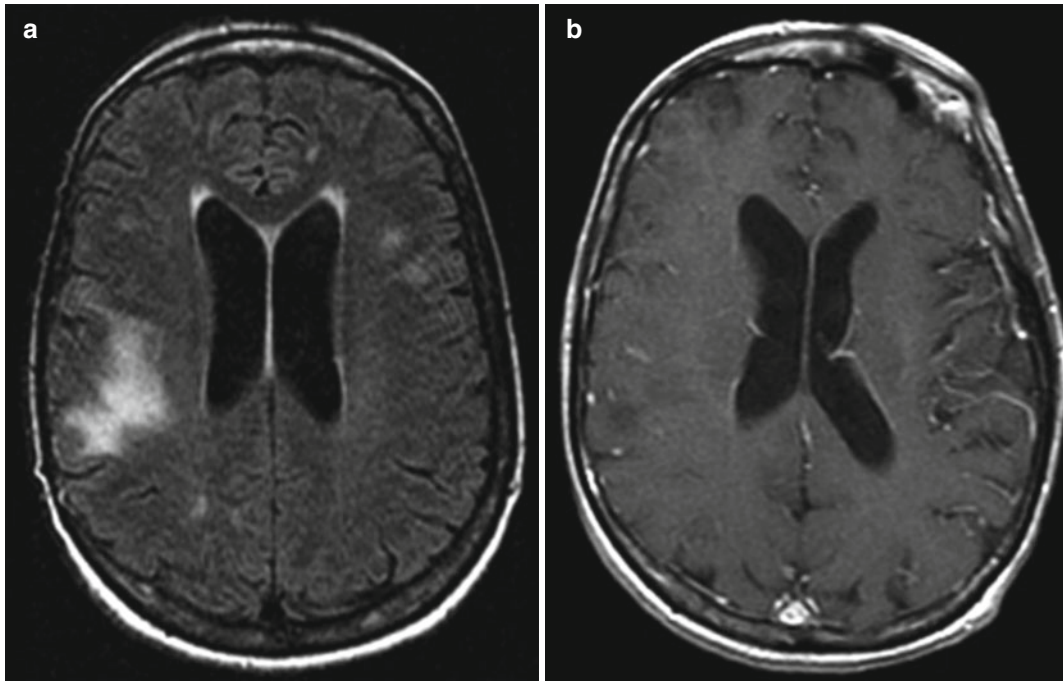

Fig. 26.2 JC virus PML. Axial FLAIR (**a**) and post-contrast T1-weighted (**b**) MRI show non-enhancing T2 hyperintense cerebral white matter lesions that are predominantly subcortical

- *JC virus PML*: Untreated PML typically presents as white matter lesions that are often subcortical with low T1 signal and high T2 signal, without mass effect and without contrast enhancement or restricted diffusion centrally (Fig. 26.2). The parietal and occipital lobes are most commonly involved, and the cerebellum is affected in one third of cases.
- *Toxoplasmosis:* Toxoplasma encephalitis in HIV patients typically presents as focal-enhancing parenchymal mass lesions, with edema and ring enhancement with or without a "target sign" appearance. The lesions commonly occur in the thalami and basal ganglia (Fig. 26.3).
- *Tuberculosis:* Although there may be a paucity of enhancement in some patients, basal meningeal enhancement, vasculitis, infarctions and focal intraparenchymal abscesses (tuberculomas), or small nodular lesions (granulomas) are also frequently observed in HIV-infected patients (Fig. 26.4). The presence of a lipid peak at 1.3 ppm on MR spectroscopy can be a useful finding suggestive of tuberculoma versus PML.
- *Cryptococcal meningitis:* Unlike cryptococcal meningitis associated with IRIS, HAART-naïve HIV-infected patients with cryptococcal meningitis typically present with leptomeningeal FLAIR hyperintensity, but without leptomeningeal enhancement due to the inability to mount a sufficient inflammatory response (Fig. 26.5). Associated communicating hydrocephalus with transependymal edema is common. In addition, gelatinous pseudocysts within dilated perivascular spaces are frequently encountered in immunocompromised patients.

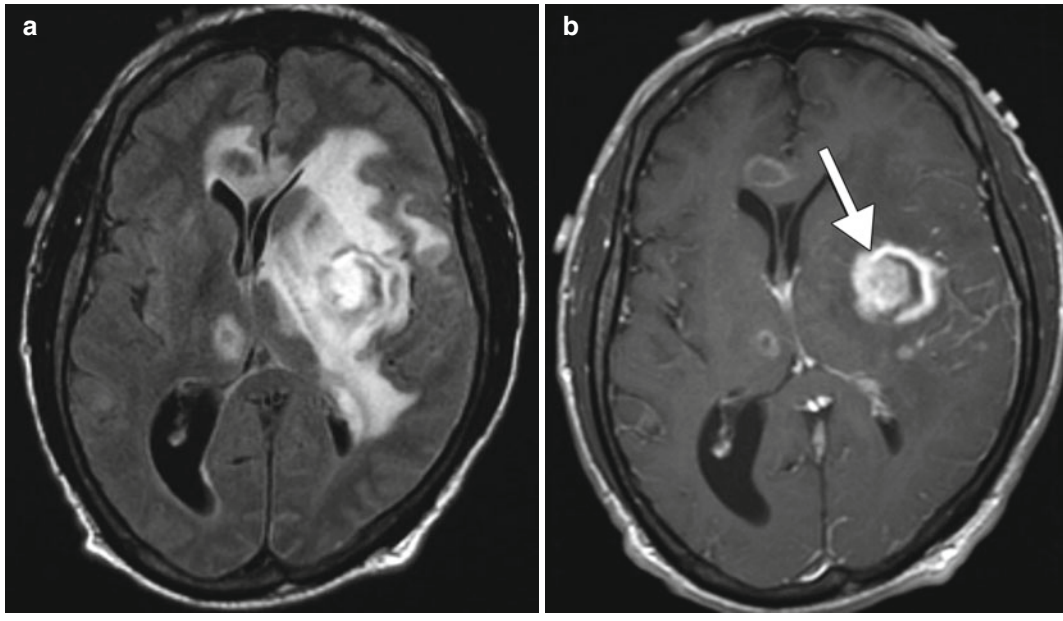

Fig. 26.3 Toxoplasma encephalitis. Axial FLAIR (**a**) and post-contrast T1-weighted (**b**) MRI show three intraparenchymal ring-enhancing lesions with associated edema and mass effect. The dominant lesion in the left basal ganglia region displays a "target sign" appearance (*arrow*)

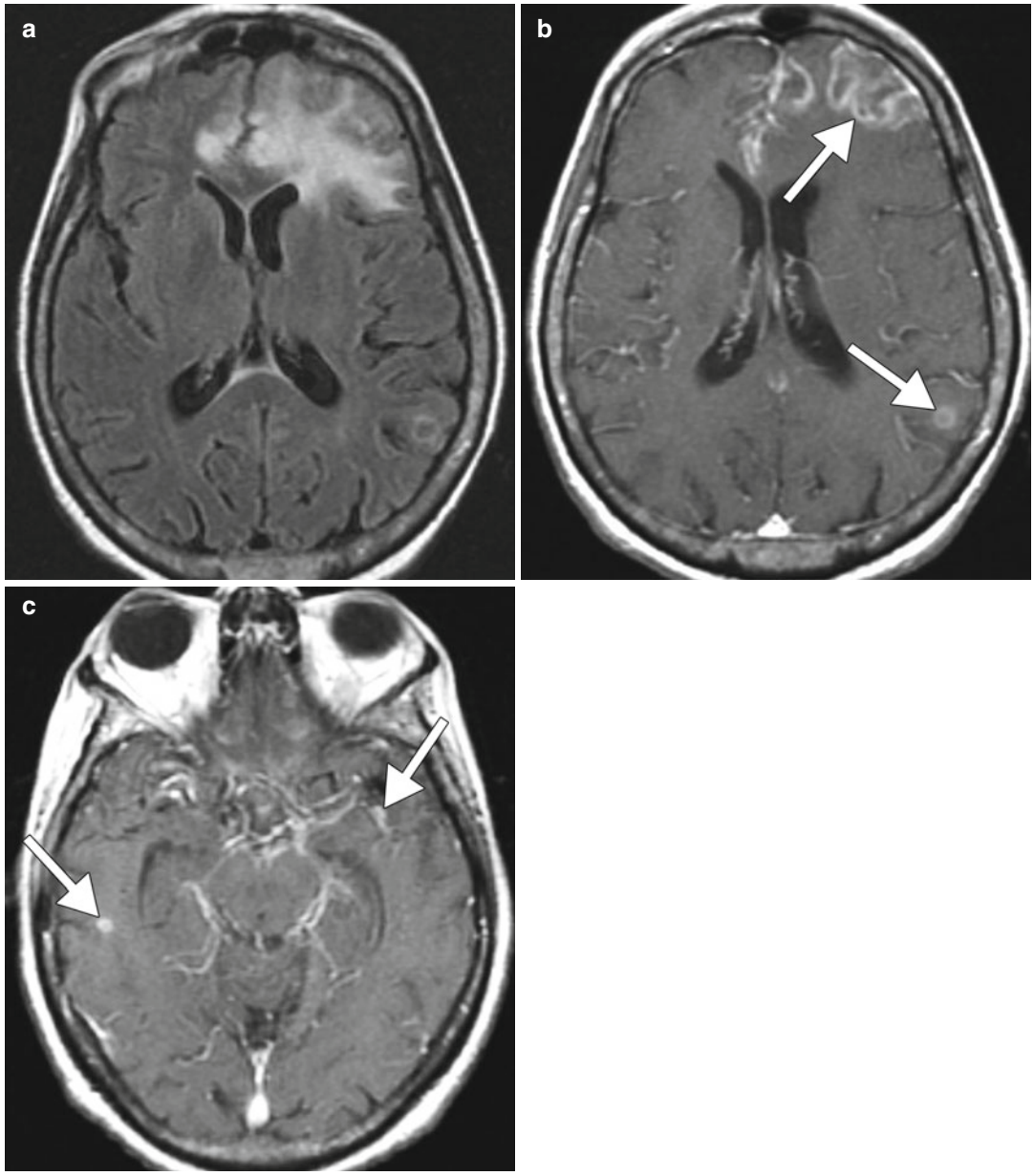

Fig. 26.4 CNS tuberculosis in an immunocompromised patient. Axial FLAIR (**a**) and axial post-contrast T1-weighted (**b**, **c**) MR images show intraparenchymal lesions with peripheral enhancement (*arrows*) as well as thick basilar leptomeningeal enhancement. MR spectroscopy (**d**) shows elevated lipid peaks at 1.3 ppm

Fig. 26.4 (continued)

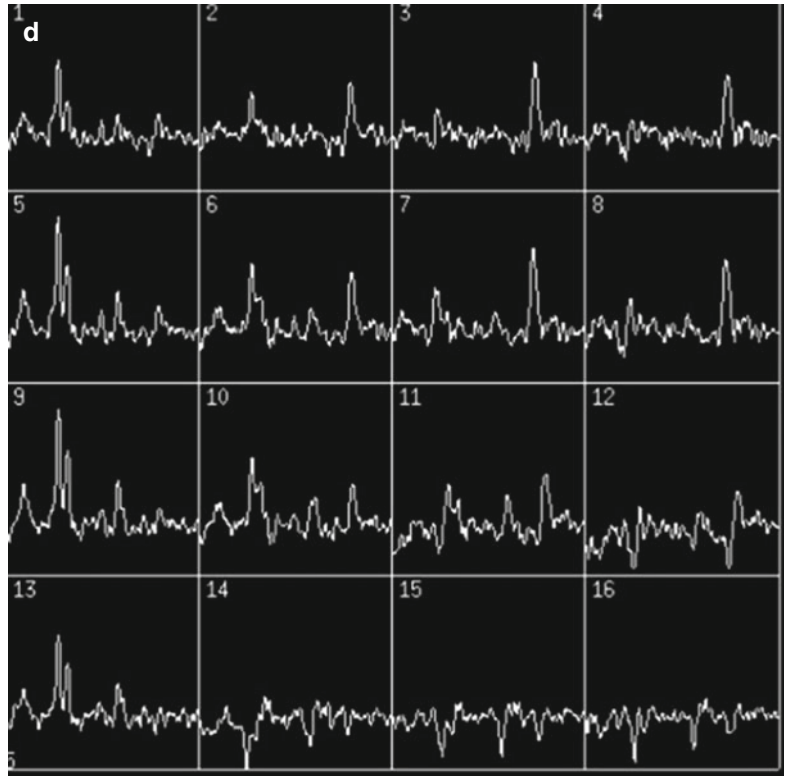

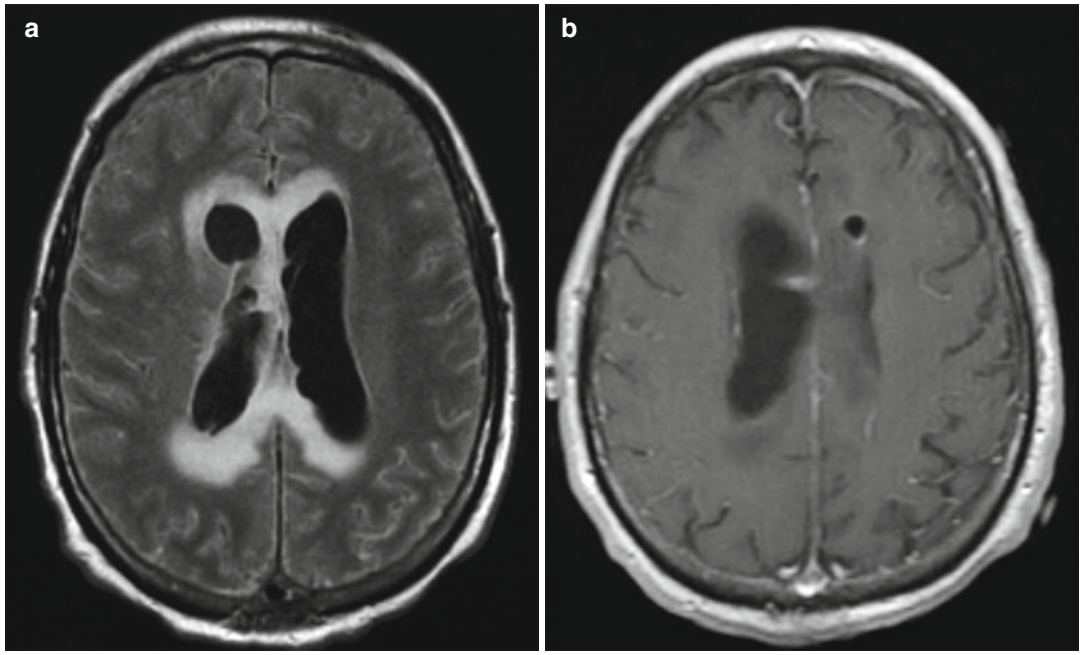

Fig. 26.5 Cryptococcal meningitis. Axial FLAIR (**a**) and axial post-contrast T1-weighted (**b**) MRI show diffuse sulcal FLAIR hyperintensity without corresponding abnormal enhancement. There is also hydrocephalus with periventricular signal abnormality, which may be related to ventriculitis

Suggested Reading

Chen KC, Chen JY, Tung GA. Case 149: immune reconstitution inflammatory syndrome. Radiology. 2009; 252(3):924–8.

Dhasmana DJ, Dheda K, Ravn P, Wilkinson RJ, Meintjes G. Immune reconstitution inflammatory syndrome in HIV-infected patients receiving antiretroviral therapy: pathogenesis, clinical manifestations and management. Drugs. 2008;68(2):191–208.

Murdoch DM, Venter WD, Van Rie A, Feldman C. Immune reconstitution inflammatory syndrome (IRIS): review of common infectious manifestations and treatment options. AIDS Res Ther. 2007;4:9.

Post MJ, Thurnher MM, Clifford DB, Nath A, Gonzalez RG, Gupta RK, Post KK. CNS-immune reconstitution inflammatory syndrome in the setting of HIV infection, part 2: discussion of neuro-immune reconstitution inflammatory syndrome with and without other pathogens. AJNR Am J Neuroradiol. 2013;34(7):1308–18.

Post MJ, Thurnher MM, Clifford DB, Nath A, Gonzalez RG, Gupta RK, Post KK. CNS-immune reconstitution inflammatory syndrome in the setting of HIV infection, part 1: overview and discussion of progressive multifocal leukoencephalopathy-immune reconstitution inflammatory syndrome and cryptococcal-immune reconstitution inflammatory syndrome. AJNR Am J Neuroradiol. 2013;34(7):1297–307.

Scharschmidt TC, Amerson EH, Rosenberg OS, Jacobs RA, McCalmont TH, Shinkai K. Immune reconstitution reactions in human immunodeficiency virus-negative patients: report of a case and review of the literature. JAMA Dermatol. 2013;149(1):74–8.

Thurnher MM, Post MJ, Rieger A, Kleibl-Popov C, Loewe C, Schindler E. Initial and follow-up MR imaging findings in AIDS-related progressive multifocal leukoencephalopathy treated with highly active antiretroviral therapy. AJNR Am J Neuroradiol. 2001; 22(5):977–84.

Dilantin (Phenytoin Sodium) 27

Maria J. Borja and Daniel Thomas Ginat

27.1 Uses

Phenytoin is an anticonvulsant used for the treatment and prevention of generalized tonic-clonic seizures, complex partial seizures, and seizures related to neurosurgical procedures.

27.2 Mechanism

Although the mechanism of action of phenytoin has not been completely elucidated, it appears to act primarily in the motor cortex by intervening with neuronal sodium channels. Phenytoin has the capability to limit the hyperexcitability of tissues by selectively blocking the neurons that fire at a high frequency. Cerebellar atrophy is attributed to loss of Purkinje cells, which may be due to toxic effects of phenytoin and/or seizure activity. Transient splenial lesions of the corpus callosum may result from the effects of the antiepileptic medication on arginine vasopressin and its function in fluid balance systems, mediated by vitamin B12 or folate deficiency. In addition, phenytoin has recently been shown to stimulate osteoblast proliferation and differentiation via upregulation of transforming growth factor-β1 and bone morphogenetic proteins.

M.J. Borja, MD
Department of Radiology, Massachusetts General Hospital, Boston, MA, USA

D.T. Ginat, MD, MS (✉)
Department of Radiology, University of Chicago, Pritzker Medical School, Chicago, IL, USA
e-mail: ginatd01@gmail.com

27.3 Discussion

The central nervous system is most commonly affected by the use of phenytoin. The effects are usually dose related and are mainly secondary to cerebellar toxicity. The manifestations include dizziness, ataxia, slurred speech, incoordination, somnolence, altered mental status, paresthesias, nystagmus, and headaches. Other less frequent reported side effects include abnormal movements such as chorea, tremor, and dystonia. Imaging findings associated with phenytoin are usually detected in patients with chronic intake of the medication, although there are a few reports of imaging changes occurring after acute exposure.

Diffuse cerebellar atrophy is a common imaging feature associated with the chronic use of phenytoin (Fig. 27.1). In particular, cerebellar atrophy caused by chronic phenytoin use manifests as enlargement of the cisterna magna, cerebellopontine angle, and superior cerebellar cisterns. The severity correlates with a longer time of exposure and a higher total dose of the medication. The atrophic changes are likely due to the combination of seizure activity and medication-related effects, including direct cellular toxicity and indirect effects on folic acid metabolism.

D.T. Ginat et al. (eds.), *Neuroimaging Pharmacopoeia*,
DOI 10.1007/978-3-319-12715-6_27, © Springer International Publishing Switzerland 2015

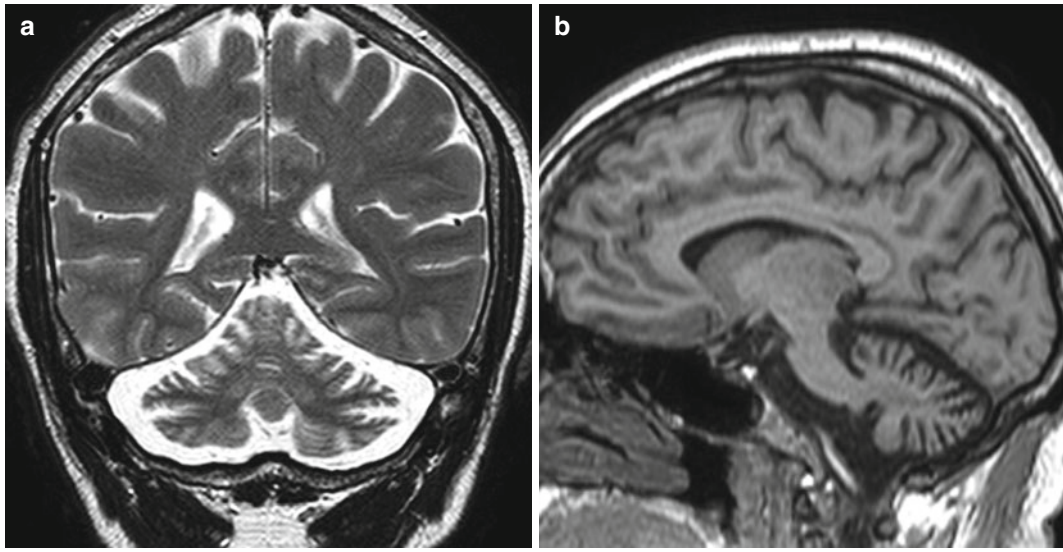

Fig. 27.1 Cerebellar atrophy related to phenytoin use. Coronal T2-weighted (**a**) and sagittal T1-weighted (**b**) MR images demonstrate disproportionate diffuse cerebellar atrophy

Another neurological effect of phenytoin is a transient focal lesion in the splenium of the corpus callosum. Splenial lesions are characteristically oval or round, measure less than 2 cm in size, and demonstrate hyperintense signal on T2-weighted sequences, hypointense signal on T1-weighted sequences, and restricted diffusion (Fig. 27.2).

Patients with chronic use of phenytoin may also present with acromegalic features with calvarial hyperostosis and coarsening of the face, hands, and feet. The incidence of calvarial thickening in epileptic patients treated with phenytoin is approximately 33 %. On imaging, progressive diffuse, smooth intramedullary expansion can be observed (Fig. 27.3).

Fetal hydantoin syndrome is a known disorder caused by the in utero exposure of phenytoin. Patients taking phenytoin during their pregnancy have two to three times the risk of birth defects compared to the general population. Although not all exposed fetuses develop the syndrome, the risk of expressing the full syndrome is 5–10 %, while the risk of expressing isolated features is 33 %. The differences in expression are determined by maternal genetic characteristics and ability to detoxify the intermediate metabolites of phenytoin. The effect of phenytoin in the metabolism of folic acid plays a crucial role in the increased risk of spina bifida. The classic features of fetal hydantoin syndrome include a dysmorphic appearance (with craniofacial anomalies, such as hypertelorism, deep nasal bridge, small nose, and cleft lip or palate), mental retardation, growth deficiencies, and limb defects. Other features include microcephaly, ocular defects, spina bifida, and cardiovascular anomalies.

Signs and symptoms related to acute cerebellar dose-related toxicity usually reverse following discontinuation of the medication. However, other effects such as cerebellar atrophy and calvarial thickening may be permanent despite a change in anticonvulsive therapy. Nevertheless, the clinical implications of calvarial thickening are mainly cosmetic.

27.4 Differential Diagnosis

The imaging findings associated with the use of phenytoin are not specific and could be related to several conditions including other antiepileptic medications. The clinical history may be the differentiating factor for making the correct diagnosis.

Cerebellar atrophy: The differential diagnosis for cerebellar atrophy is broad, including aging, alcohol, paraneoplastic syndromes, radiation, hypothyroidism, the sequela of cerebellitis,

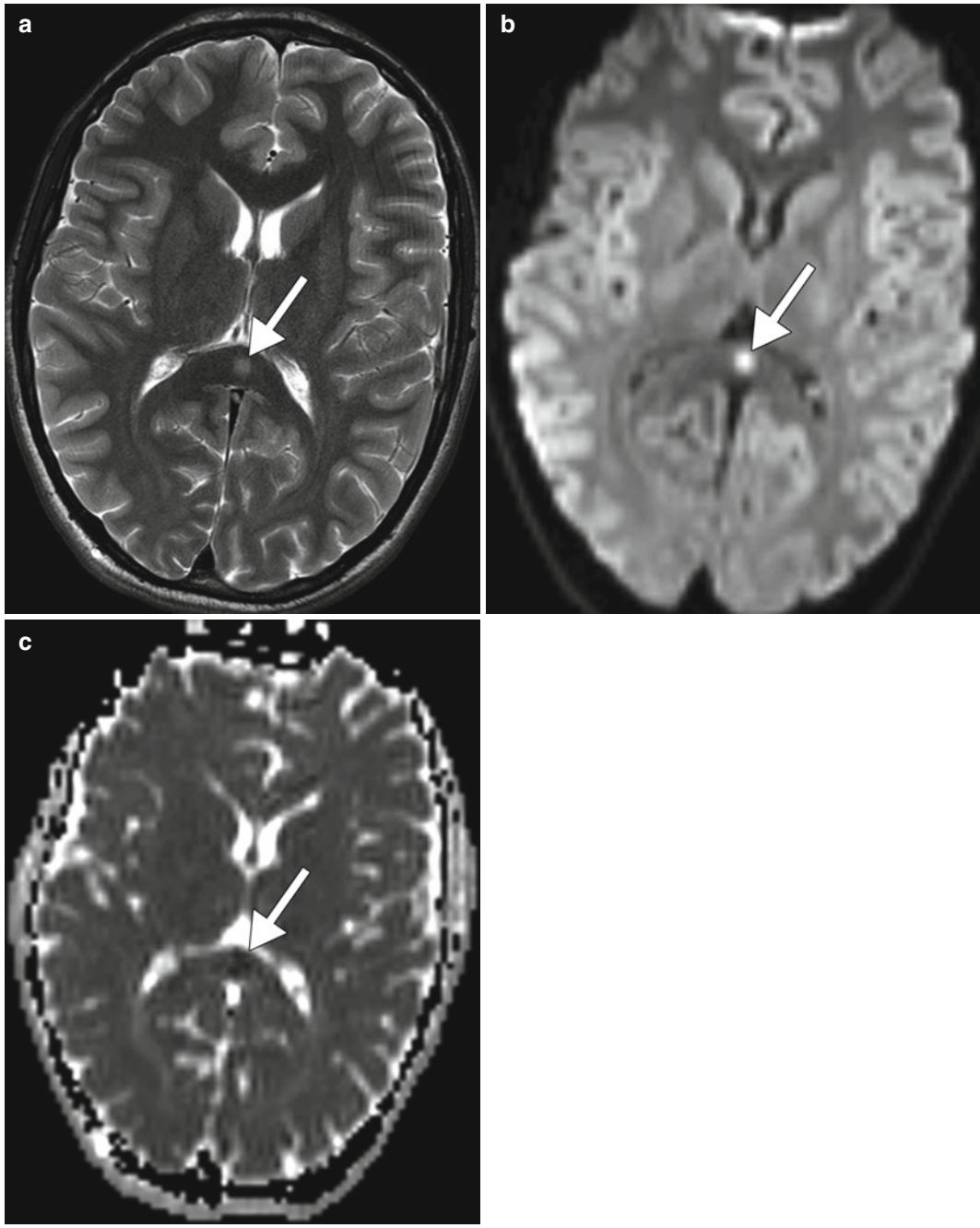

Fig. 27.2 Focal transient splenial lesion related to antiepileptic therapy. Axial T2-weighted MRI (**a**) demonstrates a focal hyperintense lesion in the splenium of the corpus callosum (*arrow*) in a patient taking phenytoin. DWI (**b**) and ADC maps (**c**) demonstrate restricted diffusion of the lesion (*arrow*)

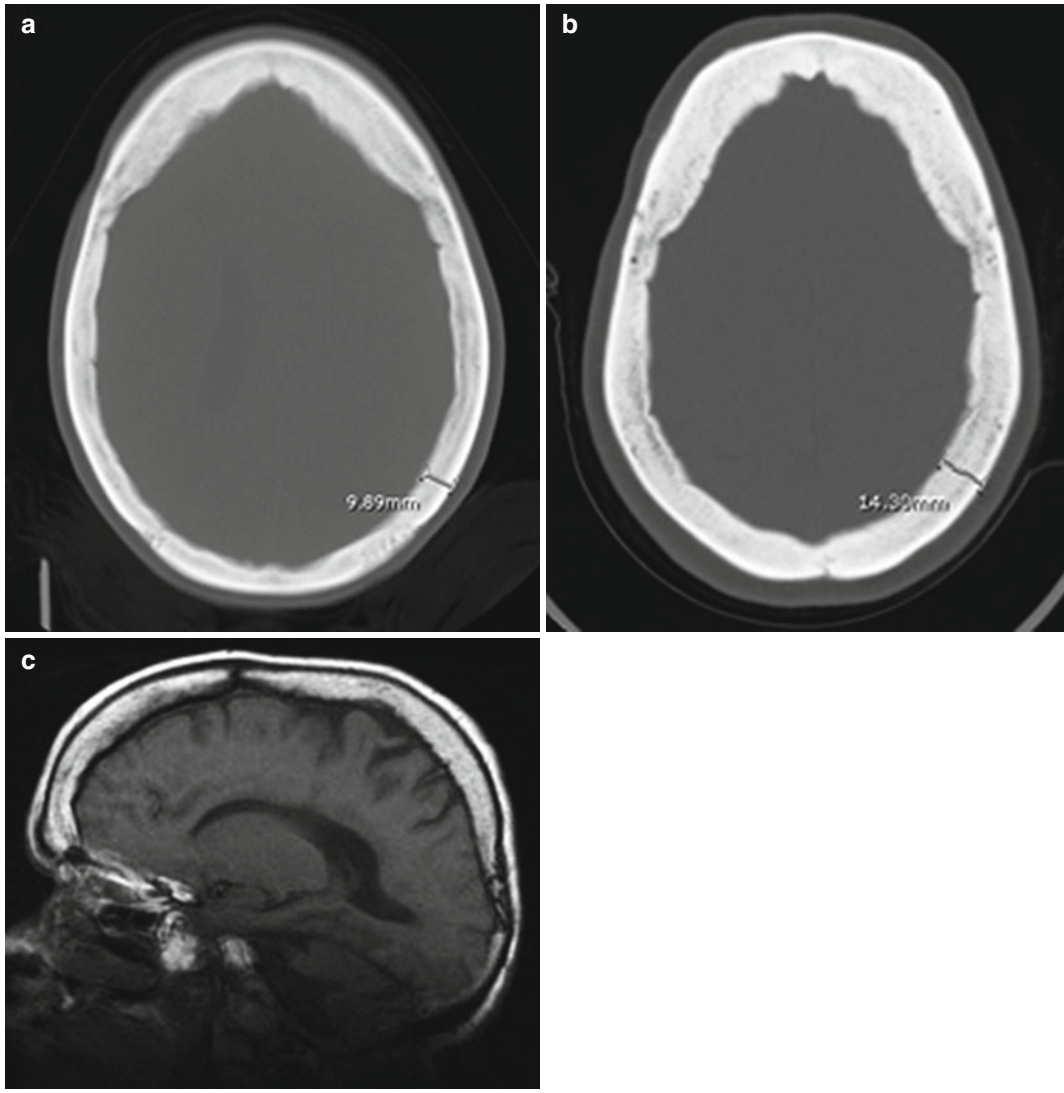

Fig. 27.3 Calvarial thickening secondary to chronic phenytoin use. Axial CT images obtained at initial presentation (**a**) and after over a decade of antiepileptic treatment (**b**) show development of substantial diffuse calvarial thickening. The sagittal T1-weighted MRI (**c**) also shows diffuse calvarial thickening with normal hyperintense fatty marrow signal

hereditary cerebellar atrophy, and multiple system atrophy.

- Alcoholic encephalopathy typically leads to disproportionate superior vermian atrophy and decrease in whole brain metabolism on F-18 FDG PET. A history of alcohol abuse is key in making the diagnosis (refer to Chap. 2).
- Paraneoplastic syndromes, most frequently from lung cancer, are a known cause of cerebellar atrophy. Concomitant findings of paraneoplastic encephalomyelitis can also be seen.
- Multiple system atrophy is a progressive neurodegenerative disease with the characteristic imaging finding of the "hot cross

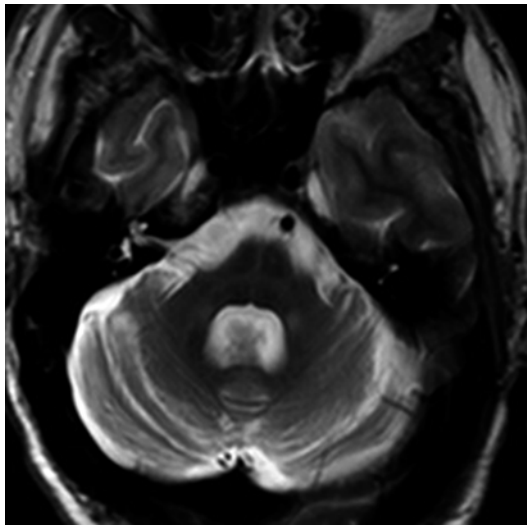

Fig. 27.4 Multisystem atrophy, type C. Axial T2WI through the posterior fossa demonstrates diffuse cerebellar atrophy, pontine hyperintense signal in the shape of a cross (the "hot cross bun" sign), and hyperintense signal in the bilateral middle cerebellar peduncles

bun" sign, consisting of T2 hyperintense signal in the pons in the form of a cross (Fig. 27.4). Spinocerebellar ataxia is another neurodegenerative condition that predominantly features volume loss in the cerebellum. Genetic testing can be helpful in confirming the diagnosis.

Diffuse calvarial thickening: Other etiologies for skull thickening include hyperparathyroidism, osteopetrosis, acromegaly, Paget's disease, fibrous dysplasia, chronically shunted hydrocephalus, diffuse metastasis, and chronic anemia. Many of these conditions have specific other features that can help differentiate them from calvarial thickening related to phenytoin use. For example, Paget's disease may contain areas of focal sclerosis giving the appearance of "cotton wool" on CT (Fig. 27.5).

Abnormal signal in the splenium of the corpus callosum: Abnormal T2 hyperintense signal in the splenium of the corpus callosum has also been described with multiple other entities including other antiepileptic drugs, seizures, hypoglycemia, multiple sclerosis, diffuse axonal injury, viral encephalitis, lymphoma, and Susac's disease (Fig. 27.6).

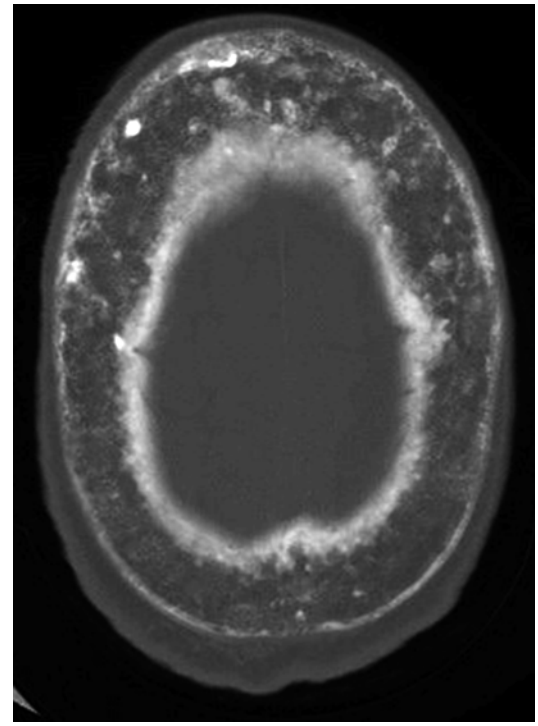

Fig. 27.5 Paget's disease. Axial CT of the skull in bone windows shows diffuse thickening of the calvarium and scattered sclerotic lesions in a "cotton wool" appearance

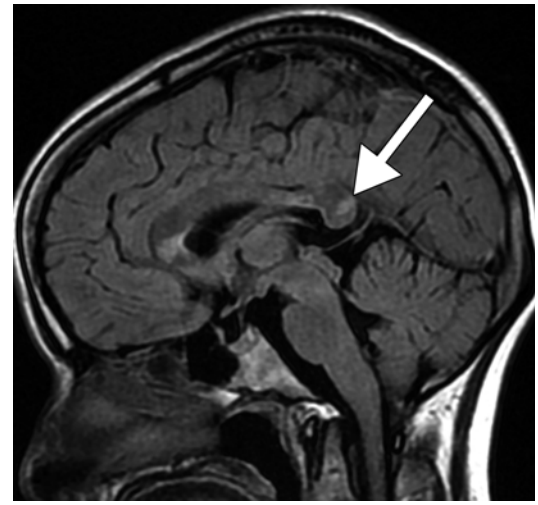

Fig. 27.6 Susac's disease. Sagittal FLAIR MRI demonstrates several hyperintense lesions in the corpus callosum, including the splenium (*arrow*)

Fetal hydantoin syndrome: Dysmorphic characteristics similar to fetal hydantoin syndrome can occur with other antiepileptic drugs such

as phenobarbital and carbamazepine, as well as with other fetal syndromes like Noonan and fetal alcohol syndrome (refer to Chap. 2). The mother's history of phenytoin use during pregnancy supports the diagnosis.

Suggested Reading

Alioğlu Z, et al. Cerebellar atrophy following acute phenytoin intoxication. J Neuroradiol. 2000;27(1):52–5.

Bourekas E, et al. Lesions of the corpus callosum: MR imaging and differential considerations in adults and children. Am J Roentgenol. 2002;179:251–7.

Buehler B, et al. Prenatal prediction of risk of the fetal hydantoin syndrome. N Engl J Med. 1990;322:1567–72.

Chow KM, et al. Cerebral atrophy and skull thickening due to chronic phenytoin. CMAJ. 2007;176(3):321–3.

Kattan K, et al. Calvarial thickening after Dilantin medication. Am J Roentgenol Radium Ther Nucl Med. 1970;110(1):102–5.

Kim SS, Chang KH, Kim ST, Suh DC, Cheon JE, Jeong SW, Han MH, Lee SK. Focal lesion in the splenium of the corpus callosum in epileptic patients: antiepileptic drug toxicity? AJNR Am J Neuroradiol. 1999;20(1):125–9.

Kima S, et al. Focal lesion in the splenium of the corpus callosum in epileptic patients: antiepileptic drug toxicity? AJNR Am J Neuroradiol. 1999;20:125–9.

Marco F, et al. Cerebellar volume and long-term use of phenytoin. Seizure. 2003;12(5):312–5.

Polster T, Hoppe M, Ebner A. Transient lesion in the splenium of the corpus callosum: three further cases in epileptic patients and a pathophysiological hypothesis. J Neurol Neurosurg Psychiatry. 2001;70(4):459–63.

Valproic Acid (Sodium Valproate, Depakote)

28

Daniel Thomas Ginat

28.1 Uses

Valproate products are FDA-approved drugs to treat seizures and manic or mixed episodes associated with bipolar disorder (manic-depressive disorder) and to prevent migraine headaches.

28.2 Mechanism

Valproate interferes with urea cycle by decreasing citrullinogenesis through inhibition of carbamoyl phosphate synthetase-I, which in turn leads to hyperammonemia. Individuals with genetic defects of the urea cycle are particularly prone to valproate-induced hyperammonemia. Valproate is also a teratogen.

28.3 Discussion

Valproate-induced hyperammonemic encephalopathy is an unusual complication characterized by a decreasing level of consciousness, focal neurological deficits, cognitive slowing, vomiting, drowsiness, and lethargy. Although valproate-induced hyperammonemic encephalopathy can occur without hepatic dysfunction, the imaging findings are the same as for other causes of hyperammonemic encephalopathy (refer to Chap. 49). The salient findings on MRI include diffuse gyriform cortical T2 hyperintensity, predominantly in the insula and temporal lobes, but occasionally the cerebellum and globi pallidi can be involved. On MRS, there is typically moderate reduced in NAA and Cho and elevated glutamate and glutamine. Administration of carnitine can lead to an early favorable clinical response. Valproate in epilepsy is also associated with reduced parietal lobe thickness, total brain volume, and white matter volume.

Valproate monotherapy during the first trimester is associated with increased risk of several congenital malformations with an absolute risk of approximately 0.6 %. The major anomalies associated with in utero exposure to valproate that may be encountered on neuroimaging include craniosynostosis, particularly trigonocephaly, spina bifida, and cleft palate (Figs. 28.1, 28.2, and 28.3).

28.4 Differential Diagnosis

Hyperammonemic encephalopathy can be caused by other drugs, such as Tylenol overdose, with identical imaging findings. The imaging findings in congenital valproate-induced malformations are rather characteristic, although there may be confounders in terms of the etiology. While the combination of anomalies and appropriate history may implicate valproate, there are many other potential causes of the associated anomalies.

D.T. Ginat, MD, MS
Department of Radiology, University of Chicago, Pritzker Medical School, Chicago, IL, USA
e-mail: ginatd01@gmail.com

D.T. Ginat et al. (eds.), *Neuroimaging Pharmacopoeia*,
DOI 10.1007/978-3-319-12715-6_28,

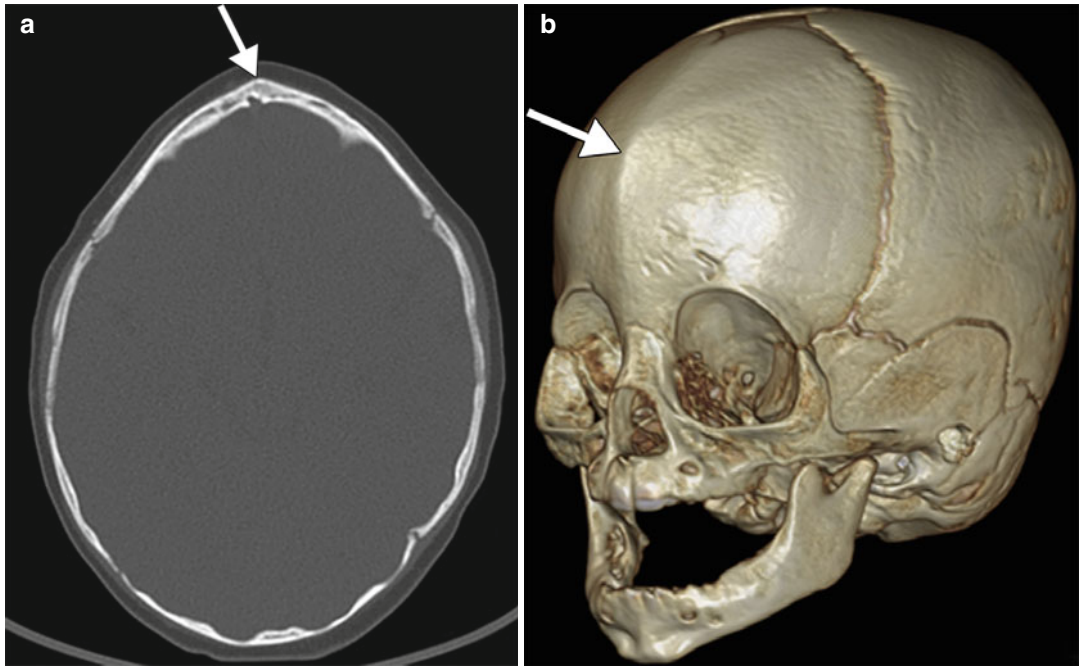

Fig. 28.1 Trigonocephaly. Axial (**a**) and 3D volume-rendered (**b**) CT images show prominence of the fused metopic suture (*arrows*)

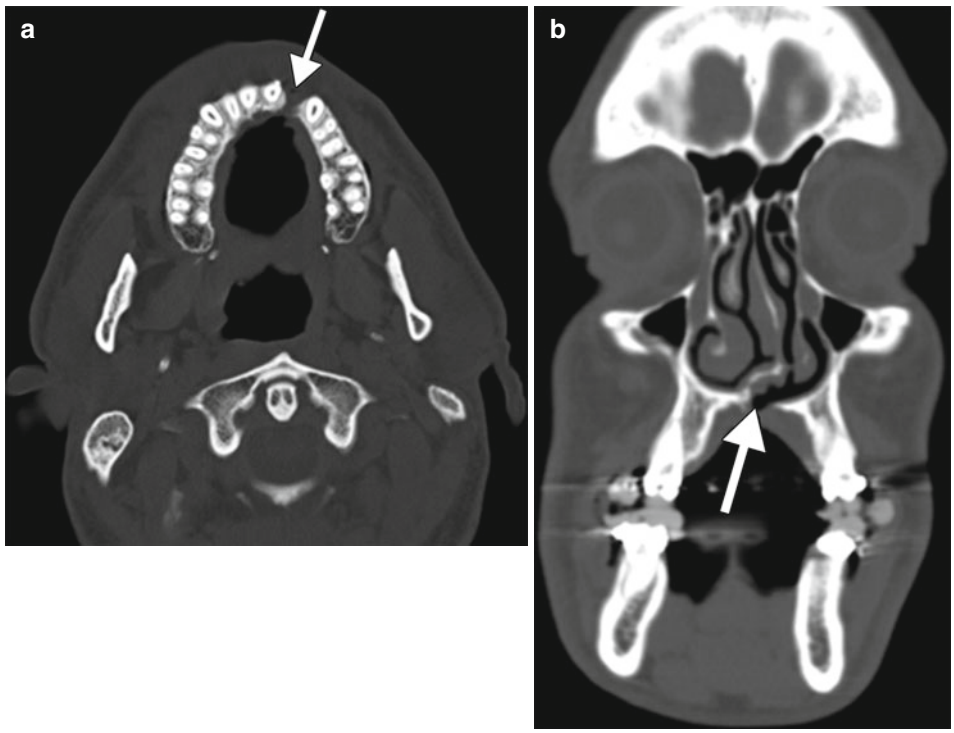

Fig. 28.2 Cleft palate. Axial (**a**) and coronal (**b**) CT images show a defect in the left parasagittal hard palate (*arrows*)

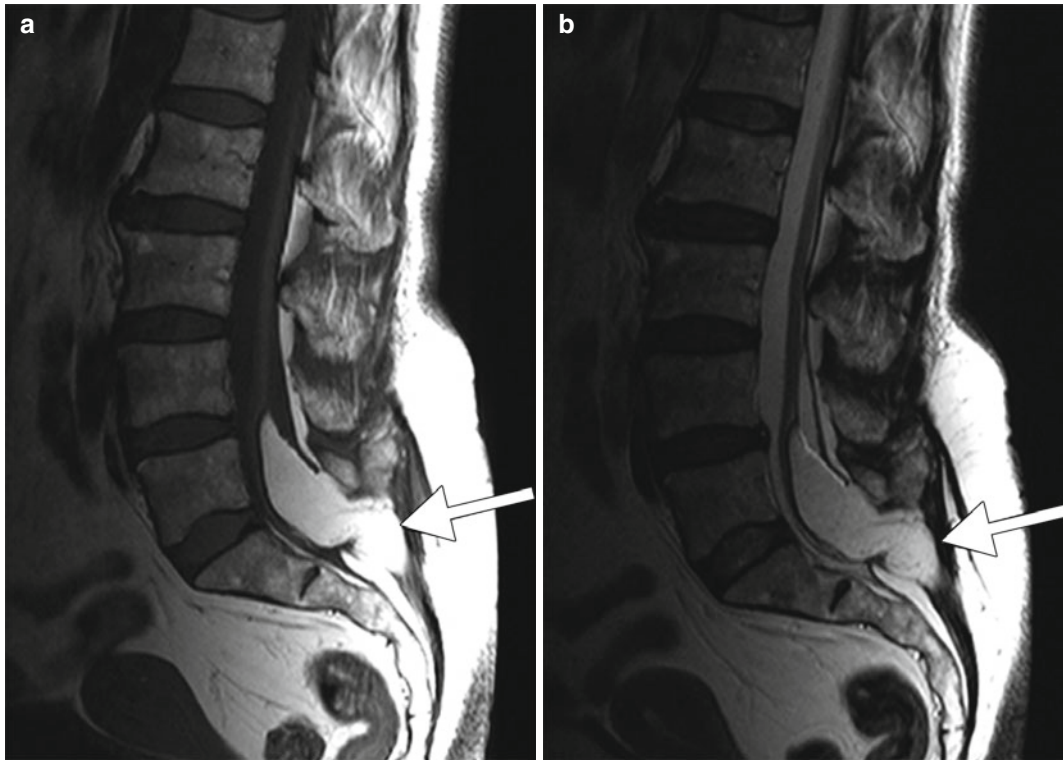

Fig. 28.3 Spina bifida. Sagittal T1-weighted (**a**) and T2-weighted (**b**) MR images show lumbosacral dysraphism associated with a lipomyelomeningocele (*arrows*)

Suggested Reading

Alsdorf R, Wyszynski DF. Teratogenicity of sodium valproate. Expert Opin Drug Saf. 2005;4(2):345–53.

Carter BS, Stewart JM. Valproic acid prenatal exposure. Association with lipomyelomeningocele. Clin Pediatr (Phila). 1989;28(2):81–5.

Dealberto MJ. Valproate-induced hyperammonaemic encephalopathy: review of 14 cases in the psychiatric setting. Int Clin Psychopharmacol. 2007;22(6):330–7.

Gilboa SM, Broussard CS, Devine OJ, Duwe KN, Flak AL, Boulet SL, Moore CA, Werler MM, Honein MA. Influencing clinical practice regarding the use of antiepileptic medications during pregnancy: modeling the potential impact on the prevalences of spina bifida and cleft palate in the United States. Am J Med Genet C Semin Med Genet. 2011;157C(3):234–46.

Jentink J, Loane MA, Dolk H, Barisic I, Garne E, Morris JK, den de Jong-van Berg LT, EUROCAT Antiepileptic Study Working Group. Valproic acid monotherapy in pregnancy and major congenital malformations. N Engl J Med. 2010;362(23):2185–93.

Lajeunie E, Barcik U, Thorne JA, El Ghouzzi V, Bourgeois M, Renier D. Craniosynostosis and fetal exposure to sodium valproate. J Neurosurg. 2001;95(5):778–82.

Pardoe HR, Berg AT, Jackson GD. Sodium valproate use is associated with reduced parietal lobe thickness and brain volume. Neurology. 2013;80(20):1895–900.

Segura-Bruna N, Rodriguez-Campello A, Puente V, Roquer J. Valproate-induced hyperammonemic encephalopathy. Acta Neurol Scand. 2006;114(1):1–7.

Wyszynski DF, Nambisan M, Surve T, Alsdorf RM, Smith CR, Holmes LB, Antiepileptic Drug Pregnancy Registry. Increased rate of major malformations in offspring exposed to valproate during pregnancy. Neurology. 2005;64(6):961–5.

Ziyeh S, Thiel T, Spreer J, Klisch J, Schumacher M. Valproate-induced encephalopathy: assessment with MR imaging and 1H MR spectroscopy. Epilepsia. 2002;43(9):1101.

Vigabatrin (Sabril)

29

Daniel Thomas Ginat

29.1 Uses

Vigabatrin can serve as adjunctive therapy for adult patients with refractory complex partial seizures who have responded inadequately to several alternative treatments and as monotherapy for pediatric patients aged 1 month to 2 years with infantile spasms.

29.2 Mechanism

Inhibition of GABA transaminase by vigabatrin results in a dose-dependent increase in GABA concentrations in the brain. The increase in GABA inhibits the excitatory processes that can initiate seizure activity. Toxicity may result from microvacuolization of glial cells in specific regions of the brain, including the brainstem, cerebellum, basal ganglia, and deep white matter tracts.

29.3 Discussion

Vigabatrin can cause reversible, often symmetric, T2 hyperintensity and restricted diffusion within the basal ganglia, thalami, brainstem, and/or dentate nuclei in approximately 30 % of patients. The histopathological correlate consists of intramyelinic edema and microvacuolation with reactive astrocytosis. The predilection of vigabatrin toxicity for these anatomic areas may depend on the stage of myelin maturation. Indeed, infants are particularly susceptible to vigabatrin-induced changes. Patients are typically asymptomatic from vigabatrin-related effects. The imaging abnormalities typically resolve within several weeks, sometimes without cessation of vigabatrin. Routine MRI surveillance of this population is not recommended, since the long-term clinical consequences of vigabatrin-associated MRI changes are unknown (Fig. 29.1).

29.4 Differential Diagnosis

The diagnosis of vigabatrin neurotoxicity should be straightforward in an infant with the described imaging findings and treatment history. Nevertheless, possible differential considerations by anatomic location include the following (many of these conditions can affect multiple anatomical sites):

- *Bilateral basal ganglia T2 hyperintensity*: Hypoxic-ischemic injury, viral encephalitis, deep cerebral vein thrombosis, glutaric aciduria type 1, biotin-responsive encephalopathy, neurofibromatosis type 1 (Fig. 29.2), and mitochondrial encephalopathies
- *Bilateral thalami*: Infiltrating neoplasms, artery of Percheron infarct, viral encephalitis, deep

D.T. Ginat, MD, MS
Department of Radiology, University of Chicago, Pritzker Medical School, Chicago, IL, USA
e-mail: ginatd01@gmail.com

D.T. Ginat et al. (eds.), *Neuroimaging Pharmacopoeia*,
DOI 10.1007/978-3-319-12715-6_29,

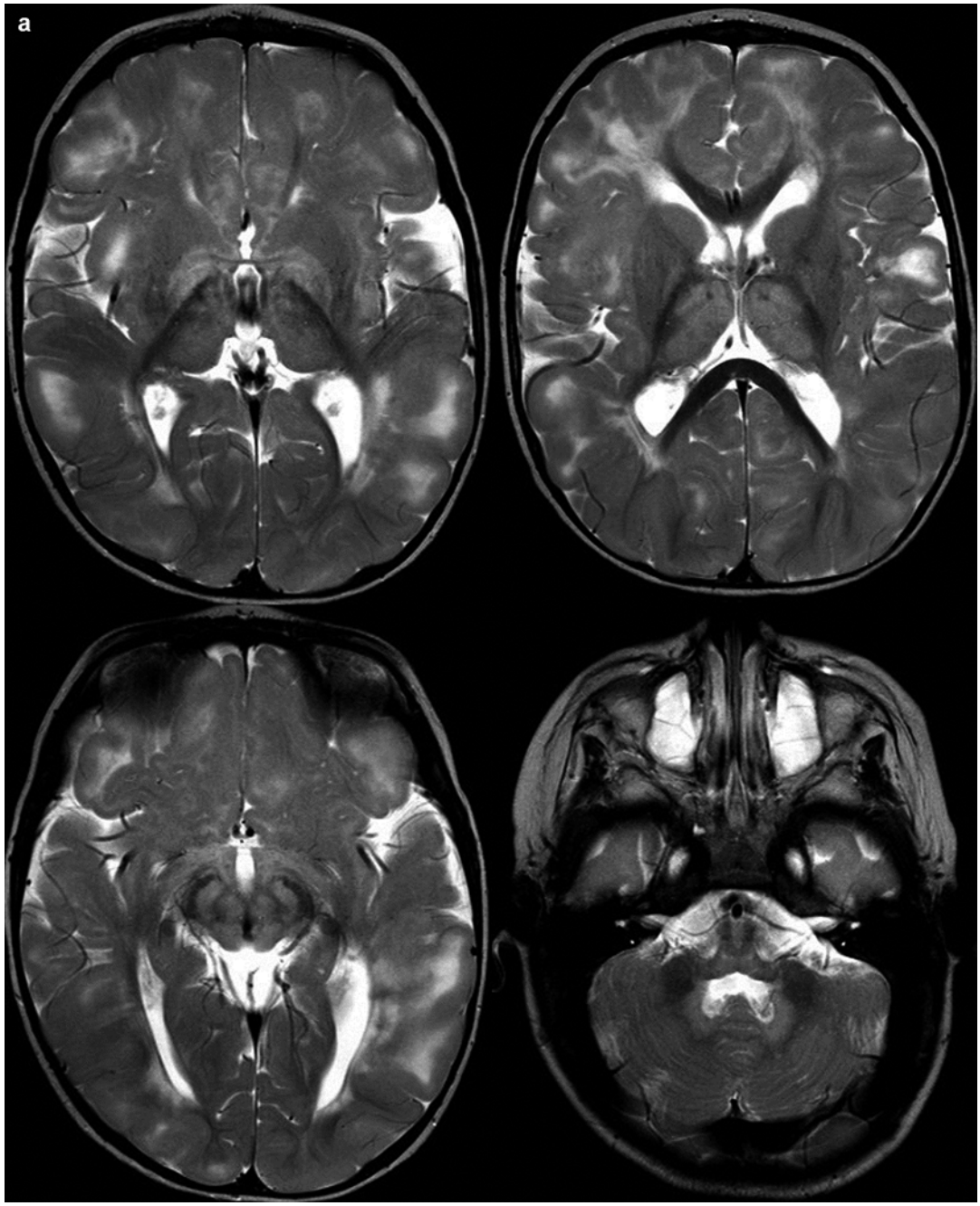

Fig. 29.1 Vigabatrin neurotoxicity. An infant with a history of tuberous sclerosis treated with vigabatrin presented with lethargy. Axial T2-weighted MR images (panel **a**), DWI (panel **b**), and ADC maps (panel **c**) show bilateral symmetric T2 hyperintensity and restricted diffusion within the thalami, basal ganglia, midbrain, and dentate nuclei. The abnormalities resolved within 2 months after cessation of vigabatrin (panel **d**)

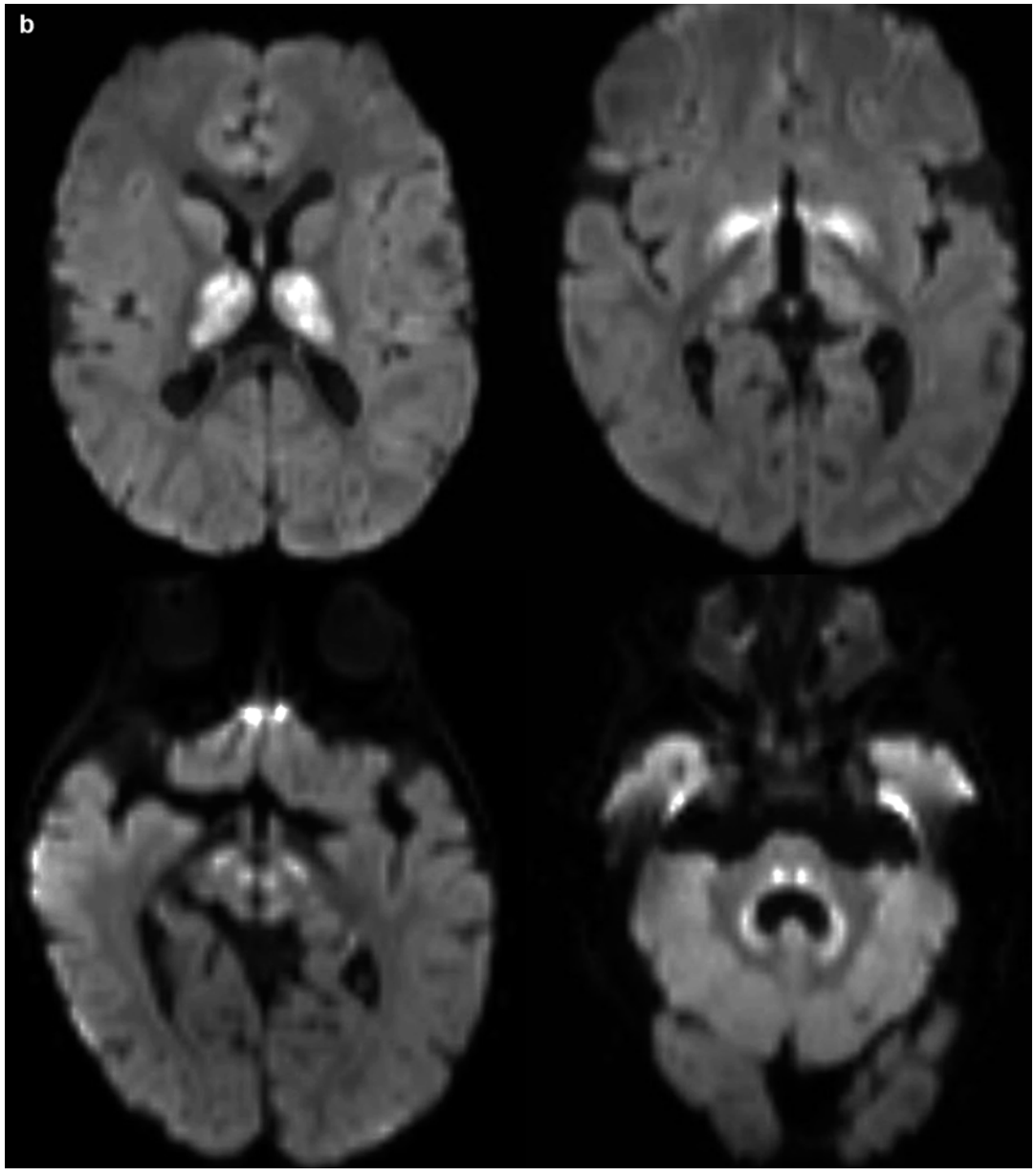

Fig. 29.1 (continued)

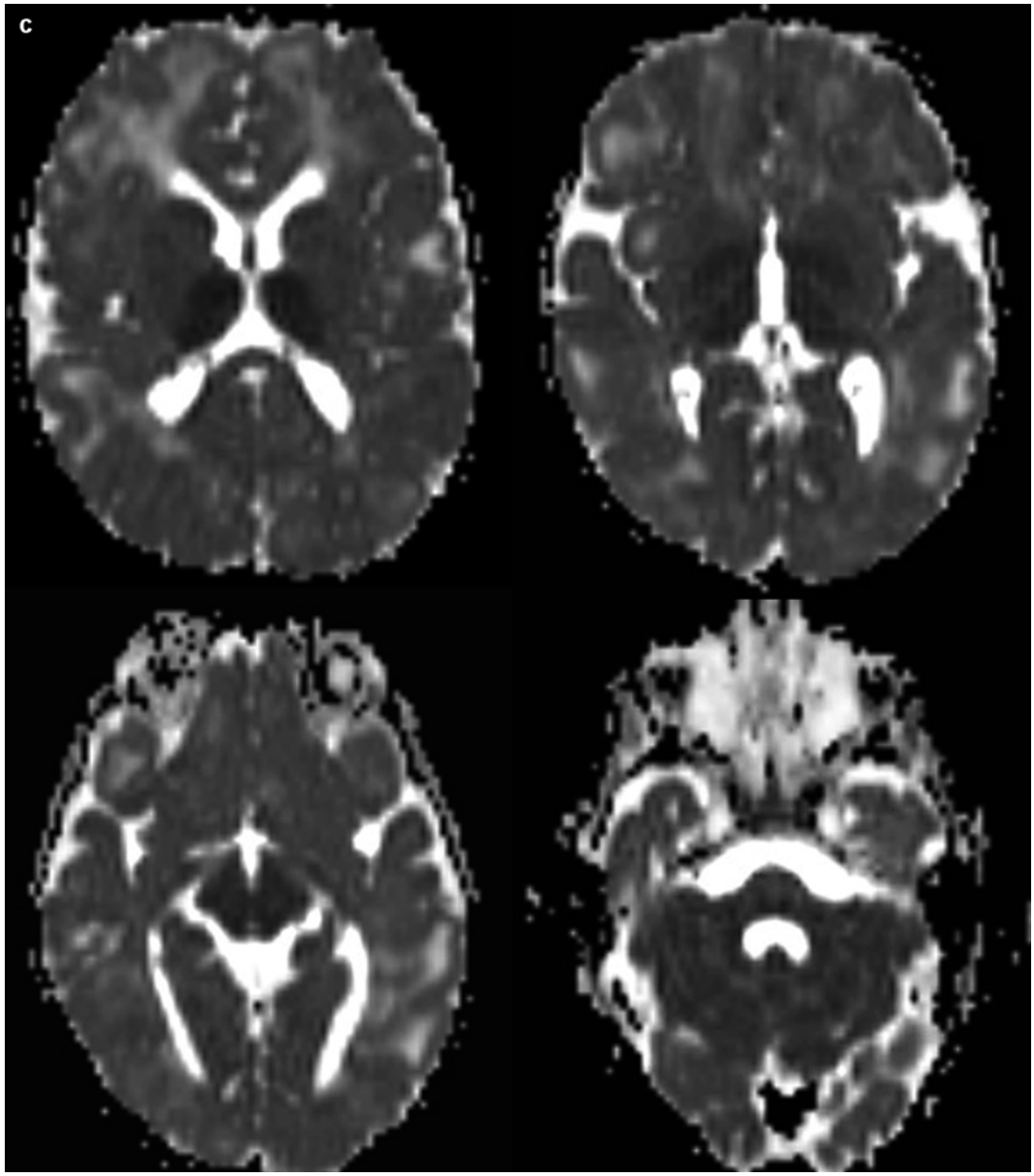

Fig. 29.1 (continued)

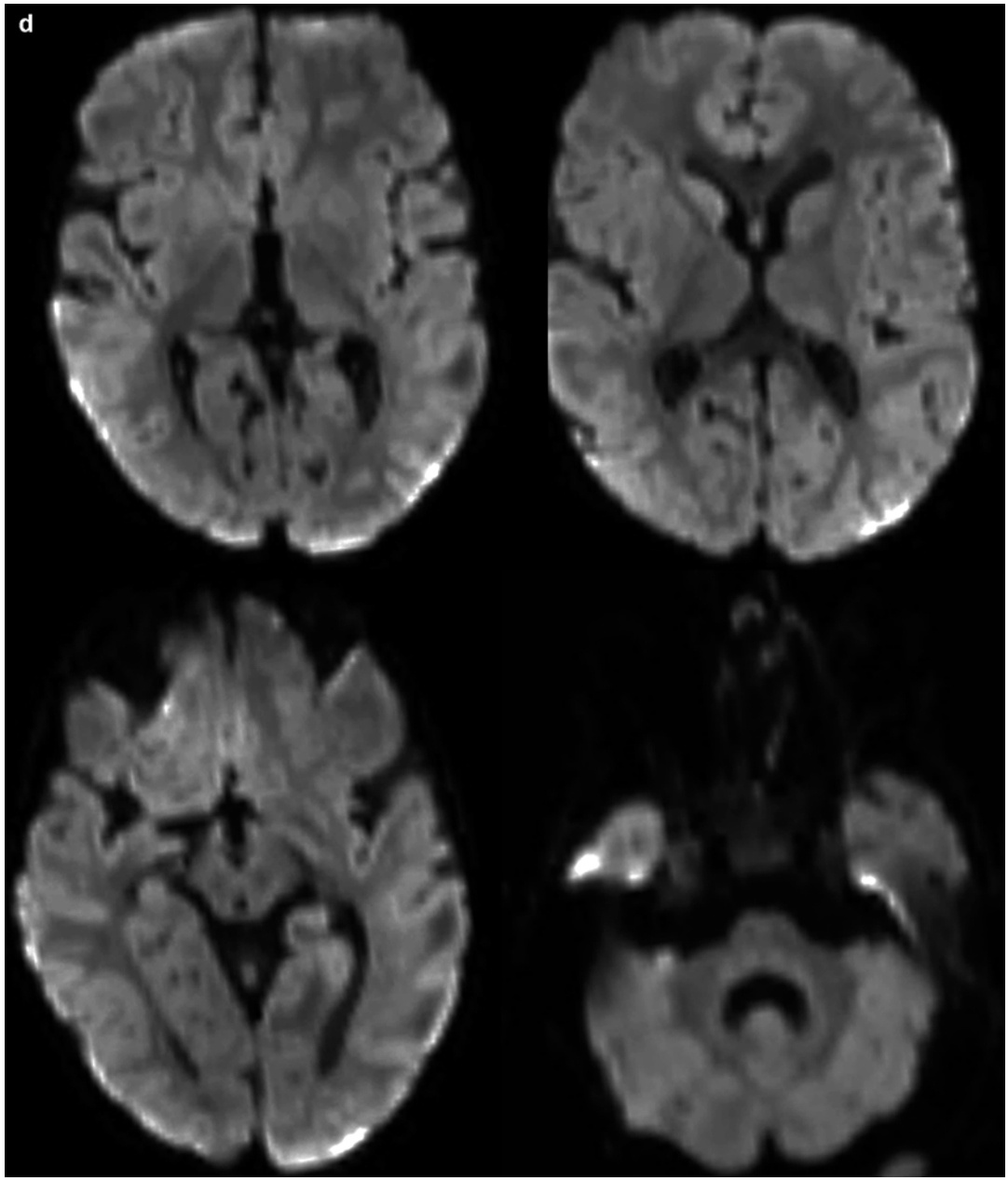

Fig. 29.1 (continued)

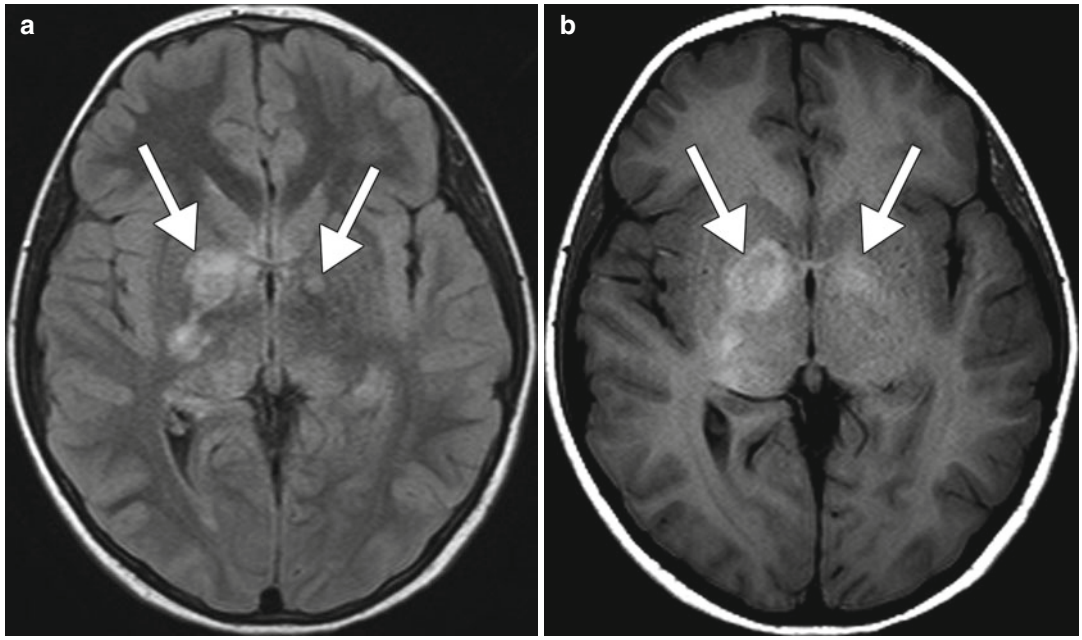

Fig. 29.2 Neurofibromatosis type 1. Axial FLAIR MRI (**a**) shows patchy hyperintensity in the bilateral basal ganglia, right greater than left (*arrows*). The corresponding axial T1-weighted MRI (**b**) shows corresponding T1 hyperintensity in the basal ganglia (*arrows*)

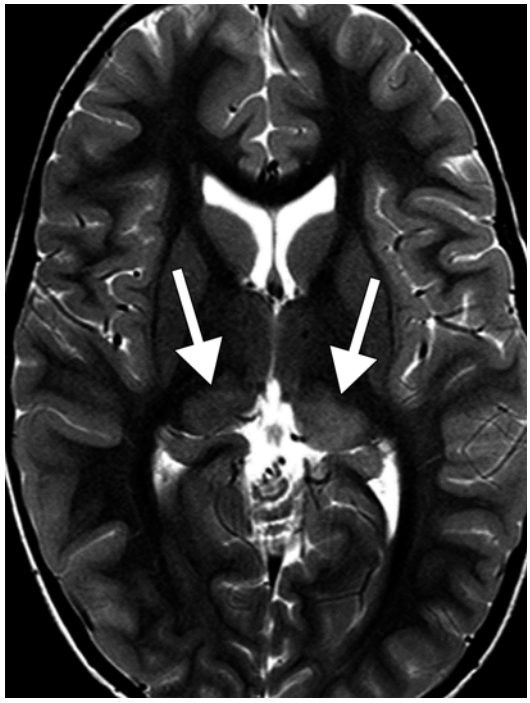

Fig. 29.3 Post-ictal thalamic changes. Axial T2-weighted MRI shows hyperintensity in the bilateral thalami (*arrows*)

cerebral vein thrombosis, and post-ictal thalamic changes resulting from excessive activity in thalamic nuclei having reciprocal connections with the involved cortex (Fig. 29.3)

- *Dentate nuclei*: Viral encephalitis, biotin-responsive encephalopathy, neurofibromatosis type 1, maple syrup urine disease, metronidazole toxicity (refer to Chap. 25) and methotrexate toxicity (refer to Chap. 19)

Suggested Reading

Ben-Menachem E. Mechanism of action of vigabatrin: correcting misperceptions. Acta Neurol Scand Suppl. 2011;192:5–15.

Dracopoulos A, Widjaja E, Raybaud C, Westall CA, Snead 3rd OC. Vigabatrin-associated reversible MRI signal changes in patients with infantile spasms. Epilepsia. 2010;51(7):1297–304.

Pearl PL, Vezina LG, Saneto RP, McCarter R, Molloy-Wells E, Heffron A, Trzcinski S, McClintock WM, Conry JA, Elling NJ, Goodkin HP, de Menezes MS, Ferri R, Gilles E, Kadom N, Gaillard WD. Cerebral MRI abnormalities associated with vigabatrin therapy. Epilepsia. 2009;50(2):184–94.

Thapa M, Khanna PC. Vigabatrin-associated diffusion MRI abnormalities in tuberous sclerosis. Pediatr Radiol. 2010;40 Suppl 1:S153.

Thelle T, Gammelgaard L, Hansen JK, Østergaard JR. Reversible magnetic resonance imaging and spectroscopy abnormalities in the course of vigabatrin treatment for West syndrome. Eur J Paediatr Neurol. 2011;15(3):260–4.

Embolic Agents

30

Lee-Anne Slater, Daniel Thomas Ginat,
and Ronil V. Chandra

30.1 Uses

Embolic agents are administered as part of an overall therapeutic approach to tumors and vascular pathology of the central nervous system. The choice of embolic agent depends on the clinical goal of the embolization procedure, i.e., permanent or temporary occlusion, taking into account the target vascular anatomy. In general, embolic agents can be classified as liquid and nonliquid embolic agents. Commonly used liquid embolic agents include n-Butyl Cyanoacrylate (nBCA) (Trufill nBCA Liquid Embolic, Codman Neurovascular, Raynham, Massachusetts, USA), ethylene vinyl alcohol copolymer (Onyx liquid embolic system, ev3 Neurovascular, Irvine, CA), and sclerosants, such as absolute alcohol and sodium tetradecyl sulfate (Sotradecol®). These agents are typically used for permanent occlusion of vascular malformations or tumor circulation. Commonly used nonliquid embolic agents are Gelfoam, polyvinyl alcohol (PVA) particles, and coils. Gelfoam and PVA are typically used temporary occlusion of tumor circulation or cessation of acute hemorrhage, while coils are typically used for permanent vessel or intracranial aneurysm occlusion.

30.2 Mechanism

nBCA rapidly polymerizes on contact with blood. When delivered, this is typically in a form mixed with ethiodized oil and tantalum powder to augment radiopacity. This forms a cast of the blood vessel, which causes immediate and permanent occlusion. On histological examination, vascular and perivascular inflammation are common, as well as angionecrosis. This is attributable to the exothermic reaction that occurs with polymerization. Over time, a foreign-body giant-cell reaction is induced with subsequent fibrosis in the vessel wall.

Onyx also polymerizes as the solvent dimethyl sulfoxide (DMSO) disperses on contact with blood. Onyx laminates on the blood vessel wall, which forms a cast of the blood vessel with continued delivery. Once the vascular cast fills the blood vessel, permanent occlusion is achieved. On histological examination, vascular and perivascular inflammation are common, as well as angionecrosis. Over time, a foreign-body giant-cell reaction is induced with subsequent fibrosis in the vessel wall.

Sclerosants, such as ethanol, cause immediate endothelial denudation on contact and consequent permanent vessel occlusion. Slower injections

L.-A. Slater, MBBS, MMed, FRANZCR
R.V. Chandra, MBBS, MMed, FRANZCR
Department of Diagnostic Imaging,
Monash Medical Center, Monash Health,
Melbourne, VIC, Australia

D.T. Ginat, MD, MS (✉)
Department of Radiology, University of Chicago,
Pritzker Medical School, Chicago, IL, USA
e-mail: ginatd01@gmail.com

D.T. Ginat et al. (eds.), *Neuroimaging Pharmacopoeia*,
DOI 10.1007/978-3-319-12715-6_30,

that prolong the contact time with endothelium result in greater cytotoxic injury.

Gelfoam is derived from porcine adipose tissue and is available in the form of a sponge or a powder. The Gelfoam sponge can be cut into small cuboids or made into a slurry and then delivered in an iodinated contrast suspension via an intravascular catheter. The small cuboids will pass into the target vasculature and mechanically occlude the lumen once the size of the Gelfoam piece is larger than the target vasculature. This also provides a matrix onto which platelet aggregation can occur. Gelfoam slurry delivery tends to form a "cast" the target vessel. Gelfoam is also commonly used during neurosurgery in the form of sheets or pledgets in order to help achieve and maintain hemostasis.

PVA particles are available in a range of sizes (typically 50–1,000 μm). Thus, the particle size can be tailored to the target vessel occlusion size required. PVA is also typically delivered in an iodinated contrast suspension via a intravascular catheter. Both Gelfoam and PVA result in temporary vessel occlusion. PVA also initially incites an acute inflammatory response, followed by a foreign-body giant-cell reaction. Vessel recanalization occurs due to absorption of the Gelfoam and vascular remodeling and collateral formation around the nonabsorbable PVA particles.

Coils induce thrombosis, which in combination with the coils themselves result in permanent occlusion. Some coils contain fibers along their length in order to increase thrombogenicity.

30.3 Discussion

When foreign material is identified within the cerebral vasculature, the presence of embolic agents should be considered. Nonliquid embolic agents and their effects are often discernible on radiographic, CT, and/or MRI imaging. The clinical history combined with characteristic imaging features can lead to accurate identification.

nBCA and Onyx are commonly used for embolization of cranial and spinal arteriovenous malformations and dural arteriovenous fistulae. Both appear as hyperdense casts that mold to the lumen of the embolized vascular structure. However, Onyx produces the greater streak artifact on CT compared to nBCA (Figs. 30.1 and 30.2).

Gelfoam and PVA particles are commonly used for preoperative embolization of tumor vasculature, in order to minimize blood loss during surgical excision. In general, the advantage of using PVA is the greater tumoral devascularization from penetration of small tumor vessels. However, the use of PVA particles <150 μm raises the risk of embolization into the vasa nervosum of the cranial nerves, and higher rates of complications have been reported during preoperative embolization. In certain situations, particularly for embolization of tumors at the skull base, larger PVA particle size and Gelfoam are preferable. At the time of embolization, Gelfoam is often mixed with contrast agents in order to increase conspicuity on X-ray modalities.

Fig. 30.1 nBCA. The patient has a history of hereditary hemorrhagic telangiectasia with a right cerebral hemisphere arteriovenous malformation. Axial non-contrast CT images shows the hyperattenuating embolic agent within the vascular malformation and associated aneurysm (*arrow*)

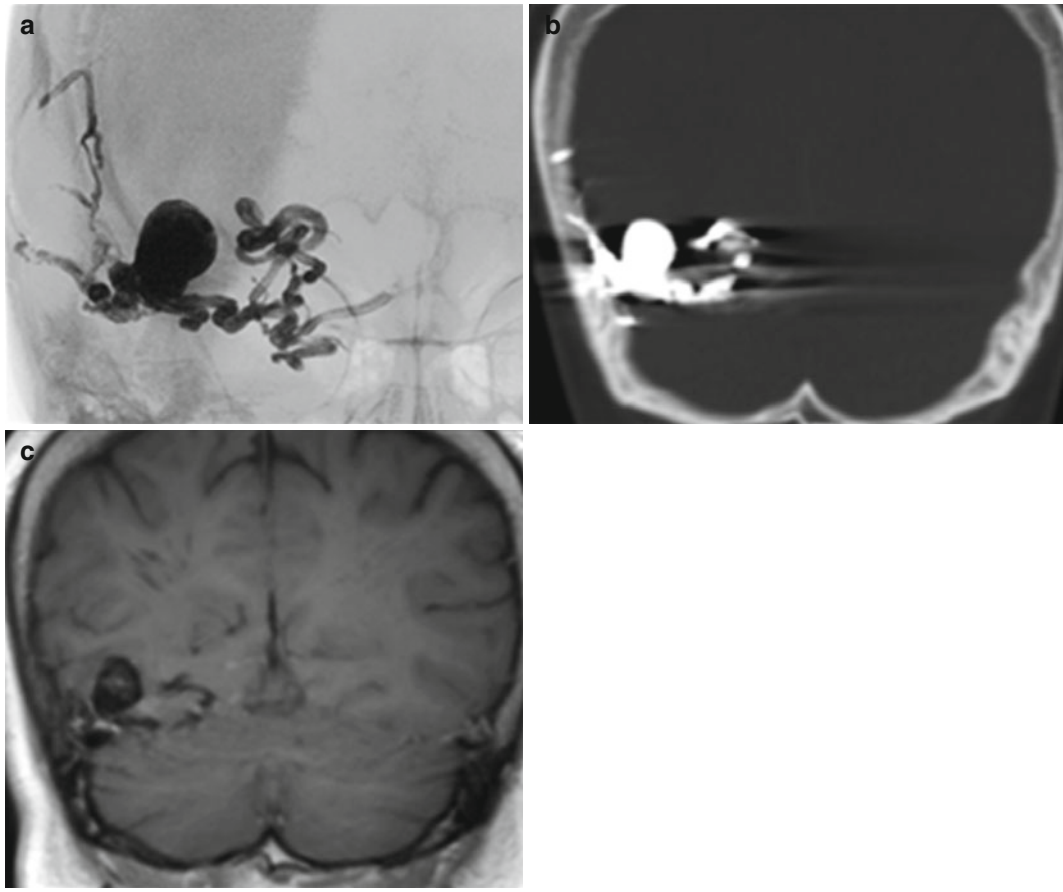

Fig. 30.2 Onyx. Frontal radiograph (**a**), coronal non-contrast CT (**b**), and coronal non-contrast T1-weighted MRI (**c**) show that the Onyx cast appears radiopaque and hyperattenuating and has molded to the shape of the arteriovenous malformation. There is associated beam-hardening artifact on CT

Otherwise, Gelfoam used for hemostasis in surgical cavity often initially appears as hypoattenuating sheets on CT but then becomes more hyperattenuating, and eventually dissolve (Fig. 30.3). On MRI, Gelfoam can appear as T1 hyperintense, which should not be mistaken for enhancement. Polyvinyl alcohol (PVA) particles are also mixed with contrast agents the time of embolization in order to facilitate visibility during angiography (Fig. 30.4). Although the particles cannot be directly visualized on imaging, the secondary effects of vascular occlusion and tissue necrosis may be evident (Fig. 30.5). With regard to meningiomas, postembolization MRI shows a variable degree of secondary revascularization and devascularization shortly after embolization. Peripheral secondary enhancement corresponds to a thin layer of viable tumor tissue, while the devitalized, necrotic portions do not enhance. MR spectroscopy may demonstrate a lactate peak in devascularized areas immediately after embolization. The tumors may or may not decrease in size following embolization.

Although coils can be used for permanent vessel occlusion, this is usually not required in the context of preoperative embolization. Coils are most commonly used in the treatment of intracranial aneurysms. Coils are radiopaque and can produce considerable streak artifact on CT, obscuring the adjacent brain parenchyma

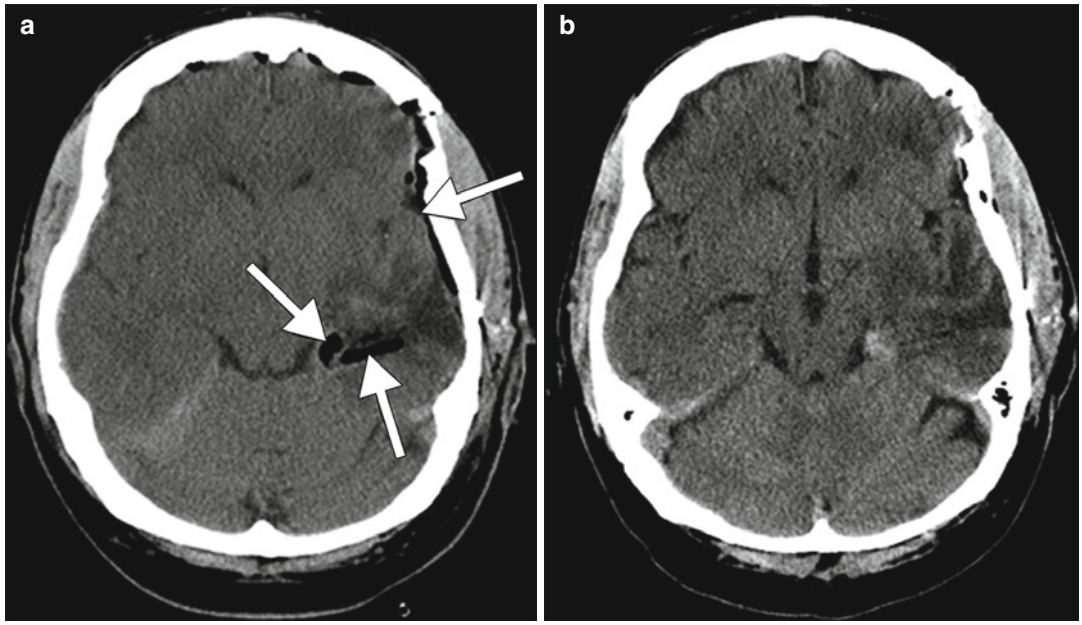

Fig. 30.3 Gelfoam. Initial postoperative CT image (**a**) obtained after left temporal lobe tumor resection shows linear hypoattenuation material lining the surgical bed, which corresponds to Gelfoam (*arrows*). Follow-up CT image (**b**) obtained several days later shows interval resorption of the Gelfoam

(Fig. 30.6). On MRI, coils are T1 and T2 hypointense and can cause local T2* susceptibility effects on MRA, which can be reduced by using short echo times.

30.4 Differential Diagnosis

Various conditions can produce cerebrovascular filling defects. Atheroembolism is a natural pathological phenomenon that is a common cause of stroke and can produce a dense vessel sign on non-contrast CT and vessel cutoff on angiography (Fig. 30.7). These lesions occur in an entirely different setting than interventional therapeutic embolization procedures, although inadvertent migration of the embolic agent and infraction of nontarget tissues can rarely occur as a complication. Very rare bullet emboli can mimic a small coil mass on CT (Fig. 30.8), while on some MRI sequences the low signal of a coil mass can potentially resemble a calcified tumor, pneumocephalus, or hemorrhage. Furthermore, aneurysm clips are also metallic, but these devices have a characteristic elongated configuration (Fig. 30.9). Calcifications that are often naturally present within vascular malformations (Fig. 30.10) may resemble the hyperdense liquid embolic agents, particularly nBCA. Without the relevant history, the tumor necrosis induced by embolic agents may be indistinguishable from spontaneous tumor necrosis and can also resemble spontaneous tumor necrosis and cystic (Fig. 30.11). The T1 hyperintensity associated with the contrast in Gelfoam can resemble natural emboli containing subacute blood products, while early Gelfoam on CT scan resemble pneumocephalus. The embolization-induced tumor necrosis can develop rapidly and be apparent on MRI within a matter of hours to days. There can be areas of restricted diffusion and the embolized mass can transient enlarge.

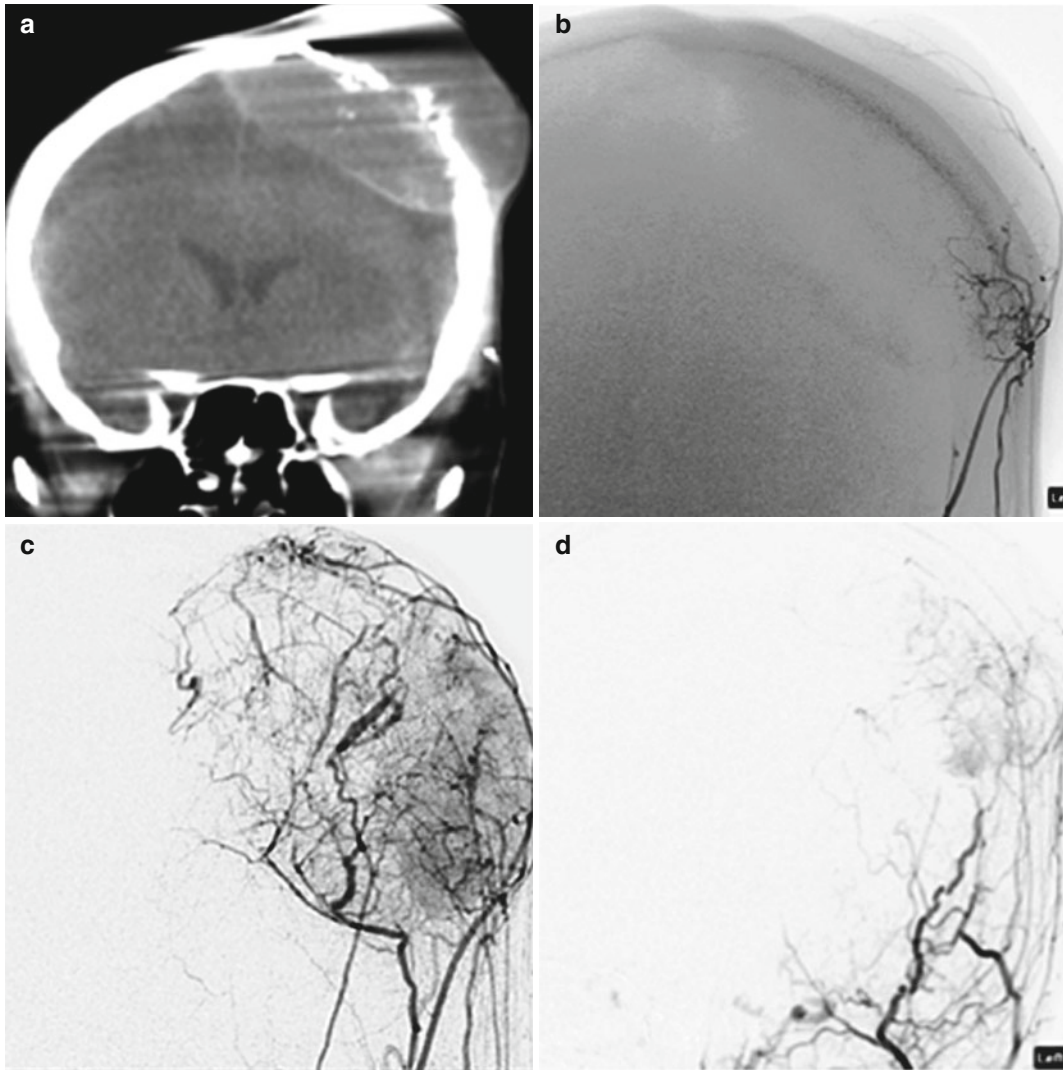

Fig. 30.4 PVA. Coronal intra-procedural CT (**a**), early arterial (**b**), and parenchymal phase (**c**) external carotid DSA shows prominent tumor vascularity in a cranial plasmacytoma. Post PVA embolization external carotid DSA (**d**) shows multiple feeding branch occlusions and absence of the tumor blush

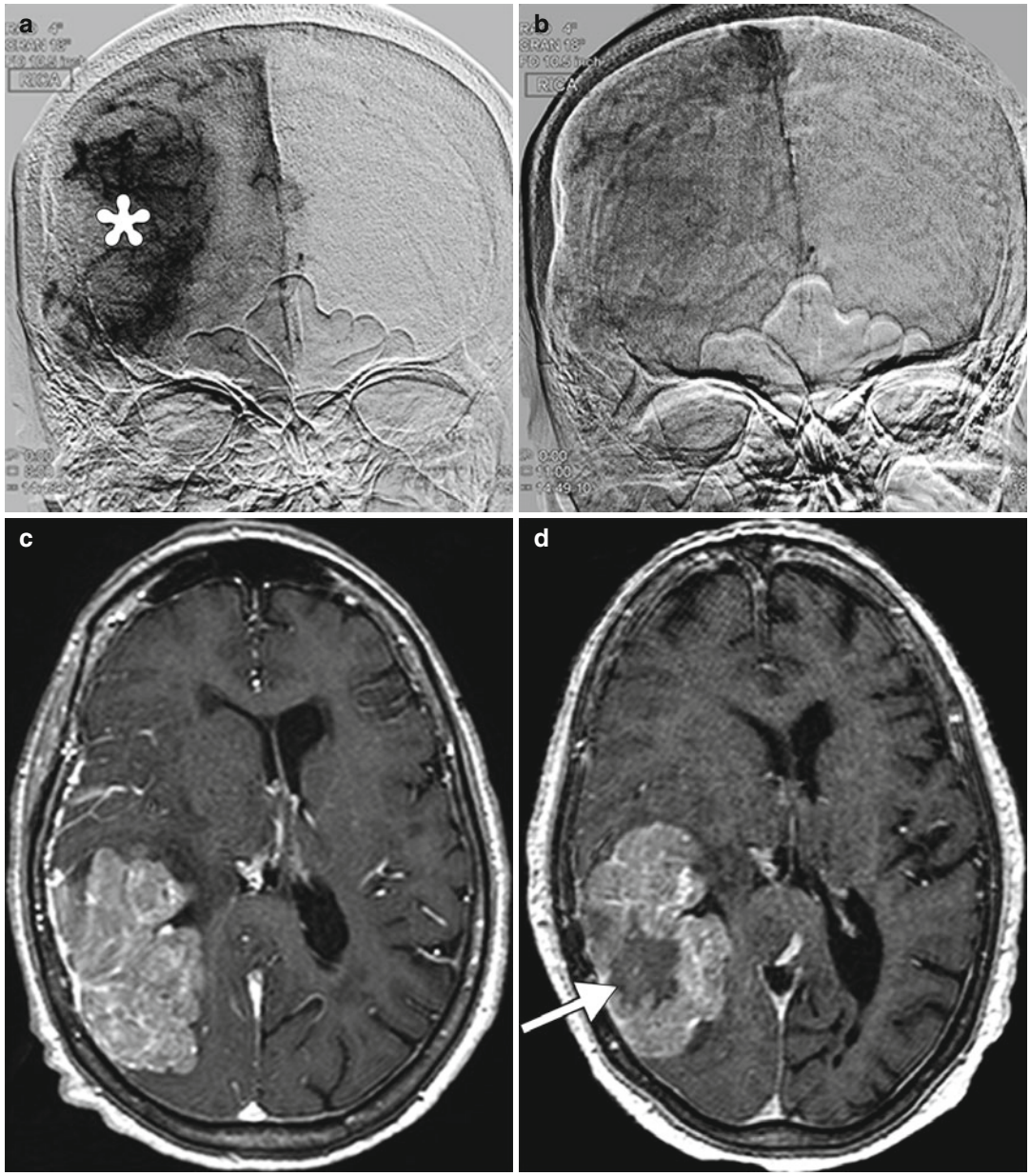

Fig. 30.5 Tumor necrosis. Initial frontal digital subtraction image (**a**) shows a large tumor blush, which corresponds to a meningioma (*). Completion digital subtraction image (**b**) obtained after Onyx embolization of the tumor shows marked diminution of the tumor blush. Pre-embolization axial post-contrast T1-weighted MRI (**c**) shows a large enhancing mass in the right temporo-occipital convexity. Post-embolization axial post-contrast T1-weighted MRI (**d**) shows interval development of central necrosis within the tumor (*arrow*)

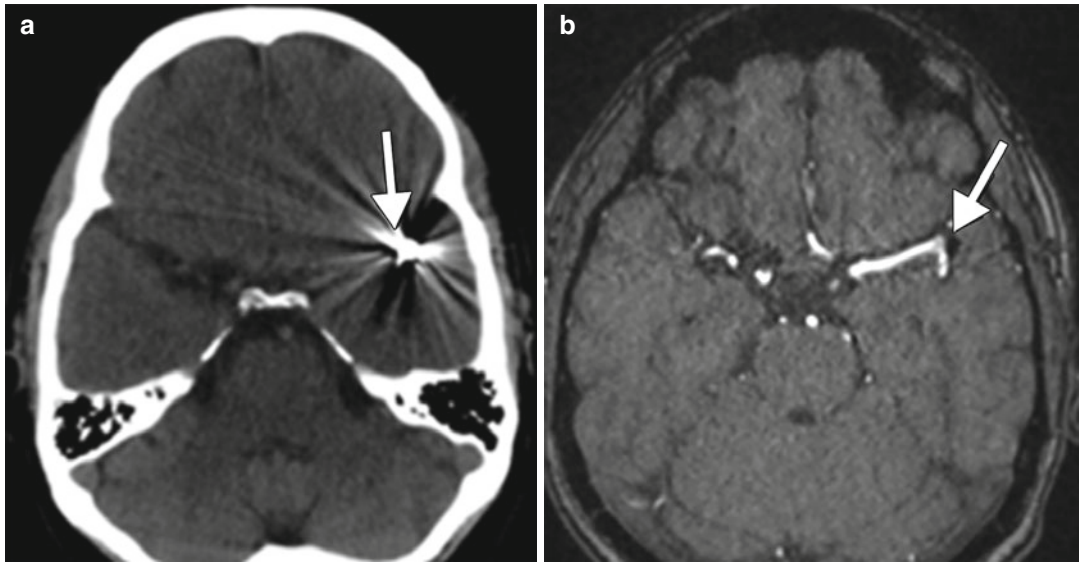

Fig. 30.6 Coil embolization. Axial CT (**a**) and axial T1 time of flight MRA (**b**) show that the coil mass (*arrows*) as radiopaque and hyperattenuating intravascular material with marked streak artifact on CT, greater than that of liquid embolic agents such as nBCA and Onyx, even on bone windows. There is minimal associated susceptibility effect on the MRA (*arrow*)

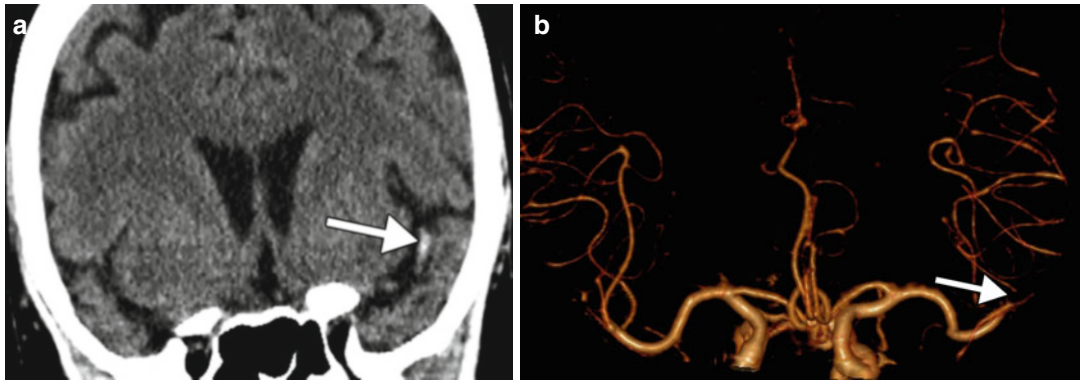

Fig. 30.7 Atheroembolus. Axial CT image (**a**) shows a dense left middle cerebral artery sign (*arrows*). Frontal projection 3D CTA reformatted image (**b**) show cutoff of the left middle cerebral artery (*arrow*)

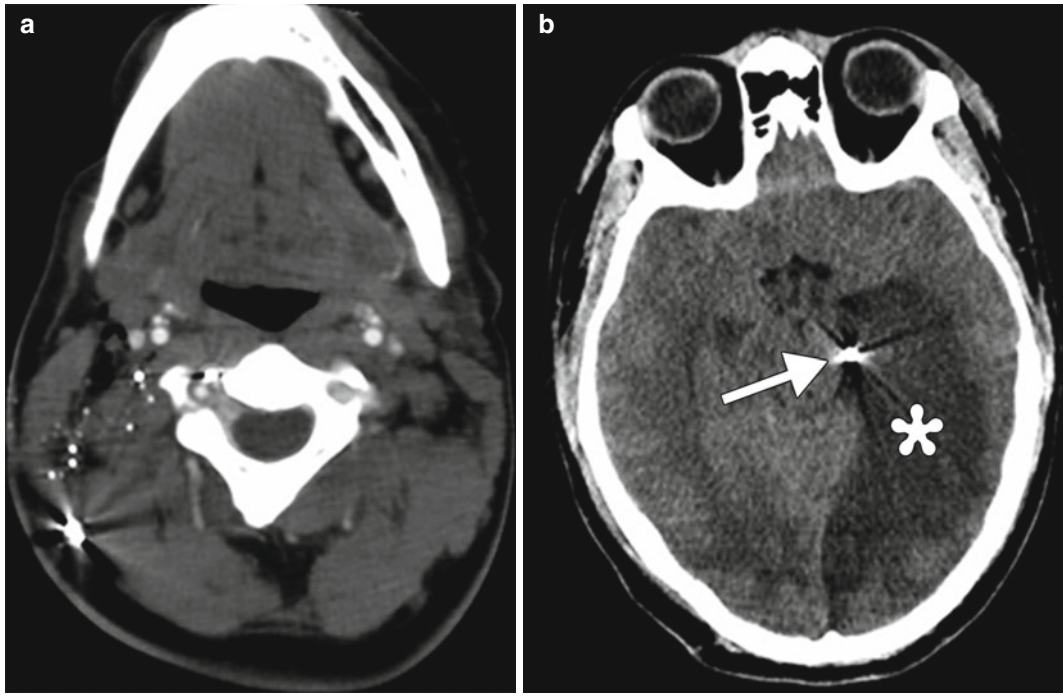

Fig. 30.8 Bullet embolization. Axial CTA of the neck (**a**) shows bullet fragments in the right neck. Axial CT image of the brain (**b**) shows a bullet fragment in the left posterior cerebral artery (*arrow*) with acute infarction in the corresponding vascular territory (*asterisk*)

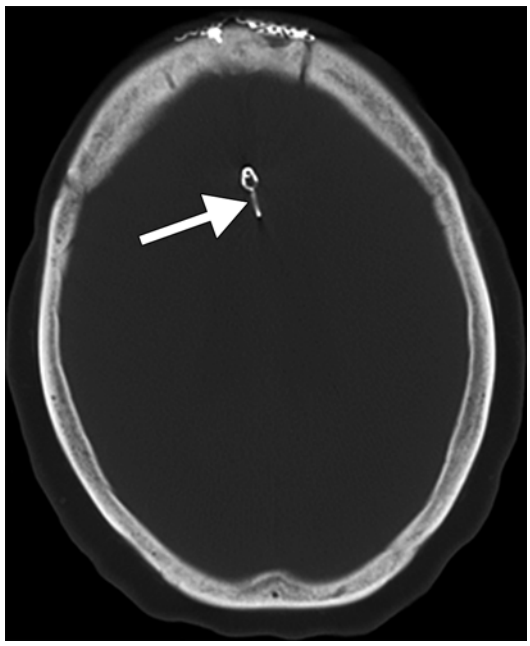

Fig. 30.9 Aneurysm clip. Axial CT image shows a linear metallic aneurysm clip (*arrow*) in the anterior cerebral artery trajectory

Fig. 30.10 Vascular malformation calcifications. Axial CT image shows punctate and curvilinear calcifications (*arrows*) associated with the arteriovenous malformation

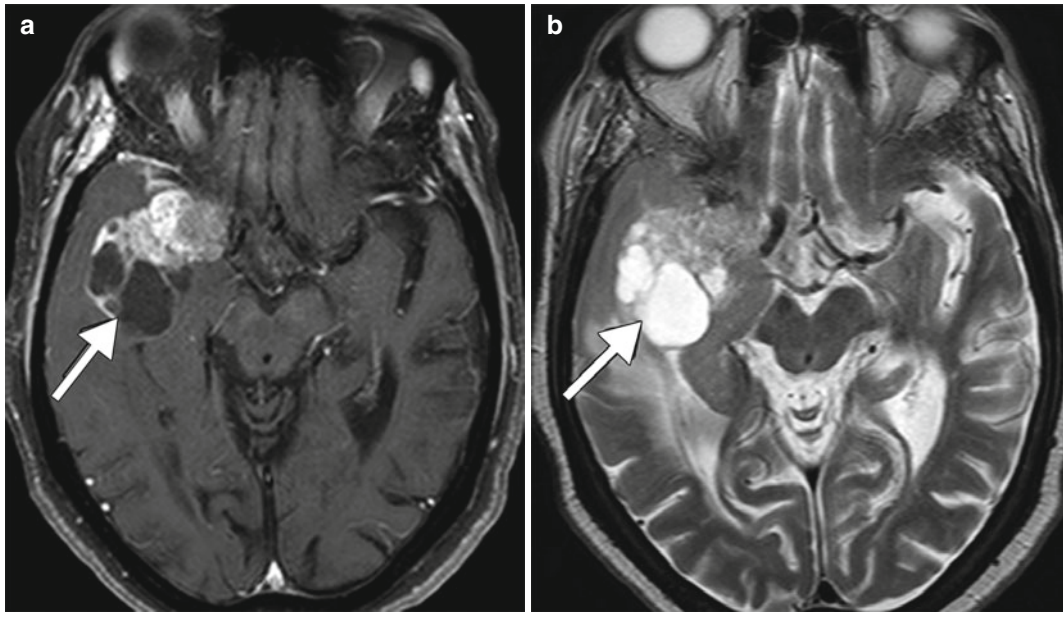

Fig. 30.11 Tumor cysts. Axial post-contrast T1-weighted (**a**) and T2-weighted (**b**) MR images show non-enhancing areas along the periphery of a right middle cranial fossa meningioma (*arrows*)

Suggested Reading

Bendszus M, Warmuth-Metz M, Klein R, Bartsch AJ, Krone A, Tonn JC, Solymosi L. Sequential MRI and MR spectroscopy in embolized meningiomas: correlation with surgical and histopathological findings. Neuroradiology. 2002;44(1):77–82.

Carli DF, Sluzewski M, Beute GN, van Rooij WJ. Complications of particle embolization of meningiomas: frequency, risk factors, and outcome. AJNR Am J Neuroradiol. 2010;31:152–4.

Lubarsky M, Ray CE, Funaki B. Embolization agents-which one should be used when? Part 1: large-vessel embolization. Semin Intervent Radiol. 2009;26:352–7.

Lubarsky M, Ray C, Funaki B. Embolization agents-which one should be used when? Part 2: small-vessel embolization. Semin Intervent Radiol. 2010;27:99–104.

Vaidya S, Tozer KR, Chen J. An overview of embolic agents. Semin Intervent Radiol. 2008;25:204–15.

Aspirin and Plavix/Clopidogrel

31

Merav Galper, Daniel Thomas Ginat, and Juan E. Small

31.1 Uses

Aspirin alone is indicated in the setting of the primary prevention of coronary heart disease in individuals who have multiple coronary risk factors. It is also recommended for the secondary prevention of ischemic stroke, patients with symptomatic peripheral arterial disease, and the long-term secondary prevention of myocardial infarction. Low-dose aspirin (81 mg) is typically prescribed in the setting of primary prevention and in the long-term after a patient suffers a myocardial infarction, while high-dose aspirin (325 mg) is typically prescribed in the acute setting post-myocardial infarction and for the long-term secondary prevention of ischemic stroke. Low-dose aspirin is typically combined with oral anticoagulants such as Coumadin in the primary prevention of embolic stroke in patients with atrial fibrillation.

While clopidogrel, like aspirin, is also recommended as monotherapy for secondary prevention of ischemic stroke and for peripheral arterial disease, it is typically combined with aspirin in the treatment of myocardial infarction. Since clopidogrel is a prodrug and requires activation by liver CYP enzymes, patients suffering a myocardial infarction that require urgent coronary revascularization are typically treated with an initial bolus of 300–600 mg of clopidogrel and 325 mg of aspirin. Thereafter patients are treated with 75 mg of clopidogrel for at least 1 month after receiving a percutaneous coronary intervention with a bare-metal coronary stent and at least 12 months if they received a drug-eluting stent. While low-dose aspirin treatment is continued indefinitely after myocardial infarction, there is active debate regarding the need to continue treatment with both aspirin and clopidogrel more than 12 months after percutaneous coronary intervention for a myocardial infarction.

31.2 Mechanism

Aspirin is an irreversible cyclooxygenase inhibitor which leads to thromboxane A2 inhibition. Clopidogrel is an irreversible inhibitor of the type 2 purinergic receptor ($P2Y_{12}$) which is an adenosine diphosphate receptor that lies on the surface of the platelet. Both drugs inhibit key steps in the activated platelet clotting cascade. Thromboxane A2 and adenosine diphosphate recruit and activate platelets. Adenosine diphosphate then binds to the type 2 purinergic receptor ($P2Y_{12}$) and the high affinity purinergic receptor (P2Y1). These receptors then increase intracellular calcium and ultimately activate the glycoprotein IIb/IIIa

M. Galper, MD • J.E. Small, MD
Department of Diagnostic Radiology, Lahey Clinic, Burlington, MA, USA

D.T. Ginat, MD, MS (✉)
Department of Radiology, University of Chicago, Pritzker Medical School, Chicago, IL, USA
e-mail: ginatd01@gmail.com

D.T. Ginat et al. (eds.), *Neuroimaging Pharmacopoeia*,
DOI 10.1007/978-3-319-12715-6_31,

complex which binds the platelets to one another forming linkages via fibrinogen molecules and thus leading to a meshwork of platelets and clot.

31.3 Discussion

Aspirin and clopidogrel combine to potently inhibit platelet function and thus lead to both a significant reduction in thrombotic events as well as an increase in risk of hemorrhage. Multiple clinical trials have demonstrated that the addition of clopidogrel to aspirin in patients presenting with myocardial infarction leads to a significant decrease in repeat ischemic events while also increasing risk of bleeding.

Aspirin and clopidogrel have also been evaluated for the prevention of ischemic stroke for patients with atrial fibrillation, and while the combination decreased the risk of recurrent stroke as compared to patients taking aspirin alone, it also led to a significant increase in the risk of hemorrhage and in particular intracranial bleeding and hemorrhagic stroke. In general the benefit of reducing ischemic stroke and myocardial infarction realized by the combination of aspirin and clopidogrel must be offset by the increased risk of bleeding, especially intracranial hemorrhage, from adding clopidogrel to aspirin therapy.

Acute intracranial hematomas appear as a hyperattenuating, round, or elliptical mass on computed tomography (Fig. 31.1) and are often associated with a peripheral area of vasogenic edema. Furthermore, anticoagulation can lead to multiple intracranial fluid-blood levels in the intracranial hematomas. Over time, the blood products in a hematoma evolve through a predictable variation in hemoglobin oxygenation states and hemoglobin by-products. This evolution manifests as gradually decreasing attenuation on CT and a specific pattern of changing signal characteristic on conventional MRI. There is generally minimal or no enhancement associated with coagulopathic hematomas. In addition to identifying hemorrhage, imaging is important for delineating associated complications, such as

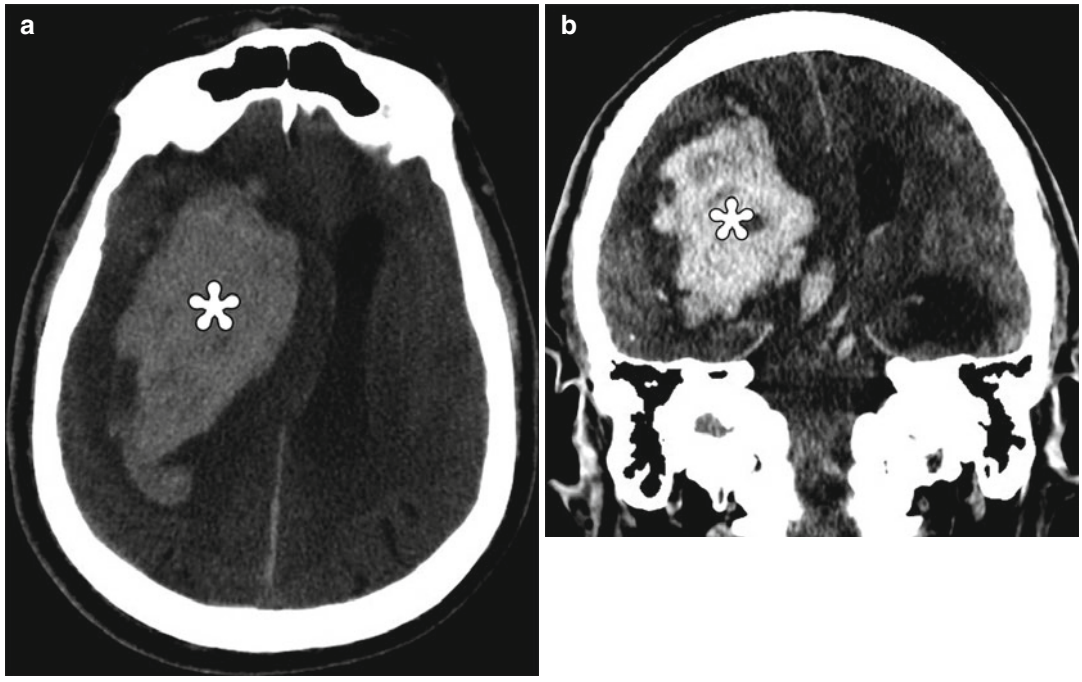

Fig. 31.1 Intraparenchymal hematoma related to aspirin and Plavix. Axial (**a**) and coronal (**b**) non-contrast CT images show a large right cerebral hemisphere hematoma (*) with associated midline shift to the left and obstructive hydrocephalus

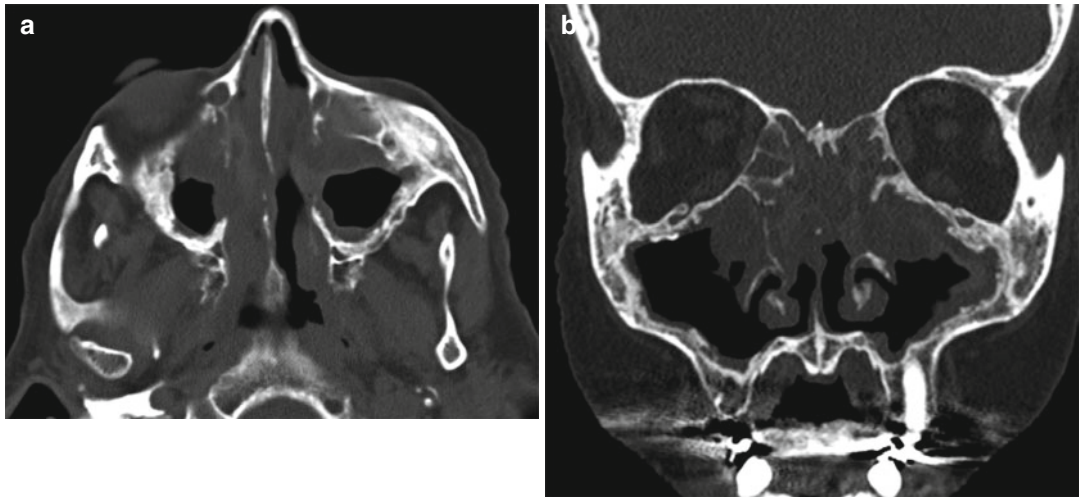

Fig. 31.2 Nasal polyps in aspirin sensitivity syndrome. Axial (**a**) and coronal (**b**) non-contrast CT images show extensive, bilateral sinonasal opacification related to multiple polypoid soft tissue densities in a patient with prior endoscopic sinus surgery

obstructive hydrocephalus, vascular compression, and herniation of brain tissue.

A rare, but devastating complication of aspirin use is Reye syndrome, which consists of hepatitis and encephalopathy in the setting of a viral illness, particularly in the pediatric population. On imaging, diffuse cerebral edema and signal alterations in brainstem, bilateral thalami, medial temporal lobes, parasagittal cortex, and cerebellar and subcortical white matter are evident. In addition, there can be diffusion restriction in the thalami, midbrain, cerebellar white matter, subcortical white matter, and watershed territories. The imaging abnormalities tend to resolve as the patients recover from this condition.

An additional complication of aspirin use that may be encountered on neuroimaging is nasal polyposis in patients with aspirin sensitivity and asthma (Samter's triad). Non-contrast CT of the sinuses often shows widespread mucosal inflammation and bilateral polypoid opacities in the sinonasal cavities (Fig. 31.2). Patients with Samter's triad tend to have a more extensive sinonasal disease and a higher rate of nasal polyp recurrence following endoscopic sinus surgery than aspirin-tolerant patients. Patients with aspirin sensitivity may also develop aural polyps.

31.4 Differential Diagnosis

Differential considerations for acute, nontraumatic cerebral hemorrhage include hypertensive hemorrhage, with characteristic locations in the basal ganglia, thalamus, pons, and cerebellum; amyloid angiopathy, which classically demonstrates a lobar distribution and associated foci of blooming or "black dots" on SWI in a subcortical distribution (Fig. 31.3); vascular malformations (Fig. 31.4); venous sinus thrombosis (refer to Chaps. 20 and 47); cocaine or alcohol abuse (refer to Chaps. 2 and 5); primary CNS vasculitis (refer to Chaps. 5, 6, and 10); hemorrhagic neoplasm, for which tumoral enhancement may be minimal; and hemorrhagic conversion of ischemic stroke. The imaging interpreter must combine imaging findings with clinical history, including age of the patient, medical comorbidities, and medication use, in order to arrive at the most probable diagnosis. In patients without a clear etiology of the intracranial hemorrhage on initial evaluation, CTA or MRA should be recommended. Furthermore, underlying lesions may not be apparent in the acute phase of hemorrhage, and follow-up imaging in 2–3 months is often warranted (Fig. 31.5).

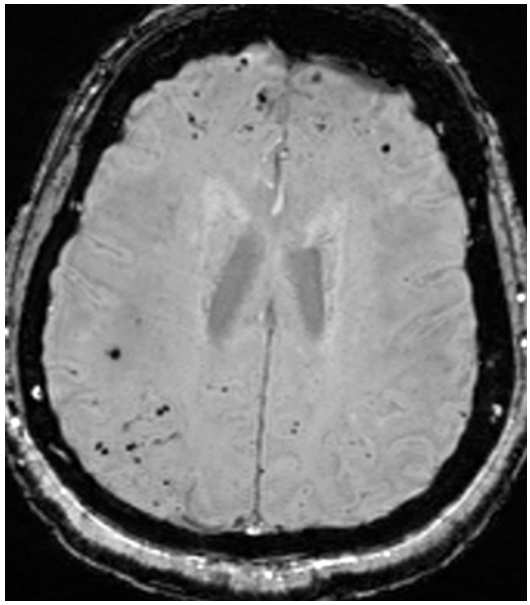

Fig. 31.3 Amyloid angiopathy. Axial SWI image demonstrates numerous subcortical punctate foci of susceptibility effect consistent with foci of chronic microhemorrhage

The differential diagnosis for sinonasal polyposis in the setting of aspirin sensitivity may include inverted papilloma (Fig. 31.6) and neoplasms, such as melanoma (Fig. 31.7). In general, CT is well suited for depicting hyperostosis that may be associated with inverted papilloma and osseous destruction that can be associated with malignant neoplasms. On the other hand, MRI is often better suited for depicting orbital and intracranial involvement.

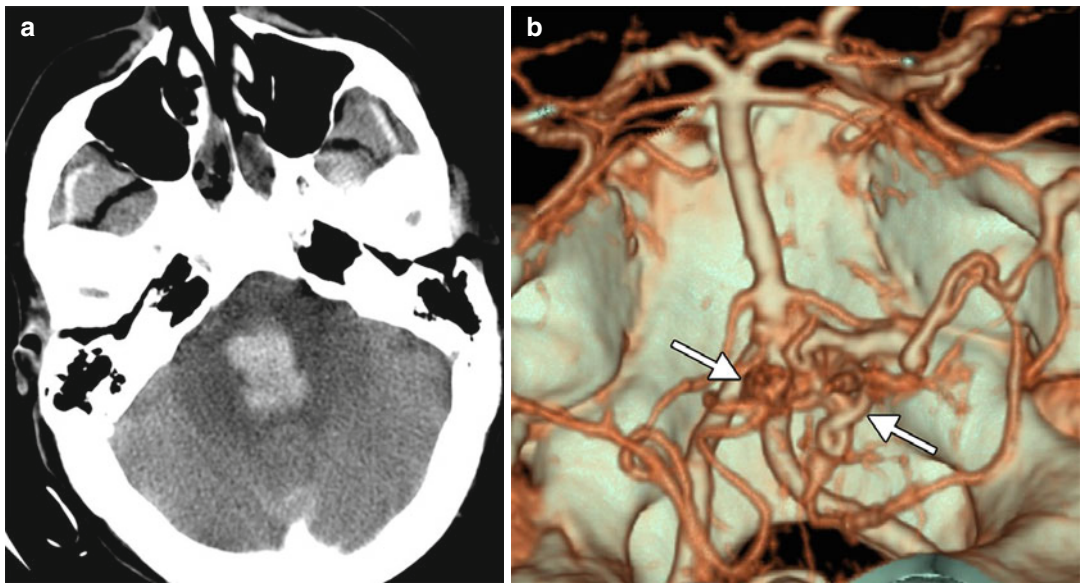

Fig. 31.4 Ruptured arteriovenous malformation. Axial non-contrast CT image (**a**) shows an acute hematoma within the pons and fourth ventricle. 3D CTA image (**b**) shows the vascular nidus of an arteriovenous malformation arising from the vertebrobasilar circulation (*arrows*)

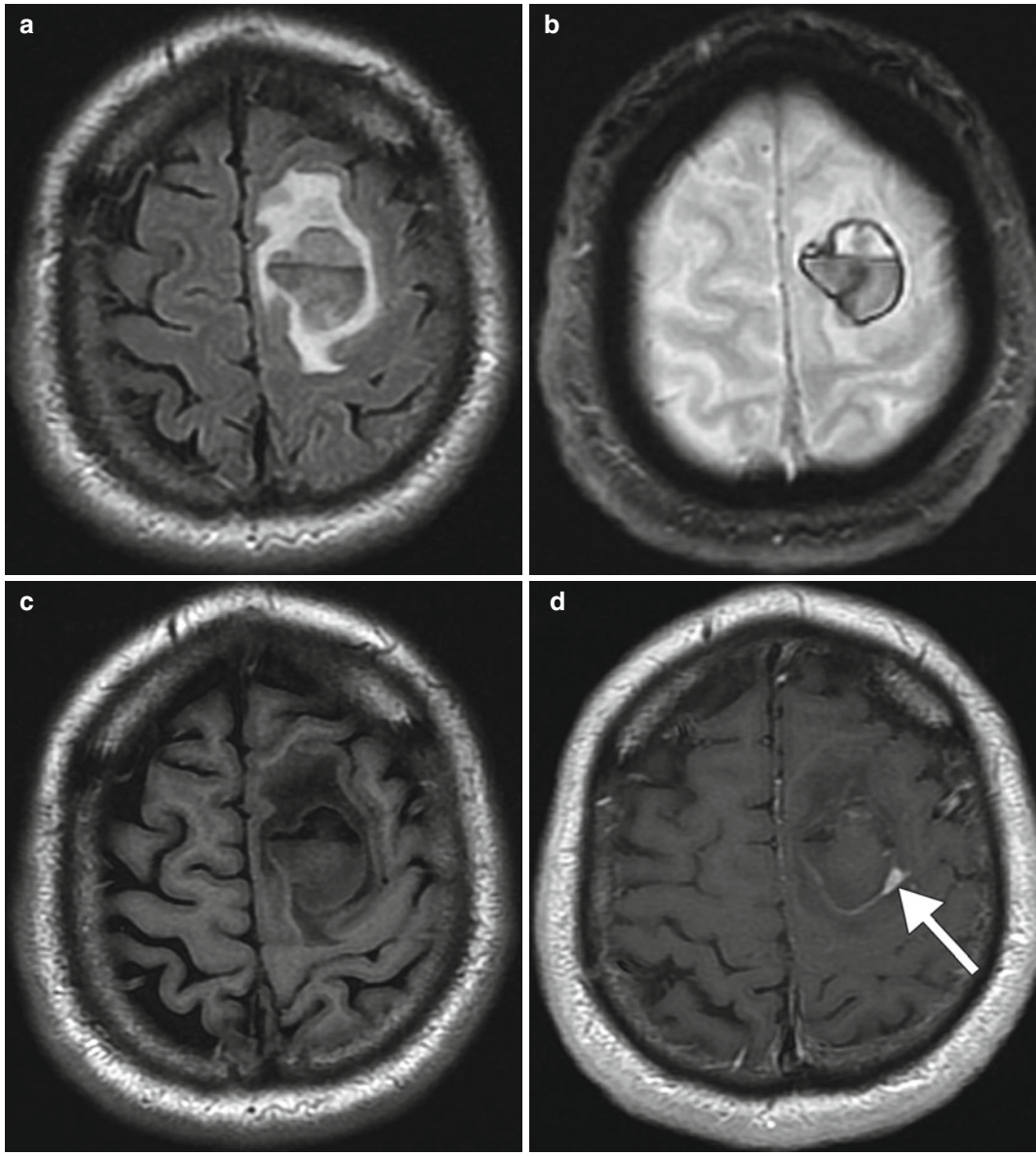

Fig. 31.5 Hemorrhagic metastasis. The patient has a history of melanoma. Axial FLAIR (**a**), T2* GRE (**b**), T1-weighted (**c**), and post-contrast T1-weighted (**d**) MR images show a mass in the left frontal lobe with layering hemorrhage, surrounding vasogenic edema, and a small focus of enhancement (*arrow*)

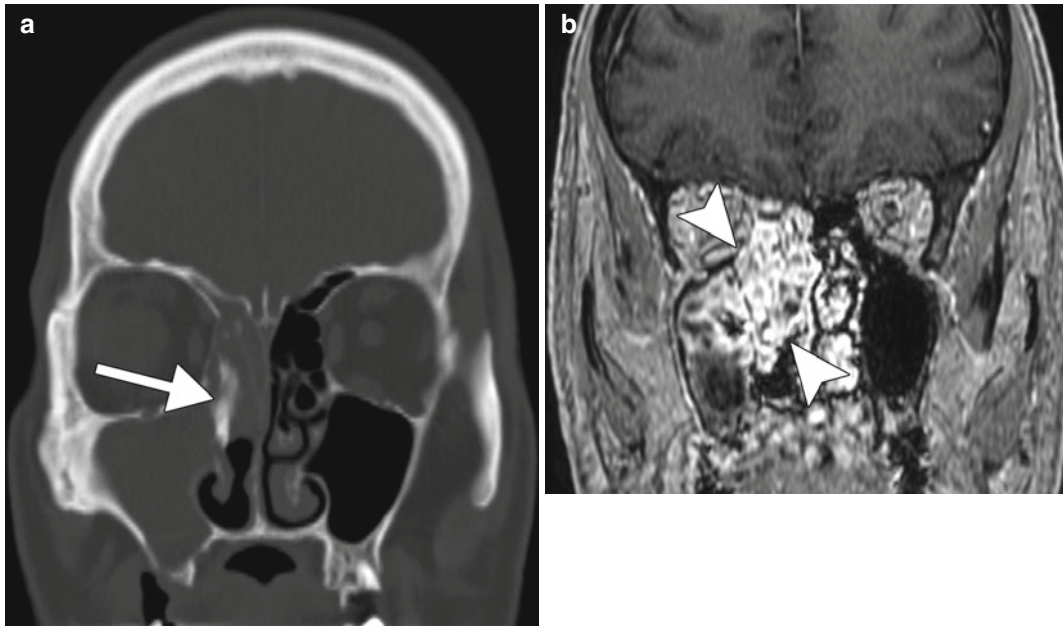

Fig. 31.6 Inverted papilloma. Coronal CT image (**a**) shows opacification in the right osteomeatal unit complex containing a dense calcification (*arrow*). Coronal post-contrast MRI (**b**) shows that the right sinonasal mass displays a cerebriform pattern of enhancement (*arrowheads*)

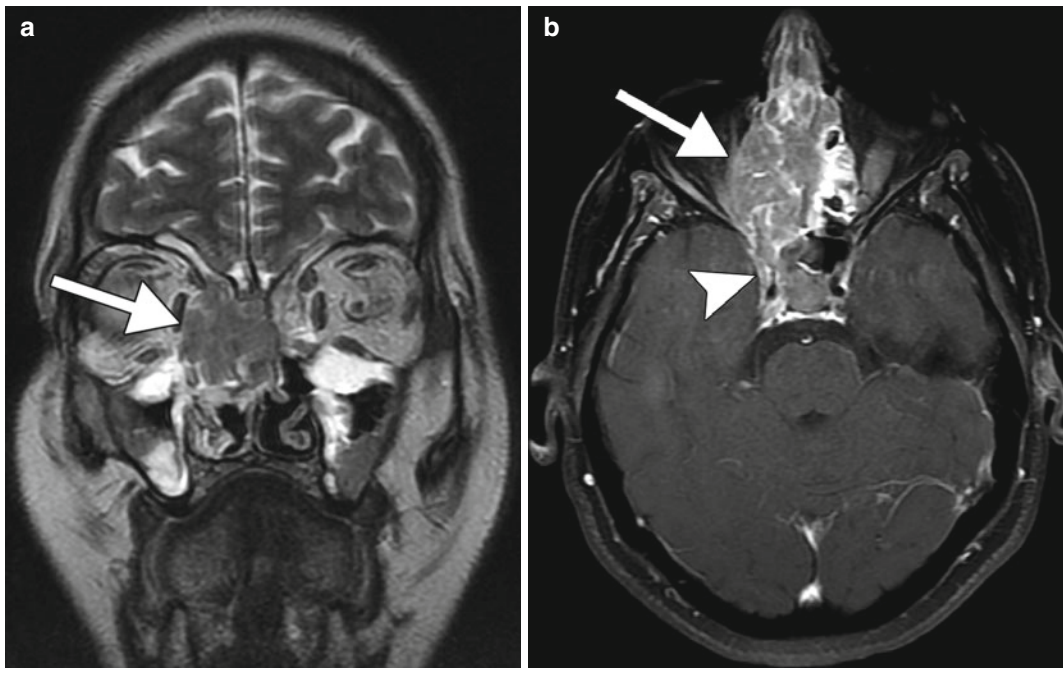

Fig. 31.7 Sinonasal melanoma. Coronal T2-weighted (**a**) and fat-suppressed post-contrast T1-weighted MR images show a low T2, enhancing mass in the right nasal cavity that invades the right orbit (*arrows*). In addition, the post-contrast T1-weighted image (**b**) shows intracranial extension (*arrowhead*)

Suggested Reading

Awad OG, Lee JH, Fasano MB, Graham SM. Sinonasal outcomes after endoscopic sinus surgery in asthmatic patients with nasal polyps: a difference between aspirin-tolerant and aspirin-induced asthma? Laryngoscope. 2008;118(7):1282–6.

Bhatt DL, Fox KAA, Hacke W, Berger PB, Black HR, Boden WE, Cacoub P, Cohen EA, Creager MA, Easton JD, Flather MD, Haffner SM, Hamm CW, Hankey GJ, Johnston SC, Mak K-H, Mas J-L, Montalescot G, Pearson TA, Steg PG, Steinhubl SR, Weber MA, Brennan DM, Fabry-Ribaudo L, Booth J, Topol EJ, for the CHARISMA Investigators. Clopidogrel and aspirin versus aspirin alone for the prevention of atherothrombotic events. N Engl J Med. 2006;354:1706–17.

Kim JE, Kountakis SE. The prevalence of Samter's triad in patients undergoing functional endoscopic sinus surgery. Ear Nose Throat J. 2007;86(7):396–9.

Mehta SR, Yusuf S, Peters RJ, Bertrand ME, Lewis BS, Natarajan MK, Malmberg K, Rupprecht H, Zhao F, Chrolavicius S, Copland I, Fox KA, Clopidogrel in Unstable angina to prevent Recurrent Events trial (CURE) Investigators. Effects of pretreatment with clopidogrel and aspirin followed by long-term therapy in patients undergoing percutaneous coronary intervention: the PCI-CURE study. Lancet. 2001;358(9281):527–33.

Ozdoba C, Pfenninger J, Schroth G. Initial and follow-up MRI in a case of early diagnosed Reye's syndrome. Neuroradiology. 1997;39(7):495–8.

Parizel PM, Makkat S, Van Miert E, Van Goethem JW, van den Hauwe L, De Schepper AM. Intracranial hemorrhage: principles of CT and MRI interpretation. Eur Radiol. 2001;11(9):1770–83.

Pfleger MJ, Hardee EP, Contant Jr CF, Hayman LA. Sensitivity and specificity of fluid-blood levels for coagulopathy in acute intracerebral hematomas. AJNR Am J Neuroradiol. 1994;15(2):217–23.

Sharis PJ, Cannon CP, Loscalzo J. The antiplatelet effects of ticlopidine and clopidogrel. Ann Intern Med. 1998;129(5):394–405.

Shen J, Peterson M, Mafee M, Nguyen QT. Aural polyps in Samter's triad: case report and literature review. Otol Neurotol. 2012;33(5):774–8.

Singh P, Goraya JS, Gupta K, Saggar K, Ahluwalia A. Magnetic resonance imaging findings in Reye syndrome: case report and review of the literature. J Child Neurol. 2011;26(8):1009–14.

The ACTIVE Investigators. Effect of clopidogrel added to aspirin in patients with atrial fibrillation. N Engl J Med. 2009;360:2066–78.

Weisberg LA.Significance of the fluid-blood interface in intracranial hematomas in anticoagulated patients. Comput Radiol. 1987;11(4):175–9

Zeitz HJ. Bronchial asthma, nasal polyps, and aspirin sensitivity: Samter's syndrome. Clin Chest Med. 1988; 9(4):567–76.

Warfarin (Coumadin)

32

Jeffrey Hashim, Daniel Thomas Ginat, and Juan E. Small

32.1 Uses

Anticoagulation therapy for stroke risk prevention, treatment of deep venous thrombosis, and pulmonary embolism.

32.2 Mechanism

Selective inhibition of vitamin K epoxide reductase enzyme by warfarin results in diminished stores of vitamin K available to the tissues. Vitamin K is essential for activation of the normal coagulation cascade through its interaction with another enzyme, gamma-glutamyl carboxylase, which is responsible for activating coagulation factors such that they will bind endothelial surfaces of blood vessels initiating blood clot formation.

32.3 Discussion

Warfarin is the most widely used anticoagulant medication in the world. The gravest of side effects of anticoagulant therapy is hemorrhage. This can occur spontaneously in the setting of a supratherapeutic INR or in the setting of a therapeutic INR where there has been trauma. Intracranial hemorrhage can be the most devastating (Fig. 32.1). However, the location of hemorrhage can also occur elsewhere in the head and neck soft tissues, resulting in rather large hematomas even with relatively minor trauma (Fig. 32.2). CT is generally the first-line modality for evaluating intracranial and maxillofacial hemorrhage.

Hemorrhage associated with warfarin can occur in any CNS compartment, including epidural, subdural, and subarachnoid locations. In addition to the complications at the site of hemorrhage, more remote complications related may later ensue. For instance, a rare complication of intracranial subarachnoid hemorrhage is the development of adhesive arachnoiditis with arachnoid adhesions, septations, and cysts that mainly involve the cervical and thoracic spine (Fig. 32.3).

Other less common side effects include warfarin necrosis and fetal warfarin syndrome (Binder phenotype). Warfarin necrosis occurs early with the initiation of warfarin therapy and is believed to occur secondary to decreased levels of protein C, which is an anticoagulant. This response is exaggerated in patients who express genetic mutations resulting in low protein C levels. When anticoagulation is initiated, vicarious administration of heparin products is used to offset these processes. Warfarin is a teratogen during the first trimester of pregnancy. Several findings are

J. Hashim, MD • J.E. Small, MD
Department of Diagnostic Radiology, Lahey Clinic, Burlington, MA, USA

D.T. Ginat, MD, MS (✉)
Department of Radiology, University of Chicago, Pritzker Medical School, Chicago, IL, USA
e-mail: ginatd01@gmail.com

D.T. Ginat et al. (eds.), *Neuroimaging Pharmacopoeia*,
DOI 10.1007/978-3-319-12715-6_32,

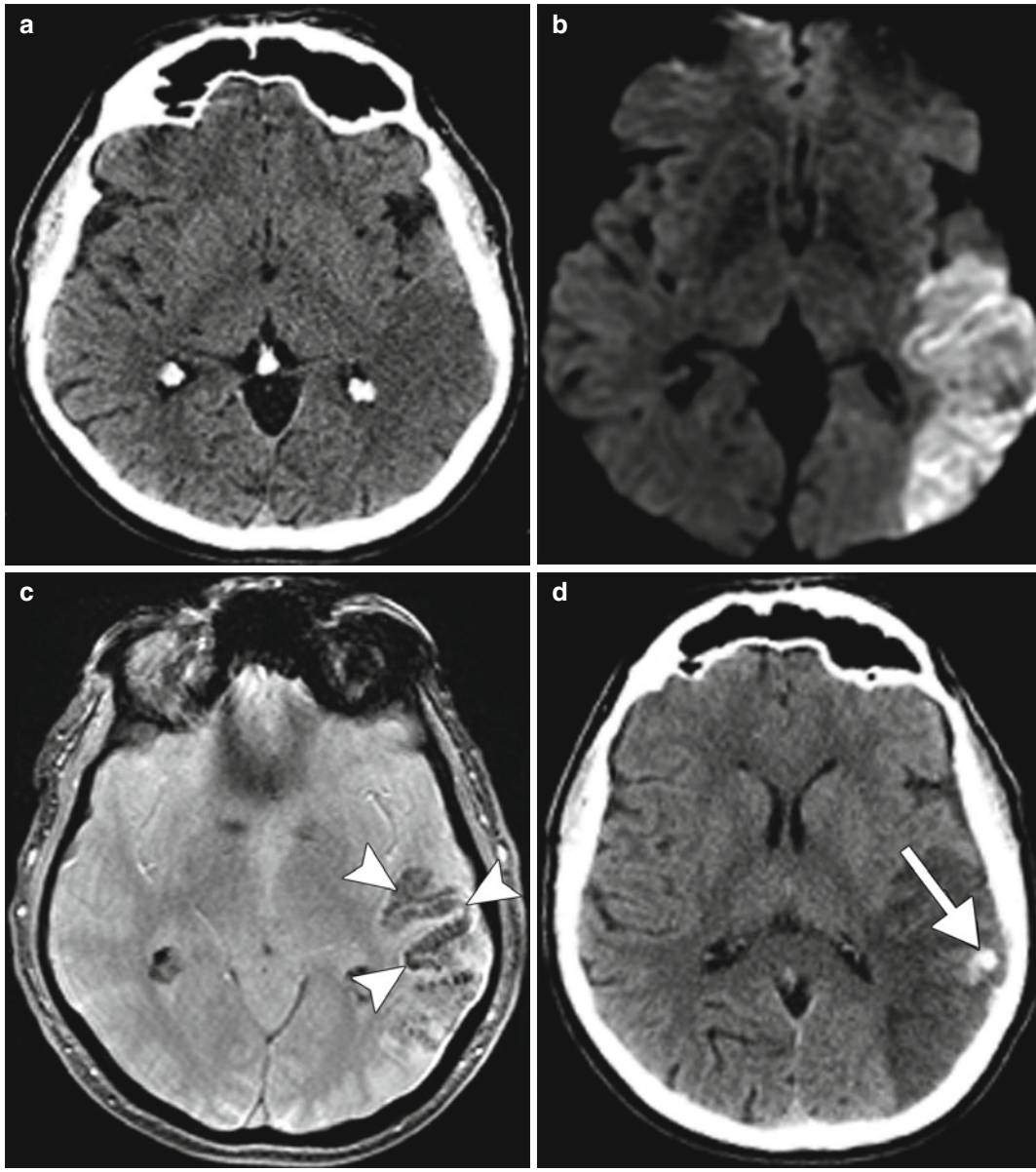

Fig. 32.1 Warfarin-associated intracranial hemorrhage. The patient underwent anticoagulation for a left MCA cardioembolic stroke shortly after atrial fibrillation ablation procedure. Axial non-contrast CT (**a**), axial DWI (**b**), and axial GRE (**c**) images demonstrate a left MCA territory infarct with cortical petechial microhemorrhage (*arrowheads*), but no gross hemorrhagic conversion apparent on CT. Axial non-contrast CT (**d**) obtained one later shows a small area of hemorrhagic conversion (*arrow*). Anticoagulation with Coumadin was reinstituted secondary to concerns of atrial fibrillation and the concern of new cardioembolic phenomena. The patient presented acutely 2 weeks later with an INR of 2.2 when axial non-contrast CT (**e**, **f**) demonstrated extensive hemorrhagic conversion with multiple hemorrhagic fluid levels

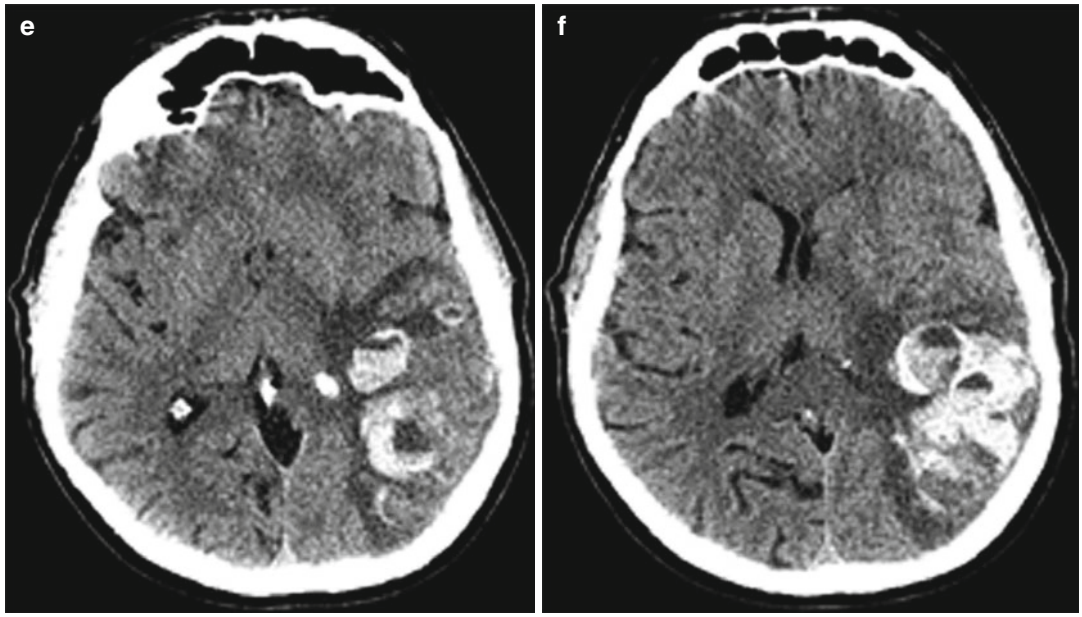

Fig. 32.1 (continued)

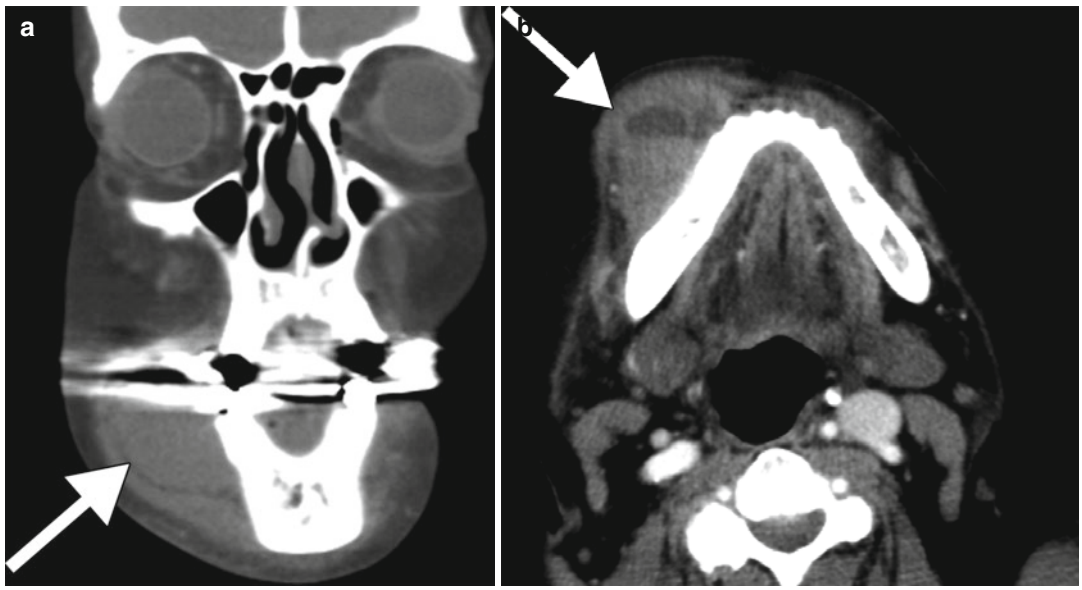

Fig. 32.2 Warfarin-associated facial hemorrhage. Coronal (**a**) and axial (**b**) CT images of the face show a large hematoma overlying the right mandible (*arrows*). Note the layering blood-fluid level on the axial image. The presence of a blood-fluid level has been found to be moderately sensitive but highly specific for the identification of a coagulopathic hemorrhage

associated with fetal warfarin syndrome, including epiphyseal stippling, nasal hypoplasia (Fig. 32.4), nasal cartilage calcification, scoliosis, and brachydactyly. Warfarin use later in pregnancy is considered impart a lower risk of birth defects.

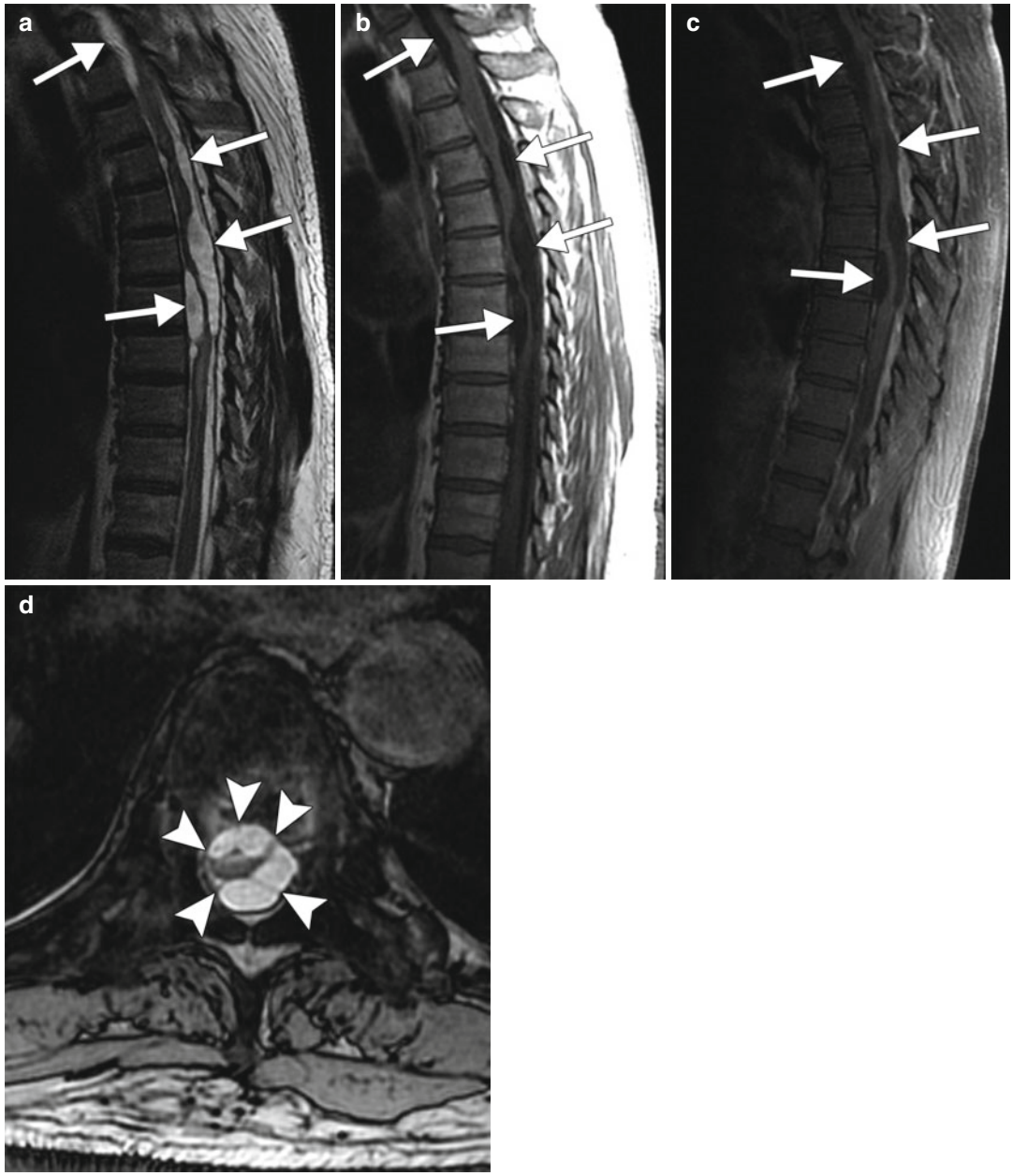

Fig. 32.3 Adhesive arachnoiditis as a late complication of Warfarin-associated subarachnoid hemorrhage. The patient has a history of prior intracranial and thoracic spine subarachnoid and subdural hemorrhage, presenting with several months of low back pain and progressive lower extremity weakness and paresthesias. Sagittal T2-weighted (**a**), sagittal T1-weighted (**b**), and sagittal T1-weighted post-contrast (**c**) images of the thoracic spine demonstrate distortion of the thoracic spinal cord in multiple areas associated extramedullary cystic spaces (*arrows*). Axial GRE (**d**) image depicts the morphologically abnormal spinal cord secondary to arachnoid adhesions (*arrowheads*)

32.4 Differential Diagnosis

The differential considerations for warfarin-induced complications encountered on imaging are numerous, and clinical history is critical for establishing the appropriate diagnosis. However, it should be cautioned that patients on Coumadin may nevertheless have a separate etiology of the abnormality encountered on imaging.

Other causes of intracranial hemorrhage: There are several causes of intracranial hemorrhage other than those secondary to anticoagulation. Some of these include hypertension, AVM, hemorrhagic neoplasm, and amyloid angiopathy. Clinical history is important in helping to narrow the differential diagnosis. Other imaging modalities including MRI/MRA as well as CTA can also be helpful to further elucidate the underlying cause of intracranial hemorrhage.

- *Hemorrhagic neoplasm*: Intracranial hemorrhage can also be secondary to intracranial neoplasm. Some of these include primary brain neoplasms, the most common being glioblastoma multiforme as well as hemorrhagic metastases. Imaging characteristics will vary depending on the type of neoplasm. The hallmark of a hemorrhagic neoplasm is nodular enhancement (Fig. 32.4), a finding that can obscured in the acute setting due to the mass effect exerted by the acute hemorrhage and edema. In such cases, it is important to obtain follow-up imaging.
- *Hypertension*: Hypertensive intracranial hemorrhage is the most common cause of spontaneous ICH in patients 45–70 years old. The location of the hemorrhage is helpful in determining its etiology. Typical sites of hypertensive hemorrhage include the basal ganglia, thalamus, pons, and cerebellum.
- *Vascular malformation*: Are several types of intracranial vascular malformations, including arteriovenous and cavernous malformations that can present with intracranial hemorrhage, usually in a younger population. CTA will better depict the enlarged arteries and draining veins (refer to Chap. 31).

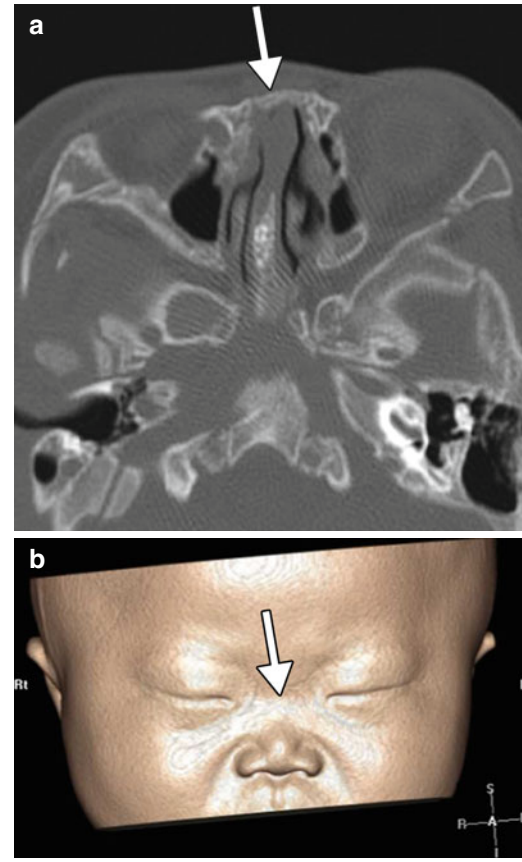

Fig. 32.4 Fetal warfarin syndrome. Axial (**a**) and non-contrast bone window CT images of the brain and a 3D surface-rendered image of the face (**b**) in an infant demonstrating dramatic midface and nasal hypoplasia (*arrows*) in the setting of warfarin use in the first trimester (Courtesy of Carolyn Robson)

- *Amyloid angiopathy*: Cerebral amyloid is responsible for 15–20 % of primary intracranial hemorrhage in patients greater than 60 years old. MR gradient echo or susceptibility-weighted sequences demonstrate multiple small foci of blooming artifact consistent with chronic microbleeds distributed throughout the supratentorial peripheral white matter (refer to Chap. 31).

Congenital skeletal dysplasias: Several congenital skeletal dysplasias can resemble fetal warfarin syndrome, including chondrodysplasia punctata, achondroplasia, epoxide reductase deficiency, and Crouzon syndrome (Fig. 32.5).

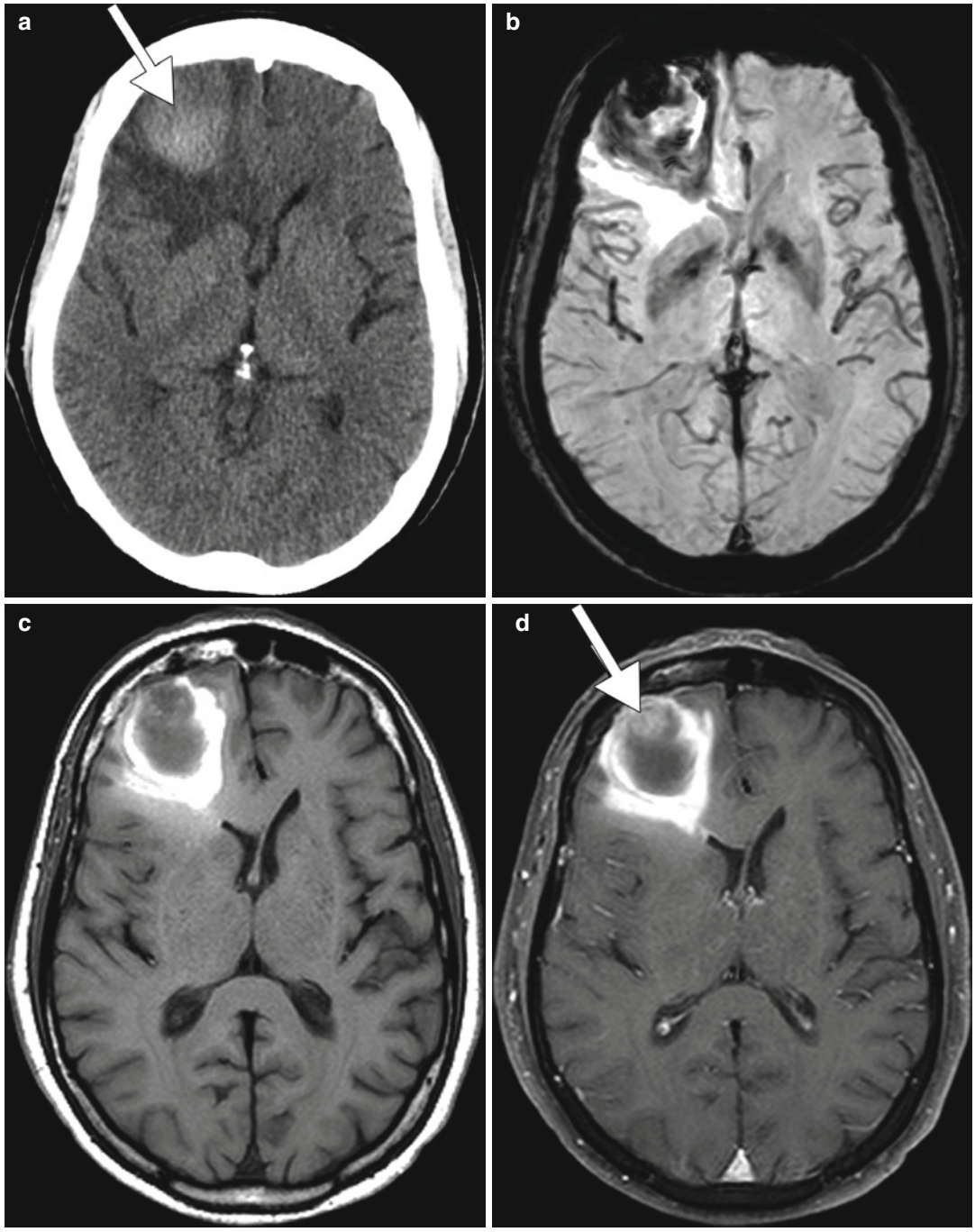

Fig. 32.5 Tumor hemorrhage. The patient has brain metastases from lung cancer. Axial CT image (**a**) shows hemorrhage within the right frontal lobe (*arrow*). The corresponding SWI (**b**), T1-weighted (**c**), and post-contrast T1-weighted (**d**) MR images show an enhancing nodule (*arrow*) amidst hemorrhage and vasogenic edema

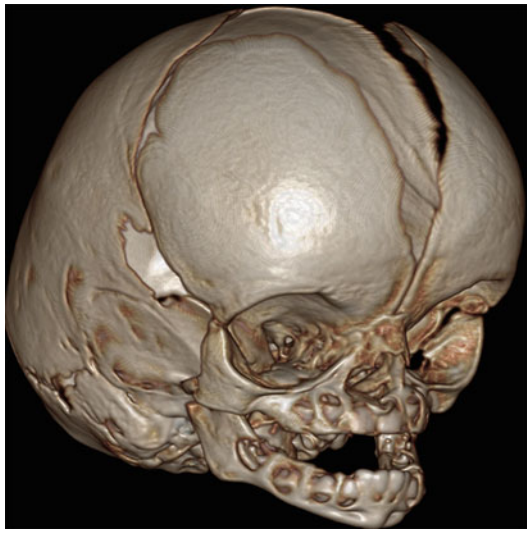

Fig. 32.6 Crouzon syndrome. 3D CT surface rendering in bone window shows substantial midface hypoplasia and a cloverleaf skull appearance

Adhesive arachnoiditis: As several important differential diagnostic considerations for arachnoiditis include leptomeningeal metastases, infection and post-surgical complications. These more commonly affect the cauda equina nerve roots (Fig. 32.6) as opposed to the thoracic spinal cord in hemorrhagic arachnoiditis. Arachnoid cysts may also be considered in the differential diagnosis. These typically appear as well-defined CSF signal intensity collections that may exert mass effect upon the spinal cord and nerve roots (Fig. 32.7).

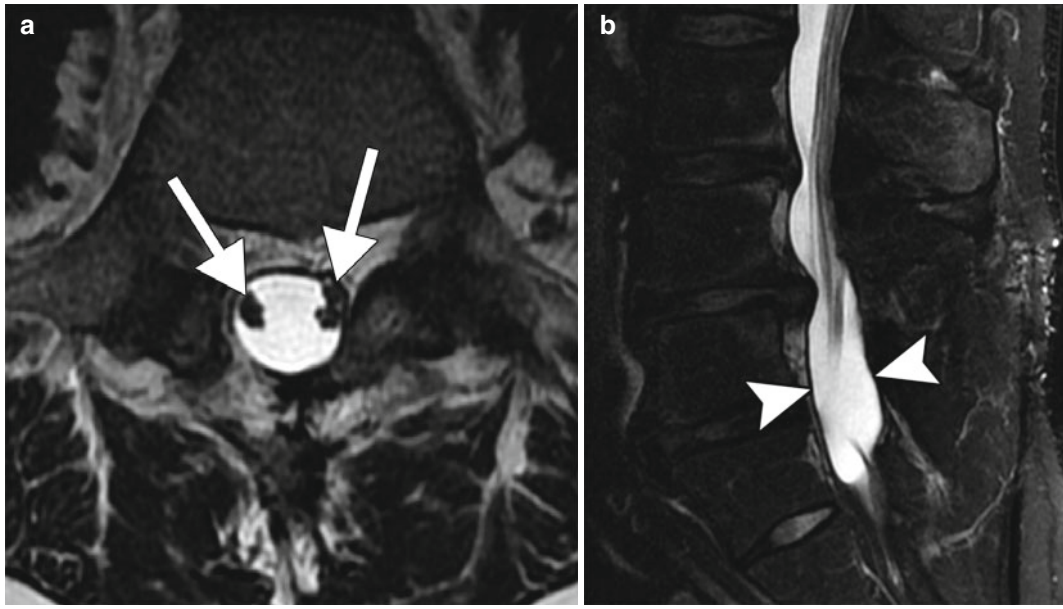

Fig. 32.7 Postsurgical arachnoiditis. The patient is status post L4–L5 laminectomy and discectomy. Axial (**a**) and sagittal (**b**) T2-weighted MR images show clumping of cauda equina nerve roots (*arrows*), resulting in an "empty sac" appearance of the lower lumbar spinal canal (*arrowheads*)

Suggested Reading

Ansell J, Hirsh J, Hylek E, et al. Pharmacology and management of the vitamin K antagonists: American College of Chest Physicians evidence-based clinical practice guidelines. Chest. 2008;133:160S–98.

Auer RN, et al. Primary intracerebral hemorrhage: pathophysiology. Can J Neurol Sci. 2005;2:S3–12.

Holbrook AM, Pereira JA, Labiris R, McDonald H, Douketis JD, Crowther M, Wells PS. Systematic overview of warfarin and its drug and food interactions. Arch Intern Med. 2005;165(10):1095–106.

Holford NH. Clinical pharmacokinetics and pharmacodynamics of warfarin. Understanding the dose-effect relationship. Clin Pharmacokinet. 1986;11:483–504.

Howe AM, Lipson AH, de Silva M, Ouvrier R, Webster WS. Severe cervical dysplasia and nasal cartilage calcification following prenatal warfarin exposure. Am J Med Genet. 1997;71(4):391–6.

Howe AM, Hawkins JK, Webster WS. The growth of the nasal septum in the 6–9 week period of foetal development–Warfarin embryopathy offers a new insight into prenatal facial development. Aust Dent J. 2004;49(4):171–6.

Ikushima I, Korogi Y, Hirai T, Yamashita Y. High-resolution constructive interference in a steady state imaging of cervicothoracic adhesive arachnoiditis. J Comput Assist Tomogr. 2007;31(1):143–7.

Jeffree RL, et al. Warfarin related intracranial hemorrhage: a case-controlled study of anticoagulation monitoring prior to spontaneous subdural or intracerebral haemorrhage. J Clin Neurosci. 2009;16(7):882–5.

Morisako H, Takami T, Yamagata T, Chokyu I, Tsuyuguchi N, Ohata K. Focal adhesive arachnoiditis of the spinal cord: imaging diagnosis and surgical resolution. J Craniovertebr Junction Spine. 2010;1(2):100–6.

Nandigam RN, et al. MR imaging detection of cerebral microbleeds: effect of susceptibility-weighted imaging, section thickness, and field strength. AJNR Am J Neuroradiol. 2009;30(2):338–43.

Pathak R, Supplee S, Aryal MR, Karmacharya P. Warfarin induced sublingual hematoma: a Ludwig angina mimic. Am J Otolaryngol. 2015;36(1):84–6.

Shah QA, et al. Acute hypertension in intracerebral hemorrhage: pathophysiology and treatment. J Neurol Sci. 2007;261(1–2):74–9.

Heparin

33

Evan Watkins and Daniel Thomas Ginat

33.1 Uses

Heparin therapy is one of the most common forms of medical intervention. It is the mainstay of treatment and prevention of thrombosis in several clinical settings, including acute venous thromboembolism, atrial fibrillation, and acute coronary syndrome and in patients undergoing invasive cardiac procedures. Unfractionated heparin had been the standard of anticoagulation for most of the twentieth century. However, more recently the development of low-molecular-weight heparins (LMWHs) represents a refinement for the use of heparin. Low-molecular-weight heparins and fondaparinux, a synthetic analog, have displaced unfractionated heparin for many indications.

33.2 Mechanism

Heparin has no intrinsic anticoagulant activity, but produces its effects indirectly by combining with antithrombin to inhibit thrombin and/or factor Xa. In addition, LMWH also increases non-antithrombin-dependent effects, such as TFPI release, modulation of adhesion molecules, and release of profibrinolytic and antithrombotic mediators from the blood vessels. Fondaparinux is an analog of a unique pentasaccharide found in heparin and LMWH. Heparin is cleared by predominantly extrarenal mechanisms. The binding of unfractionated heparin to numerous plasma proteins, some of which are acute phase reactants, causes patient dosing and response to be quite variable as compared to the newer agents. LMWH and fondaparinux are cleared exclusively by the kidneys; therefore, doses are more predictable and can be adjusted in patients with renal insufficiency. The mechanism by which anticoagulation increases the incidence of ICH is unclear. One theory suggests that small hemorrhages that would be otherwise subclinical expand and become clinically significant in the anticoagulated patient. One study suggests that findings of such small-vessel disease on MRI may be predictive of an anticoagulation-treated patient's risk for spontaneous bleeding.

The main nonhemorrhagic side effects of heparin are heparin-induced thrombocytopenia (HIT) and osteopenia. HIT is caused by heparin-dependent IgG antibodies. Binding of these antibodies to receptors on the platelet surface causes platelet activation. Activated platelets then shed highly prothrombotic microparticles. These activated platelets and microparticles provide a surface for the formation of coagulation factor complexes, which promote thrombin generation. This phenomenon can then trigger venous or

E. Watkins, MD
Department of Diagnostic Radiology, Lahey Clinic, Burlington, MA, USA

D.T. Ginat, MD, MS (✉)
Department of Radiology, University of Chicago, Pritzker Medical School, Chicago, IL, USA
e-mail: ginatd01@gmail.com

D.T. Ginat et al. (eds.), *Neuroimaging Pharmacopoeia*,
DOI 10.1007/978-3-319-12715-6_33,

arterial thrombosis, with venous thrombosis being more common. Osteopenia may be caused by binding of heparin to osteoblasts, which then release factors that promote osteoclastic activity.

33.3 Discussion

Cerebral hemorrhage is a major complication of heparin therapy. Approximately 70 % of intracranial hemorrhage episodes associated with anticoagulation consists of intraparenchymal hemorrhage (Fig. 33.1), whereas most of the remainder are subdural hematomas (Fig. 33.2). Anticoagulant-related intracranial hemorrhage differs from that due to other causes in several ways. Most significantly, intracranial hemorrhage related to anticoagulation often develops gradually and insidiously, over many hours or even days. Anticoagulant- related intracranial hemorrhages are also more likely to enlarge after they are first seen on imaging. The mortality rate associated with anticoagulant-related intracranial hemorrhage has been reported to be as high as 60 %. Advanced age, trauma, and prior history of infarct are risk factors that have been definitively linked to increased rates of ICH in anticoagulated patients. The incidence of major hemorrhage depends upon the form of heparin therapy. For example, extracorporeal membrane oxygenation (ECMO) is associated with a 7–15 % incidence of intracranial hemorrhage, which can be supratentorial or less commonly infratentorial (Fig. 33.3). Heparin prophylaxis for DVT has a much lower risk for intracranial hemorrhage but can nevertheless occur in patients with predisposing factors, such as brain metastases (Fig. 33.4).

Heparin-induced thrombocytopenia (HIT) occurs in 1–5 % of patients treated with heparin and can occur immediately, although usually occurs after several days of treatment. It is a life-threatening condition in which at least half of the patients develop arterial or venous thrombosis that can lead to amputation or death.

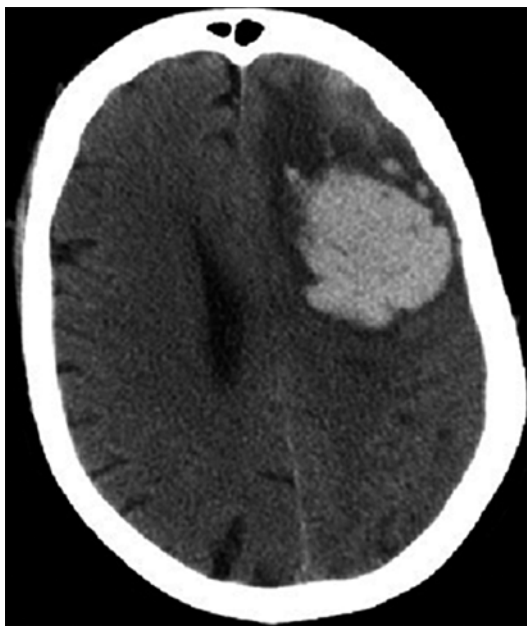

Fig. 33.1 Heparin-related intraparenchymal hemorrhage. The patient received large amounts of heparin during cardiac catheterization. Coronal CT image shows a large left frontal lobe hematoma with surrounding vasogenic edema

Fig. 33.2 Heparin-related subdural hematomas. The patient incurred head trauma. Axial CT image shows bilateral mixed attenuation subdural hematomas (*arrowheads*) and a right subgaleal hematoma (*arrow*)

In neuroimaging, the most common manifestation of HIT is venous sinus thrombosis, in which hyperattenuating venous structures can be encountered on non-contrast CT, although it is best demonstrated as filling defect on post-contrast imaging. This can occur in conjunction with venous infarct/hemorrhage in 50 % of cases and should be suspected in cases of infarcts appearing to evolve in a non-arterial distribution. Thrombus tends to form initially in a dural sinus and then propagate into deep cerebral and/or cortical veins. Once venous drainage is obstructed, venous pressure will rise, resulting in vasogenic edema and possibly parenchymal infarct and/or hemorrhage secondary to venous hypertension. If infarction occurs, cytotoxic edema will ensue. Venous sinus thrombosis is the presenting event of HIT in 3 % of cases.

Fig. 33.3 ECMO-associated hemorrhage. Sagittal CT image shows large posterior fossa hematomas with associated obstructive hydrocephalus

If sinus thrombosis is suspected in a patient who is currently using or has recently used heparin, HIT must be excluded, since this condition represents an absolute contraindication to further anticoagulant therapy. Diagnosis of HIT is made primarily by detecting the presence of HIT antibodies, although a decrease in platelet count of >50 % is also considered diagnostic. Given their high risk of clot formation, patients receive antithrombotic therapy even in the absence of known

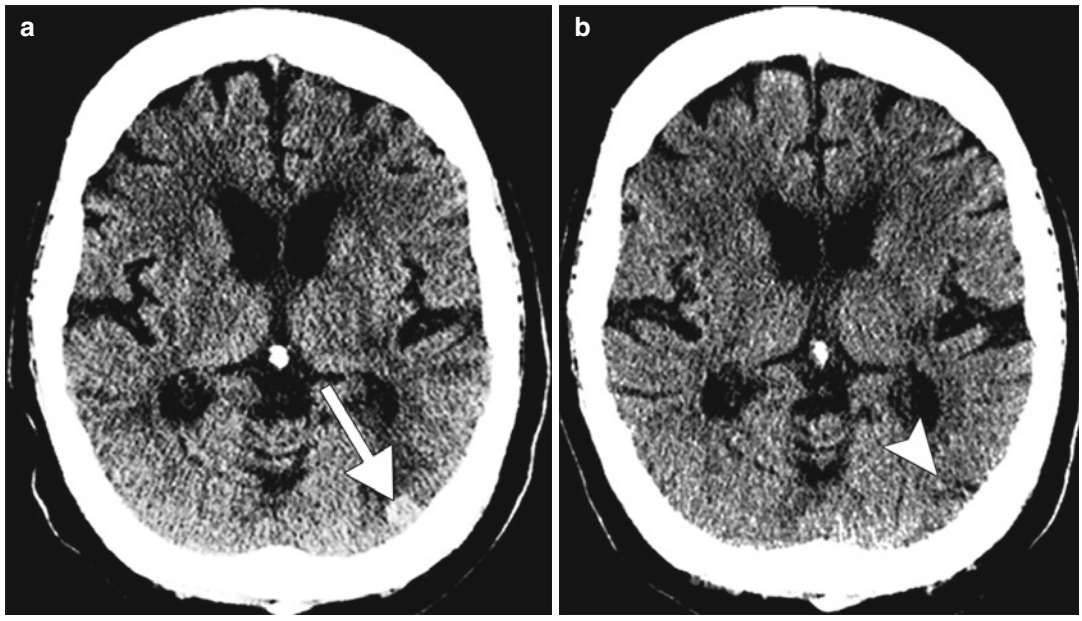

Fig. 33.4 Concurrent anticoagulation and metastatic disease. The patient has a history of metastatic lung cancer and was on heparin DVT prophylaxis. Axial CT image (**a**) shows hemorrhage that developed suddenly within a left occipital lobe metastasis (*arrow*) after instituting prophylactic heparin. The lesion (*arrowhead*) was barely perceptible not long previously (**b**)

thrombus. Treatment is continued until the platelet count has rebounded. Despite thrombocytopenia, increased bleeding is not seen in patients with HIT.

The first published clinical report of heparin-related osteopenia appeared in 1965. Griffith et al. described spontaneous vertebral and rib fractures in adult patients treated with 15,000–30,000 units daily for 6 months or longer. The effects were found to be reversible with the cessation of therapy. A more recent study of patients receiving heparin therapy during pregnancy showed no clinically significant osteoporosis, with approximately 1/3 of patients developing subclinical osteoporosis.

33.4 Differential Diagnosis

Intracranial hemorrhage. A broad differential diagnosis exists in the setting of acute, nontraumatic cerebral hemorrhage, and both clinical history as well as imaging findings are needed to arrive at the appropriate diagnosis (refer to Chaps. 2, 5, 16, 21, 30, 31, and 34). In addition to anticoagulation, hypertensive hemorrhage may also be considered in patients with the appropriate history. Hypertensive hemorrhages are typically parenchymal hemorrhages, commonly striatocapsular and thalamic. Amyloid angiopathy is an important consideration in older patients, especially those who are normotensive and present with lobar hemorrhage. On the other hand, parenchymal hemorrhage associated with enhancement may be secondary to bleeding related to a vascular malformation as well as hemorrhagic metastasis. Patient age, clinical history, and medical comorbidities are all vital tools that assist in determining the most likely etiology of an intracranial bleed.

Heparin-induced thrombocytopenia. Other potential etiologies for venous sinus thrombosis include local trauma or infection, hypovolemic and hypercoagulable states, pregnancy, vasculitis, and various pharmaceuticals (refer to Chaps. 21 and 47).

Osteopenia. When considering a differential, it is important to realize that 95 % of osteopenia is age-related or postmenopausal. Corticosteroids (refer to Chap. 46) and heparin are the two most common therapy-related causes. Alcohol, liver failure, calcium deficiency, and malnutrition can also lead to osteoporosis. Several relatively rare metabolic conditions, such as hyperparathyroidism, Cushing's syndrome, acromegaly, and hypogonadism have also been known to cause osteopenia. Clinical history is vital to narrowing the differential, as there are no specific imaging findings that have been known to suggest heparin-related osteopenia in relation to other potential etiologies.

Suggested Reading

Barbour LA, Kick SD, Steiner JF, LoVerde ME, Heddleston LN, Lear JL, Baron AE, Bartón PL. A prospective study of heparin-induced osteoporosis in pregnancy using bone densitometry. Am J Obstet Gynecol. 1994;170(3):862–9.

Bulas DI, Taylor GA, Fitz CR, Revenis ME, Glass P, Ingram JD. Posterior fossa intracranial hemorrhage in infants treated with extracorporeal membrane oxygenation: sonographic findings. AJR Am J Roentgenol. 1991;156(3):571–5.

Crowther MA, Warkentin TE. Bleeding risk and the management of bleeding complications in patients undergoing anticoagulant therapy: focus on new anticoagulant agents. Blood. 2008;111(10):4871–9.

Fareed J, Hoppensteadt DA, Bick RL. An update on heparins at the beginning of the new millennium. Semin Thromb Hemost. 2000;26(s1):5–22.

Garcia DA, Baglin TP, Weitz JI, Samama MM. Parenteral anticoagulants: antithrombotic therapy and prevention of thrombosis, 9th ed: American College of Chest Physicians evidence-based clinical practice guidelines. Chest. 2012;141(2 Suppl):e24S–43.

Griffith GC, Nichols JD, Flanagan B. Heparin osteoporosis. J Am Med Assoc. 1965;196:85–8.

Madhugiri VS, Mahadevan A, Gundamaneni SK, Singh M. Heparin-induced tumour bleed. BMJ Case Rep. 2012;2012.

Pohl C, Klockgether T, Greinacher A, Hanfland P, Harbrecht U. Neurological complications in heparin-induced thrombocytopenia. Lancet. 1999;353:1678–9.

Quinones-Hinojosa A, Gulati M, Singh V, Lawton MT. Spontaneous intracerebral hemorrhage due to coagulation disorders. Neurosurg Focus. 2003;15(4):E3.

Resnick SB, Resnick SH, Weintraub JL, Kothary N. Heparin in interventional radiology: a therapy in evolution. Semin Intervent Radiol. 2005;22(2):95–107.

Roob G, Fazekas F. Magnetic resonance imaging of cerebral microbleeds. Curr Opin Neurol. 2000;13:69–73.

Sackler JP, Liu L. Heparin-induced osteoporosis. Br J Radiol (Impact Factor: 131). 1973;46(547):548–50.

Weitz DS, Weitz JI. Update on heparin: what do we need to know? J Thromb Thrombolysis. 2010;29(2):199–207.

Tissue Plasminogen Activator (tPA) 34

Evan Watkins, Juan E. Small, and
Daniel Thomas Ginat

34.1 Uses

Tissue plasminogen activator (tPA) is used in the setting of acute ischemic stroke. tPA is also utilized for several additional thrombolytic indications, including acute MI, pulmonary embolism, and central venous catheter occlusion.

34.2 Mechanism

tPA is a fibrinolytic agent which activates the body's fibrinolytic system by converting plasminogen to plasmin. Plasmin binds to fresh fibrin clots, dissolving them and generating fibrinogen degradation products. Tissue plasminogen activator theoretically has a clinical advantage over urokinase and streptokinase in that it is relatively clot specific, activating fibrin-bound plasminogen preferentially over circulating plasminogen. Contraindications to the use of tPA relate mainly to probability of developing hemorrhage and include recent intracranial hemorrhage or surgery, intracranial neoplasm, aneurysm, AVM, and severe uncontrolled hypertension. Any active hemorrhage, recent hemorrhage (within 3 months), including gastrointestinal and genitourinary bleeding, is also considered a contraindication.

34.3 Discussion

Fortunately, intracranial hemorrhage as a result of tPA infusion is a relatively rare complication, seen in less than 1 % of patients. However, careful assessment of the patient's risk profile is vital to avoid this complication. ICH secondary to thrombolytic therapy presents as lobar hemorrhage in 70–90 % of cases and causes multiple hemorrhages in about one third of patients. Hemorrhage usually occurs soon after treatment has begun, with studies finding that 40 % of TPA-related ICH occur during the infusion, with another 25 % occurring within 24 h of treatment. Compared with other types of ICH, patients with hemorrhage from tPA therapy are more likely to have fluid levels in the hematomas, which suggests active hemorrhage. Hemorrhages also often occur in several different intracranial compartments (intraventricular, subarachnoid, subdural, and parenchymal).

Some studies have suggested that patient age greater than 65, aspirin use, and history of hypertension are found to be independent risk factors for ICH on tPA therapy. However, the importance of these potential clinical risk factors has been debated. Other studies have shown no relationship between the aforementioned factors and suggest the existence of cerebral amyloid

E. Watkins, MD • J.E. Small, MD
Department of Diagnostic Radiology, Lahey Clinic, Burlington, MA, USA

D.T. Ginat, MD, MS (✉)
Department of Radiology, University of Chicago, Pritzker Medical School, Chicago, IL, USA
e-mail: ginatd01@gmail.com

D.T. Ginat et al. (eds.), *Neuroimaging Pharmacopoeia*,
DOI 10.1007/978-3-319-12715-6_34, © Springer International Publishing Switzerland 2015

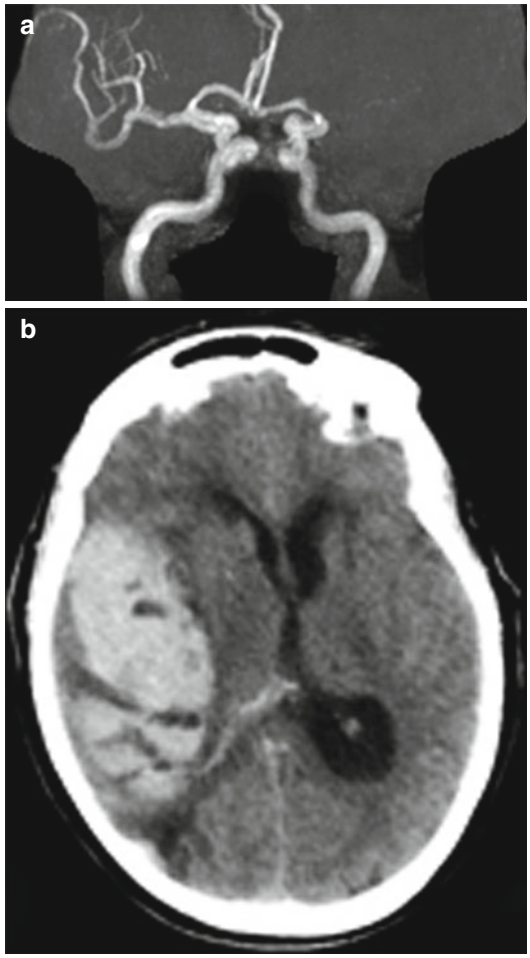

Fig. 34.1 Parenchymal hemorrhage after tPA. Middle-aged female presenting with acute complete occlusion of the left M1 segment seen on MRA (**a**). After tPA infusion, the patient developed a large parenchymal hemorrhage in the contralateral hemisphere evident on the axial non-contrast CT image (**b**)

angiopathy is the underlying process in many of those patients with ICH. Several pretreatment findings have also been identified as predictors of hemorrhage, such as the hyperdense vessel sign on CT, as well as volume of ischemic tissue and the presence of lacunes on MRI (Fig. 34.1).

34.4 Differential Diagnosis

Although hemorrhage in the setting of tPA administration might imply that the etiology is treatment related, it is important to consider the differential of nontraumatic intracranial hemorrhage, which includes hypertension, amyloid angiopathy, vascular malformations, and hemorrhagic metastases (refer to Chaps. 2, 5, 16, 20, 29, 30, and 32). Hypertensive hemorrhages are typically parenchymal hemorrhages, commonly striatocapsular and thalamic. Amyloid angiopathy is common in older patients and often presents with lobar hemorrhage. Patients with bleeding secondary to a vascular malformation often present at a younger age, and an enhancing underlying lesion is eventually evident. Hemorrhage associated with the presence of enhancement may also occur secondary to a hemorrhagic neoplastic process, such as metastasis.

Suggested Reading

Derex L, Hermier M, Adeleine P, Pialat J-B, Wiart M, Bertheze'ne Y, Philippeau F, Honnorat J, Froment J-C, Trouillas P, Nighoghossian N. Clinical and imaging predictors of intracerebral haemorrhage in stroke patients treated with intravenous tissue plasminogen activator. J Neurol Neurosurg Psychiatry. 2005;76:70–5.

Gore JM, Sloan M, Price TR, et al. Intracerebral hemorrhage, cerebral infarction, and subdural hematoma after acute myocardial infarction and thrombolytic therapy in the Thrombolysis in Myocardial Infarction Study. Thrombolysis in Myocardial Infarction, Phase II, pilot and clinical trial. Circulation. 1991;83:448–59.

Kase CS, Williams JP, Wyatt DA, et al. Lobar intracerebral hematomas: clinical and CT analysis of 22 cases. Neurology. 1982;32:1146–50.

O'Connor CM, Califf RM, Massey EW, et al. Stroke and acute myocardial infarction in the thrombolytic era: clinical correlates A. Quinones-Hinojosa, et al. 16 *Neurosurg. Focus/Volume 15/October, 2003* and long-term prognosis. J Am Coll Cardiol. 1990;16:533–40.

Quinones-Hinojosa A, Gulati M, Singh V, Lawton MT. Spontaneous intracerebral hemorrhage due to coagulation disorders. Neurosurg Focus. 2003;15(4):E3.

Wijdicks EF, Jack Jr CR. Intracerebral hemorrhage after fibrinolytic therapy for acute myocardial infarction. Stroke. 1993;24:554–7.

Supplemental Oxygen

35

Daniel Thomas Ginat

35.1 Uses

The administration of supplemental oxygen is integral to the management of a wide range of clinical conditions, including acute hypoxemia (shock, asthma, pneumonia, heart failure), ischemia (myocardial infarction but only if associated with hypoxemia), and abnormality in quality or type of hemoglobin.

35.2 Mechanism

With two unpaired electrons, supplemental oxygen has a weakly paramagnetic effect that results in reduction of CSF T1-weighted relaxation time and high signal intensity on FLAIR sequences.

35.3 Discussion

Oxygen diffuses from the blood to the CSF at the pia-arachnoid surface of the brain. Consequently, high concentration supplemental oxygen results in diffuse hyperintensity within the subarachnoid and basal cisterns on FLAIR MRI sequences (Fig. 35.1). This finding develops within the first 5 min of oxygen administration. This effect has occasionally been exploited in order to perform noninvasive cisternography. However, the presence of high FLAIR signal can be mistaken for actual pathology. The use of oxygen concentrations less than 50 % and shorter FLAIR inversion times can avoid this effect.

35.4 Differential Diagnosis

Many conditions can produce the appearance of subarachnoid FLAIR hyperintensity, including subarachnoid hemorrhage, meningitis, sluggish blood flow in acute stroke, moyamoya, leptomeningeal carcinomatosis, leptomeningeal melanosis, delayed contrast leakage, CSF and vascular pulsation artifact, metal susceptibility artifact, and motion artifact. Some of these conditions are discussed and illustrated below:

- *Subarachnoid hemorrhage*: High protein content and the diamagnetic properties of oxyhemoglobin in acute subarachnoid hemorrhage result in FLAIR hyperintensity. FLAIR is more sensitive than CT for the detection of acute subarachnoid hemorrhage (refer to Chap. 4). Susceptibility effect may also be present.
- *Meningitis*: The presence of increased CSF cellular and protein content in inflammatory meningitis alters the CSF nulling point on FLAIR (Fig. 35.2). There may also be prominent leptomeningeal enhancement as well as associated cerebritis, abscess, and empyema.

D.T. Ginat, MD, MS
Department of Radiology, University of Chicago, Pritzker Medical School, Chicago, IL, USA
e-mail: ginatd01@gmail.com

D.T. Ginat et al. (eds.), *Neuroimaging Pharmacopoeia*,
DOI 10.1007/978-3-319-12715-6_35,

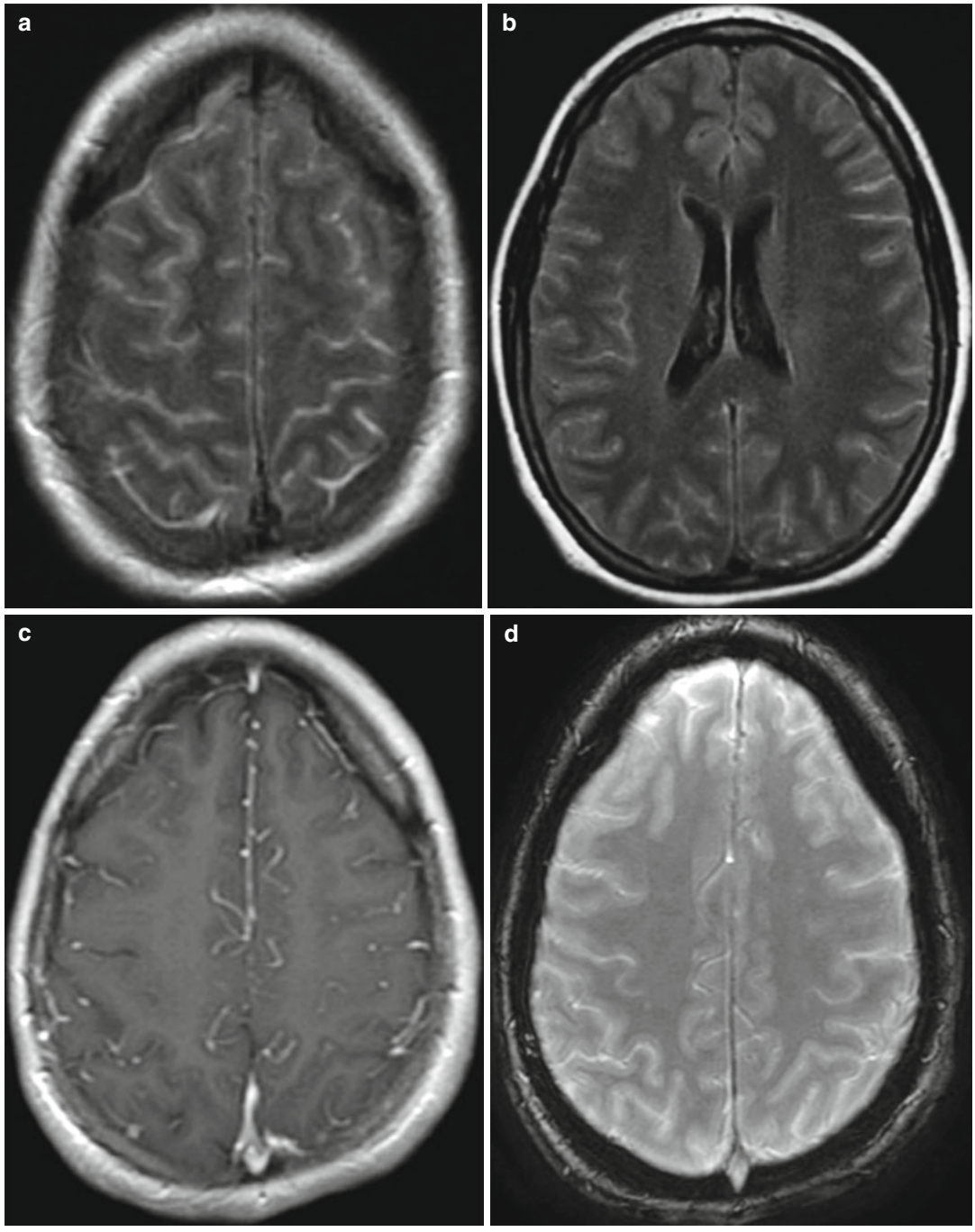

Fig. 35.1 Supplemental oxygen. Axial FLAIR MR images (**a**, **b**) show diffuse sulcal hyperintensity. The corresponding axial post-contrast T1-weighted (**c**) and susceptibility-weighted (**d**) MR images show no associated abnormal enhancement or evidence of blood products. Sagittal T1-weighted MRI (**e**) shows the presence of an airway mask (*arrow*)

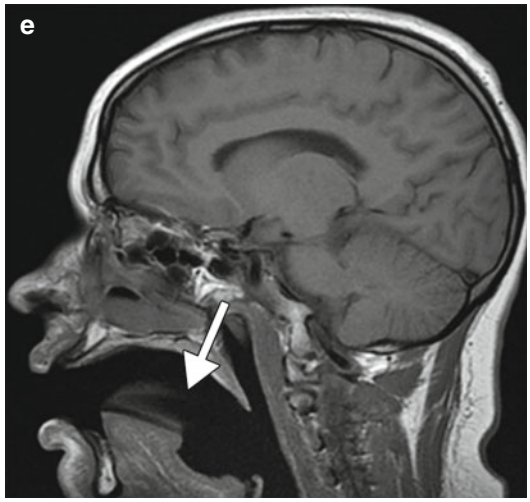

Fig. 35.1 (continued)

- *Cerebral ischemia*: Vascular hyperintensity in the subarachnoid space on FLAIR results from severe stenosis or occlusion of major cerebral vessels, including moyamoya with slow pial blood flow that results in the "ivy sign" on FLAIR images (Fig. 35.3).
- *Leptomeningeal carcinomatosis*: Dissemination of neoplasm in the subarachnoid space can manifest as FLAIR hyperintensity with linear and/or nodular enhancement (Fig. 35.4).
- *Metal susceptibility artifact*: Local magnetic field inhomogeneity at tissue interfaces results in incomplete nulling of CSF by the slice-selection inversion pulse. This phenomenon can extend some distance from the metal object (Fig. 35.5).

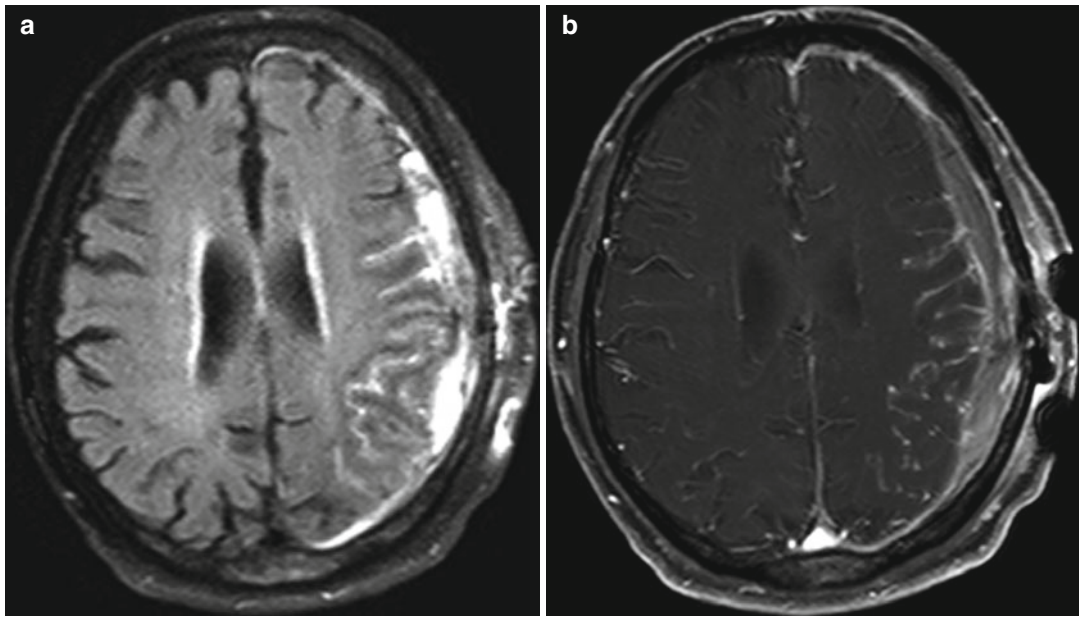

Fig. 35.2 Meningoencephalitis. Axial FLAIR (**a**) and axial post-contrast T1-weighted (**b**) MR images show sulcal FLAIR hyperintensity and enhancement, as well as cortical swelling in the left cerebral hemisphere

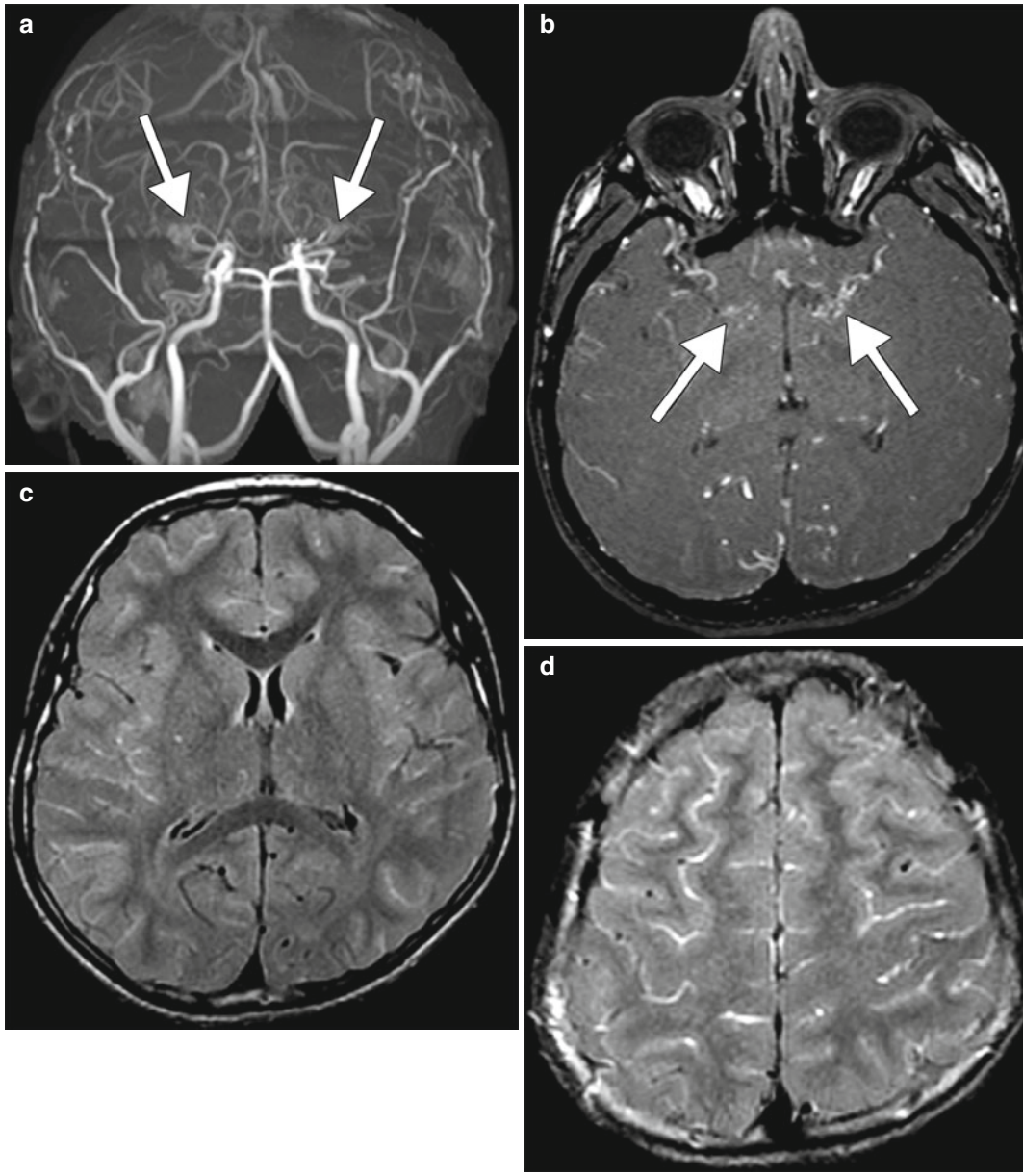

Fig. 35.3 Moyamoya. Frontal MIP MRA (**a**) and axial post-contrast T1-weighted MRI (**b**) show occlusion of the supraclinoid artery with associated prominent lenticulostriate collateral vessels (*arrows*). Axial FLAIR images (**c**, **d**) show diffuse sulcal hyperintensity

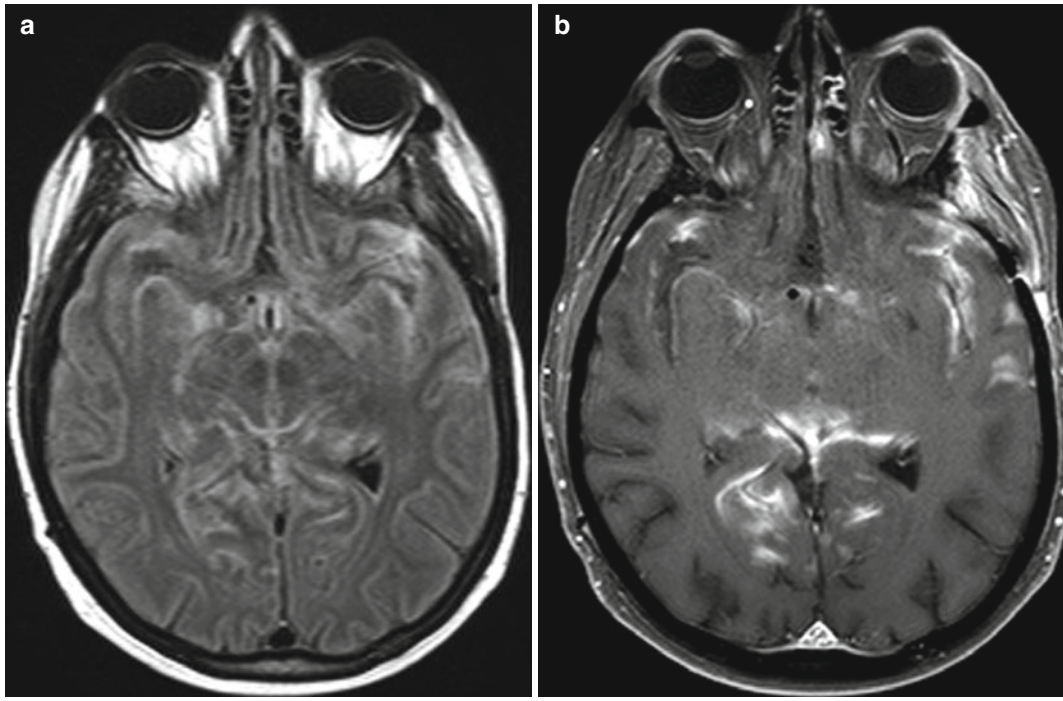

Fig. 35.4 Leptomeningeal carcinomatosis. Axial FLAIR (**a**) shows scattered areas of sulcal hyperintensity with corresponding leptomeningeal enhancement on the post-contrast T1-weighted image (**b**)

- *CSF pulsation artifact*: CSF flow in the subarachnoid space can introduce CSF that may not have been exposed to the inversion pulse into the imaging plane. This phenomenon is most frequently encountered in the basal, prepontine, and cerebellopontine angle cisterns, as well as within the ventricular system (Fig. 35.6).

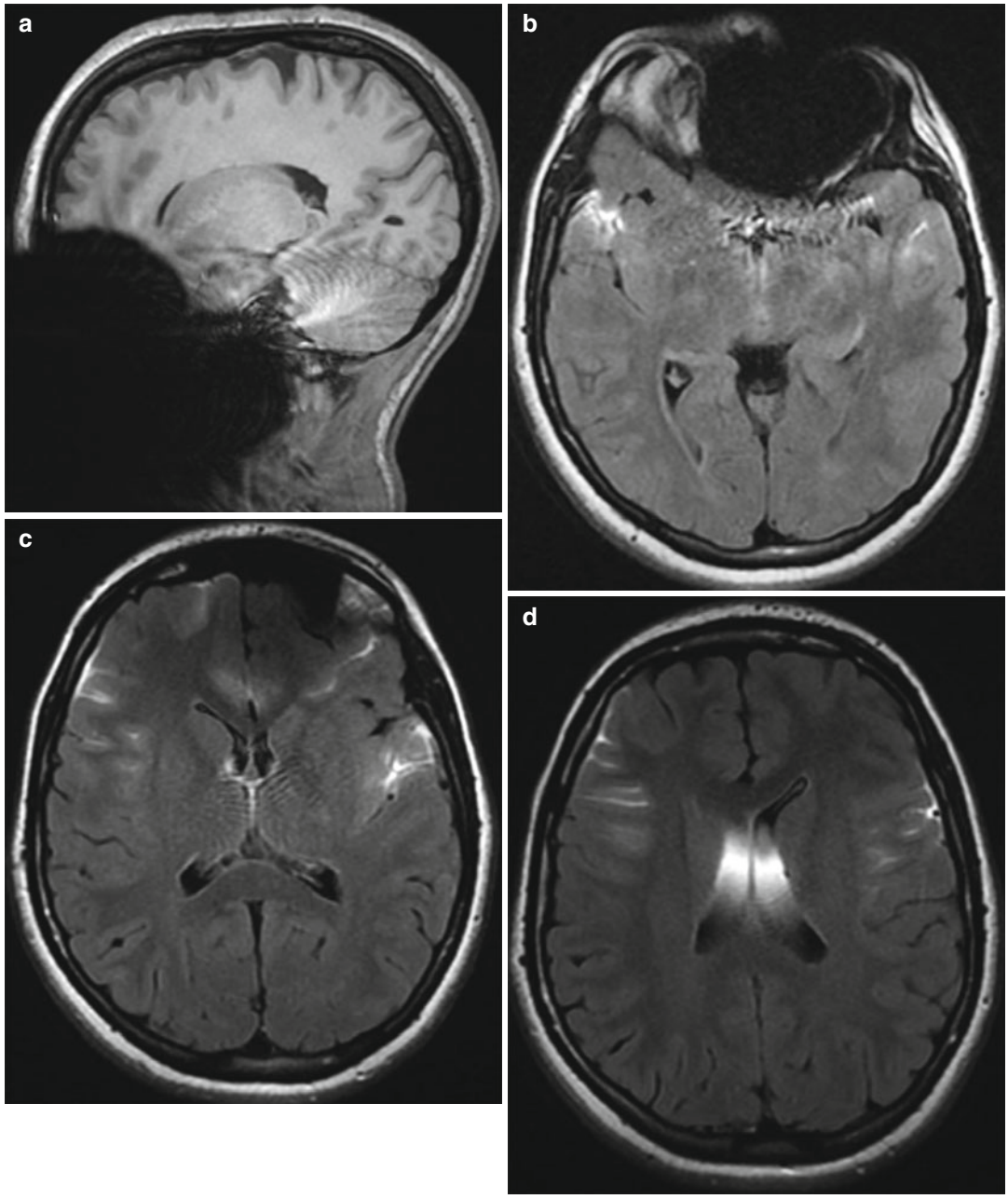

Fig. 35.5 Metal susceptibility artifact. Sagittal T1-weighted MRI (**a**) shows loss of signal and distortion surrounding the oral cavity due to dental braces. Axial FLAIR MR images (**b–d**) show areas of artifactual high signal within the sulci and ventricles

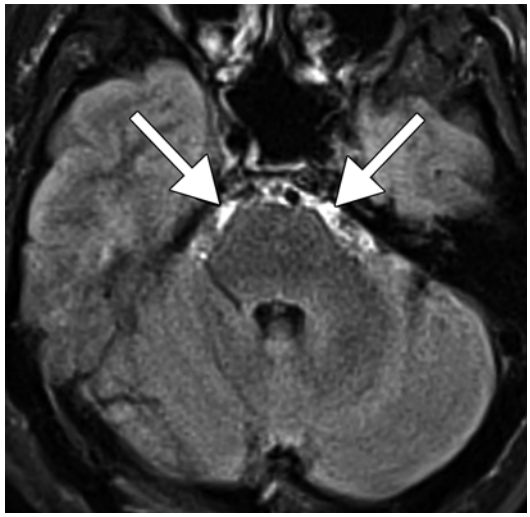

Fig. 35.6 CSF flow artifact. Axial FLAIR image shows hyperintense signal within the prepontine cistern (*arrows*)

Suggested Reading

Anzai Y, Ishikawa M, Shaw DW, Artru A, Yarnykh V, Maravilla KR. Paramagnetic effect of supplemental oxygen on CSF hyperintensity on fluid-attenuated inversion recovery MR images. AJNR Am J Neuroradiol. 2004;25(2):274–9.

Braga FT, da Rocha AJ, Hernandez Filho G, Arikawa RK, Ribeiro IM, Fonseca RB. Relationship between the concentration of supplemental oxygen and signal intensity of CSF depicted by fluid-attenuated inversion recovery imaging. AJNR Am J Neuroradiol. 2003; 24(9):1863–8.

Frigon C, Shaw DW, Heckbert SR, Weinberger E, Jardine DS. Supplemental oxygen causes increased signal intensity in subarachnoid cerebrospinal fluid on brain FLAIR MR images obtained in children during general anesthesia. Radiology. 2004;233(1):51–5.

Hypertonic Saline

36

Daniel Thomas Ginat

36.1 Uses

There are three main indications for the use of hypertonic saline in critical care, including hyponatremia, volume resuscitation, and brain injury. Although the syndrome of inappropriate antidiuretic hormone secretion (SIADH) and cerebral salt wasting syndrome may require sodium replacement, most cases of hyponatremia can be managed without administration of hypertonic saline.

36.2 Mechanism

Rapid or excessive rise in serum sodium from a hyponatremic state is believed to cause intramyelinic splitting, vacuolization, and rupture of myelin sheaths due to the sensitivity of oligodendrocytes to osmotic changes. Alcoholic and malnourished patients are particularly vulnerable to osmotic demyelination due to deficiency in organic osmolytes.

36.3 Discussion

Patients with osmotic demyelination often present acutely with seizures and encephalopathy, followed by transient improvement with correction of the sodium level and then neurological decline towards coma or delirium several days later.

On MRI, the characteristic finding of osmotic demyelination is a symmetric trident-shaped area in the central pons on T2-weighted and FLAIR MRI sequences, with relative sparing of the ventrolateral pons and corticospinal tracks (pontine myelinolysis). Bilateral symmetric signal abnormalities of the deep grey nuclei (thalami and basal ganglia) as well as subcortical white matter can also be observed (extra-pontine myelinolysis) (Fig. 36.1). The lesions typically do not have significant mass effect or enhancement. ADC values vary depending on the location of the lesion and the time at which imaging is obtained, ranging from initially decreased to subsequently elevated ADC values. CT is less sensitive than MRI for identifying osmotic demyelination, but may show hypoattenuation in the affected areas. The imaging findings tend to lag behind the clinical symptoms. The prognosis for osmotic demyelination syndrome varies without correlation to clinical features or imaging findings.

36.4 Differential Diagnosis

Osmotic demyelination can also occur in the setting of hyperglycemia, hypoglycemia, normonatremia, and hypernatremia. Without the pertinent clinical history, however, the differential considerations for the imaging findings may include microangiopathy (Fig. 36.2), infarct (Fig. 36.2),

D.T. Ginat, MD, MS
Department of Radiology, University of Chicago, Pritzker Medical School, Chicago, IL, USA
e-mail: ginatd01@gmail.com

D.T. Ginat et al. (eds.), *Neuroimaging Pharmacopoeia*,
DOI 10.1007/978-3-319-12715-6_36,

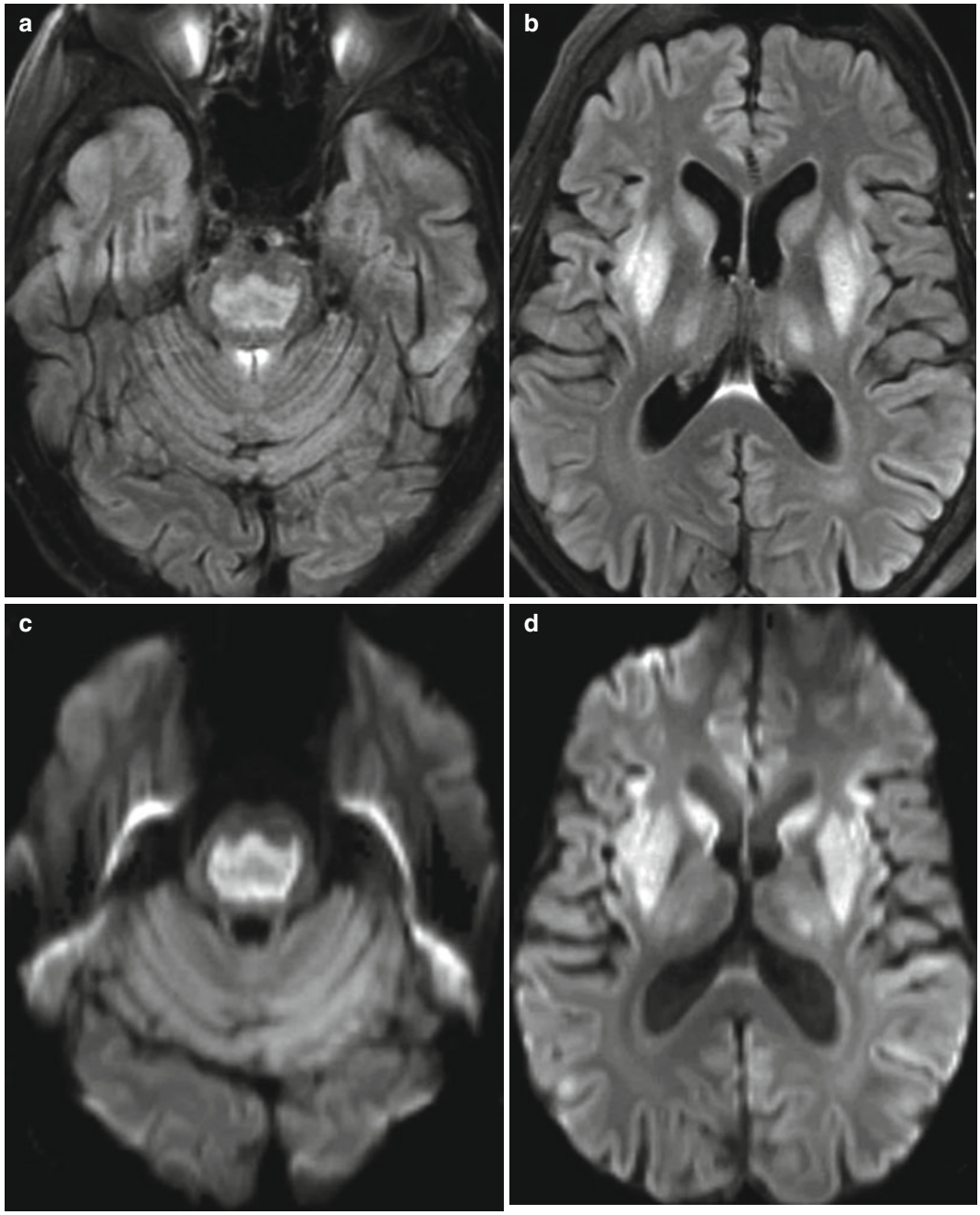

Fig. 36.1 Osmotic demyelination related to rapid correction of hyponatremia with hypertonic saline. Axial FLAIR (**a**, **b**), axial DWI (**c**, **d**), and axial ADC maps (**e**, **f**) show a trident-shaped area of abnormal signal with peripheral sparing within the mid-pons, consistent with pontine myelinolysis. In addition, bilateral symmetric signal abnormality within the basal ganglia, thalami, and external capsules is noted, consistent with extra-pontine myelinolysis. There is restricted diffusion in the pons, but not in the affected portions of the supratentorial brain

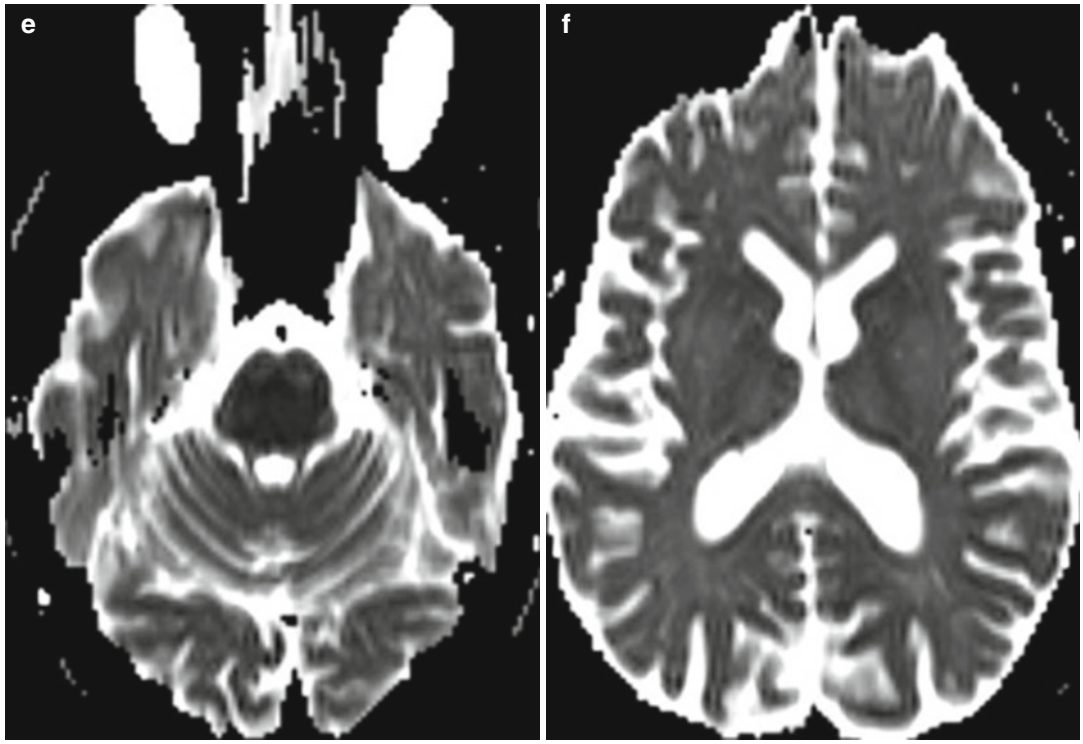

Fig. 36.1 (continued)

neoplasms, such as glioma (Fig. 36.3), and viral encephalitis (Fig. 36.4). Microangiopathy is a chronic process that can produce streaky FLAIR hyperintensity in the central pons and supratentorial white matter without associated restricted diffusion. Unlike central pontine myelinolysis, pontine infarcts can involve the corticospinal tracts and are often unilateral, with a sharp margin along the midline. Furthermore, concomitant involvement of the brainstem and bilateral basal ganglia with stroke is distinctly uncommon. Pontine gliomas tend to present with a mass-like appearance and may or may not demonstrate enhancement. In certain cases, viral encephalitis can affect the brainstem and basal ganglia in a bilateral symmetric manner similar to osmotic demyelination, although involvement of the external capsules is relatively uncommon.

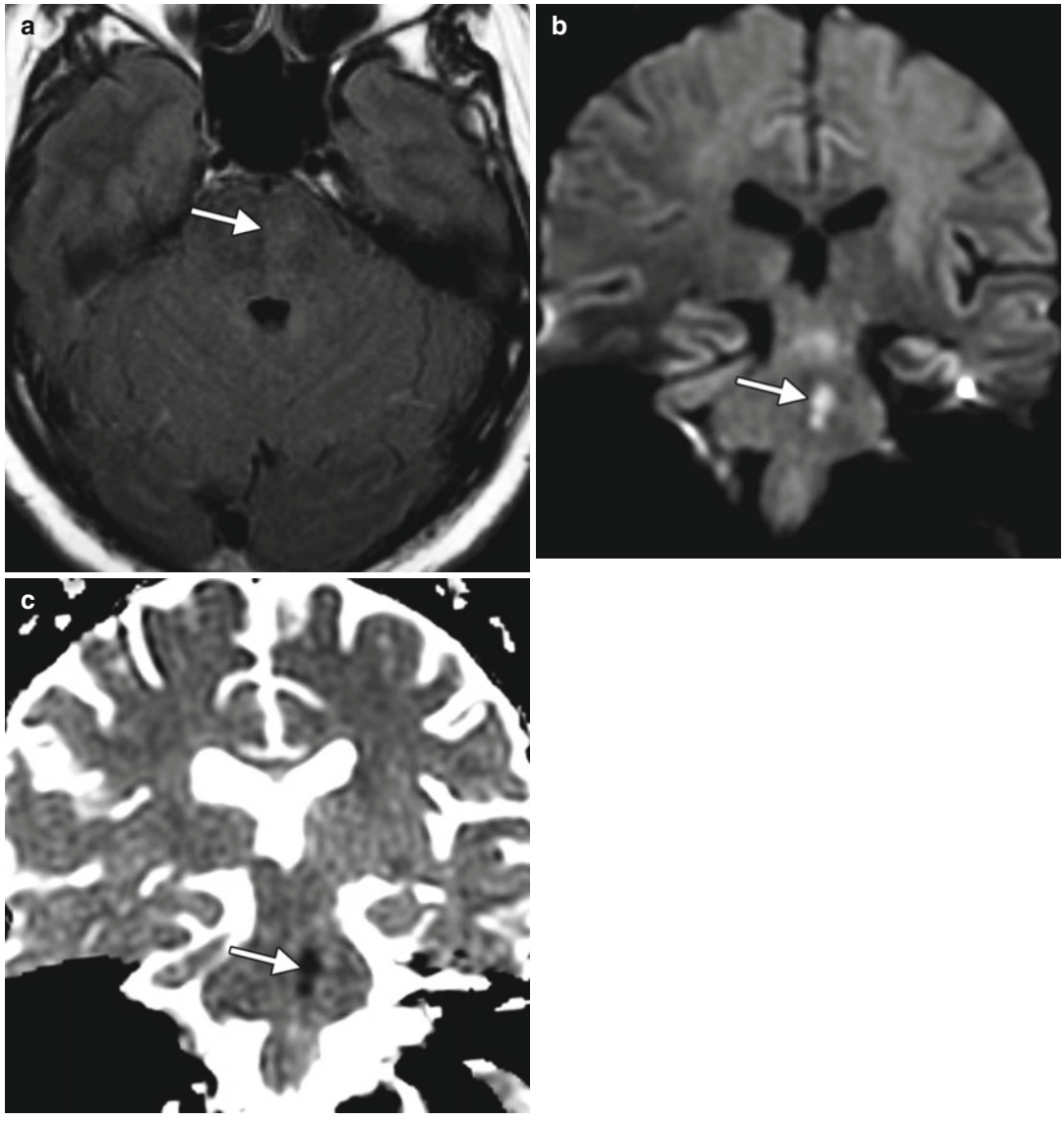

Fig. 36.2 Pontine infarct. Axial FLAIR (**a**) shows faint hyperintensity within the left pons (*arrow*). Coronal DWI (**b**) and ADC map (**c**) show corresponding restricted diffusion (*arrows*)

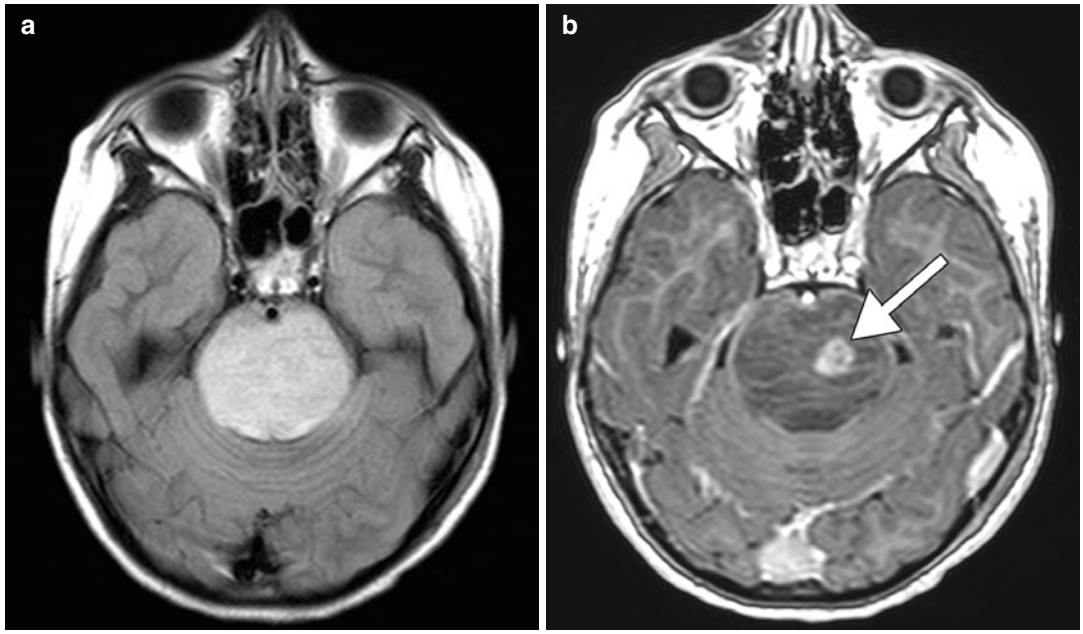

Fig. 36.3 Pontine glioma. Axial FLAIR (**a**) and post-contrast T1-weighted (**b**) MR images show an expansile and infiltrative mass in the pons with an area of enhancement (*arrow*)

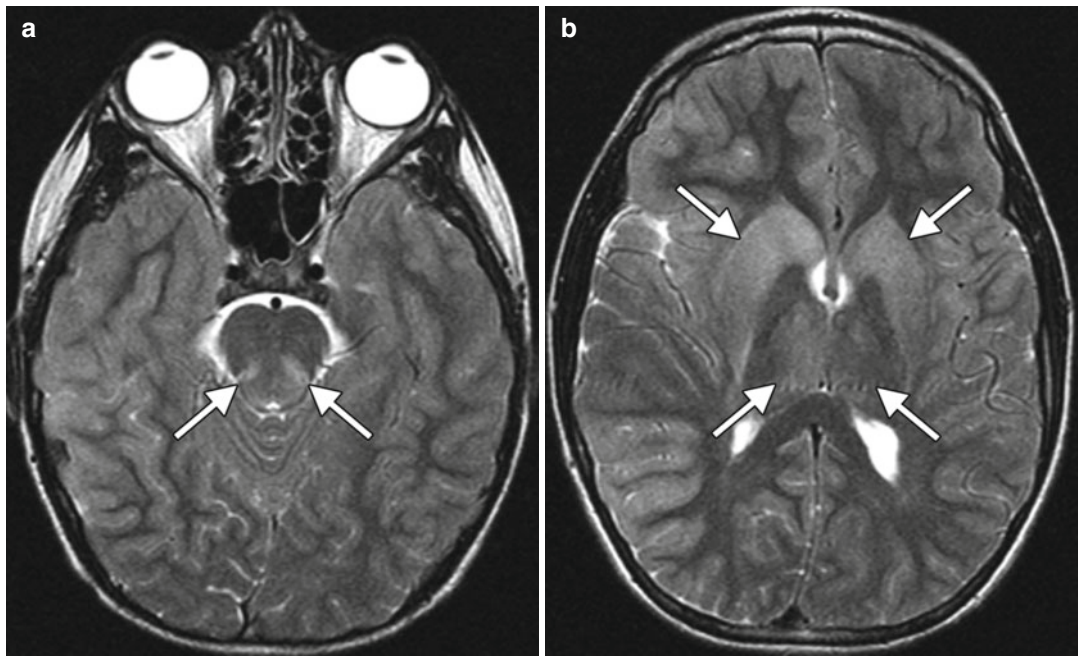

Fig. 36.4 Viral encephalitis in the setting of Eastern equine encephalitis. Axial T2-weighted MR images (**a**, **b**) show bilateral symmetric hyperintensity in the posterior pons, basal ganglia, and thalami (*arrows*)

Suggested Reading

Bourgouin PM, Chalk C, Richardson J, Duang H, Vezina JL. Subcortical white matter lesions in osmotic demyelination syndrome. AJNR Am J Neuroradiol. 1995; 16(7):1495–7.

Brunner JE, Redmond JM, Haggar AM, Elias SB. Central pontine myelinolysis after rapid correction of hyponatremia: a magnetic resonance imaging study. Ann Neurol. 1988;23(4):389–91.

Brunner JE, Redmond JM, Haggar AM, Kruger DF, Elias SB. Central pontine myelinolysis and pontine lesions after rapid correction of hyponatremia: a prospective magnetic resonance imaging study. Ann Neurol. 1990; 27(1):61–6.

Johnson AL, Criddle LM. Pass the salt: indications for and implications of using hypertonic saline. Crit Care Nurse. 2004;24(5):36–8, 40–4, 46 passim.

Singh TD, Fugate JE, Rabinstein AA. Central pontine and extrapontine myelinolysis: a systematic review. Eur J Neurol. 2014;21(12):1443–50.

Martin RJ. Central pontine and extrapontine myelinolysis: the osmotic demyelination syndromes. J Neurol Neurosurg Psychiatry. 2004;75 Suppl 3:iii22-8.

Mannitol (1,2,3,4,5,6-Hexanehexol)

37

Daniel Thomas Ginat

37.1 Uses

Mannitol is a form of hyperosmolar therapy for the reduction of intracranial pressure, including vasogenic edema associated with brain tumors and cerebral edema related to traumatic brain injury and infarcts. However, the use of mannitol is not supported by strong evidence and can produce deleterious effects.

37.2 Mechanism

Mannitol initially produces plasma expansion followed by volume depletion.

37.3 Discussion

Mannitol is a sugar alcohol osmotic diuretic available in sterile solutions of 10 and 20 %. It is believed that mannitol can leak into tissues with altered blood-brain barrier and contribute to rebound increases in intracranial pressure by reversing the initial plasma-to-blood osmotic gradient. The presence of mannitol in edematous tissue can be detected on proton MRS. All 6-CH protons of mannitol resonate in the range of 3.65–3.91 ppm, such that the integral is characterized by a wide-based peak centered at 3.8 ppm (Fig. 37.1). This finding can remain detectable for at least several hours after the last dose of mannitol and supports the theory that mannitol leakage into the peritumoral region may contribute to rebound increases in ICP.

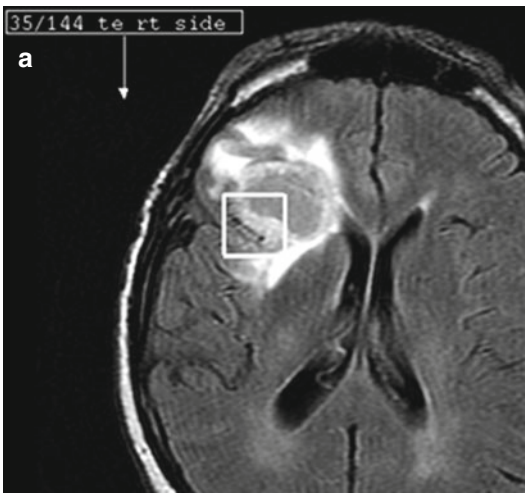

Fig. 37.1 Mannitol. The patient with a right frontal glioblastoma received mannitol. Intratumoral and peritumoral single-voxel spectroscopy (**a**) of the right frontal lobe(square region of interest) performed at short TE of 35 ms (**b**) and at intermediate TE of 144 ms (**c**) show a peak centered at 3.8 ppm (*)

D.T. Ginat, MD, MS
Department of Radiology, University of Chicago, Pritzker Medical School, Chicago, IL, USA
e-mail: ginatd01@gmail.com

D.T. Ginat et al. (eds.), *Neuroimaging Pharmacopoeia*,
DOI 10.1007/978-3-319-12715-6_37, © Springer International Publishing Switzerland 2015

Fig. 37.1 (continued)

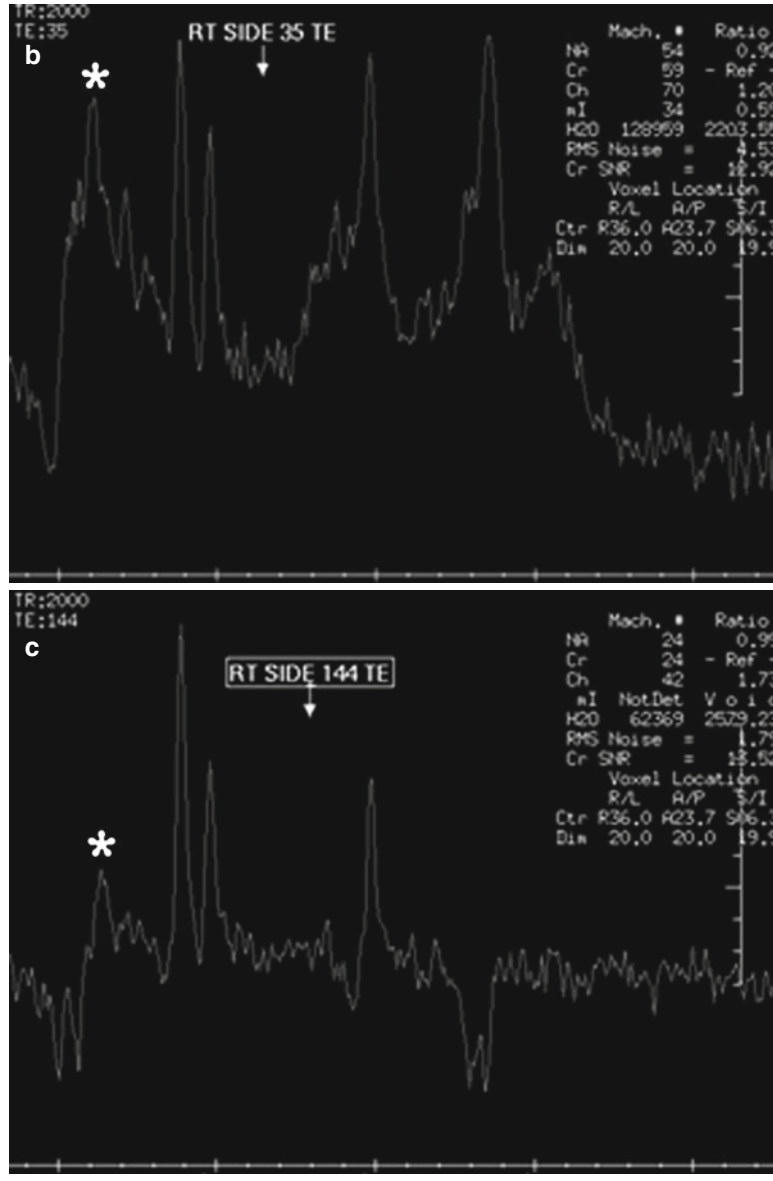

37.4 Differential Diagnosis

A broad peak on MRS between 3.6 and 3.8 ppm can also be found in the peritumoral edema associated with glioblastoma (Fig. 37.2), which is attributable to the α-hydrogens of amino acids, such as Glx, myo-inositol, and other metabolites. A peak at 3.8 ppm can be observed at low TE MRS in meningiomas (Fig. 37.3), which can help differentiate these from other brain tumors.

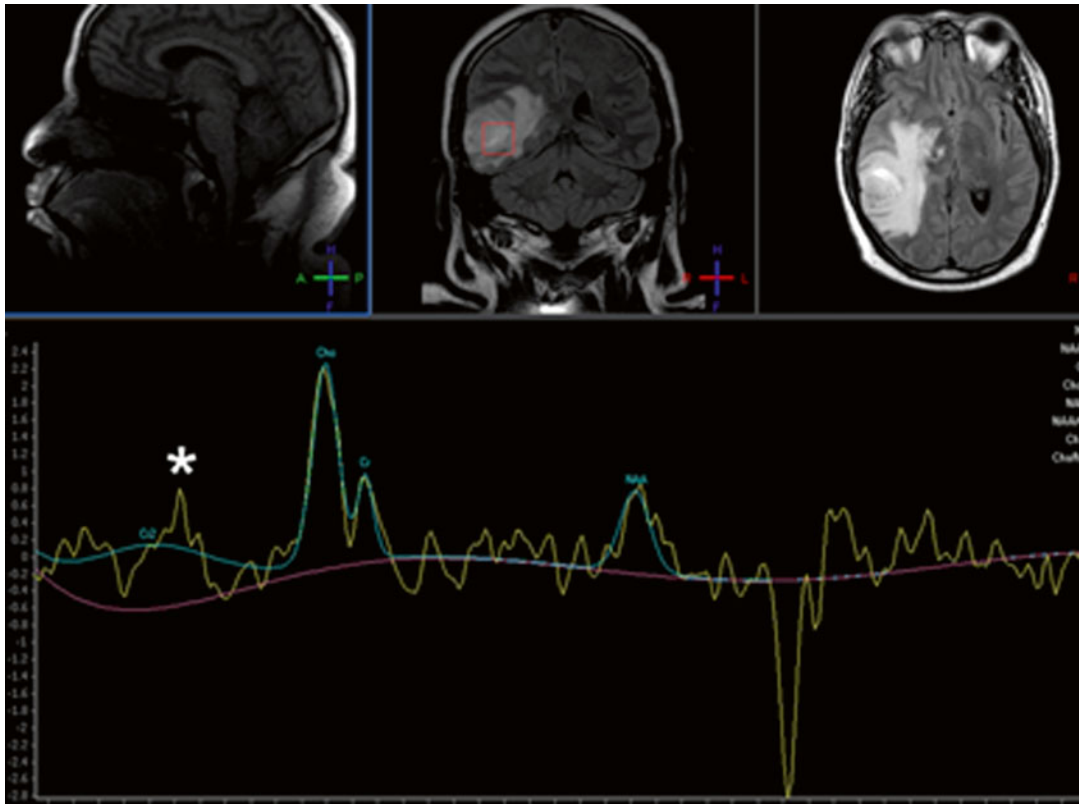

Fig. 37.2 Peritumoral edema. Single-voxel MRS of the right temporo-occipital glioblastoma shows metabolite peaks in the 3.6–3.8 range (*)

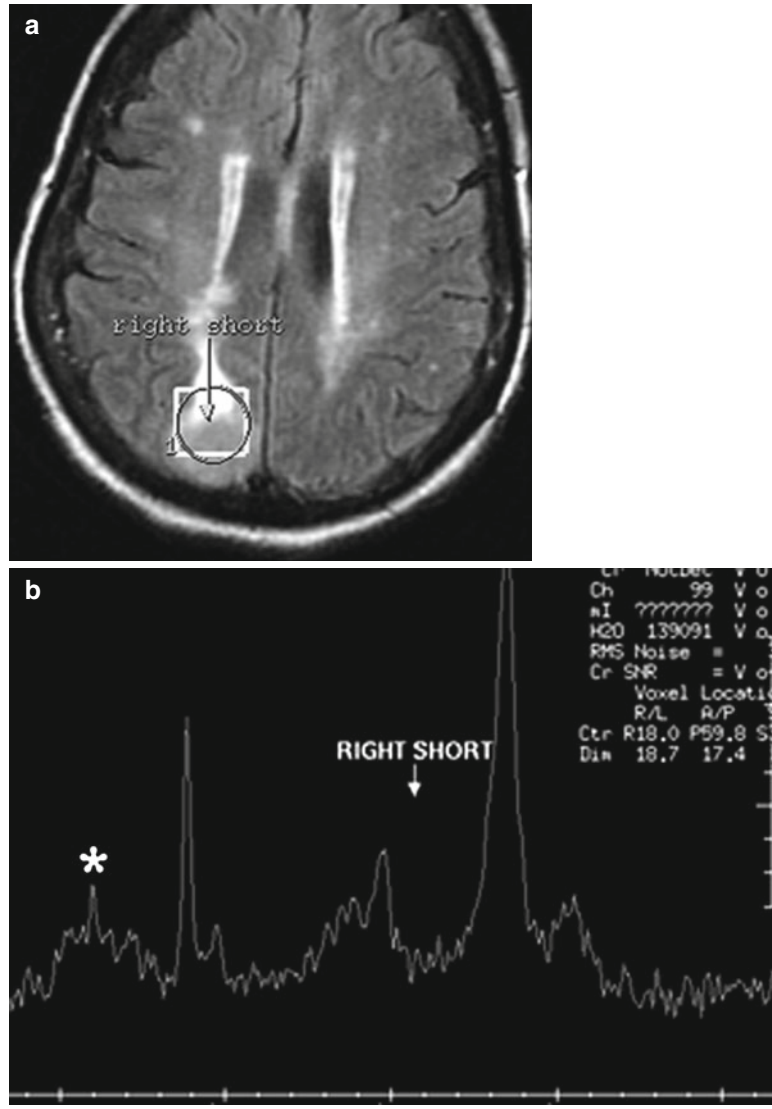

Fig. 37.3 Meningioma. MR spectroscopy (**a**, **b**) performed with a single voxel positioned over the right parietal meningioma and associated peritumoral edema shows a peak at approximately 3.8 ppm (*). The patient did not receive mannitol

Suggested Reading

Grände PO, Romner B. Osmotherapy in brain edema: a questionable therapy. J Neurosurg Anesthesiol. 2012; 24(4):407–12.

Kousi E, Tsougos I, Fountas K, Theodorou K, Tsolaki E, Fezoulidis I, Kapsalaki E. Distinct peak at 3.8 ppm observed by 3T MR spectroscopy in meningiomas, while nearly absent in high-grade gliomas and cerebral metastases. Mol Med Rep. 2012;5(4):1011–8.

Palma L, Bruni G, Fiaschi AI, Mariottini A. Passage of mannitol into the brain around gliomas: a potential cause of rebound phenomenon. A study on 21 patients. J Neurosurg Sci. 2006;50(3):63–6.

Ricci R, Bacci A, Tugnoli V, Battaglia S, Maffei M, Agati R, Leonardi M. Metabolic findings on 3T 1H-MR spectroscopy in peritumoral brain edema. AJNR Am J Neuroradiol. 2007;28(7):1287–91.

Sankar T, Assina R, Karis JP, Theodore N, Preul MC. Neurosurgical implications of mannitol accumulation within a meningioma and its peritumoral region demonstrated by magnetic resonance spectroscopy: case report. J Neurosurg. 2008;108(5): 1010–3.

HiDAC (High-Dose Ara-C; Cytarabine; Cytosine Arabinoside; Cytosar-U; Depocyt)

38

Daniel Thomas Ginat

38.1 Uses

Ara-C remains one of the most effective drugs used in the treatment of acute leukemia and other hematopoietic malignancies. In particular, high-dose ara-C is used during remission induction or as consolidation therapy after complete remission of acute myeloid leukemia in adults. Ara-C has also been used as an antiviral agent, particularly against herpes, although this application has been limited by the relatively high toxicity of the pharmaceutical.

38.2 Mechanism

Ara-C is an antimetabolite of the nucleoside analog class of antineoplastic agents. The activity of ara-C depends on conversion to its lethal triphosphate derivative, ara-CTP, which interferes with one or more DNA polymerases, leading to DNA fragmentation and chain termination. Ultimately, ara-C-mediated DNA damage induces apoptosis.

D.T. Ginat, MD, MS
Department of Radiology, University of Chicago, Pritzker Medical School, Chicago, IL, USA
e-mail: ginatd01@gmail.com

38.3 Discussion

Bone marrow necrosis is an uncommon complication of HiDAC. This complication tends to occur either immediately during chemotherapy or at the time of relapse. High-dose ara-C may be responsible for increased IL-6 production and hematopoietic overstimulation, which can lead to hematopoietic cell necrosis. Bone marrow necrosis is separate from avascular necrosis and has a distinctive MRI appearance, consisting of a diffuse, extensive geographic pattern of signal abnormality with a central area of variable signal intensity that corresponds to necrotic bone marrow surrounded by a peripheral enhancement, which represents reactive granulation tissue (Fig. 38.1). Furthermore, bone marrow necrosis does not progress to vertebral body collapse. Ultimately, the necrotic bone marrow can heal and become repopulated by normal hematopoietic tissue, leaving residual areas of fibrosis that are hypointense on MRI. Portions of the affected bone marrow can also be hypermetabolic on ^{18}FDG-PET.

38.4 Differential Diagnosis

A variety of other chemotherapy agents have been implicated in the development of bone marrow necrosis, including imatinib mesylate and G-CSF. Otherwise, a variety of bone marrow alterations can be encountered on MRI in

D.T. Ginat et al. (eds.), *Neuroimaging Pharmacopoeia*,
DOI 10.1007/978-3-319-12715-6_38,

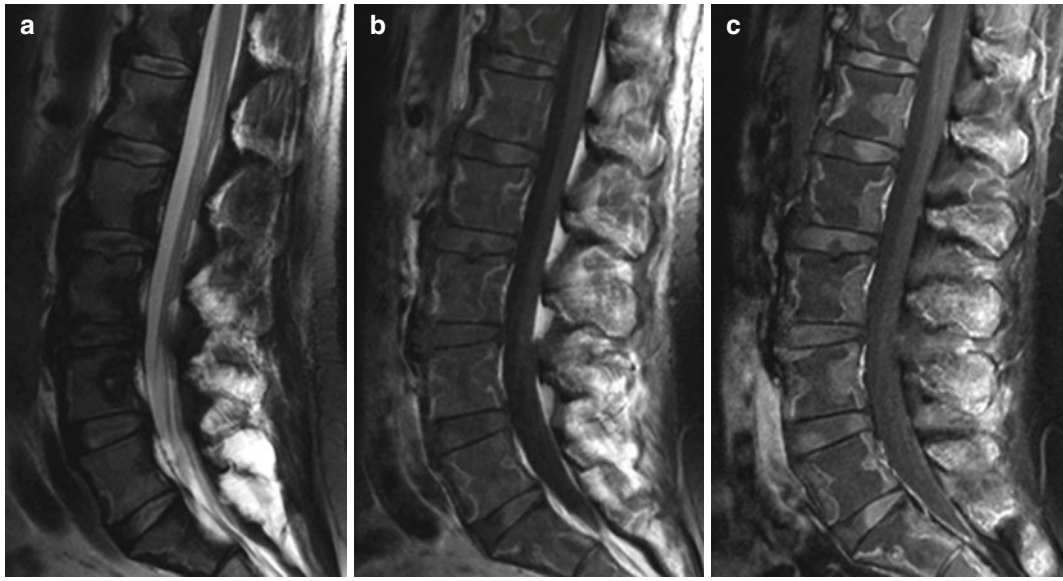

Fig. 38.1 Bone marrow necrosis related to HiDAC. Sagittal T2-weighted (**a**), T1-weighted (**b**), and post-contrast T1-weighted (**c**) images show diffuse, extensive geographic signal abnormality and peripheral enhancement within the vertebral bone marrow without vertebral body height loss or expansion

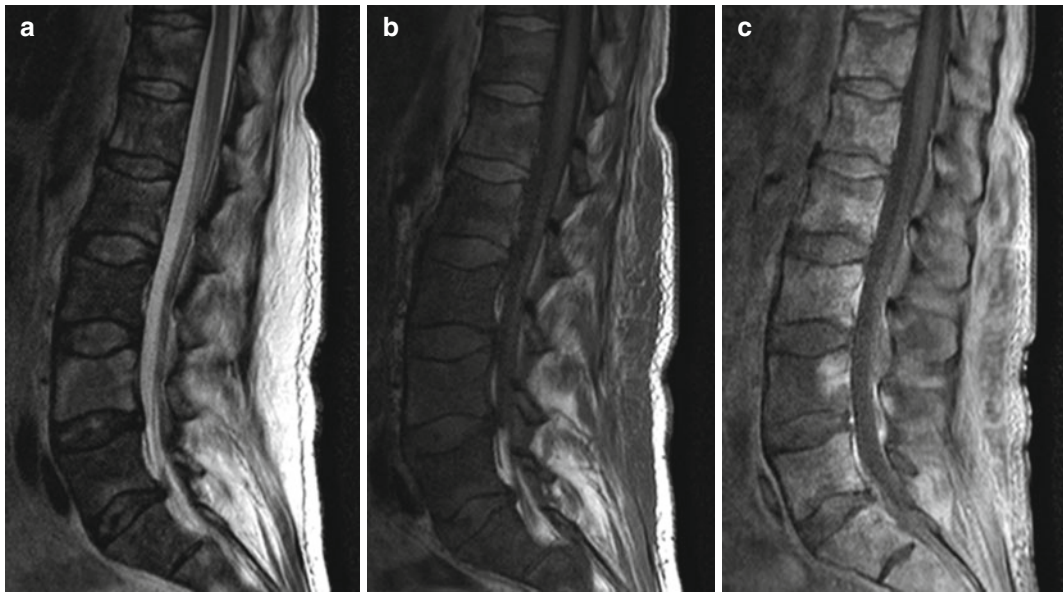

Fig. 38.2 Acute myelogenous leukemia. Sagittal T2-weighted (**a**), T1-weighted (**b**), and post-contrast T1-weighted (**c**) MR images show diffusely heterogeneous bone marrow signal and enhancement

patients being treated for malignancies. For example, on MRI leukemia can manifest as heterogeneous areas of enhancement (Fig. 38.2), anemia appears as diffuse low T1 and T2 signal due to red marrow conversion (Fig. 38.3), while spinal irradiation produces diffuse high T1 and T2 signal due to fatty marrow conversion (Fig. 38.4).

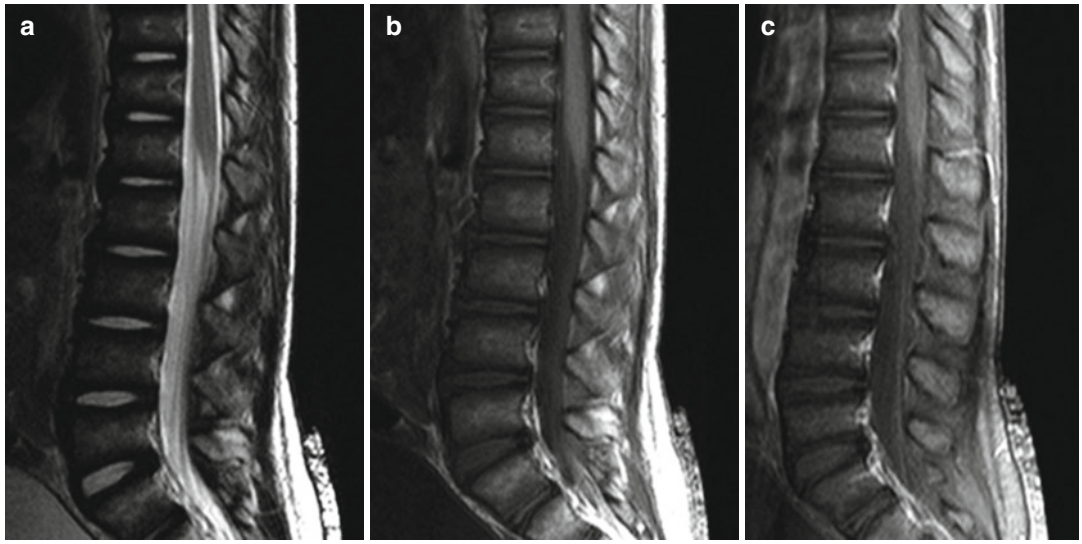

Fig. 38.3 Anemia. Sagittal T2-weighted (**a**), T1-weighted (**b**), and post-contrast T1-weighted (**c**) MR images show diffuse low signal intensity on all sequences throughout the vertebral bone marrow without associated enhancement

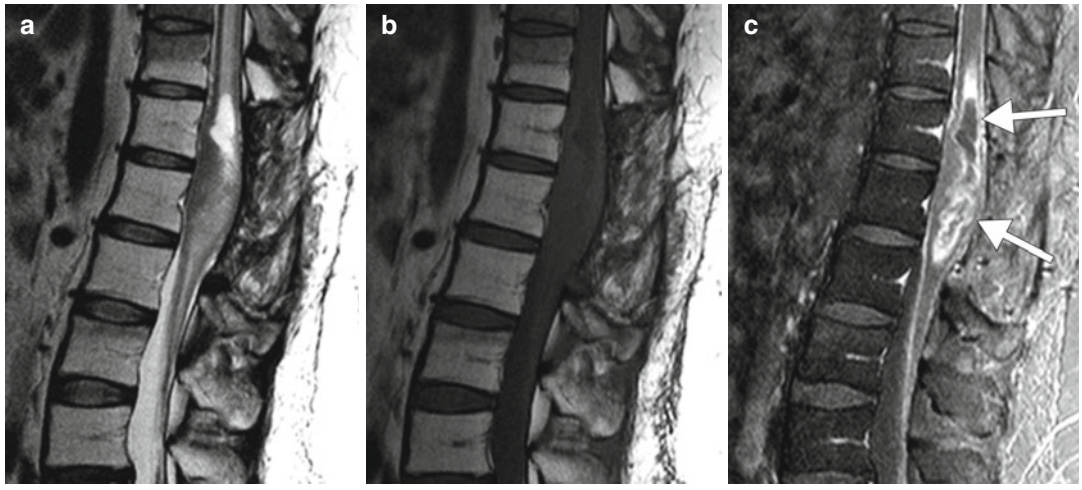

Fig. 38.4 Irradiated bone marrow. Sagittal T2-weighted (**a**), T1-weighted (**b**), and fat-suppressed post-contrast T1-weighted (**c**) MR images show diffuse T1 and T2 hyperintensity with loss of signal on fat suppression, compatible with fatty marrow conversion. There is a conus medullaris astrocytoma (*arrows*)

Suggested Reading

Aras Y, Akcakaya MO, Unal SN, Bilgic B, Unal OF. Bone marrow necrosis secondary to imatinib usage, mimicking spinal metastasis on magnetic resonance imaging and FDG-PET/CT. J Neurosurg Spine. 2012;16(1):57–60.

Grant S. Ara-C: cellular and molecular pharmacology. Adv Cancer Res. 1998;72:197–233.

Paydas S, Ergin M, Baslamisli F, Yavuz S, Zorludemir S, Sahin B, Bolat FA. Bone marrow necrosis: clinicopathologic analysis of 20 cases and review of the literature. Am J Hematol. 2002;70(4):300–5.

Tang YM, Jeavons S, Stuckey S, Middleton H, Gill D. MRI features of bone marrow necrosis. AJR Am J Roentgenol. 2007;188(2):509–14.

Triple H Therapy

39

Daniel Thomas Ginat

39.1 Uses

The combination of induced hypertension, hypervolemia, and hemodilution constitutes triple H therapy, which may be carried out by the administration of albumin, phenylephrine, and/or dopamine. Triple H therapy is an option for preventing and treating cerebral vasospasm after aneurysmal subarachnoid hemorrhage. Although strong clinical evidence is lacking, this therapy may be appropriate for selected cases.

39.2 Mechanism

The rationale for triple H therapy is to increase cerebral perfusion. In order to achieve hypertension, hypervolemia, and hemodilution, 70 % dextran, 4–5 % albumin, and catecholamines, such as phenylephrine or dopamine, are commonly administered.

39.3 Discussion

The occurrence of ischemia as a complication of subarachnoid hemorrhage is associated with high morbidity and mortality due to vasospasm. Triple H therapy has been devised in order to overcome the effects of vasospasm and prevent cerebral ischemia. However, many reports suggest that triple H therapy has only modest effects on regional cerebral blood flow but can have a potentially negative impact on brain tissue oxygenation as well as complications, such as posterior leukoencephalopathy syndrome. A pattern of predominantly bilateral posterior cerebral hemisphere vasogenic edema resulting from dysfunction of cerebral blood vessel autoregulation can be depicted on imaging (Fig. 39.1). CT perfusion can detect alterations in cerebral blood flow and volume caused by these hemodynamic changes.

39.4 Differential Diagnosis

The main differential consideration for new neurological deficits following subarachnoid hemorrhage is vasospasm-associated ischemia (Fig. 39.2). Although infarction secondary to vasospasm and posterior reversible encephalopathy can both appear as bilateral hypoattenuating foci on CT, infarcts typically demonstrate perfusion deficits, while posterior reversible encephalopathy tends to show elevated perfusion. Diffusion-weighted imaging can also be useful for characterizing these lesions, whereby acute infarcts display restricted diffusion, while posterior reversible encephalopathy more commonly demonstrates elevated diffusivity.

D.T. Ginat, MD, MS
Department of Radiology, University of Chicago, Pritzker Medical School, Chicago, IL, USA
e-mail: ginatd01@gmail.com

D.T. Ginat et al. (eds.), *Neuroimaging Pharmacopoeia*,
DOI 10.1007/978-3-319-12715-6_39,

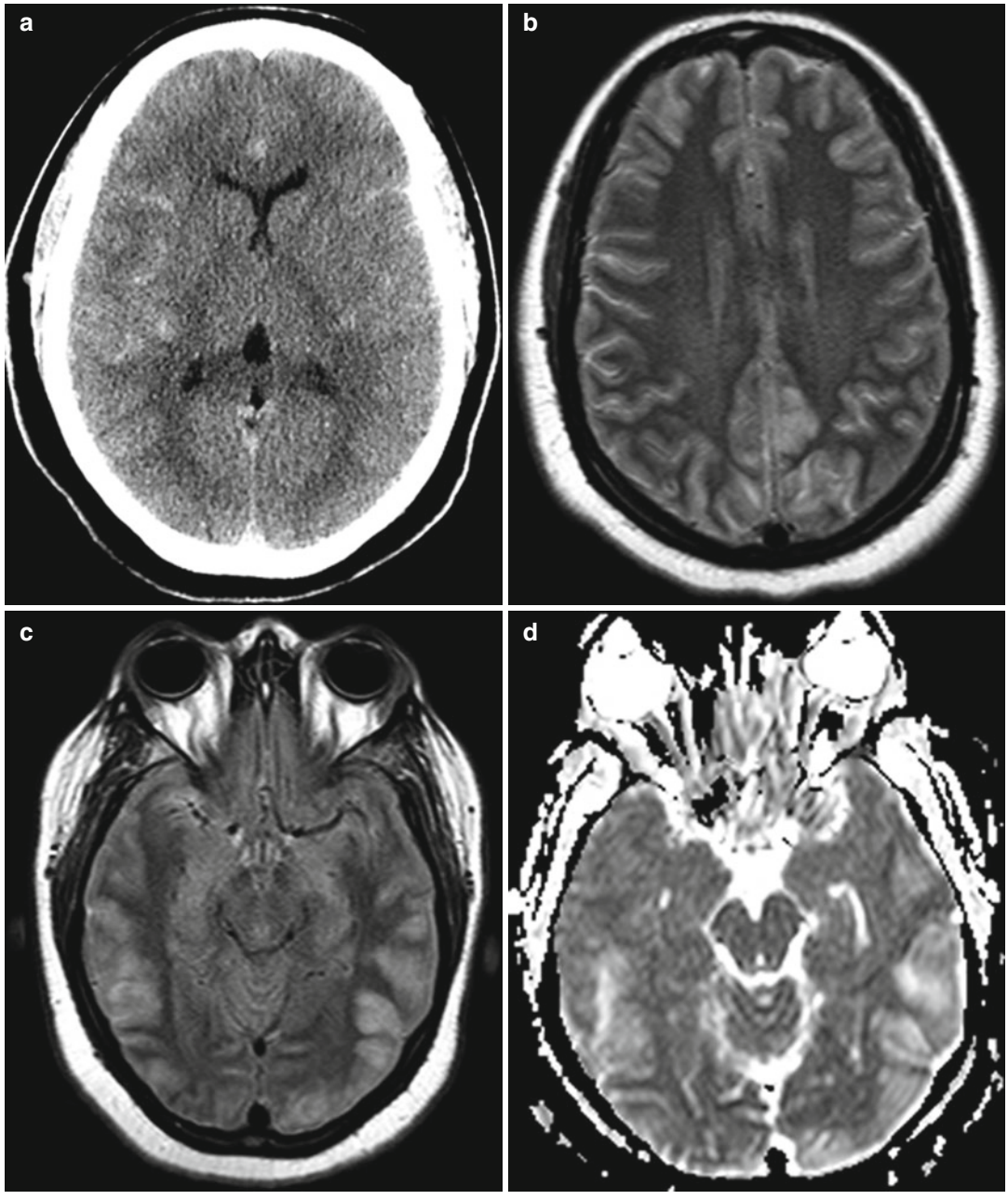

Fig. 39.1 Triple H-associated posterior reversible encephalopathy syndrome. Axial CT image (**a**) shows scattered subarachnoid hemorrhage. Follow-up MRI (**b**–**d**) shows bilateral posterior cerebral hemisphere cortical and subcortical vasogenic edema

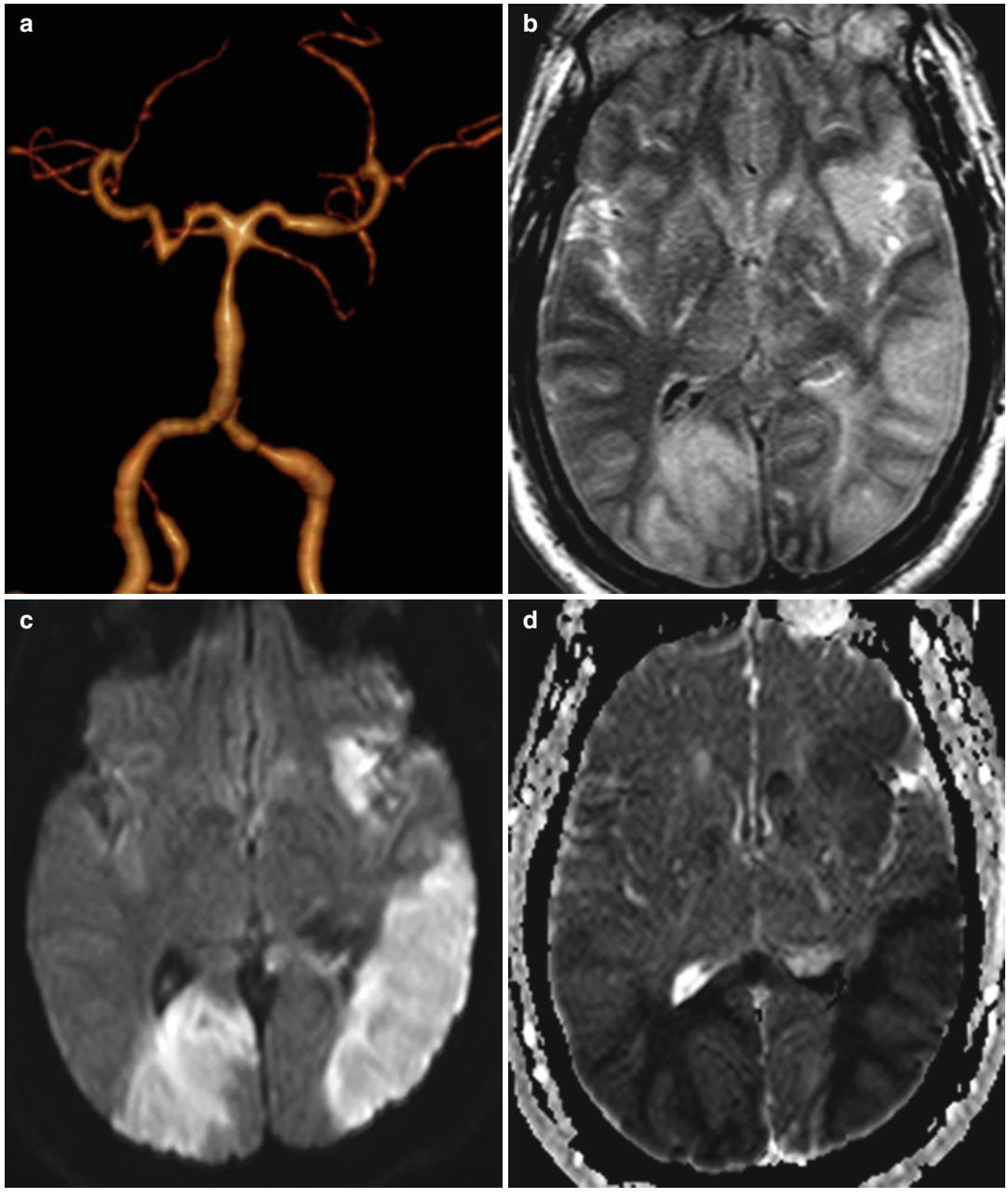

Fig. 39.2 Infarct related to vasospasm after subarachnoid hemorrhage. Posterior circulation 3-D reformatted CTA image (**a**) shows multiple stenotic lesions. Axial FLAIR (**b**), DWI (**c**), and ADC map (**d**) show that acute infarcts predominantly affect the posterior hemispheres bilaterally

Suggested Reading

Dankbaar JW, Slooter AJ, Rinkel GJ, Schaaf IC. Effect of different components of triple-H therapy on cerebral perfusion in patients with aneurysmal subarachnoid haemorrhage: a systematic review. Crit Care. 2010;14(1):R23.

Jang HW, Lee HJ. Posterior reversible leukoencephalopathy due to "triple H" therapy. J Clin Neurosci. 2010; 17(8):1059–61.

Lee KH, Lukovits T, Friedman JA. "Triple-H" therapy for cerebral vasospasm following subarachnoid hemorrhage. Neurocrit Care. 2006;4(1):68–76.

Meyer R, Deem S, Yanez ND, Souter M, Lam A, Treggiari MM. Current practices of triple-H prophylaxis and therapy in patients with subarachnoid hemorrhage. Neurocrit Care. 2011;14(1):24–36.

Sen J, Belli A, Albon H, Morgan L, Petzold A, Kitchen N. Triple-H therapy in the management of aneurysmal subarachnoid haemorrhage. Lancet Neurol. 2003; 2(10):614–21.

Wartenberg KE, Parra A. CT and CT-perfusion findings of reversible leukoencephalopathy during triple-H therapy for symptomatic subarachnoid hemorrhage-related vasospasm. J Neuroimaging. 2006;16(2): 170–5.

Insulin

40

Lee-Anne Slater, Stephen L. Stuckey,
and Ronil V. Chandra

40.1 Uses

Insulin is the cornerstone of therapy in patients with type 1 diabetes. Patients with type 2 diabetes who fail to achieve glycemic control with oral hypoglycemics are also treated with insulin. The clinical aim is to achieve glycemic control within, or close to, the normal physiological levels. Insulin is typically administered via intermittent subcutaneous injection or occasionally via subcutaneous infusion pump.

40.2 Mechanism

The physiological secretion of insulin by the pancreas is regulated via a closed feedback loop linked to plasma glucose levels. An endogenous rate of glucose production results in a basal rate of insulin secretion. Ingestion of meals leads to elevation of plasma glucose levels and consequent increased in pancreatic insulin secretion. Insulin binds to insulin receptor sites on hepatic and muscle cells, leading to increased cellular glucose uptake, reduced gluconeogenesis, and increased glycogenesis. The aim of exogenous insulin use in patients with diabetes is to replace the basal and prandial actions of endogenous insulin. The availability of human recombinant or animal (bovine/porcine) insulin has been supplemented with genetically modified insulins known as the insulin analogues. These insulin analogues have more predictable absorption and action profiles reducing the risk of hypoglycemia.

40.3 Discussion

Excessive exogenous insulin administration is the most common reason for hypoglycemia in diabetic patients. Symptoms of mild hypoglycemia vary and include trembling, sweating, headache, dizziness, and difficulty with concentration. Some patients remain asymptomatic. Even with the introduction of insulin analogues, episodes of mild hypoglycemia occur on average twice a week in type 1 diabetic patients and are typically self-treated. Neuroimaging is typically not performed for such cases. However, 30–40 % of type 1 diabetics experience an episode of severe hypoglycemia that requires external assistance. Severe hypoglycemia can lead to seizures, coma, and death. Neuroimaging is commonly performed soon after acute presentation. Acute hypoglycemic lesions are commonly bilateral (and often symmetrical), which is the usual

L.-A. Slater, MBBS, MMed, FRANZCR
S.L. Stuckey, MBBS, MMed, MD, FRANZCR
Department of Diagnostic Imaging,
Monash Medical Center, Monash Health,
Melbourne, VIC, Australia

R.V. Chandra, MBBS, MMed, FRANZCR (✉)
Department of Diagnostic Imaging,
Monash Medical Center, Monash Health,
Melbourne, VIC, Australia
e-mail: ronilvchandra@gmail.com

D.T. Ginat et al. (eds.), *Neuroimaging Pharmacopoeia*,
DOI 10.1007/978-3-319-12715-6_40, © Springer International Publishing Switzerland 2015

harbinger for a toxic or acquired metabolic process. The lesions are hypoattenuating on CT and T2 hyperintense and may have restricted diffusion. Common imaging patterns include involvement of the corticospinal tracts, corona radiata, posterior limb of the internal capsule, splenium of the corpus callosum, basal ganglia, and occipital and temporal (hippocampi) cortices.

Importantly, patterns are variable and unilateral cortical or basal ganglia involvement can mimic acute arterial ischemic stroke. The temporal evolution of MR imaging findings is also similar with diffusion-weighted imaging most likely to be abnormal early after insult, followed by T2 hyperintensity (Fig. 40.1), and then hypoattenuation on CT. Notably, hypoglycemic injury may cross vascular territories, and thalamic involvement is rare. Those with good clinical outcome can have neuroimaging findings reverse as early as 6 h after clinical recovery.

Emergent management involves cardiorespiratory support in cases of coma and prompt restoration of euglycemia. The prognosis is determined by the duration and severity of hypoglycemia, which in turn impacts on the extent of brain injury. Basal ganglia and cortical involvement is generally associated with poor prognosis. Patients with poor neurological outcome who survive often eventually show generalized cerebral atrophy.

40.4 Differential diagnosis

All patients presenting with neurological symptoms, in particular seizure or coma, have measurement of their plasma glucose levels. Insulin overdose typically occurs in known diabetic patients. The history and laboratory investigations are key in making a diagnosis. Bilateral T2 hyperintensity involving the deep white matter, basal ganglia, and cerebral cortices can be seen in a variety of conditions. Symmetrical involvement favors a toxic, acquired metabolic or hypoxic process. Differential considerations include carbon monoxide, methotrexate, methanol, and cyanide toxicity, viral encephalopathy, and hypoxic ischemic injury.

- *Toxic-metabolic conditions and other drug toxicities, including carbon monoxide, methotrexate, methanol, and cyanide toxicity:* Bilateral T2 hyperintensities involving the deep white matter, basal ganglia, and cerebral cortices can occur with all three toxins with overlapping neuroimaging appearances (Fig. 40.2). There are some specific features that can be helpful. In carbon monoxide poisoning, there is a predilection for involvement of the globus pallidus and temporal cortices. Bilateral T2 hyperintensities with diffusion restriction involving the deep white matter, in particular the centrum semiovale, are the most typical neuroimaging finding of methotrexate encephalopathy (refer to Chap. 19). Methanol toxicity typically results in bilateral hemorrhagic putaminal necrosis (refer to Chap. 3). Cyanide toxicity typically results in bilateral hemorrhagic caudate, putaminal, and sensorimotor cortex necrosis.
- *Hypoxic brain injury*: Neuroimaging findings depend on brain maturity, severity, and length of hypoxia. In severe adult hypoxia, bilateral symmetric T2 hyperintensities with diffusion restriction involving the basal ganglia and cortices (typically sensorimotor and visual) are the most common manifestations. Delayed post-anoxic leukoencephalopathy may also occur after the initial insult, manifesting as bilateral symmetric T2 hyperintensities with diffusion restriction in the cerebral white matter (refer to Chaps. 3, 19, and 48).

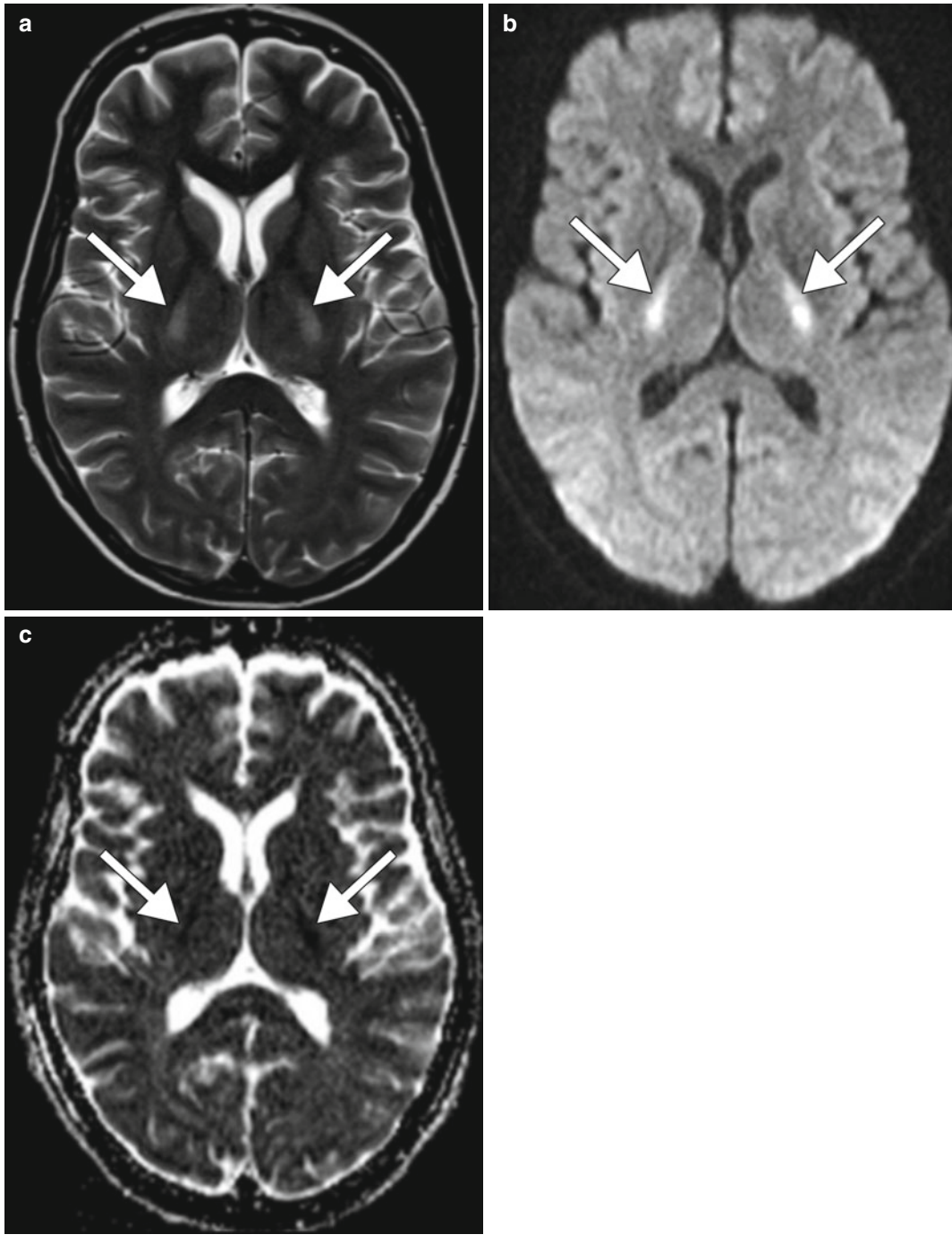

Fig. 40.1 Insulin-induced hypoglycemic encephalopathy. The type 1 diabetic patient presented in coma. Axial T2-weighted (**a**), DWI (**b**), and ADC map (**c**) imaging reveal symmetrical corona radiata T2 hyperintensity with diffusion restriction (*arrows*)

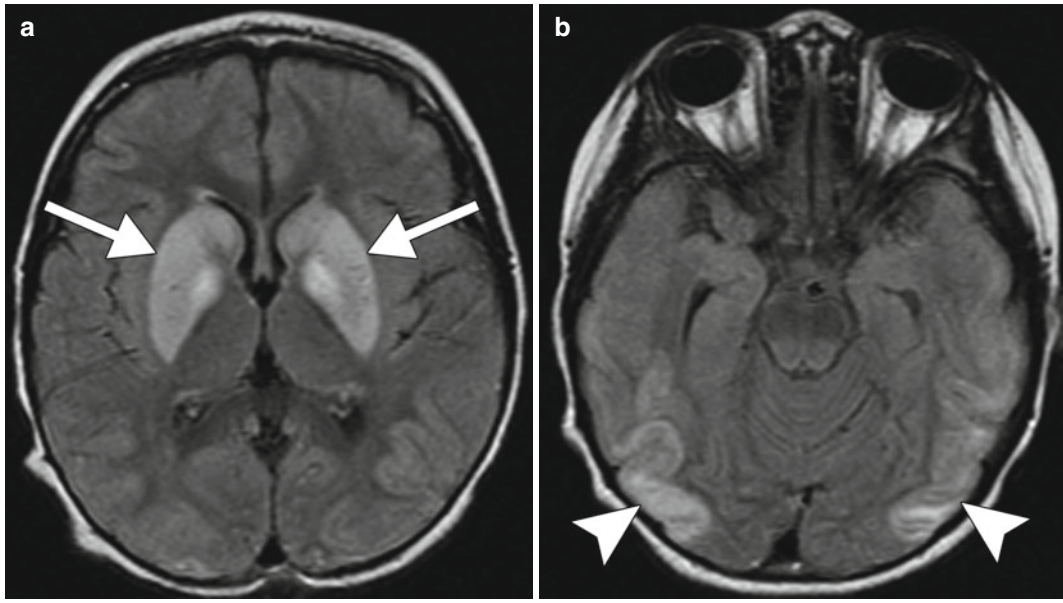

Fig. 40.2 Carbon monoxide poisoning. Axial FLAIR MR images (**a**, **b**) show edema in the bilateral basal ganglia (*arrows*) and occipital lobe cortex (*arrowheads*)

Suggested Reading

Frier BM. How hypoglycaemia can affect the life of a person with diabetes. Diabetes Metab Res Rev. 2008;24:87–92.

Mégarbane B, Deye N, Bloch V, Sonneville R, Collet C, Launay JM, Baud FJ. Intentional overdose with insulin: prognostic factors and toxicokinetic/toxicodynamic profiles. Crit Care. 2007;11(5):R115.

Pickup JC. Insulin-pump therapy for type 1 diabetes mellitus. N Engl J Med. 2012;366:1616–24.

Tofade TS, Liles EA. Intentional overdose with insulin glargine and insulin aspart. Pharmacotherapy. 2004;24(10):1412–8.

Yong AW, Morris Z, Shuler K, Smith C, Wardlaw J. Acute symptomatic hypoglycaemia mimicking ischaemic stroke on imaging: a systemic review. BMC Neurol. 2012;12:139.

Manganese in Total Parenteral Nutrition

41

Daniel Thomas Ginat

41.1 Uses

Manganese is a trace element included in total parenteral nutrition therapy preparations in order to prevent development of deficiency symptoms such as nausea, vomiting, weight loss, dermatitis, and changes in growth and color of hair. Manganese intoxication can also result from intravenous methcathinone (ephedrone) abuse.

41.2 Mechanism

When manganese is administered parenterally, the normal regulatory mechanisms that prevent excess absorption are bypassed, leading to its deposition in specific locations within the brain. Manganese is a paramagnetic transition metal with T1 shortening effects on MRI.

41.3 Discussion

Hyperintense signal on T1-weighted MRI sequences is frequently observed in the basal ganglia bilaterally and symmetrically in patients receiving long-term total parenteral nutrition therapy. This increased signal intensity is homogeneous and is most pronounced in the globus pallidus (Fig. 41.1). In addition, intrinsic high signal on T1-weighted sequences can also be found in the cerebral peduncles, dorsal brainstem, and anterior pituitary. The hyperintense signal normalizes after cessation of TPN therapy. Transcranial ultrasound can be TCS sensitive in detecting the trace metal accumulation in the lenticular nuclei, which appears as abnormal hyperechogenicity.

41.4 Differential Diagnosis

Besides excess total parenteral nutrition, a variety of conditions can produce T1 shortening in the basal ganglia, including hepatic encephalopathy (refer to Chap. 2), hypoxic ischemic injury (refer to Chaps. 3, 29, and 40), hypertensive hemorrhage, mineralizing angiopathy (refer to Chap. 19), hypoparathryroidism, pseudohypoparathyroidism, Fahr disease (refer to Chap. 19), Cockayne syndrome (Fig. 41.2), neurofibromatosis type 1 (Fig. 41.3), and neurodegenerative Langerhans cell histiocytosis (Fig. 41.4), among other conditions. In addition to clinical history, other imaging findings may help differentiate these conditions from the effects of manganese deposition. The differential diagnosis for T1 shortening in the anterior pituitary may include pituitary apoplexy (Fig. 41.5), although this has an acute presentation and appears as a mass on

D.T. Ginat, MD, MS
Department of Radiology, University of Chicago, Pritzker Medical School, Chicago, IL, USA
e-mail: ginatd01@gmail.com

D.T. Ginat et al. (eds.), *Neuroimaging Pharmacopoeia*,
DOI 10.1007/978-3-319-12715-6_41,

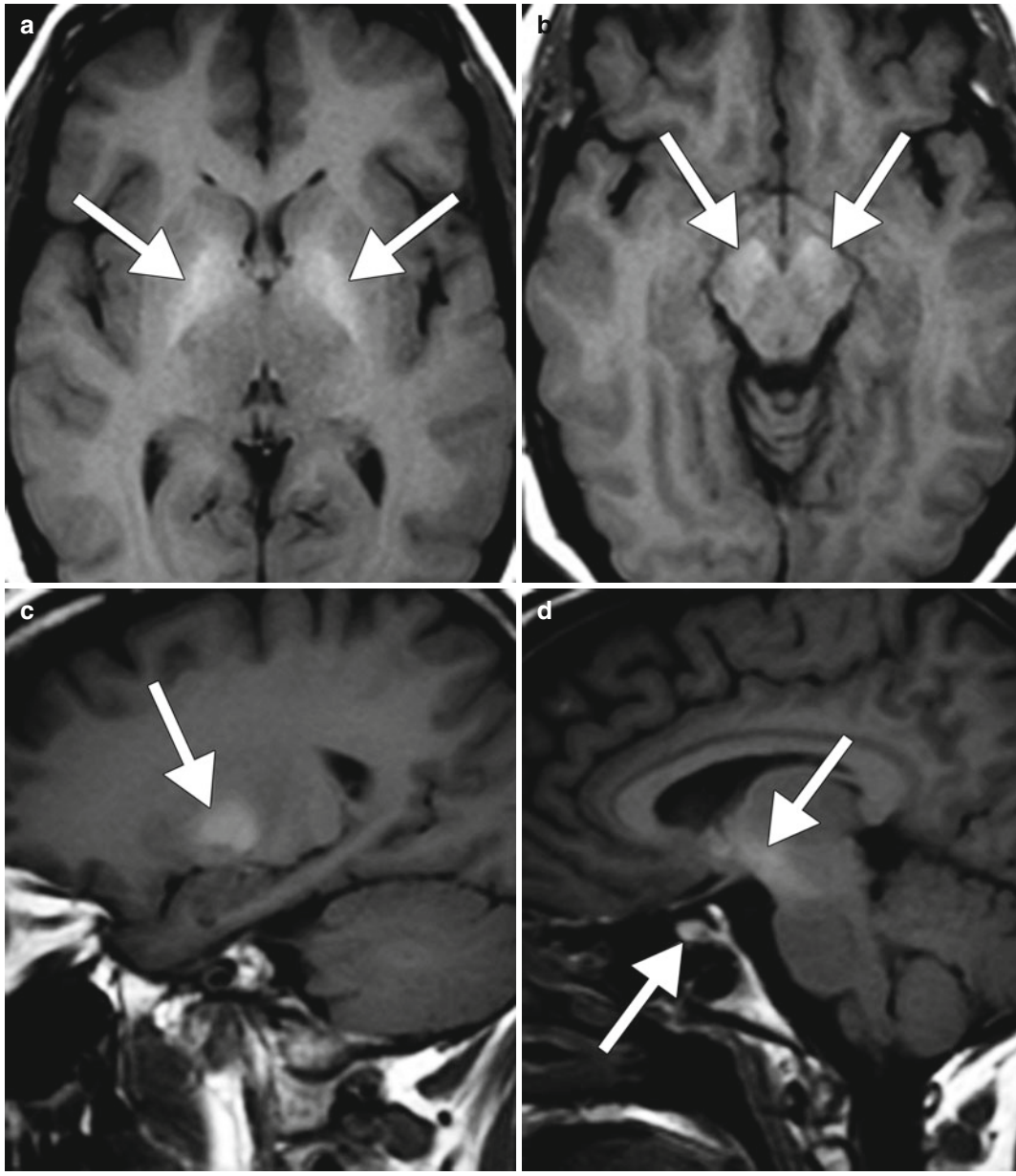

Fig. 41.1 Manganese toxicity in total parenteral nutrition. Axial (**a**, **b**) and sagittal (**c**, **d**) T1-weighted MRI images show patchy hyperintensity within the bilateral basal ganglia, cerebral peduncles, and anterior pituitary (*arrows*)

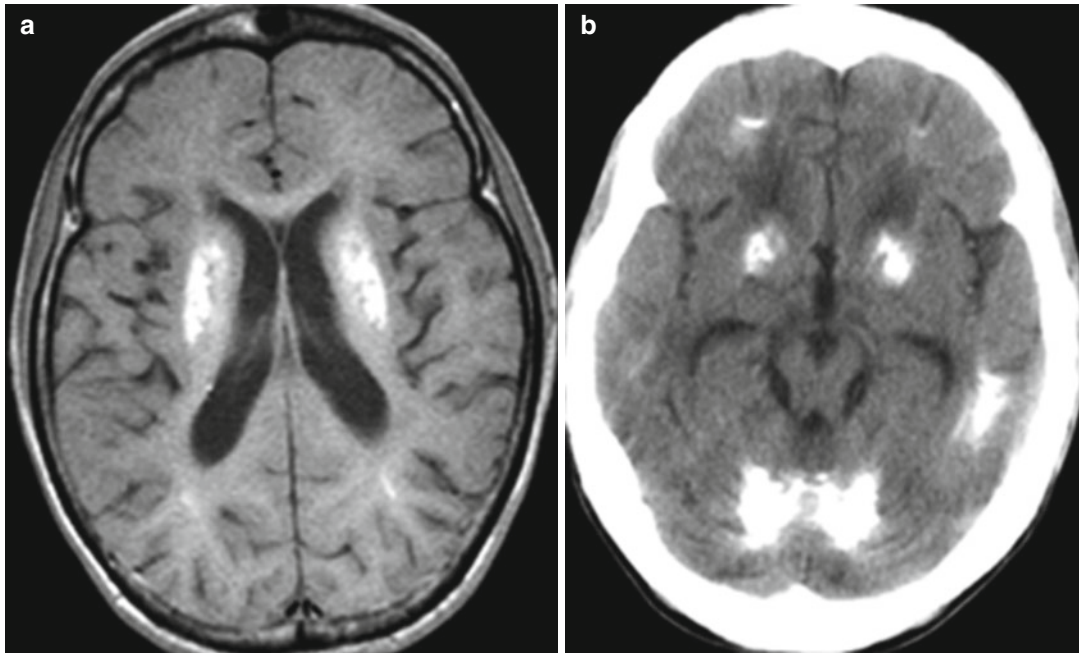

Fig. 41.2 Cockayne syndrome. Axial T1-weighted MRI (**a**) shows hyperintensity within the bilateral basal ganglia. Axial CT image (**b**) shows extensive cerebral calcifications

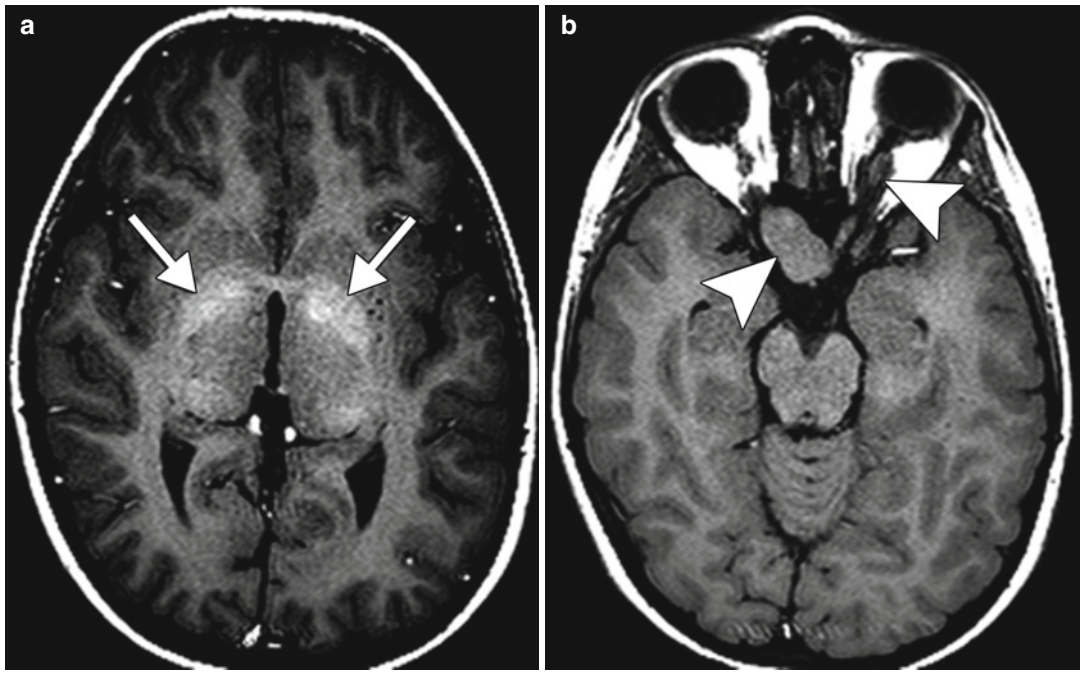

Fig. 41.3 Neurofibromatosis type 1. Axial T1-weighted MR image (**a**) shows irregular areas of high signal in the bilateral basal ganglia (*arrows*), bridging across the anterior commissure. Axial T1-weighted MR image (**b**) shows bilateral optic gliomas (*arrowheads*)

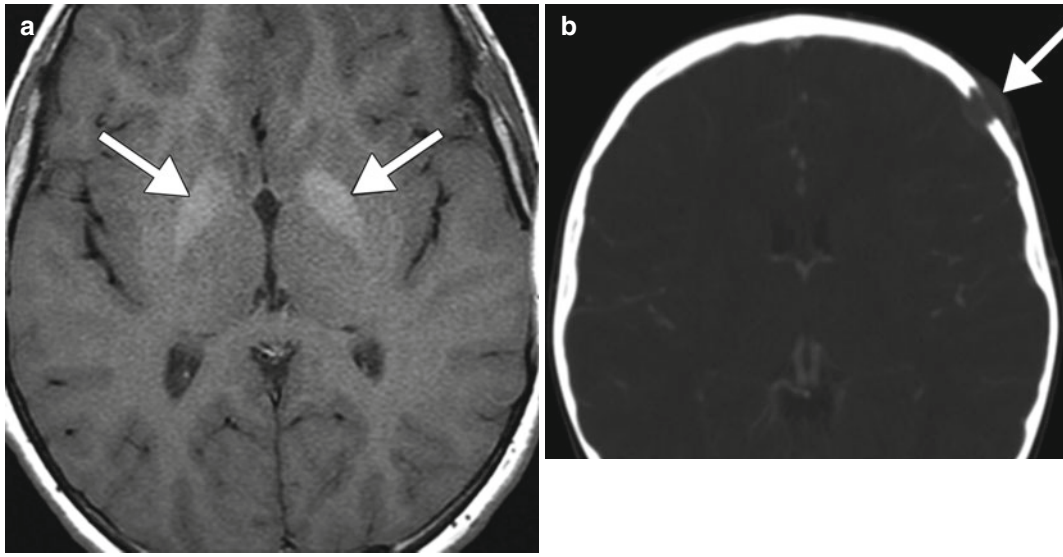

Fig. 41.4 Neurodegenerative Langerhans cell histiocytosis. Axial T1-weighted MRI (**a**) shows bilateral symmetric T1 hyperintensity within the globi pallidi (*arrows*). Axial CT image (**b**) shows an expansile lytic lesion within the left frontal bone (*arrow*)

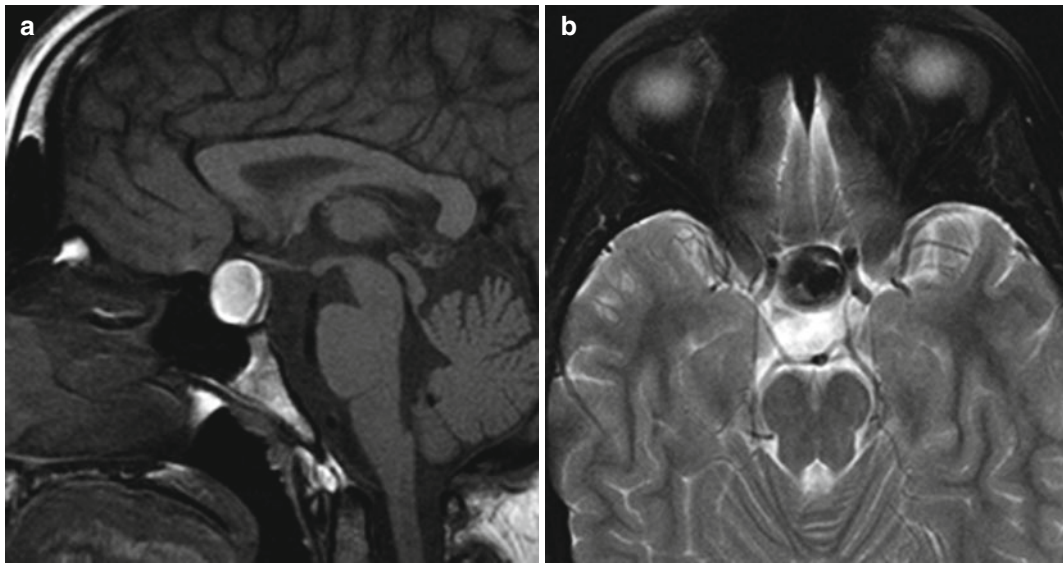

Fig. 41.5 Pituitary apoplexy. Sagittal T1-weighted MRI (**a**) shows diffuse hyperintensity within an enlarged anterior pituitary gland. There is hypointensity within the lesion on the corresponding T2-weighted MRI (**b**)

imaging. Ultimately, the history of hyperalimentation in manganese toxicity versus the presence of finding beyond the basal ganglia in the other conditions is key for elucidating the diagnosis.

Suggested Reading

Fitzgerald K, Mikalunas V, Rubin H, McCarthey R, Vanagunas A, Craig RM. Hypermanganesemia in patients receiving total parenteral nutrition. JPEN J Parenter Enteral Nutr. 1999;23(6):333–6.

Ginat DT, Meyers SP. Intracranial lesions with high signal intensity on T1-weighted MR images: differential diagnosis. Radiographics. 2012;32(2):499–516.

Lucchini R, Albini E, Placidi D, Gasparotti R, Pigozzi MG, Montani G, Alessio L. Brain magnetic resonance imaging and manganese exposure. Neurotoxicology. 2000;21(5):769–75.

Mirowitz SA, Westrich TJ. Basal ganglial signal intensity alterations: reversal after discontinuation of parenteral manganese administration. Radiology. 1992;185(2): 535–6.

Okamoto K, Ito J, Furusawa T, Sakai K, Tokiguchi S. Reversible hyperintensity of the anterior pituitary gland on T1-weighted MR images in a patient receiving temporary parenteral nutrition. AJNR Am J Neuroradiol. 1998;19(7):1287–9.

Skowronska M, Dziezyc K, Czlonkowska A. Transcranial sonography in manganese-induced parkinsonism caused by drug abuse. Clin Neuroradiol. 2014; 24(4):385–7.

Zinc Oxide (ZnO)

42

Daniel Thomas Ginat and Juan E. Small

42.1 Uses

Zinc is an essential trace element that is available in over-the-counter supplements. Despite the lack of convincing evidence for effectiveness, some individuals use zinc oxide supplements in order to prevent infections such as the common cold, recurrent ear infections, and lower respiratory infections. Zinc may also be used to treat certain eye conditions and skin conditions and is a component of adhesive denture creams.

42.2 Mechanism

Zinc is a necessary cofactor in biological reactions, including those associated with immune response, wound healing, blood clotting, and visual and thyroid function. However, excess zinc ingestion can result in copper deficiency. In particular, zinc overload results in intestinal metallothionein induction. Since copper binds tightly to metallothionein in enterocytes, copper is excessively eliminated. Copper is a critical component of metalloenzymes, which have a role in bone marrow and neurologic function. The most common neurologic manifestations of copper deficiency myelopathy are spastic gait and prominent sensory ataxia.

42.3 Discussion

Copper deficiency myelopathy caused by excessive zinc supplementation is a potentially avoidable and reversible cause of subacute combined degeneration. Patients typically present with polyneuropathy, gait difficulty due to sensory ataxia from the dorsal column dysfunction, and spasticity. In conjunction with a relevant exposure history, low ceruloplasmin levels can help suggest the diagnosis. The myelopathy most commonly exhibits abnormal long-segment T2 hyperintensity without enhancement in the dorsal columns of the cervical spinal cord and to a lesser extent the thoracic spinal cord (Fig. 42.1). Cerebral demyelination, peripheral neuropathy, and optic neuritis have also been described. Copper supplementation in the acute setting can prevent further deterioration.

42.4 Differential Diagnosis

The main considerations for the abnormal findings of zinc-induced copper deficiency myelopathy on imaging include other causes of subacute

D.T. Ginat, MD, MS (✉)
Department of Radiology, University of Chicago, Pritzker Medical School, Chicago, IL, USA
e-mail: ginatd01@gmail.com

J.E. Small, MD
Department of Diagnostic Radiology, Lahey Clinic, Burlington, MA, USA

D.T. Ginat et al. (eds.), *Neuroimaging Pharmacopoeia*,
DOI 10.1007/978-3-319-12715-6_42,

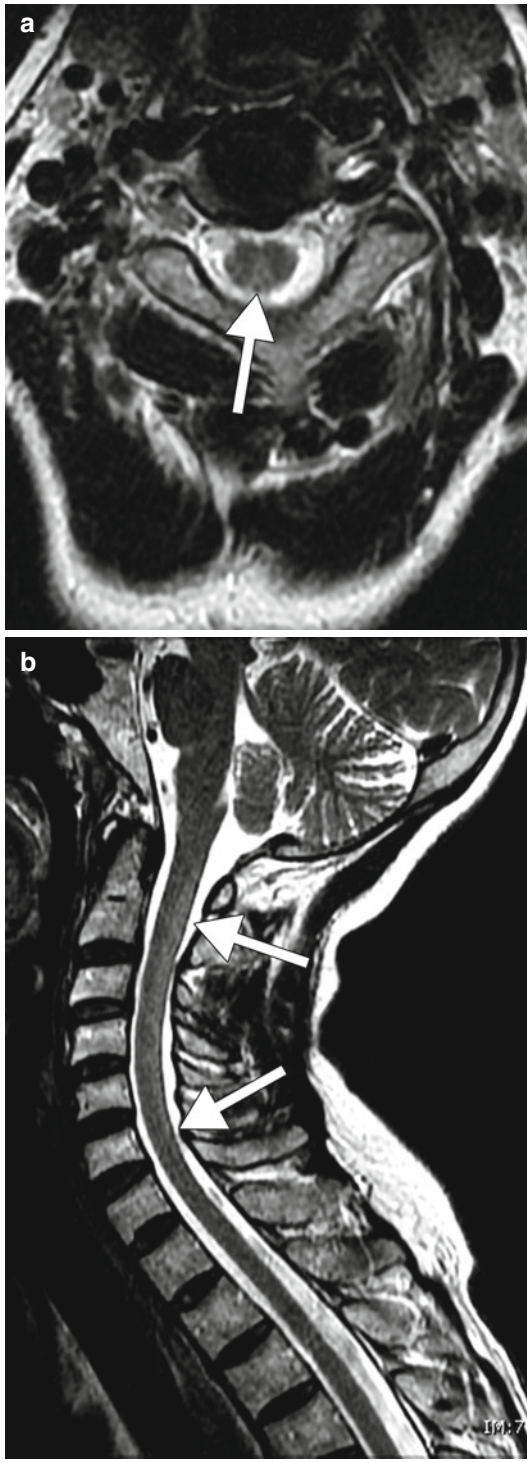

combined degeneration, such as from vitamin B12 deficiency and nitrous oxide toxicity (refer to Chap. 11). Since the imaging findings of these various cases of subacute degeneration are essentially indistinguishable, clinical parameters may point to the precise etiology. Other conditions that may less closely resemble subacute combined degeneration on imaging include spinal cord infarction; Wallerian degeneration; HIV myelopathy; demyelinating conditions, such as multiple sclerosis (refer to Chap. 11); and compressive myelopathy (Fig. 42.2).

Fig. 42.1 Zinc-induced copper deficiency myelopathy. The patient had a history of using large quantities of zinc supplements and subsequently presented with the subacute onset of progressive numbness and paresthesias affecting all four limbs in a non-length-dependent pattern with a prominent Romberg sign and vibratory loss in her legs without weakness or atrophy on exam. The patient's zinc level at the time of presentation was 152 (reference range 60–120), the vitamin B6 and B12 levels were normal, and serum copper level was at the lower limit of normal at the time of imaging. Axial (**a**) and sagittal (**b**) T2-weighted MR images of the cervical spine demonstrate long-segment T2 hyperintensity, predominantly involving the cervical dorsal columns (*arrows*)

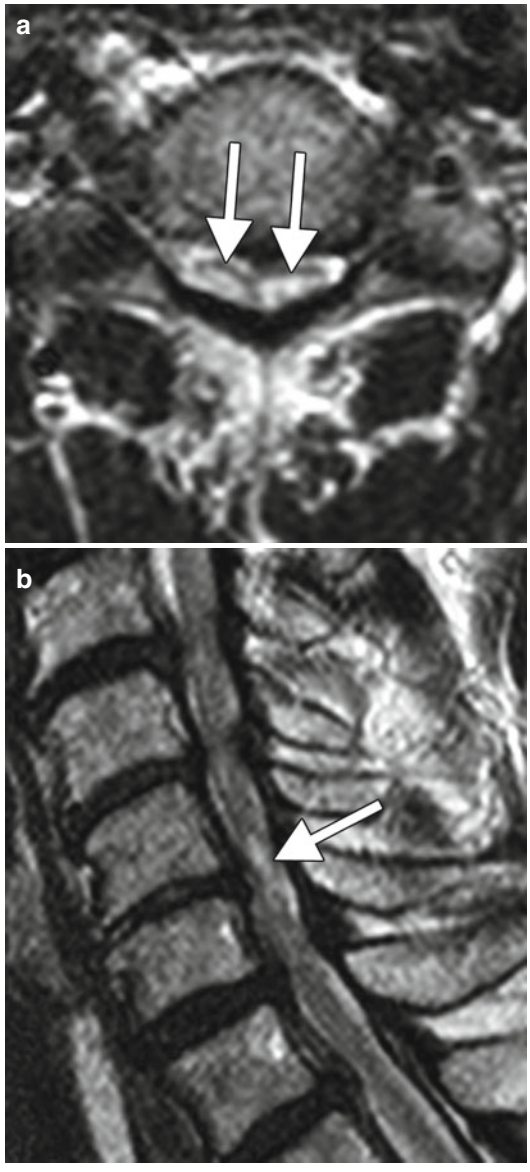

Fig. 42.2 Compressive myelopathy. Axial (**a**) and sagittal (**b**) T2-weighted MR images show an area of myelomalacia in the cervical spinal cord (*arrows*) associated with severe spinal canal stenosis

Suggested Reading

Jaiser SR, Winston GP. Copper deficiency myelopathy. J Neurol. 2010;257(6):869–81.

Kumar N, Gross Jr JB, Ahlskog JE. Copper deficiency myelopathy produces a clinical picture like subacute combined degeneration. Neurology. 2004;63(1):33–9.

Kumar N, Ahlskog JE, Klein CJ, Port JD. Imaging features of copper deficiency myelopathy: a study of 25 cases. Neuroradiology. 2006;48(2):78–83.

Nations SP, Boyer PJ, Love LA, Burritt MF, Butz JA, Wolfe GI, Hynan LS, Reisch J, Trivedi JR. Denture cream: an unusual source of excess zinc, leading to hypocupremia and neurologic disease. Neurology. 2008;71(9):639–43.

Yaldizli O, Johansson U, Gizewski ER, Maschke M. Copper deficiency myelopathy induced by repetitive parenteral zinc supplementation during chronic hemodialysis. J Neurol. 2006;253(11):1507–9.

Angiotensin Converting Enzyme (ACE) Inhibitors

43

Daniel Thomas Ginat and Jason M. Johnson

43.1 Uses

ACE inhibitors are commonly used to treat hypertension and congestive heart failure.

43.2 Mechanism

ACE inhibitors are believed to result in angioedema through increased bradykinin activity, which causes transient vasodilation and extravasation of fluid into the extracellular space, resulting in soft tissue edema. ACE inhibitor-induced angioedema is a class effect and is not dose dependent.

43.3 Discussion

The use of ACE inhibitors is believed to be the most common cause of angioedema, comprising approximately 35 % of all cases of angioedema. Conversely, angioedema occurs in approximately 0.1–1 % of patients treated with ACE inhibitors. ACE inhibitor-induced angioedema is primarily localized in the head and neck, especially in the face, mouth, tongue, lips, and larynx. The distribution of involvement tends to be diffuse and bilateral (Fig. 43.1), although focal or unilateral lingual and peritonsillar edema have been reported (Fig. 43.2). Patients with suspected angioedema are typically assessed clinically and via laryngoscopy, but may present for radiological imaging. The edema of the affected tissues appears as relatively low attenuation on CT and as low T1 and high T2 signal on MRI, without much abnormal enhancement. Patients often present shortly after initiating ACE inhibitors, but can sometimes develop angioedema many years after starting the medication. The severity of angioedema can also vary considerably from benign facial swelling to severe airway obstruction. Treatment consists of stopping the medication, instituting steroids and antihistamines, and supportive care for airway protection, which may require intubation or tracheotomy.

43.4 Differential Diagnosis

Several other drugs, such as rituximab, alteplase, fluoxetine, laronidase, lepirudin, and tacrolimus, can also cause angioedema. Otherwise, the imaging differential diagnosis for angioedema includes infection, longus coli calcific tendonitis, vascular malformations (Fig. 43.5), and neoplasms (Fig. 43.6).

- Phlegmon appears as ill-defined areas of hypoattenuation and swelling on CT, while abscess is characterized by a rim-enhancing

D.T. Ginat, MD, MS (✉)
Department of Radiology, University of Chicago, Pritzker Medical School, Chicago, IL, USA
e-mail: ginatd01@gmail.com

J.M. Johnson, MD
Department of Diagnostic Radiology, MD Anderson Cancer Center, Houston, TX, USA

D.T. Ginat et al. (eds.), *Neuroimaging Pharmacopoeia*,
DOI 10.1007/978-3-319-12715-6_43,

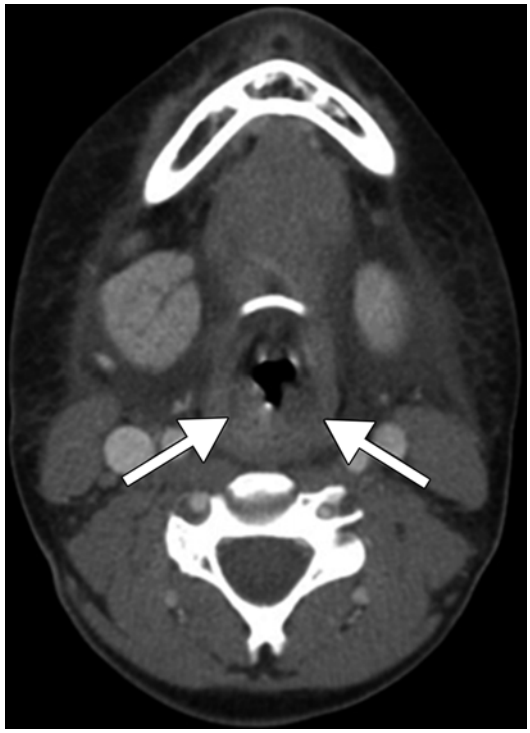

Fig. 43.1 Diffuse AACE inhibitor induced angioedema. Axial contrast-enhanced CT image shows circumferential mucosal pharyngeal swelling (*arrows*) and diffuse stranding of the parapharyngeal and subcutaneous fat bilaterally

fluid collection (Fig. 43.3). Clinical parameters, such as fever and elevated white blood cell count, are typically present.

- Longus colli calcific tendonitis can present with prevertebral space edema. Identifying a calcification on CT along the course of the tendon helps to make the diagnosis (Fig. 43.4). Patients can present with neck pain and fever.
- Vascular malformations, such as lymphatic malformations (Fig. 43.5), can present as focal or diffusely infiltrative trans-spatial lesions. These lesions are often initially diagnosed in children or young adults. Patients may present acutely due to hemorrhage within such a lesion.
- Neoplasms, such as squamous cell carcinoma (refer to Chaps. 1, 2, and 8), can present as an infiltrative mass in the oral cavity or pharynx. Tumors typically demonstrate enhancement, but may contain areas of necrosis that do not enhance.
- Radiation therapy for head and neck cancers of the aerodigestive track often produces diffuse pharyngeal mucosal edema (Fig. 43.6). This is generally mild and chronic and may be accompanied by other changes, such as subcutaneous fat reticulation.

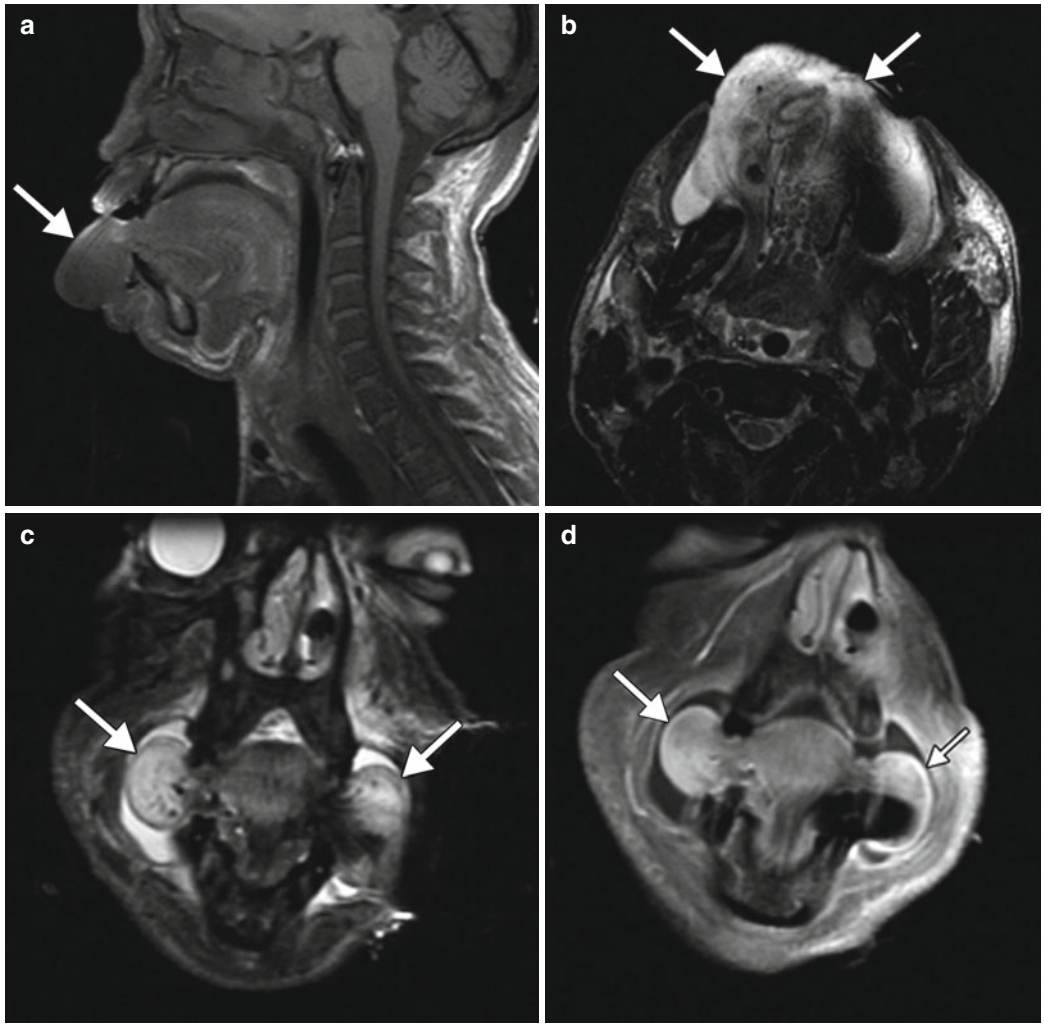

Fig. 43.2 Focal ACE inhibitor angioedema. Sagittal T1-weighted (**a**), axial (**b**) and coronal T2-weighted (**c**), and coronal post-contrast T1-weighted (**d**) MR images show diffusely massive tongue edema (*arrows*)

Fig. 43.3 Retropharyngeal abscess. Axial contrast-enhanced CT image shows a discrete rim-enhancing fluid collection in the left retropharyngeal space (*arrow*), consistent with abscess

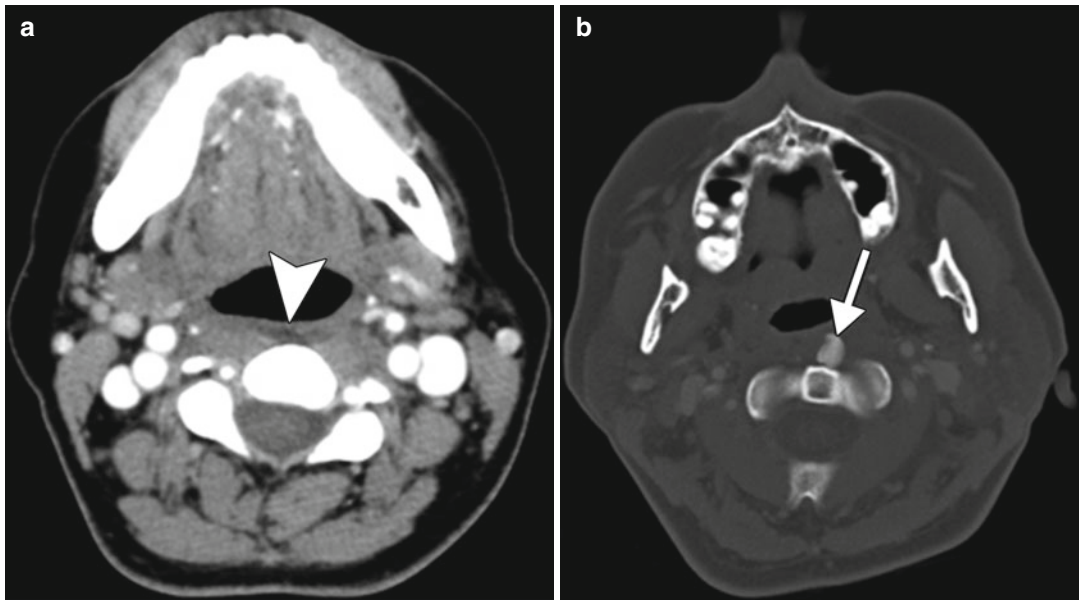

Fig. 43.4 Longus colli calcific tendonitis. Axial contrast-enhanced CT images in the soft tissue (**a**) and bone (**b**) windows obtained at different levels show an effusion in the prevertebral space (*arrowhead*) and a rounded calcification in the left longus colli tendon (*arrow*)

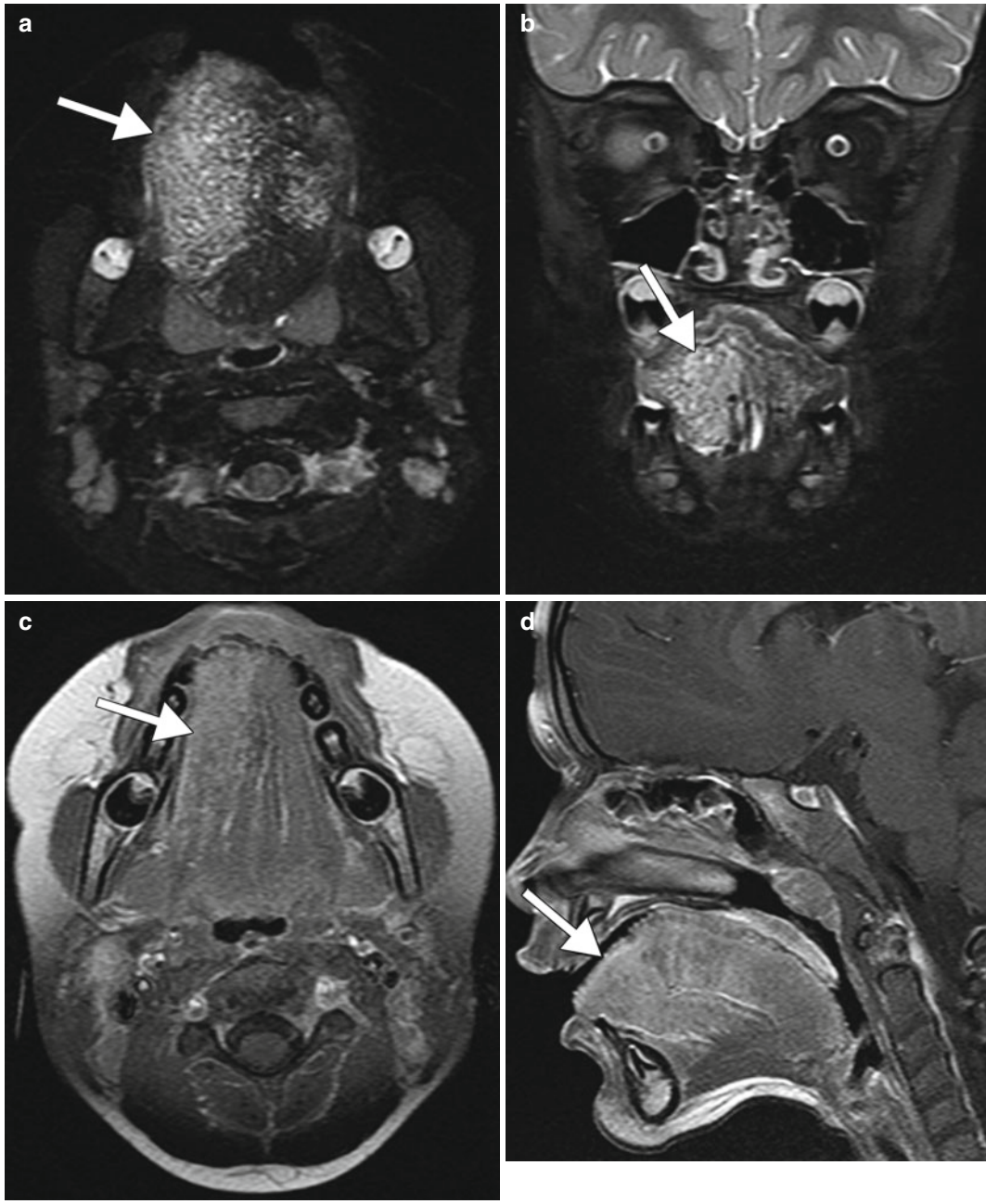

Fig. 43.5 Microcystic lymphatic malformation of the tongue. Axial (**a**) and coronal (**b**) fat-suppressed T2 and axial (**c**) and coronal (**d**) post-contrast fat-suppressed T1 MR images show a lesion mainly in the right oral tongue (*arrows*)

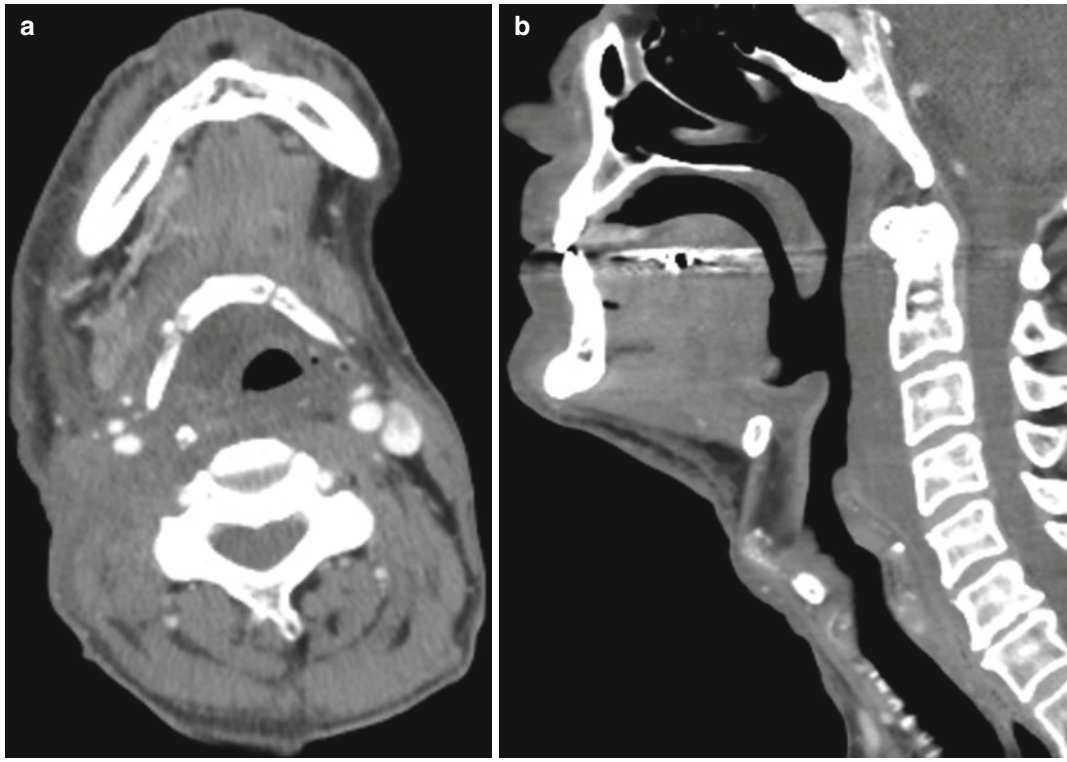

Fig. 43.6 Radiation-induced pharyngeal mucosal edema. The patient had a history of head and neck squamous cell cancer treated with chemoradiotherapy. Axial (**a**) and coronal (**b**) CT images show diffuse edema in the region of the hypopharynx as well as stranding of the subcutaneous fat

Suggested Reading

Al-Khudari S, Loochtan MJ, Peterson E, Yaremchuk KL. Management of angiotensin-converting enzyme inhibitor-induced angioedema. Laryngoscope. 2011; 121(11):2327–34.

Chiu AG, Newkirk KA, Davidson BJ, Burningham AR, Krowiak EJ, Deeb ZE. Angiotensin-converting enzyme inhibitor-induced angioedema: a multicenter review and an algorithm for airway management. Ann Otol Rhinol Laryngol. 2001;110(9):834–40.

Ee YS, Sow AJ, Goh BS. Unilateral tongue angioedema caused by angiotensin-converting enzyme inhibitor. J Laryngol Otol. 2010;124(12):1337–9.

Raman SP, Lehnert BE, Pruthi S. Unusual radiographic appearance of drug-induced pharyngeal angioedema and differential considerations. AJNR Am J Neuroradiol. 2009;30(1):77–8.

Winters ME, Rosenbaum S, Vilke GM, Almazroua FY. Emergency department management of patients with ACE-inhibitor angioedema. J Emerg Med. 2013; 45:775–80.

Acetazolamide (Diamox) 44

Daniel Lopes Noujaim, Juan E. Small, and Daniel Thomas Ginat

44.1 Uses

Acetazolamide (ACZ) is used as a medication to treat glaucoma, altitude sickness, pseudotumor cerebri, cystinuria, and hypokalemic periodic paralysis and to diminish edema related to epileptic activity. In addition, acetazolamide is used as part of the acetazolamide challenge test, which can be implemented to evaluate cerebrovascular reserve in patients with chronic cerebrovascular disease.

44.2 Mechanism

Acetazolamide is a carbonic anhydrase inhibitor that dilates the vasculature by increasing carbon dioxide levels within the bloodstream. ACZ inhibition of carbonic anhydrase causes carbonic acidosis, which induces a considerable increase in cerebral blood flow (CBF). ACZ penetrates the blood-brain barrier slowly, and vasodilation occurs over 3–4 min with maximal effect at 10 min and changes apparently on imaging lasting up to 45 min.

44.3 Discussion

Identification of the degree of autoregulatory vasodilation capacity is a reflection of cerebrovascular reserve (CVR), which is a significant prognostic factor in chronic cerebrovascular disease. Patients with poor CVR are at risk for stroke and should be treated more aggressively with medical therapies and considered for surgical interventions (carotid endarterectomy or extracranial–intracranial bypass). CVR can be assessed with the use of paired blood flow measurements, with the initial measurement obtained at baseline and the second, after a vasodilatory stimulus, such as acetazolamide. In normal patients, cerebral blood flow increases three- to fourfold after ACZ, as demonstrated on perfusion imaging, which can be performed using SPECT, MRI, or CT. Regional cerebral blood flow attains a maximum 10 min after administration of acetazolamide and then gradually decreases. On the other hand, areas of the brain where perfusion reserve is diminished due to cerebrovascular disease exhibit maximal vasodilation at baseline through autoregulatory mechanisms that attempt to maintain perfusion pressure. These regions demonstrate unchanged or paradoxical decreased perfusion (potential steal phenomenon) relative to non-diseased territories after vasodilatory stimulus (Fig. 44.1).

D.L. Noujaim, MD • J.E. Small, MD
Department of Diagnostic Radiology, Lahey Clinic, Burlington, MA, USA
e-mail: Juan.E.Small@Lahey.org

D.T. Ginat, MD, MS (✉)
Department of Radiology, University of Chicago, Pritzker Medical School, Chicago, IL, USA
e-mail: ginatd01@gmail.com

D.T. Ginat et al. (eds.), *Neuroimaging Pharmacopoeia*,
DOI 10.1007/978-3-319-12715-6_44,

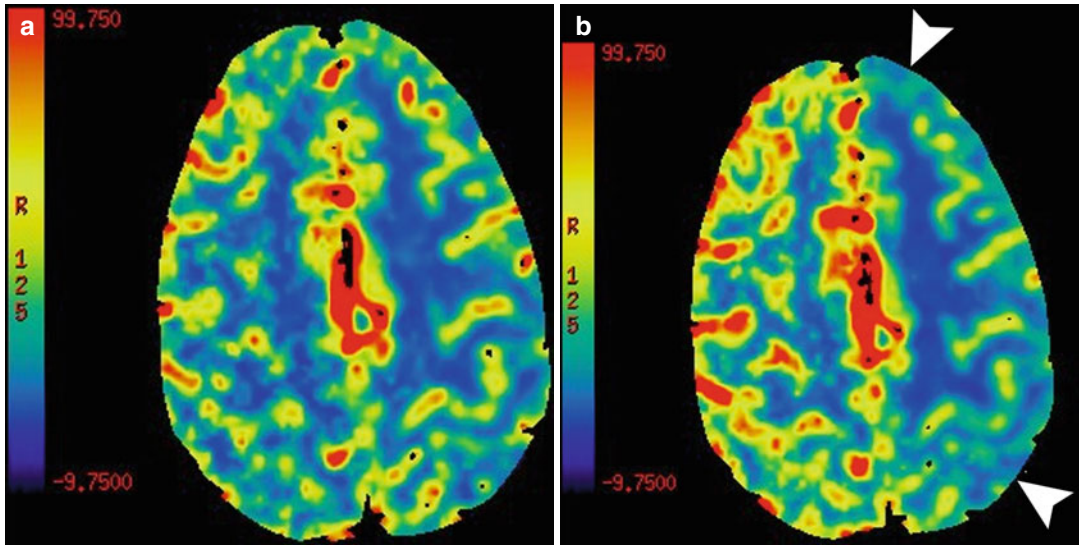

Fig. 44.1 Acetazolamide challenge test. Baseline (**a**) and post-acetazolamide (**b**) CT perfusion studies demonstrate paradoxical decrease in cerebral blood flow (CBF) within the left cerebral hemisphere (*arrowheads*) 10 min after vasodilatory stimulus consistent with poor cerebrovascular reserve in this patient with chronic left ICA vascular disease. There is a normal increase in CBF in the unaffected right cerebral hemisphere following vasodilatory stimulus

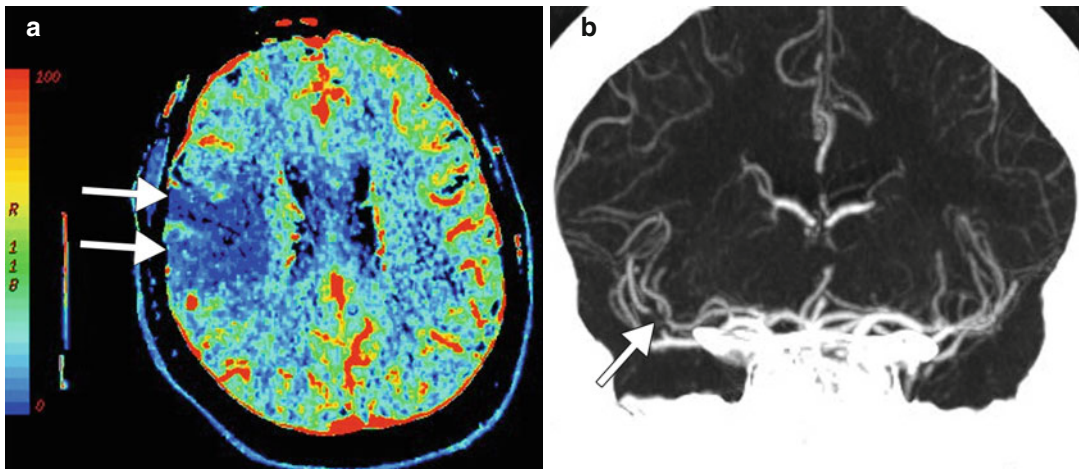

Fig. 44.2 Acute thromboembolic stroke. The patient presented with acute left hemiparesis. CT perfusion imaging (**a**) demonstrates regional diminished cerebral blood flow within the right MCA territory (*arrows*). Coronal CTA MIP image (**b**) demonstrates a focal filling defect within the right MCA superior division (*arrow*)

Contraindications to ACZ administration include allergy to other sulfonamides, electrolyte disturbances, severe kidney and liver disease, adrenocortical insufficiency, and long-term use in treatment of chronic noncongestive angle-closure glaucoma. Although well tolerated, there has been a case report of reversible pontine ischemia related to ACZ challenge testing.

44.4 Differential Diagnosis

Acute thromboembolic infarction and delayed reactive cerebrovascular vasoconstriction in the setting of subarachnoid hemorrhage (vasospasm) can also demonstrate regional decreases in cerebral blood flow (Figs. 44.2 and 44.3), although the presenting clinical scenarios are distinct.

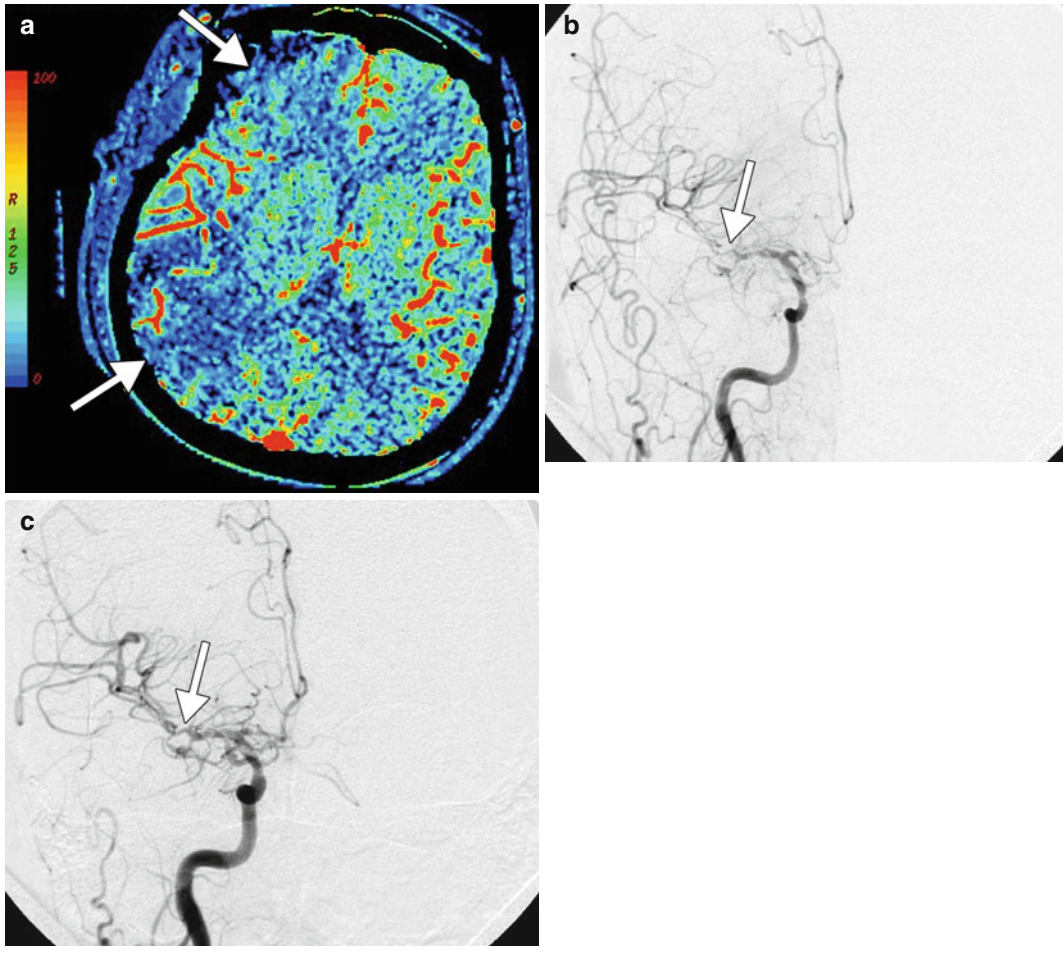

Fig. 44.3 Vasospasm. The patient presented with new neurologic deficits 12 days post-clipping of ruptured right PCOM aneurysm. CT perfusion study (**a**) demonstrates decreased cerebral blood flow within the right MCA and ACA territories (*arrows*), consistent with failing perfusion and cerebral ischemia. Cerebral digital subtraction angiography before (**b**) and after (**c**) intra-arterial therapy with vasodilatory agent demonstrates partially resolved vasospasm (*arrows*)

Suggested Reading

Inoue Y, Tanaka Y, Hata H, Hara T. Arterial spin-labeling evaluation of cerebrovascular reactivity to acetazolamide in healthy subjects. AJNR Am J Neuroradiol. 2014;35(6):1111–6.

Komiyama M, Nishikawa M, Yasui T, et al. Reversible pontine ischemia cause by acetazolamide challenge. AJNR Am J Neuroradiol. 1997;18:1782–4.

Ohnishi T, Nakano S, Yano T, Hoshi H, Jinnouchi S, Nagamachi S, Flores 2nd L, Watanabe K, Yokogami K, Ohta H. Susceptibility-weighted MR for evaluation of vasodilatory capacity with acetazolamide challenge. AJNR Am J Neuroradiol. 1996;17(4):631–7.

Settakis G, Molnár C, Kerényi L, Kollár J, Legemate D, Csiba L, Fülesdi B. Acetazolamide as a vasodilatory stimulus in cerebrovascular diseases and in conditions affecting the cerebral vasculature. Eur J Neurol. 2003; 10(6):609–20.

Vagal AS, Leach JL, Fernandez-Ulloa M, Zuccarello M. The acetazolamide challenge: techniques and applications in the evaluation of chronic cerebral ischemia. AJNR Am J Neuroradiol. 2009;30(5): 876–84.

Facial Fillers

45

Daniel Thomas Ginat and Charles J. Schatz

45.1 Uses

Injectable filler materials are used for cosmetic purposes, including smoothing wrinkles, effacing acne scars, restoring youthful tissue volume, and treating HIV lipoatrophy.

45.2 Mechanism

Fillers can either add volume without associated foreign body reaction (volumizers) or they can stimulate tissue and elicit a foreign body reaction (stimulators). Volumizers include Bio-Alcamid, certain polyacrylamides, collagen, and hyaluronic acid (HA); stimulators include polylactic acid (PLA), dextrans, calcium hydroxyapatite (CaHA), hydroxyethyl methacrylate (HEMA), and polymethylmethacrylate (PMMA). PLA and dextrans cause a foreign body reaction for a limited time period before they are absorbed, whereas PMMA microspheres stimulate collagen deposition indefinitely and are never absorbed. Collagen, hyaluronic acid gels, PLA microspheres, calcium hydroxyapatite, and HEMA particles are biodegradable, while certain polyacrylamide (PAAG) gels and PMMA microspheres are not. Non-medical grade liquid injectable silicone has a particular propensity to elicit inflammatory reactions, perhaps due to the presence of impurities.

45.3 Discussion

Facial fillers are often injected into the nasolabial folds and perioral region and can be discerned on imaging due to their distinctive imaging features. Calcium hydroxyapatite-based fillers are semi-solid pastes created by suspending calcium hydroxyapatite microspheres of 25–45 μm diameter in a gel carrier. The gel carrier consists primarily of sterile water and glycerin; the gel structure is formed by the addition of a small amount of carboxymethylcellulose. The calcium hydroxyapatite component imparts high attenuation on CT (Fig. 45.1). Over time, breakdown of the particles occurs via phagocytosis and the gel eventually dissipates in vivo and is replaced with soft tissue. This process is likely responsible for the hypermetabolism observed on ^{18}FDG-PET at the site of the filler (Fig. 45.1). Bio-Alcamid tends to appear as well-defined globular clusters due to the formation of a thin collagenous capsule that separates the fillers from surrounding tissues. Bio-Alcamid gels are comprised of 96 % water and 4 % synthetic polymeric polyalkylimide and therefore have CT attenuation and

D.T. Ginat, MD, MS (✉)
Department of Radiology, University of Chicago, Pritzker Medical School, Chicago, IL, USA
e-mail: ginatd01@gmail.com

C.J. Schatz, MD, FACR
Department of Radiology, Beverly Tower Wilshire Advanced Imaging, University of Southern California Keck School of Medicine, Los Angeles, CA, USA

D.T. Ginat et al. (eds.), *Neuroimaging Pharmacopoeia*,
DOI 10.1007/978-3-319-12715-6_45,

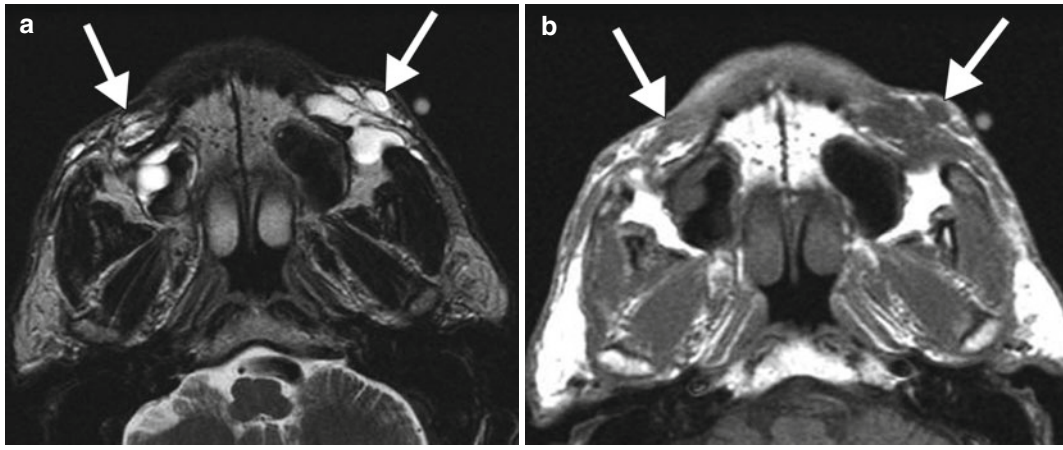

Fig. 45.1 Bio-Alcamid. Axial T1-weighted (**a**) and T2-weighted (**b**) MR images show T1 hypointense and T2 hyperintense lobulated material within the subcutaneous tissues of the bilateral cheeks (*arrows*)

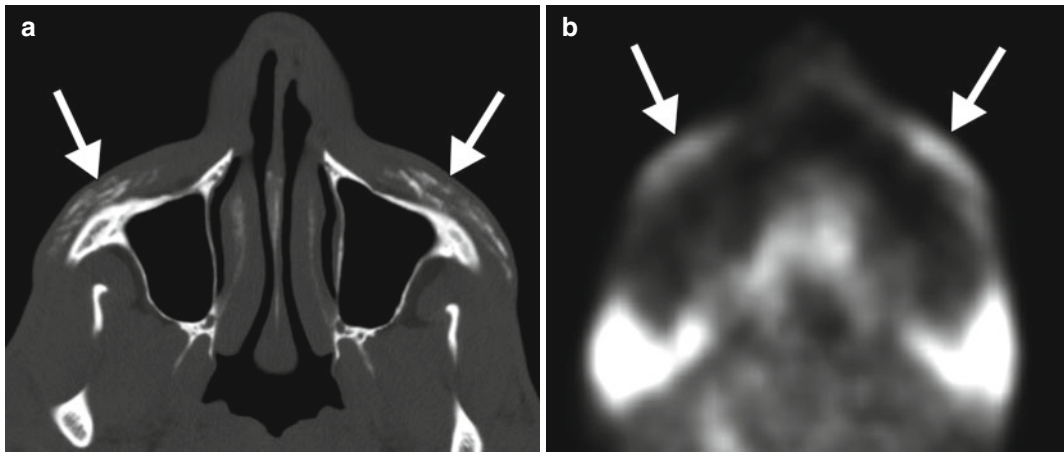

Fig. 45.2 Calcium hydroxyapatite (Radiesse). Axial CT image (**a**) shows patchy hyperattenuation fillers within the bilateral malar subcutaneous tissues (*arrows*). Axial ^{18}FDG-PET image (**b**) shows corresponding hypermetabolism at the site of the fillers (*arrows*)

MRI signal characteristics very similar to that of water (Figs. 45.2 and 45.3). Likewise, collagen and hyaluronic acid-based fillers are mainly composed of water, and the deposits of these fillers also have imaging characteristics similar to those of water with minimal peripheral enhancement (Fig. 45.4). Familiarity with the imaging features of various types of facial fillers is important to avoid misdiagnosing these as pathology, particularly if the relevant history has not been disclosed. Conversely, facial fillers may be associated with complications such as granuloma formation, which more commonly occurs with silicone oil. Such lesions can appear as partially calcified subcentimeter nodules (Fig. 45.5).

45.4 Differential Diagnosis

A variety of conditions can potentially resemble facial fillers on imaging:

- *Skin and vascular calcifications*: Punctate dystrophic skin calcifications in the cheeks are commonly encountered on CT (Fig. 45.6). These can be rather numerous, but are of little clinical significance. Occasionally vascular calcifications form along the facial artery, particularly in diabetic patients. These can be distinguished from calcium hydroxyapatite facial fillers by their distribution and at times branching tubular configuration.

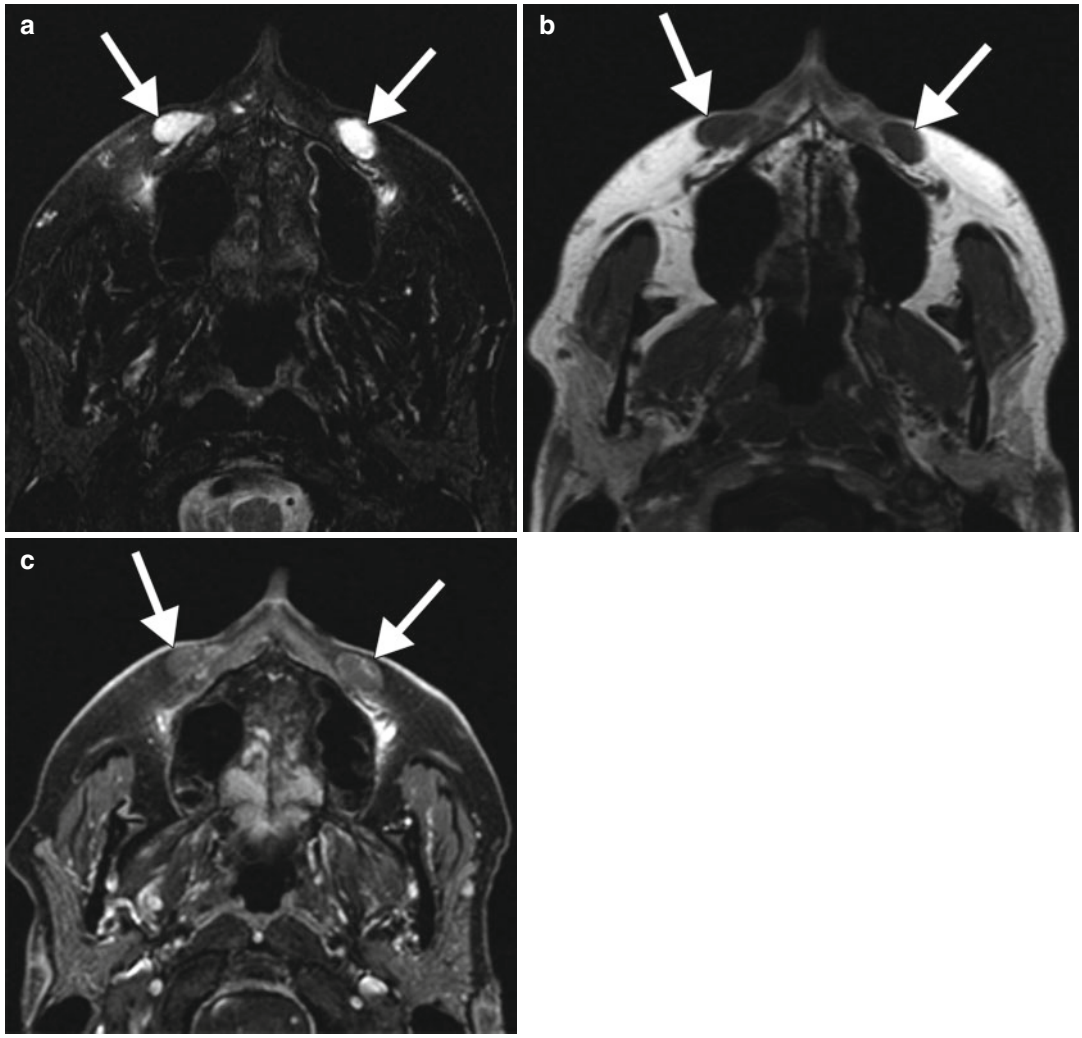

Fig. 45.3 Hyaluronic acid (Restylane). Axial fat-suppressed T2-weighted (**a**), T1-weighted (**b**), and fat-suppressed post-contrast T1-weighted (**c**) MR images show the filler within the bilateral nasolabial folds (*arrows*). The fillers demonstrate signal characteristics similar to fluid and minimal peripheral enhancement

- *Lymphatic malformations*: These are congenital vascular malformations that appear as transspatial masses that can involve the subcutaneous tissues of the face. Venous predominant lesions are typically T2 hyperintense, may have fluid levels, demonstrate enhancement (Fig. 45.7), and may contain phleboliths.
- *Epidermal inclusion cysts*: These are common subcutaneous lesions that often demonstrate fluid attenuation on CT (Fig. 45.8), but may be hyperattenuating. A portion of these lesions typically contacts the epidermis. They are well-defined, unless they are ruptured or infected.
- *Pilomatrixomas*: These are benign tumors derived from the matrix of hair follicles and often occur in the preauricular region and cheeks. Coarse calcifications within these lesions are typical and evident on CT (Fig. 45.9).
- *Hematomas*: Subcutaneous hematomas often occur in the cheeks over the zygomatic arch and malar eminence in the setting of facial trauma. The imaging appearances of facial hematomas range from diffuse soft tissue stranding of the fat to more discrete mass-like collections (Fig. 45.10). On MRI, signal characteristics vary depending on hematoma age. Facial fractures may be present in the vicinity the hematomas as another indicator of trauma.

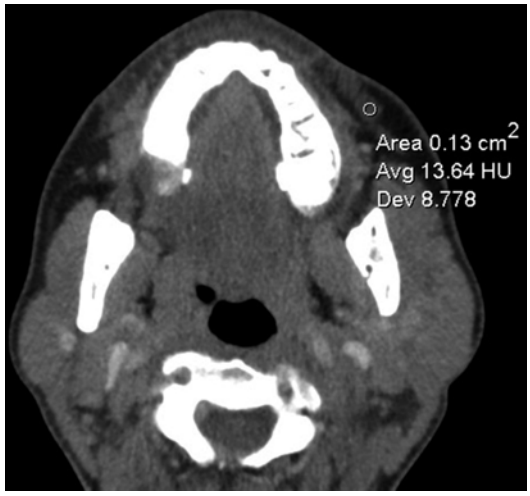

Fig. 45.4 Hyaluronic acid (Juvederm). Axial CT with a region of interest marker shows that the perioral filler is of fluid attenuation

Fig. 45.5 Silicone oil. Axial CT image shows a rim calcified nodule in the subcutaneous tissues in a patient who received silicone injections many years before (*arrow*)

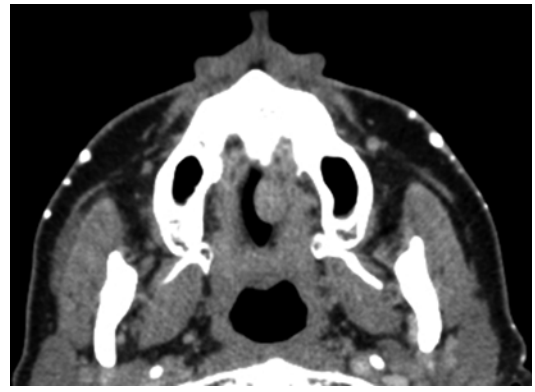

Fig. 45.6 Dystrophic skin calcifications. Axial CT image shows multiple punctuate calcifications in the skin of the bilateral cheeks

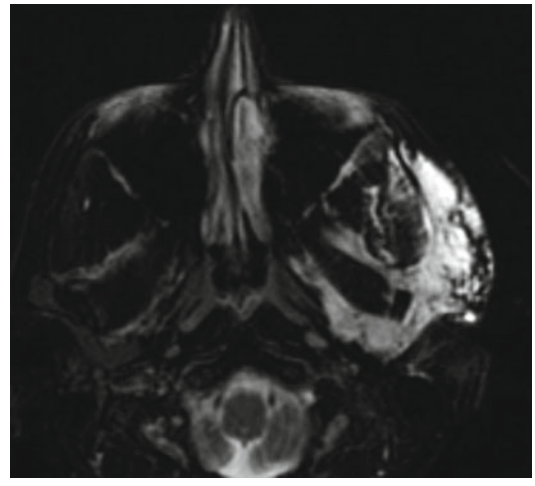

Fig. 45.7 Lymphatic malformation. Axial fat-suppressed T2-weighted MRI shows an infiltrative hyperintense lesion in the left face

Fig. 45.8 Epidermal inclusion cyst. Axial CT image shows a well-defined fluid attenuation lesion within the right cheek subcutaneous tissues (*arrow*)

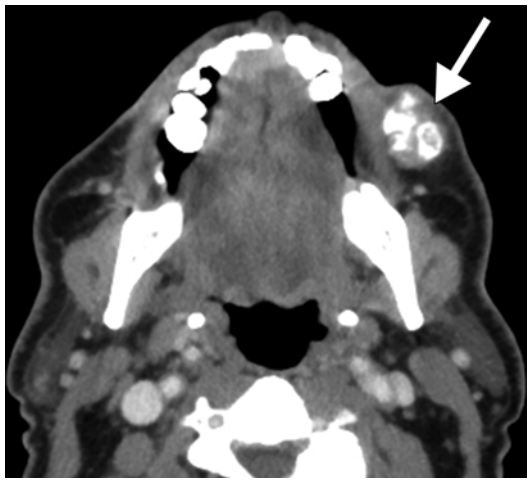

Fig. 45.9 Pilomatrixoma. Axial CT image shows a nodular lesion in the left cheek subcutaneous tissues with multiple coarse calcifications (*arrow*)

Fig. 45.10 Hematoma. The patient incurred trauma to the face. Axial CT image shows stranding and swelling of the right cheek subcutaneous tissues (*arrow*)

Suggested Reading

Bentkover SH. The biology of facial fillers. Facial Plast Surg. 2009;25(2):73–85.

De Beuckeleer LH, De Schepper AM, Neetens I. Magnetic resonance imaging of pilomatricoma. Eur Radiol. 1996;6(1):72–5.

Feeney JN, Fox JJ, Akhurst T. Radiological impact of the use of calcium hydroxylapatite dermal fillers. Clin Radiol. 2009;64(9):897–902.

Fordham LA, Chung CJ, Donnelly LF. Imaging of congenital vascular and lymphatic anomalies of the head and neck. Neuroimaging Clin N Am. 2000;10(1):117–36, viii.

Ginat DT, Schatz CJ. Imaging features of midface injectable fillers and associated complications. AJNR Am J Neuroradiol. 2013;34(8):1488–95.

Hönig J. Cheek augmentation with Bio-Alcamid in facial lipoatrophy in HIV seropositive patients. J Craniofac Surg. 2008;19(4):1085–8.

Kontis TC. Contemporary review of injectable facial fillers. JAMA Facial Plast Surg. 2013;15(1):58–64.

Redbord KP, Busso M, Hanke CW. Soft-tissue augmentation with hyaluronic acid and calcium hydroxyl apatite fillers. Dermatol Ther. 2011;24(1):71–81.

Tansavatdi K, Mangat DS. Calcium hydroxyapatite fillers. Facial Plast Surg. 2011;27(6):510–6.

Synthetic Corticosteroids

46

Jason M. Johnson, Yi Li, and Daniel Thomas Ginat

46.1 Uses

Synthetic corticosteroids are exogenous analogues of naturally occurring glucocorticoids and mineral corticoids produced by the adrenal glands. In particular, synthetic glucocorticoids serve an important role in anti-inflammatory and immunosuppressive therapies. Indeed, they are widely used to treat inflammatory conditions such as rheumatoid arthritis, lupus, inflammatory bowel disease, multiple sclerosis, psoriasis, asthma, and eczema. Glucocorticoids are also used in neuro-oncology in the treatment of CNS lymphoma and leukemia, as well as treatment of tumor and radiation-associated edema. In addition, they are included as part of immunosuppressive regimes following organ transplant. Furthermore, oral and topical corticosteroids are used in the treatment of allergic rhinitis and nasal polyposis.

J.M. Johnson, MD
Department of Diagnostic Radiology, MD Anderson Cancer Center, Houston, TX, USA

Y. Li, MD
Department of Radiology, University of California, San Francisco, CA, USA

D.T. Ginat, MD, MS (✉)
Department of Radiology, University of Chicago, Pritzker Medical School, Chicago, IL, USA
e-mail: ginatd01@gmail.com

46.2 Mechanism

The anti-inflammatory effects of synthetic glucocorticoids are mediated by activation of several genes. These include the NF-kB inhibitor IkB and dual-specificity phosphatase 1 (mitogen-activated protein kinase (MAPK) phosphatase 1), a crucial anti-inflammatory gene, as well as interleukin (IL)-10, a potent immunomodulatory and anti-inflammatory cytokine; GC-induced leucine zipper, a protein for which the mechanism of action is unclear but which interacts with, and inhibits the function of, NF-kB and AP-1; and annexin A1, a calcium-dependent phospholipid-binding protein. In particular, glucocorticoids interfere with the ability of NF-κB and AP-1 to induce transcription by increasing the compaction of unwound chromosomal DNA in a process that involves deacetylation of histone proteins. Glucocorticoids also inhibit the vasodilation and increased vascular permeability that occurs following inflammatory insult and decrease leukocyte emigration into inflamed sites, which are processes that require protein synthesis. Corticosteroids produce their anti-edema effects by reducing the permeability of tumor capillaries through upregulation of the tight junction component occluding endothelial cells. Furthermore, corticosteroid-induced repression of NF-κB causes reduction of edema via inhibition of cytokine-induced barrier breakdown and expression of cell adhesion molecules, which mediate leukocyte recruitment across the blood-

D.T. Ginat et al. (eds.), *Neuroimaging Pharmacopoeia*,
DOI 10.1007/978-3-319-12715-6_46, © Springer International Publishing Switzerland 2015

brain barrier. Similarly, glucocorticosteroids reduce nasal mucosa inflammation by inhibition of antigen presentation associated with decreased Langerhans cell and eosinophil infiltration and suppression the expression of interleukins.

46.3 Discussion

Treatment of Tumor-Related Edema. Glucocorticoids have been used for decades in the treatment of tumor-associated edema and minimizing the risk of encephalopathy in patients undergoing radiation therapy. In particular, glucocorticoid therapy (prednisone, prednisolone, dexamethasone, and methylprednisolone) is one of the main first-line treatments for primary CNS lymphoma. Activation of cytoplasmic steroid receptors in proliferative lymphoid cells triggers apoptosis. Thus, glucocorticoids provide rapid reduction of cerebral masses related to lymphoma, as depicted by the marked decline in edema and enhancement of these masses on imaging (Fig. 46.1). Consequently, when primary CNS lymphoma is suspected based on imaging, steroids should not be administered prior to biopsy, as steroids may obscure histologic diagnosis. However, long-term glucocorticoids use may lead to inevitable relapse and side effects. Thus, follow-up imaging is important for detecting recurrence.

Epidural Lipomatosis. Epidural lipomatosis is characterized by pathologic overgrowth of normal fat in the epidural space and is problematic when it causes spinal stenosis and/or cord compression. Glucocorticoids increase hydrolysis of circulating triglycerides, thereby increasing the amount of fatty acids in circulation and available for ectopic fat distribution. Glucocorticoids also increase *de novo* lipid production in the liver and in adipocytes and promote adipocyte maturation. No minimum glucocorticoid dose or minimum period of usage has been determined for disease onset, and time to symptom onset ranges from several months to many years after initiation of steroid therapy. Patients typically present with gradually worsening low back pain, radiculopathy, and even cauda equina symptoms. Epidural lipomatosis displays fat signal characteristics on all MRI sequences and can be confirmed by fat suppression techniques (Fig. 46.2).

Dorsocervical Fat. Dorsocervical fat (buffalo hump) is a lipodystrophy that represents a manifestation of the cushingoid features associated with chronic glucocorticoid use. The fat has a propensity to accumulate in the posterior lower neck and upper back and is continuous with the adjacent subcutaneous fat. On CT, this process is readily recognized by fat attenuation and on MRI by the fat signal characteristics on all sequences (Fig. 46.3). The appearance of iatrogenic dorsocervical fat is identical to a buffalo hump that results from endogenous Cushing's syndrome.

Osteoporosis and Insufficiency Fractures. Glucocorticoids directly inhibit bone formation and promote bone resorption. Glucocorticoids also decrease calcium absorption from the intestine and increase renal excretion. Osteoporosis occurs in at least 50 % of persons who require long-term glucocorticoid therapy. Glucocorticoids inhibit osteoblast function, preventing the formation of new bone in normal bone turnover. Osteoporosis can be diagnosed by DEXA scan or by relative subjective visual assessment of radiographs or CT. Insufficiency fracture should be suspected in an osteoporotic individual who presents with severe focal pain. MRI provides more sensitive and early diagnosis, in which the edema associated with acute fractures appears as hyperintensity on T2 and STIR sequences (Fig. 46.4).

Steroid-Associated Infections. Patients receiving chronic steroids have an increased susceptibility to many different types of infections. The risk of infection is related to the dose of steroid and the duration of therapy. Although pyogenic bacteria are the most common pathogens, chronic steroid use increases the risk of infection with intracellular pathogens such as Listeria, various fungi, herpes viruses, and certain parasites. On MRI, CNS pyogenic abscesses typically appear as ring enhancing lesions with restricted diffusion centrally. On the other hand, atypical infections can form abscesses without associated central diffusion restriction (Fig. 46.5).

Corticosteroid-Associated Apparent Cerebral Atrophy. The mechanism by which corticosteroids affect brain volume is not well-elucidated.

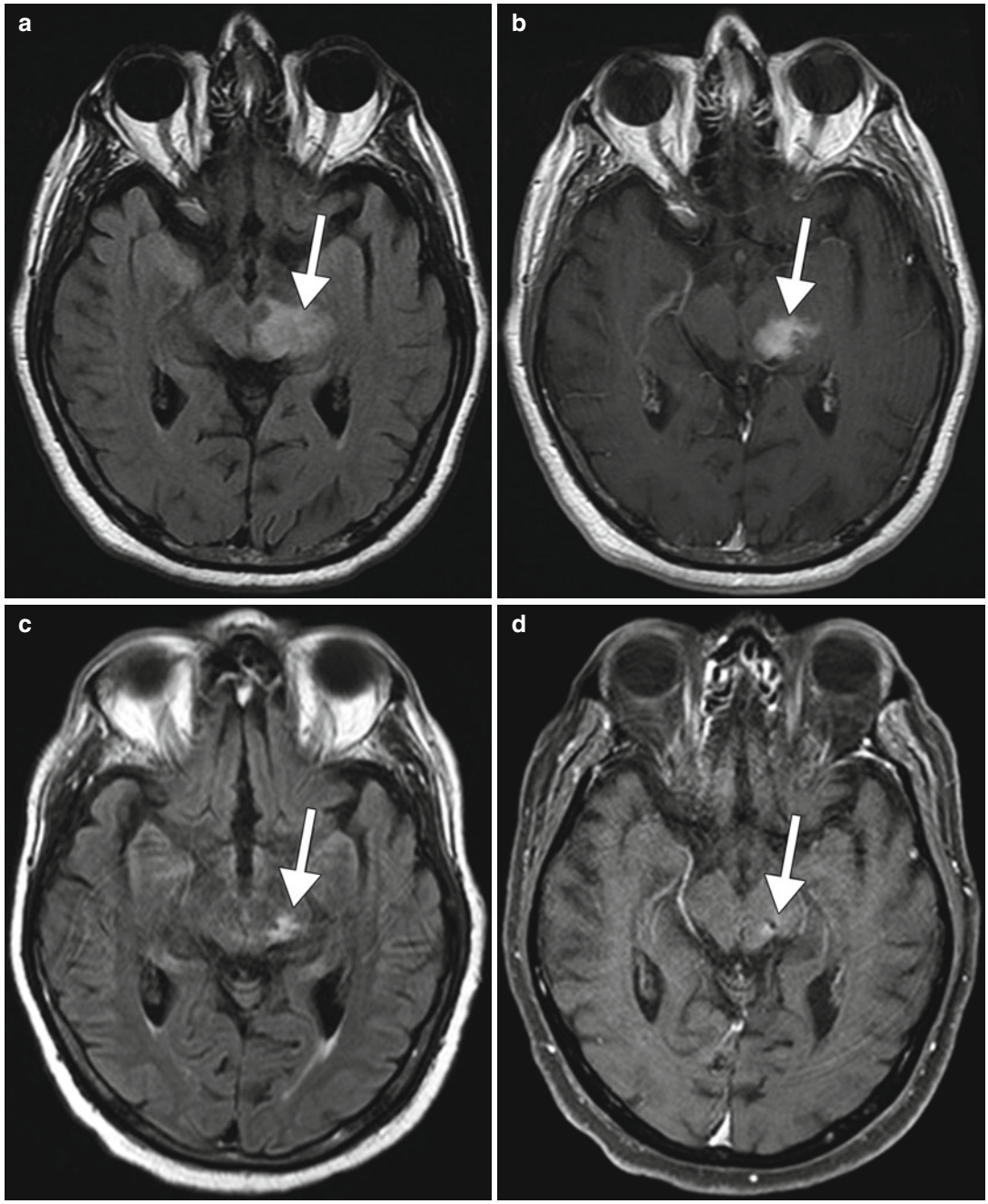

Fig. 46.1 Corticosteroid therapy for lymphoma. Initial FLAIR (**a**) and post-contrast T1-weighted (**b**) MR images show patchy edema and enhancement within the left midbrain (*arrows*). Follow-up FLAIR (**c**) and post-contrast T1-weighted (**d**) MR images obtained after corticosteroid administration show considerable interval decrease in the edema and abnormal enhancement (*arrows*)

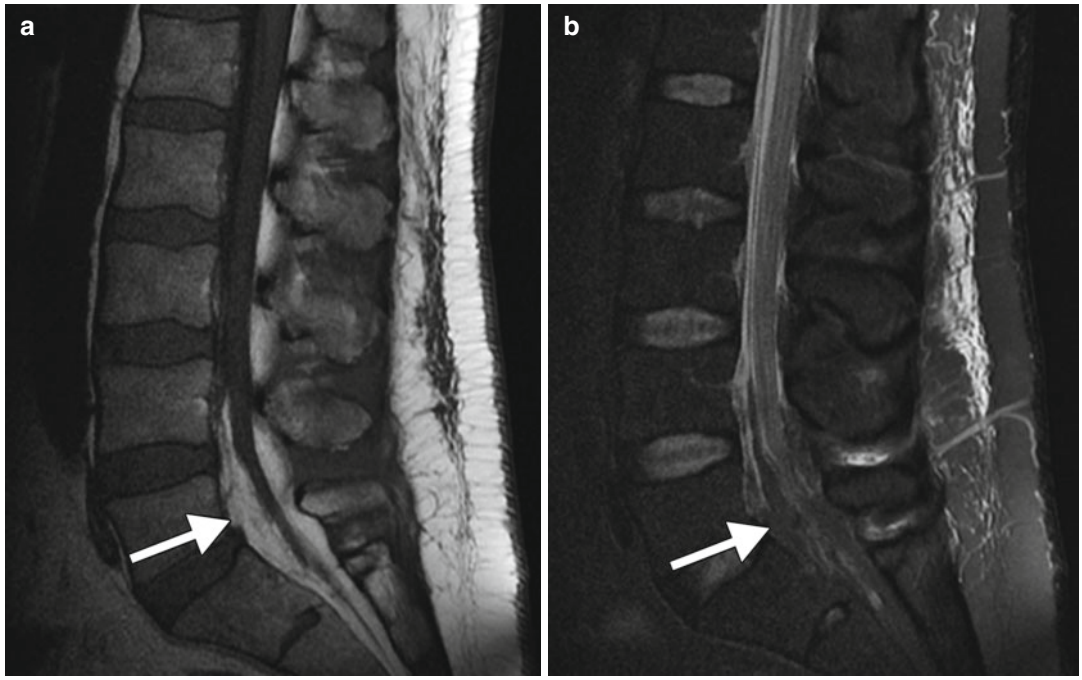

Fig. 46.2 Steroid-induced epidural lipomatosis. Sagittal T1 MRI (**a**) shows prominent T1 hyperintensity in the lumbosacral epidural space (*arrow*). The corresponding sagittal STIR MRI (**b**) shows suppression of signal in the epidural space, consistent with fat (*arrow*)

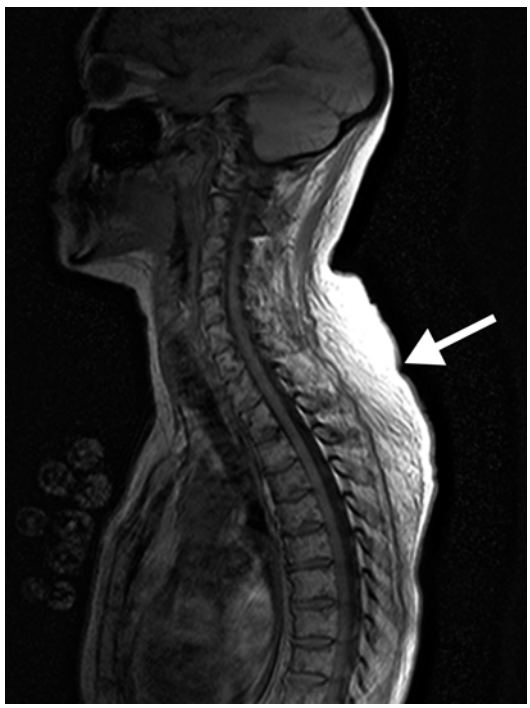

Fig. 46.3 Dorsocervical fat. Sagittal T1 MRI shows disproportionate increased thickness of subcutaneous fat in the posterior lower neck and upper back (*arrow*)

Several possibilities include reduction of vasogenic edema due to decreased vascular permeability, steroid-induced protein catabolism, increased neuronal apoptosis by inhibition of the calcium-dependent mitogen-activated protein kinase mechanism, and inhibition of adult neurogenesis. On cross-sectional imaging, the apparent volume loss can be shown to affect the cerebral hemispheres diffusely (Fig. 46.6). These findings can be reversible and other factors may be contributory.

Sinonasal Mucosa Effects. The anti-inflammatory action of corticosteroids can produce a significant decrease in the thickness of the sinonasal mucosa and associated secretions, which can be detected on post-treatment CT (Fig. 46.7).

46.4 Differential Diagnosis

- *Epidural Lipomatosis:* Differential considerations for epidural lipomatosis include other epidural lesions, including subacute

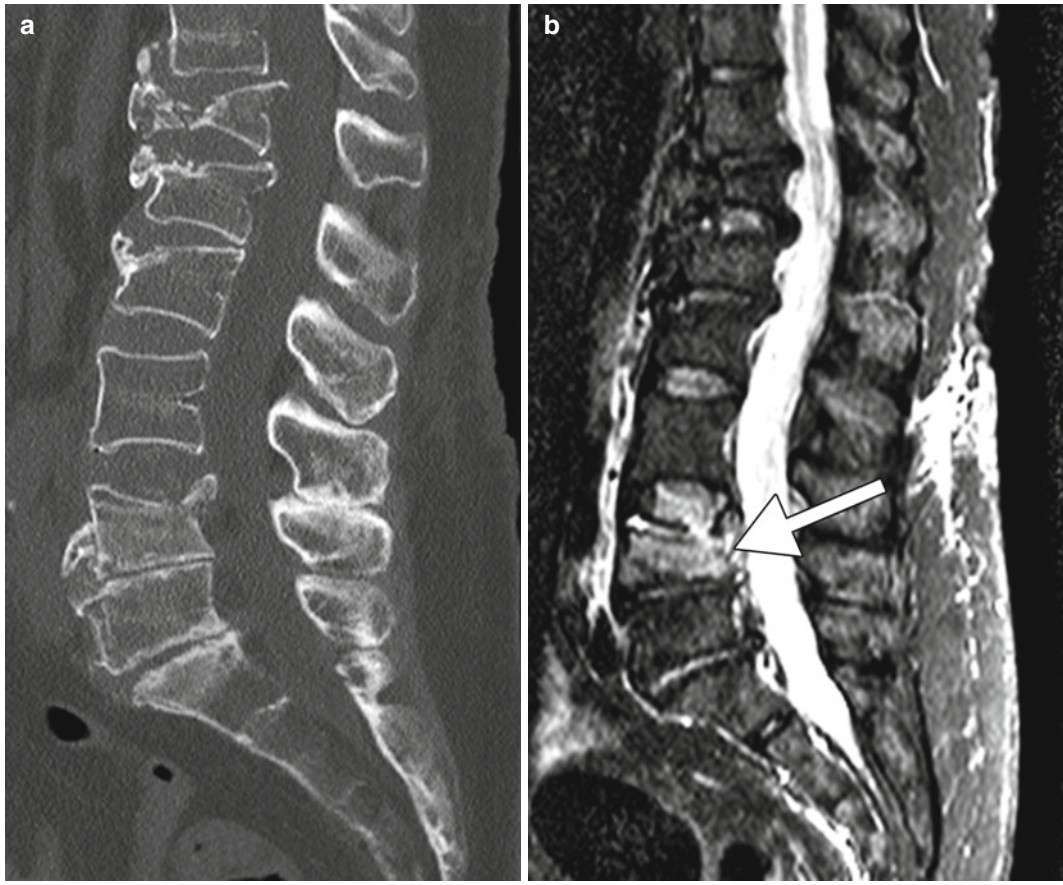

Fig. 46.4 Steroid-induced osteopenia and compression fractures. Sagittal CT (**a**) shows diffuse osteopenia and multiple compression fractures. The corresponding sagittal STIR MRI (**b**) shows edema in the L4 vertebral body (*arrow*), indicating an acute fracture, while the other compression fractures are chronic

epidural hematoma, spinal angiolipoma, epidural metastasis, and epidural abscess. While subacute hematomas are T1 hyperintense on MRI (Fig. 46.8), there will not be loss of signal with fat suppression. Unlike epidural lipomatosis, angiolipomas, metastases, and abscess are generally associated with some form of enhancement and tend to be more focal. Although most patients with epidural lipomatosis will have a history of glucocorticoid use, this condition can also be idiopathic or associated with excess endogenous corticosteroid production and obesity.

- *Dorsocervical Fat:* Although cosmetically problematic, dorsocervical fat is benign and should not be misinterpreted as neoplasms, such as lipoma or liposarcoma. Alternatively, the relatively focal distribution of the fat in the buffalo hump is distinguished from the more diffuse presence of fat related to obesity and Madelung disease (refer to Chap. 2).
- *Osteoporosis and Insufficiency Fractures*. An important differential consideration for insufficiency fracture is pathologic fracture due to neoplasm, for example. On MRI, the presence of diffuse or focal abnormal bone marrow with well-defined or ill-defined enhancement that does not follow fracture lines is suggestive of a pathologic fracture (Fig. 46.9).
- *Steroid-Associated Infections.* Several other immunosuppressive agents and the use of illicit drugs are associated with infections of the CNS. Otherwise, conditions that can

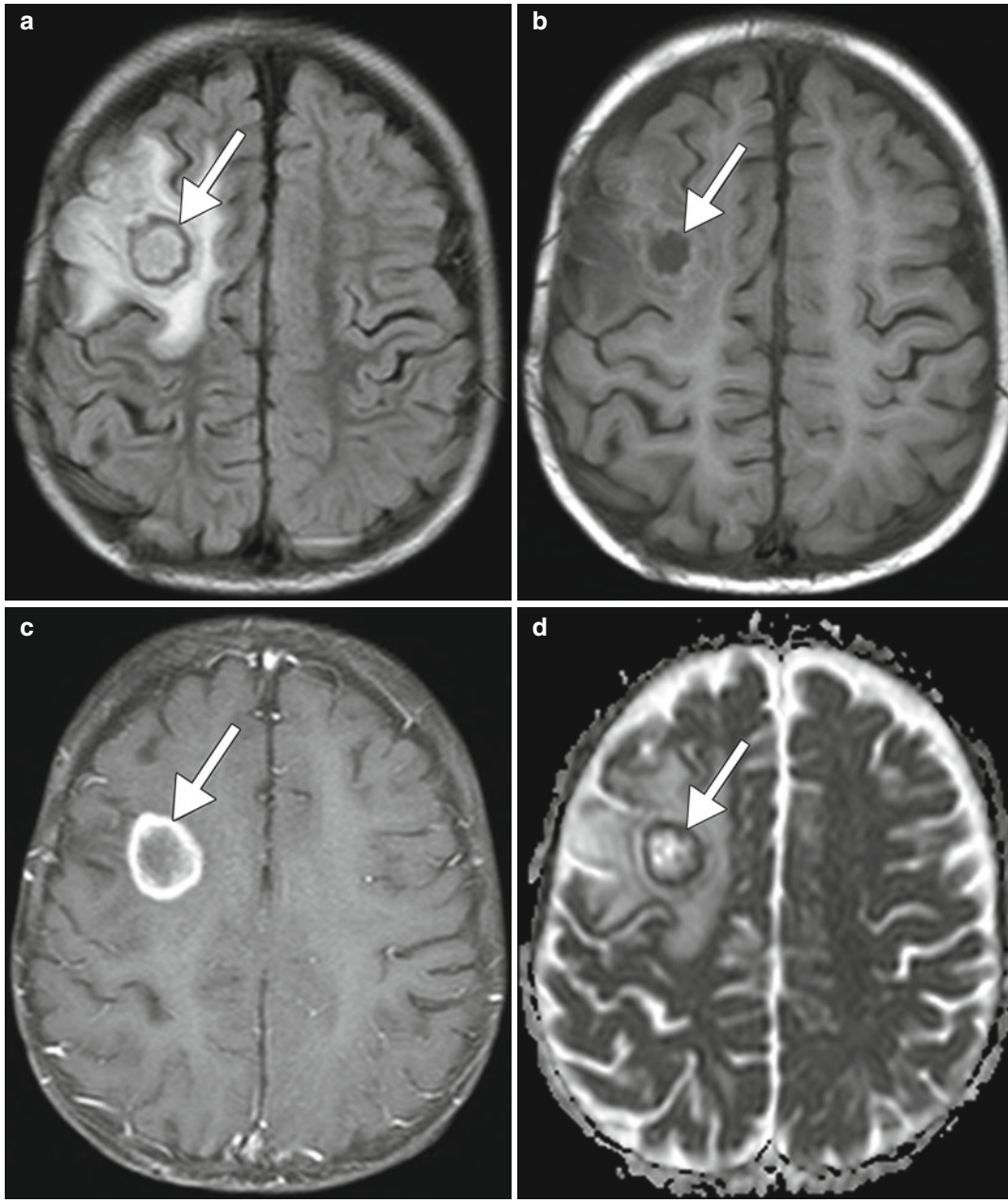

Fig. 46.5 Steroid-associated infection. This transplant recipient was on steroid therapy for immunosuppression and developed a Nocardia brain abscess. Axial FLAIR (**a**), T1-weighted (**b**), post-contrast T1-weighted (**c**), and ADC map (**d**) show a ring enhancing lesion with surrounding edema, but no restricted diffusion of the contents, in the right frontal lobe (*arrows*)

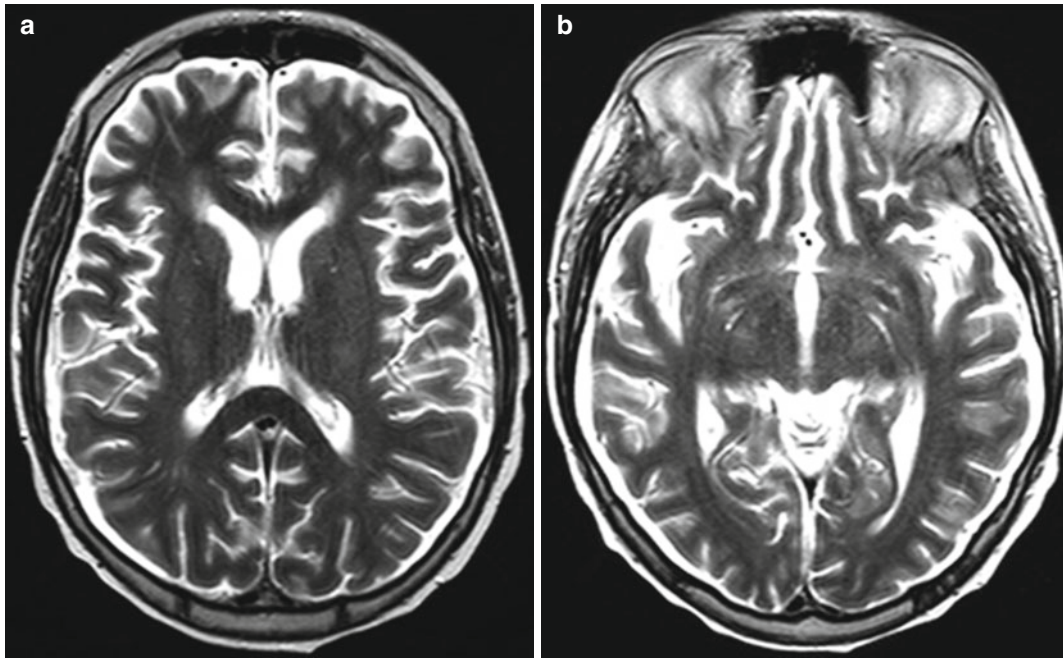

Fig. 46.6 Corticosteroid-associated cerebral atrophy. The patient is a 17-year-old male who underwent transplantation and received immunosuppressive therapy, including steroids. Axial T2 MR images (**a**, **b**) show diffuse prominence of the ventricles and sulci consistent with generalized volume loss

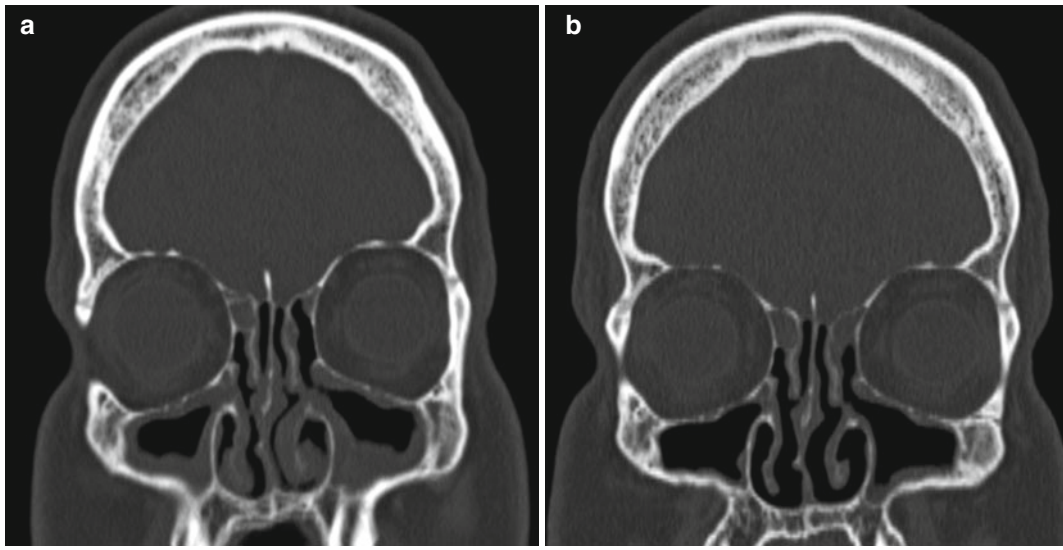

Fig. 46.7 Sinonasal mucosa effects of corticosteroids. Initial coronal CT image (**a**) shows diffuse sinonasal mucosal thickening related to allergic rhinitis. There are also findings related to prior endoscopic sinus surgery. Follow up coronal CT image (**b**) obtained after corticosteroid therapy shows interval marked decrease in the degree of mucosal thickening

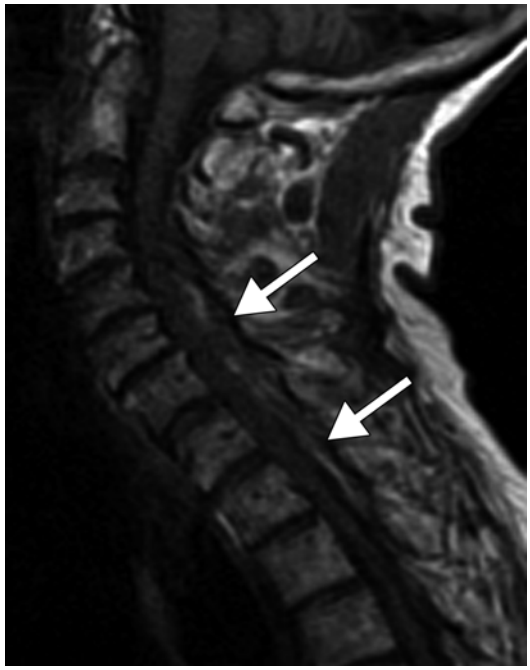

Fig. 46.8 Epidural hematoma. Sagittal T1-weighted MRI of the cervical spine shows a partially T1 hyperintense posterior epidural collection (*arrows*)

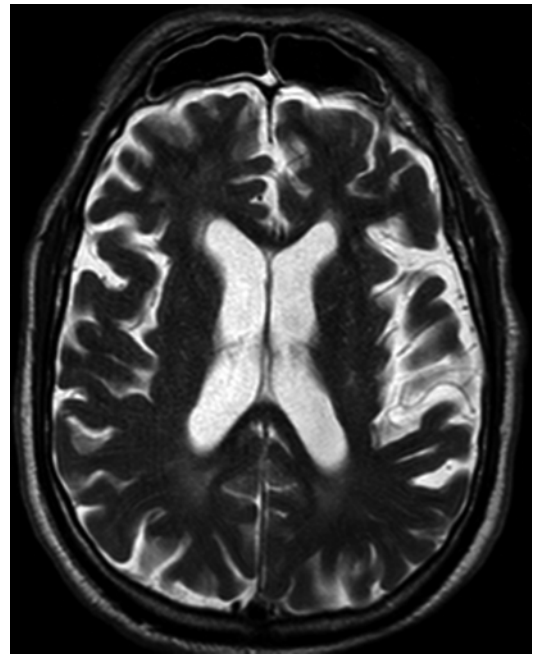

Fig. 46.10 Age-related cerebral volume loss in an elderly patient. Axial T2-weighted MRI shows diffuse prominence of the sulci and ventricles

Fig. 46.9 The patient has a history of metastatic bladder cancer. Sagittal fat-suppressed post-contrast T1-weighted MRI shows a compression fracture and diffuse enhancement of L4 vertebral body (*arrow*)

resemble brain abscesses include other ring-enhancing lesions, such as neoplasms, demyelinating diseases, and subacute infarcts. In addition, conditions that can mimic subdural, epidural, and scalp or paraspinal abscesses mainly include tumors and hematomas.

- *Corticosteroid-Associated Apparent Cerebral Atrophy.* Chemotherapy agents used in conjunction with steroid therapy for certain neoplasms may also result in reduced brain volume. In addition, certain disease processes that are treated with steroids, such as lupus and multiple sclerosis, may contribute to cerebral volume loss. Otherwise, apparent cerebral atrophy caused by steroids can resemble age-related cerebral volume loss (Fig. 46.10).
- *Sinonasal Mucosa Effects.* Other nasal decongestants can lead to decreased mucosal thickness, overuse of these medications can lead to rebound inflammation, known as rhinitis medicamentosa (refer to Chap. 55). Otherwise, the

effects of corticosteroids should not be confused with alterations resulting from endoscopic sinus surgery, which entails the removal of obstructive sinonasal osseous structures.

Suggested Reading

Coutinho AE, Chapman KE. The anti-inflammatory and immunosuppressive effects of glucocorticoids, recent developments and mechanistic insights. Mol Cell Endocrinol. 2011;335(1):2–13.

Fassett DR, Schmidt MH. Spinal epidural lipomatosis: a review of its causes and recommendations for treatment. Neurosurg Focus. 2004;16(4):E11.

Klein NC, Go CH, Cunha BA. Infections associated with steroid use. Infect Dis Clin North Am. 2001;15(2):423–32, viii.

Lukert BP, Raisz LG. Glucocorticoid-induced osteoporosis: pathogenesis and management. Ann Intern Med. 1990;112(5):352–64.

Nishimura J, Ikuyama S. Glucocorticoid-induced osteoporosis: pathogenesis and management. J Bone Miner Metab. 2000;18(6):350–2.

Pujols L, Alobid I, Benítez P, Martínez-Antón A, Roca-Ferrer J, Fokkens WJ, Mullol J, Picado C. Regulation of glucocorticoid receptor in nasal polyps by systemic and intranasal glucocorticoids. Allergy. 2008;63(10):1377–86.

Rhen T, Cidlowski JA. Antiinflammatory action of glucocorticoids–new mechanisms for old drugs. N Engl J Med. 2005;353(16):1711–23.

Spies CM, Strehl C, van der Goes MC, Bijlsma JW, Buttgereit F. Glucocorticoids. Best Pract Res Clin Rheumatol. 2011;25(6):891–900.

Venekamp RP, Thompson MJ, Hayward G, Heneghan CJ, Del Mar CB, Perera R, Glasziou PP, Rovers MM. Systemic corticosteroids for acute sinusitis. Cochrane Database Syst Rev. 2011;7(12):CD008115.

Zanardi VA, Magna LA, Costallat LT. Cerebral atrophy related to corticotherapy in systemic lupus erythematosus (SLE). Clin Rheumatol. 2001;20(4):245–50.

Oral Contraceptives (Estrogen and Progestin)

47

Kimberly Kallianos, Daniel Thomas Ginat, and Jason M. Johnson

47.1 Uses

Oral contraceptive agents are used for the prevention of pregnancy in addition to non-contraceptive indications, such as for the treatment of menorrhagia or hyperandrogenism.

47.2 Mechanism

Oral contraceptives act primarily via the inhibition of ovulation through suppression of the cyclic release of luteinizing hormone. Other mechanisms of action include direct effects on follicular maturation, endometrium, cervical mucus, and tubal transport. Venous thromboembolic disease (VTE) is a major side effect associated with the administration of estrogen- and progestin-containing contraceptives, contributed to by the thrombotic effects of estrogen. Lower estrogen dose has been shown to decrease the risk of thromboembolism; however, there is increased risk of VTE in patients receiving both high- and low-dose oral contraceptives. In addition, an association has been shown between the class of progestin and risk of VTE.

K. Kallianos, MD
Department of Radiology, University of California, San Francisco, California, USA

J.M. Johnson, MD
Department of Diagnostic Radiology, MD Anderson Cancer Center, Houston, TX, USA

D.T. Ginat, MD, MS (✉)
Department of Radiology, University of Chicago, Pritzker Medical School, Chicago, IL, USA
e-mail: ginatd01@gmail.com

47.3 Discussion

Venous thromboembolic disease in patients treated with oral contraceptives may manifest as thrombosis of the dural venous sinuses. Thrombus formation within the cerebral veins and dural sinuses leads to obstruction of venous drainage and can result in cerebral edema, hemorrhage, or venous infarction. Patients with dural sinus thrombosis present with a variety of nonspecific symptoms, including nausea, vomiting, headache, and focal neurological deficits. Anticoagulation is a major component of the treatment for dural sinus thrombosis.

The CT findings of dural sinus thrombosis may be subtle. The hyperattenuating appearance of a venous sinus or cerebral vein on noncontrast CT (Fig. 47.1), known as the "cord sign," is relatively insensitive. On contrast-enhanced CT, enhancing dura surrounding a non-enhancing thrombus, known as the "empty delta sign," has been shown to be more sensitive and can be seen in 30–70 % of cases. CT venography can directly demonstrate a filling defect in the vessel lumen; however, noncontrast images are useful for comparison to avoid misinterpretation of hyperattenuating clot. Secondary findings that are demonstrated on noncontrast CT include signs of

D.T. Ginat et al. (eds.), *Neuroimaging Pharmacopoeia*,
DOI 10.1007/978-3-319-12715-6_47, © Springer International Publishing Switzerland 2015

venous infarction including parenchymal hypoattenuation with or without hemorrhage.

On MRI, acute thrombus appears as isointense to the brain parenchyma on T1-weighted sequences, while subacute thrombus will appear hyperintense. On T2-weighted sequences, acute thrombus appears as hypointense, while subacute to chronic thrombus appears as hyperintense. T2* or gradient echo (GRE) sequences demonstrate blooming and can increase the conspicuity of thrombus; however, susceptibility weighting (SWI) is not useful for the evaluation of sinus thrombosis (Fig. 47.1). FLAIR and diffusion-weighted (DWI) sequences are useful for the evaluation of associated brain parenchymal abnormalities, such as venous infarction or edema (Fig. 47.1).

Absence of flow-related signal on a time-of-flight MR venogram (MRV) is suggestive of thrombosis. Gadolinium-enhanced MRV can be performed for confirmation, demonstrating the "empty delta sign" with dural enhancement surrounding a non-enhancing thrombus. One must be cautious not to misinterpret subacute hyperintense thrombus on T1-weighted contrast-enhanced MRV. Other potential pitfalls on gadolinium-enhanced MRV include the enhancement or recanalization of chronic thrombus. Cerebral angiography can be performed for confirmation in equivocal cases.

47.4 Differential Diagnosis

There are numerous other causes of venous sinus thrombosis, including other pharmaceuticals, such as L-asparaginase (refer to Chap. 20); malignancy; pregnancy; infections; disorders of coagulation, such as factor V deficiency; granulomatous diseases; connective tissue disorders; dehydration; trauma; and surgery. In addition, several conditions can also mimic the appearance of venous sinus thrombosis on imaging.

- *Dehydration and polycythemia*: In addition to predisposing to venous sinus thrombosis, these conditions can also mimic the appearance of thrombosis on imaging. For example, there is hyperattenuation of the venous sinuses on CT in a patient with elevated hematocrit (Fig. 47.2). This effect is particularly pronounced in pediatric patients, who have a high relative attenuation of the dural sinuses compared to the brain parenchyma secondary to stage of myelination. Certainly, infants are not expected to be on oral contraceptives!
- *Dural sinus hypoplasia/aplasia*: Congenitally absent or hypoplastic dural venous sinuses can occur, with hypoplasia/aplasia of the transverse sinuses seen in up to 20 % of patients on time-of-flight venography (Fig. 47.3). In addition, the combined effect of slow flow within a diminutive venous sinus may be mistaken for acute thrombosis. Evaluation of collateral venous pathways or the size of the ipsilateral jugular foramen may be useful when considering a case with hypoplastic or aplastic dural sinuses. Apparent discontinuity of flow on maximum intensity projection (MIP) images should be evaluated on the source images in order to exclude the presence of hypoplastic or aplastic sinus anatomic variants.
- *Arachnoid granulations*: Arachnoid granulations appear as rounded filling defects within the venous sinuses, which when elongated may be mistaken for sinus thrombosis. These are typically rounded or lobulated foci that display low T1 and high T2 signal (Fig. 47.4)
- *Idiopathic intracranial hypertension*: Constrictions of the lateral portions of the transverse sinuses are often present, along with flattening or even bulging of the optic nerve discs and a partially empty sella, particularly in obese individuals (Fig. 47.5).
- *Hemorrhage*: Acute subdual hematomas layering along the cerebellar tentorium may mimic thrombosis of the transverse sinus, but the hemorrhage can be distinguished from the venous sinuses and often extend well beyond the region o the venous sinuses. Venous epidural hematomas can compress the venous sinuses, mimicking thrombus, but have a convex margin and are typically associated with calvarial fractures (Fig. 47.6).
- *MRI artifact*: Flow-related artifacts can mimic thrombosis of the dural sinuses. Specifically in

time-of-flight venography, flow parallel to the plane of image acquisition may experience signal loss leading to the appearance of thrombus. Other MRI artifacts that can mimic thrombus include slow flow on flow-sensitive sequences or the normal flow void on contrast-enhanced MRV. The lack of restricted diffusion within the venous sinus favors flow artifact over thrombus.

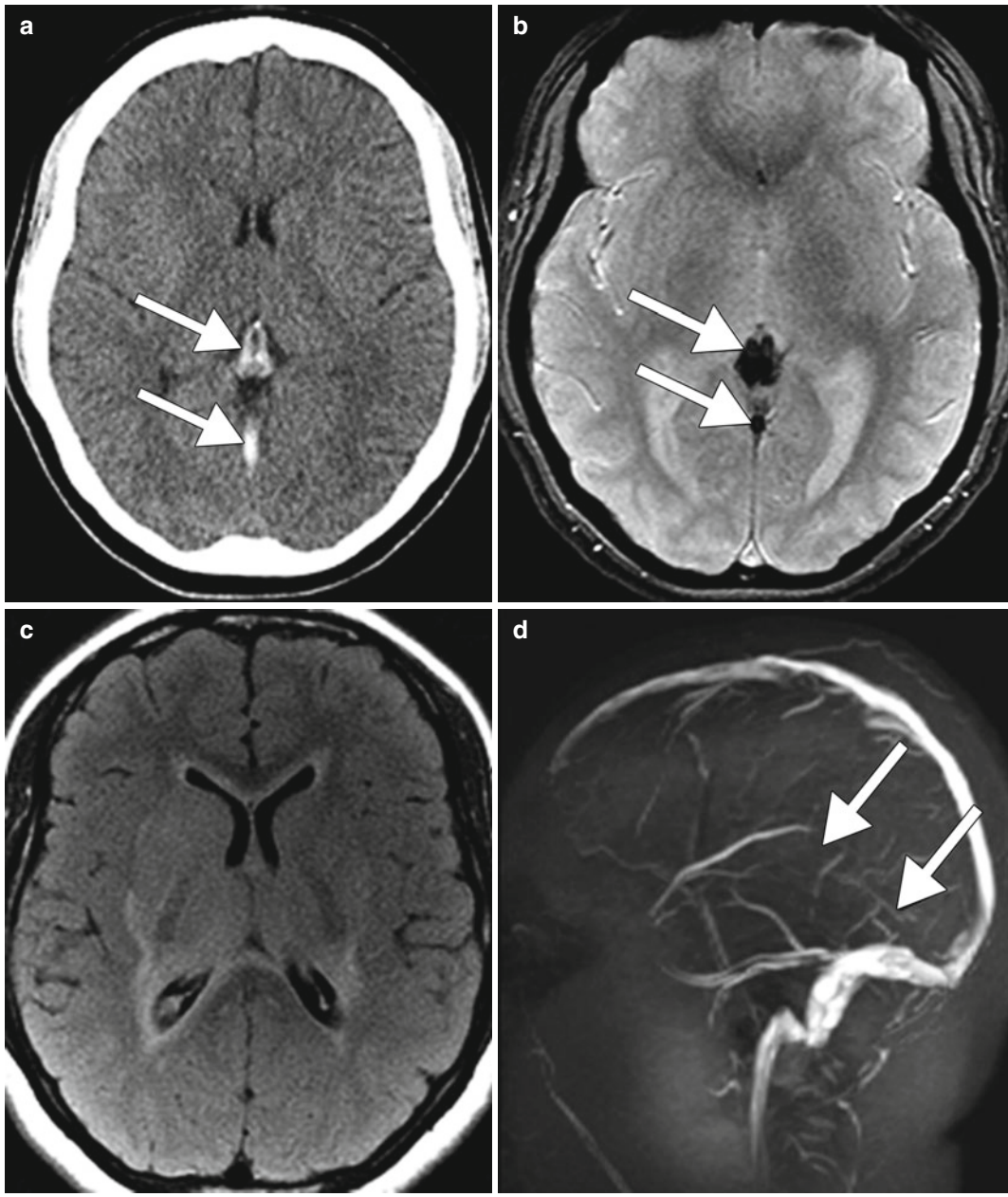

Fig. 47.1 Venous sinus thrombosis associated with oral contraceptive use. Axial noncontrast CT image (**a**) shows hyperattenuation of the internal cerebral veins and straight sinus (*arrows*). The corresponding T2*GRE MRI (**b**) shows susceptibility effect within these venous structures (*arrows*). The FLAIR image (**c**) shows edema in the bilateral deep gray matter and periventricular white matter. Time-of-flight MRA (**d**) shows absent flow-related enhancement of the internal cerebral veins and straight sinus (*arrows*)

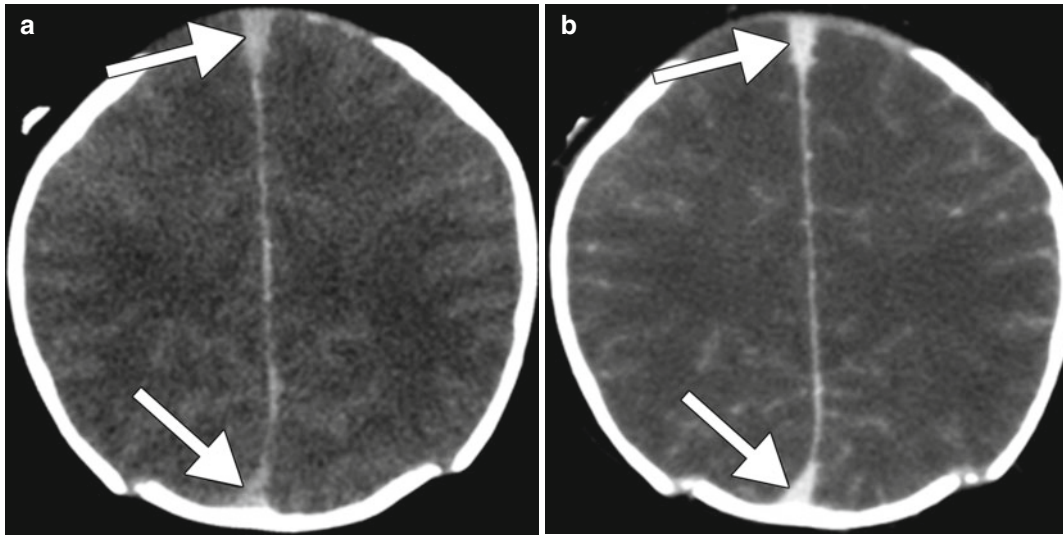

Fig. 47.2 Polycythemia. Axial noncontrast CT (**a**) shows markedly hyperattenuating superior sagittal sinus contents (*arrows*). The corresponding CTV (**b**) shows normal opacification of the venous sinuses (*arrows*)

Fig. 47.3 Hypoplastic venous sinus. Top view MIP MRA shows diffusely narrow right transverse sinus (*arrow*) and prominent left transverse and sigmoid sinuses

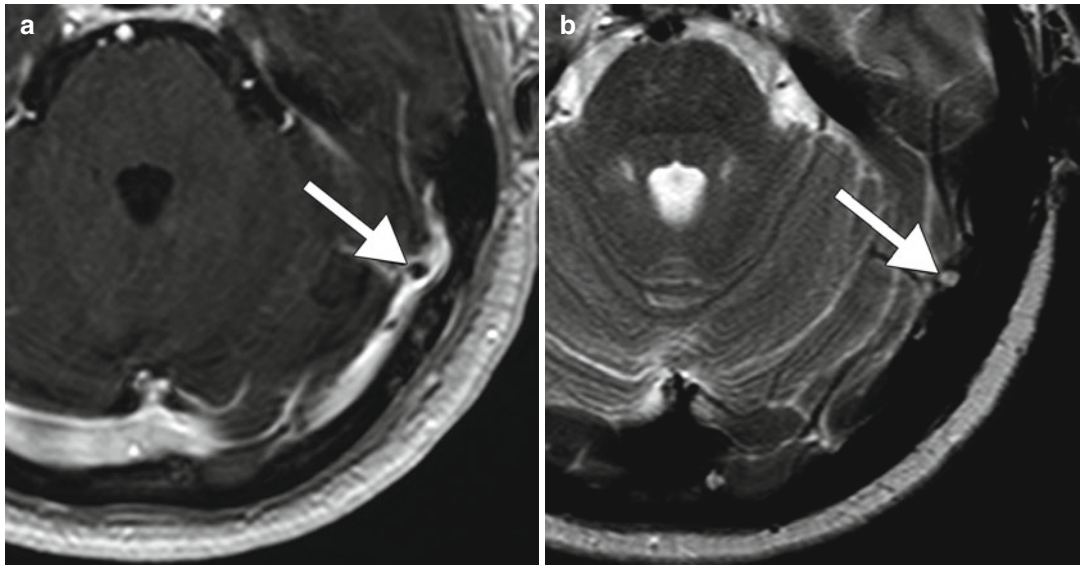

Fig. 47.4 Arachnoid granulation. Axial post-contrast T1-weighted (**a**) and T2-weighted (**b**) MR images show a rounded filling defect within the left transverse sinus with CSF signal characteristics (*arrows*)

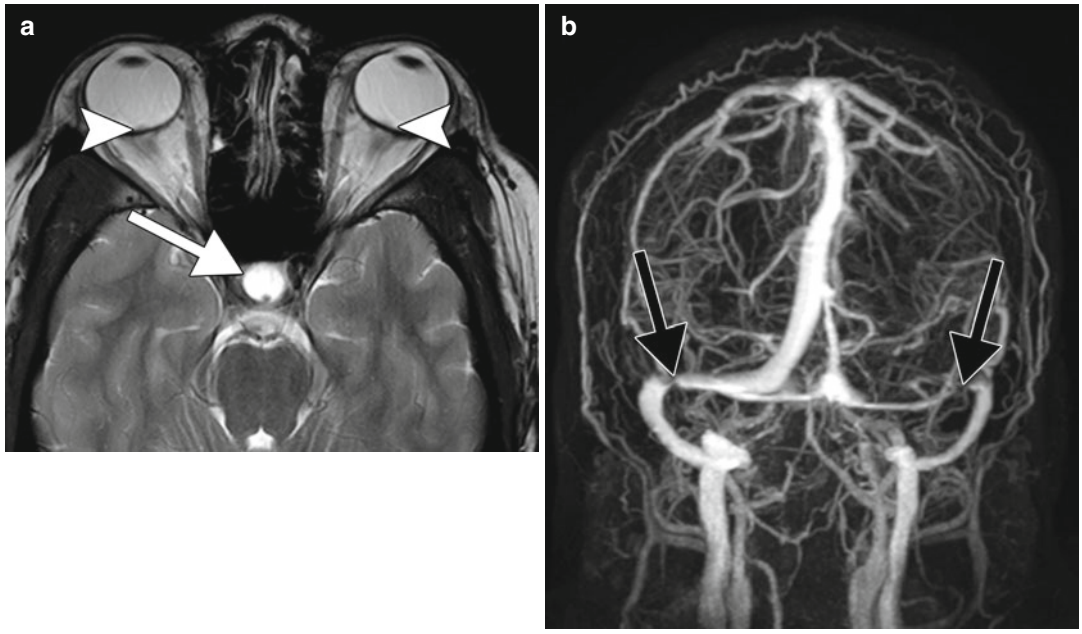

Fig. 47.5 Idiopathic intracranial hypertension. Axial T2-weighted MRI (**a**) shows a partially empty sella (*arrow*) and bulging of the bilateral optic nerves (*arrowheads*). MIP MRA image (**b**) shows constriction of the bilateral transverse sinuses (*black arrows*)

Fig. 47.6 Venous epidural hematoma. Sagittal noncontrast CT image shows a small convex hematoma (*arrow*) adjacent to the transverse sinus (*arrowhead*) and a depressed calvarial fracture

Suggested Reading

Alper F, Kantarci M, Dane S, Gumustekin K, Onbas O, Durur I. Importance of anatomical asymmetries of transverse sinuses: an MR venographic study. Cerebrovasc Dis. 2004;18:236–9.

Ayanzen RH, Bird CR, Keller PJ, McCully FJ, Theobald MR, Heiserman JE. Cerebral MR venography: normal anatomy and potential diagnostic pitfalls. AJNR Am J Neuroradiol. 2000;21:74–8.

Carr BR, Ory H. Estrogen and progestin components of oral contraceptives: relationship to vascular disease. Contraception. 1997;55(5):267–72.

Healy JF, Nichols C. Polycythemia mimicking venous sinus thrombosis. AJNR Am J Neuroradiol. 2002;23:1402–3.

Kawaguchi T, et al. Classification of venous ischaemia with MRI. J Clin Neurosci. 2001;8 Suppl 1:82–8.

Leach JL, et al. Normal appearance of arachnoid granulations on contrast-enhanced CT and MR of the brain: differentiation from dural sinus disease. AJNR Am J Neuroradiol. 1996;17(8):1523–32.

Lewin JS, Masaryk TJ, Smith AS, Ruggieri PM, Ross JS. Time-of-flight intracranial MR venography: evaluation of the sequential oblique section technique. AJNR Am J Neuroradiol. 1994;15:1657–64.

Liang L, Korogi Y, Sugahara T, et al. Normal structures in the intracranial dural sinuses: delineation with 3D contrast-enhanced magnetization prepared rapid acquisition gradient-echo imaging sequence. AJNR Am J Neuroradiol. 2002;23:1739–46.

Provenzale JM, Kranz PG. Dural sinus thrombosis: sources of error in image interpretation. Am J Roentgenol. 2011;196(1):23–31.

Provenzale JM, Joseph GJ, Barboriak DP. Dural sinus thrombosis: findings on CT and MR imaging and diagnostic pitfalls. Am J Roentgenol. 1998;170(3):777–83.

Rollins N, Ison C, Booth T, Chia J. MR venography in the pediatric patient. AJNR Am J Neuroradiol. 2005;26:50–5.

Rosendaal FR, Van Hylckama Vlieg A, Tanis BC, Helmerhorst FM. Estrogens, progestogens and thrombosis. J Thromb Haemost. 2003;1(7):1371–80.

Tanis BC, Rosendaal FR. Venous and arterial thrombosis during oral contraceptive use: risks and risk factors. Semin Vasc Med. 2003;3(1):69–84. Review.

Vaccines

48

Daniel Thomas Ginat

48.1 Uses

Many types of vaccines are available and routinely used for the prevention of many microbial diseases. The development of immunization has been a major boon to public health.

48.2 Mechanism

The main types of vaccines include live attenuated vaccines (such as smallpox, yellow fever, measles, mumps, rubella, and chicken pox vaccines), subunit vaccines (such as the vaccine against recombinant hepatitis B), toxoid vaccines that consist of inactivated toxins (such as vaccines against diphtheria and tetanus), carbohydrate vaccines (such as vaccines against pneumococcus), and conjugate vaccines (such as vaccines against *Haemophilus influenzae* type B and meningococcus). Ultimately, most vaccines are believed to confer protection through neutralizing antibodies. On the other hand, while it was initially believed that postvaccination ADEM is caused by the viral component in vaccines, evidence suggests that the complications may be related to contamination with the central nervous system tissue in which the vaccine was propagated. Indeed, there is a lower incidence of ADEM with vaccines based on recombinant proteins than with *in vivo* infected tissue.

48.3 Discussion

Although generally safe and effective, vaccines can rarely lead to neurological complications, most notably acute disseminated encephalomyelitis (ADEM). ADEM is a monophasic inflammatory demyelinating condition that has been associated with several vaccines, including the rabies, diphtheria-tetanus-polio, smallpox, measles, mumps, rubella, Japanese B encephalitis, pertussis, influenza, hepatitis B, and the hog vaccine. Patients may present several weeks to months following exposure to the precipitant with decreased level of consciousness that varies from lethargy to coma, convulsions, and multifocal neurologic symptoms such as paralysis, and movement disorders. Pathologic findings of ADEM include inflammatory reactions around the vessels, edema, and perivenous demyelination. CT is rather insensitive to the white matter changes in ADEM, although corresponding hypoattenuation may be observed. On MRI, typical findings include bilateral asymmetric T2 hyperintense subcortical white matter lesions (Fig. 48.1) that may or may not exhibit enhancement and peripheral diffusion restriction. The cortex, thalami, and brainstem can be involved on occasion. Associated hemorrhage is rare and may

D.T. Ginat, MD, MS
Department of Radiology, University of Chicago, Pritzker Medical School, Chicago, IL, USA
e-mail: ginatd01@gmail.com

D.T. Ginat et al. (eds.), *Neuroimaging Pharmacopoeia*,
DOI 10.1007/978-3-319-12715-6_48, © Springer International Publishing Switzerland 2015

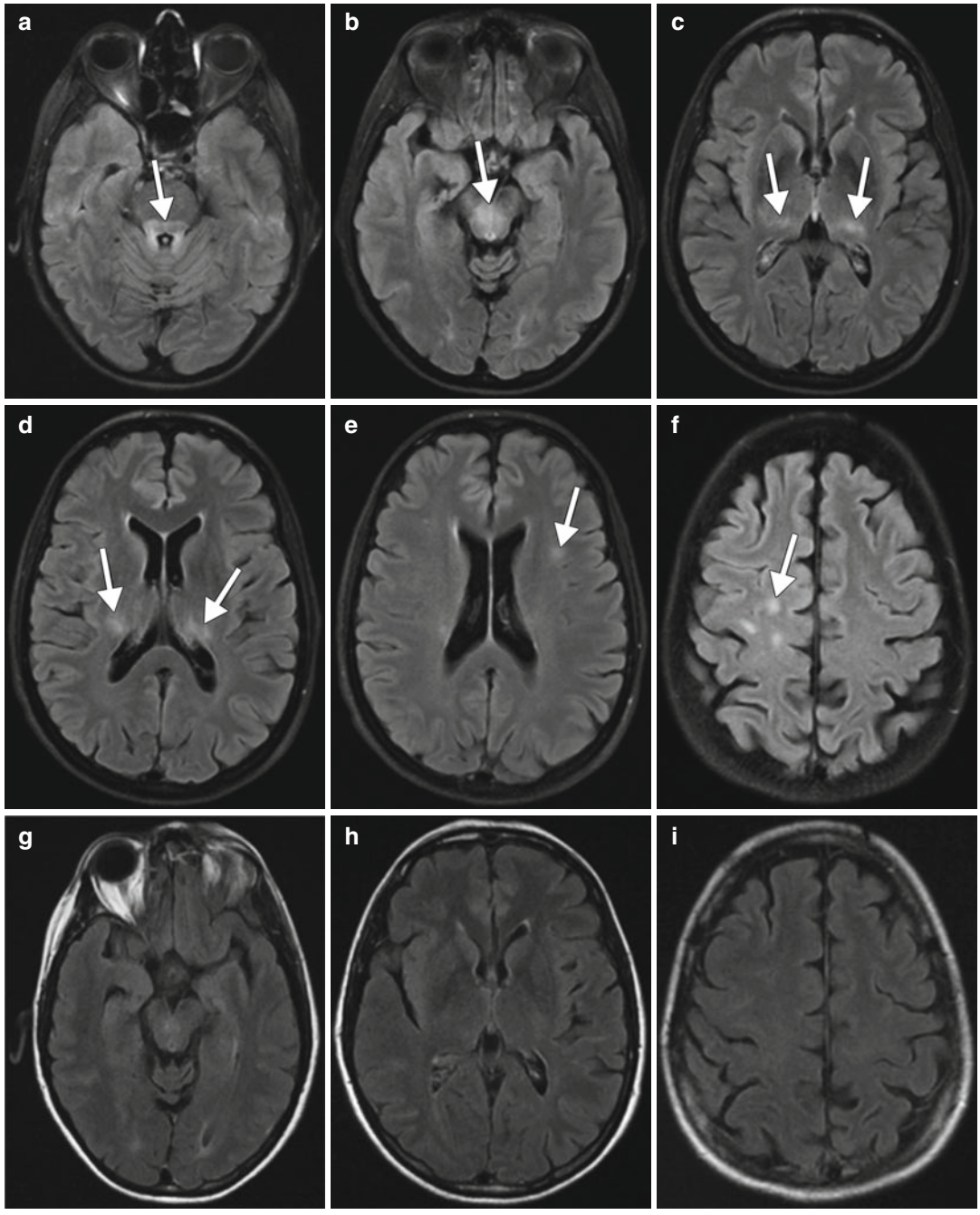

Fig. 48.1 ADEM related to vaccination. Axial FLAIR images (**a**–**f**) obtained approximately 2 weeks after the administration of the vaccine demonstrate numerous hyperintense foci (*arrows*) involving the infratentorial and supratentorial white matter and thalami. Selected FLAIR images (**g**–**i**) obtained approximately 1 month later show interval resolution of the lesions

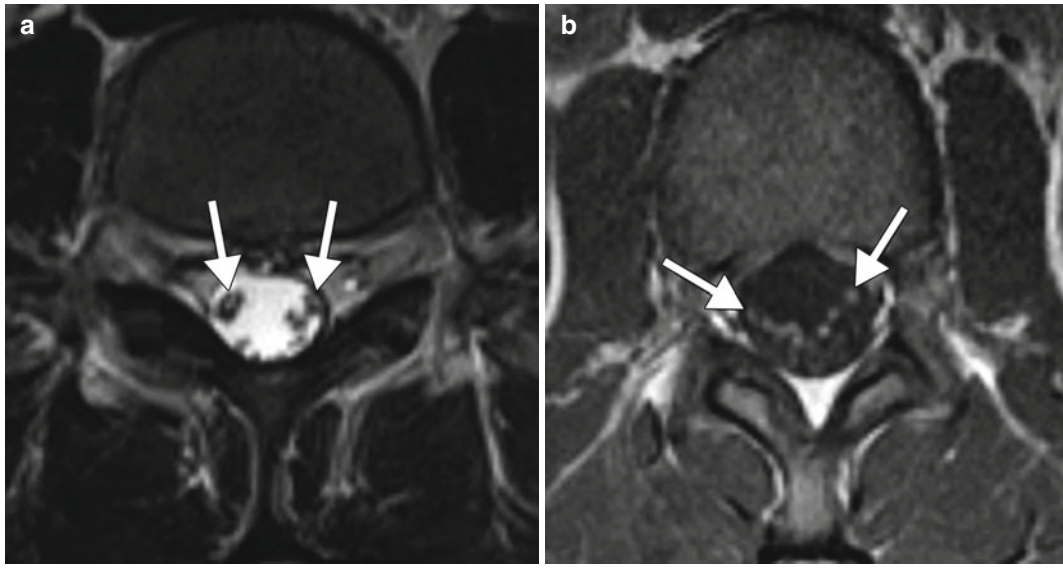

Fig. 48.2 Guillain-Barre disease related to vaccination. Axial T2-weighted (**a**) and post-contrast T1 (**b**) MR images show preferential thickening and enhancement of the anterior cauda equina nerve roots (*arrows*)

be a manifestation of a fulminant form of ADEM, known as acute hemorrhagic leukoencephalopathy or Hurst disease. Patients with postimmunization ADEM typically recover spontaneously or improve after administration of corticosteroids.

Certain vaccines can also result in Guillain-Barre syndrome. Patients present with acute flaccid paralysis, as well as sensory abnormalities and autonomic dysfunction. Salient features of Guillain-Barre syndrome on MRI include diffuse, smooth mild thickening and enhancement of the cauda equina nerve roots, preferentially the anterior nerve roots (Fig. 48.2). The spinal cord can also be affected, demonstrating patchy areas of high T2 signal and variable degrees of enhancement. There may be concomitant brain involvement; therefore, the brain should be imaged as well in these cases. Ultimately, the diagnosis is based on the temporal relation to vaccination and exclusion of other potential etiologies.

48.4 Differential Diagnosis

- The main differential diagnoses for vaccine-induced ADEM include ADEM caused by other etiologies, other demyelinating conditions such as multiple sclerosis, and viral encephalitis. Postinfectious ADEM is essentially indistinguishable from postimmunization ADEM on imaging, and clinical history may suggest the precipitating factor. Although multiple sclerosis may resemble ADEM on MRI, multiple sclerosis is a progressive disease rather than a monophasic one. Nevertheless, findings on conventional MRI that favor multiple sclerosis over ADEM include the absence of a diffuse bilateral lesion pattern, presence of black holes, and presence of two or more periventricular lesions (Fig. 48.3). In addition, magnetization transfer sequences can help distinguish ADEM from MS, in that normal-appearing brain on T2-weighted images has normal magnetization transfer ratio, whereas in multiple sclerosis measurements are decreased in both areas. It is important, but not always straightforward to differentiate viral encephalitis from ADEM. On MRI, viral encephalitis typically demonstrates bilateral diffuse areas of T2 hyperintensity involving the cerebral cortex and the underlying white matter and, to a lesser extent, the basal ganglia, brainstem, and cerebellum (refer to Chap. 3). However, the particular distribution of the

lesions may depend upon the particular viral agent. Associated enhancement may or may not be present, but tends to be leptomeningeal when present.

- Guillain-Barre syndrome can be caused by other entities besides vaccination, most commonly viral infections. Otherwise, the finding of thickened and enhancing nerve roots on MRI can be caused by chronic inflammatory demyelinating polyneuropathy (CIDP), which may be considered to be a chronic form of Guillain-Barre syndrome; hereditary polyneuropathies, such as Charcot-Marie-Tooth disease; and carcinomatous and lymphomatous meningitis. CIDP can appear essentially identical to Guillain-Barre syndrome on MRI (Fig. 48.4), and these conditions are mainly differentiated by the time course of the symptoms. The other lesions in the differential diagnosis tend to produce a greater degree of nerve root enlargement (hereditary polyneuropathies) and more irregular or nodular lesions (neoplasms).

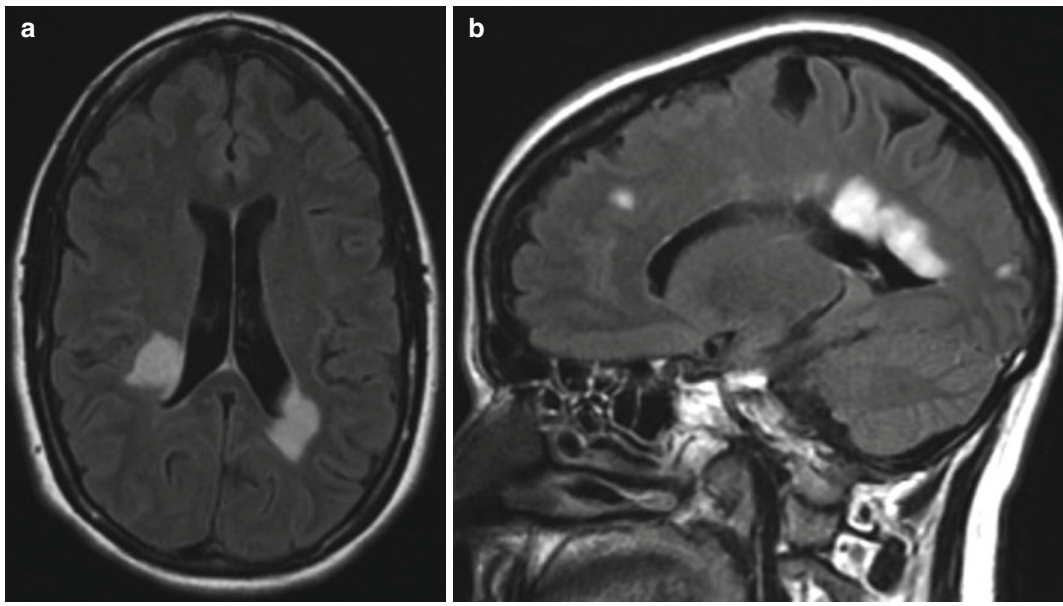

Fig. 48.3 Multiple sclerosis. Axial (**a**) and sagittal (**b**) FLAIR images show bilateral periventricular and callosal hyperintense flame-shaped lesions

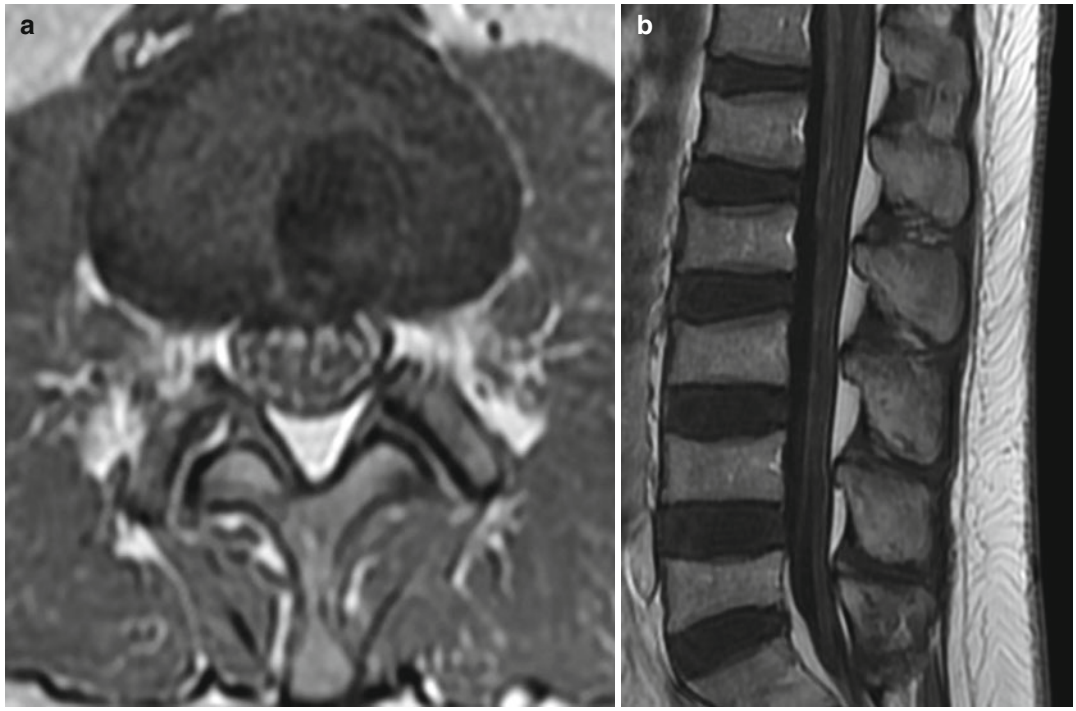

Fig. 48.4 CIDP. The patient has a history of protracted motor and sensory deficits in the lower extremities. Axial (**a**) and sagittal (**b**) post-contrast T1 MR images show diffuse enlargement and enhancement of the cauda equina nerve roots

Suggested Reading

Callen DJ, Shroff MM, Branson HM, Li DK, Lotze T, Stephens D, Banwell BL. Role of MRI in the differentiation of ADEM from MS in children. Neurology. 2009;72(11):968–73.

DeStefano F, Verstraeten T, Jackson LA, Okoro CA, Benson P, Black SB, Shinefield HR, Mullooly JP, Likosky W, Chen RT; Vaccine Safety Datalink Research Group, National Immunization Program, Centers for Disease Control and Prevention. Vaccinations and risk of central nervous system demyelinating diseases in adults. Arch Neurol. 2003;60(4):504–9.

Haber P, DeStefano F, Angulo FJ, Iskander J, Shadomy SV, Weintraub E, Chen RT. Guillain-Barré syndrome following influenza vaccination. JAMA. 2004;292(20):2478–81.

Haber P, Sejvar J, Mikaeloff Y, DeStefano F. Vaccines and Guillain-Barré syndrome. Drug Saf. 2009;32(4):309–23.

Hoshino T, Uchiyama Y, Ito E, Osawa S, Ohashi T. Simultaneous development of acute disseminated encephalomyelitis and Guillain-Barré syndrome associated with H1N1 09 influenza vaccination. Intern Med. 2012;51(12):1595–8.

Huynh W, Cordato DJ, Kehdi E, Masters LT, Dedousis C. Post-vaccination encephalomyelitis: literature review and illustrative case. J Clin Neurosci. 2008;15(12):1315–22.

Inglese M, Salvi F, Iannucci G, et al. Magnetization transfer and diffusion tensor MR imaging of acute disseminated encephalomyelitis. AJNR Am J Neuroradiol. 2002;23(2):267–72.

Mader I, Stock KW, Ettlin T, Probst A. Acute disseminated encephalomyelitis: MR and CT features. AJNR Am J Neuroradiol. 1996;17(1):104–9.

Pulendran B, Ahmed R. Immunological mechanisms of vaccination. Nat Immunol. 2011;12(6):509–17.

Acetominophen (Tylenol, Paracetamol)

49

Daniel Thomas Ginat

49.1 Uses

Tylenol is a mild nonnarcotic analgesic and antipyretic agent that is widely used for pain relief and fever reduction. The maximum safe daily dosage is less than 4 g in a 24-h period.

49.2 Mechanism

The precise mechanism of analgesic action has not been clearly defined. Nevertheless, Tylenol appears to produce analgesia by elevation of the pain threshold. The potential mechanism may involve the inhibition of the nitric oxide pathway. In relation to its antipyretic action, acetaminophen has been shown to inhibit endogenous pyrogens and block the formation of central nervous system prostaglandins. Tylenol is also a COX-2 inhibitor, which exerts its therapeutic effects by decreasing the production of thromboxanes. However, centrilobular necrosis can result from abundance of the reactive metabolite of acetaminophen, N-acetyl-*p*-benzoquinone imine, which is formed by cytochrome P-450 by a direct two-electron oxidation of acetaminophen. Ammonia is produced in the gastrointestinal tract from digestion of protein and bacterial metabolism. Normally, ammonia is metabolized primarily in the liver as urea via the urea cycle. However, when the metabolic capacity of the liver is overwhelmed, elimination becomes dependent on the kidneys, brain, and skeletal muscle. Astrocytes metabolize ammonia and glutamate to glutamine via the glutamine synthetase pathways, which leads to an increase in cellular osmolarity and astrocyte swelling. Inflammatory cascades, apoptosis, and various metabolic pathways ensue, resulting in elevation in lactate, loss of cerebral autoregulation, and cerebral edema.

49.3 Discussion

The acute symptoms can be nonspecific, ranging from mild altered mental status to varying degrees of unresponsiveness, with coma and death occurring in severe cases. The toxic levels of glutamine caused by Tylenol overdose predominantly lead to cerebral cortical injury. CT can demonstrate diffuse cerebral edema, which manifests as loss of gray-white mater differentiation, hypoattenuation, and sulcal effacement (Fig. 49.1). MRI, particularly FLAIR, and DWI sequences are useful for depicting acute hyperammonemic encephalopathy. The most common findings on MRI are bilateral symmetric high FLAIR and DWI signal in the cerebral cortex, especially the insular and cingulate cortices, with relative sparring of the perirolandic and occipital regions. In addition, the basal ganglia,

D.T. Ginat, MD, MS
Department of Radiology, University of Chicago, Pritzker Medical School, Chicago, IL, USA
e-mail: ginatd01@gmail.com

D.T. Ginat et al. (eds.), *Neuroimaging Pharmacopoeia*,
DOI 10.1007/978-3-319-12715-6_49,

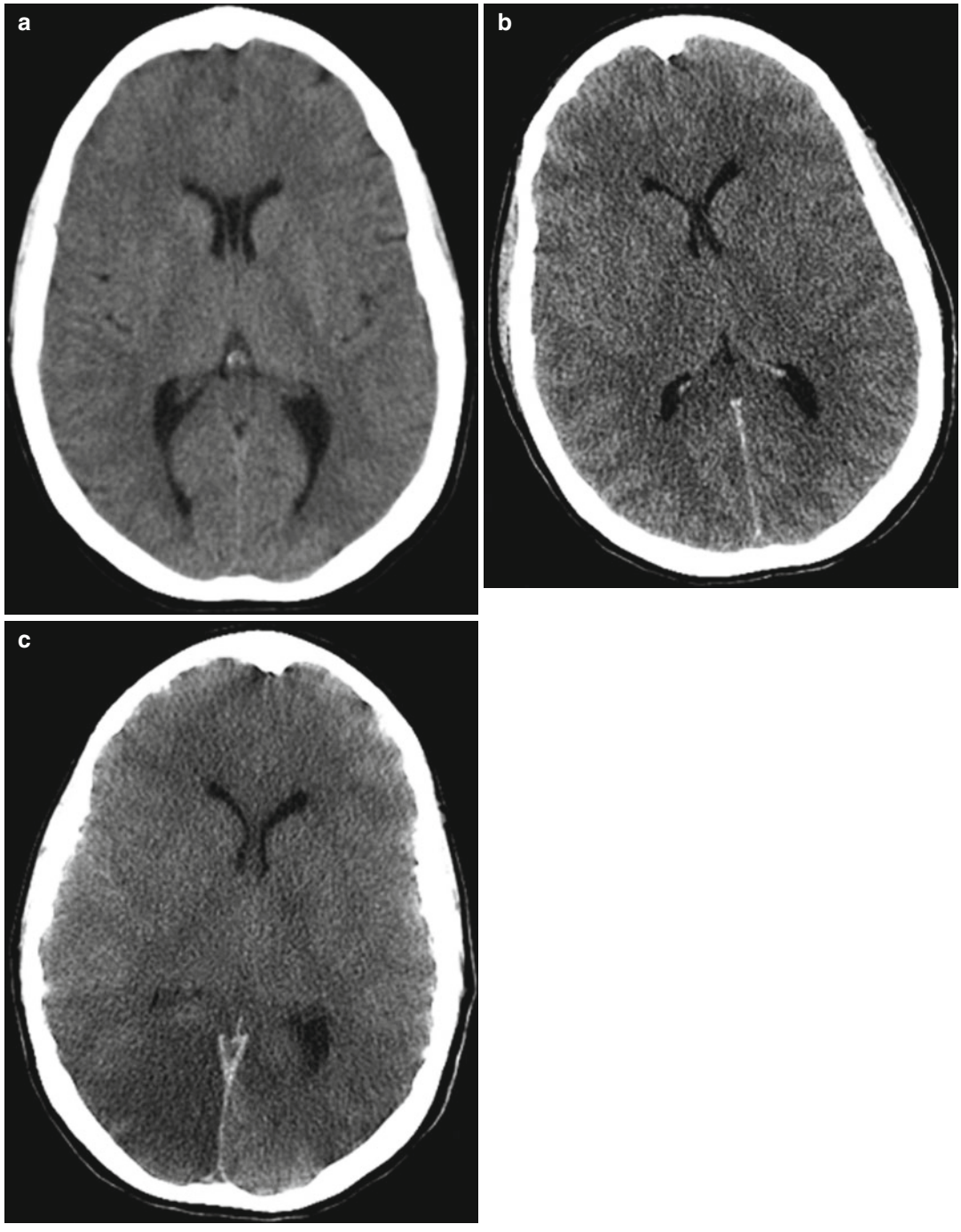

Fig. 49.1 Cerebral edema secondary to fulminant acute liver failure associated with acetaminophen overdose. Axial CT image obtained at the time of presentation soon after ingestion (**a**) demonstrates an unremarkable appearance of the brain. Axial CT images obtained 4 days (**b**) and 7 days (**c**) after ingestion demonstrate progressive loss of gray-white differentiation and severe diffuse cerebral cytotoxic edema secondary to acute liver failure with markedly elevated ammonia levels. There is also progressive effacement of the lateral ventricles secondary to diffuse brain edema

thalamus, and brainstem may also be affected. The high DWI signal can correspond to restricted diffusion. Treatment consists of administration of acetylcysteine, ideally within 8 h of Tylenol ingestion. Thus, prompt diagnosis is crucial. The signal abnormalities in hyperammonemic encephalopathy are potentially reversible with prompt and aggressive treatment, but may also evolve to variable degrees of atrophy in the cingulate and insular cortex after treatment.

49.4 Differential Diagnosis

Other causes of hyperammonemia include acute hepatic encephalopathy from other cases, such as alcohol and valproate toxicity (refer to Chaps. 2 and 28), as well as citrullinemia and proximal urea cycle disorders. Otherwise, the differential considerations for cerebral edema secondary to acetaminophen overdose on imaging include diffuse hypoxic-ischemic injury (Fig. 49.2), posterior reversible encephalopathy syndrome (refer to Chap. 23), seizure activity (Fig. 49.3), and Creutzfeldt-Jakob disease (Fig. 49.4). Seizure activity can result in reversible cortical FLAIR and DWI hyperintensity, which can be localized or generalized, and with or without associated contrast enhancement. Although Creutzfeldt-Jakob disease can produce T2 cortical and/or deep gray matter hyperintensity and restricted diffusion, it classically presents with rapidly progressive dementia.

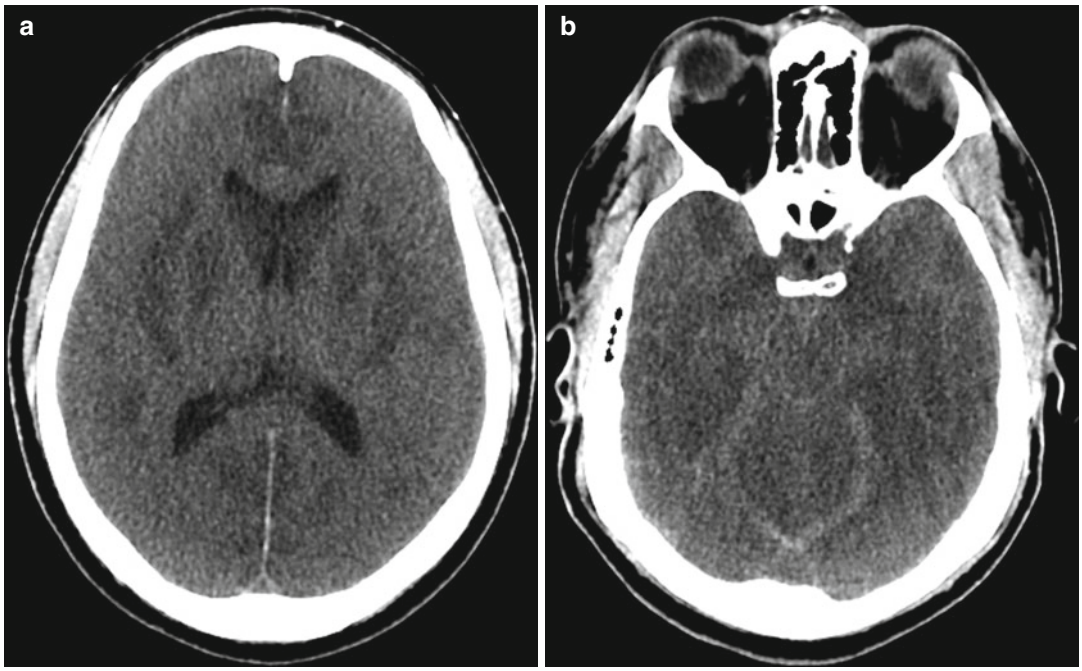

Fig. 49.2 Hypoxic-ischemic encephalopathy. The patient has a history of insulin-dependent diabetes mellitus status post cardiac arrest secondary to DKA status post resuscitation. Axial CT images (**a**, **b**) show diffuse cerebral edema with sulcal, ventricular, and basal cistern effacement, as well as more pronounced areas of hypoattenuation within the bilateral basal ganglia

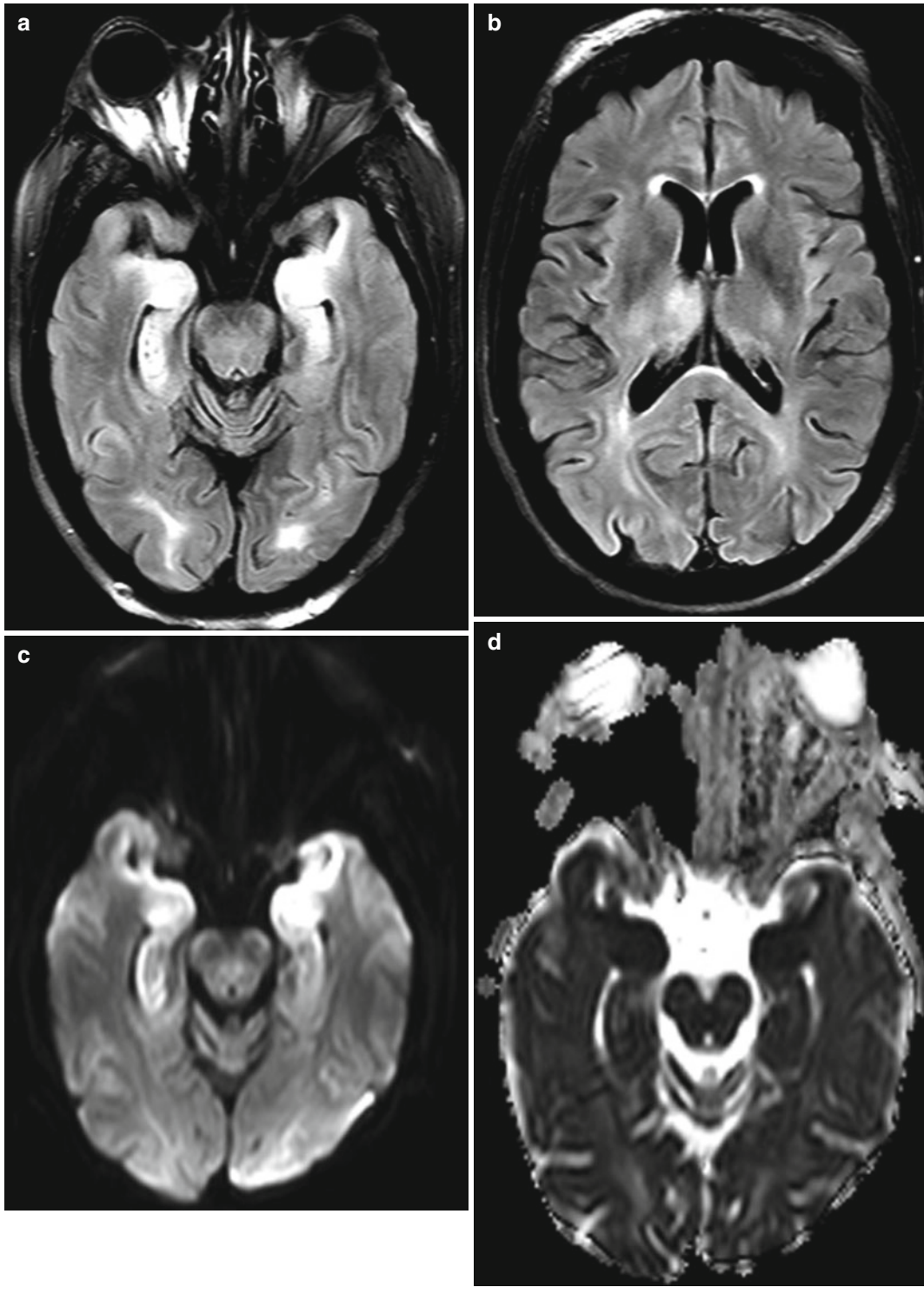

Fig. 49.3 Status epilepticus. Axial FLAIR images (**a**, **b**) show hyperintensity within the bilateral medial temporal lobes and thalami. The DWI (**c**) and ADC map (**d**) show corresponding restricted diffusion

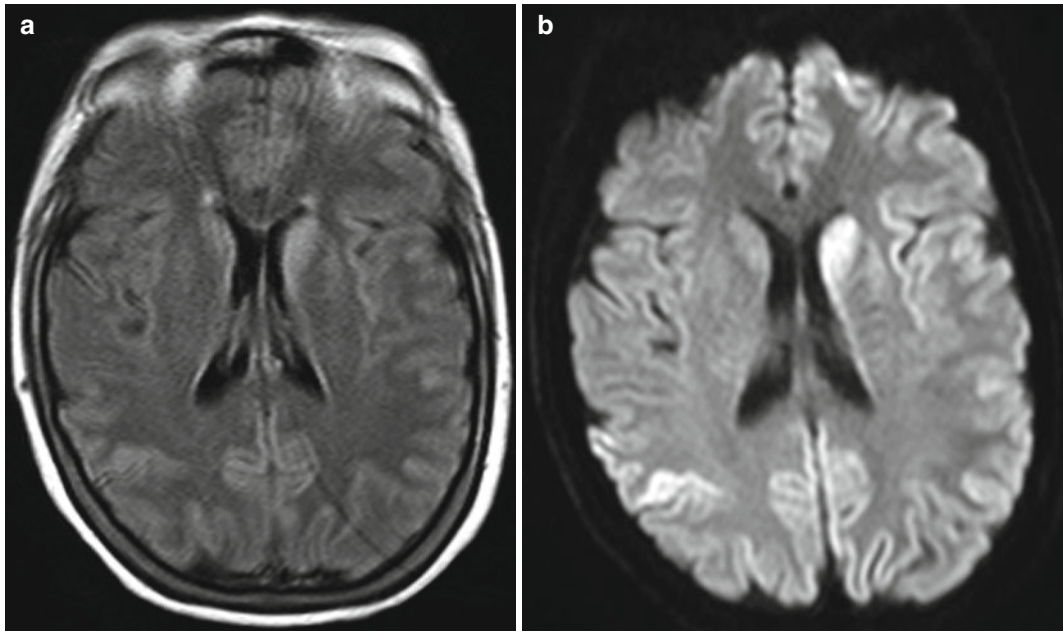

Fig. 49.4 Creutzfeldt-Jakob disease. Axial FLAIR (**a**) and DWI (**b**) sequences show diffuse peripheral and central gray matter hyperintensity involving the cerebral cortex and left caudate head

Suggested Reading

Butterworth RF. Neuroinflammation in acute liver failure: mechanisms and novel therapeutic targets. Neurochem Int. 2011;59(6):830–6.

Desjardins P, Du T, Jiang W, Peng L, Butterworth RF. Pathogenesis of hepatic encephalopathy and brain edema in acute liver failure: role of glutamine redefined. Neurochem Int. 2012;60(7):690–6.

Larson AM. Acetaminophen hepatotoxicity. Clin Liver Dis. 2007;11(3):525–48, vi.

McKinney AM, Lohman BD, Sarikaya B, Uhlmann E, Spanbauer J, Singewald T, Brace JR. Acute hepatic encephalopathy: diffusion-weighted and fluid-attenuated inversion recovery findings, and correlation with plasma ammonia level and clinical outcome. AJNR Am J Neuroradiol. 2010;31(8):1471–9.

Thayaparajah SW, Gulka I, Al-Amri A, Das S, Young GB. Acute fulminant hepatic failure, encephalopathy and early CT changes. Can J Neurol Sci. 2013;40(4):553–7.

U-King-Im JM, Yu E, Bartlett E, Soobrah R, Kucharczyk W. Acute hyperammonemic encephalopathy in adults: imaging findings. AJNR Am J Neuroradiol. 2011;32(2):413–8.

Vaquero J, Butterworth RF. Mechanisms of brain edema in acute liver failure and impact of novel therapeutic interventions. Neurol Res. 2007;29(7):683–90.

Vaquero J, Chung C, Blei AT. Brain edema in acute liver failure. A window to the pathogenesis of hepatic encephalopathy. Ann Hepatol. 2003;2(1):12–22.

Vaquero J, Chung C, Blei AT. Cerebral blood flow in acute liver failure: a finding in search of a mechanism. Metab Brain Dis. 2004;19(3–4):177–94.

Propofol

50

Mariam Aboian, Jason M. Johnson,
and Daniel Thomas Ginat

50.1 Uses

Propofol (2,6-diisopropylphenol) is used for induction of anesthesia, maintenance of anesthesia, and treatment of refractory status epilepticus. Propofol has very rapid time to onset of unconsciousness (15–30 s) and is rapidly metabolized. Patients rapidly recover from sedation with few side effects, thus making it an anesthetic of choice for ambulatory surgery.

50.2 Mechanism

Propofol modulates the inhibitory function of neurotransmitter gamma-aminobutyric acid (GABA) through GABA-A receptors.

M. Aboian, MD
Department of Radiology, University of California, San Francisco, San Francisco, CA, USA

J.M. Johnson, MD
Department of Diagnostic Radiology, MD Anderson Cancer Center, Houston, TX, USA

D.T. Ginat, MD, MS (✉)
Department of Radiology, University of Chicago, Pritzker Medical School, Chicago, IL, USA
e-mail: dtg1@uchicago.edu

50.3 Discussion

In clinical imaging, propofol has commonly been used to decrease motion. One of the described artifacts associated with propofol sedation is increased hyperintensity of CSF within the subarachnoid cisterns and sulci on FLAIR (Fig. 50.1). This phenomenon is sometimes observed in children under propofol sedation, which could be due to propofol solution having a smaller T1 value than CSF, transient increase in protein content within CSF, or hyperdynamic CSF pulsations due to propofol-induced changes in vascular tone. One of the main functions of propofol is inhibition of connectivity in the brain, in particular on intralaminar thalamic nuclei. There is decreased connectivity of the thalamus with increase in eigenvector centrality in the brainstem, which is likely a consequence of its increased influence over highly central cortical regions during sedation with propofol. The effect of propofol on memory has also been widely studied using functional magnetic resonance imaging. Propofol has an effect on explicit memory at any dose, but implicit memory is affected only in deep propofol sedation. This has been shown by inhibition of activation of middle temporal gyrus and parietal lobule as opposed to only superior temporal gyrus, which is inhibited by mild propofol sedation. On evaluation of auditory verbal memory with functional MRI in subjects under deep sedation with propofol, primary auditory cortex activity was present on auditory stimuli, but activation

D.T. Ginat et al. (eds.), *Neuroimaging Pharmacopoeia*,
DOI 10.1007/978-3-319-12715-6_50,

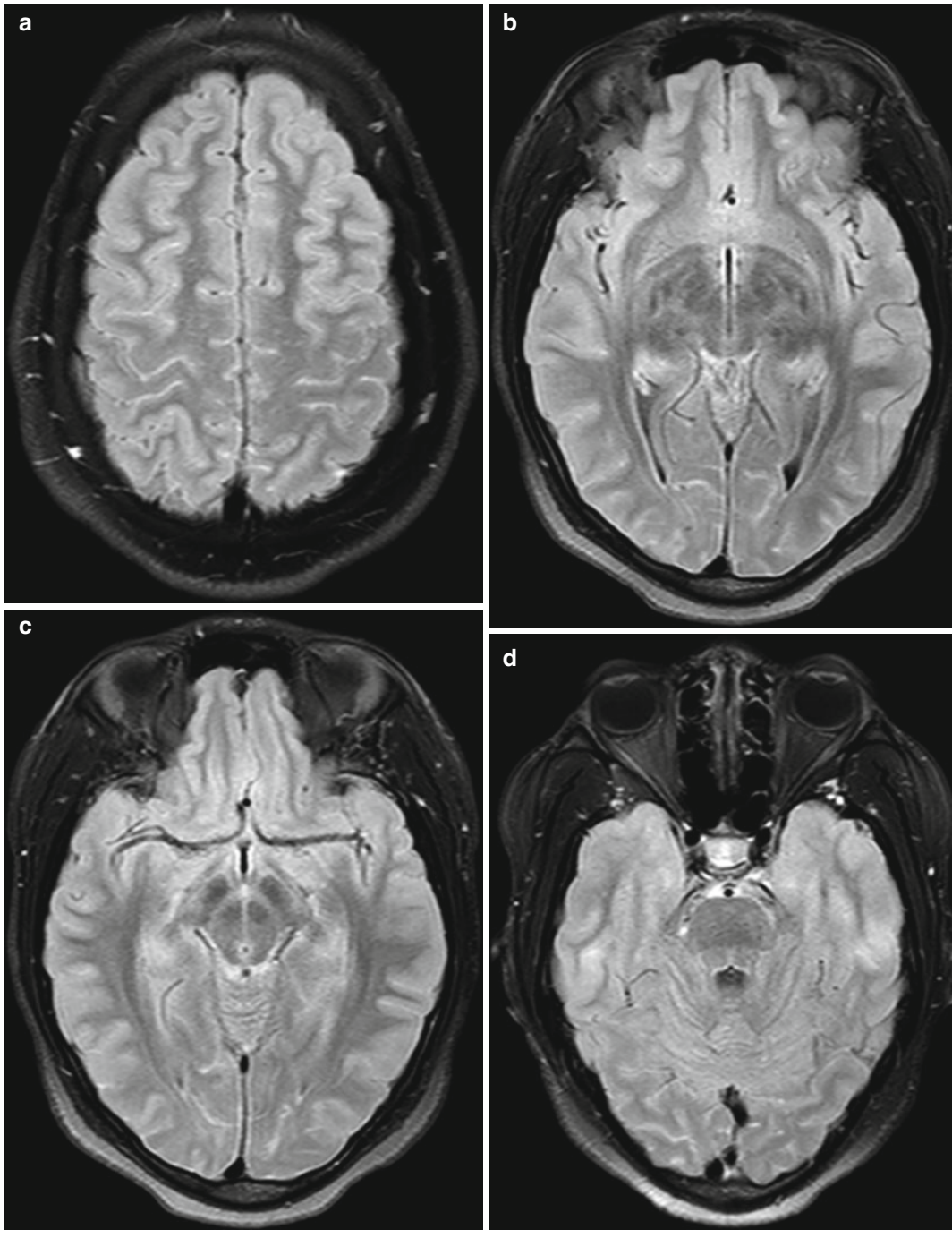

Fig. 50.1 Propofol effects on MRI. Axial FLAIR images (**a**–**d**) show diffuse high signal within the subarachnoid spaces of the sulci and basal cisterns

of inferior frontal gyrus and premotor areas were not detected. These results showed that integration of auditory sensory stimuli with high-order processing networks is inhibited under deep sedation with propofol, thus suggesting that propofol acts by disrupting connections between the sensory areas of the brain with the executive areas.

50.4 Differential Diagnosis

Subarachnoid FLAIR hyperintensity has been observed in a variety of other conditions, including meningitis, leptomeningeal carcinomatosis, hemorrhage, leptomeningeal melanosis, stroke, and supplemental oxygen administration (refer to Chap. 35).

Suggested Reading

Fillipi CG, Ulug AM, Lin D, Heir LA, Zimmerman RD. Hyperintense signal abnormality in subarachnoid spaces and basal cisterns on MR images of children anesthetized with propofol: new fluid-attenuated inversion recovery finding. AJNR Am J Neuroradiol. 2001;22:394–9.

Fugii J, Miyachi S, Matsubara N, Kinkori T, Takebayashi S, Izumi T, Ohshima T, Tsurumi A, Hososhima O, Wakabayashi T, Yoshida J. Selective propofol injection into the M1 segment of the middle cerebral artery (MCA Wada test) reduces adverse effects and enhances the reliability of the Wada test for determining speech dominance. World Neurosurg. 2011;75(3–4):503–8.

Gili T, Saxena N, Diukova A, Murphy K, Hall JE, Wise RG. The thalamus and brainstem act as key hubs in alterations of human brain network connectivity induced by mild propofol sedation. J Neurosci. 2013;33(9):4024–31.

Li W, Walt SD, Ogg RJ, Scoggins MA, Zou P, Wheless J, Boop FA. Functional magnetic resonance imaging of the visual cortex performed in children under sedation to assist in presurgical planning. J Neurosurg Pediatr. 2013;11(5):543–6.

Liu X, Lauer KK, Ward BD, Rao SM, Li SJ, Hudetz AG. Propofol disrupts functional interactions between sensory and high-order processing of auditory verbal memory. Hum Brain Mapp. 2012;33(10):2487–98.

Maeda M, Yagishita A, Yamamoto T, Sakuma H, Takeda K. Abnormal hyperintensity within the subarachnoid space evaluated by fluid-attenuated inversion-recovery MR imaging: a spectrum of central nervous system diseases. Eur Radiol. 2003;13:L192–201.

Quan X, Yi J, Ye T, Tian SY, Zou L, Yu XR, Huang YG. Propofol and memory: a study using a process dissociation procedure and functional magnetic resonance imaging. Anaesthesia. 2013;68(4):391–9.

Stoner T, Braff S, Khoshyomn S. High signal in subarachnoid spaces on FLAIR MR images in an adult with propofol sedation. Neurology. 2002;59:292.

Stuckey SL, Goh TD, Heffernan T, Rowan D. Hyperintensity in the subarachnoid space on FLAIR MRI. Am J Radiol. 2007;189:913–21.

Zijlmans M, Hulskamp GM, Cremer OL, Ferrier CH, van Huffelen AC, Leijten FS. Epileptic high frequency oscillations in intraoperative electrocorticography: the effect of propofol. Epilepsia. 2012;53(10):1799–809.

Bisphosphonates

51

Ana M. Franceschi, Daniel Thomas Ginat, and Jason M. Johnson

51.1 Uses

Oral bisphosphonates are primarily used for treatment of osteoporosis and osteopenia, as well as some less common metabolic bone disorders including Paget's disease of the bone, osteogenesis imperfecta, and fibrous dysplasia. Intravenous bisphosphonates are used for the management of cancer-related conditions, such as hypercalcemia of malignancy and skeletal complications associated with bone metastases in patients with solid tumors including breast, prostate, and lung cancer, and treatment of lytic lesions in patients with multiple myeloma.

51.2 Mechanism

Bisphosphonates are inorganic pyrophosphate analogs that inhibit osteoclast activity, thereby suppressing bone remodeling and resorption. Simple bisphosphonates, such as clodronate and etidronate, act at the cellular level via induction of osteoclast apoptosis. Specifically, clodronate generates a toxic analog of adenosine triphosphate (ATP), AppCCl2p, which inhibits adenine nucleotide translocase, a component of the permeability transition pore complex in the inner mitochondrial membrane. This leads to the disruption of the mitochondrial membrane potential, which causes release of cytochrome C, caspase activation, and initiates other steps in the process of apoptosis. The direct intracellular target of nitrogen-containing aminobisphosphonates, such as alendronate and risedronate and the intravenously administered pamidronate and zoledronate, is the isoprenoid biosynthetic enzyme farnesyl diphosphate (FPP) synthase in the cholesterol biosynthesis pathway. Inhibition of FPP synthase suppresses protein geranylgeranylation, which then causes GTPase inactivation resulting in deregulation of vesicular trafficking (e.g., formation of ruffled border) and cytoskeletal structures necessary for bone-resorbing osteoclast activity.

51.3 Discussion

Bisphosphonate-related osteonecrosis of the jaw (BRONJ) presents as painful or painless bone exposure in the mandible (2/3 cases), maxilla (1/4 cases), or both, which is usually preceded by various dental manipulations, such as tooth extraction or infection. According to the American Association of Oral and Maxillofacial Surgeons

A.M. Franceschi, MD
Diagnostic Radiology, New York University Medical Center, New York, NY, USA

J.M. Johnson, MD
Department of Diagnostic Radiology, MD Anderson Cancer Center, Houston, TX, USA

D.T. Ginat, MD, MS (✉)
Department of Radiology, University of Chicago, Pritzker Medical School, Chicago, IL, USA
e-mail: ginatd01@gmail.com

D.T. Ginat et al. (eds.), *Neuroimaging Pharmacopoeia*,
DOI 10.1007/978-3-319-12715-6_51,

(AAOMS), patients are considered to have BRONJ if the following conditions are met: (1) current or previous treatment with a bisphosphonate; (2) exposed, necrotic bone in the maxillofacial region that has persisted for more than 8 weeks; and (3) no history of radiation therapy to the jaws. The estimated incidence of osteonecrosis ranges from 1 to 10 % among patients on IV bisphosphonate treatment, while it is much less common (<1/100,000 patient-treatment years with a reported prevalence of 0.0004–0.04 %) in patients receiving oral bisphosphonate therapy. The onset of BRONJ has been reported at 6–60 months following initiation of bisphosphonate therapy, and the risk of osteonecrosis increases with the duration of bisphosphonate exposure.

It is hypothesized that BRONJ has a predilection for the jaw since the hypodynamic and hypovascular bone is unable to meet increased demand for remodeling secondary to physiologic stress, iatrogenic trauma, or tooth infection. The exposed, nonhealing bone is generally unresponsive to conventional medical and surgical treatment. Attempts at debridement and removal of painful teeth or tissue flaps have all been reported to cause additional bone exposure and exacerbation of the process. Management strategies emphasize prevention of BRONJ, including preventive dental treatment, patient education, and optimal periodontal health prior to initiation of IV bisphosphonates in cancer patients as well as periodic drug "holidays" in patients on chronic oral bisphosphonate therapy. Once patients develop BRONJ, treatment is focused on the control of chronic pain and infection with antibiotics (oral antimicrobial rinses and systemic antibiotic therapy) as well as attempts at hyperbaric oxygen therapy, while surgical resection/debridement is reserved for advanced stages with a goal of long-term palliation and resolution of acute infection and pain.

While BRONJ is a clinical diagnosis made primarily on the basis of history and physical exam, imaging studies can be helpful in delineating the extent of the necrotic process, therefore guiding therapeutic and clinical management plans, excluding other diseases of the jaw, monitoring disease progression, and diagnosing complications such as pathologic fractures. However, in the early stages of osteonecrosis, plain film studies frequently demonstrate no significant abnormalities, especially when the lesions are smaller than 1 cm, with little or no ossification at a previous tooth extraction site often being the first sign of disease. As the osteonecrosis progresses, areas of ill-defined lucency, thickening of the lamina dura, osseous fragmentation, osteosclerosis, periosteal reaction, and regions of bony sequestrum may form. In advanced cases of BRONJ, osteolytic changes can spread to affect the inferior border of the mandible and lead to pathologic fracture. Additionally, there may be associated narrowing of the inferior alveolar canal. The abnormalities associated with BRONJ may be predominantly lytic, predominantly sclerotic, or mixed.

CT is often obtained to delineate the area of necrosis, which can appear as osteosclerotic and osteolytic lesions. Focal medullary sclerosis with disorganized microtrabeculae and poor corticomedullary differentiation corresponds to areas of delayed socket healing and is typically the earliest finding of disease. As the pathologic process progresses, proliferative periosteal reactions and bony sequestrum become predominant lesions, resulting in a bone-within-a-bone appearance on CT (Fig. 51.1). Additional findings on CT images include narrowing of the marrow space, cortical bone resorption and disruption, osseous fragmentation, involvement of the inferior alveolar canal, as well as complications such as pathologic fractures (Fig. 51.2). If the maxilla is involved, it is often accompanied by abnormalities of the adjacent maxillary sinus, including mucoperiosteal thickening, air-fluid levels, and oroantral fistula formation (Fig. 51.3). Additionally, there is often evidence of reactive cervical lymphadenopathy secondary to infection of the exposed bone, and there can be thickening of the masticator muscles, which can be a diagnostic dilemma and raises concern for tumor. Similar to radiography, CT has not been proven useful in detecting early changes in asymptomatic patients with osteonecrosis.

MRI can be used to further delineate involvement of the surrounding soft tissues and neurovascular bundle, lymphadenopathy, as well as bone marrow edema, which may be an early indicator of bone ischemia and necrosis. Therefore, in the

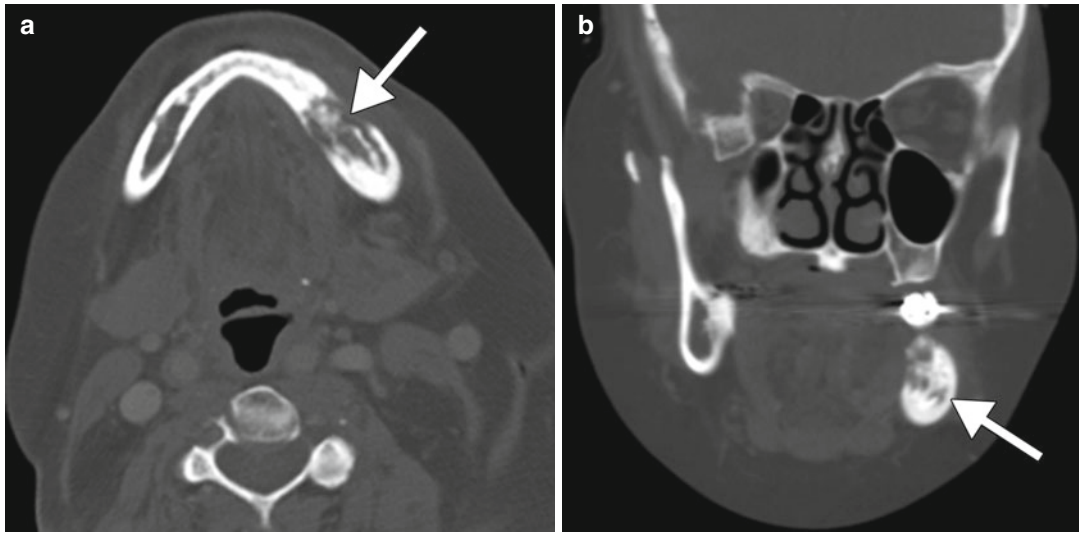

Fig. 51.1 Bisphosphonate-induced osteonecrosis of the mandible. Axial (**a**) and coronal (**b**) CT images show a mixed sclerotic and lucent lesion within the left mandibular body that has a bone-within-a-bone appearance (*arrows*)

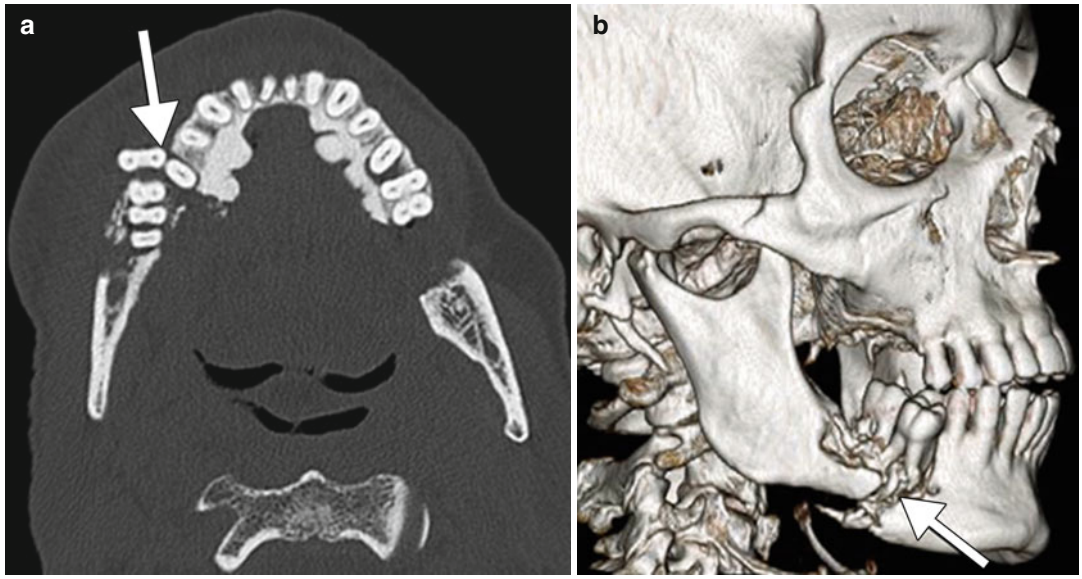

Fig. 51.2 Bisphosphonate-induced osteonecrosis of the mandible with pathological fracture. Axial (**a**) and 3D surface rendered (**b**) CT images show a displaced fracture of the right mandibular body (*arrows*), adjacent to a lucent focus of osteonecrosis. There is also torus mandibularis internis (Courtesy of Christine Glastonbury)

early stages of BRONJ, findings classically include decreased bone marrow signal intensity on non-contrast T1-weighted images, accompanied by increased signal intensity of the surrounding soft tissues on contrast-enhanced T1-weighted images. Findings on T2-weighted and short inversion time inversion-recovery (STIR) images are variable and can appear normal in early stages of

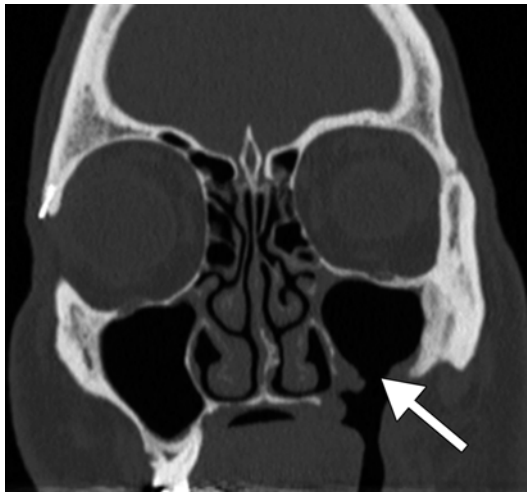

Fig. 51.3 Bisphosphonate-induced osteonecrosis of the maxilla. Coronal CT image shows a defect in the left maxillary sinus wall and alveolus with associated oroantral fistula (*arrow*) (Courtesy of Christine Glastonbury)

disease. Areas with low signal intensity on T2-weighted and STIR images correspond to osteonecrosis. Additionally, there is increased T2-weighted signal intensity and enhancement on contrast-enhanced T1-weighted images at the periphery of the necrotic bone, corresponding to formation of a reactive fibrotic margin and surrounding soft tissue inflammation. In clinically advanced cases, development of a sequestrum is recognized by identifying areas with centrally decreased signal intensity on T2-weighted images, which are surrounded by a high T2-weighted signal intensity peripheral rim. Enhancement of the bone marrow corresponds to low signal intensity on T1-weighted images and indicates the degree of fatty marrow replacement, which often spares the central bony sequestrum. It is important to remember that the signal intensity changes on MRI in patients with BRONJ are not isolated to the affected bony cortex, but encompass adjacent areas including the surrounding soft tissues, bone marrow, inferior alveolar canal, and maxillary sinuses. Enhancement of the adjacent soft tissues often involves the mylohyoid ridge, buccinator muscle, orbicularis oris muscle, and masticator space, with focal areas of mass-like muscle thickening. Additionally, reactive cervical lymphadenopathy is frequently present, most commonly in the submental and jugulodigastric areas secondary to infection of the affected bone.

Nuclear medicine studies, such as 99mTc-methylene diphosphonate (99mTc-MDP) planar and single-photon emission computerized tomography (SPECT) bone scintigraphy, hybrid SPECT/CT systems, as well as [18F] sodium fluoride (NaF) or [18F] fluorodeoxyglucose (FDG) positron emission tomography (PET/CT), are highly sensitive for the detection of BRONJ, especially in the early stages of disease. Typically, these modalities demonstrate increased radiotracer uptake in the majority of cases, which is thought to be secondary to surrounding areas of soft tissue inflammation as well as infection at the site of necrosis. Furthermore, 3-phase bone scintigraphy characteristically reveals increased perfusion and increased blood pool, which is caused by areas of hypervascularity in the affected region. The limiting factor of these functional imaging modalities is their poor spatial resolution and low specificity. However, hybrid systems such as SPECT/CT are able to demonstrate the metabolic difference between the necrotic sequestrum (decreased radiotracer uptake) and surrounding areas of reactive osteoblastic hyperactivity, therefore allowing for precise localization of the osteonecrotic core and enabling differentiation from the adjacent viable bone.

51.4 Differential Diagnosis

The differential diagnosis for bisphosphonate-induced osteonecrosis of the jaw includes osteoradionecrosis, neuralgia-inducing cavitational osteonecrosis, osteomyelitis, bone metastases, and primary bone tumors (osteosarcoma).

- *Osteoradionecrosis:* There is always an accompanying clinical history of radiation therapy to the oral cavity. Osteoradionecrosis causes an increase in the marrow space which is filled with necrotic tissue, followed by bony sequestration demonstrating a typical moth-eaten appearance. Furthermore, osteoradionecrosis may present with ill-defined regions of cortical thickening and sclerosis, loss of trabeculation, soft tissue edema, and pathologic fractures (Fig. 51.4).

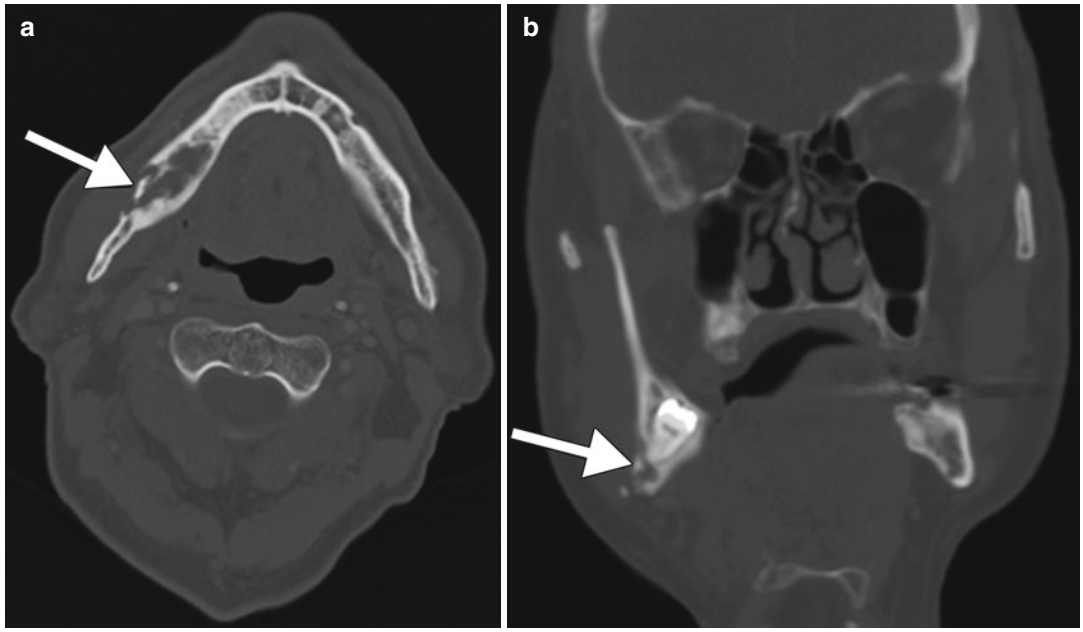

Fig. 51.4 Osteoradionecrosis. Axial (**a**) and coronal (**b**) CT images show fragmentation of the lingual cortex of the right mandible body (*arrows*) associated with surrounding irregular lucency and sclerosis in a patient who received radiation therapy for a right tonsillar squamous cell cancer several years before

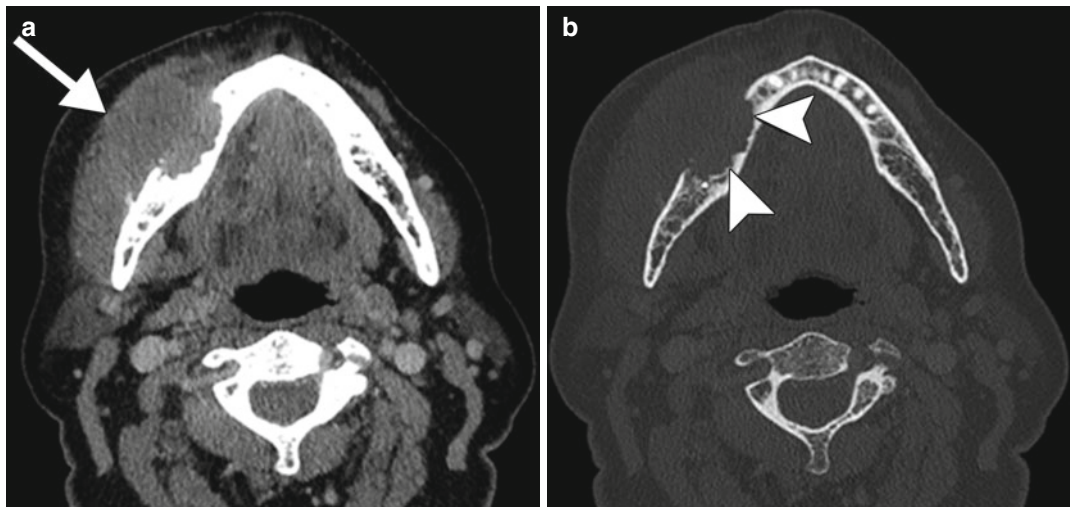

Fig. 51.5 Squamous cell carcinoma. Axial CT images in soft tissue (**a**) and bone (**b**) windows show a bulky soft tissue mass (*arrow*) in the anterior right oral cavity that erodes into the adjacent mandible (*arrowheads*)

- *Squamous cell carcinoma:* On head and neck cancer patients, new or recurrent tumor may be a consideration when a mandibular lesion is identified on imaging. The presence of mandibular involvement affects staging and management. An associated soft tissue mass is often apparent on imaging (Fig. 51.5), which is otherwise unusual for BRONJ.
- *Neuralgia-inducing cavitational osteonecrosis:* There is dissolution of the alveolar medullary

bone with subsequent loosening and loss of teeth. Patients typically present with severe atypical facial pain or trigeminal neuralgia. CT can demonstrate lucency of the affected bone with irregular borders (Fig. 51.6).

- *Osteomyelitis*: An acute presentation with constitutional symptoms suggests suppurative osteomyelitis. However, it can be difficult to differentiate chronic osteomyelitis of the jaw from BRONJ on imaging, since there is often considerable overlap between these entities. Abnormal enhancement on contrast-enhanced T1-weighted images secondary to soft tissue inflammation and edema is common in both BRONJ and osteomyelitis. The bone marrow in osteomyelitis frequently demonstrates low signal intensity on T1-weighted images and high signal intensity on T2-weighted images, with the bony sequestrum identified by low signal intensity on both T1-weighted and T2-weighted images. In addition, there is often an accompanying periosteal reaction with reactive bone formation as well as regions of diffuse osteolytic destruction. Nuclear medicine studies, including In-111 can be useful for differentiating infection from BRONJ, in which osteomyelitis will demonstrate increased uptake of radiolabelled white blood cells, while BRONJ typically will not (Fig. 51.7).
- *Metastases*: Primary tumors most likely to cause bony metastases include the breast, kidney, prostate, lung, and stomach, with metastases most frequently found at the mandible. Imaging findings include focal or diffuse areas of bone destruction and elevated radiotracer uptake on bone scan (Fig. 51.8). There may be multiple lesions and accompanying lymphadenopathy. However, the development of a bony sequestrum or the presence of exposed areas of bone is uncommon.
- *Osteosarcoma*: Osteosarcoma can develop many years after radiation therapy has been administered to the head and neck and typically appears as an aggressive lesion with moth-eaten or permeative borders, irregular sclerosis, and soft tissue components on CT (Fig. 51.9). The tumors are often accompanied by prominent periosteal reaction.

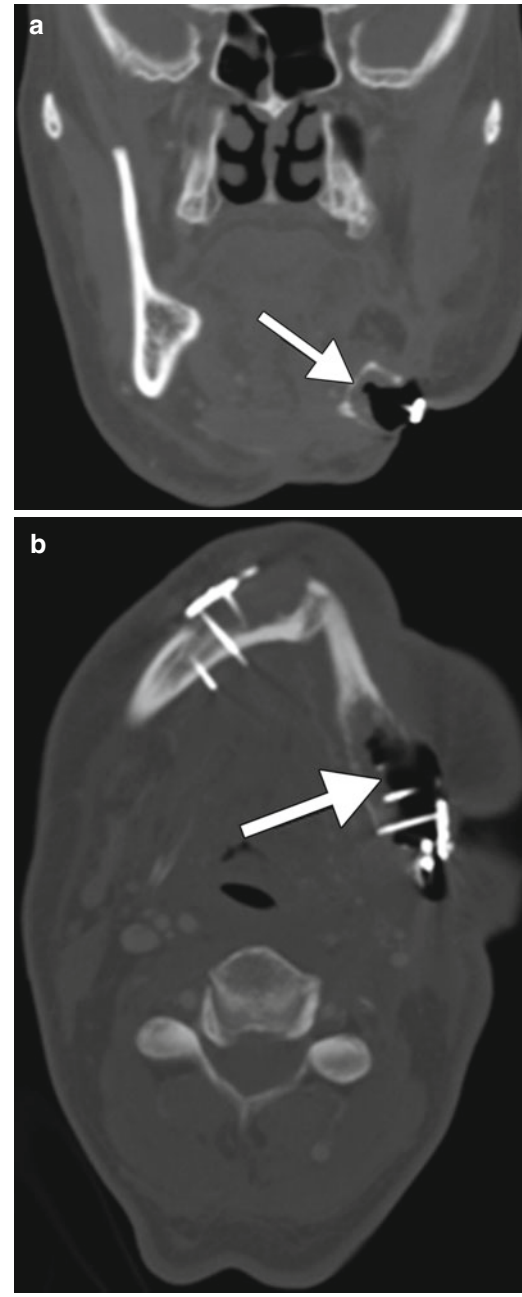

Fig. 51.6 Cavitation necrosis. Coronal (**a**) and axial (**b**) CT images show air within a defect that extends from the overlying skin to the marrow of the left mandibular bone graft (*arrows*)

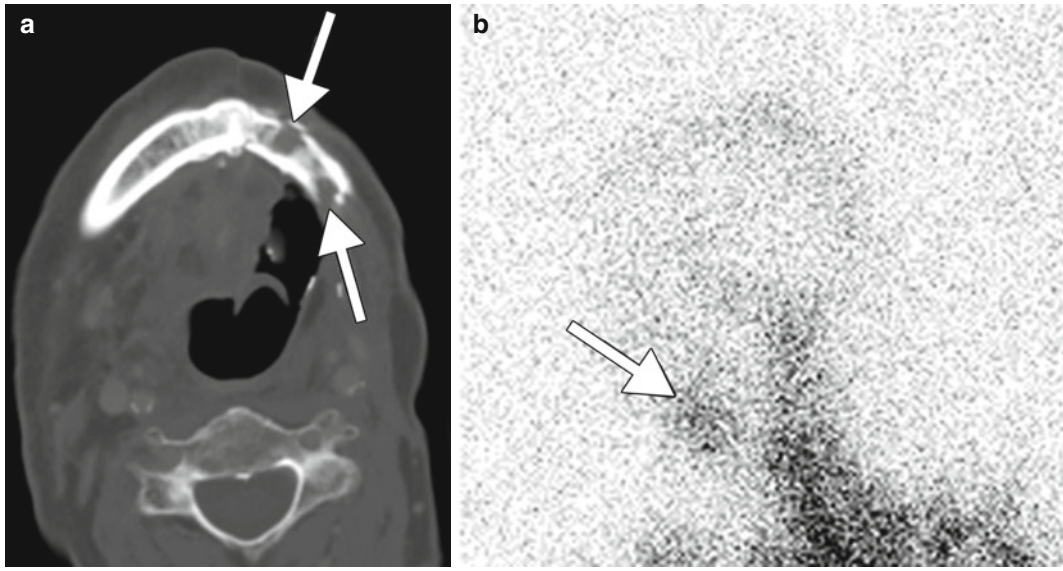

Fig. 51.7 Osteomyelitis. Axial CT image (**a**) shows lytic foci with erosion of the overlying left mandibular cortex (*arrows*). In-111 tagged white blood cell exam, left lateral oblique view (**b**) shows uptake in the corresponding region of the left mandible (*arrow*)

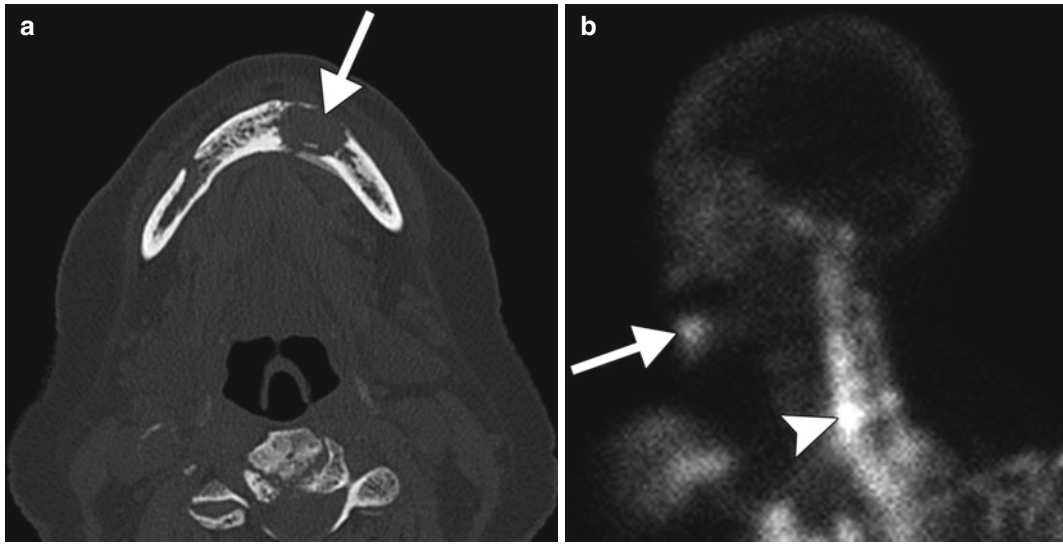

Fig. 51.8 Metastasis. Axial CT image (**a**) show a lytic lesion within the left mandible body with associated defects in the cortex (*arrow*). The bone scan (**b**) shows elevated radiotracer uptake in the lesion (*arrow*) and another metastasis involving the C7 vertebra (*arrowhead*)

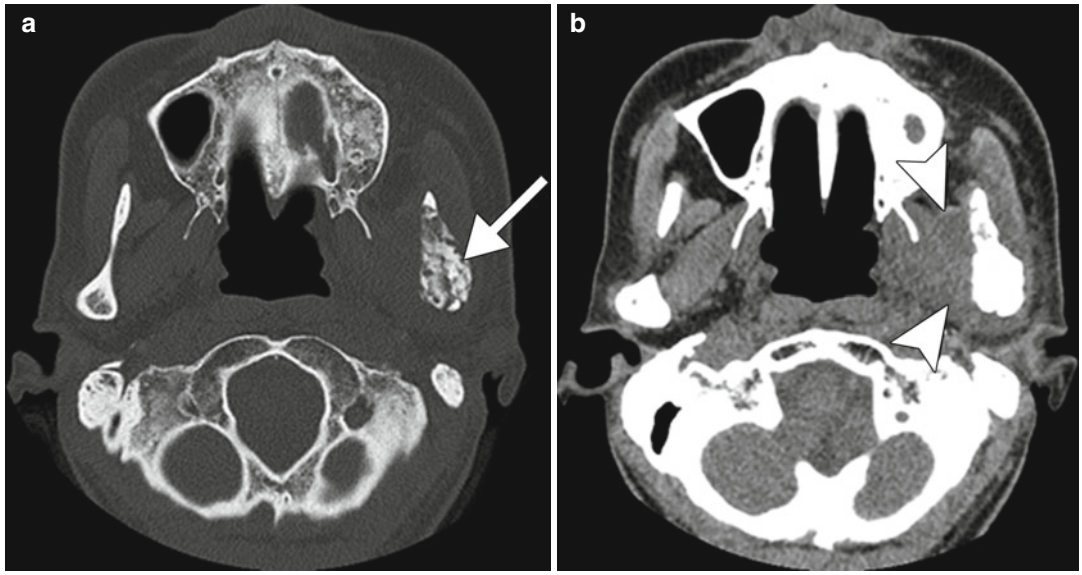

Fig. 51.9 Radiation-induced osteosarcoma. Axial CT images in bone (**a**) and soft tissue (**b**) windows show an irregular osteoblastic mass (*arrow*) with an ill-defined soft tissue component (*arrowheads*) arising from the left mandibular ramus

Suggested Reading

Arce K, Assael LA, Weissman JL, Markiewicz MR. Imaging findings in bisphosphonate-related osteonecrosis of jaws. J Oral Maxillofac Surg. 2009;67:75–84.

Ariji Y, Ariji E. Role of magnetic resonance imaging in diagnosis of bisphosphonate-related osteonecrosis of the jaw. Oral Radiol. 2013;29:111–20.

Durie BG, Katz M, Crowley J. Osteonecrosis of the jaw and bisphosphonates. N Engl J Med. 2005;353:99–102.

Garcia-Ferrer L, Bagan JV, Martinez-Sanjuan V, Hernandez-Bazan S, Garcia R, Jimenez-Soriano Y, et al. MRI of mandibular osteonecrosis secondary to bisphosphonates. AJR Am J Roentgenol. 2008;190:949–55.

Gill SB, Valencia MP, Sabino ML, Heideman GM, Michel MA. Bisphosphonate-related osteonecrosis of the mandible and maxilla: clinical and imaging features. J Comput Assist Tomogr. 2009;33:449–54.

Krishnan A, Arslanoglu A, Yildirm N, Silbergleit R, Aygun N. Imaging findings of bisphosphonate-related osteonecrosis of the jaw with emphasis on early magnetic resonance imaging findings. J Comput Assist Tomogr. 2009;33:298–304.

Morag Y, Morag-Hezroni M, Jamadar DA, Ward BB, Jacobson JA, Zwetchkenbaum SR, et al. Bisphosphonate-related osteonecrosis of the jaw: a pictorial review. Radiographics. 2009;29:1971–84.

Phal PM, Myall RWT, Assael LA, Weissman JL. Imaging findings of bisphosphonate-associated osteonecrosis of the jaws. AJNR Am J Neuroradiol. 2007;28:1139–45.

Reszka AA, Rodan GA. Mechanism of action of bisphosphonates. Curr Osteoporos Rep. 2003;1:45–52.

Reszka AA, Rodan GA. Nitrogen-containing bisphosphonate mechanism of action. Mini Rev Med Chem. 2004;4:711–9.

Van den Wyngaert T, Huizing MT, Fossion E, Vermorken JB. Prognostic value of bone scintigraphy in cancer patients with osteonecrosis of the jaw. Clin Nucl Med. 2011;36(1):17–20.

Recombinant Human Bone Morphogenetic Protein

52

Marianne S. Reed, Jason M. Johnson, and Daniel Thomas Ginat

52.1 Uses

Bone morphogenetic proteins (BMPs) are a group of growth factors that induce the differentiation of osteoprogenitor cells into osteoblasts and stimulate the formation of new bone in areas requiring repair. Recombinant human BMP (rhBMP) is sometimes used in spinal fusion surgery and in the treatment of nonunion in long bone fractures where the formation of new bone is desired.

52.2 Mechanism

BMPs are members of the transforming growth factor-B superfamily, which exist within bone matrix and act locally as growth and differentiation factors by binding to receptors on the surface of mesenchymal stem cells and causing a cascade of events that leads to their differentiation into bone- and cartilage-forming cells. In this important role, they regulate bone volume and initiate healing after a fracture through pleiotropic effects on chemotaxis, mitosis, differentiation, extracellular matrix production, and apoptosis. BMPs can now be manufactured in large quantities through the use of recombinant genetic methods.

52.3 Discussion

There are two commercially available rhBMP products available, one of which has been approved by the FDA for anterior fusion of the lumbar spine and the other for the treatment of long bone fractures. rhBMP is applied to the operative site via a collagen sponge in combination with bone graft and/or interbody fusion devices. The addition of rhBMP promotes osseous fusion at a faster rate than with bone grafts alone. However, rhBMP influences all phases of the bone healing process, including both osteolysis and bone formation (Fig. 52.1). Initially, there can be an intense early inflammatory phases resulting in edema, swelling, and abnormal enhancement. Osteolysis at the vertebral endplate is a common finding on postoperative imaging following spinal surgery with rhBMP, occurring in up to 100 % of cases in the cervical spine and over 80 % of cases in the lumbar spine. On radiographs and CT, this can manifest as cortical irregularities and well-defined lucencies at the vertebral endplates. Endplate resorption can be radiographically evident as early as 1.5 months following surgery and typically resolves by

M.S. Reed, MD
Diagnostic Radiology, Yale University, New Haven, CT, USA

J.M. Johnson, MD
Department of Diagnostic Radiology, MD Anderson Cancer Center, Houston, TX, USA

D.T. Ginat, MD, MS (✉)
Department of Radiology, University of Chicago, Pritzker Medical School, Chicago, IL, USA
e-mail: ginatd01@gmail.com

D.T. Ginat et al. (eds.), *Neuroimaging Pharmacopoeia*,
DOI 10.1007/978-3-319-12715-6_52, © Springer International Publishing Switzerland 2015

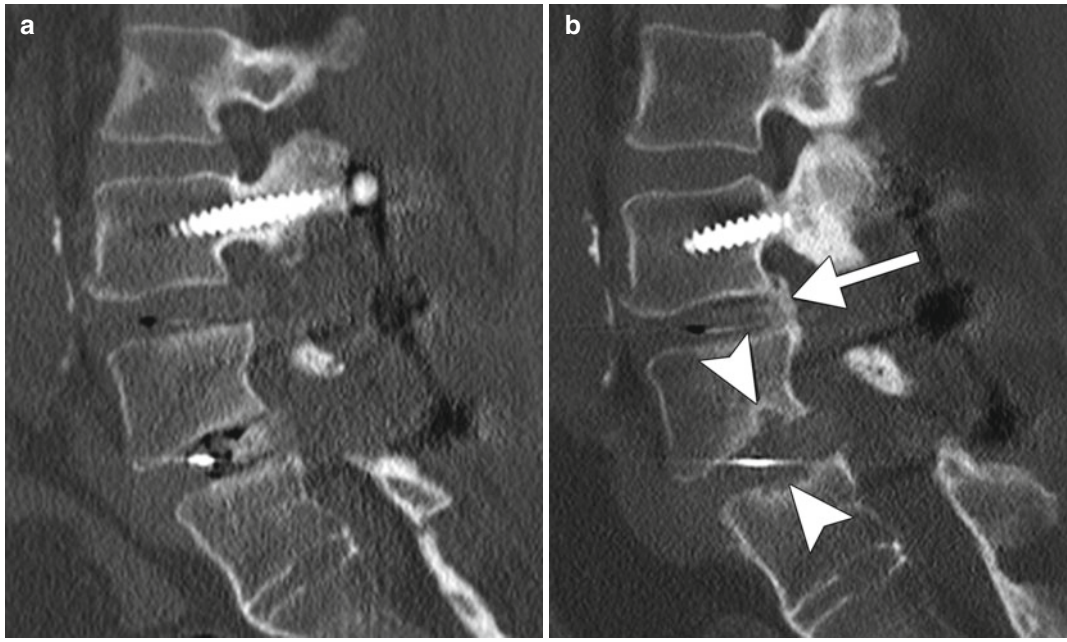

Fig. 52.1 rhBMP-induced osteolysis and heterotopic bone formation. Initial postoperative sagittal CT image (**a**) shows unremarkable vertebral bodies adjacent to the intervertebral disc spacers. Follow-up sagittal CT image (**b**) shows interval heterotopic bone formation posterior to the upper intervertebral disc spacer (*arrow*) and vertebral body cortical irregularity and endplate lucencies adjacent to the lower spacer (*arrowheads*)

9 months. On MRI, this process can demonstrate extensive vertebral bone marrow and disc space signal abnormality and paravertebral soft tissue swelling. The occurrence of heterotopic bone formation is most common in the lumbar spine, particularly in association with polyetheretherketone cage inserted using a transforaminal approach. The clinical significance of the ectopic bone growth has not been fully elucidated, as patients were often asymptomatic. CT findings include bony osteophytes extending into the spinal canal or neural foramina, while MRI can further delineate neural or thecal sac compression.

52.4 Differential Diagnosis

Imaging findings following spinal fusion surgery in which rhBMP is used include heterotopic bone formation, bone resorption/osteolysis, cage migration, and soft tissue inflammation. A history of spinal surgery in which rhBMP has been utilized and comparison with preoperative imaging studies are most helpful in assessing the presence of these findings and determining if findings warrant further investigation or are part of the expected postoperative course. The differential diagnosis for rhBMP-induced osteolysis includes Schmorl's node, interbody spacer subsidence, fracture, postoperative discitis/osteomyelitis, and lytic tumor (Fig. 52.2). On the other hand, the differential diagnosis for heterotopic bone formation with rhBMP includes graft migration or extrusion, adjacent level degenerative changes, calcified disc herniation, myositis ossificans, and osteoblastic tumor (Fig. 52.3).

Fig. 52.2 Postoperative subsidence and fracture. Sagittal CT image shows a vertebral body fracture at one operated level (*arrow*) and subsidence of the interbody spacer device into the adjacent vertebral body at another level (*arrowheads*) in an osteopenic patient

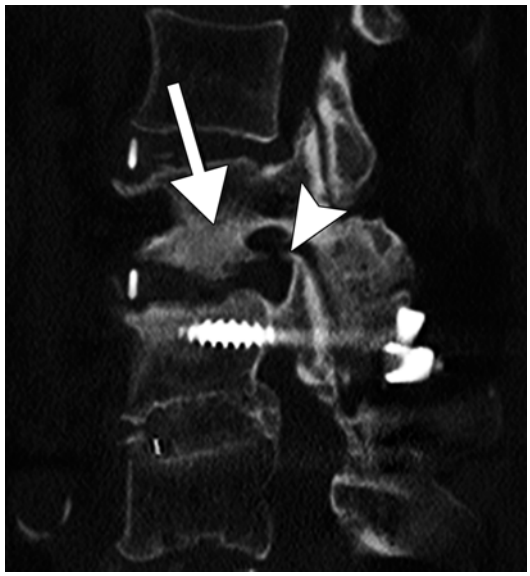

Fig. 52.3 Postoperative degenerative spondylosis. Sagittal CT image shows endplate sclerosis (*arrow*) and uncovertebral osteophytosis (*arrowhead*)

Suggested Reading

Agarwal R, Williams K, Umscheid CA, Welch WC. Osteoinductive bone graft substitutes for lumbar fusion: a systematic review. J Neurosurg Spine. 2009; 11(6):729–40.

Carragee EJ, Hurwitz EL, Weiner BK. A critical review of recombinant human bone morphogenetic protein-2 trials in spinal surgery: emerging safety concerns and lessons learned. Spine J. 2011;11(6):471–91.

Dimar 2nd JR, Glassman SD, Burkus JK, Pryor PW, Hardacker JW, Carreon LY. Clinical and radiographic analysis of an optimized rhBMP-2 formulation as an autograft replacement in posterolateral lumbar spine arthrodesis. J Bone Joint Surg Am. 2009;91(6): 1377–86.

Joseph V, Rampersaud YR. Heterotopic bone formation with the use of rhBMP2 in posterior minimal access interbody fusion: a CT analysis. Spine (Phila Pa 1976). 2007;32(25):2885–90.

Katayama Y, Matsuyama Y, Yoshihara H, Sakai Y, Nakamura H, Imagama S, Ito Z, Wakao N, Kamiya M, Yukawa Y, Kanemura T, Sato K, Iwata H, Ishiguro N. Clinical and radiographic outcomes of posterolateral lumbar spine fusion in humans using recombinant human bone morphogenetic protein-2: an average five-year follow-up study. Int Orthop. 2009;33(4):1061–7.

Mroz TE, Wang JC, Hashimoto R, Norvell DC. Complications related to osteobiologics use in spine surgery: a systematic review. Spine (Phila Pa 1976). 2010;35(9 Suppl):S86–104.

Murtagh RD, Quencer RM, Castellvi AE, Yue JJ. New techniques in lumbar spinal instrumentation: what the radiologist needs to know. Radiology. 2011;260(2): 317–30.

Saigal G, Quencer R, Guest JD, Cristescu MM, Lebwohl N. Vertebral body osteolysis following the use of bone morphogenetic protein in spinal surgery: a mimicker of infection. J Neuroradiol. 2012;39(5):354–9.

Sethi A, Craig J, Bartol S, Chen W, Jacobson M, Coe C, Vaidya R. Radiographic and CT evaluation of recombinant human bone morphogenetic protein-2-assisted spinal interbody fusion. AJR Am J Roentgenol. 2011; 197(1):W128–33.

Valdes MA, Thakur NA, Namdari S, Ciombor DM, Palumbo M. Recombinant bone morphogenic protein-2 in orthopaedic surgery: a review. Arch Orthop Trauma Surg. 2009;129(12):1651–7.

Valentin-Opran A, Wozney J, Csimma C, Lilly L, Riedel GE. Clinical evaluation of recombinant human bone morphogenetic protein-2. Clin Orthop Relat Res 2002;(395):110–120.

Retinoids (13-cis-Retinoic Acid, Isotretinoin, Accutane, All-trans-retinoic acid)

53

Daniel Thomas Ginat

53.1 Uses

Isotretinoin is a synthetic form of vitamin A that has been used in the United States since 1983 mainly for the treatment of severe cystic acne. Long-term therapy with low-dose isotretinoin has also been used for prevention of basal cell carcinoma and treatment of cutaneous T-cell lymphomas, and all-trans-retinoic acid (ATRA) has been used in patients with acute promyelocytic leukemia (APL).

53.2 Mechanism

Retinoids promote skin cell turnover prompting new cell growth and hamper the breakdown of collagen. In addition, they normalize abnormal keratinocyte growth and differentiation. Furthermore, they inhibit various immune factors including leukocyte activity, proinflammatory cytokines, and immunomodulatory transcription factors. These effects are exerted by nuclear receptor interaction and gene activation. Retinoic acid also appears to promote the proliferation of chondrocytes and endochondral ossification in the anterior longitudinal ligaments and the epiphyseal region of the vertebral bodies leading to radiologic manifestations.

53.3 Discussion

Hyperostosis associated with retinoic acid consists of focal calcification or ossification of the anterior longitudinal ligament, which initially appears as elongation of the corner of a vertebral body, resulting in a "pointed" rather than a normal "squared" appearance, mainly occurring at the anterosuperior and anteroinferior margins of the cervical vertebrae. There can also be milder "pointing" of the anterior and posterior margins of vertebral bodies and facets. Over time, the hyperostosis can enlarge and fuse across adjacent vertebrae (Fig. 53.1). The thoracic and lumbar spines tend to be less extensively affected. Occasionally, there can also be sacroiliac involvement, which manifests as bilateral ossification of the inferior margins of the ventral sacroiliac ligaments. Patients with retinoic acid-induced hyperostosis are usually asymptomatic, but can experience dysphagia from extensive anterior longitudinal ligament involvement or spinal canal stenosis from extensive posterior longitudinal ligament involvement.

ATRA has been implicated as a cause of differentiation syndrome (previously known as retinoic acid syndrome) in patients with acute promyelocytic leukemia, which consists of

D.T. Ginat, MD, MS
Department of Radiology, University of Chicago, Pritzker Medical School, Chicago, IL, USA
e-mail: ginatd01@gmail.com

D.T. Ginat et al. (eds.), *Neuroimaging Pharmacopoeia*,
DOI 10.1007/978-3-319-12715-6_53, © Springer International Publishing Switzerland 2015

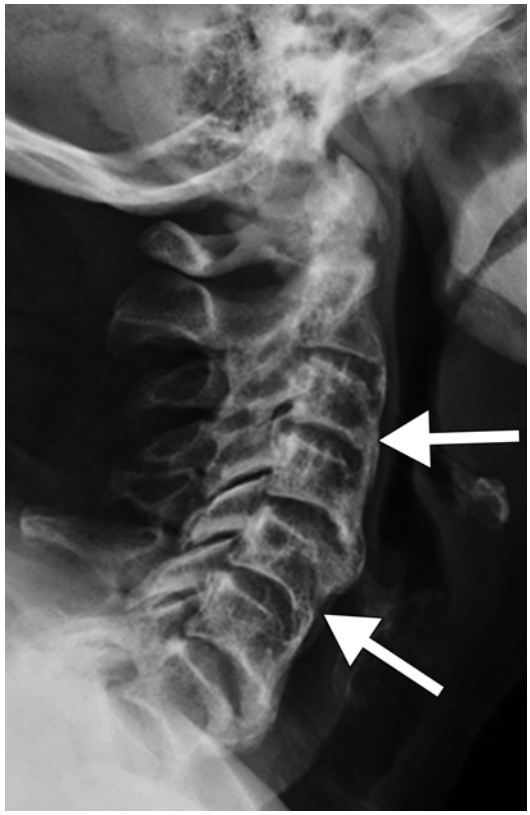

Fig. 53.1 Hyperostosis in a patient with long-term retinoid therapy. Lateral radiograph of the cervical spine shows multilevel flowing ossification in the distribution of the anterior longitudinal ligament (*arrows*)

differentiation of leukemic blasts and promyelocytes that leads to cellular migration, endothelial activation, and release of interleukins and vascular factors responsible for tissue damage. This syndrome may consist of unexplained fever, weight gain, dyspnea with pulmonary infiltrates, pleuropericardial effusion, hypotension, and renal failure, and may present shortly after starting ATRA. There can also be pseudotumor cerebri and intracranial, subhyoid, or retinal hemorrhage. Administration of steroids can alleviate the differential syndrome.

Retinoic acid is also a teratogen that results in a constellation of congenital anomalies, most commonly the central nervous system and cardiovascular system. The central nervous system anomalies include microcephaly and hydrocephalus. Microtia or anotia is another frequent complication.

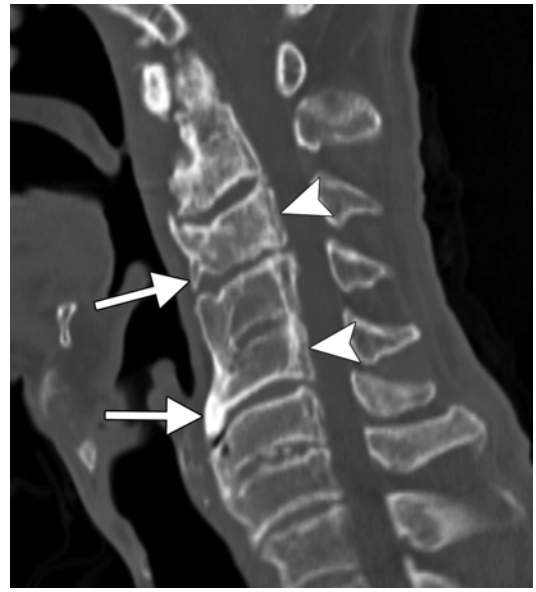

Fig. 53.2 Diffuse idiopathic skeletal hypertrophy and ossification of the posterior longitudinal ligament. Sagittal CT shows flowing ossification along the anterior aspect of the entire cervical spine (*arrows*), as well as ossification of the posterior longitudinal ligament (*arrowheads*)

53.4 Differential Diagnosis

Early cervical hyperostotic changes consist of pointing of the anteroinferior margins of the vertebral bodies (unlike the hyperostoses found in diffuse idiopathic skeletal hyperostosis (DISH)), while later changes resemble the typical hyperostoses of DISH, and both conditions can be associated with ossification of the posterior longitudinal ligament (Fig. 53.2). Furthermore, patients with DISH often have relatively high levels of vitamin A. Other differential considerations for multilevel hyperostosis of the spine may include degenerative spondylosis and ankylosing spondylitis. Degenerative spondylosis is associated with increased age and includes the constellation of disc space narrowing, vacuum phenomenon, disc desiccation, vertebral osteophyte formation, disc herniation, and facet arthrosis (Fig. 53.3). Ankylosing spondylitis is an inflammatory process related to HLA-B27 positivity. The hallmark features include erosions and fusion of the sacroiliac joints and enthesitis at the edges of the discovertebral joints resulting in syndesmophyte

Fig. 53.3 Degenerative spondylosis. Sagittal CT shows multiple disc-osteophyte complexes (*arrowheads*), a calcified disc (*arrow*), and facet joint arthropathy (*curved arrow*)

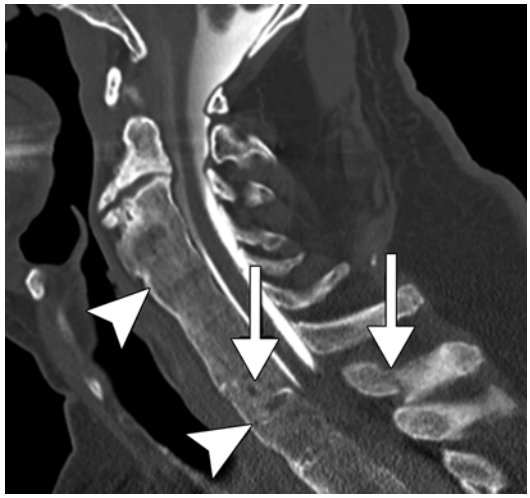

Figure 53.4 Ankylosing spondylitis. Sagittal CT myelogram shows syndesmophytes with multilevel fusion of the cervical vertebrae (*arrowheads*) and a vertebral fracture (*arrows*) with associated spinal canal stenosis, presumably related to hemorrhage

development. Syndesmophytes start as thin vertically oriented projections of the bone that develop due to ossification within the outer fibers of the annulus fibrosus of the intervertebral disc. The cervical spine is less commonly involved than the lumbosacral spine, but can also have the characteristic bamboo spine appearance when multiple vertebral bodies are fused (Fig. 53.4). Patients with ankylosing spondylitis are also particularly susceptible to vertebral fractures.

Suggested Reading

Ellis CN, Pennes DR, Hermann RC, Blauvelt A, Martel W, Voorhees JJ. Long-term radiographic follow-up after isotretinoin therapy. J Am Acad Dermatol. 1988;18(6):1252–61.

Lammer EJ, Chen DT, Hoar RM, Agnish ND, Benke PJ, Braun JT, Curry CJ, Fernhoff PM, Grix Jr AW, Lott IT, et al. Retinoic acid embryopathy. N Engl J Med. 1985;313(14):837–41.

Pennes DR, Martel W, Ellis CN, Voorhees JJ. Evolution of skeletal hyperostoses caused by 13-cis-retinoic acid therapy. AJR Am J Roentgenol. 1988;151(5):967–73.

Rogers JE, Yang D. Differentiation syndrome in patients with acute promyelocytic leukemia. J Oncol Pharm Pract. 2012;18(1):109-14.

Stern RS, Rosa F, Baum C. Isotretinoin and pregnancy. J Am Acad Dermatol. 1984;10(5 Pt 1):851–4.

Tangrea JA, Kilcoyne RF, Taylor PR, Helsel WE, Adrianza ME, Hartman AM, Edwards BK, Peck GL. Skeletal hyperostosis in patients receiving chronic, very-low-dose isotretinoin. Arch Dermatol. 1992;128(7):921–5.

Vincent V, Zabraniecki L, Loustau O, Godfrin B, Latour FB, Railhac JJ, Fournié B. Acitretin-induced enthesitis in a patient with psoriatic arthritis. Joint Bone Spine. 2005;72(4):326–9.

Wendling D, Hafsaoui C, Laurain JM, Runge M, Magy-Bertrand N, Prati C. Dysphagia and hypervitaminosis A: cervical hyperostosis. Joint Bone Spine. 2009;76(4):409–11.

Topical Prostaglandin Analogues

54

Daniel Thomas Ginat and Nurhan Torun

54.1 Uses

Topical prostaglandin analogue drops such as latanoprost and bimatoprost are considered potent agents for reducing intraocular pressure associated with glaucoma.

54.2 Mechanism

Prostaglandin receptors and associated mRNAs are present in the trabecular meshwork, ciliary muscle, and sclera. Prostaglandin analogues (latanoprost acid, travoprost acid, tafluprost acid, bimatoprost, bimatoprost acid, and unoprostone) result in a considerable increase in uveoscleral outflow and may also improve trabecular outflow and stimulate aqueous flow. Prostaglandin analogues also have the potential to inhibit adipogenesis through prostaglandin F (FP) receptor stimulation.

D.T. Ginat, MD, MS (✉)
Department of Radiology, University of Chicago, Pritzker Medical School, Chicago, IL, USA
e-mail: ginatd01@gmail.com

N. Torun, MD
Department of Ophthalmology, Beth Israel Deaconess Medical Center, Boston, MA, USA

54.3 Discussion

Chronic topical prostaglandin use for the treatment of glaucoma has been associated with the development of periorbitopathy. Prostaglandin-associated periorbitopathy consists of enophthalmos associated with the atrophy of orbital and periorbital fat. The incidence of prostaglandin-associated periorbitopathy is in the range of 70 to over 90 %, depending upon the particular agent. The loss of the periorbital fat pad is the first sign of prostaglandin-associated periorbitopathy, especially in older patients. CT or MRI can be used to demonstrate the diffusely decreased orbital and periorbital fat volume in the absence of inflammatory changes. This finding is particularly conspicuous if the process is unilateral (Fig. 54.1). Imaging is also of utility in order to exclude other conditions that may result in enophthalmos. Prostaglandin-associated periorbitopathy has cosmetic implications and can render the task of measuring intraocular pressure difficult. Some cases improve with discontinuation of the prostaglandin.

54.4 Differential Diagnosis

The differential diagnosis for an adult patient who presents with enophthalmos includes orbital blow-out fracture, silent sinus syndrome, scirrhous breast carcinoma metastases, localized scleroderma, and postirradiation atrophy. For example, orbital blow-out fractures can

D.T. Ginat et al. (eds.), *Neuroimaging Pharmacopoeia*,
DOI 10.1007/978-3-319-12715-6_54,

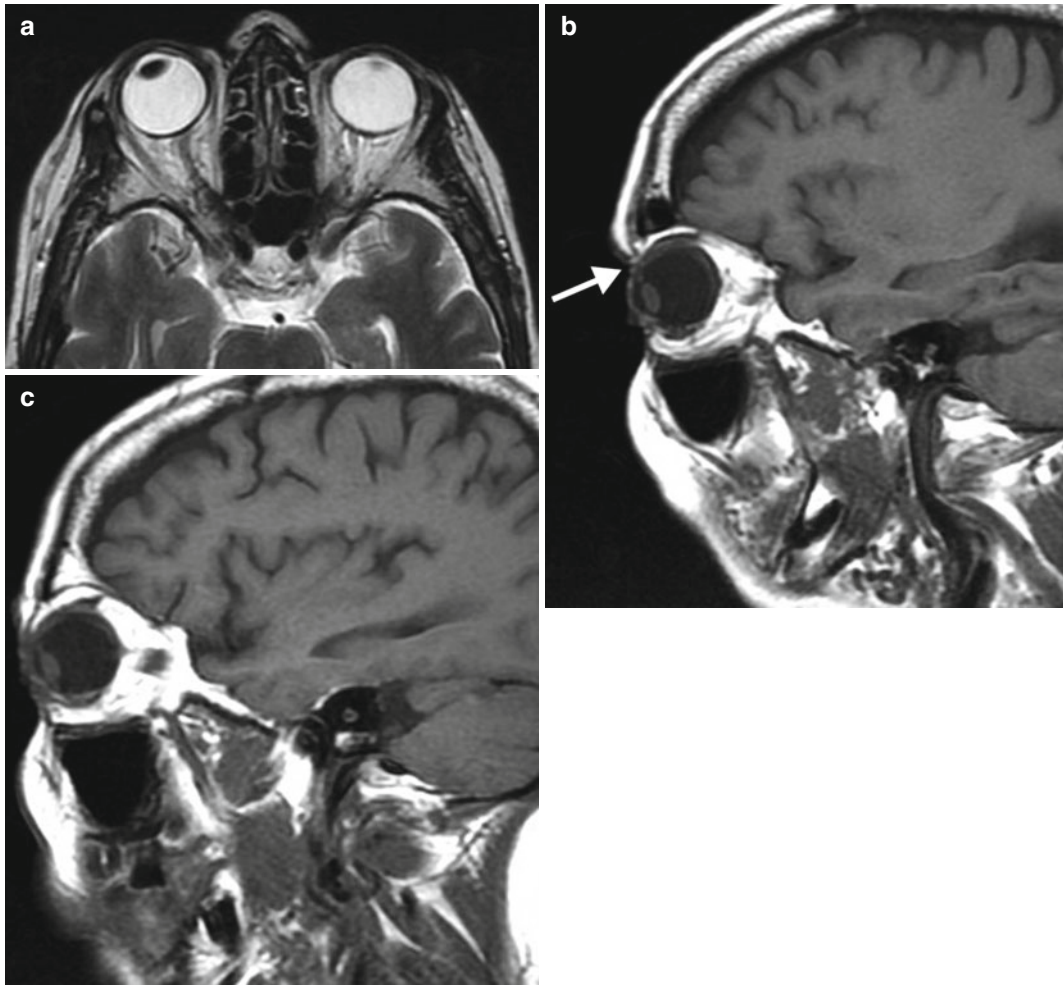

Fig. 54.1 Prostaglandin-associated periorbitopathy. The patient has a history of the left eye only Lumigan use for a number of years and had left enophthalmos along with superior sulcus deformity due to the loss of orbital fat. Axial T2-weighted (**a**) and sagittal T1-weighted (**b**) MR images show left-sided enophthalmos with a deep superior sulcus (*arrow*) due to diffusely diminished orbital and periorbital fat. The patient's unaffected right eye is shown on the sagittal T1-weighted image for comparison (**c**)

lead to enophthalmos when there is persistent orbital fat herniation through orbital wall defects or persistently displaced fracture fragments that lead to orbital cavity expansion (Fig. 54.2). While a history of trauma may be given, patients may not always recall this. Silent sinus syndrome consists of enophthalmos secondary to orbital vault expansion associated with atelectasis of the ipsilateral maxillary sinus. It can also develop after orbital trauma that damages the ostiomeatal complex. The maxillary sinus is often completely opacified, and the infundibulum is collapsed (Fig. 54.3). Scirrhous breast carcinoma metastases to the orbit can lead to retraction of the globes rather than proptosis due to desmoplastic fibrosis. These metastases can appear as infiltrative enhancing lesions (Fig. 54.4).

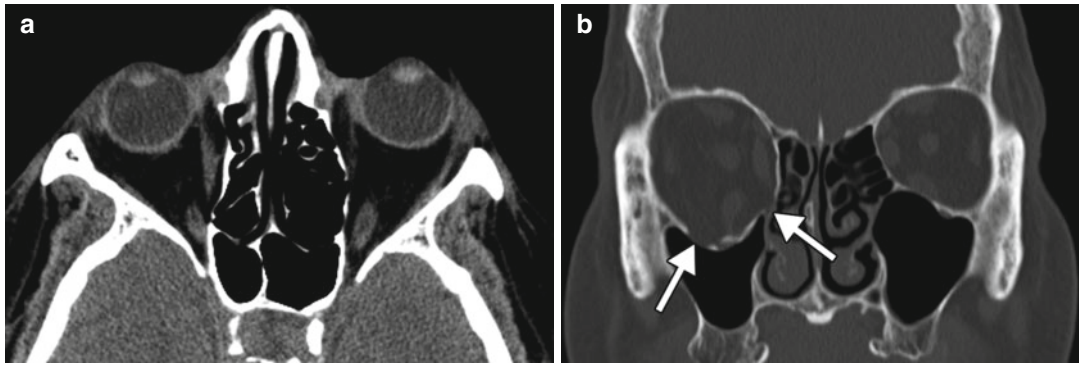

Fig. 54.2 Orbital blow-out fracture. Axial CT image (**a**) shows mild right enophthalmos and medial bowing of the right lamina papyracea. The coronal CT image (**b**) shows outward displacement of the inferior and medial orbital walls (*arrows*) and a relatively voluminous right orbital cavity

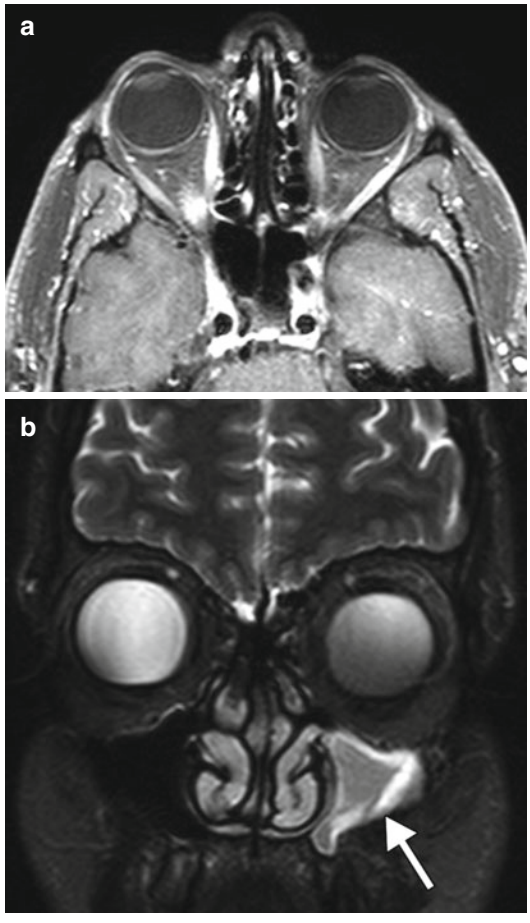

Fig. 54.3 Silent sinus syndrome. Axial post-contrast fat-suppressed T1-weighted MRI (**a**) shows left enophthalmos. The coronal fat-suppressed T2-weighted MRI (**b**) shows that the left maxillary sinus is relatively small in size and filled with secretions (*arrow*)

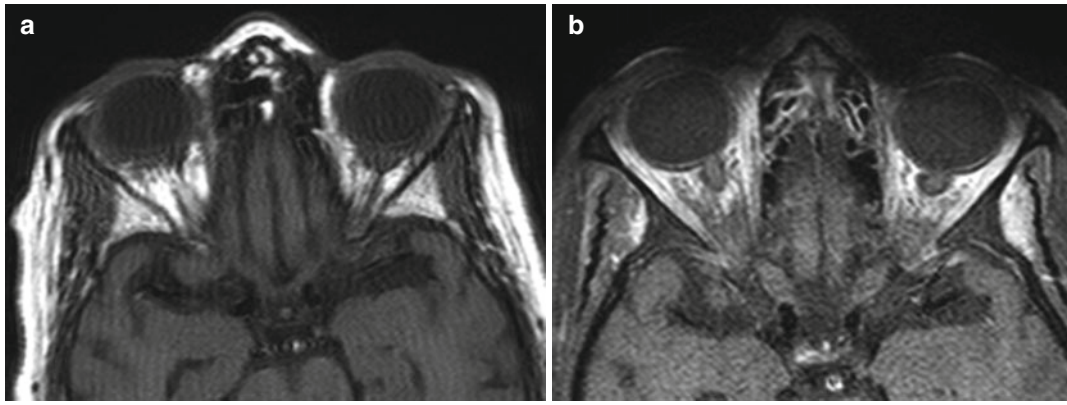

Fig. 54.4 Scirrhous breast metastases. Axial T1-weighted (**a**) and fat-suppressed post-contrast T1-weighted (**b**) MR images show retraction of the bilateral globes and ill-defined retrobulbar enhancement. There is also an abnormal enhancement of the bilateral temporalis muscles, the left greater than the right

Suggested Reading

Filippopoulos T, Paula JS, Torun N, Hatton MP, Pasquale LR, Grosskreutz CL. Periorbital changes associated with topical bimatoprost. Ophthal Plast Reconstr Surg. 2008;24(4):302–7.

Jayaprakasam A, Ghazi-Nouri S. Periorbital fat atrophy – an unfamiliar side effect of prostaglandin analogues. Orbit. 2010;29(6):357–9.

Johnson TV, Fan S, Zhan G, Camras CB, Toris CB. Efficacy and mechanisms of intraocular pressure reduction with latanoprost and timolol in participants with ocular hypertension: a comparison of 1 and 6 weeks of treatment. J Glaucoma. 2010;19(6):356–64.

Kucukevcilioglu M, Bayer A, Uysal Y, Altinsoy HI. Prostaglandin associated periorbitopathy in patients using bimatoprost, latanoprost and travoprost. Clin Experiment Ophthalmol. 2014;42(2):126–31.

Montezuma SR, Gopal H, Savar A, Turalba A, Cestari DM, Torun N. Silent sinus syndrome presenting as enophthalmos long after orbital trauma. J Neuroophthalmol. 2008;28:107–10.

Sakata R, Shirato S, Miyata K, Aihara M. Incidence of deepening of the upper eyelid sulcus on treatment with a tafluprost ophthalmic solution. Jpn J Ophthalmol. 2014;58(2):212–7.

Taketani Y, Yamagishi R, Fujishiro T, Igarashi M, Sakata R, Aihara M. Activation of the prostanoid FP receptor inhibits adipogenesis leading to deepening of the upper eyelid sulcus in prostaglandin-associated periorbitopathy. Invest Ophthalmol Vis Sci. 2014;55(3):1269–76.

Tan J, Berke S. Latanoprost-induced prostaglandin-associated periorbitopathy. Optom Vis Sci. 2013;90(9):e245–7; discussion 1029.

Toris CB, Gabelt BT, Kaufman PL. Update on the mechanism of action of topical prostaglandins for intraocular pressure reduction. Surv Ophthalmol. 2008;53 Suppl 1:S107–20.

Nasal Decongestants

55

Daniel Thomas Ginat

55.1 Uses

Systemic and topical nasal decongestants are widely used for the management of acute and, in certain cases, chronic rhinosinusitis. Specific decongestant agents include ephedrine, phenylephrine, and phenylpropanolamine, among others.

55.2 Mechanism

Nasal decongestant agents contain substances that have sympathomimetic effects by acting upon epinephrine, norepinephrine, or alpha-adrenergic receptors, which results in vasoconstriction. However, overuse of these nasal decongestant agents can result in rebound congestion, nasal hyperreactivity, tolerance, and histologic changes of the nasal mucosa, which is a phenomenon known as rhinitis medicamentosa.

D.T. Ginat, MD, MS
Department of Radiology, University of Chicago, Pritzker Medical School, Chicago, IL, USA
e-mail: dtg1@uchicago.edu

55.3 Discussion

Rhinitis medicamentosa is characterized by nasociliary loss, squamous cell metaplasia, epithelial edema, epithelial cell denudation, goblet cell hyperplasia, increased expression of the epidermal growth factor receptor, and inflammatory cell infiltration. Thus, on imaging, these changes are frequently characterized by diffuse swelling of the nasal mucosa, particularly in the inferior turbinates (Fig. 55.1). The findings may subside with cessation of the vasoconstrictive nasal decongestants and administration of steroids. Besides nasal decongestants, other pharmaceuticals may be associated with rhinitis medicamentosa, including oral beta-adrenoceptor antagonists, antipsychotics, oral contraceptives, and antihypertensive medications.

55.4 Differential Diagnosis

Allergic and infectious rhinitis can also lead to swelling of the nasal mucosa and secretions within the nasal cavity and can have similar appearances on CT (Fig. 55.2). The distinction between allergic or infectious rhinitis and rhinitis medicamentosa depends on the clinical scenario. Unilateral enlargement of the nasal turbinate mucosa can occur naturally during the process of

D.T. Ginat et al. (eds.), *Neuroimaging Pharmacopoeia*,
DOI 10.1007/978-3-319-12715-6_55, © Springer International Publishing Switzerland 2015

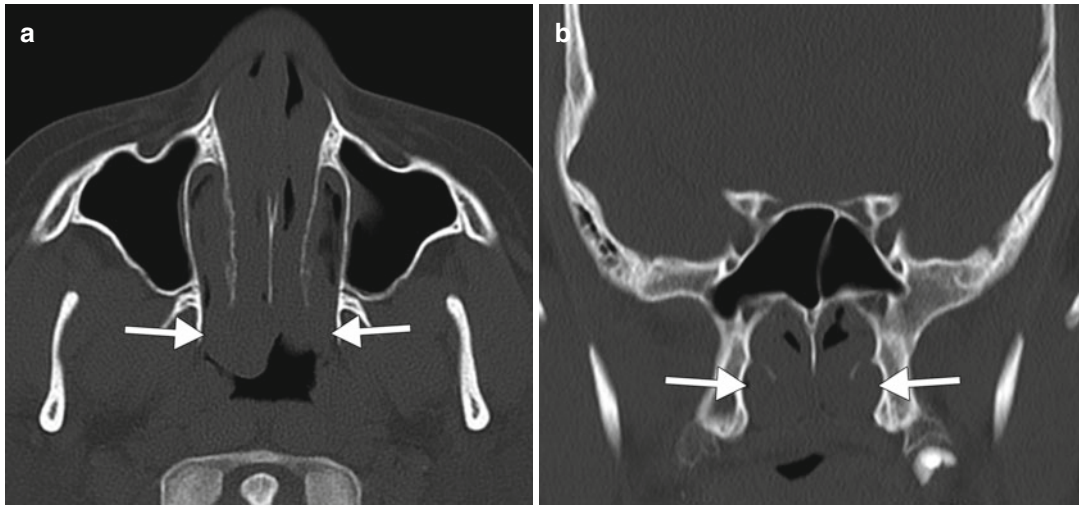

Fig. 55.1 Rhinitis medicamentosa. Axial (**a**) and coronal (**b**) CT images show marked mucosal thickening of the bilateral inferior turbinates (*arrows*), with resultant nasal airway obstruction

Fig. 55.2 Allergic hypertrophic rhinitis. Coronal CT image shows swelling of the bilateral inferior turbinate mucosa. There are also bilateral concha bullosa, which are partially opacified

the nasal cycle (Fig. 55.3), in which there is alternating turgescence of the mucosa on one side versus the other. Although the middle turbinate can appear enlarged with concha bullosa, it is a developmental variant that affects the bony anatomy rather than the mucosa. The pneumatized middle turbinates are readily identified on CT (Fig. 55.4). Other potential mimics of turbinate hypertrophy are various nasal cavity neoplasms, including recurrent tumors that occupy the space of resected turbinates (Fig. 55.5).

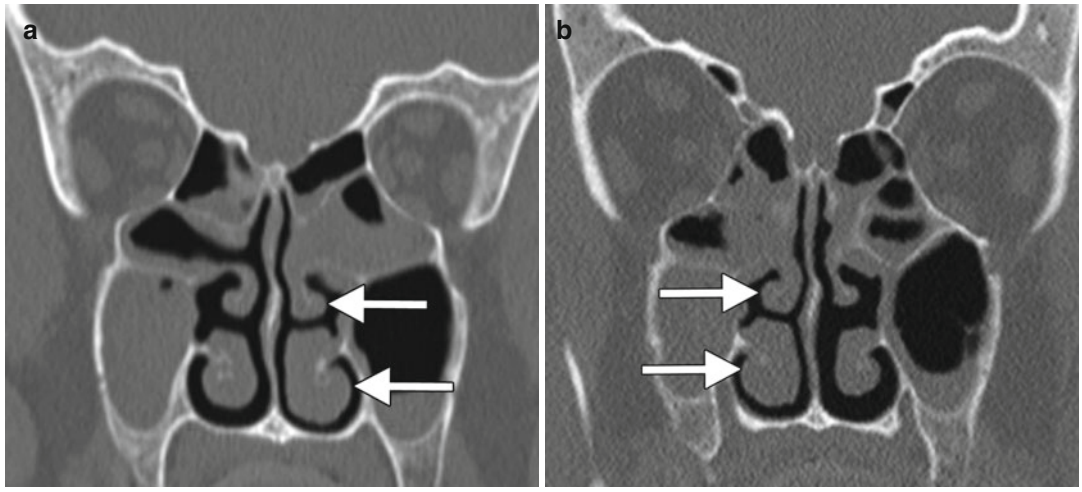

Fig. 55.3 Coronal CT image (**a**) shows relative enlargement of the left inferior and middle turbinate mucosa (*arrows*) with respect to the right side. Coronal CT image (**b**) obtained 2 weeks later in the same patient now shows relative enlargement of the right inferior and middle turbinate mucosa (*arrows*) with respect to the left side

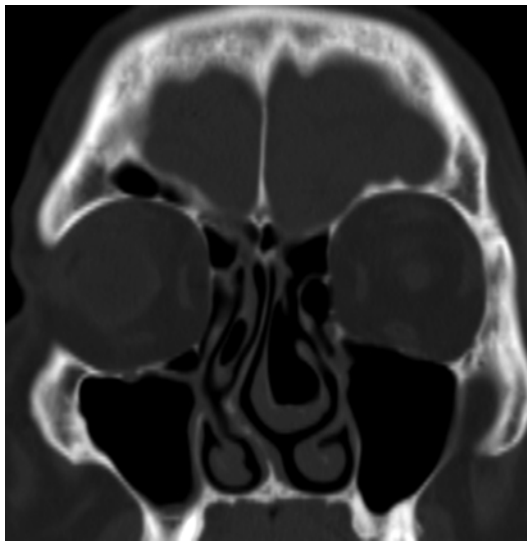

Fig. 55.4 Concha bullosa. Coronal CT image shows a large left and smaller right pneumatized middle turbinates with associated nasal septal deviation. The nasal cavity mucosa is not thickened

Fig. 55.5 Recurrent nasal melanoma. Coronal post-contrast CT image shows an enhancing mass (*arrow*) in the left nasal cavity, which occupies the site of the previously resected left inferior and middle turbinates

Suggested Reading

Carr WW, Nelson MR, Hadley JA. Managing rhinitis: strategies for improved patient outcomes. Allergy Asthma Proc. 2008;29(4):349–57.

Graf P. Rhinitis medicamentosa: aspects of pathophysiology and treatment. Allergy. 1997;52(40 Suppl): 28–34.

Mortuaire G, de Gabory L, François M, Massé G, Bloch F, Brion N, Jankowski R, Serrano E. Rebound congestion and rhinitis medicamentosa: nasal decongestants in clinical practice. Critical review of the literature by a medical panel. Eur Ann Otorhinolaryngol Head Neck Dis. 2013;130(3):137–44.

Ramey JT, Bailen E, Lockey RF. Rhinitis medicamentosa. J Investig Allergol Clin Immunol. 2006;16(3):148–55.

Index

D.T. Ginat et al. (eds.), *Neuroimaging Pharmacopoeia*,
DOI 10.1007/978-3-319-12715-6,